

N73 24865

NASA CR 121103



VOLUME I

# SPACE VEHICLE INTEGRATED THERMAL PROTECTION/STRUCTURAL/ METEOROID PROTECTION SYSTEM

FINAL REPORT

# CASE FILE COPY

by

D. H. Bartlett & D. K. Zimmerman

**BOEING**

AEROSPACE COMPANY

April 1973

Prepared For

NATIONAL AERONAUTICS AND SPACE ADMINISTRATION

NASA LEWIS RESEARCH CENTER

Contract NAS3-13316

J. R. Barber, Project Manager

1. Report No. NASA CR-121103	2. Government Accession No.	3. Recipient's Catalog No.	
4. Title and Subtitle Space Vehicle Integrated Thermal Protection/Structural/ Meteoroid Protection System		5. Report Date April 1973	6. Performing Organization Code
		8. Performing Organization Report No. D180-15172-1	
7. Author(s) D. H. Bartlett, D. K. Zimmerman		10. Work Unit No.	
9. Performing Organization Name and Address Boeing Aerospace Company (A division of The Boeing Company) P.O. Box 3999 Seattle, Washington 98124		11. Contract or Grant No. NAS3-13316	
		13. Type of Report and Period Covered Final Contractor Report	
12. Sponsoring Agency Name and Address National Aeronautics & Space Administration Lewis Research Center		14. Sponsoring Agency Code	
		15. Supplementary Notes J. R. Barber, Project Manager	
16. Abstract  A program was conducted to determine the merit of a combined structure/thermal meteoroid protection system for a cryogenic space vehicle propulsion module. Structural concepts were evaluated to identify leastweight designs. Thermal analyses determined optimum tank arrangements and insulation materials. Meteoroid penetration experiments provided data for design of protection systems. Preliminary designs were made and compared on the basis of payload capability. Thermal performance tests demonstrated heat transfer rates typical for the selected design. Meteoroid impact tests verified the protection characteristics. A mockup was made to demonstrate protection system installation. The best design found combined multilayer insulation with a truss structure vehicle body. The multilayer served as the thermal/meteoroid protection system.			
17. Key Words (Suggested by Author(s)) Multilayer Insulation Meteoroid Protection Cryogenic Propellants Composite Structure		18. Distribution Statement  Unclassified - Unlimited	
19. Security Classif. (of this report) Unclassified	20. Security Classif. (of this page) Unclassified	21. No. of Pages 396	22. Price* \$3.50

\* For sale by the National Technical Information Service, Springfield, Virginia 22151

## TABLE OF CONTENTS

	<u>Page</u>
ILLUSTRATIONS	v
TABLES	xvi
INTRODUCTION	1
SUMMARY	3
1.0 TASK I - DESIGN EVALUATION	7
1.1 Screening and Conceptual Design Investigation	9
1.1.1 Tank Arrangement Screening	11
1.1.2 Tank Arrangement Thermal Efficiency	38
1.1.3 Vehicle Structure Evaluation	45
1.1.4 Insulation Concept Development	58
1.1.5 Combined Systems Evaluation	131
1.2 Preliminary Evaluation	139
1.2.1 Solar Panel Emittance Study	139
1.2.2 Selection of Vehicle 1-14 Tank Arrangement	139
1.2.3 Preliminary Design Development	160
1.3 Final Evaluation	229
1.3.1 Final Design Development	229
1.3.2 Thermal Analysis	230
1.3.3 Weights	239
1.3.4 Meteoroid Protection Sensitivity	245
1.3.5 Thermal Conductivity Sensitivity	249
1.3.6 Tank Mounted MLI Comparison	249
2.0 TASK II - EXPERIMENTAL EVALUATION	257
2.1 Meteoroid Impact Testing	257
2.1.1 Tank Wall Penetration Criteria	257
2.1.2 Design Curve Derivation	257
2.1.3 Final Design Proof Tests	263

## TABLE OF CONTENTS (Cont.)

	<u>Page</u>
2.2 Thermal Performance and Launch Environment Testing	265
2.2.1 Test Program	265
2.2.2 Test System Description	272
2.2.3 Test Results and Analysis	289
2.3 Mockup Evaluation	354
3.0 TASK III - DATA EVALUATION AND FINAL DESIGN CORRECTION	367
3.1 Design Heat Leak Corrections	367
3.2 Thermal Systems Optimization	367
3.3 Recommendations	369
4.0 CONCLUSIONS	371
5.0 ACKNOWLEDGEMENTS	372
REFERENCES	373
DISTRIBUTION LIST	375

## LIST OF ILLUSTRATIONS

<u>Figure No.</u>	<u>Title</u>	<u>Page</u>
1.1-1	Task 1 - Study Flow Diagram	8
1.1-2	Propulsion Vehicle Description	10
1.1-3	Typical Vehicle Layouts	12
1.1-4	Structural Arrangement - Vehicle 1-1	16
1.1-5	Structural Arrangement - Vehicle 1-3	17
1.1-6	Structural Arrangement - Vehicle 1-6	18
1.1-7	Structural Arrangement - Vehicle 1-7	19
1.1-8	Structural Arrangement - Vehicle 1-8	20
1.1-9	Structural Arrangement - Vehicle 1-14	21
1.1-10	Structural Arrangement - Vehicle 1-20	22
1.1-11	Structural Arrangement - Vehicle 2-1	23
1.1-12	Structural Arrangement - Vehicle 2-2	24
1.1-13	Structural Arrangement - Vehicle 2-8	25
1.1-14	Structural Arrangement - Vehicle 2-16	26
1.1-15	Structural Arrangement - Vehicle 2-18	27
1.1-16	Structural Arrangement - Vehicle 2-19	28
1.1-17	Structural Arrangement - Vehicle 2-20	29
1.1-18	Propellant Feed System Concept - Individual Tankage	30
1.1-19	Propellant Feed System Concept - Manifolded Tankage	31
1.1-20	Tank Arrangement Configuration Selection	37
1.1-21	Payload Definition	40
1.1-22	Thermal Model Vehicle 1-1	41
1.1-23	Thermal Model Vehicle 1-1 (Inverted)	41
1.1-24	Thermal Program Printout Data - Vehicle 1-1	42
1.1-25	Thermal Program Printout Data - Vehicle 1-1 (Inverted)	42
1.1-26	Tank Arrangement Thermal Efficiency Study Results LF <sub>2</sub> - LH <sub>2</sub> Propellants	43
1.1-27	Tank Arrangement Thermal Efficiency Study Results FLOX - CH <sub>4</sub> Propellants	44

<u>Figure No.</u>	<u>Title</u>	<u>Page</u>
1.1-28	Vehicle Structure Evaluation Representative Configurations	46
1.1-29	Structure Analysis Model - Vehicle 1-8	47
1.1-30	OPTRAN Code Flow Chart	51
1.1-31	OPTRAN Optimization Strategy	51
1.1-32	Vehicle Construction Concepts	53
1.1-33	Continuous Shell Construction Weights	56
1.1-34	Tubular Strut Weights	56
1.1-35	Vehicle Structure Evaluation Results	57
1.1-36	Multilayer Insulation Panel Attachment Concept to a Cylindrical Shell	63
1.1-37	Conical Insulation Concept	64
1.1-38	Lower Cone Insulation Concept	65
1.1-39	Insulation Bulkhead - Single Piece	66
1.1-40	Inner Insulation Concept	67
1.1-41	Thermal/Meteoroid Protection Concepts	68
1.1-42	Thermal/Meteoroid Protection Concepts	69
1.1-43	Thermal/Meteoroid Protection Concepts	70
1.1-44	Multilayer Insulation For Truss Structure	71
1.1-45	Lacing Concept For Multilayer Blanket Assembly	72
1.1-46	Insulation/Sidewall Panel Assembly Concept	74
1.1-47	Insulation Installation Weight Vs Insulation Thickness	76
1.1-48	Insulation Installation Weight Vs Insulation Thickness	76
1.1-49	Insulation Installation Weight Vs Insulation Thickness	77
1.1-50	Insulation Installation Weight Vs Insulation Thickness	77
1.1-51	Ground Heat Transfer to H <sub>2</sub> With Helium Purge	81
1.1-52	Ground Heat Transfer to H <sub>2</sub> With Helium Purge and Foam on Tank	81
1.1-53	Ground Heat Transfer to H <sub>2</sub> With Helium Purge and Foam Outside of Multilayer	82
1.1-54	Ground Heat Transfer to H <sub>2</sub> With Nitrogen Purge and Foam on Tank	82

<u>Figure No.</u>	<u>Title</u>	<u>Page</u>
1.1-55	Ground Heat Transfer to H <sub>2</sub> With Helium Flow Thru Insulation	85
1.1-56	Ground Heat Transfer to LF <sub>2</sub> With Basic Helium & Nitrogen Purges	85
1.1-57	Ground Heat Transfer to F <sub>2</sub> With Nitrogen Purge and Foam on Tank	86
1.1-58	Ground Heat Transfer to LF <sub>2</sub> & LH <sub>2</sub> With CO <sub>2</sub> Filled Fiberglass Honeycomb Structure	87
1.1-59	Heat Transfer Distribution on LH <sub>2</sub> Tank With Cold Helium Purge	88
1.1-60	Heat Transfer Distribution on LF <sub>2</sub> Tank With Cold Helium Purge	88
1.1-61	Ground Hold Design Concept #1	91
1.1-62	Ground Hold Design Concept #2	92
1.1-63	Ground Hold Design Concept #3	93
1.1-64	Ground Hold Design Concept #4	94
1.1-65	Ground Hold Design Concept #5	95
1.1-66	Ground Hold Design Concept #6	96
1.1-67	Ground Hold Design Concept #7	97
1.1-68	Tank Mounted Insulation Concept	101
1.1-69	Tank Mounted Insulation Concept	102
1.1-70	Tank Mounted Insulation Concept	103
1.1-71	Comparison of Analysis to Evacuation Test	107
1.1-72	Residual Gas Pressure in Perforated NRC-2 and Aluminized Mylar - Nylon Net	108
1.1-73	Calculated Pressure History for Aluminized Mylar-2 Silk Net Insulation Evacuated Along Layers, Helium Purge, Room Temperature	109
1.1-74	Effect of Ascent Heating and Evacuation Method on Total Mission Heating - Sidewall	110
1.1-75	Effect of Ascent Heating and Evacuation Method on Total Mission Heating - Top Deck	111
1.1-76	Mission Time/Temperature Phasing	112

<u>Figure No.</u>	<u>Title</u>	<u>Page</u>
1.1-77	Conductivity-Density Product for Several Multilayer Insulations	116
1.1-78	Conductivity-Density Product for Several Multilayer Insulations	117
1.1-79	Conductivity Parallel to Layers for Several Multilayer Insulations	118
1.1-80	Emittance of Vacuum Metallized Polyester Film at 553°R (307°K) for Various Coating Materials and Thicknesses	121
1.1-81	Effect of Metallizing on Conductivity/Density Product	121
1.1-82	Effect of Fasteners on Insulation Material Choice - .25 Mil Mylar	124
1.1-83	Effect of Fasteners on Insulation Material Choice - 0.15 Mil Mylar	125
1.1-84	Effect of Fasteners on Insulation Material Choice - Large Fasteners	127
1.1-85	Effect of Fasteners on Insulation Material Choice - Small Fasteners	129
1.1-86	Tank Support - Multilayer Penetration Concepts	130
1.1-87	Thermal Model for Tank Support - Insulation Interaction and Temperature Results for Case 1	132
1.1-88	Weight Comparison - LF <sub>2</sub> /LH <sub>2</sub> Vehicles	135
1.1-89	Weight Comparison - FLOX/CH <sub>4</sub> Vehicles	135
1.1-90	Vehicle Evaluation LH <sub>2</sub> /LF <sub>2</sub> Propellants	136
1.1-91	Vehicle Evaluation FLOX/Methane Propellants	136
1.1-92	Screening and Conceptual Design Investigation - Vehicle Selections	137
1.2-1	Analytical Model for Solar Panel Temperature Analysis	140
1.2-2	Effect of Solar Panel Lower Surface Emittance on Temperatures	141
1.2-3	Effect of Solar Panel Lower Surface Emittance on Solar Cell Output and Required Panel Size	142
1.2-4	Vehicle 1-14 Configuration Options	145
1.2-5	Vehicle 1-14 Thermal Environment	146

<u>Figure No.</u>	<u>Title</u>	<u>Page</u>
1.2-6	End Fitting Weight Data	155
1.2-7	Attachment Bracket Weight Data	156
1.2-8	Honeycomb Sandwich Edge Attachment Details	157
1.2-9	Corrugated Construction Edge Attachment Details	158
1.2-10	Preliminary Design Vehicle Structure Evaluation Results	163
1.2-11	Vehicle Structure Evaluation Results	164
1.2-12	Vehicle 1-14 Fluid Line Arrangement	165
1.2-13	Vehicle 1-2B Fluid Line Arrangement	166
1.2-14	Vehicle 1-2A Fluid Line Arrangement	167
1.2-15	Vehicle 1-3 Fluid Line Arrangement	168
1.2-16	Vehicle 1-7 Fluid Line Arrangement	169
1.2-17	Vehicle 2-19 Fluid Line Arrangement	170
1.2-18	Vehicle 2-18 Fluid Line Arrangement	171
1.2-19	Vehicle 2-2 Fluid Line Arrangement	172
1.2-20	Vehicle 2-3 Fluid Line Arrangement	173
1.2-21	Vehicle 2-14 Fluid Line Arrangement	174
1.2-22	Comparison of Heat Leaks Thru Compartment Wall to Heat Leaks to Tank	178
1.2-23	Vehicle 2-3 Nodal Network (Insulation Outside)	179
1.2-24	Comparison of Optimization Program Heat Transfer Analysis Method to Thermal Analyzer Results - Insulation Thickness Dependent Heat Transfer	181
1.2-25	Comparison of Optimization Program Heat Transfer Analysis Method to Thermal Analyzer Results - Heat Leaks "Independent" of Insulation Thickness	182
1.2-26	Vehicle 1-14 Node Numbers	184
1.2-27	System Weights, Vehicle 1-14	191
1.2-28	System Weights, Vehicle 1-2B	191
1.2-29	System Weights, Vehicle 1-2A	195
1.2-30	System Weights, Vehicle 1-3	195
1.2-31	System Weights, Vehicle 1-7	197

<u>Figure No.</u>	<u>Title</u>	<u>Page</u>
1.2-32	System Weights, Vehicle 2-2	197
1.2-33	System Weights, Vehicle 2-3	199
1.2-34	System Weights, Vehicle 2-18	199
1.2-35	System Weights, Vehicle 2-14	201
1.2-36	System Weights, Vehicle 2-19	201
1.2-37	Payload Support Data	207
1.2-38	Meteoroid Protection Design Data - MLI	214
1.2-39	Meteoroid Protection Design Data - $\beta$ Cloth & MLI	214
1.2-40	Meteoroid Protection Design Data - Aluminum & MLI	218
1.2-41	Meteoroid Protection Design Data - Fiberglass & MLI	218
1.2-42	Vehicle Preliminary Design, Weight Summary	223
1.2-43	Operational Complexity Evaluation - FLOX/CH <sub>4</sub> Vehicles	224
1.2-44	Operational Complexity Evaluation - FLOX/CH <sub>4</sub> Vehicles	225
1.2-45	Operational Complexity Evaluation - LH <sub>2</sub> /LF <sub>2</sub> Vehicles	226
1.2-46	Operational Complexity Evaluation - LH <sub>2</sub> /LF <sub>2</sub> Vehicles	227
1.3-1	Structural Design - Vehicle 1-14	231
1.3-2	Insulation Details - Vehicle 1-14	232
1.3-3	Structural Design - Vehicle 2-18	234
1.3-4	Insulation Details - Vehicle 2-18	235
1.3-5	Configuration 1-14 Thermal Analysis Network - Structure and Penetrations	237
1.3-6	Configuration 1-14 Thermal Analysis Network - Insulation	238
1.3-7	Configuration 1-14 Insulation Temperatures	240
1.3-8	Reliability of Meteoroid Protection as a Function of the Model of the Meteoroid Flux and of the Penetration Dependence of Velocity	250
1.3-9	Meteoroid Protection Weight Sensitivity - Vehicle 1-14	250
1.3-10	Meteoroid Protection Weight Sensitivity - Vehicle 2-18	250
1.3-11	Tank Mounted Thermal/Meteoroid Protection Design	252
1.3-12	Meteoroid Protection Design Data - Tank Mounted MLI	254

<u>Figure No.</u>	<u>Title</u>	<u>Page</u>
2.1-1	Flaw Growth-Thru-The-Thickness of 2219-T6E46 Aluminum	258
2.1-2	Tank Mounted Meteoroid Protection Design Data	260
2.1-3	Meteoroid Protection Design Data - MLI	260
2.1-4	Meteoroid Protection Design Data - $\beta$ Cloth & MLI	262
2.1-5	Meteoroid Protection Design Data - $\beta$ Cloth & MLI	262
2.1-6	Meteoroid Protection Design Data - $\beta$ Cloth & MLI	264
2.1-7	Meteoroid Protection Design Data - MLI & Aluminum	264
2.1-8	Meteoroid Protection Design Data - MLI	266
2.1-9	Proof Test Sample - Vehicle 1-14	266
2.1-10	Proof Test Sample - Vehicle 1-14	267
2.1-11	Proof Test Sample - Vehicle 1-14	267
2.1-12	Proof Test Sample - Vehicle 2-18	267
2.1-13	Proof Test Sample - Vehicle 1-14	267
2.1-14	Proof Test Sample - Vehicle 2-18	268
2.1-15	Witness Plate Damage	268
2.1-16	Witness Plate Damage	268
2.1-17	Witness Plate Damage	268
2.2-1	Thermal Performance and Launch Environment Test Program	269
2.2-2	Depressurization Rates	270
2.2-3	Thermal Test Site - Area 8 Tulalip	273
2.2-4	Schematic - Thermal Test System	274
2.2-5	Guard and Test Tank Assembly	276
2.2-6	Test Article Details	277
2.2-7	Gas Measurement System Components	282
2.2-8	Test Article	283
2.2-9	Test Article	283
2.2-10	Test Article	282
2.2-11	Test Article - Fluid Line Penetration	286
2.2-12	Test Article - Fluid Line and Support Strut	286

<u>Figure No.</u>	<u>Title</u>	<u>Page</u>
2.2-13	Test Article Base Plate	287
2.2-14	Test Article Base Plate	287
2.2-15	Test Article Base Plate Installation	287
2.2-16	Thermal Test System Components	288
2.2-17	Thermal Test System Assembly	288
2.2-18	Experimental and Analytical Temperatures - Main Insulation Outer Sidewall Area	297
2.2-19	Experimental and Analytical Temperatures - Main Insulation Inner Sidewall Area	297
2.2-20	Experimental and Analytical Temperatures - Longitudinal Joint Area	298
2.2-21	Experimental and Analytical Temperatures - Typical Fastener Area	298
2.2-22	Experimental and Analytical Temperatures - Main Insulation Outer Sidewall Area	299
2.2-23	Experimental and Analytical Temperatures - Main Insulation Inner Sidewall Area	299
2.2-24	Experimental and Analytical Temperatures - Longitudinal Joint Area	300
2.2-25	Analytical Temperatures - Typical Fastener Area	300
2.2-26	Experimental and Analytical Temperatures - Main Insulation Sidewall Area	301
2.2-27	Experimental and Analytical Temperatures - Longitudinal Joint Area	302
2.2-28	Analytical Temperatures - Typical Fastener Area	302
2.2-29	Experimental and Analytical Temperatures - Fluid Line Penetration Area	303
2.2-30	Experimental and Analytical Temperatures - Strut Penetration Area	304
2.2-31	Experimental and Analytical Temperatures - Tank Support Strut	304
2.2-32	Experimental and Analytical Temperatures - Fluid Line Penetration Area	305
2.2-33	Experimental and Analytical Temperatures - Strut Penetration Area	306

<u>Figure No.</u>	<u>Title</u>	<u>Page</u>
2.2-34	Experimental and Analytical Temperatures - Strut Penetration Area	306
2.2-35	Experimental and Analytical Temperatures - Fluid Line and Truss	307
2.2-36	Experimental and Analytical Temperatures - Fluid Line Penetration Area	307
2.2-37	Experimental and Analytical Temperatures - Fluid Line Penetration Area	308
2.2-38	Experimental and Analytical Temperatures - Fluid Line Penetration Area	308
2.2-39	Experimental and Analytical Temperatures - Fluid Line & Truss	309
2.2-40	Experimental and Analytical Temperatures - Fluid Line Penetration Area	309
2.2-41	Experimental and Analytical Temperatures - Fluid Line Penetration Area	310
2.2-42	Experimental and Analytical Temperatures - Fluid Line Penetration Area	310
2.2-43	Experimental and Analytical Temperatures - Base Lap Joint Area	311
2.2-44	Experimental and Analytical Temperatures - Base Area	312
2.2-45	Heat Flow, Test T-1	314
2.2-46	Typical Data Printout	315
2.2-47	Test Tank Outlet Temperature, Test T-1	317
2.2-48	Test Tank and Barometric Pressure, Test T-1	317
2.2-49	Longitudinal Joint Instrumentation	318
2.2-50	Guard Area Instrumentation	318
2.2-51	Heat Flow, Test T-2	321
2.2-52	Test Tank and Barometric Pressures, Test T-2	321
2.2-53	Test Tank Outlet Temperature, Test T-2	323
2.2-54	Heat Flow, Test T-3	324
2.2-55	Test Tank Outlet Temperature, Test T-3	326
2.2-56	Test Tank and Barometric Pressure, Test T-3	327

<u>Figure No.</u>	<u>Title</u>	<u>Page</u>
2.2-57	Vibration Test Assembly	329
2.2-58	Vibration Test Envelope	330
2.2-59	Vibration Test Results	330
2.2-60	Acoustic Test Assembly	331
2.2-61	Acoustic Environment	332
2.2-62	Centrifuge	332
2.2-63	Heat Flow, Test T-4	334
2.2-64	Test Tank and Barometric Pressures, Test T-4	334
2.2-65	Test Tank Outlet Temperature, Test T-4	335
2.2-66	Heat Flow, Test T-5	335
2.2-67	Test Tank and Barometric Pressures, Test T-5	337
2.2-68	Test Tank Outlet Temperature, Test T-5	337
2.2-69	Heat Flow, Test T-6	341
2.2-70	Test Tank and Barometric Pressure, Test T-6	342
2.2-71	Test Tank Outlet Temperature, Test T-6	343
2.2-72	Heat Flow, Test T-7	343
2.2-73	Test Tank and Barometric Pressure, Test T-7	347
2.2-74	Test Tank Outlet Temperature, Test T-7	347
2.2-75	Heat Flow, Test T-8	349
2.2-76	Test Tank and Barometric Pressure, Test T-8	350
2.2-77	Test Tank Outlet Temperature, Test T-8	351
2.3-1	Mockup - Vehicle 1-14 Structure	356
2.3-2	Mockup - LH <sub>2</sub> Fill Line/MLI Penetration	356
2.3-3	Mockup - Vehicle 1-14 MLI Assembly	359
2.3-4	Mockup - Top Deck MLI Blanket	360
2.3-5	Mockup - Internal View, LF <sub>2</sub> Compartment	360
2.3-6	Mockup - Inside View, LF <sub>2</sub> Compartment	361
2.3-7	Mockup - Top Deck/Sidewall Blanket Junction	361
2.3-8	Mockup - Mid Body Ring And MLI Joint	362

<u>Figure No.</u>	<u>Title</u>	<u>Page</u>
2.3-9	Mockup - Section View, Longitudinal Joint	362
2.3-10	Mockup - Tank Support/MLI Blanket Penetration	363
2.3-11	Mockup - Compartment Separation Blanket	363
2.3-12	Mockup - Compartment Separation Blanket Attachment	364
2.3-13	Mockup - Compartment Separation/Sidewall Blanket Junction	364
2.3-14	Mockup - Compartment Separation Blanket, Inside View	365
2.3-15	Mockup - Conical Base Area	365
2.3-16	Mockup - Base Blanket Penetrations	366
2.3-17	Mockup - Sidewall/Conical Base Blanket Junction	366

## LIST OF TABLES

<u>Table No.</u>	<u>Title</u>	<u>Page</u>
1.1-1	LH <sub>2</sub> /LF <sub>2</sub> Vehicle Screening Data	13
1.1-2	FLOX/CH <sub>4</sub> Vehicle Screening Data	14
1.1-3	Feed System Weight Summary Concept 1-1 (4 LF <sub>2</sub> Tanks)	33
1.1-4	Vehicle Concept Rating	36
1.1-5	Material Properties	54
1.1-6	Continuous Shell Structure Dimensions	57
1.1-7	Ground Hold Protection Weights	98
1.1-8	Tank Mounted Insulation Weights	104
1.1-9	Insulation Conductivity Equations	115
1.1-10	Effect of Insulation on Fastener Heat Leak	122
1.1-11	Effect of Insulation on Fastener Heat Leak - Internal Insulation, Sidewall, Large Fasteners	126
1.1-12	Effect of Insulation on Fastener Heat Leak - Internal Insulation, Top Deck, Small Fasteners	128
1.1-13	Tank Support - Insulation Interaction Analysis	133
1.2-1	Tank Arrangement Thermal Efficiency Study Results	147
1.2-2	Ring Stiffened Corrugated Shell Data	148
1.2-3	Honeycomb Sandwich Data	150
1.2-4	Truss Structure Data	152
1.2-5	Vehicle and Adaptor Weights	159
1.2-6	Preliminary Design Study Flow Diagram	161
1.2-7	Temperatures for Several Insulation Thickness - Vehicle 2-3	180
1.2-8	Vehicle 1-14 System Weights with Three Insulation Combinations, Aluminum Truss Structure, Insulation Inside, 4" (10 cm) Payload Separation	180
1.2-9	Penetration Conductances - Configuration 1-14	185
1.2-10	Vehicle Structure Conductances - Configuration 1-14 Insulation Outside Only	186

<u>Table No.</u>	<u>Title</u>	<u>Page</u>
1.2-11	Coast Phase Temperature, Vehicle 1-14	187
1.2-12	Coast Phase Temperature, Vehicle 1-14	187
1.2-13	Coast Phase Temperature, Vehicle 1-14	188
1.2-14	Coast Phase Temperature, Vehicle 1-14	188
1.2-15	Coast Phase Temperature, Vehicle 1-14	189
1.2-16	Coast Phase Temperature, Vehicle 1-14	189
1.2-17	Optimum System Weights, Vehicle 1-14	190
1.2-18	Optimum System Weights, Vehicle 1-2B	192
1.2-19	Optimum System Weights, Vehicle 1-2A	196
1.2-20	Optimum System Weights, Vehicle 1-3	196
1.2-21	Optimum System Weights, Vehicle 1-7	198
1.2-22	Optimum System Weights, Vehicle 2-2	198
1.2-23	Optimum System Weights, Vehicle 2-3	200
1.2-24	Optimum System Weights, Vehicle 2-18	200
1.2-25	Optimum System Weights, Vehicle 2-14	202
1.2-26	Optimum System Weights, Vehicle 2-19	202
1.2-27	Meteoroid Protection Initial Screening Results, Vehicle 1-14	208
1.2-28	Meteoroid Protection Initial Screening Results, Vehicle 1-2B	209
1.2-29	Meteoroid Protection Initial Screening Results, Vehicle 1-2A	209
1.2-30	Meteoroid Protection Initial Screening Results, Vehicle 1-3	209
1.2-31	Meteoroid Protection Initial Screening Results, Vehicle 1-7	209
1.2-32	Meteoroid Protection Initial Screening Results, Vehicle 2-14	210
1.2-33	Meteoroid Protection Initial Screening Results, Vehicle 2-3	210
1.2-34	Meteoroid Protection Initial Screening Results, Vehicle 2-18	210
1.2-35	Meteoroid Protection Initial Screening Results, Vehicle 2-19	211
1.2-36	Meteoroid Protection Initial Screening Results, Vehicle 2-2	211
1.2-37	Meteoroid Protection Evaluation 4" (10 cm) Payload Height, Vehicle 1-14	215
1.2-38	Meteoroid Protection Evaluation 4" (10 cm) Payload Height, Vehicle 1-2B, LF <sub>2</sub> on Top	215

<u>Table No.</u>	<u>Title</u>	<u>Page</u>
1.2-39	Meteoroid Protection Evaluation 4" (10 cm) Payload Height, Vehicle 1-2A	220
1.2-40	Meteoroid Protection Evaluation 4" (10 cm) Payload Height, Vehicle 1-3	220
1.2-41	Meteoroid Protection Evaluation 4" (10 cm) Payload Height, Vehicle 1-7	220
1.2-42	Meteoroid Protection Evaluation 4" (10 cm) Payload Height, Vehicle 2-3	220
1.2-43	Meteoroid Protection Evaluation 4" (10 cm) Payload Height, Vehicle 2-14	221
1.2-44	Meteoroid Protection Evaluation 4" (10 cm) Payload Height, Vehicle 2-18	221
1.2-45	Meteoroid Protection Evaluation 4" (10 cm) Payload Height, Vehicle 2-19	221
1.2-46	Meteoroid Protection Evaluation 4" (10 cm) Payload Height, Vehicle 2-2	221
1.3-1	System Weight Comparisons	241
1.3-2	Final Evaluation Vehicle Weights	242
1.3-3	Weight Data - Structure	243
1.3-4	Weight Data - Insulation	243
1.3-5	Weight Data - Fuel System	243
1.3-6	Weight Data - Oxidizer System	244
1.3-7	Weight Data - Pneumatic System	244
1.3-8	Effect of Variations in Mean Thermal Conductivity on Tank Weight	251
1.3-9	Vehicle & Tank Mounted MLI Weight Comparisons	255
1.3-10	Weight Data - Tank Mounted MLI	256
2.2-1	Properties Used in Thermal Analyses	291
2.2-2	Heat Flow Summary	313
3.1-1	Revised Thermal Properties	368
3.1-2	Final Design System Weights - Experimental Thermal Properties	370

## INTRODUCTION

This report describes the results of a design, analytical and experimental investigation conducted by the Boeing Aerospace Company for the NASA/Lewis Research Center. The period of performance was October 14, 1969, through August 31, 1972. Mr. James R. Barber was the NASA Project Manager.

A companion document, Volume II, NASA CR-121104, contains appendixes with detailed information relating to both the analytical and experimental phases of the study.

The purpose of this program was to evaluate, for both a cryogenic and space storable propellant combination, a thermal protection system that was integrated with the vehicle structure and meteoroid protection system. Design definition, detailed system evaluation, fabrication feasibility and experimental demonstration were required for a complete assessment of the potential of this concept. A propulsion vehicle having maximum payload capability with minimum operational complexity was the primary goal.

**Page Intentionally Left Blank**

## SUMMARY

The program was performed in three phases. These were (1) a design evaluation, (2) an experimental evaluation, and (3) data evaluation and final design correction.

In the first task, Design Evaluation, the objective was to identify preliminary vehicle design concepts which provided maximum payload capability with design and operational simplicity. This task was conducted in three parts.

The first part was a screening and conceptual design study. Critical vehicle areas were identified and design solutions were evaluated. Example of critical areas were vehicle structure, meteoroid protection system, thermal protection system, tank arrangements, and ground hold thermal protection. Designs and/or analytical studies were performed in sufficient detail to identify advantages or disadvantages of selected approaches. These results were summarized and a large field of candidate tank arrangements and vehicle structural concepts were narrowed to ten design configurations.

The second part of Task I consisted of development of the ten vehicle preliminary designs. Structural and thermal analyses were conducted. Meteoroid impact data was obtained and used to define least-weight protection systems. An operational evaluation was made to determine relative vehicle complexity. Design drawings of each vehicle were prepared giving critical dimensions, insulation thicknesses and attachment concepts in sufficient detail to prepare a weight statement. Weights, payload capability and operational complexity were obtained for the ten study vehicles. The concepts which appeared most promising at this stage for LH<sub>2</sub>-LF<sub>2</sub> propellants were truss structure with MLI (multilayer insulation) suspended inside the structure, two oblate spheroid tanks in a tandem (LF<sub>2</sub> forward) configuration and MLI as the meteoroid protection system. For FLOX-CH<sub>4</sub> propellants a common bulkhead tank configuration appeared best, suspended within a truss structure. MLI mounted inside the vehicle structure provided optimum thermal/meteoroid protection. Continuous shell structures, such as honeycomb sandwich, incurred significant weight penalties because of low shell loadings.

The third part of Task I involved selection of the two most promising vehicle configurations, described above, and further design development. The sensitivity to errors in the velocity and flux parameters of the meteoroid environment were evaluated for both vehicles. Sensitivity to errors in the prediction of MLI thermal conductivity were also determined. It was found that both of these were only of minor importance in terms of vehicle weight.

Task I was concluded with a weight summary of each vehicle. The results showed that a mass fraction of 0.81 was possible for the LH<sub>2</sub>-LF<sub>2</sub> propellants and 0.86 for the FLOX-CH<sub>4</sub> propellants. Payload weight capability for the

LH<sub>2</sub>-LF<sub>2</sub> propellants was 4791 lbs (2130 kg), and 4642 lbs (2110 kg) for the FLOX-CH<sub>4</sub> propellants. A comparison with a tank mounted MLI design was made and it was found that there was only a slight weight difference.

Task II consisted of an experimental program to obtain meteoroid impact data for construction of design curves, thermal performance data for the selected MLI system with and without typical penetrations, structural response of the MLI system to launch environment loads, and the ease and accuracy of installation on a full scale mockup.

The meteoroid tests were conducted with a light gas gun which propelled polyethylene cylinders at  $\approx$  25000 fps (7.6 km/sec). Five MLI concepts; aluminum and Beta fiber cloth bumpers; aluminum, and fiberglass honeycomb sandwich shell constructions were tested to determine penetration depth in a simulated tank wall. These data were used to derive curves relating penetration depth to protection system thickness. In general, MLI systems alone produced the least-weight protection system.

Thermal performance tests were made with a 2 ft diameter by 4 ft long (0.61 x 1.22 m) thermal model consisting of an aluminum trusswork frame with MLI suspended from the inside. Baseline tests of the "as fabricated" system were made. Results were obtained by measuring boiloff gas and converting to heat transfer rate. Launch loads were applied and the boiloff test repeated for an assessment of damage. The MLI was then modified to incorporate a fiberglass tank support strut and later, a fluid line penetration. Thermal performance tests were made with each configuration. The thermal model was modified to include a lap joint typical of the preliminary designs and the boiloff test repeated.

A cumulative increase in heat transfer rate was noted as testing progressed. The launch load tests caused approximately a 10% increase in heat flow. The cumulative effects of tank support and fluid line penetrations caused a 50% increase in heat flow. Correlations with predicted heat transfer rates and temperatures were reasonable in most cases.

A full scale mockup was made of the LH<sub>2</sub>-LF<sub>2</sub> vehicle with two oblate spheroid tanks in tandem. MLI blankets were assembled and installed to verify fit-up and clearances. The design improvements necessitated by this investigation were incorporated on the detail design drawings of both vehicles.

Task III involved correction of the analytically derived designs in light of the test results. Correlations between prediction methods and test results were made, and heat transfer values for MLI and penetrations in the thermal analysis computer program were adjusted to be representative of experimental values. The vehicle weights were recalculated with the program and it was found that the inert weight of the LH<sub>2</sub>-LF<sub>2</sub> vehicle increased by only 1.5% and the FLOX-CH<sub>4</sub> vehicle decreased by 1.2%.

In conclusion, it was found that combining the continuous structural shell of a vehicle body, e.g., honeycomb sandwich, with the integrated thermal/meteoroid protection system was impractical because of the excessive weight attendant in the continuous shell structure. An efficient design was obtained however, when the integrated thermal/meteoroid protection system was combined with a truss structure vehicle. The MLI by itself was found to be the most weight efficient meteoroid protection system.

Comparisons with a tank mounted protection system indicated there was little weight difference between the two approaches.

**Page Intentionally Left Blank**

## 1.0 TASK 1 - DESIGN EVALUATION

A design evaluation of a space vehicle propulsion module was performed. The vehicle incorporated an integral structural/thermal/meteoroid protection system. The design evaluation was conducted in three phases:

- (1) Screening and conceptual design investigations
- (2) Preliminary evaluation
- (3) Final evaluation.

The study flow is shown in the diagram of Figure 1.1-1. The sections of text describing each element of the task are referenced in the figure. The Tank Arrangement Screening and Insulation Concept Development were started concurrently. The Vehicle Structure Evaluation was started during the initial screening stage of the Tank Arrangement Screening study. A large number of configurations were initially considered as candidates, which were reduced in number in successive study phases. For this reason, the vehicle configurations used in the structural evaluation were not the final choices from the screening study in two cases. The Tank Arrangement Thermal Efficiency study was conducted with the ten vehicle configurations derived from the final tank arrangement screening. The results of the screening and conceptual design investigation were evaluated in the Combined Systems Evaluation phase and ten promising configurations were identified. The subsequent studies of Task 1, i.e., the Preliminary and Final Evaluations, were conducted in chronological order, resulting in final definition of two vehicle configurations, one for each propellant combination.

The representative vehicle and mission constraints were:

Launch Vehicle:	Titan 3D/Centaur
Launch Load Factors:	Axial G's    +4.0 -2.5 Lateral G's $\pm 1.5$
Factors of Safety:	Structure/Thermal/Meteoroid Protection 1.25 ultimate Propellant tanks 1.4 ultimate, 1.25 yield
Mission:	Mars Orbiter; 208-day trip time; $\Delta v =$ 5000 ft/sec to orbit.
Earth Injected Weight:	7500 lbs for propulsion vehicle, payload and Centaur Adaptor. Boost shroud excluded.
Propellants:	LH <sub>2</sub> /LF <sub>2</sub> , O/F ratio = 12:1 168 lb LH <sub>2</sub> ; 2002 lb LF <sub>2</sub> ; total weight = 2170 lbs (includes 2% residuals).

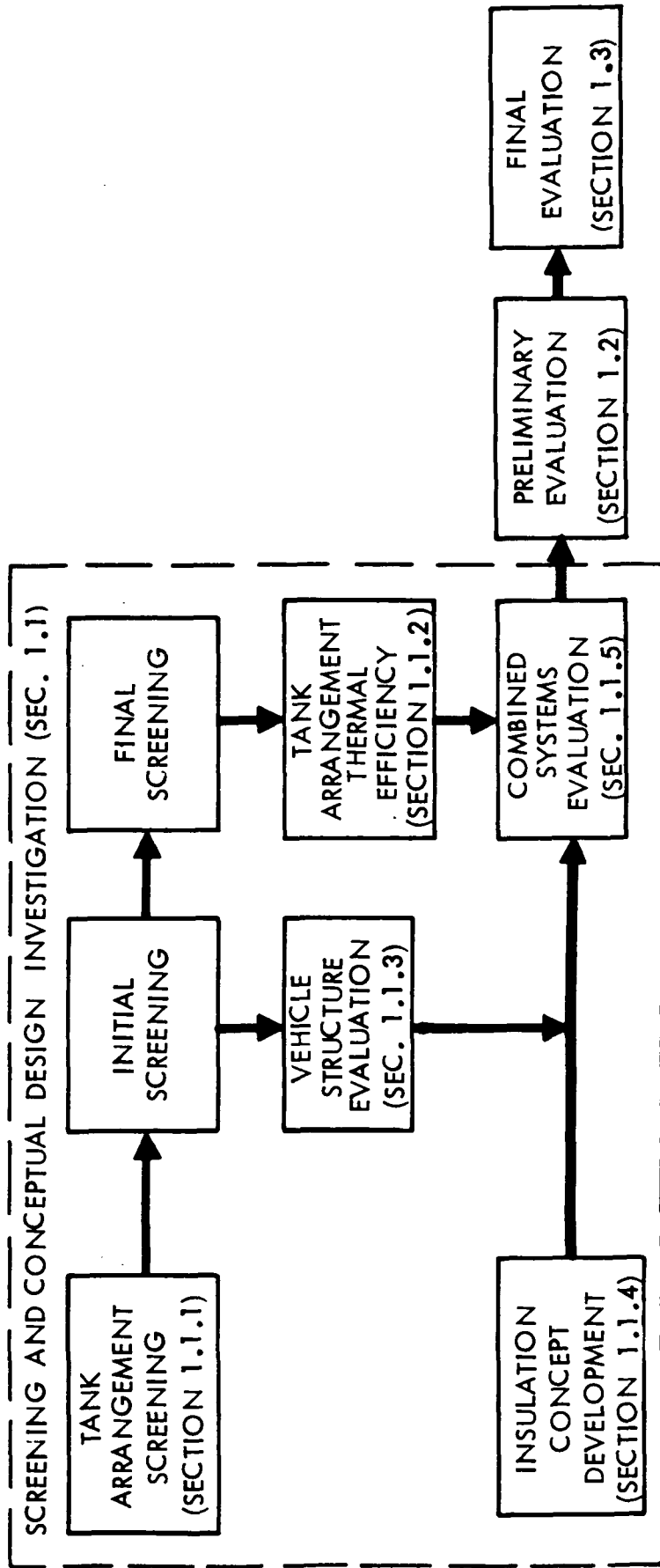


Figure 1.1-1: TASK 1 - STUDY FLOW DIAGRAM

	FLOX/CH <sub>4</sub> (82.6% by weight F <sub>2</sub> ), O/F ratio = 5.25:1 2050 lb (931 kg) FLOX; 390 lb (177 kg) CH <sub>4</sub> ; total weight = 2440 lb (1108 kg) (includes 2% residuals)
Propulsion Vehicle:	Maximum diameter 10 ft (3.06 m); contained within a boost shroud; payload diameter identical to vehicle; payload oriented towards the sun; solar panels and antennas extended beyond 10 ft (3.06 m) diameter after launch.
Propellant Tanks:	Non-vented during coast. Thermally mixed propellants. Supported by fiberglass tubular struts.
Engine System:	5000 lb thrust; oxidizer NPSP = 12 psig, fuel NPSP = 8 psig; helium pressurant for LF <sub>2</sub> , CH <sub>4</sub> and FLOX, autogenous pressurization for LH <sub>2</sub> . Engine weight = 108 lb.
Meteoroid Protection:	Probability of no failure due to meteoroid impacts = 0.999.

## 1.1 Screening and Conceptual Design Investigation

In order to provide information for development of designs in the Preliminary Evaluation phase it was necessary to conduct a conceptual design and screening investigation. The investigation was concerned with propellant tank arrangements, vehicle structural concepts and material choices, and thermal protection concepts. This phase was concluded with an evaluation of the effects of combined systems on vehicle weight and complexity, and the identification of 10 promising vehicle concepts for further study.

A "vehicle" as defined for purposes of this study consisted of a structural body, a centaur adaptor structure, a payload support system, a payload, propellant tanks, an engine and attendant fluid lines, pressurization systems and electrical systems. These items are identified on the sketch of Figure 1.1-2. Thermal/meteoroid protection blanket locations are identified also. For example, a "top deck" blanket is one which separated the payload from the propellant tanks located in the uppermost compartment.

The items which are discussed later in the section entitled, "Tank Arrangement Thermal Efficiency", comprise those components of the vehicle which were variables as a function of heat transfer rate. Specifically, the items were tank size and gage, insulation thickness, propellant vapor mass, helium tank size and

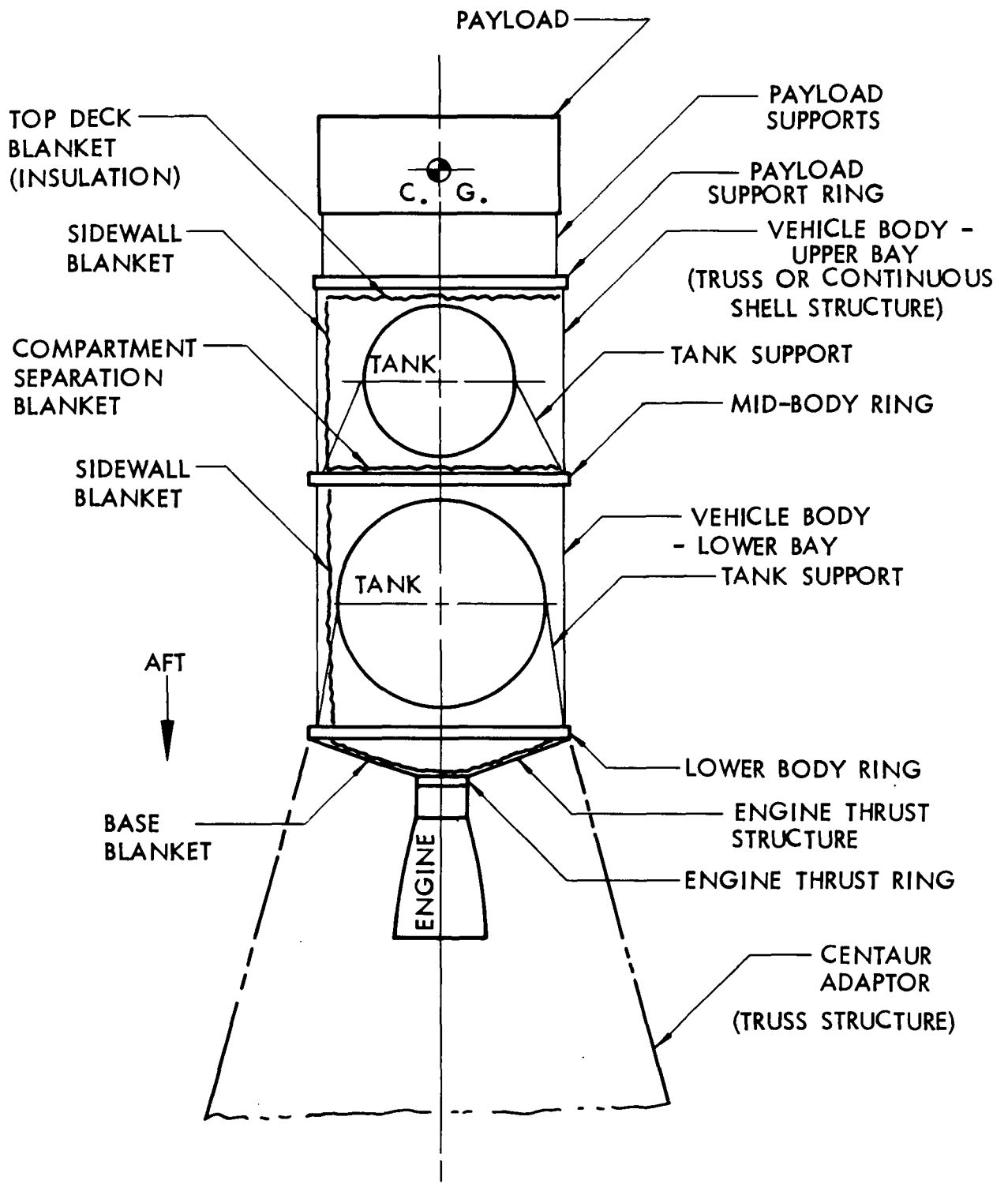


Figure 1.1-2: PROPULSION VEHICLE DESCRIPTION

gage, and helium mass. The weights of these components were derived and used as a basis for comparisons between various tank arrangements.

### 1.1.1 Tank Arrangement Screening

#### Initial Screening

The tank arrangement screening was accomplished in two phases. An initial screening was made based on data from simple layouts of a wide range of vehicle concepts. The layouts were prepared by grouping the tanks as compactly as plumbing and structure would allow. A minimum clearance of 6 inches (15.2 cm) was established between adjacent tanks or tanks and vehicle structure.

Propellant tanks were sized to contain 2170 lb (984 kg) LH<sub>2</sub>/LF<sub>2</sub> and 2440 lb (1110 kg) FLOX/CH<sub>4</sub>.

An engine configuration was obtained from Reference 1.1-1. This design was considered typical for FLOX/CH<sub>4</sub> and LH<sub>2</sub>/LF<sub>2</sub> propellants.

Figure 1.1-3 shows representative design layouts for two vehicle configurations. These were used to calculate surface areas, lengths and ratio of vehicle to tank volume.

The surface area parameter was selected because it was indicative of thermal/meteoroid protection, ground hold protection, and structural shell weight.

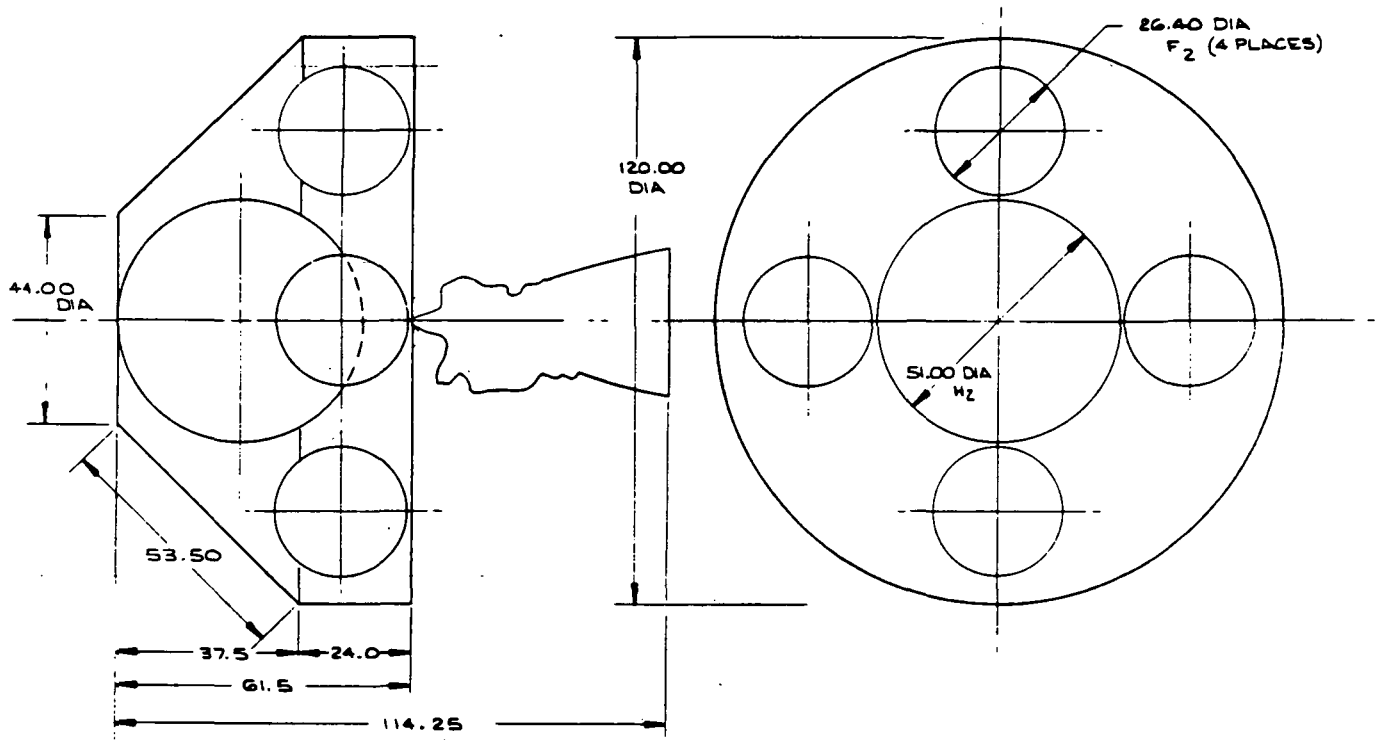
Vehicle length was selected as an evaluation parameter since vehicle bending moments influenced structure weight.

The vehicle to tank volume ratio parameter was selected because it indicated the amount of space available for other system components. A high ratio meant more useable volume for a particular vehicle.

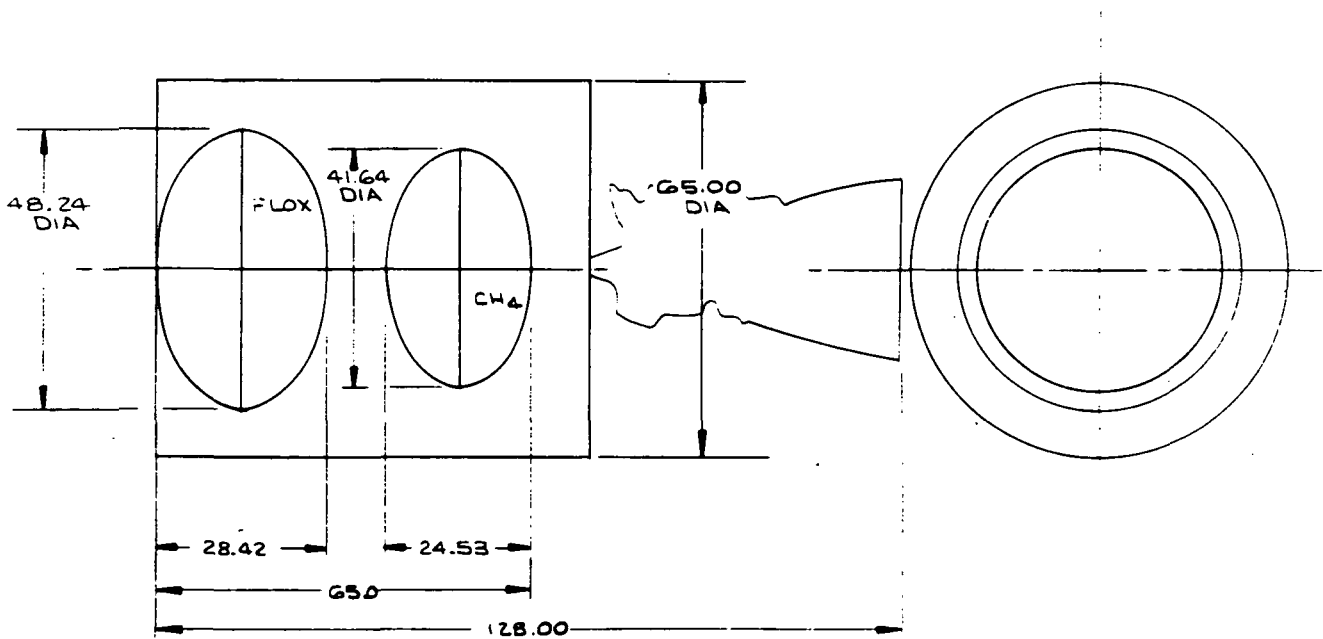
The results of the initial screening are contained in Tables 1.1-1 and 1.1-2. The vehicle configurations are categorized into general types by the heavy horizontal lines. Selections were made from these charts for a more thorough evaluation and screening. An "ideal" configuration was one with minimum surface area and vehicle length, a high volume ratio and no significant disadvantages. Selections were made so that at least one concept from each general type was retained in the investigation, with the exception of Vehicles 2-14 and 2-4. In this case neither vehicle was chosen since it was planned to evaluate the LH<sub>2</sub>/LF<sub>2</sub> counterpart, Vehicle 1-14.

#### Final Screening

The final screening was made with concepts selected from Tables 1.1-1 and 1.1-2.



CONCEPT 1-1 ( $LH_2/LF_2$ )



CONCEPT 2-14 (FLOX/ $CH_4$ )

Figure 1.1-3: TYPICAL VEHICLE LAYOUTS

Table 1.1-1: LH<sub>2</sub>/LF<sub>2</sub> VEHICLE SCREENING DATA

CONCEPT NUMBER	CONFIGURATION	DESCRIP - TION	SURF AREA INCHES <sup>2</sup> (METERS <sup>2</sup> )	VEHICLE LENGTH INCHES (METERS)	VEHICLE TO TANK VOLUME RATIO	DISADVANTAGES	SELECTED FOR FINAL SCREENING
1-8		4 CYLINDERS	18,350 (11.8)	111 (2.82)	2.9		X
1-3		4 SPHERES	26,750 (17.3)	94 (2.4)	4.3		X
1-14		2 OBLATE SPHEROIDS	16,400 (10.6)	140 (3.6)	2.5		X
1-4		2 SPHERES	23,270 (15.0)	151 (3.8)	3.0	LARGE LENGTH & AREA	
1-15		1 OBL. SPHEROID 4 SPHERES	23,040 (14.9)	118 (3.0)	4.1		
1-1		5 SPHERES	24,350 (15.8)	114 (2.9)	4.5		X
1-12		1 OBL. SPHEROID 4 CYL	26,750 (17.3)	94 (2.4)	4.3		
1-11		1 SPHERE 4 CYL	27,500 (17.7)	104 (2.6)	4.5		
1-16		1 OBL. SPHEROID 3 SPHERES	25,035 (16.2)	109 (2.8)	4.7		
1-2		4 SPHERES	25,623 (16.5)	119 (3.1)	4.7	LARGE LENGTH & AREA	
1-6		4 SPHERES	25,760 (16.6)	119 (3.1)	4.9		X
1-13		1 CYLINDER 3 SPHERES	29,424 (18.9)	134 (3.4)	5.9	LARGE LENGTH & AREA	
1-17		1 OBL. SPHEROID 3 CYL	31,670 (20.3)	102 (2.6)	5.7	LARGE LENGTH & AREA	
1-10		1 SPHERE 3 CYL	28,220 (18.1)	108 (2.7)	4.8	LARGE LENGTH & AREA	
1-20		2 TOROIDS	19,620 (12.6)	103 (2.6)	2.8		X
1-7		3 CYLINDERS	17,830 (11.4)	117 (2.8)	2.0		X
1-18		COMMON	—	—	—	COMMON BULK'D STRUCTURAL & THERMAL PROBLEMS	
1-19		COMMON	—	—	—		
1-9		3 SPHERES	—	—	—	C. G. ECCENTRICITY	
1-5		6 SPHERES	—	—	—	COMPLEX MANIFOLDING & TANK SUPPORT	

Table 1.1-2: FLOX/CH<sub>4</sub> VEHICLE SCREENING DATA

CONCEPT NUMBER	CONFIGURATION	DESCRIPTION	SURF. AREA INCHES <sup>2</sup> (METER <sup>2</sup> )	VEHICLE LENGTH INCHES (METERS)	VEHICLE TO TANK VOLUME RATIO	DISADVANTAGES	SELECTED FOR FINAL SCREENING	
2-19A		FLOX ABOVE CH <sub>4</sub>				FLOX LOAD ON COMMON BULKHEAD		
2-19		COMMON CH <sub>4</sub> ABOVE FLOX	14,129 (9.1)	118 (3.0)	2.5		X	
2-18A		COMMON CH <sub>4</sub> ABOVE FLOX	12,954 (8.4)	124 (3.2)	2.2	FLOX PRESSURE EST. HIGHER THAN CH <sub>4</sub>		
2-18		COMMON FLOX ABOVE CH <sub>4</sub>	13,005 (8.4)	125 (3.2)	2.2		X	
2-1		5 SPHERES	22,990 (14.8)	115 (2.9)	4.2	LARGE SURFACE AREA	X	
2-15		1 OBL. SPHEROID 4 SPHERES	24,500 (15.8)	100 (2.5)	5.8			
2-11		1 SPHERE 4 CYLINDERS	21,356 (13.8)	107 (2.7)	5.0			
2-12		1 OBL. SPHEROID 4 CYLINDERS	21,984 (14.2)	110 (2.8)	5.2			
2-16		1 OBL. SPHEROID 3 SPHERES	22,453 (14.5)	100 (2.5)	5.9	LARGE SURFACE AREA	X	
2-17		1 OBL. SPHEROID 3 CYLINDERS	24,010 (15.5)	102 (2.59)	5.9			
2-10		1 SPHERE 3 CYLINDERS	21,916 (14.2)	108 (2.7)	5.2			
2-13		1 CYLINDER 3 SPHERES	21,335 (13.8)	108 (2.7)	5.1			
2-2		4 SPHERES	22,118 (14.3)	108 (2.7)	5.8			X
2-6		4 SPHERES	22,883 (14.8)	113 (2.87)	6.6		LARGE LENGTH & AREA	
2-14		2 OBL. SPHEROIDS	16,584 (10.7)	128 (3.3)	3.2			
2-4		2 SPHERES	16,995 (10.9)	151 (3.8)	3.1	LARGE LENGTH		
2-20		1 OBL. SPHEROID 1 TORUS	15,970 (10.3)	112 (2.8)	3.0	LIMITED SPACE FOR TANK SUPPORTS	X	
2-21		2 TOROIDS						
2-3		4 SPHERES	19,925 (12.9)	87 (2.2)	4.4			
2-8		4 CYLINDERS	16,437 (10.6)	135 (3.4)	3.3		X	
2-9		3 CYLINDERS				C. G. ECCENTRICITY		
2-7		3 CYLINDERS				C.G ECCENTRICITY		
2-5		6 SPHERES				COMPLEX MANI- FOLDING & TANK SUPPORT		

Structural arrangements were prepared with emphasis placed on (1) definition of internal structure to support tanks and 5K engine loads and (2) primary vehicle and payload support members.

Structural members were sized for the boost or 5K engine thrust loads as applicable. Payload weight was derived by subtracting the estimated structure, tank and propellant weights from the 7500 lb (3410 kg) vehicle launch weight. Structural members and propellant tanks were assumed to be aluminum.

In some cases vehicle length or diameter was altered from the values shown in Tables 1.1-1 and 1.1-2 to accommodate structural members which had been neglected in the initial screening. An example of this is Vehicle 2-8 which was initially configured with the engine gimbal point located on the bottom plane of the propellant tanks. A crossed-beam structural arrangement was selected for the engine and lower tank support of this design resulting in a vehicle length increase of 20 in (50.8 cm).

The propellant tank operating pressures used for this preliminary evaluation were:  $\text{LH}_2$  - 30 psia (206.8 kN/m<sup>2</sup>),  $\text{LF}_2$  - 50 psia (344.7 kN/m<sup>2</sup>), FLOX - 100 psia (689.5 kN/m<sup>2</sup>), and  $\text{CH}_4$  - 40 psia (275.8 kN/m<sup>2</sup>). The cryogenic properties of 2219 aluminum were utilized. In the majority of cases the tank gage was set by an arbitrarily established minimum fabrication thickness of 0.025 in (0.064 cm). Propellant tank supports were fiberglass/epoxy tubular struts. These were sized by the compressive load condition.

The design layouts for the seven  $\text{LH}_2/\text{LF}_2$  and seven FLOX/ $\text{CH}_4$  vehicles are shown in Figures 1.1-4 through 1.1-17. The structural arrangements chosen were those which appeared to best satisfy the load path requirements for each particular tank arrangement. Component weights are also shown on the figures. These weights formed the basis for a further ranking of concepts.

An evaluation of propellant feed system complexity was made for single and multiple tank arrangements. Representative feed and pressurization system design schematics are shown in Figures 1.1-18 and 1.1-19. The ground rules established for constructing these system designs were:

1. Multiple fuel or oxidizer tanks were manifolded together and a single fuel supply valve used between the manifold and the engine. The reasons were to decrease system complexity by eliminating multiple valve operations and to reduce valve weight.
2. A reaction control system was available for settling propellants prior to engine burn, thus eliminating C.G. shift problems in the manifolded tank configurations.

COMPONENT WEIGHTS

ENGINE MOUNT BEAM (8 BEAMS)	40
P/L INTERFACE CROSS BEAM	25
LOWER RING	30
UPPER RING	20
STIFFENED SHELL	30
LH <sub>2</sub> TANK SUPPORTS	6
LF <sub>2</sub> TANK SUPPORTS	18
TANKS	43
	<u>212</u> LBS

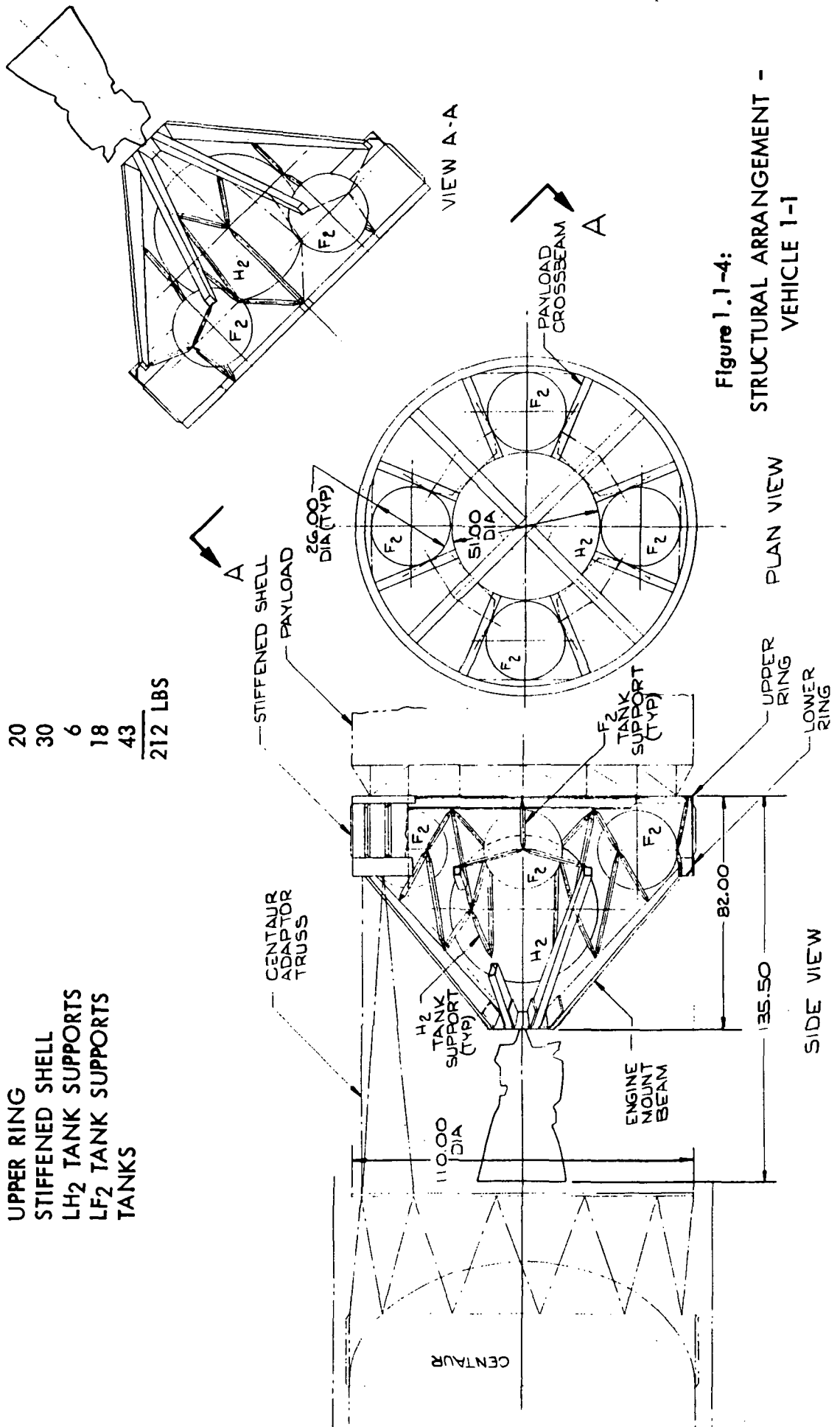


Figure 1.1-4:  
STRUCTURAL ARRANGEMENT -  
VEHICLE 1-1

COMPONENT WEIGHTS

INSULATION SUPPORTS (PROJECTING ARMS)	10
PAYLOAD SUPPORT RING	20
LOWER BODY RING	20
DIAGONALS	40
CENTER POST	5
TRUSS SUPPORT RING	10
TANK SUPPORTS	30
TANKS	44
	<hr/> 179 LBS

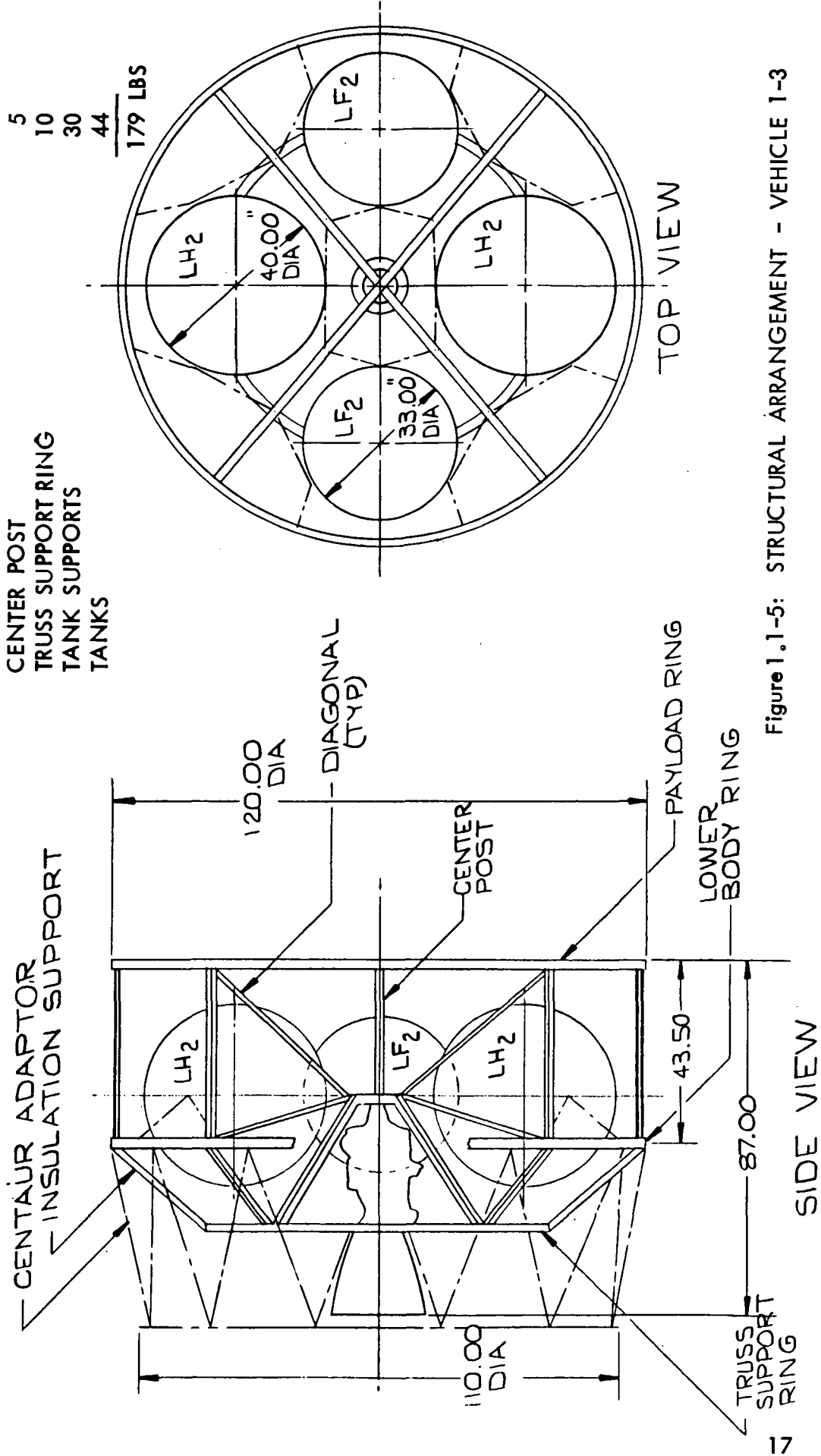


Figure 1.1-5: STRUCTURAL ARRANGEMENT - VEHICLE 1-3



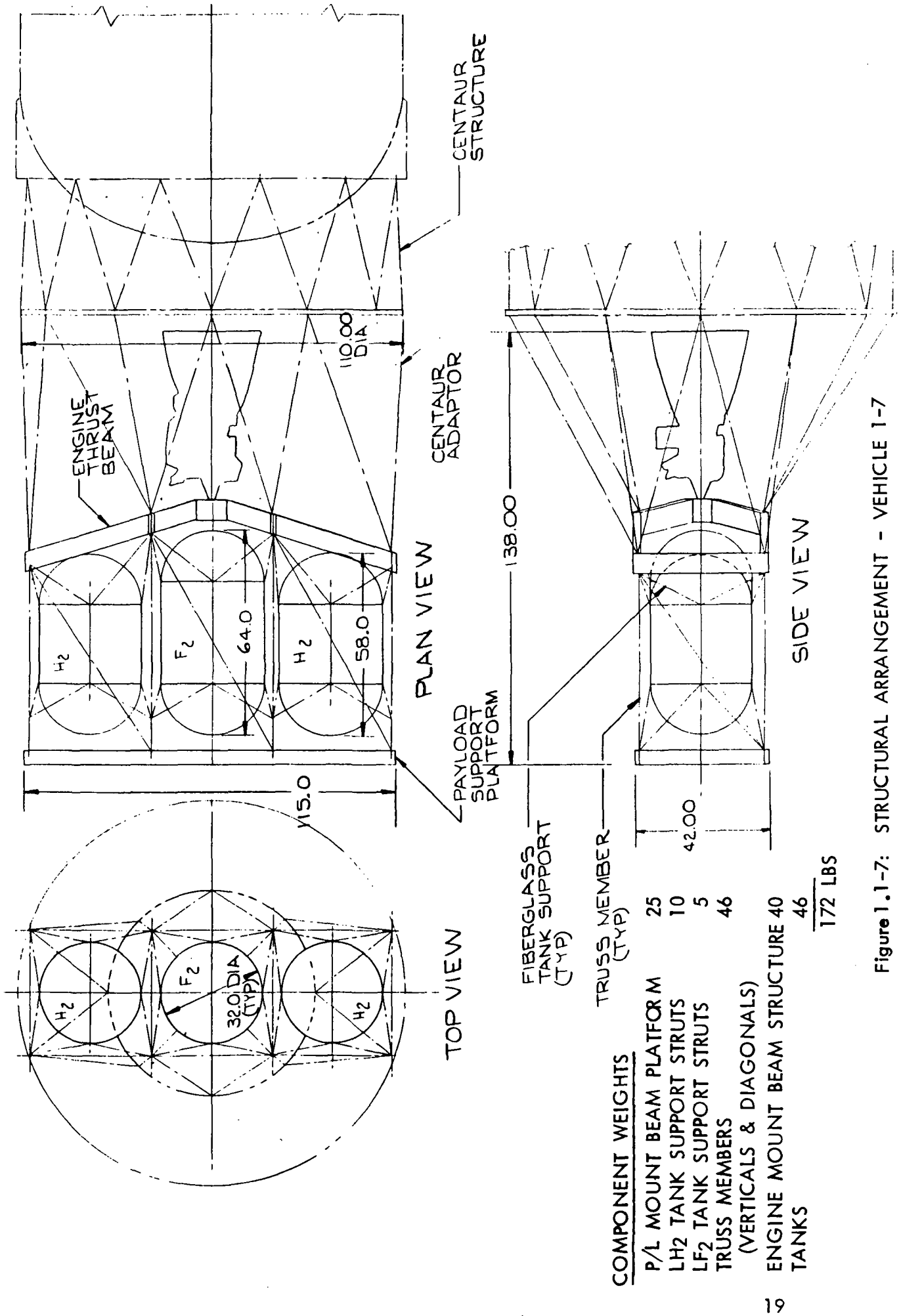


Figure 1.1-7: STRUCTURAL ARRANGEMENT - VEHICLE 1-7

COMPONENT WEIGHTS

TANK SUPPORT CROSS BEAM	30
CYLINDRICAL BODY SHELL	75
LF <sub>2</sub> & LH <sub>2</sub> TANK SUPPORT STRUTS	20
ENGINE MOUNT CONE	40
BODY-CONE INTERSECTION RING	18
PAYLOAD SUPPORT RING	18
TANKS	45
	<hr/>
	246 LBS

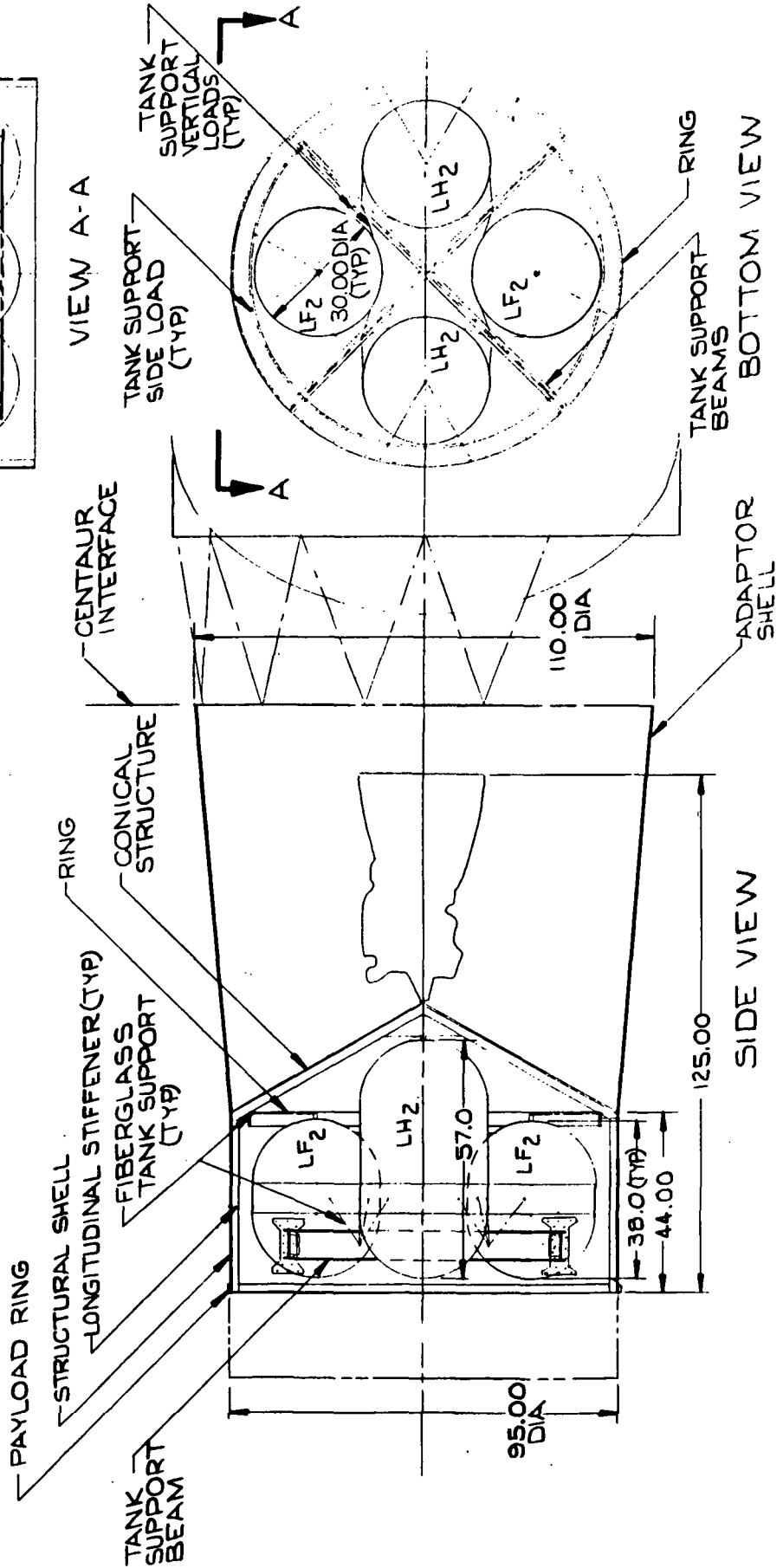
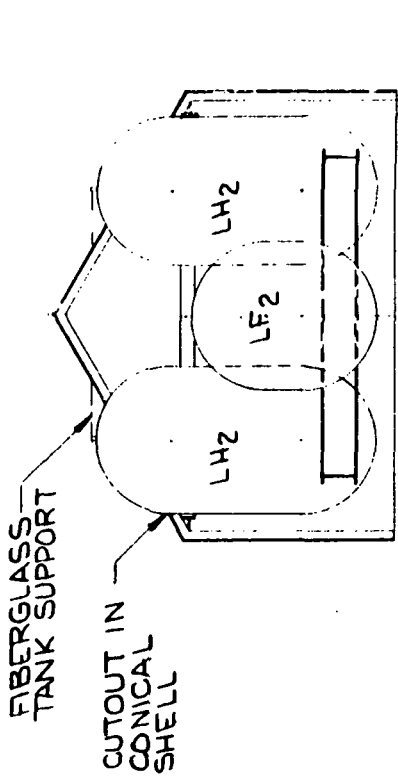


Figure 1.1-8: STRUCTURAL ARRANGEMENT - VEHICLE 1-8

COMPONENT WEIGHTS

P/L SUPPORT RING  
 MID-BODY RING  
 LOWER BODY RING  
 UPPER TRUSS STRUCTURE  
 LOWER TRUSS STRUCTURE  
 ENGINE MOUNT TRUSS STRUCTURE  
 LF<sub>2</sub> TANK SUPPORTS  
 LH<sub>2</sub> TANK SUPPORTS  
 TANKS

20  
 20  
 20  
 20  
 25  
 20  
 5  
 5  
 36  
 171 LBS

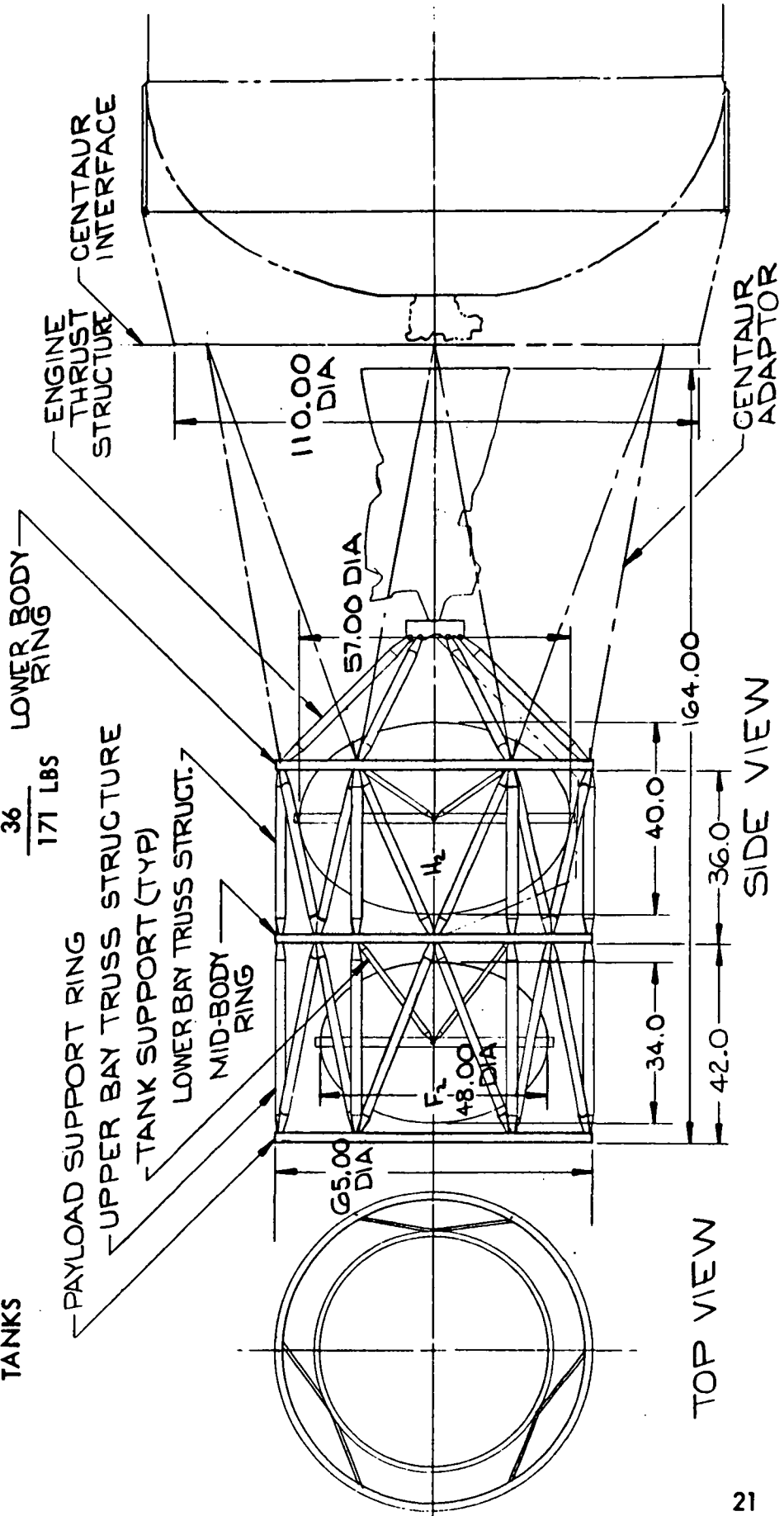


Figure 1.1-9: STRUCTURAL ARRANGEMENT - VEHICLE 1-14

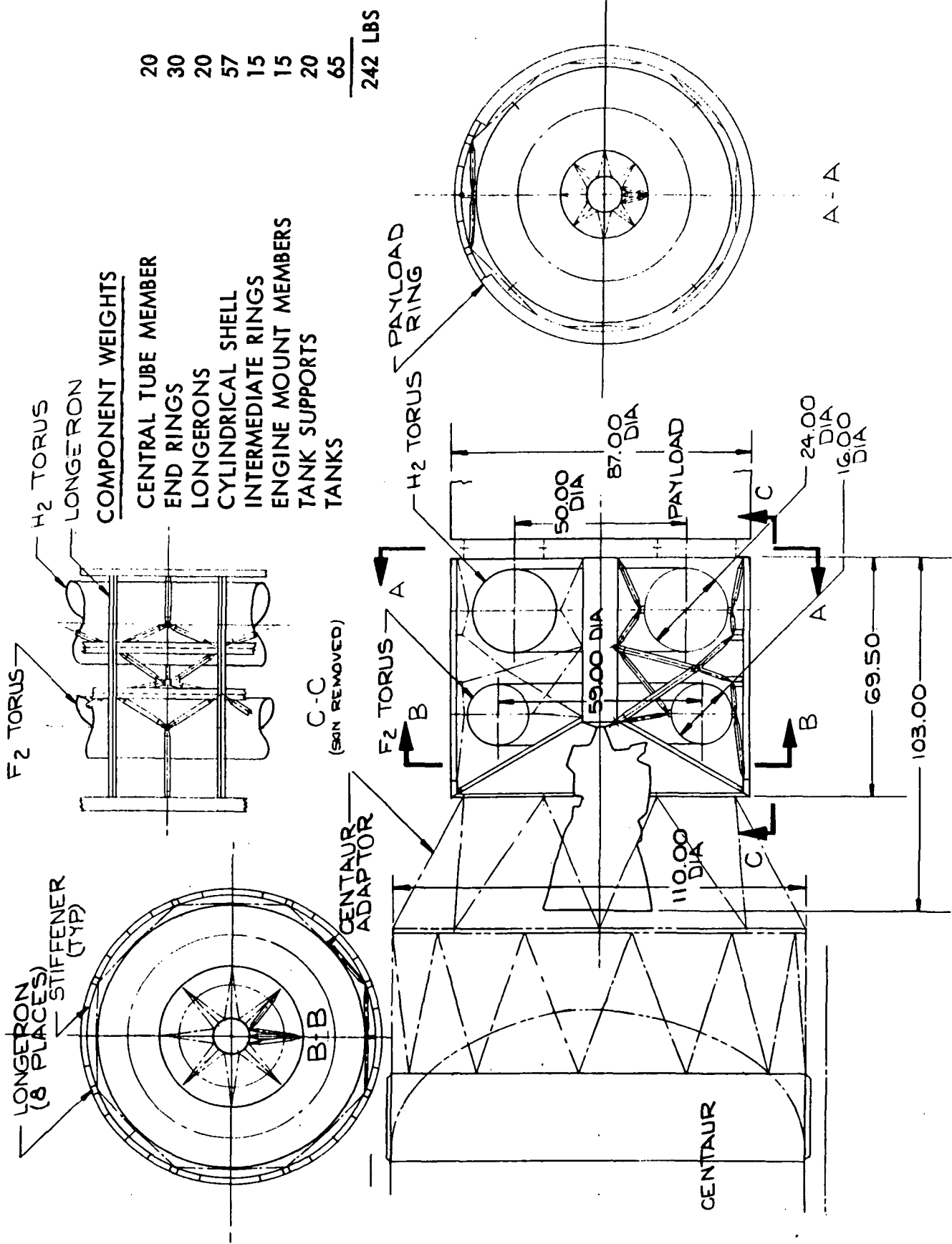


Figure 1.1-10 : STRUCTURAL ARRANGEMENT - VEHICLE 1-20

SIDE VIEW  
(SKIN REMOVED)

COMPONENT WEIGHTS

- FLOX TANK SUPPORTS
- CH<sub>4</sub> TANK SUPPORTS
- ENGINE MOUNT BEAM
- P/L SUPPORT CONICAL SHELL
- P/L SUPPORT RING
- ADAPTOR INTERFACE RING
- TANKS

10	
8	
25	
70	
10	
20	
33	
<hr/>	
176	LBS

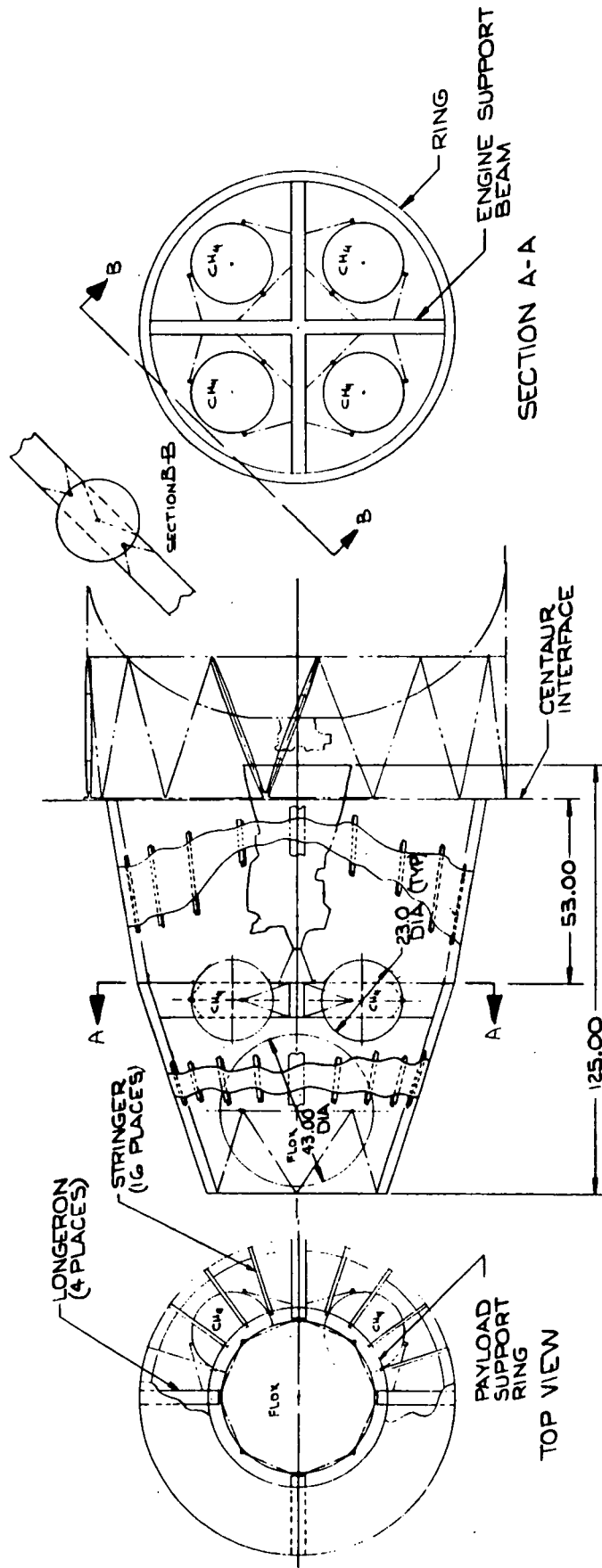


Figure 1.1-11: STRUCTURAL ARRANGEMENT - VEHICLE 2-1

COMPONENT WEIGHTS

UPPER TRUSS (P/L SUPPORT)	20
LOWER TRUSS	10
P/L SUPPORT FRAME	15
MID-FRAME	20
ADAPTOR INTERFACE FRAME	20
CH <sub>4</sub> TANK SUPPORT STRUTS	8
FLOX TANK SUPPORT STRUTS	10
ENGINE MOUNT TRUSS	20
TANKS	32
	<hr/> 155 LBS

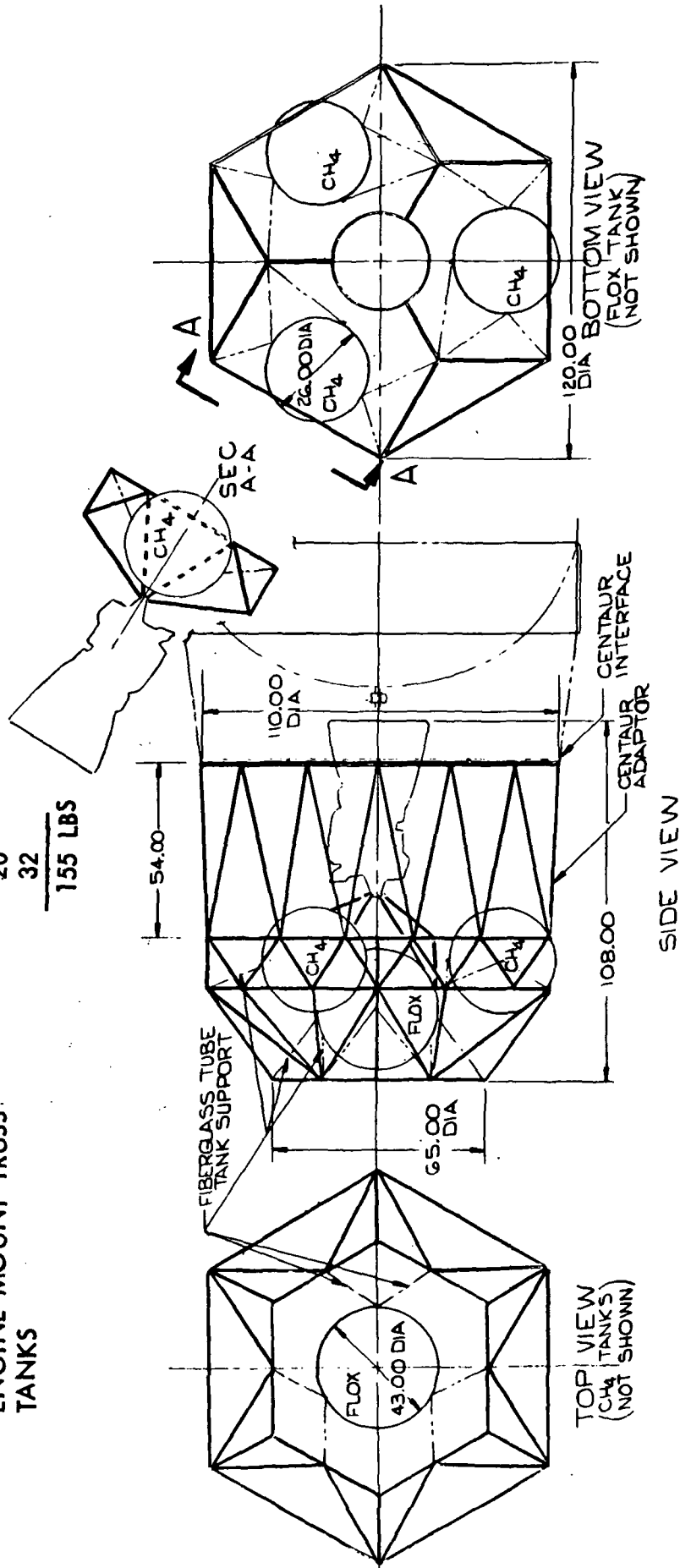


Figure 1.1-12: STRUCTURAL ARRANGEMENT - VEHICLE 2-2

COMPONENT WEIGHTS

- LONGERONS
- INTERMEDIATE RINGS
- END RINGS
- P/L CROSS BEAM
- ENGINE MOUNT BEAMS
- TANK SUPPORTS
- STRINGERS
- TANKS

- 30
- 20
- 30
- 20
- 25
- 15
- 15
- 41

196 LBS

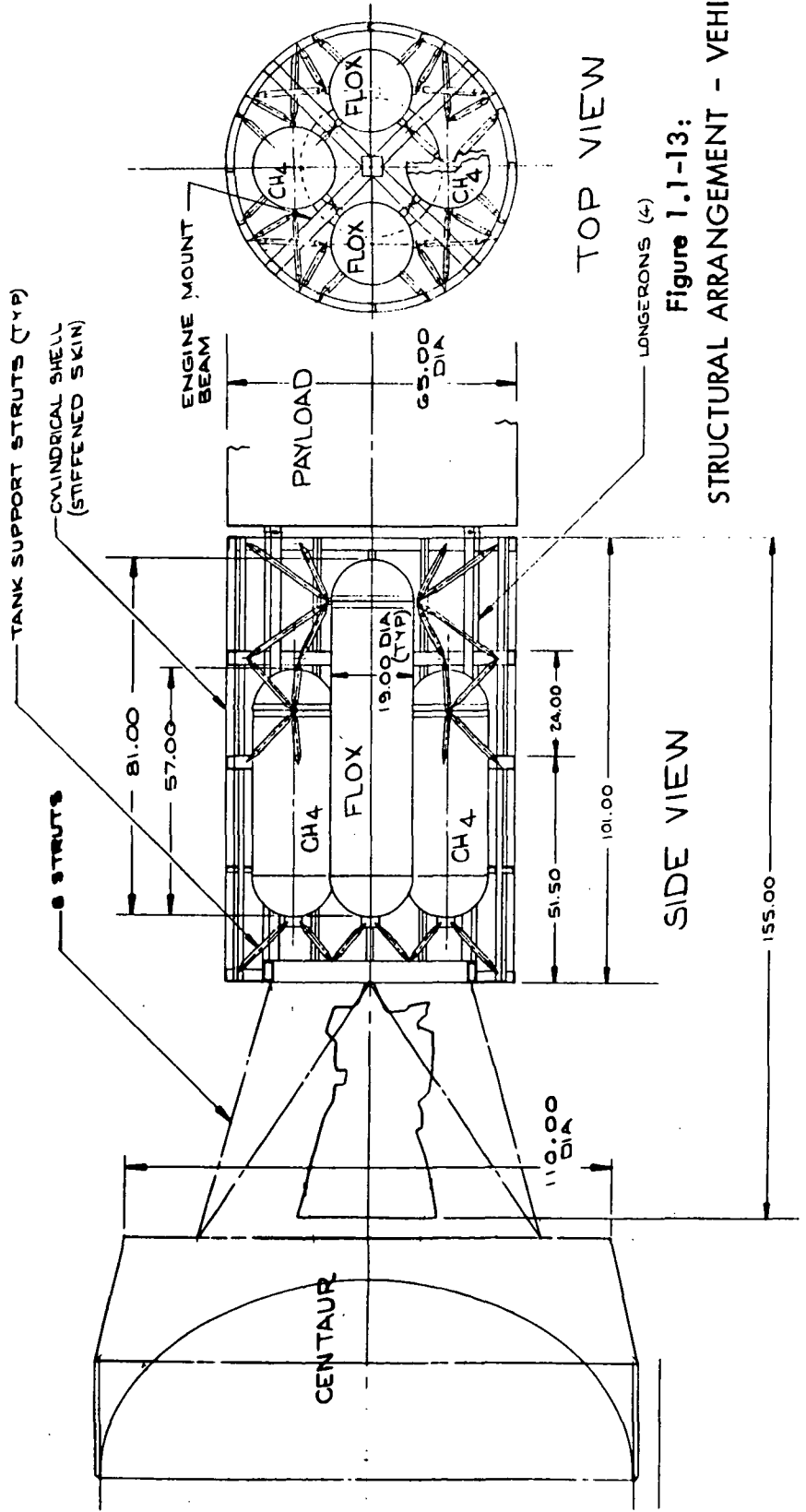


Figure 1.1-13:

STRUCTURAL ARRANGEMENT - VEHICLE 2-8

COMPONENT WEIGHTS

P/L SUPPORT VERTICAL STRUTS	5
TRIANGULAR FLOX SUPPORT FRAME	85
ENGINE MOUNT TRUSS	45
P/L DIAGONAL SUPPORT STRUTS	5
CH <sub>4</sub> SUPPORT TRUSSWORK	25
P/L SUPPORT TRIANGULAR FRAME	20
TANK SUPPORTS	18
TANKS	34
	<hr/>
	237 LBS

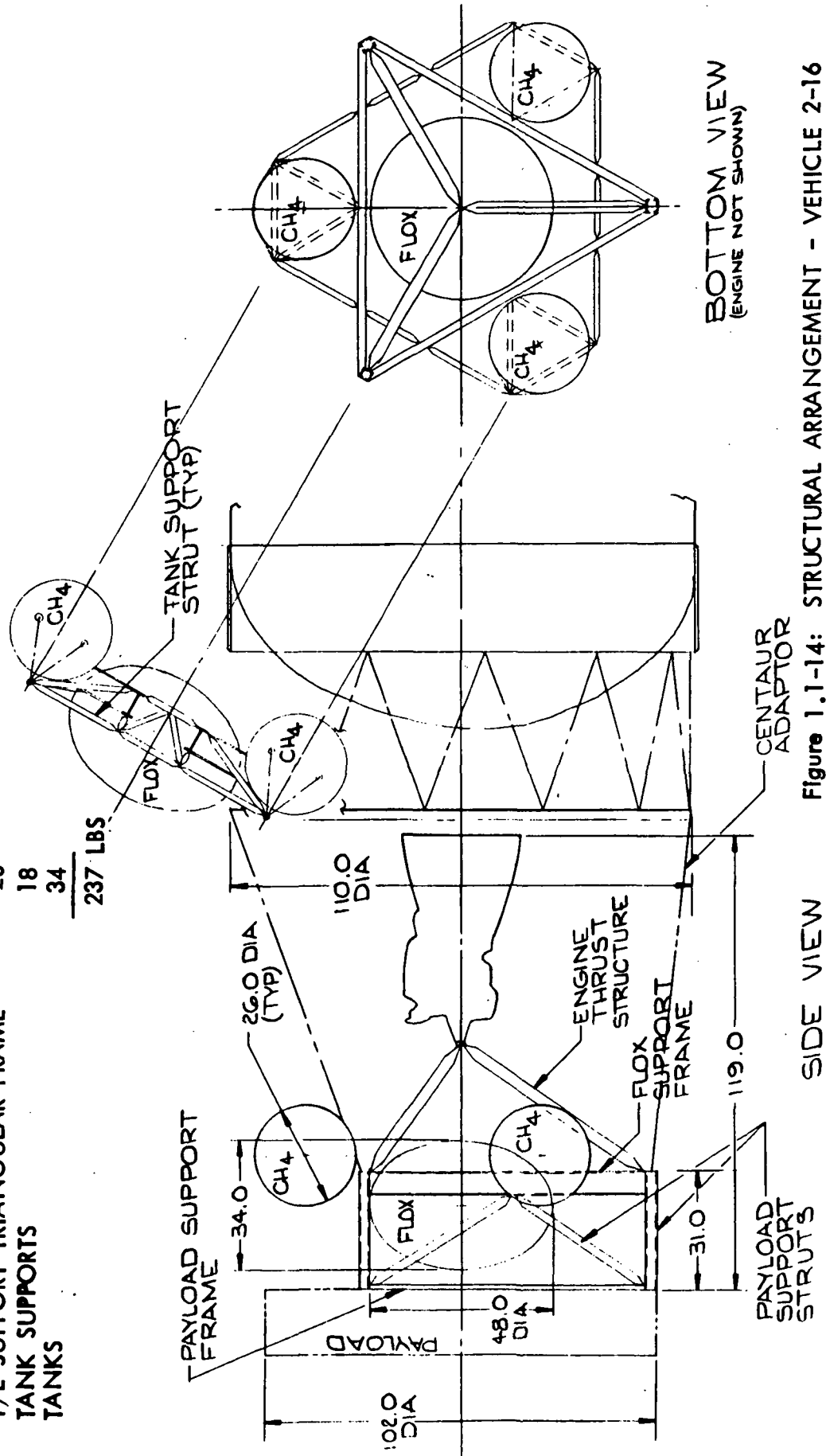


Figure 1.1-14: STRUCTURAL ARRANGEMENT - VEHICLE 2-16

COMPONENT WEIGHTS

- BODY SKIN
- CONICAL ENGINE SUPPORT
- BODY INTERFACE RING
- P/L SUPPORT TRUSS
- P/L SUPPORT RING
- TANKS

- 40
- 20
- 15
- 15
- 10
- 35

135 LBS

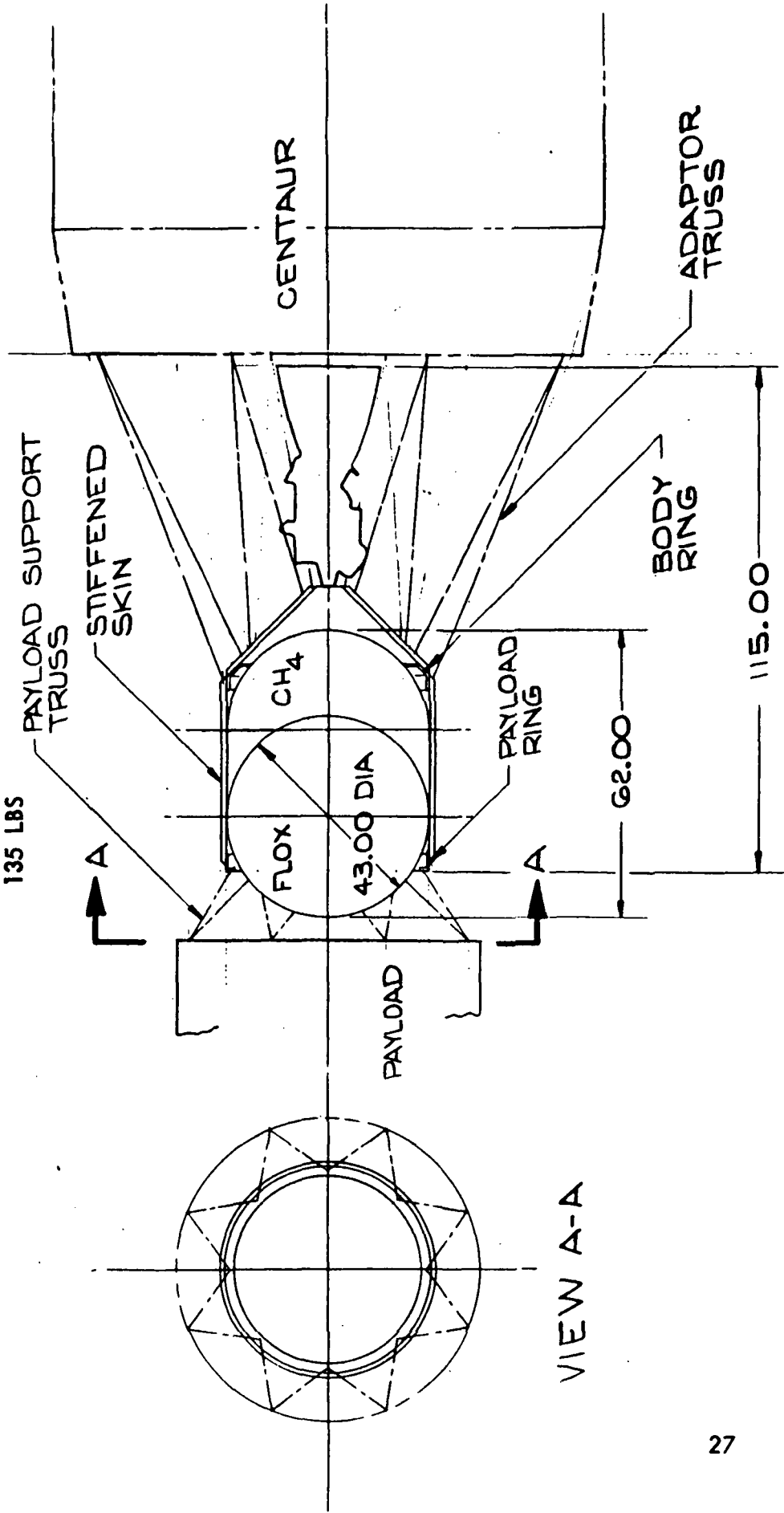


Figure 1.1-15 : STRUCTURAL ARRANGEMENT - VEHICLE 2-18

COMPONENT WEIGHTS

BODY SKIN	40
CONICAL ENGINE SUPPORT	20
BODY INTERFACE RING	15
P/L SUPPORT TRUSS	15
P/L SUPPORT RING	10
TANKS	46
	<hr/>
	146

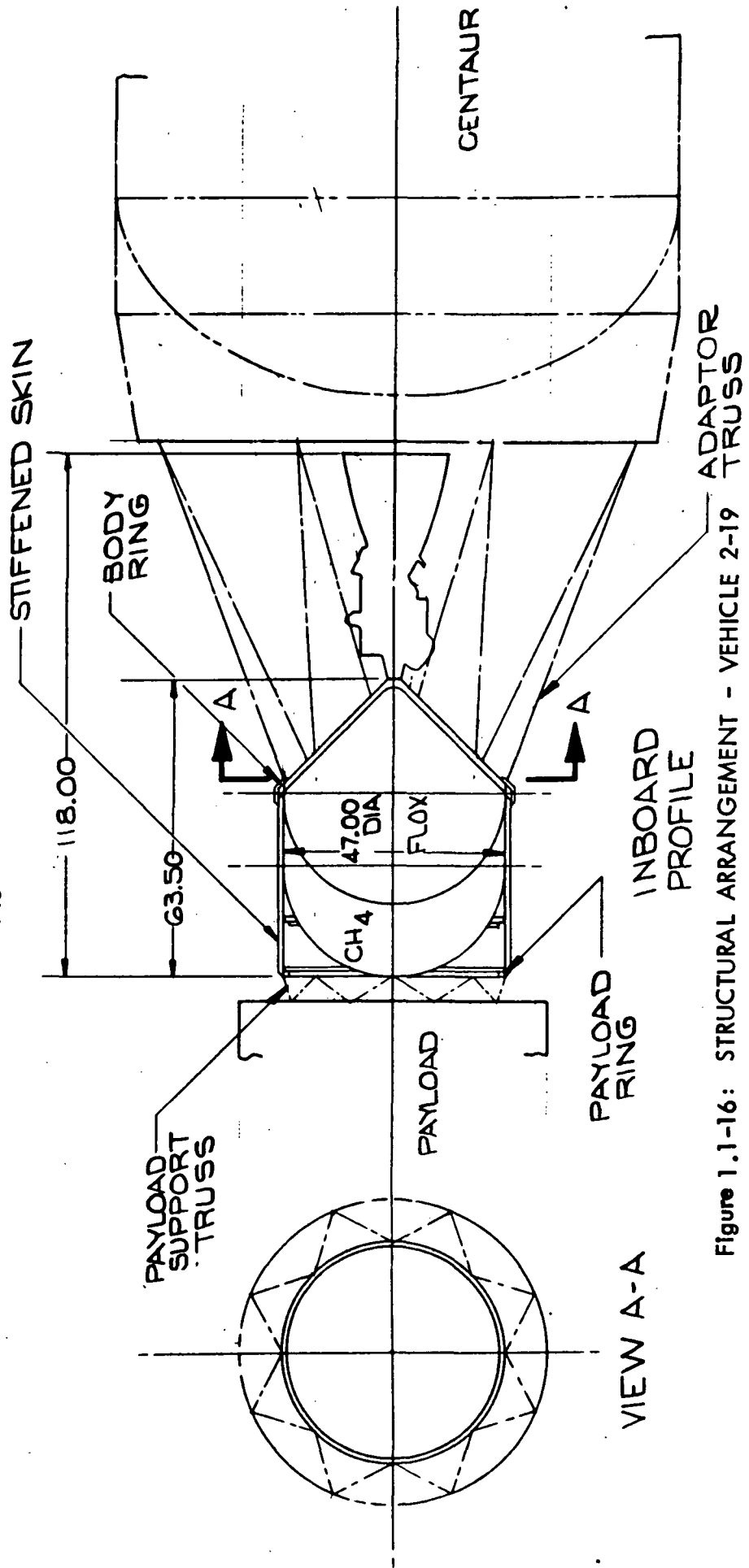


Figure 1.1-16: STRUCTURAL ARRANGEMENT - VEHICLE 2-19

COMPONENT WEIGHTS

OUTER TRUSS STRUCTURE

P/L SUPPORT BEAM FRAME

CH<sub>4</sub> TANK SUPPORTS

FLOX TANK SUPPORTS

ENGINE TRUSS STRUCTURE

ADAPTOR INTERFACE FRAME

TANKS

- 10
- 10
- 13
- 9
- 9

9

20

26

9

40

155 LBS

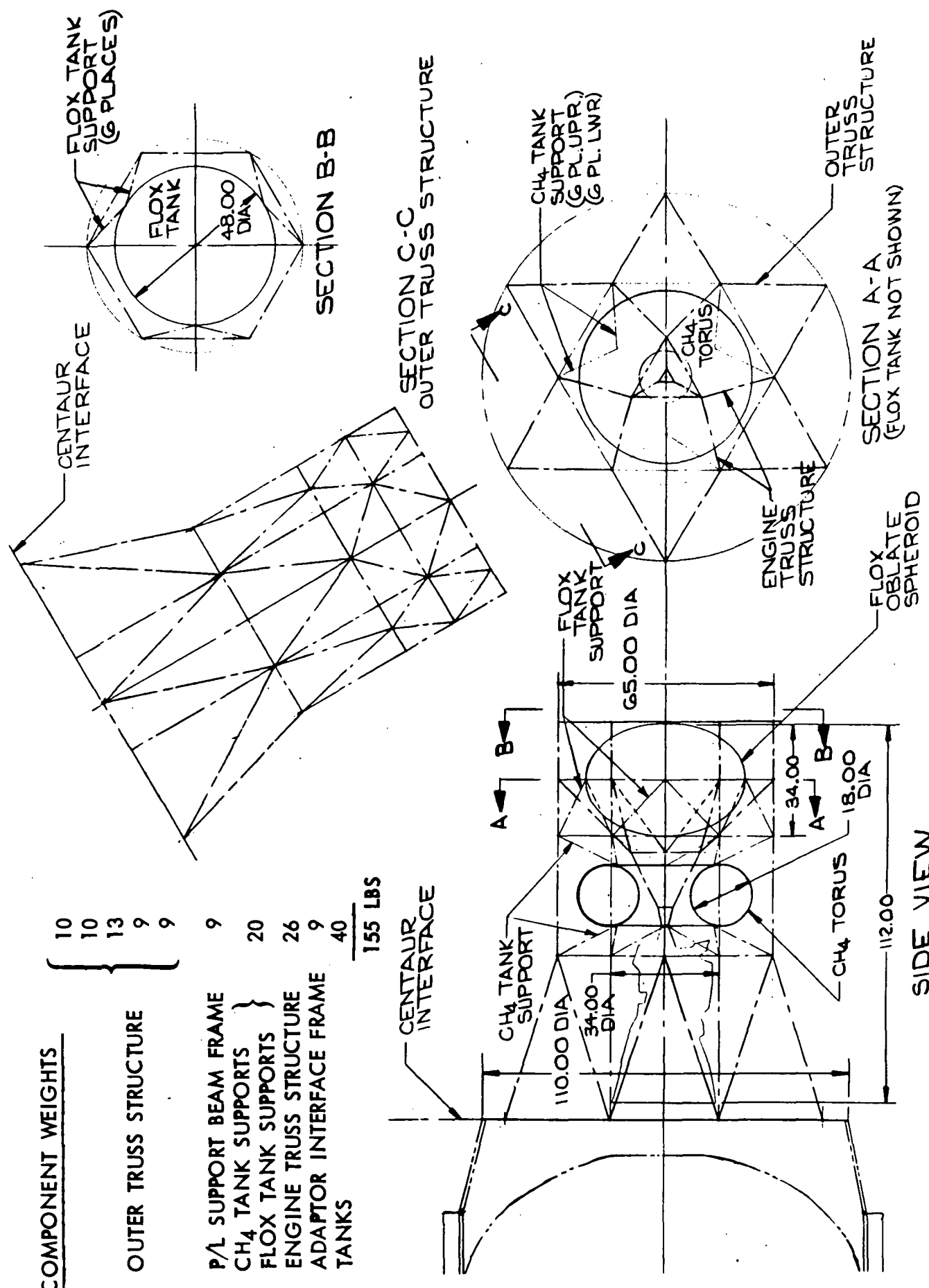


Figure 1.1-17: STRUCTURAL ARRANGEMENT - VEHICLE 2-20

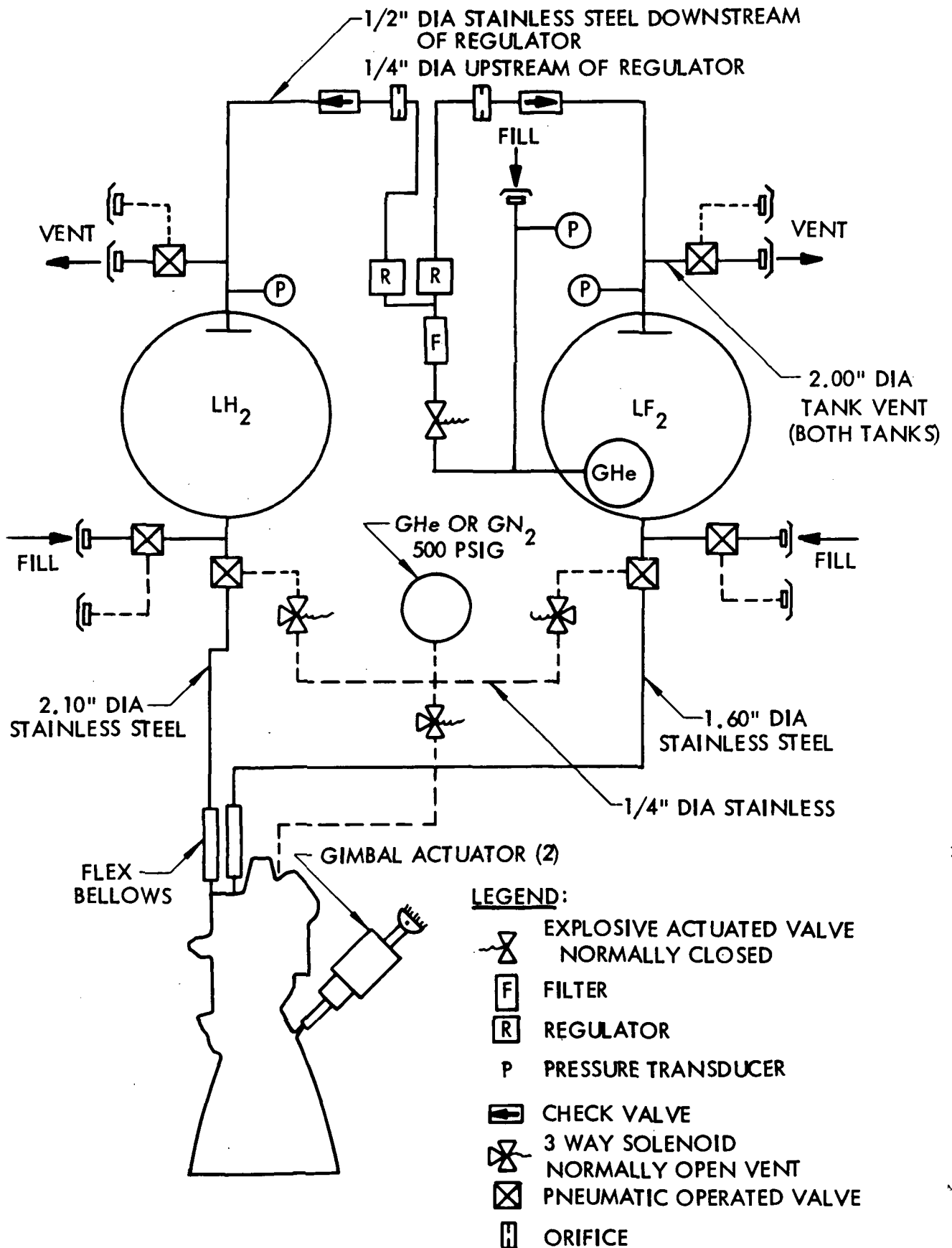


Figure 1.1-18: PROPELLANT FEED SYSTEM CONCEPT - INDIVIDUAL TANKAGE

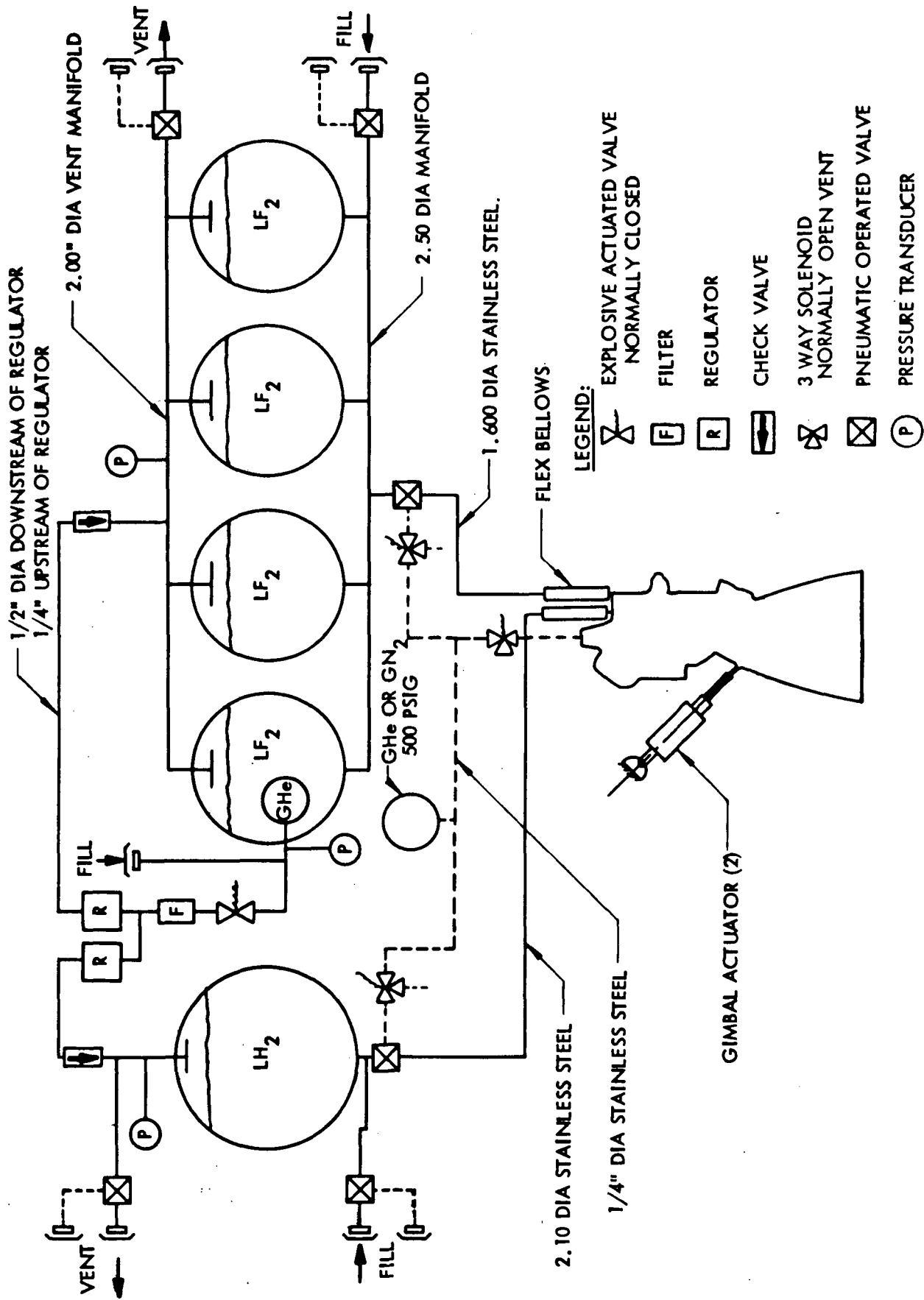


Figure 1.1-19: PROPELLANT FEED SYSTEM CONCEPT - MANIFOLDED TANKAGE

3. The helium gas pressurant for propellant expulsion was stored in  $LF_2$  or  $CH_4$  tanks. The cryogenic temperatures resulted in minimum vessel weight and storage in the warmer of the two cryogen tanks eliminated the need for a heat exchanger for conditioning the pressurant.
4. Helium or nitrogen gas for valve actuation was stored in a separate bottle, external to the cryogen tanks. The high pressure needs of valve actuators and low pressures of propellant tanks necessitated a two stage regulator if common pressurant storage was employed. With the approach selected, no regulator is needed in the "blow down" valve actuation supply system since the quantity of pressurant required is small. It was assumed that the valves operated only once during the mission.
5. Separate pressure regulators were necessary for the fuel and oxidizer sides of the propellant supply system. This approach was selected because natural pressure rise will differ between cryogens, thus a single regulator results in an unwarranted tank weight penalty for one system.

A preliminary weight statement for the propellant feed system components is presented in Table 1.1-3. Several component weights were estimated from parametric trend data assembled from various valve manufacturers, therefore, the total weight was only an approximation. Manifolding the four  $LF_2$  tanks together had a minor effect on system weight, thus the main disadvantages of multiple tank storage were in (1) providing thermal protection for the "wet" lines and manifold and (2) the operational complexity, i.e. assembly, leak checking and repair, and reduced reliability associated with multiple plumbing joints. The weight of the feed and pressurization system was not used in determining structural loads or ranking of the vehicle concepts at this stage of the study because of the slight differences noted.

### Vehicle Concept Ranking

Propulsion vehicle concepts were ranked on the basis of (1) weight trends, (2) operational complexity, and (3) thermal isolation complexity. The  $LH_2/LF_2$  and FLOX/ $CH_4$  vehicle evaluations were conducted independently. An objective of this ranking was to retain variety in the configurations selected.

Weight trends were given the highest priority in the evaluation. Thermal isolation and operational complexity had equal but lesser importance. A point system was assigned these latter two items to obtain a quantitative appraisal. The point system is described below. A high point value assignment indicated the best design.

WEIGHTS IN LBS (KILOGRAMS)  
 DIMENSIONS IN INCHES (METERS)

Table 1.1-3: - FEED SYSTEM WEIGHT SUMMARY  
 CONCEPT 1-1 (4 LF<sub>2</sub> TANKS)

FEED SYSTEMS		61.5 (27.9)
LF <sub>2</sub> Feed Lines	12.7 (5.77)	
LF <sub>2</sub> Manifold	8.5 (3.86)	
LH <sub>2</sub> Feed Lines	2.2 (.99)	
Fittings	14.9 (6.76)	
Gimbal Bellows	9.2 (4.18)	
LF <sub>2</sub> Shutoff Valve	7.6 (3.45)	
LH <sub>2</sub> Shutoff Valve	6.4 (2.91)	
FILL & DRAIN 1" (.0254)		17.0 (7.7)
Lines	4.2 (1.9)	
Fittings	1.8 (.82)	
Quick Disconnects 1/2 (.0127)	5.2 (2.4)	
Fill Valve	5.8 (2.6)	
PNEUMATIC CONTROL SYSTEM		16.0 (7.2)
Bottle Instl.	10.0 (4.5)	
Helium	1.0 (.45)	
Lines & Fittings	2.5 (1.14)	
Solenoid Valves (3)	2.5 (1.14)	
PRESSURIZATION SYSTEM HARDWARE *		51.5 (23.38)
LF <sub>2</sub> Vent Manifold 2" (.0508)	5.0 (2.27)	
LF <sub>2</sub> Press Lines 1/2" (.0127)	2.8 (1.27)	
LH <sub>2</sub> Press Line 1/2" (.0127)	0.7 (.32)	
LH <sub>2</sub> Vent Line 1" (.0254)	2.5 (1.14)	
Supply Lines	0.6 (.27)	
Fittings	10.0 (4.5)	
1/4" N.C. Squib (1)	0.7 (.32)	
Filter (1)	1.0 (.45)	
Pressure Regulator & Relief (2)	7.5 (3.4)	
Check Valves 1/2" (.0127)	1.2 (.55)	
LH <sub>2</sub> Vent Valve 1" (.0254)	4.3 (1.95)	
LF <sub>2</sub> Tanks Vent Valve 2" (.0508)	9.0 (4.09)	
Vent Quick Disconnects (2)	5.0 (2.27)	
Pneumatic Quick Disconnects (2)	1.2 (5.45)	
SUPPORTS (20%)		29 (13.2)
TOTAL		175 (79.5)

\* Does not include helium, helium bottle installation or Tank pressurant deflector installations.

### Operational Complexity

<u>Ranking Items in Increasing Order of Importance</u>	<u>Points Available</u>
1) Distance from C.G. to gimbal point	1 - 8
2) Tank quantity	9 - 16
3) Tank accessibility	17 - 24

### Thermal Isolation Complexity

<u>Ranking Items in Increasing Order of Importance</u>	<u>Points Available</u>
1) Minimum tank supports	1 - 8
2) Prelaunch thermal protection	9 - 16
3) Tank isolation from payload	17 - 24
4) Oxidizer isolation from fuel (LH <sub>2</sub> /LF <sub>2</sub> only)	17 - 24

A description of the ranking items follows:

The distance from vehicle C.G. to the gimbal point was important in terms of vehicle maneuvering capability. A long distance was favored.

Tank quantity influenced such operational factors as ullage management, filling, residuals, pressurization and manifolding. A minimum number of tanks was favored.

Tank accessibility was important for modifications, removal or inspection. Accessibility from the outside of the vehicle without removal of other tanks or structure was favored.

A minimum number of fiberglass tank supports was desirable to reduce heat transfer. The number and location of tank supports was dictated by tank size and location of vehicle "hard points" in some instances.

The ease of providing prelaunch thermal protection and non-condensing purge gas supply was important. Simplicity in routing purge lines, compartment isolation and evacuation of compartments during ascent were favored.

The payload comprised the major source of radiative heating to the propellants. A small vehicle diameter with a minimum of tankage surface area in view of the payload was favored.

Thermal isolation of  $\text{LH}_2$  from  $\text{LF}_2$  was important because of their large temperature difference. A minimal surface area between tanks and availability of structure for mounting internal thermal protection blankets was desirable.

The vehicle concept ranking results are summarized in Table 1.1-4. Weight trends are listed first in the table and a numerical ranking value assigned to each. The least weight design received the highest rank (1). For the  $\text{LH}_2/\text{LF}_2$  propellants, this design was Vehicle 1-14. Vehicles 1-7 and 1-3 were nearly the same weight and were ranked second and third. Vehicle 1-1 had a heavy engine thrust structure and a stiffened cylindrical shell which caused it to be rated fourth. Vehicles 1-20, 1-8 and 1-6 all had stiffened skin shell structures which resulted in greater weights. Vehicle 1-6 was particularly heavy because of the payload support cone.

For the  $\text{FLOX}/\text{CH}_4$  propellants, Vehicles 2-18 and 2-19 with common bulkheads were the least weight and were ranked first and second. Vehicle 2-16 was the heaviest because of the  $\text{FLOX}$  tank support beam arrangement.

The operational and thermal isolation complexity rankings follow weight rankings in Table 1.1-4. The conclusion from this evaluation for  $\text{LH}_2/\text{LF}_2$  propellants was that Vehicles 1-14 and 1-7 were the least complex and all the others were about comparable in complexity. The common bulkhead tank configurations 2-18 and 2-19 rated high for  $\text{FLOX}/\text{CH}_4$  propellants. Vehicles 2-2, 2-1, 2-8 and 2-16 were about equally complex, but with more disadvantages than Vehicle 2-18. Vehicle 2-20 was ranked the lowest.

Five  $\text{LH}_2/\text{LF}_2$  and five  $\text{FLOX}/\text{CH}_4$  vehicle concepts were selected for further evaluation as a result of the ranking effort. Some choices were obvious, for example Vehicles 1-14, 1-7 and 2-18. Vehicle 1-6 was eliminated because of weight. Vehicle 1-8 was eliminated because of weight and similarity to Vehicle 1-3. Vehicles 1-3, 1-1 and 1-20 were retained because they were third, fourth and fifth in order of weight and represented distinctly different vehicle configurations. For the  $\text{FLOX}/\text{CH}_4$  designs, Vehicle 2-19 was eliminated because of similarity to 2-18. Vehicle 2-20 was eliminated due to complexity and instead, Vehicle 2-14 with  $\text{CH}_4$  above the  $\text{FLOX}$  was substituted. This change was made because of the favorable rating received by Vehicle 1-14. Vehicle 2-1 was retained because it was similar to Vehicles 2-2 and 2-16 and represented a multi-tank configuration. Vehicle 2-8 was retained but converted to spherical tankage (2-3) because it appeared to be a good choice for  $\text{LH}_2/\text{LF}_2$  propellants and it was representative of a different vehicle configuration. A new configuration, Vehicle 2-7, was introduced as the fifth choice because of the favorable rating received by Vehicle 1-7.

The final selections are illustrated in Figure 1.1-20. The tank arrangement screening phase was not expected to yield firm conclusions on the best choice of vehicle concepts due to the preliminary nature of the evaluation. Some

Table 1.1-4: VEHICLE CONCEPT RATING

CONCEPTS	LH <sub>2</sub> /LF <sub>2</sub>										FLOX-CH <sub>4</sub>											
	1-1	1-3	1-6	1-7	1-8	1-12	1-14	1-15	1-16	1-20	2-1	2-2	2-3	2-8	2-11	2-12	2-13	2-15	2-16	2-18	2-19	2-20
TANKS	43 (19.5)	44 (20.0)	44 (20.0)	46 (20.8)	45 (20.4)	44 (20.0)	36 (16.3)	44 (20.0)	42 (19.1)	65 (29.5)	33 (14.9)	32 (14.5)	33 (14.9)	41 (18.6)	35 (15.9)	38 (17.3)	42 (19.1)	36 (16.4)	34 (15.4)	35 (15.9)	46 (20.9)	40 (18.2)
TANK SUPPORT STRUCTURE	24 (10.9)	125 (56.8)	10 (4.54)	15 (6.8)	50 (22.7)		10 (4.54)			20 (9.08)	18 (8.2)			15 (6.8)					128 (58.1)	0	0	20 (9.08)
STRUCT. SHELL, ENG. THRUST & PAYLOAD SUPRT.	145 (65.8)	10 (4.54)	247 (112.2)	111 (50.3)	151 (68.6)		125 (56.8)			157 (71.3)	125 (56.8)	105 (47.7)		140 (63.6)					75 (34.1)	100 (45.4)	100 (45.4)	95 (43.1)
TOTAL WEIGHT	212 (96.3)	179 (81.3)	301 (136.7)	172 (78.1)	246 (111.7)		171 (77.6)			242 (109.9)	176 (79.9)	155 (70.4)		196 (89)					237 (107.6)	135 (61.3)	146 (66.3)	155 (70.4)
NUMERICAL RANK	4	3	7	2	6		1			5	5	4		6					7	1	2	3
TANK QTY.	10	13	12	14	13		16			13	11	13		13					13	16	13	10
ACCESS	17	22	18	23	22		20			19	22	22		24					22	19	19	17
LONG C.G. TO GIMBAL DIST.	8	5	7	6	6		8			4	5	4		6					4	7	4	4
TOTALS	35	40	37	43	41		44			36	38	39		43					39	42	36	31
TANKS FROM PAYLOAD	20	20	23	22	20		24			20	22	23		20					22	24	24	20
TANKS FROM EACH OTHER (LH <sub>2</sub> -LF <sub>2</sub> )	22	19	22	23	19		24			20												
MINIMUM TANK SUPPORTS	4	5	5	7	5		8			6	5	5		4					5	8	8	6
PRELAUNCH THERMAL PROTECT.	11	13	12	16	13		16			14	11	11		9					11	16	16	12
TOTALS	57	57	62	68	57		68			60	38	39		33					38	48	48	38
TOTALS (OPERATIONAL COMPLEXITY & THERMAL ISOLATION)	92	97	99	111	98		112			96	76	78		76					77	90	84	69
NUMERICAL RANK	7	5	3	2	4		1			6	5	3		6					4	1	2	7

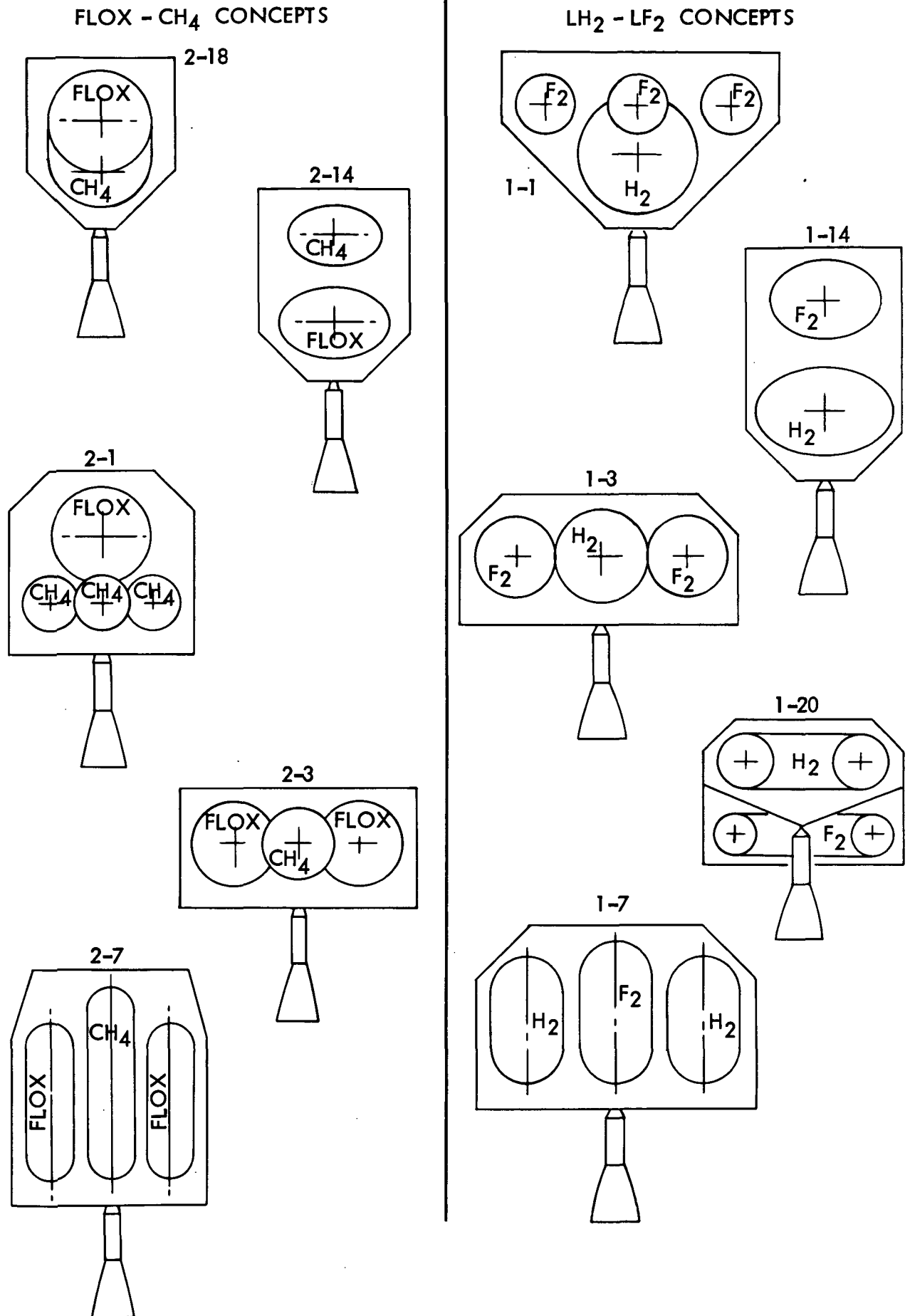


Figure 1.1-20 : TANK ARRANGEMENT CONFIGURATION SELECTION

definite trends were established, however. The configurations with two oblate spheroid tanks (1-14) and the common bulkhead tankage for FLOX/CH<sub>4</sub> propellants offered the most advantages. The choice of vehicle concepts shown in the figure was influenced by the need for retaining configurations which presented a variety of external shapes, thus allowing a thorough evaluation of advantages or disadvantages in integrating the thermal/meteoroid protection/structural systems.

### 1.1.2 Tank Arrangement Thermal Efficiency

A tank arrangement thermal efficiency study was conducted with the configurations defined in Figure 1.1-20. The study was initiated by assigning MLI (Multilayer Insulation) blanket locations to each design sketch. Typical blankets were those which separated the payload from the tankage and oxidizer from fuel tanks. A radiation view factor calculation program was utilized to find view factors for the configurations. These were used to determine boundary temperatures which were subsequently employed in another program to calculate radiation heat balance and optimize insulation thicknesses in all locations of a given vehicle configuration. Steady state heat flow was determined parametrically as a function of insulation thickness. The calculations included only the radiant interchange and conduction through the MLI thickness. Structure and penetration heat flow were not included because of the limited time available for this phase of the study and the large number of analyses required. Propellant temperatures were held constant at one-atmosphere values for this study, since the most efficient heat balance was one in which there was no propellant pressure rise.

The computer aided optimization program which was developed was entitled TATE (Tank Arrangement Thermal Efficiency). This program randomly selected insulation thicknesses and calculated heat flow to and from the propellants. It also determined tank pressure rise, tank dimensions and weight, insulation weight, helium pressurant and helium tank weight, and residual propellant vapor weight. The program saved and printed out the five least-weight cases out of 10,000 random selections for each vehicle configuration. These results were only relative, allowing identification of advantages and disadvantages of each arrangement, but not true weights. A detailed explanation of the program is contained in Appendix A located in Volume II, NASA CR-121104.

The MLI used in the analyses was 15 gage (0.15 mil) double aluminized mylar with nylon net spacers. The layer ratio was 70 shields per inch and the density was 3.25 lbs/ft<sup>3</sup> (0.052 gm/cm<sup>3</sup>).

Propellant tanks were assumed to be 2219-T6E46 aluminum alloy. The helium pressurant tank was assumed to be 301 stainless steel with a 5000 psia (34,474 kN/m<sup>2</sup>) design limit pressure. The helium tank was stored within the warmer of the two tanks (CH<sub>4</sub> and F<sub>2</sub>) for each propellant combination. The appropriate

cryogenic material properties from Boeing design manuals were used in determining tank gages.

The solar panel and antenna sizes selected for the study were typical of those used in the Viking project. The configuration is shown in Figure 1.1-21. Payload diameter was a variable depending upon propulsion vehicle tank configuration and arrangement, therefore, the solar panels and antenna were assumed to retain their position relative to the edge of the vehicle. The lower surface temperature of these appendages was assumed to be  $520^{\circ}\text{R}$  ( $289^{\circ}\text{K}$ ) and the emittance was 1.0. This thermal environment was considered constant throughout the entire 208 day mission.

Figures 1.1-22 and 1.1-23 show typical thermal models of the one  $\text{LH}_2/\text{LF}_2$  vehicle concept. In this case, the thermal efficiency of tank arrangements was evaluated in normal and inverted positions. The sketches show MLI panel locations, the thicknesses selected by the program and the external temperatures obtained by the heat balance analysis. Emissivity values for the various surfaces are also shown. A value of 0.2 was used for aluminum tankage, 0.4 for sidewall and aft facing surfaces, 0.05 for the exterior of the MLI facing the heat source and 0.03 for the interior of the MLI.

Figures 1.1-24 and 1.1-25 are printouts from the TATE program for the two vehicles discussed in the preceding paragraph. In addition to the information shown on Figures 1.1-22 and 1.1-23 these printouts give data on tank pressures and wall thickness, heat flow and component weights. In all but one case the tank wall thicknesses derived were less than the 0.025 in (0.064 cm) minimum fabrication limit. Tank design pressures were obtained by adding the NPSP, 8 psi ( $55.2 \text{ kN/m}^2$ ) for the fuel, 12 psi ( $82.7 \text{ kN/m}^2$ ) for the oxidizer, to the vapor pressure and multiplying by a factor of 1.25. This pressure was used to calculate the wall thickness, based on the yield strength of the material.

The results of the study are shown graphically in Figures 1.1-26 and 1.1-27. Figure 1.1-27 includes two graphs, one representing  $\text{FLOX}/\text{CH}_4$  with insulation separating the fuel and oxidizer and one without insulation between the tanks. In the latter case a propellant equilibrium temperature of  $170^{\circ}\text{R}$  ( $94.4^{\circ}\text{K}$ ) was maintained.

For the  $\text{LH}_2/\text{LF}_2$  vehicles, the configuration using two oblate spheroid tanks (1-14) was the most efficient regardless of tank arrangement. Vehicle 1-1 with the  $\text{LH}_2$  tank forward was also very efficient. This was due to the small heat flow to the hydrogen on the conical surface because of the open configuration and the large base area for heat rejection resulting in low  $\text{LF}_2$  tank pressures.

The two-oblate spheroid configuration (2-14) was also the most efficient for the  $\text{FLOX}/\text{CH}_4$  vehicles, followed by the common bulkhead concept, 2-18. Vehicle 2-1 was evaluated in two configurations. The inverted position, with the  $\text{FLOX}$

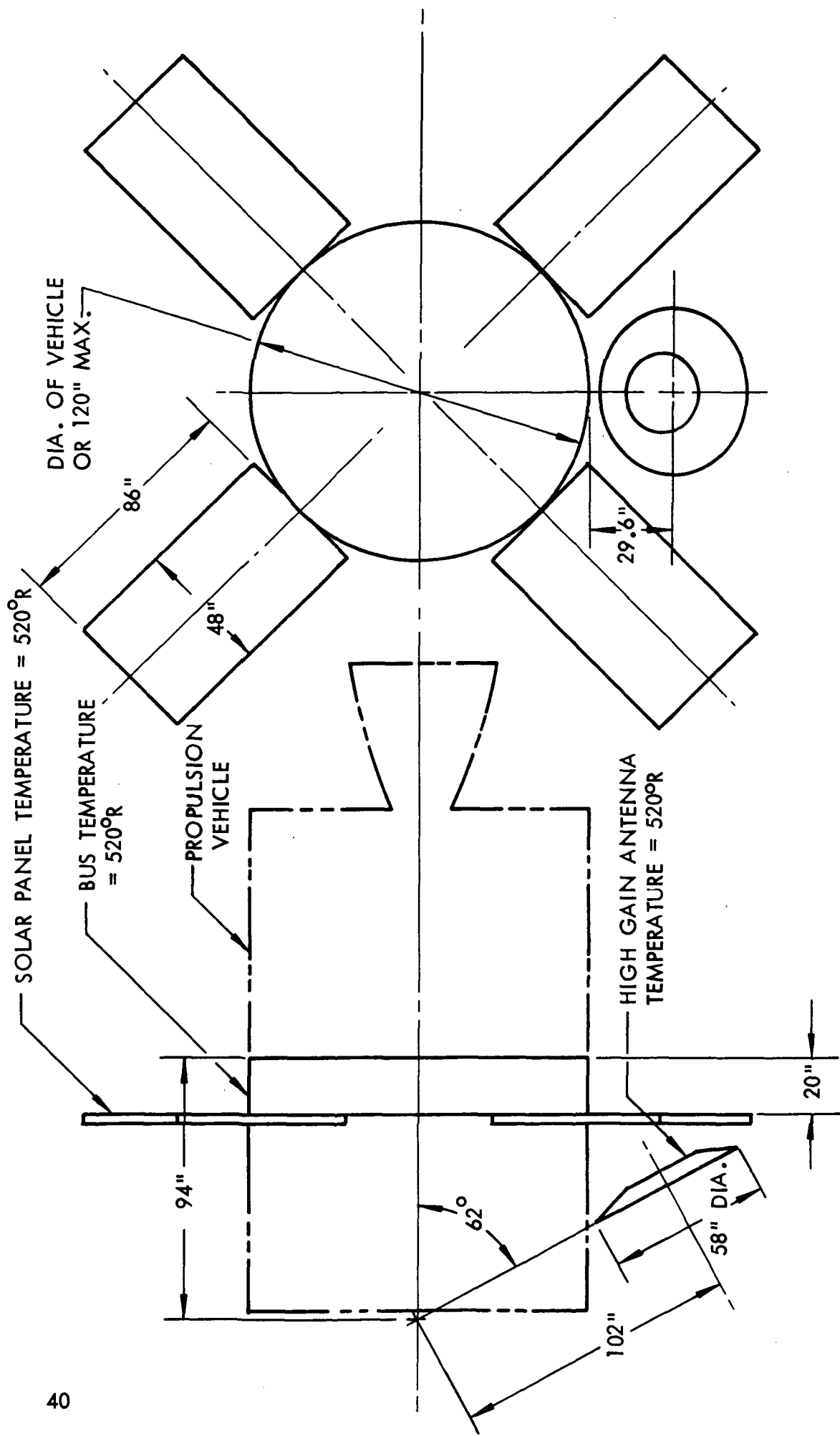


Figure 1.1-21: - PAYLOAD DEFINITION

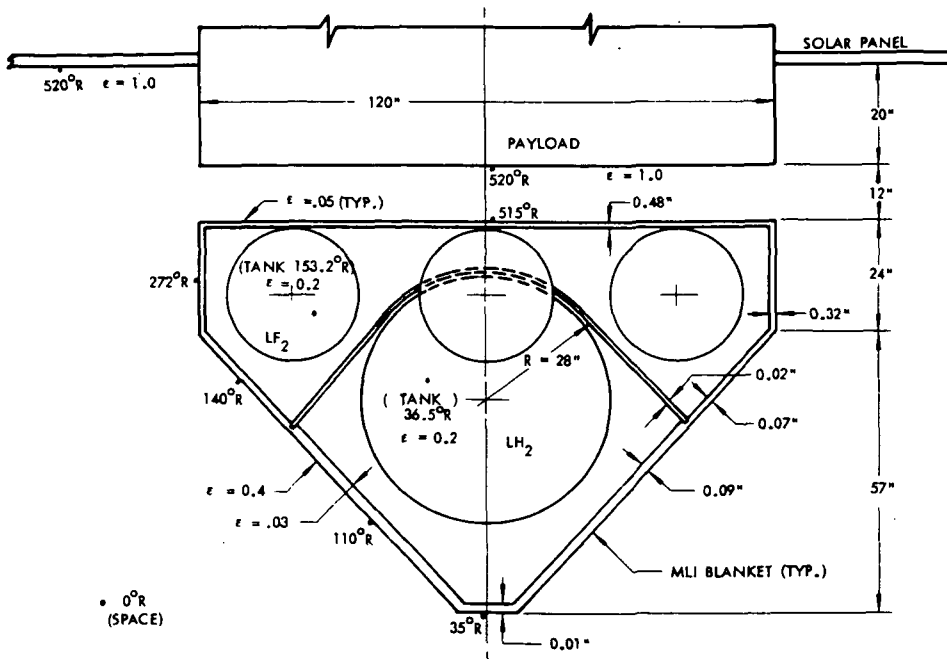


Figure 1.1-22: THERMAL MODEL VEHICLE 1-1

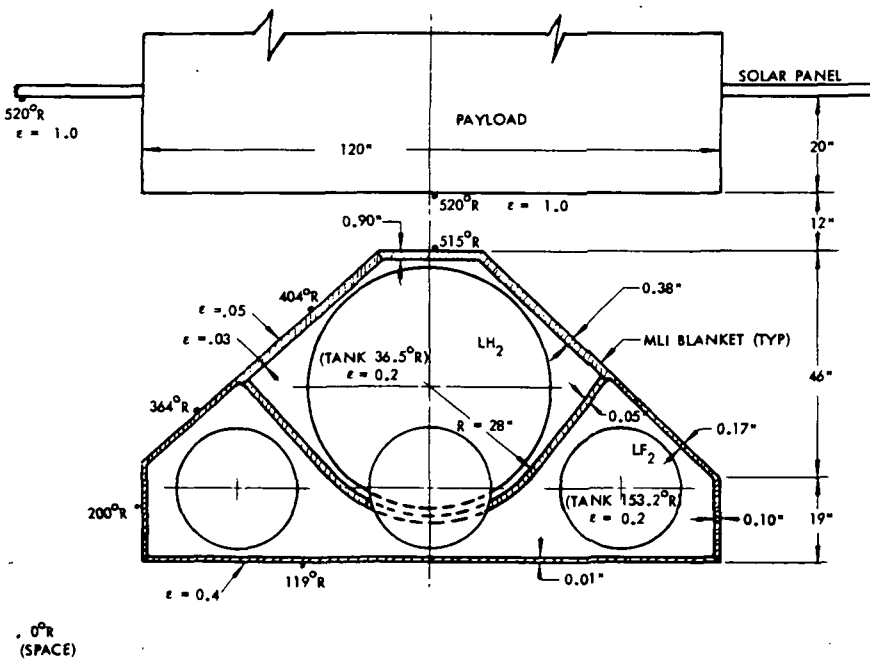


Figure 1.1-23: THERMAL MODEL VEHICLE 1-1 (INVERTED)

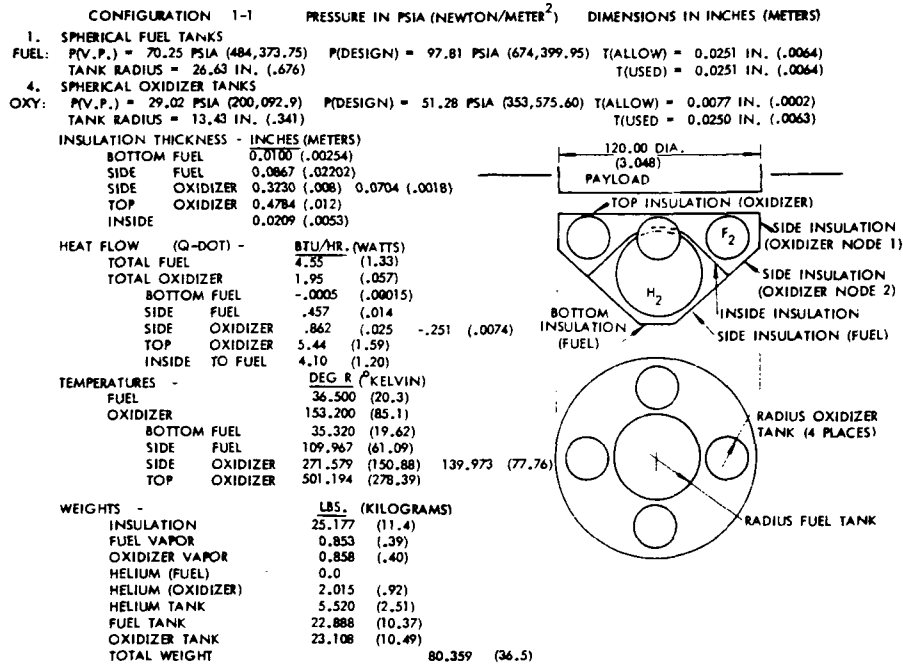


Figure 1.1-24: THERMAL PROGRAM PRINTOUT DATA - VEHICLE 1-1

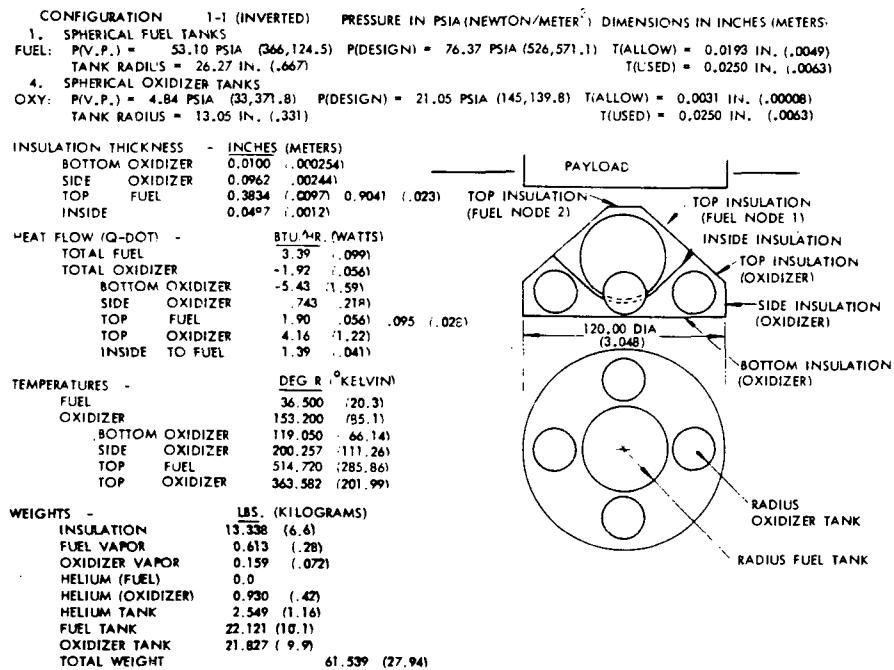


Figure 1.1-25: THERMAL PROGRAM PRINTOUT DATA - VEHICLE 1-1 (INVERTED)

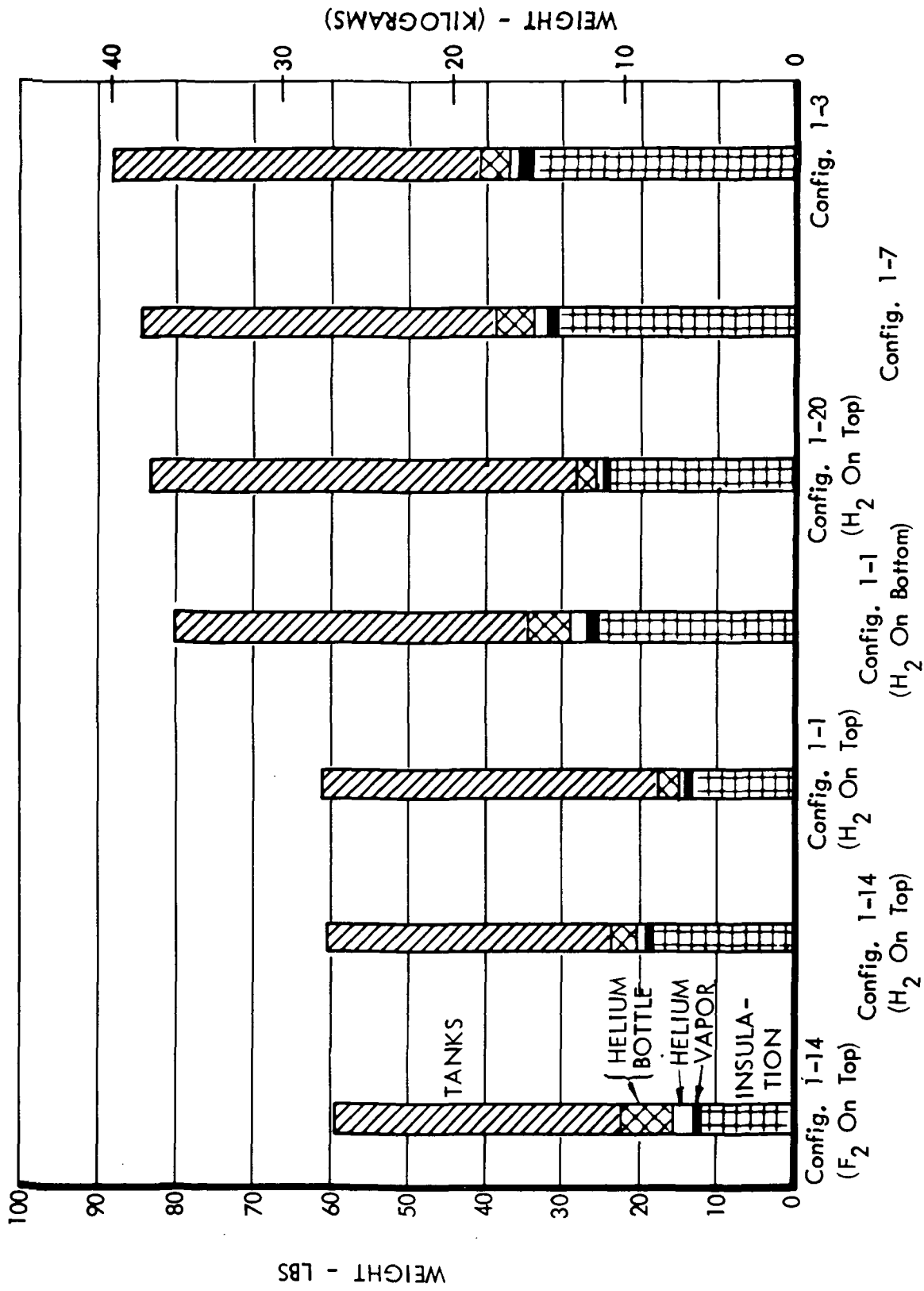


Figure 1.1-26 : TANK ARRANGEMENT THERMAL EFFICIENCY STUDY RESULTS

LF<sub>2</sub> - LH<sub>2</sub> PROPELLANTS

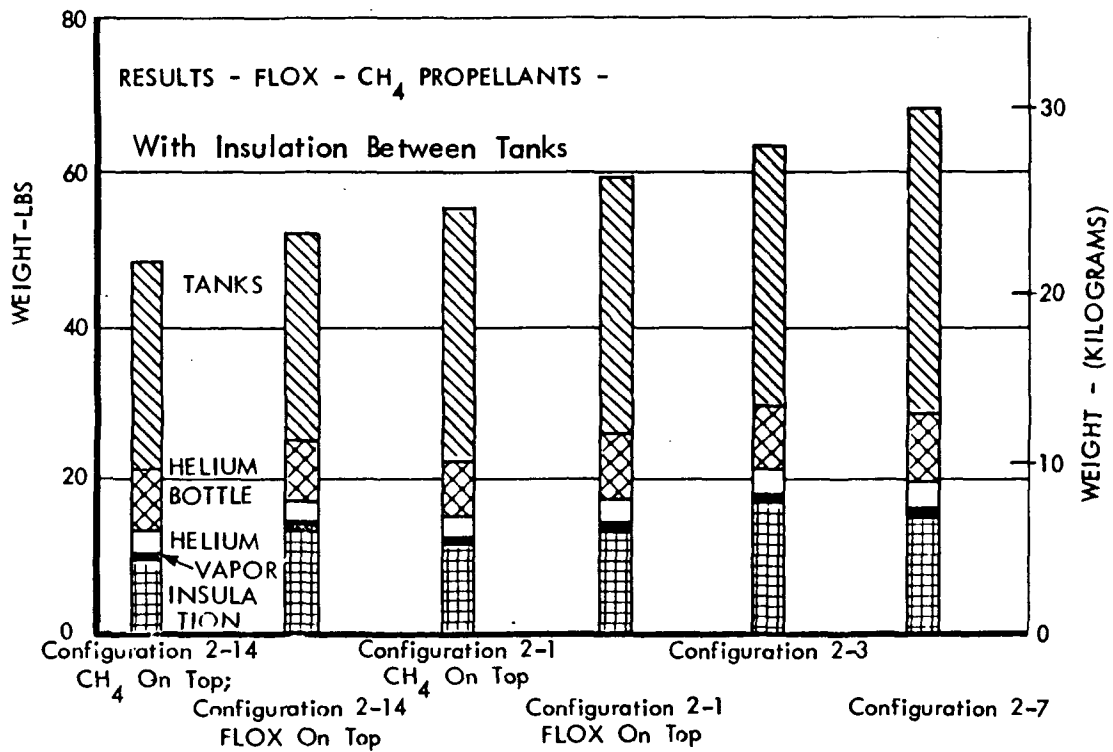
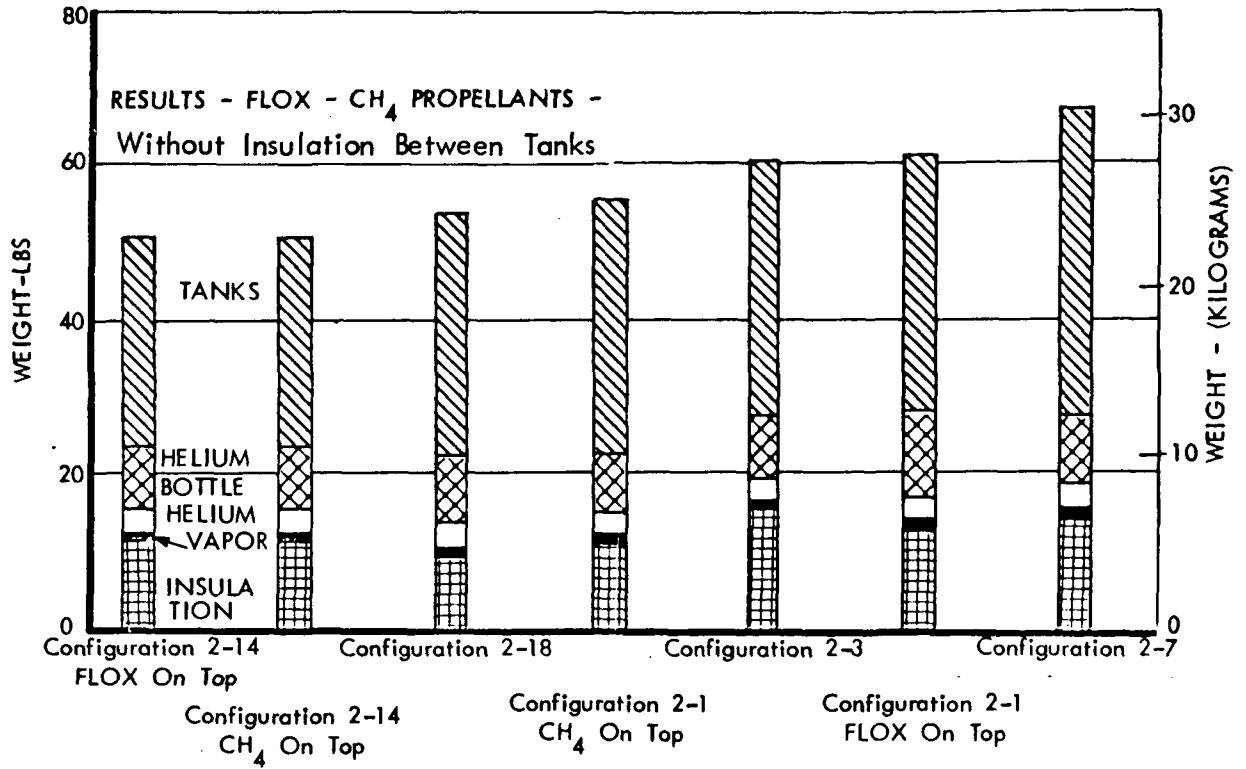


Figure 1.1-27: TANK ARRANGEMENT THERMAL EFFICIENCY STUDY RESULTS  
FLOX - CH<sub>4</sub> PROPELLANTS

tank on the bottom proved the best because the conical surface radiated heat from the vehicle instead of gaining heat as was the case for Vehicle 1-1. The conical surface temperature of Vehicle 2-1 inverted was 125°R (69.5°K), considerably cooler than the 170°R (94.5°K) oxidizer.

Insulation between oxidizer and fuel had only a slight influence on system weights. Realizing that this insulation would incur an additional weight penalty in the form of supporting structure, fasteners and joints, this approach was abandoned.

### 1.1.3 Vehicle Structure Evaluation

The purpose of this study was to determine preliminary least-weight approaches for construction of the vehicle body and Centaur adaptor as required by the boost load environment. Meteoroid protection and heat transfer characteristics of the structure were not considered in this evaluation.

The study was conducted with representative vehicle configurations selected from the initial phase of the "Tank Arrangement Screening". The vehicles were selected so that a broad range of sizes and loads were represented. Five configurations, shown in Figure 1.1-28, with diameters ranging from 65 to 120 in (1.65 to 3.05 m) were chosen. Three of these were Vehicles 1-14, 1-8 and 1-2. The other two structures were adaptors for Configurations 1-14 and 1-8.

The structural concepts which were evaluated included several types of continuous shells and truss members in a "sawtooth" arrangement. Materials used included titanium and aluminum, and non-metallic composites consisting of epoxy resins reinforced with boron, carbon and fiberglass filaments. These materials were used individually and in combination to produce the lightest structure possible.

An estimate of weights for tanks, basic vehicle structure, adaptor, propellants and payload was made for determining axial, lateral and bending loads. Figure 1.1-29 illustrates the model used for analysis of Vehicle 1-8.

For the adaptor designs using continuous shell structures, the axis of moments was taken at the base of the adaptor. Since both axial and shear loads were introduced into truss structure adaptors at the vehicle/adaptor interface, this plane was used as the axis of moments for truss construction. A tabulation of loads and moments for the adaptor of Figure 1.1-29 is given below:

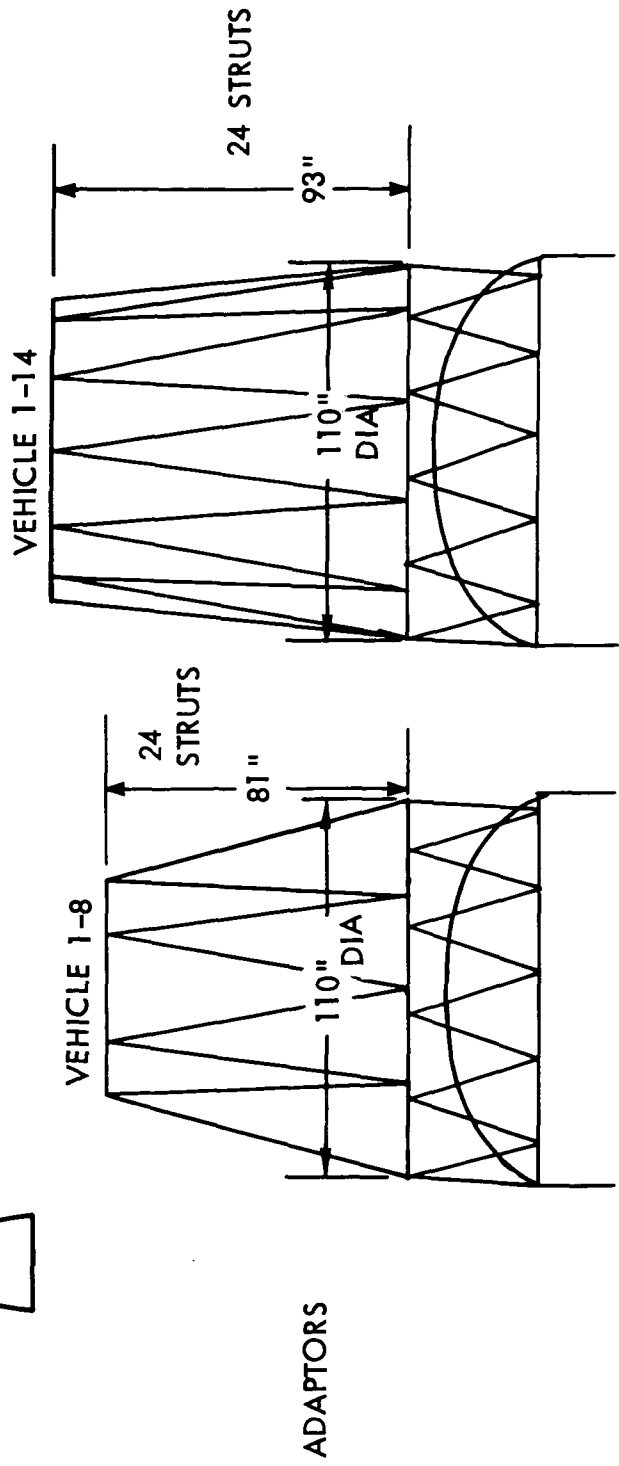
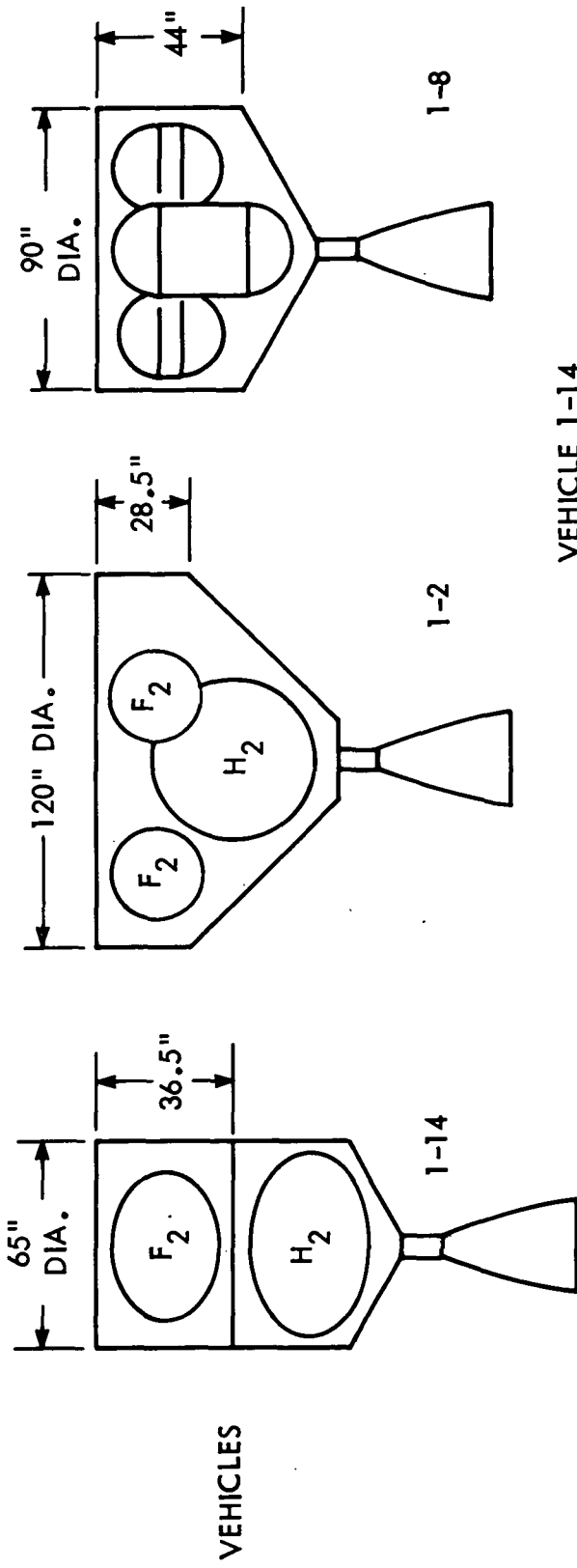
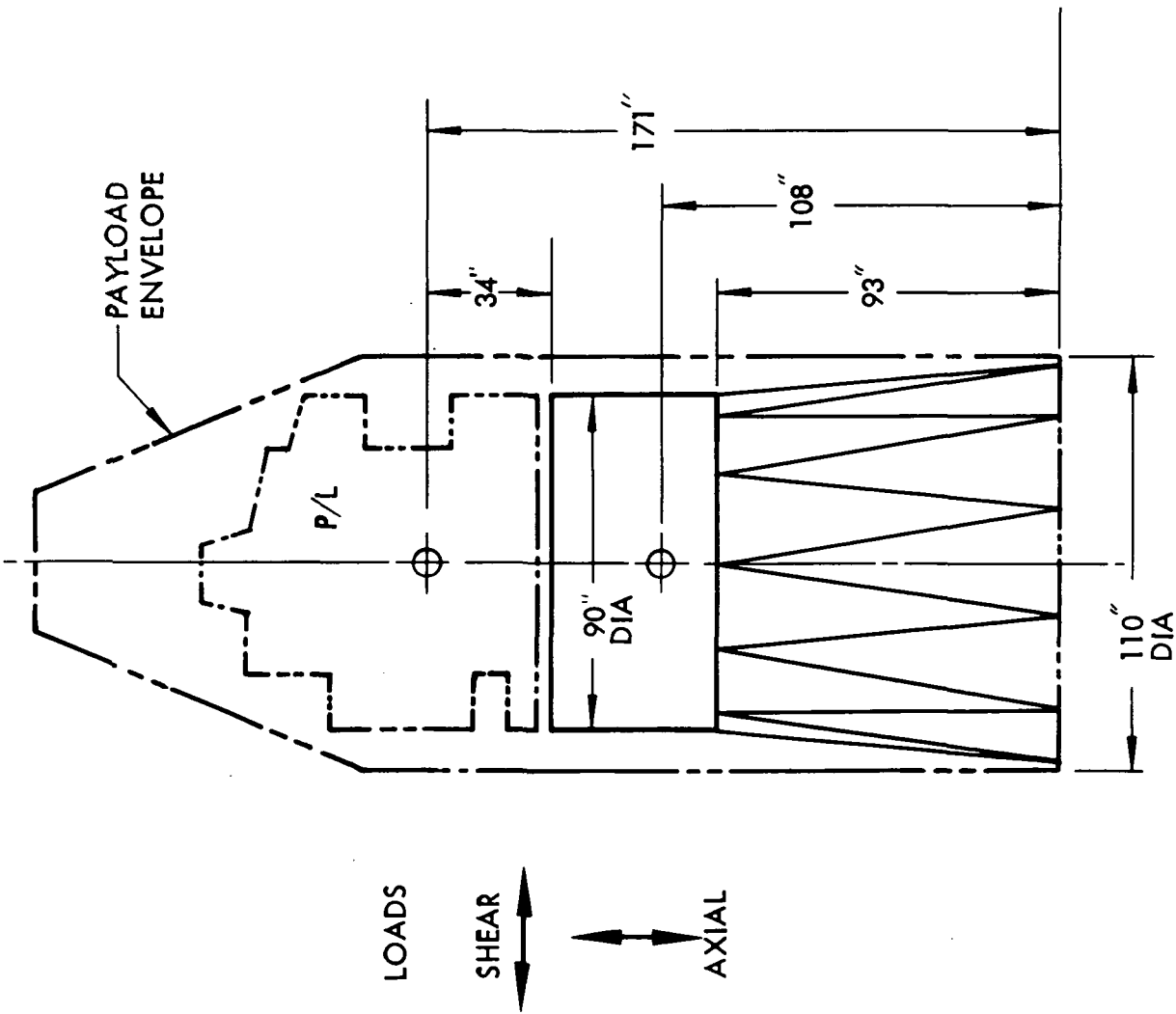


Figure 1.1-28: VEHICLE STRUCTURE EVALUATION REPRESENTATIVE CONFIGURATIONS



DESIGN ACCELERATIONS	
LIMIT	ULTIMATE
AXIAL +4.0	+5.0
-2.5	-3.125
LATERAL ±1.5	±1.875

VEHICLE STRUCTURE 1-8	lb	kg
INERT WEIGHT	246	112
MISC.	50	22.7
	<u>296</u>	<u>135</u>
PROPELLANT LF <sub>2</sub>	2010	912
LH <sub>2</sub>	160	72.6
VEHICLE WEIGHT	<u>2466</u>	<u>1120</u>
ADAPTOR WEIGHT	100	45.4
	<u>2566</u>	<u>1165</u>
PAYLOAD	4934	2240
	<u>7500</u>	<u>3410</u>

Figure 1.1-29: STRUCTURE ANALYSIS MODEL - VEHICLE 1-8

			Limit Loads			
Continuous Shell Structure	Vehicle Adaptor 1-8	Weight lb (kg)	Moment Arm in (m)	Moment @ 1.5G M lb-in (N m)	Axial Load F @ 4G lb (N)	Shear Load V @ 1.5G lb (N)
	Continuous Shell Structure	Vehicle Body	2466 (1120)	108 (2.74)	400,000 (45,100)	9,900 (44,000)
Payload		4934 (2240)	171 (4.34)	1,265,000 (142,900)	19,700 (87,500)	7,400 (32,900)
				<u>1,665,000</u> (188,000)	<u>29,600</u> (131,500)	<u>11,100</u> (49,300)
Truss Structure	Vehicle Body	2466 (1120)	15 (0.38)	55,500 (6,250)	9,900 (44,000)	3,700 (16,400)
	Payload	4934 (2240)	78 (1.98)	578,000 (65,300)	19,700 (87,500)	7,400 (32,900)
				<u>633,500</u> (71,550)	<u>29,600</u> (131,500)	<u>11,100</u> (49,300)

For the vehicle body designs using continuous shell structures the axis of moments was taken at the base of the body. For designs using truss structures the axis of moments was taken at the vehicle/payload interface. All of the body weight was applied at the payload interface for the axial load condition. The table below lists axial loads and moments for the vehicle body of Figure 1.1-29.

			Limit Loads		
Continuous Shell Structure	Vehicle Body 1-8	Weight lb (kg)	Moment Arm in (m)	Moment @ 1.5G M lb-in (N m)	Axial Load @ 4G F lb (N)
	Continuous Shell Structure	Vehicle Body	2466 (1120)	15 (0.38)	55,500 (6,250)
Payload		4934 (2240)	78 (1.98)	578,000 (65,300)	19,700 (87,500)
				<u>633,500</u> (71,550)	<u>29,600</u> (131,500)
Truss Structure	Vehicle Body	2466 (1120)	0 (0)	0 (0)	9,900 (44,000)
	Payload	4934 (2240)	34 (0.87)	252,000 (28,400)	19,700 (87,500)
				<u>252,000</u> (28,400)	<u>29,600</u> (131,500)

The ultimate design loads used in sizing structural elements for the adaptor and vehicle bodies using continuous shell structures were derived as follows:

$$N_X = (N_{XM} + N_{XA}) \quad (1.25)$$

where:  $N_X$  = The ultimate applied load

$N_{XM}$  = The limit applied load due to bending moment =

$$\frac{M}{\pi R^2}$$

$R$  = Vehicle or adaptor radius

$N_{XA}$  = The limit applied axial load =  $\frac{F}{2 \pi R}$

The ultimate design loads used in sizing truss members (tubular struts) for the adaptor and vehicle bodies were derived as follows:

$$P = (P_A + P_M) \quad (1.25)$$

where:  $P$  = The ultimate strut load

$P_A$  = The limit strut load due to axial loading =  $F_A/2 \cos\beta$

$F_A$  = The limit axial load at the apex of two struts =  $F/N_C$

$2 \cos\beta$  = A geometric correction for the angularity of the strut

$N_C$  = The number of strut apex's  
(e.g. twelve for Vehicle 1-8)

$P_M$  = The limit strut load due to bending moment =  $F_M/2 \cos\beta$

$F_M$  =  $\frac{2M}{N_C R}$

The ultimate design loads obtained for the study vehicles are tabulated below:

Vehicle	Shell Height in (m)	Strut Length in (m)	Shell Radius in (m)	Shell $N_x$ lb-in (N/m)	Strut P lb (N)
1-14	36.5 (0.93)	49.3 (1.25)	32.5 (0.83)	586 (120,000)	10,000 (44,480)
1-8	44 (1.12)	45 (1.14)	45 (1.14)	258 (45,100)	2,225 (9,870)
1-2	28.5 (0.72)	-	60 (1.52)	139 (24,300)	-
1-14 Adaptor	81 (2.06)	83 (2.11)	32.5 (0.83)	550 (96,000)	4,230 (18,800)
1-8 Adaptor	93 (2.36)	94.2 (2.39)	49.2 (1.25)	347 (60,600)	3,050 (13,550)

A computer aided optimization method was employed to determine the minimum weight designs.

The computer aided design study involved screening optimum designs of a large number of concepts. Because of the large number of variables and failure modes which had to be treated, extensive use was made of a multi-variable search technique coded as the OPTRAN (OPTimization by RANDom search algorithm) code. A flow chart is given in Figure 1.1-30 for the basic OPTRAN code. Closed form analysis code modules for calculating weight, constitutive stiffness coefficients and constraint conditions (failure modes) were inserted in appropriate locations in the basic FORTRAN IV OPTRAN deck to specialize the deck for a specific structural concept. OPTRAN established designs by random selection of values for the dimensional parameters (skin thickness, stiffener spacing, stiffener thickness, etc.) from specified search ranges. Minimum gage design constraints were accomplished by proper specification of the search ranges. If a design was found that had lower weight than the best preceding design, the constraints were then checked. If all constraints were satisfied for the design load condition, then the design became the current best design. The process was repeated until a specified number of good designs were found, say 5 out of about 200 trial designs, which completed a search cycle. Design refinement was achieved by resizing the respective variable search ranges and conducting another search cycle; the search cycles were repeated until the variable search ranges were squeezed down to a specified size which signified convergence to an acceptable optimum design.

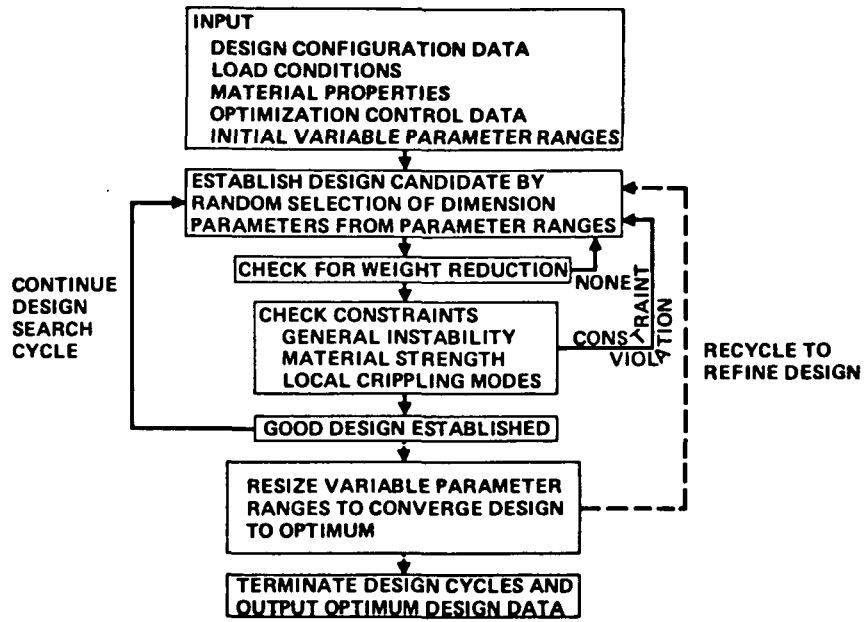


Figure 1.1-30: OPTRAN CODE FLOW CHART

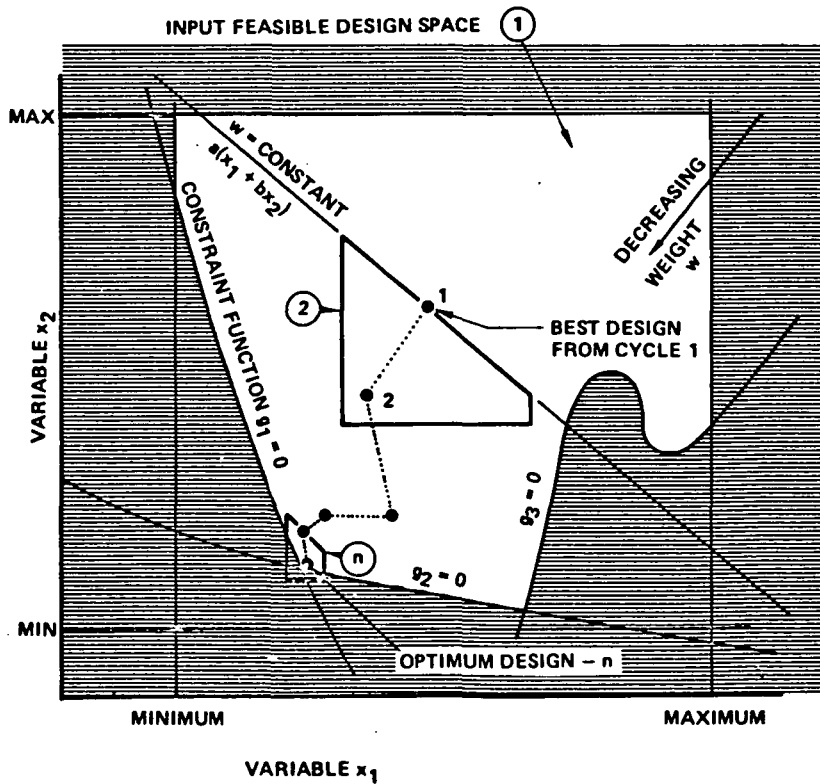


Figure 1.1-31: OPTRAN OPTIMIZATION STRATEGY

The search method was made adaptive by resizing the variable search ranges for each new cycle according to changes in the respective variables for the best designs from the preceding two cycles. Thus if one variable showed greater variation from cycle to cycle, its range was made broader to increase the probability of directing the design to a true minimum. The use of discrete variables (standard structural sections, number of composite laminate plies, etc.) presented no difficulties in this search method.

The optimization strategy coded in OPTRAN is illustrated by a simplified two variable design optimization problem shown in Figure 1.1-31 having linear weight characteristics. The feasible design space at the beginning of the first cycle consisted of the unshaded area which contained all possible configurations that did not violate any constraints. The point 1 represents the values of the design parameters  $x_1$  and  $x_2$  constituting the best design found during the first cycle. The feasible design space for the second cycle was established by applying an arbitrary factor to the input search ranges. For following cycles, the boundaries were established as a function (subject to an arbitrary minimum band width) of the variations of  $x_1$  and  $x_2$  for successive best designs found during the preceding two cycles. The current best weight formed an upper boundary to the new feasible design space because each new best design must show a decrease in weight.

The optimum minimum weight design, point n, was the best design from the final cycle and was bounded by the two constraint functions,  $g_1 = 0$  and  $g_2 = 0$ . The third constraint function did not govern the final design, although it might have been encountered during previous cycles. Trapping of the design at a non-global minimum, such as the weight valley on the  $g_3 = 0$  constraint curve, was generally avoided by using the random point search.

Figure 1.1-32 shows the concepts and materials considered. The geometric variables are also identified. In several instances the fabrication characteristics of some materials limited their use, e.g., boron filaments cannot be formed around small radii, thus they could not be used as the core for truss core concepts. Table 1.1-5 lists the material properties used in the analysis.

The failure mode constraints for tubular struts were: Euler buckling, local buckling (Reference 1.1-2) and material yielding. The failure mode constraints for honeycomb sandwich were: material strength, general instability (Reference 1.1-3), panel instability, face dimpling and face wrinkling (Reference 1.1-4). The failure mode constraints for corrugated construction were: material strength, general instability (Reference 1.1-2), local panel instability, corrugation web crippling and corrugation flange crippling (Reference 1.1-5). Failure mode constraints for truss core and stiffened skin construction methods were: general crippling, stiffener web crippling and stiffener flange crippling (Reference 1.1-5).

CONCEPT	MATERIAL VARIATIONS	GEOMETRIC VARIABLES		
		MATERIAL VARIATIONS		
		GEOMETRIC VARIABLES		
RING STIFFENED CORRUGATIONS	Corrugations	X	X	Corrugation - width (w), thickness (t), Slope ( $\theta$ ), height (h)
	Corrugation Reinforcements	X	X	Corrugation Reinforcement - Thickness (ct)
	Rings	X	X	Ring - height (rh), width ( $\frac{rh}{2}$ ), spacing
	Ring Reinforcements	X	X	Ring Reinforcement - thickness (rt)
RING STIFFENED STIFFENED SKIN	Skin	X	X	Skin - thickness (t)
	Hat Sections	X	X	Stiffener - spacing, height (h), width ( $\frac{h}{2}$ )
	Hat Section Reinforcements	X	X	Stiffener Reinforcement - thickness (st)
	Ring	X	X	Ring - spacing, height (rh), width ( $\frac{rh}{2}$ )
	Ring Reinforcement	X	X	Ring Reinforcement - thickness (rt)
HONEYCOMB SANDWICH	Face Skins	X	X	Face Skins - thickness (tf)
	Core	X	X	Core - ribbon thickness, cell size (cs), height (h)
RING STIFFENED TRUSS CORE	Face Skins	X	X	Face Skins - thickness (t)
	Core	X	X	Core - thickness (ct), Slope ( $\theta$ ), height (h)
	Ring	X	X	Ring - spacing, height (rh), width ( $\frac{rh}{2}$ )
	Ring Reinforcement	X	X	Ring Reinforcement - thickness (rt)
TUBULAR STRUTS	Radius	X	X	Radius (r)
	Ply Orientation	X	X	Ply Orientation
				Number of plies or tube thickness (t)

Figure 1.1-32: VEHICLE CONSTRUCTION CONCEPTS

Table 1.1-5: MATERIAL PROPERTIES

	MATERIAL	LONGITUDINAL MODULUS OF ELASTICITY $E_L$ $10^6$ LB/IN <sup>2</sup> (N/m <sup>2</sup> )	TRANSVERSE MODULUS OF ELASTICITY $E_T$ $10^6$ LB/IN <sup>2</sup> (N/m <sup>2</sup> )	SHEAR MODULUS G $10^6$ LB/IN <sup>2</sup> (N/m <sup>2</sup> )	POISSONS RATIO $\nu$	COMPRESSIVE YIELD STRENGTH $F_{cy}$ LB/IN <sup>2</sup> (N/m <sup>2</sup> )	COMPRESSIVE ULTIMATE STRENGTH $F_{cu}$ LB/IN <sup>2</sup> (N/m <sup>2</sup> )	TENSILE YIELD STRENGTH $F_{ty}$ LB/IN <sup>2</sup> (N/m <sup>2</sup> )	TENSILE ULTIMATE STRENGTH $F_{tu}$ LB/IN <sup>2</sup> (N/m <sup>2</sup> )	DENSITY LB/IN <sup>3</sup> (Kg/m <sup>3</sup> )
	AL 7075-T6	10.5 (72,450)	10.5 (72,450)	3.9 (26,910)	0.33	67 (462,300)				0.1 (1.6)
	Ti 6AL4V	16.5 (113,850)	16.5 (113,850)	6.2 (42,780)	0.3	152 (1,048,800)				0.16 (2.56)
UNIDIRECTIONAL	HS <sup>*</sup> C/E $E_f = 35$	18 (124,200)	1 (6,900)	1 (6,900)	0.3		90 (620,000)		125 (862,500)	0.054 (.864)
ISOTROPIC	HS C/E $E_f = 35$	7.2 (49,680)	7.2 (49,680)	2.6 (17,940)	0.3		40 (276,000)		43 (296,700)	0.054 (.864)
UNIDIRECTIONAL	HM <sup>+</sup> C/E $E_f = 55$	28 (119,320)	1 (6,900)	1 (6,900)	0.3		75 (517,500)		100 (690,000)	0.058 (.928)
ISOTROPIC	HM C/E $E_f = 55$	11.2 (77,280)	11.2 (77,280)	3.8 (26,220)	0.3		30 (207,000)		33 (227,700)	0.058 (.928)
UNIDIRECTIONAL	B <sup>++</sup> E/E $E_f = 60$	30 (207,000)	1 (6,900)	1 (6,900)	0.3		250 (1,725,000)		200 (1,380,000)	0.067 (1.072)
ISOTROPIC	B/E $E_f = 60$	12 (82,800)	12 (82,800)	4 (27,600)	0.3		80 (552,000)		70 (483,000)	0.067 (1.072)
UNIDIRECTIONAL	SG <sup>+++</sup> E/E $E_f = 12$	7.5 (51,750)	1 (6,900)	1 (6,900)	0.3		100 (690,000)		230 (1,587,000)	0.066 (1.056)
ISOTROPIC	SG/E $E_f = 12$	3.0 (20,700)	3.0 (20,700)	J. (6,900)	0.3		60 (414,000)		77 (531,300)	0.066 (1.056)

\* HIGH STRENGTH CARBON/EPOXY \*\* FILAMENT MODULUS OF ELASTICITY

+ HIGH MODULUS CARBON/EPOXY ++ BORON/EPOXY +++ "S" GLASS/EPOXY

Results of the vehicle structure investigations are shown in Figures 1.1-33 and 1.1-34. In Figure 1.1-33, the weights of continuous shell structures are plotted versus shell load. The weights include stiffening rings smeared uniformly over the surface. Each vertical line represents a specific vehicle with a certain height, diameter, and center of gravity. The vehicles shown range from the relatively short, large diameter, Vehicle 1-2 with low shell loading to the long, narrow, Vehicle 1-14 adaptor with high shell loading, thus a reasonably wide range of vehicle types was bracketed.

Carbon/epoxy and boron/epoxy laminates in both corrugated construction and honeycomb sandwich provided the least structural shell weight for the entire range of vehicles. Fiberglass corrugations and fiberglass and aluminum honeycomb sandwich showed promise except in lightly loaded structure where minimum gages were obtained. Titanium structure in any of the forms considered had no particular advantage. Truss core and stiffened skin concepts were investigated for Configuration 1-14 using the full range of materials. These two approaches resulted in relatively heavy structure, therefore further investigation was limited to Vehicle 1-2.

Some typical dimensions of the four least-weight configurations of Figure 1.1-33 are listed in order of increasing weight in Table 1.1-6. The 0.02 skin thickness obtained for most of the cases was the minimum gage limit used in the analysis. This explains why titanium was not competitive.

In Figure 1.1-34 individual tubular strut weights are plotted versus strut length. As in the previous plot, the vertical lines each define a specific vehicle. The lines connecting similar points for each vehicle do not indicate weight trends as a function of member length, because the member loads are different for each case.

The advanced composite materials exhibited the most potential for minimizing weight and titanium had the least. Fiberglass offered no particular advantage at this stage of the study.

Comparisons of tubular strut and shell structures are presented in Figure 1.1-35. The weights presented are not representative of entire vehicles and therefore comparisons between vehicle types would not give an accurate assessment. Instead, this data is presented to show the relative ranking of truss and continuous shell structural concepts as candidates for construction of individual vehicles. Such items as tank support beams, fittings, engine thrust members, payload supports and miscellaneous hardware are not included in these estimates. In the case of Vehicle 1-14, approximately one-half of the total shell weight is represented because the vehicle is divided into two vertical compartments and only one of these was considered. For each vehicle, truss structure consistently offered the least weight.

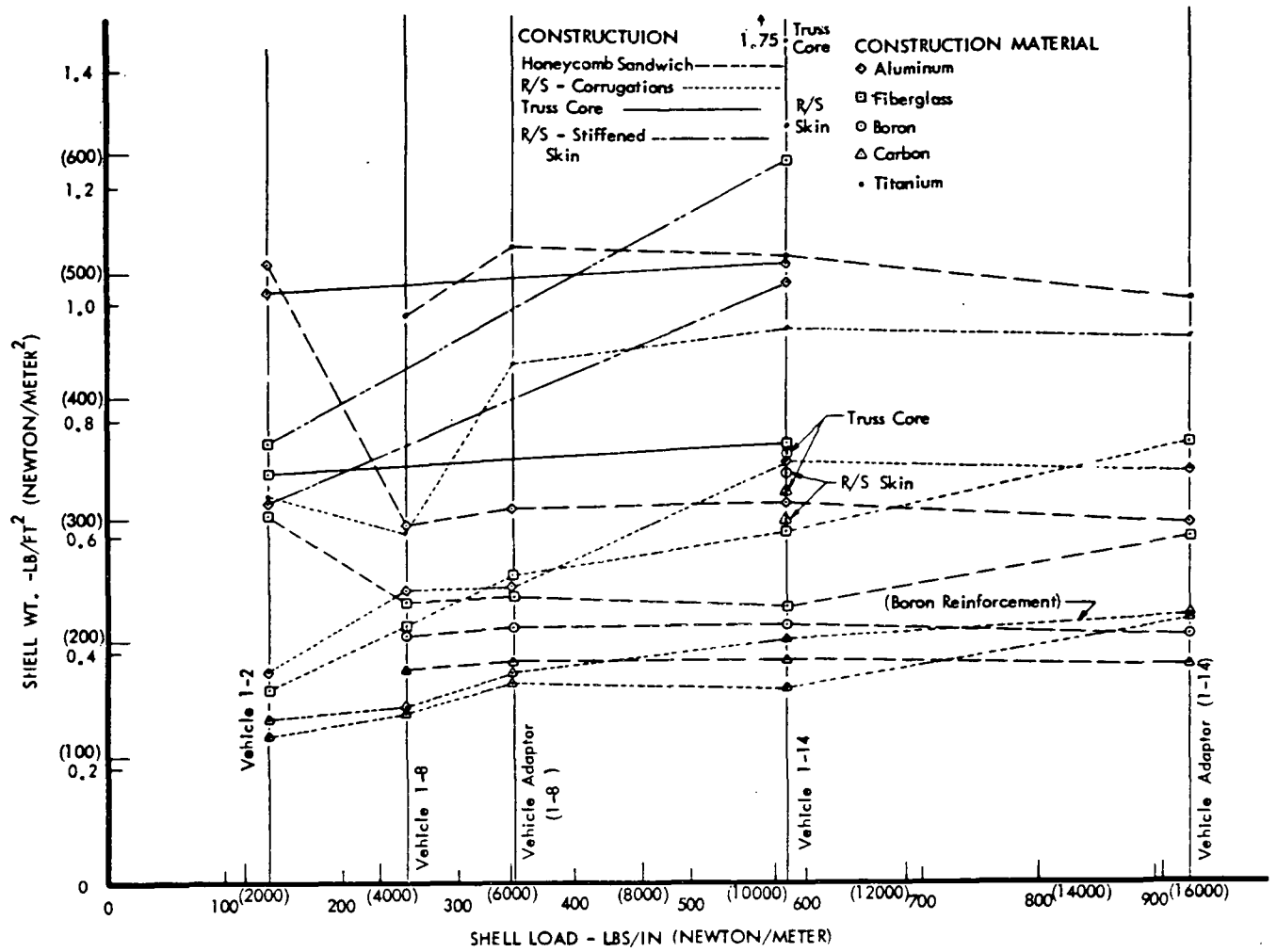


Figure 1.1-33: CONTINUOUS SHELL CONSTRUCTION WEIGHTS

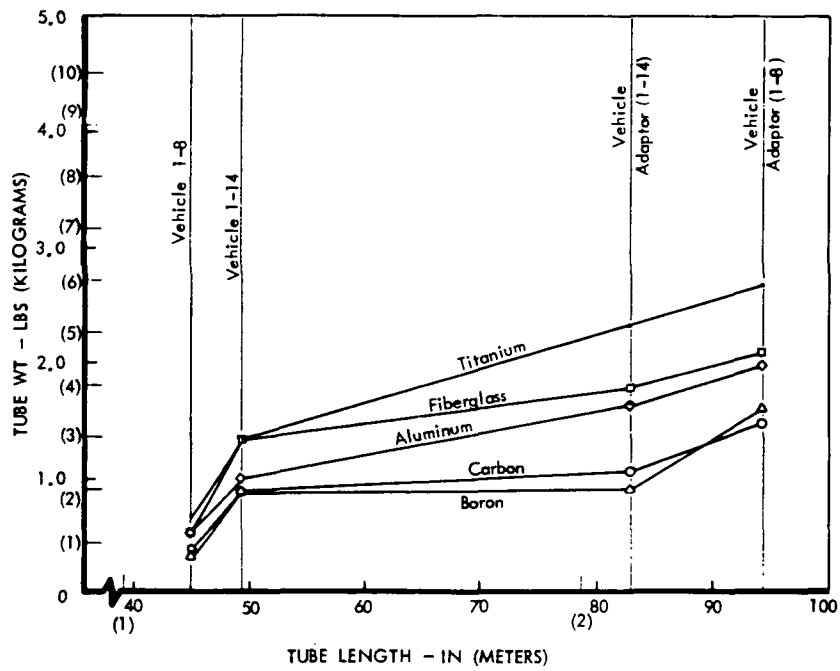
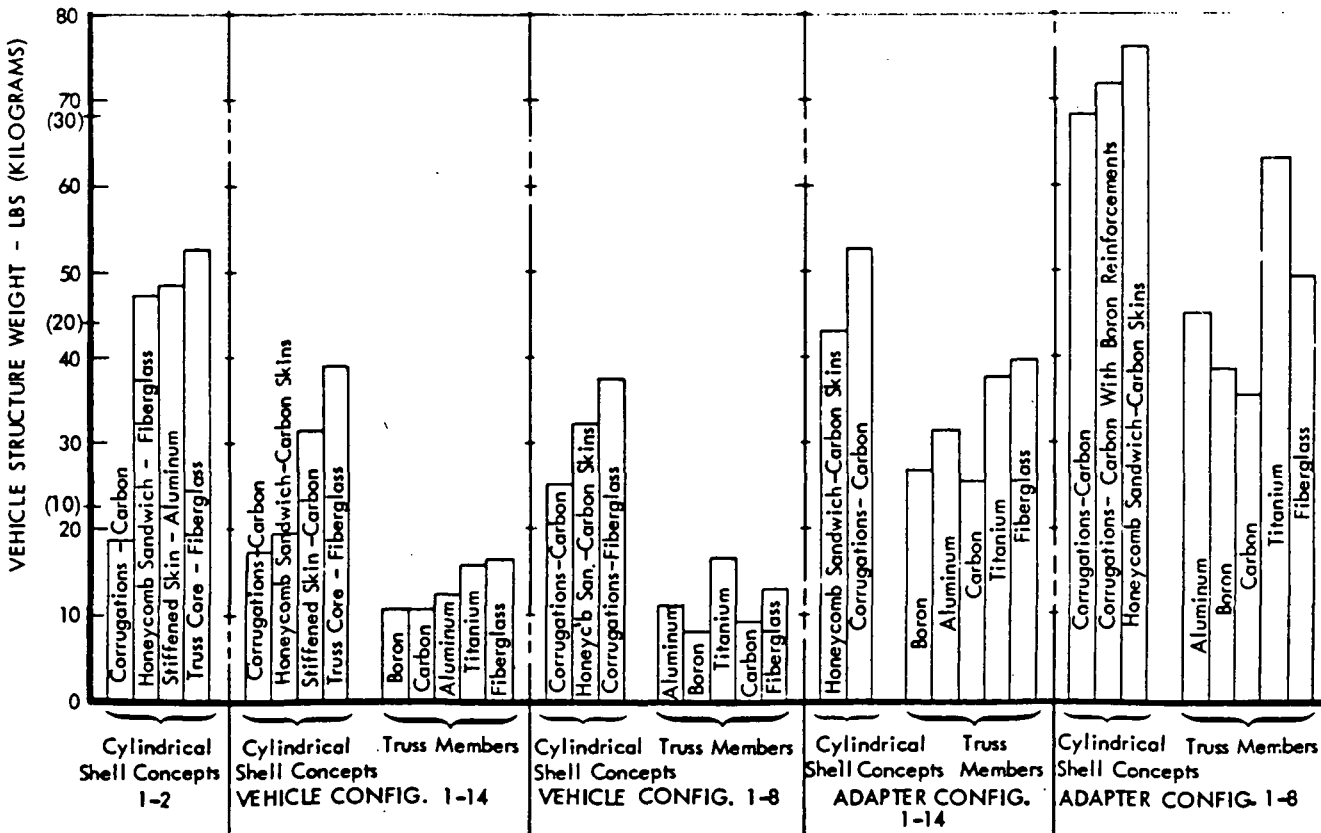


Figure 1.1-34: TUBULAR STRUT WEIGHTS

**Table 1.1-6: CONTINUOUS SHELL STRUCTURE DIMENSIONS**

STRUCTURAL CONCEPTS	SHELL PROPERTIES		THICKNESS		HEIGHT		WIDTH		SPACING		SLOPE (°)	
	VEHICLE		1-14	1-8	1-14	1-8	1-14	1-8	1-14	1-8	1-14	1-8
STRUCTURAL CONCEPTS	Carbon/Epoxy Corrugations	{	0.02 (.00051)	0.03 (.00076)	0.57 (.0145)	1.38 (.0351)	0.80 (.0203)	1.51 (.0384)	-	-	45.6 (1.16)	46.1 (1.17)
	Carbon Corrugation Reinforcements	{	0.006 (.00015)	0.001 (.000025)	-	-	-	-	-	-	-	-
	Aluminum Ring	{	0.003 (.000076)	-	0.74 (.0188)	-	0.37 (.0094)	-	18.3 (.465)	-	-	-
	Carbon Ring Reinforcements	{	0.22 (.0056)	-	-	-	-	-	-	-	-	-
	Carbon/Epoxy Honeycomb Sandwich	{	0.02 (.00051)	0.02 (.00051)	-	-	-	-	-	-	-	-
	Carbon Face Skins	{	-	-	-	-	-	-	-	-	-	-
	Aluminum Core	{	Ribbon Thick. .0013 (.00003)	0.0011 (.000028)	0.31 (.0079)	0.28 (.0071)	Cell Size 0.33 (.0084)	0.32 (.0082)	-	-	-	-
	Carbon/Epoxy Corrugations	{	0.03 (.00076)	0.02 (.00051)	1.26 (.032)	1.30 (.033)	1.47 (.0373)	0.92 (.0234)	-	-	77.6 (1.97)	50.8 (1.29)
	Boron Corrugation Reinforcements	{	0.006 (.00015)	0.006 (.00015)	-	-	-	-	-	-	-	-
	Boron/Epoxy Honeycomb Sandwich	{	0.02 (.00051)	0.02 (.00051)	-	-	-	-	-	-	-	-
	Boron Face Skins	{	-	-	-	-	-	-	-	-	-	-
	Aluminum Core	{	Ribbon Thick. 0.0016 (.000041)	0.0011 (.00003)	0.26 (.0066)	0.29 (.0074)	Cell Size 0.37 (.0094)	0.36 (.0092)	-	-	-	-

DIMENSIONS IN INCHES (METERS) ANGLE IN DEGREES (RADIANS)



**Figure 1.1-35: VEHICLE STRUCTURE EVALUATION RESULTS**

#### 1.1.4 Insulation Concept Development

Work in this phase of the program consisted of (1) the development of conceptual designs of insulation panels for attachment to both truss and shell type vehicle structures, (2) an analytical evaluation of various ground hold thermal protection schemes preparatory to development of design configurations, (3) tank mounted MLI comparisons, and (4) an insulation evacuation analysis and evaluation of candidate MLI materials. The design study was performed with several propulsion vehicle structural arrangements, which presented different insulating problems.

##### Insulation Panel Designs

During the development of conceptual designs, consideration was given to ease of MLI panel installation and removal, attachment methods, prelaunch purging and thermal protection provisions. The following sections describe concepts for thermal protection of tankage along vehicle sidewalls, between payload and tankage, between oxidizer and fuel tanks and along the vehicle base.

It was necessary to establish certain ground rules so that the results of the thermal and weight efficiency analysis of concepts would be meaningful. These were; (1) the diameter of the vehicle was fixed at 120 in (3.1 m); (2) the height at 36 in (0.9 m); (3) a 45° conical lower surface extending to the engine was selected; (4) all external surfaces required meteoroid protection, a preliminary selection consisted of either the structural shell or Beta fiber cloth or 3 mil aluminum; and (5) one inch (2.54 cm) of 0.15 mil aluminized mylar/nylon net MLI on all surfaces.

Weight and thermal efficiency comparisons were expected to reveal the advantages or disadvantages of specific design features such as the number and type of panel joints, panel fasteners, MLI blanket retainers, panel encapsulation and corner joints. The design concepts presented would be suitable for use with some of the other more common MLI materials which possess adequate strength. Examples of these are (1) sliced foam/aluminized mylar, (2) dacron net/aluminized mylar, (3) silk net/aluminized mylar, (4) scrim cloth (fortrel or dacron)/aluminized mylar, (5) NRC-2, (6) NRC-2 in combination with any of the spacers mentioned, and (7) tissuglas/aluminized mylar.

Figure 1.1-36 presents a concept for assembly and attachment of three prefabricated MLI multilayer panels to the inside of a vehicle shell structure. The shell structure served as the meteoroid shield. The MLI blanket would be attached to the structural shell by means of two rows of fiberglass studs. One row of studs would be bonded near the top of the shell and the other bonded near the bottom. Blanket buildup and installation was simplified by the use of removable layup posts that positioned layers during assembly. After buildup, the blanket would be removed from the layup board with posts retained in the blanket to control layer alignment. The assembly would then be installed on the shell by slipping

the layup posts inside the hollow fiberglass studs. After the posts are removed, fiberglass buttons would be installed in the studs to hold the insulation in place. In addition, fiberglass filaments or titanium screen could be installed between the studs to provide lateral support.

Installation of the MLI in the lower conical area of a vehicle is depicted in Figure 1.1-37. Here there is no structural shell for meteoroid protection, consequently the blankets were encapsulated in Beta fiber cloth. The conical multi-layer blanket would be built up on a cone shaped layup board using removable layup posts similar to those described in previous paragraphs. The blanket would be supported on hollow fiberglass studs at top and bottom. For additional lateral support, fiberglass filaments or titanium screens were provided on both sides of the blanket.

Initial study results indicated that very thin insulation blankets were all that was necessary on the aft facing surfaces of the vehicle. The drawing of Figure 1.1-38 presents a concept which combined both ground hold and flight thermal protection. Panel construction consisted of fiberglass honeycomb core, foam filled, with 3 mil polished aluminum face skins. The panels were fastened to engine thrust members by means of mounting clips insulated from the member by fiberglass studs or foam barriers.

Two approaches for flat MLI bulkheads between tanks and payload or adjacent tanks are shown in Figure 1.1-39.

The version shown in Section B-B (Bulkhead Concept 1) was supported by a honeycomb sandwich which was both support structure and part of the insulation. During the gas purged ground hold phase, the cryopumped honeycomb would be an effective portion of the insulation bulkhead since gas purged MLI is relatively inefficient. In space the MLI blanket would become effective after evacuation.

The bulkhead would be supported in the vehicle by low heat leak fiberglass brackets which tie it to the upper ring and tank support beams.

In the MLI bulkhead design shown in Section C-C (Bulkhead Concept II), MLI would be supported by a titanium screen that rests on the vehicle upper ring and tank support beams. The blanket would be built-up on hollow fiberglass studs fastened to the titanium screen. After assembly on the bench the insulation bulkhead would be installed on the vehicle and secured against lateral movement by velcro patches.

A method of supporting a multilayer insulation blanket to separate hydrogen and fluorine tanks is shown in Figure 1.1-40. A titanium wire mesh was used on both sides of the blanket to provide lateral support. The blanket would be built-up on a cone shaped layup board using the removable layup posts discussed previously. The blanket would have openings and be slit to provide for tank

supports and piping. After removal from the layup board, the blanket assembly would be installed in the vehicle and supported at its edge and center by hollow fiberglass studs attached to secondary structure. A method of providing access from the top for vent valve replacement is shown.

The drawing of Figure 1.1-41 shows a method of utilizing the Beta fiber cloth meteoroid bumper as a building platform and support structure for the MLI blanket. Three of these integrated panels would be required for the cylindrical portion of the vehicle and eight for the conical base. The Beta fiber cloth would be rigidized with epoxy resin, and molded in a curved contour. The MLI blanket would be assembled on the Beta fiber cloth and attached with nylon retainers. Holes could be formed in the blanket with a hot needle. The melt down head approach for retainer studs would provide a quick and permanent means of attachment and stabilization of layers, however boost loads are expected to cant these fasteners due to poor moment carrying capacity. This approach might be limited to thin MLI blankets. An alternate stud approach is shown wherein lock washers were used to stabilize the studs and the Beta fiber cloth. When flight loads are applied the Beta fiber cloth could buckle locally, however the material is so flexible that no damage is expected.

Complete panels were held to truss members, upper and lower rings, and adjacent panels with Velcro tape. Abutting MLI edges were thermally disconnected by net, thin foam or fiberglass batting.

The approach selected for payload thermal isolation was a continuous blanket of MLI supported by polypropylene netting stretched across an aluminum hoop. The MLI would be laid-up from 48 in (122 cm) wide roll stock with 1/2 in (1.27 cm) overlaps along the edges. These overlaps would be staggered to avoid excessive thickness. The polypropylene net would be reinforced with dacron webbing and stitched along the perimeter of the hoop, thus producing an encapsulating envelope with strength and resilience. The hoop was held in place in the vehicle with snap rings which permitted easy removal. The MLI blanket was restrained by means of nylon retainers.

A radiation window occurred at the corner joint and this was shielded with a MLI blanket mounted to a fiberglass tray. The tray, with insulation installed, was mounted to the structure in segments.

In this concept it was assumed that perforated radiation shields were used for evacuation of purge gasses, therefore it was necessary to perforate the Beta fiber cloth/epoxy laminate.

The insulation panels in Figure 1.1-42 were cut to fit the spaces between truss members. The MLI materials were encapsulated with Beta fiber cloth on the outside for meteoroid protection and netting on the inside. The edges of the panels were reinforced and provided with metal grommets. The panels would be

laced to the truss members. This approach leaves the truss members exposed to the cryogenic tankage, therefore a method of thermal isolation is also shown. The truss member covers consist of MLI built-up on open weave epoxy impregnated fiberglass cloth. The layers would be stitched to the fiberglass as necessary. The multilayer on these covers would have perforated radiation shields providing an escape path for purge gasses. The triangular shaped panels had no perforations and would be edge pumped. The covers were attached to truss members with patches of Velcro tape.

The payload isolation MLI blanket would be constructed in a manner similar to the previously described concept, however, the aluminum hoop would be replaced with an extruded nylon edge member. The panel would be drawn taut by lacing along the edges. A radiation window is also present at the corner in this design. The corner would be protected by a MLI patch mounted on a nylon film substrate. This would be perforated like the MLI to allow purge gasses to exit. The substrate was made flexible with a hinge to accommodate variations in fit-up.

Figure 1.1-43 shows an approach for assembling MLI blankets on the inside of a shell, using a fiberglass latticework structure as an assembly aid, and to support flight loads. The structural shell served as the meteoroid barrier in this concept.

MLI materials would be assembled on the bonded latticework and attached using the slotted nylon tubes. These were located at the midpoint between lattice member intersections. The attachments were slotted to allow purge gases to exit from the MLI and serve as the main exhaust ports for the vehicle purge system. A lattice assembly would be installed on the vehicle over fiberglass studs at predetermined locations on the shell or shell rings. The studs were designed with a floating base feature which allowed for minor misalignment. A "snap" cap was used to lock the lattice assembly in place. Joints along panel abutting edges were step lapped to minimize radiation "windows", and were thermally isolated with foam strips.

The conical base of the vehicle was insulated in the same manner, however, eight panels were required because of material width limitations. To produce the conical curvature it was assumed that aluminized mylar roll stock was used in a radial pattern, cutting each layer to a pie shaped piece. The material would conform to the conical shape without wrinkling using this approach.

The payload isolation approach consists of four discrete shields of 2 mil aluminized mylar. These would be applied to a fiberglass framework in one-quarter segments using Velcro tape, thus making it possible to remove a single quadrant for access to the interior. The framework could also be assembled in four sections by sliding into channels on a center hub. The sections would be locked in place by a rotating cap on the hub. Four fiberglass diagonal channels were used to space and support the shields on their longest span. This same structural approach could be used to support a MLI blanket.

The concept of Figure 1.1-44 used three separate insulation systems. The first and outermost was a single layer of Beta fiber cloth that surrounded the outside of the truss structure on the sides and was coupled with a 5 shield blanket of MLI to reduce heating of the structural members. The second system was comprised of the MLI blanket panels which were mounted on the inside of the truss structure. Beta fiber cloth meteoroid protection was provided with the bottom panels. The third system was a foam substrate layer (fiberglass reinforced) which was assembled on the cryogenic tanks.

The MLI panels were mounted on two fiberglass or nylon rings which were attached to the structural rings. These were the only points of attachment of the MLI to the structure. The panel system would be perforated to simplify purging. The outer Beta fiber cloth/MLI shield would reduce direct radiation to the perforated multilayer insulation, and was not perforated. The cryogenic tanks were encapsulated in a foam covering for ground hold protection.

Figure 1.1-45 shows lacing concepts for MLI blanket assemblies. The radiation shields and nylon net spacers would be loosely laced together with nylon cord as shown in Detail B. Since the aluminized mylar shields are easily torn when pierced, holes for lacing would be burned in with a hot needle. Detail C shows typical hole and slit patterns. Two shields with a separating spacer would be laced together into sub-assembly "A" using the holes in the shields. Two sub-assembly "A's" with a separating spacer would then be laced together into sub-assembly "B" using the slits in the shields. This lacing arrangement maintains a separation between shields. Fabrication difficulties are foreseen in design of tooling for accurately locating the lacing holes and slits. Accessibility to perform the lacing operation may also be a problem. On this particular arrangement, since the individual spacers would be attached to the vehicle support structure, the blanket assembly would be laced together only along the edges.

Detail E shows a stepped joint. This arrangement would be used to join panel blankets along the seams. The first step after the blankets were attached at both ends was to pull back the outer stepped layers of the one blanket to expose the inner seam. Inner net layers from both blankets would be pulled through this seam and laced together. This inner step would be packed with spacer material to prevent shorting between misaligned radiation shields in the adjacent blankets. The outer stepped layers would be returned to position and the gap packed with spacers. The outer layers of nylon net would be overlapped and laced together.

The payload deck blanket is shown in Section A-A. This blanket, although laced together as shown in Detail B, required a special arrangement of holes and slits in the radiation shields to accommodate the pie-shaped shield sections. This section shape was necessary due to material width limitations. The shield seams would be rotated with respect to adjacent shields in order to uniformly distribute thickness buildup. This blanket assembly extended beyond the outer diameter of

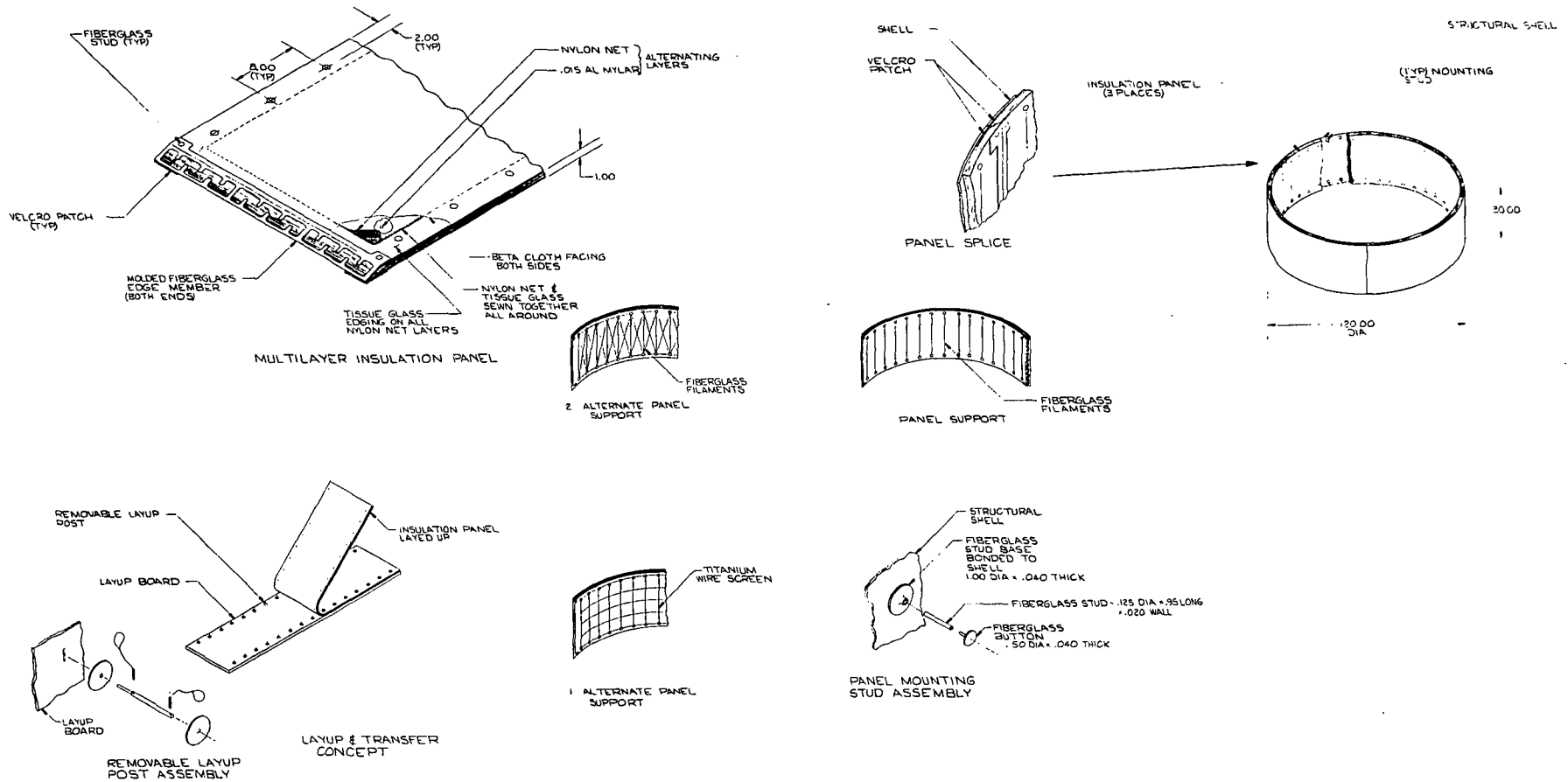


Figure 1.1-36: MULTILAYER INSULATION PANEL ATTACHMENT CONCEPT TO A CYLINDRICAL SHELL

**Page Intentionally Left Blank**

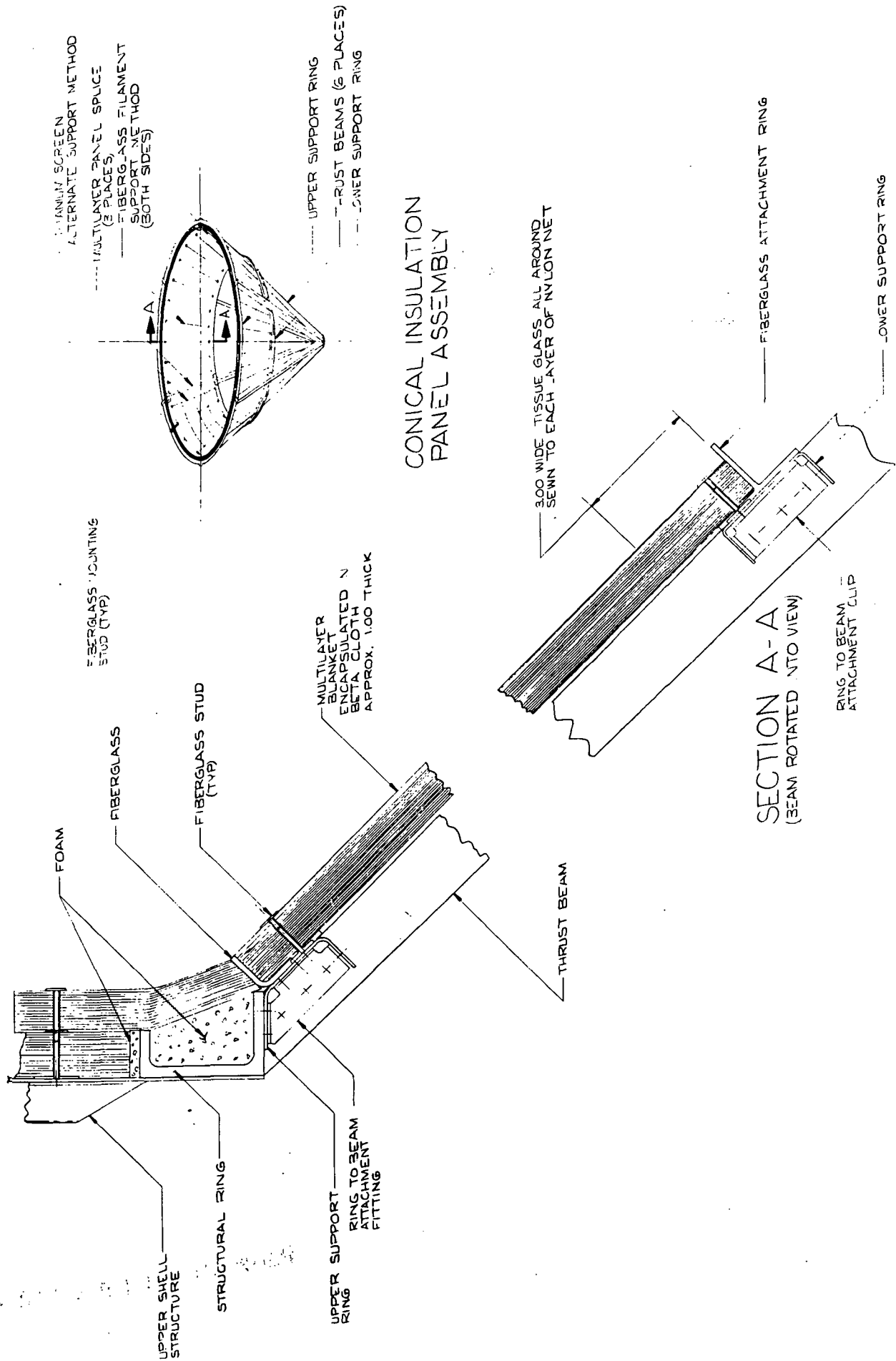


Figure 1.1-37: CONICAL INSULATION CONCEPT

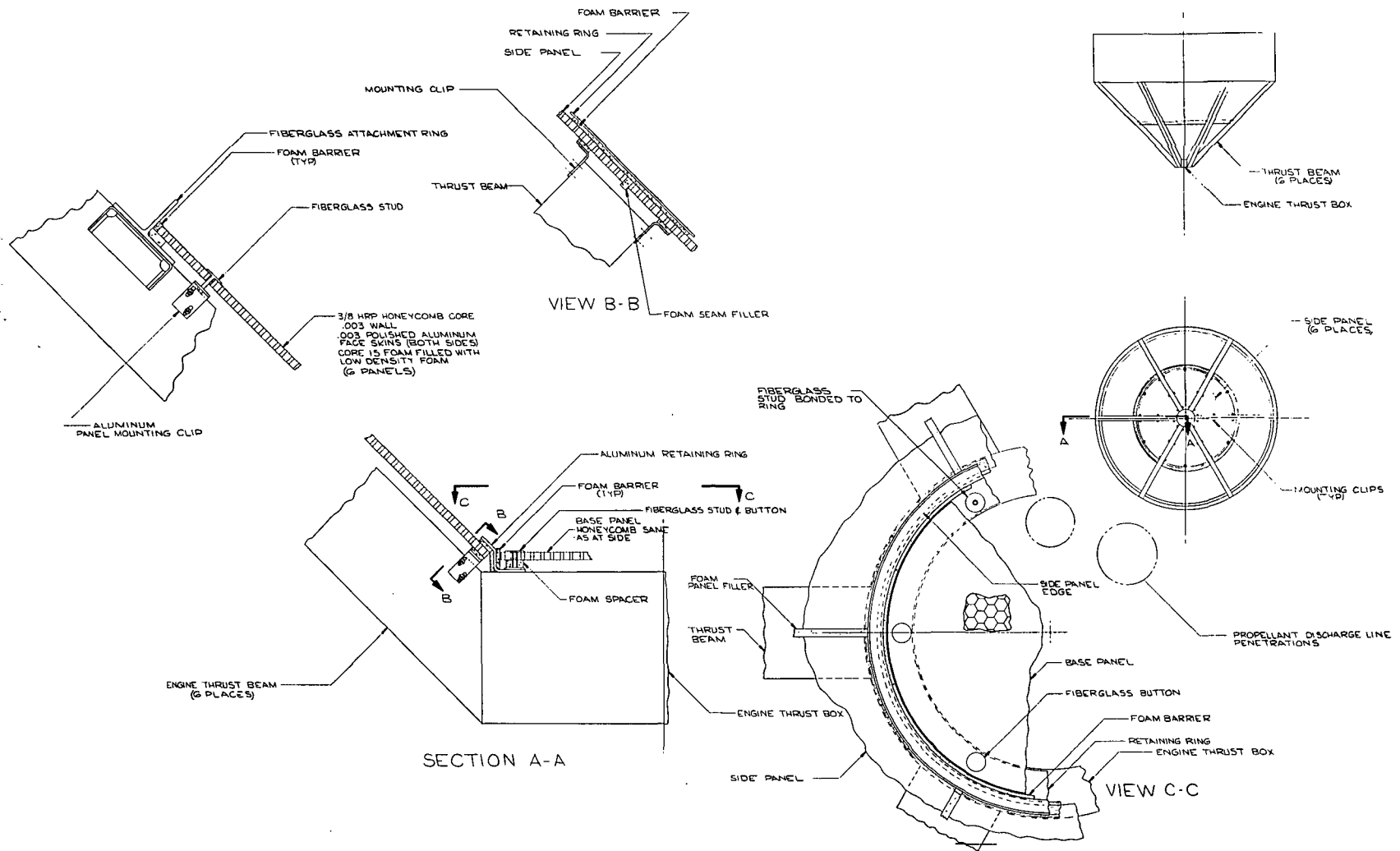
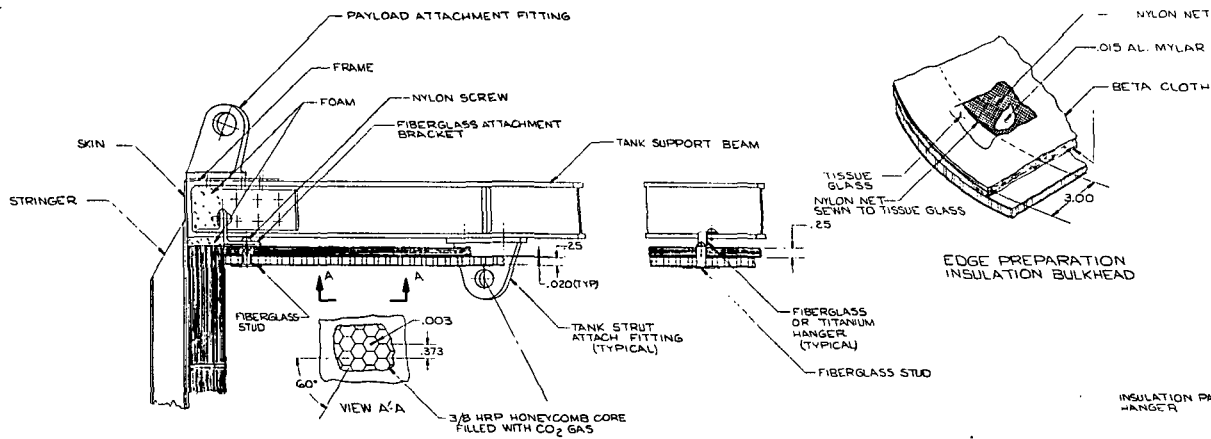
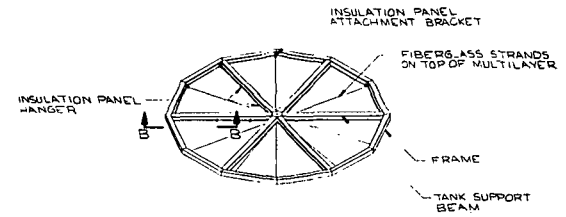


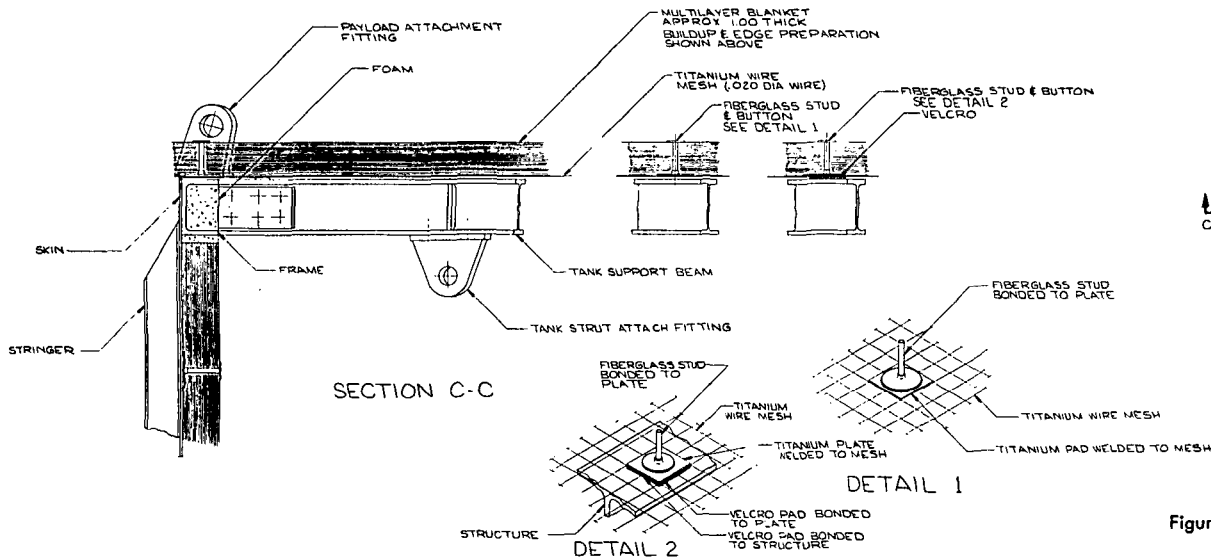
Figure 1.1-38: LOWER CONE INSULATION CONCEPT



SECTION B-B  
 FLAT, ONE PIECE, INSULATION BULKHEAD  
 INSULATION BULKHEAD IS INSTALLED BEFORE TANK SUPPORT BEAMS ARE INSTALLED



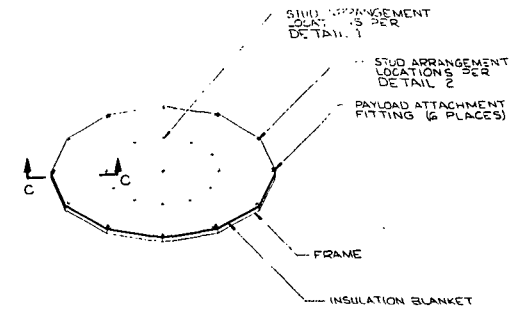
BULKHEAD CONCEPT I



SECTION C-C

DETAIL 1

DETAIL 2



BULKHEAD CONCEPT II

Figure 1.1-39: INSULATION BULKHEAD-SINGLE PIECE

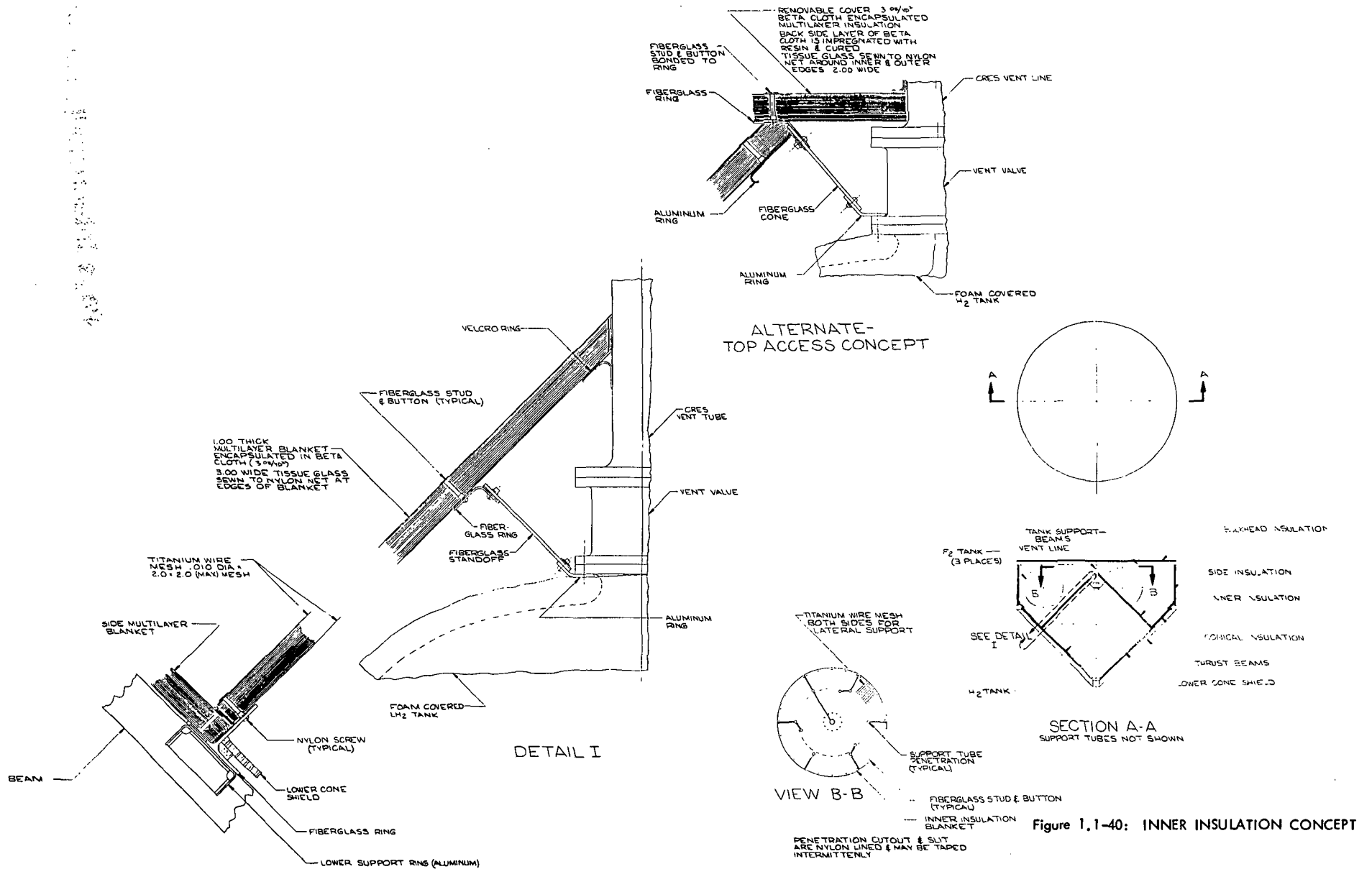
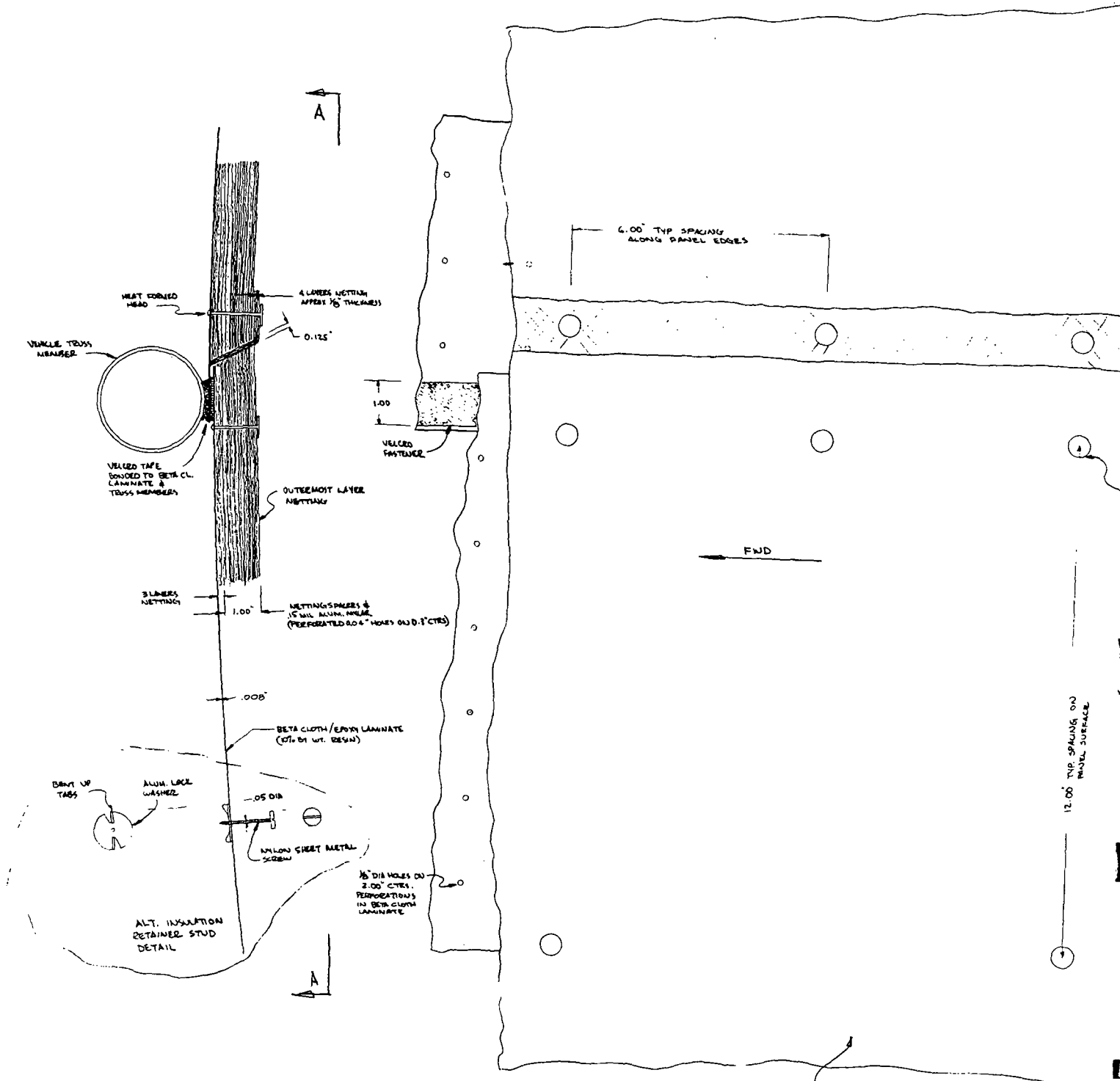


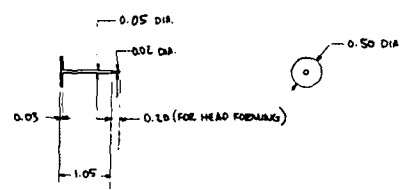
Figure 1.1-40: INNER INSULATION CONCEPT



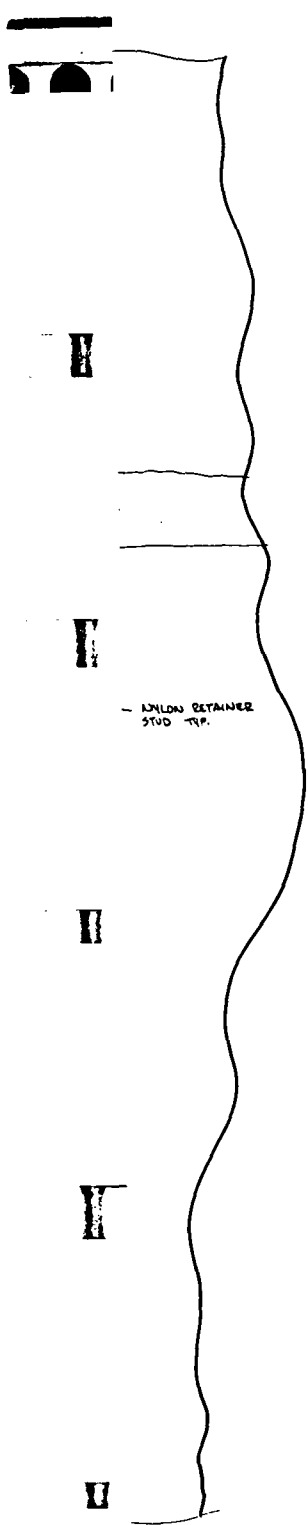
MULTILAYER BLANKET  
 .15 MIL ALUM. MYLAR PERFORATED SHEETS  
 NETTING (MILKIN OR DRENN) .007 THK.

SECT A-A

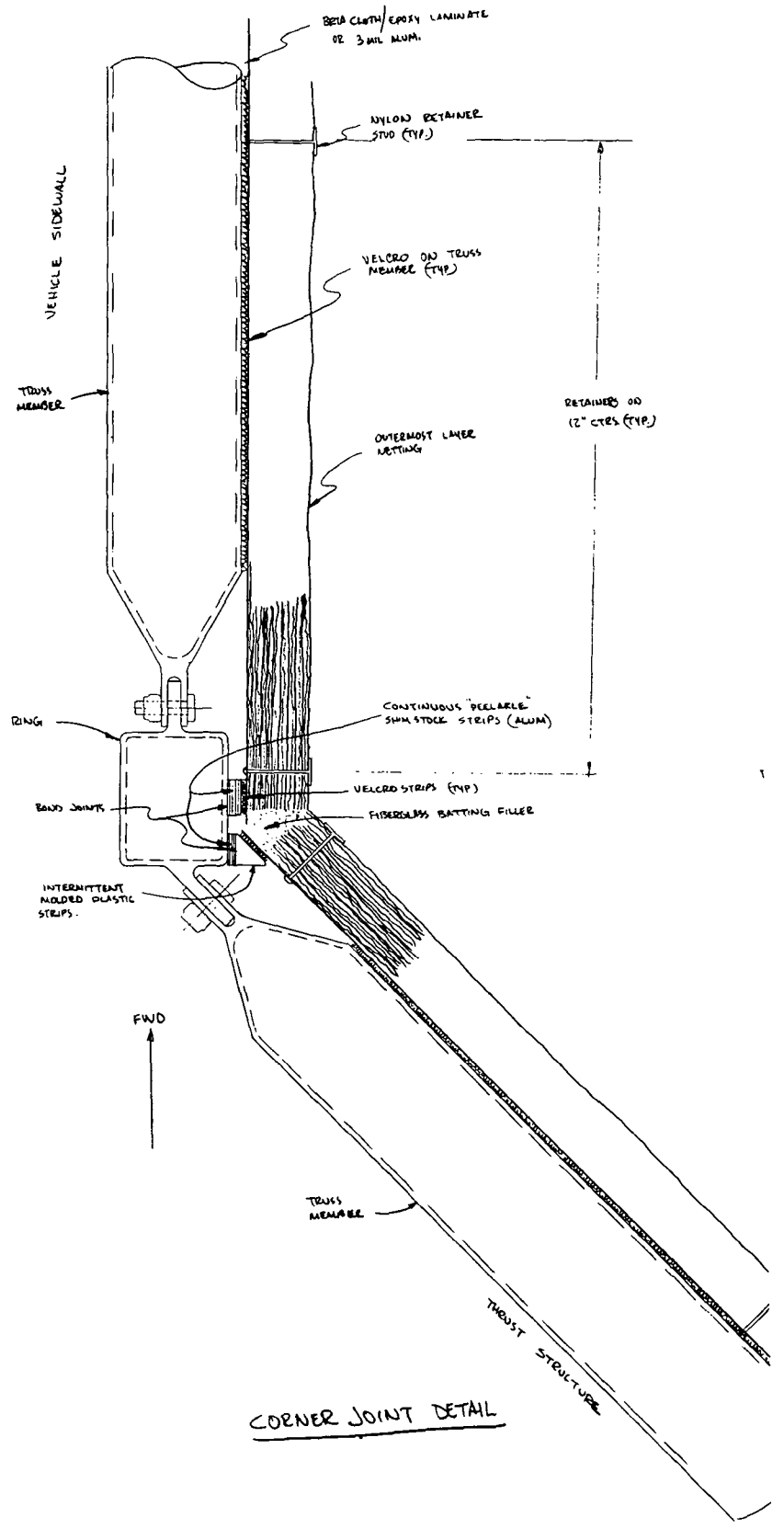
- NOTES:
1. BETA CLOTH/EPoxy LAMINATE CAN BE READED FOR ADDITIONAL STIFFNESS IF NECESSARY.
  2. ALUMINUM (.3 MIL) SHEET CAN BE SUBSTITUTED FOR BETA CLOTH LAMINATE BUMPER.



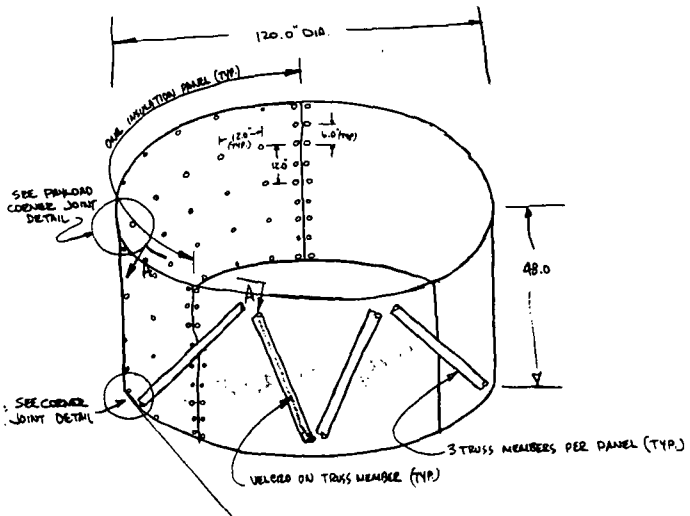
NYLON RETAINER STUD  
 DETAIL



NYLON RETAINER STUD (TYP.)



CORNER JOINT DETAIL



U

**Page Intentionally Left Blank**

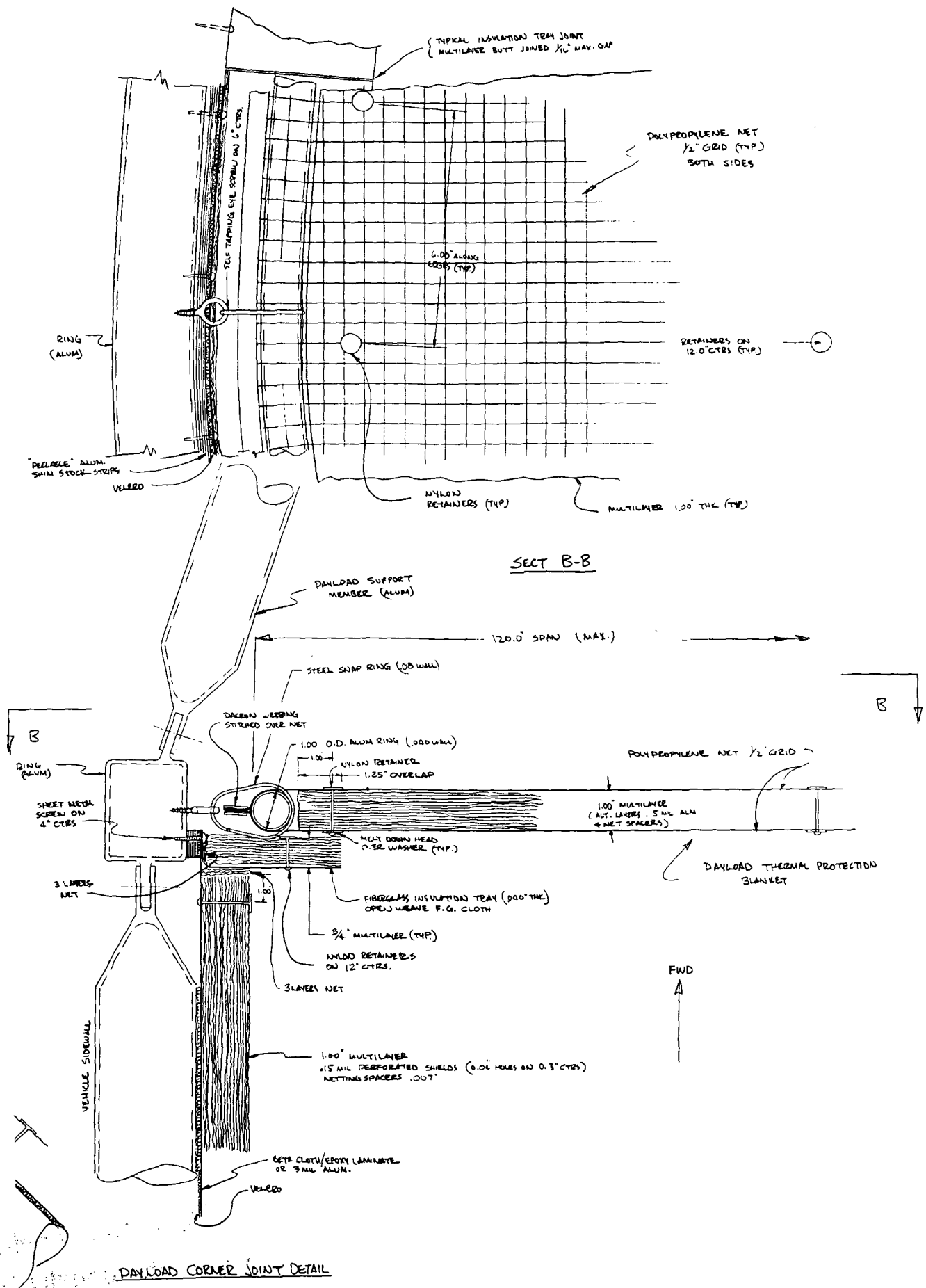
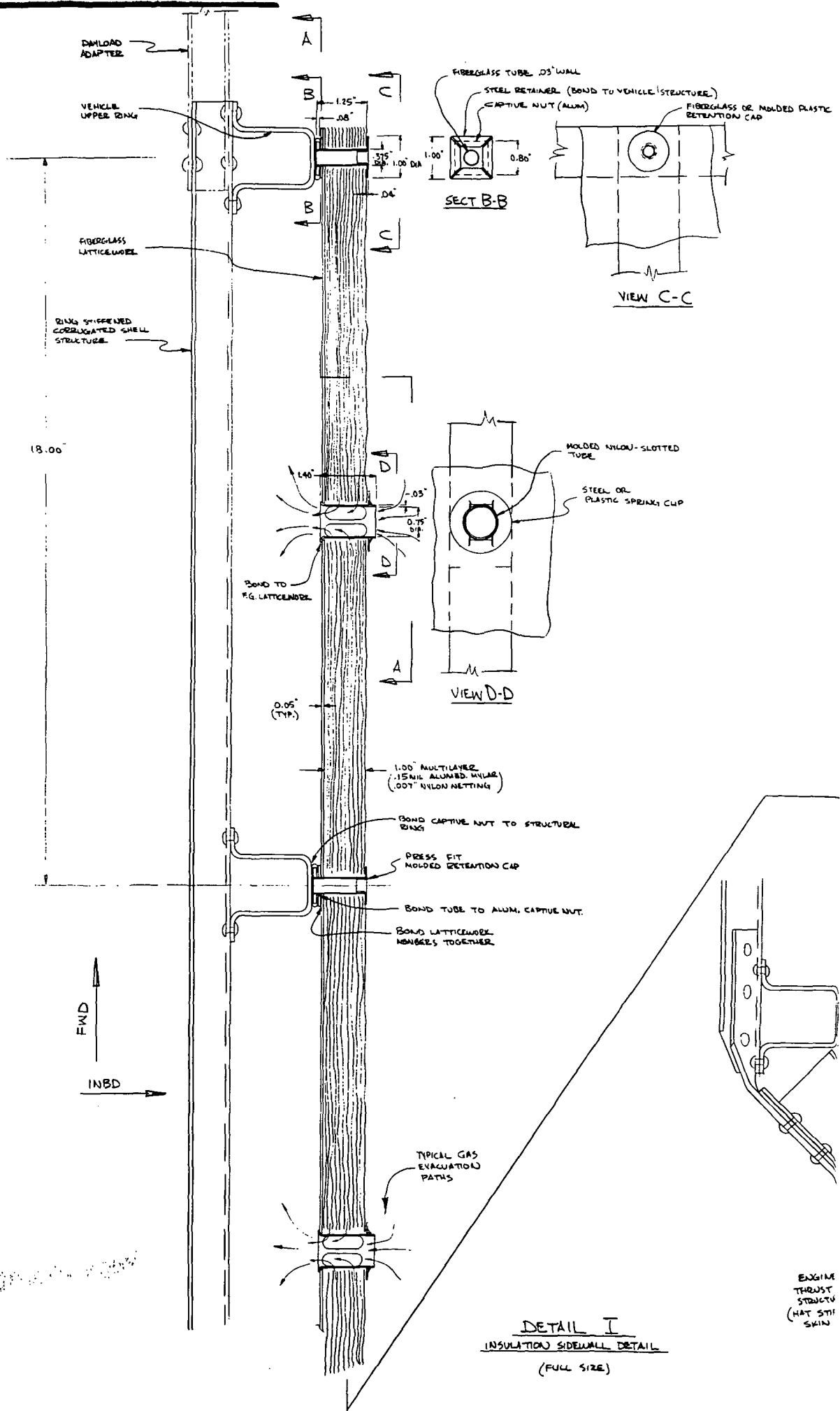
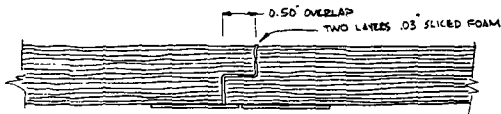
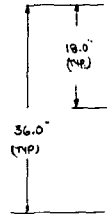
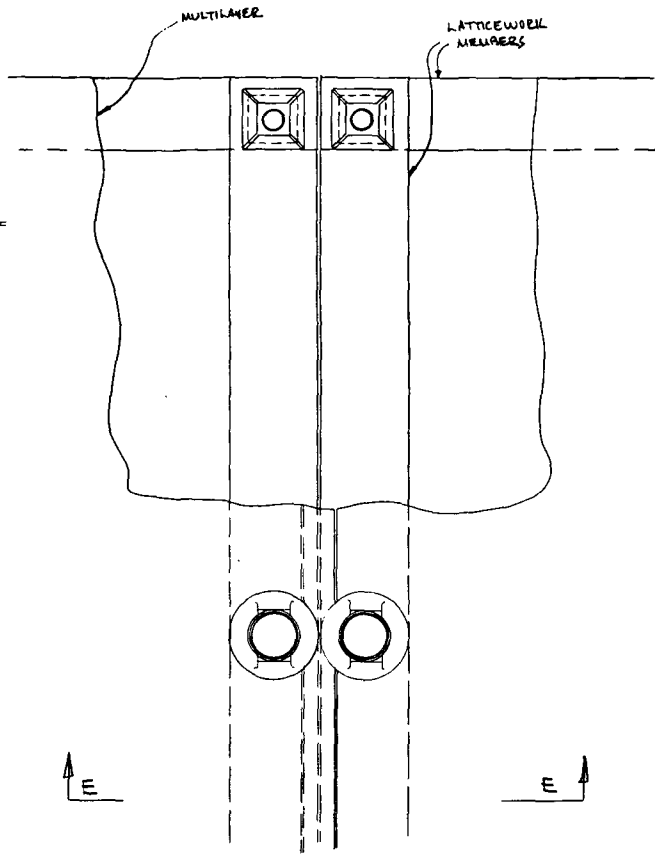


Figure 1.1-41: THERMAL/METEOROID PROTECTION CONCEPTS

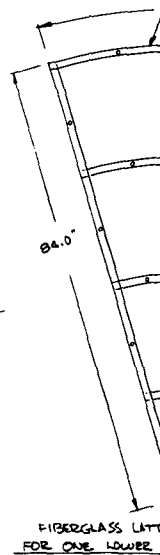
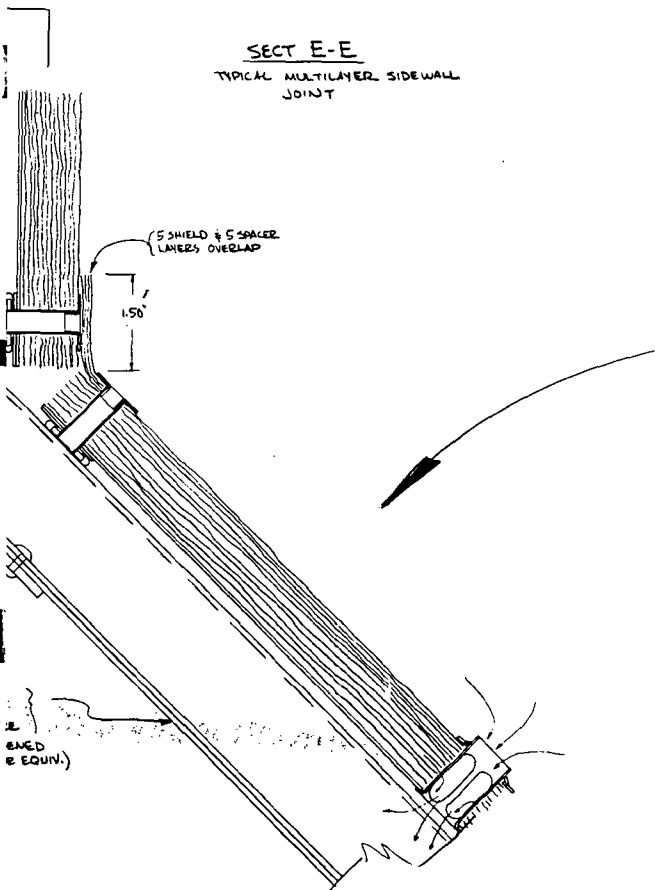




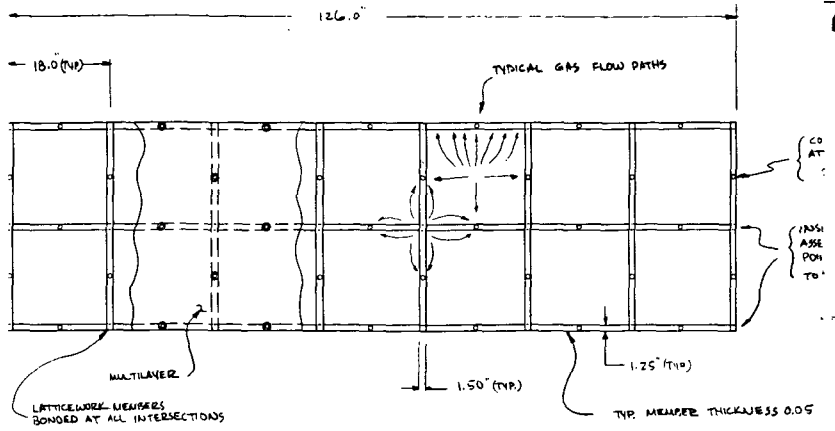
**DETAIL I**  
 INSULATION SIDEWALL DETAIL  
 (FULL SIZE)



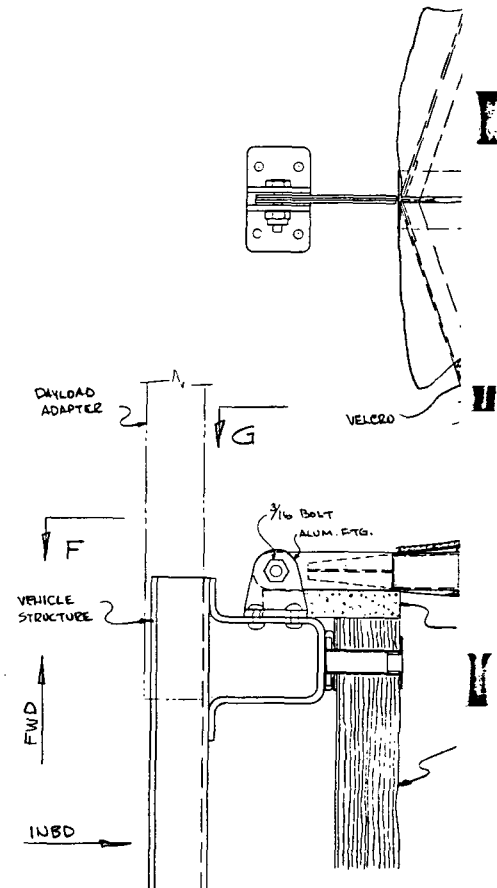
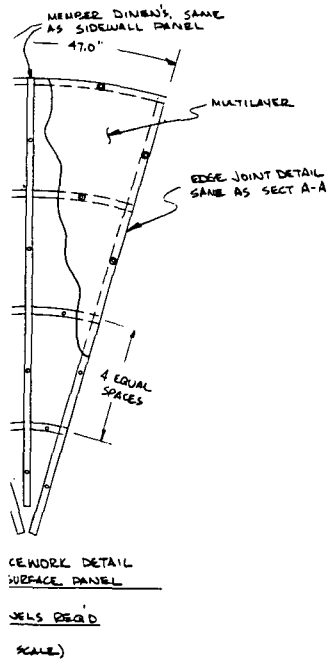
SECT E-E  
TYPICAL MULTILAYER SIDEWALL JOINT



B DA  
(X0)

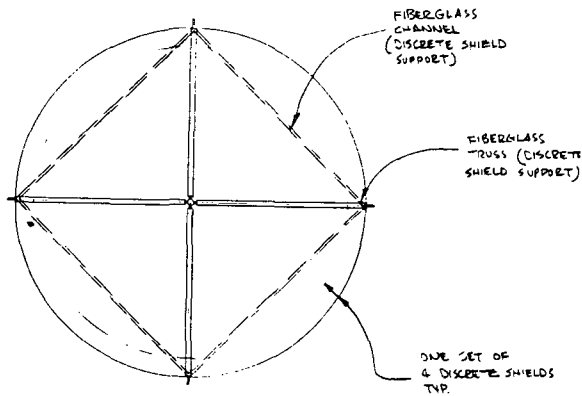
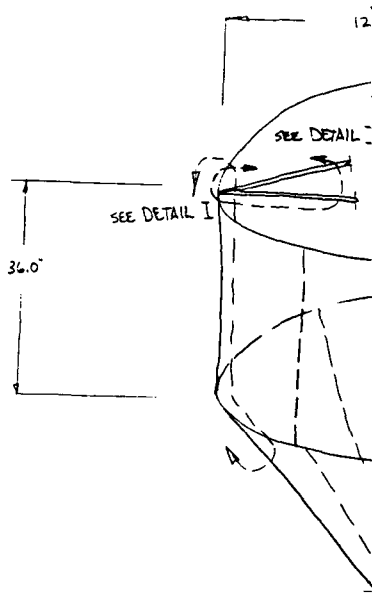


FIBERGLASS LATTICEWORK DETAIL  
 FOR ONE PANEL  
 3 PANELS REQ'D  
 (NO SCALE)

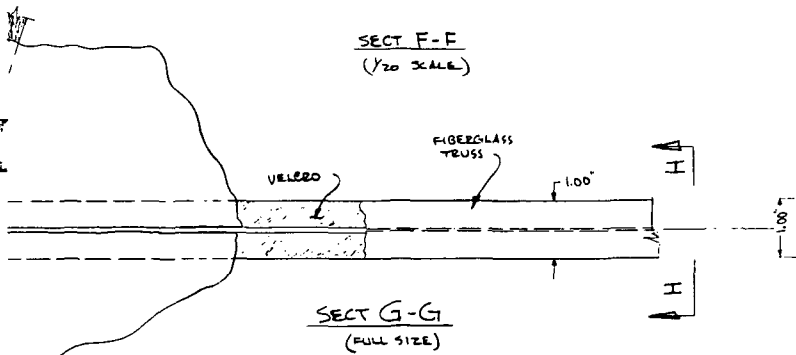


UNITED INSULATION  
ACHUMENTS & VENT PORTS  
SEE VIEW D-D

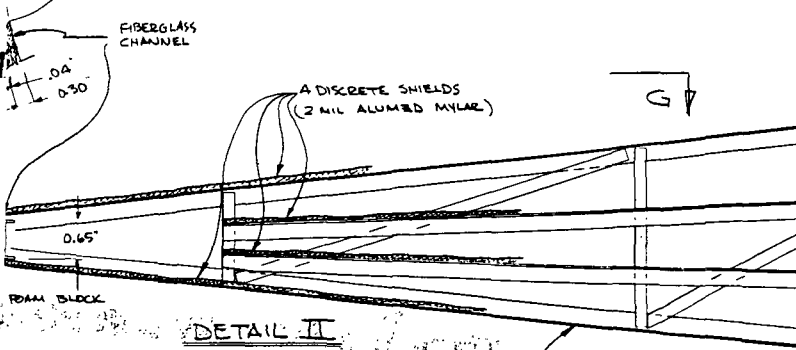
RATION/LATTICEWORK  
MAIN ATTACHMENT  
PTS. (FASTENERS BONDED  
VEHICLE STRUCTURE)



SECT F-F  
(1/20 SCALE)



SECT G-G  
(FULL SIZE)



DETAIL II

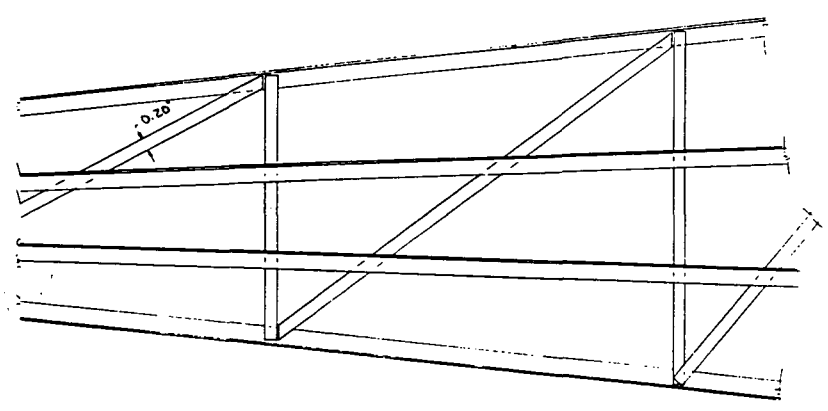
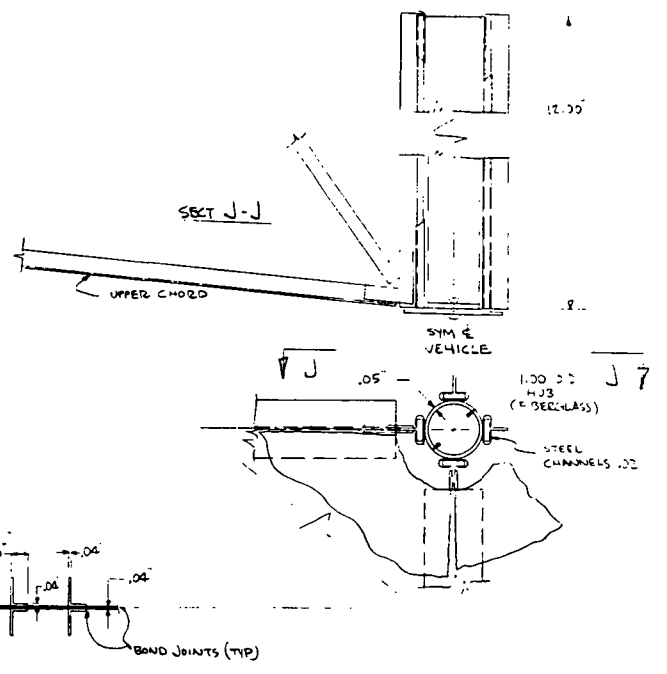
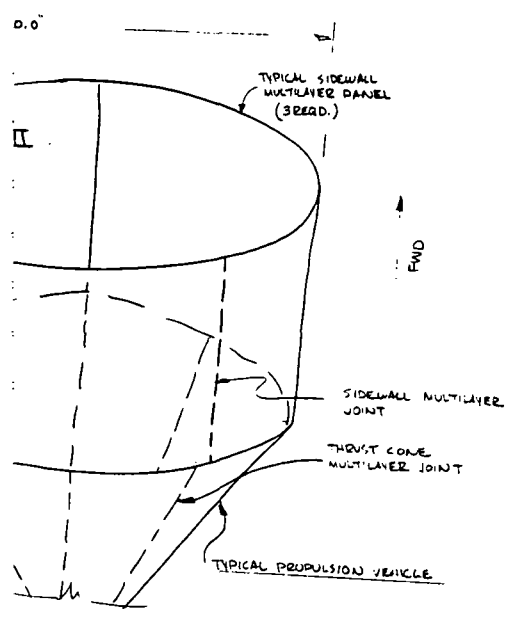
INSULATION DECK DETAIL  
TYPICAL FOR BETWEEN TANK  
COMPARTMENTS OR BETWEEN  
TANK AND PAYLOAD.

(FULL SIZE)

SIDEWALL  
MULTILAYER

FIBERGLASS TRUSS  
(FORWARD ASSEMBLY)

Figure 1.1-43: THEI



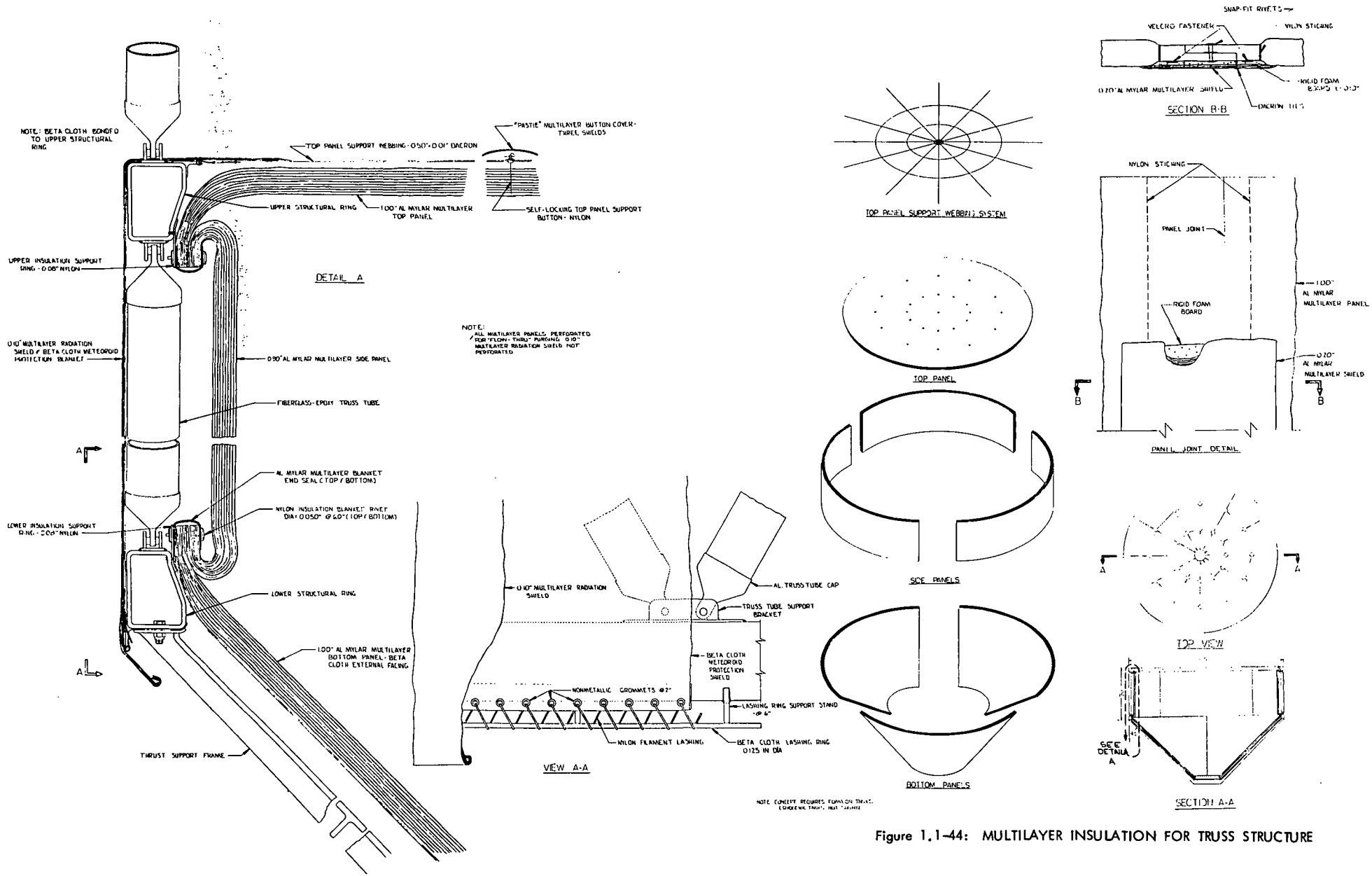
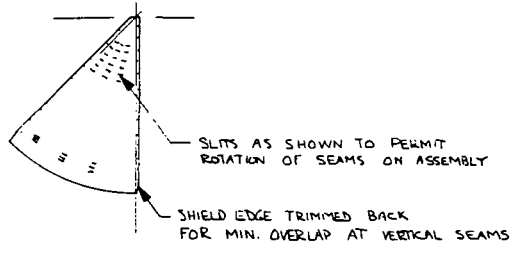
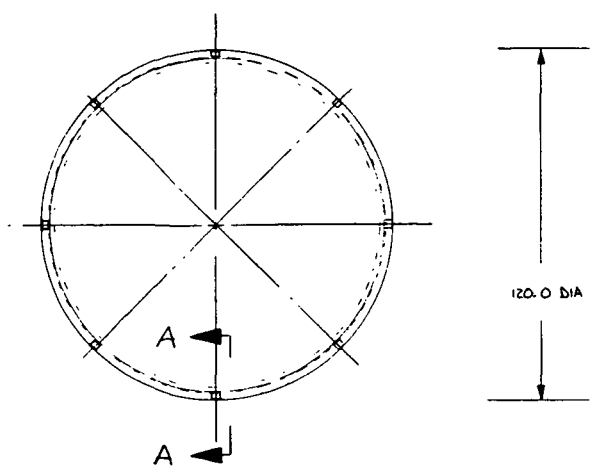


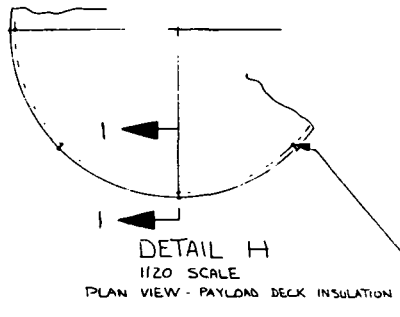
Figure 1.1-44: MULTILAYER INSULATION FOR TRUSS STRUCTURE



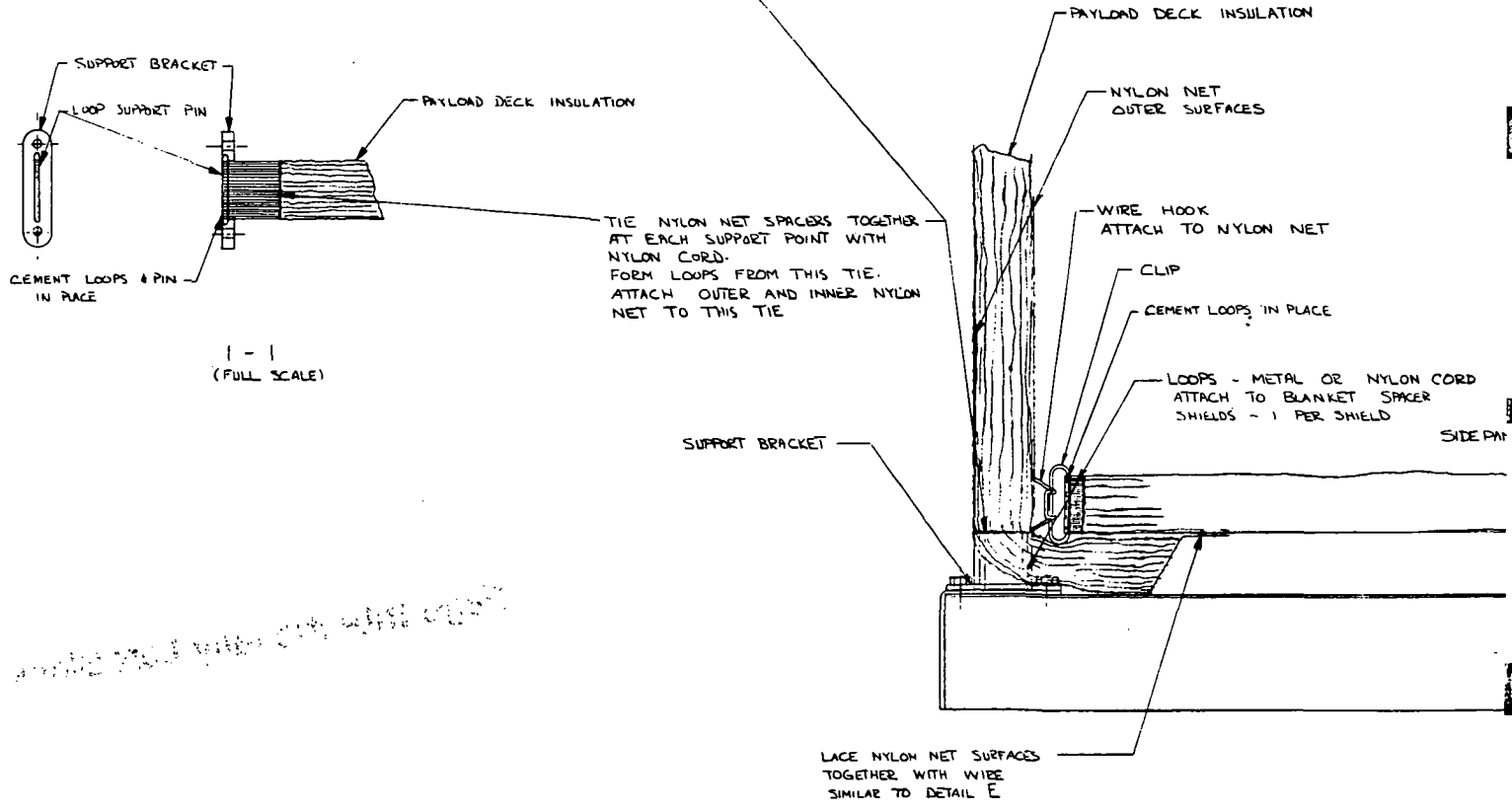
DETAIL G  
(1/20 SCALE)  
REFLECTOR SHIELD - PAYLOAD DECK - TYP SECTION



STAGE  
(1/20 SCALE)

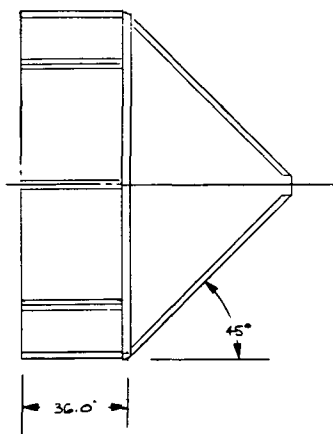


DETAIL H  
1/20 SCALE  
PLAN VIEW - PAYLOAD DECK INSULATION



1-1  
(FULL SCALE)

*Handwritten note:* using 2x4 with 2x4 with 2x4



FOLD INNER NYLON NET LAYER  
& LACE TOGETHER WITH WIRE

DETAIL F  
(NOT TO SCALE)

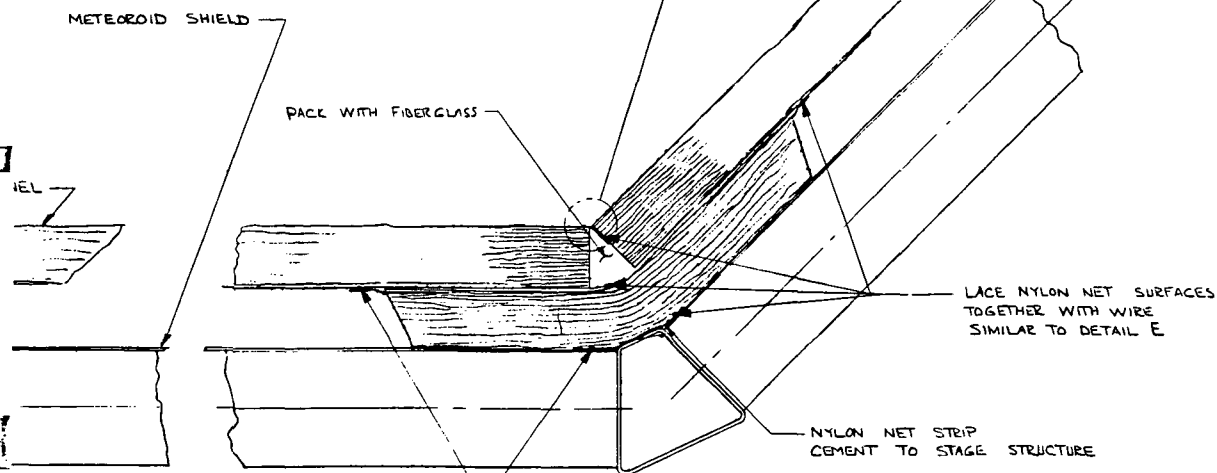
SPACERS TO PREVENT  
SHORTING ACROSS REF

NYLON NET

DETAIL E  
SHOWING SECTION THROUGH STEPPED  
JOINT FOR SIDE PANELS  
(FULL SCALE)

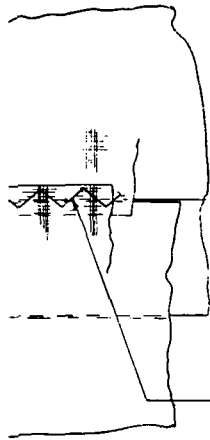
(2 REFL

(2 SUB-

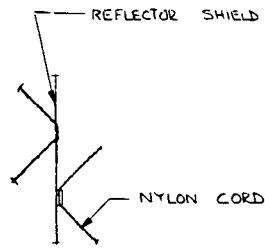


A - A  
(FULL SCALE)

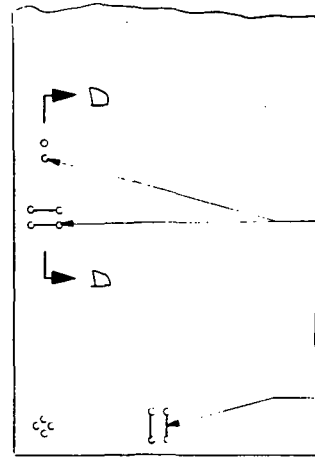
REFLECTOR SHIELDS



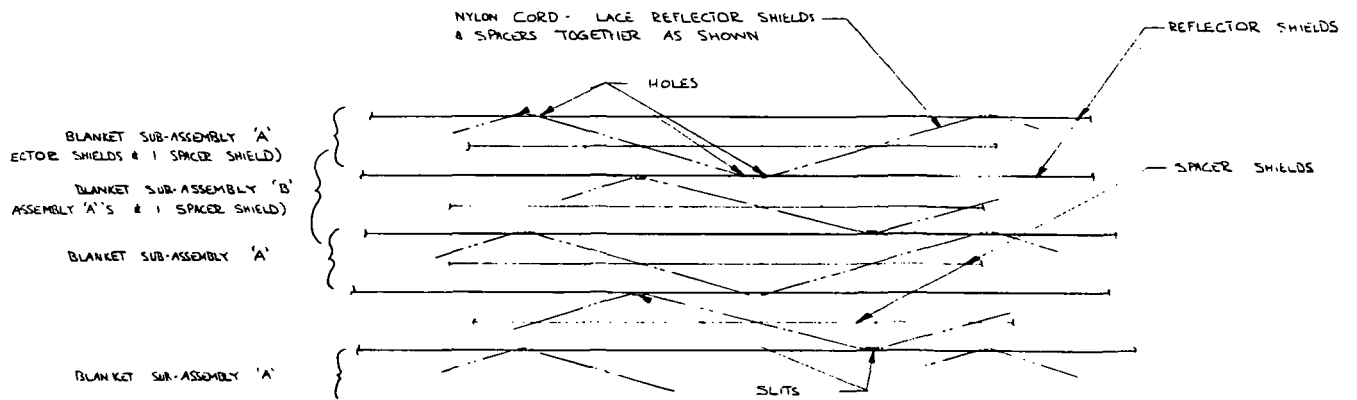
OVER LAP OUTER LAYER OF NYLON NET AND LACE TOGETHER WITH WIRE



D-D  
(NOT TO SCALE)



DETAIL C  
TYPICAL REFLECTOR SHIELD  
(NOT TO SCALE)



DETAIL B  
ENLARGED SECTION THROUGH MULTILAYER BLANKET  
(NOT TO SCALE)

Figure 1.1-45: LACING CONCEPT FOR MULTILAYER BLANKET ASSEMBLY

the side panel to provide insulation for covering the radiation window at the side panel intersection. At each structural attachment point the shields were slit and cut to permit folding down with a minimum overlap at the seams. At the end of the slit the spacers were tied together with nylon cord. Attachment loops were formed from the tie, and the outer and inner nylon net was attached to this tie. The loops extended to the support bracket attached to the vehicle structure. The portion of the blanket which extended down along the side panel was held in place by lacing through the adjacent nylon net surfaces.

For the upper side panel attachment wire hooks were embedded in inner nylon net covering the payload deck insulation. This inner nylon net supported the upper end of the side panels. Metal or nylon cord loops were attached to the side panel spacer shields. A support pin through these loops was mounted to a clip. This arrangement permitted attaching the clip to the hook in a limited access condition.

The lower side panel and the thrust structure insulation were attached together at their intersection (Section A-A, Figure 1.1-45). An overlapping insulation blanket covered the radiation window at the intersection and provided the attachment tie from the vehicle structure to the side panel and thrust structure insulation blankets. In all cases the attachments in this area were made by lacing overlapping nylon net surfaces together. A strip of nylon net was bonded to the vehicle structure for this attachment.

Figure 1.1-46 shows insulation/sidewall panel assembly concepts. These concepts provided the integration of structural panels with insulation and meteoroid shields. The panel assemblies were adaptable to the cylindrical portion of the vehicle structure and to the thrust cone section. Joints were along the longerons or the thrust beams. A gap was maintained between the structural panels and the insulation for channelling the purge gas flow. In the cases shown, the insulation was perforated and the purge gas was vented either into the compartment or outside the compartment. Intermediate attachment of insulation to the structural panels in both cases used nylon support rods with washers bonded in place.

Detail E shows a stepped joint concept for an assembly with the insulation outside of the structural panel. The overlap insulation strip assembly would be manufactured using thin diameter nylon pins. This strip was attached to the insulation panels with overlapping nylon layers laced together. Radiation windows along the steps were packed with separator material.

Detail H shows a stepped joint concept with the insulation and inner and outer fiberglass support structure. The assembly was bonded to the vehicle structure longeron or beam; along with the anchor nuts for panel installation. There was a fiberglass standoff frame along the edge of the panel to align panel insulation with joining strip insulation.

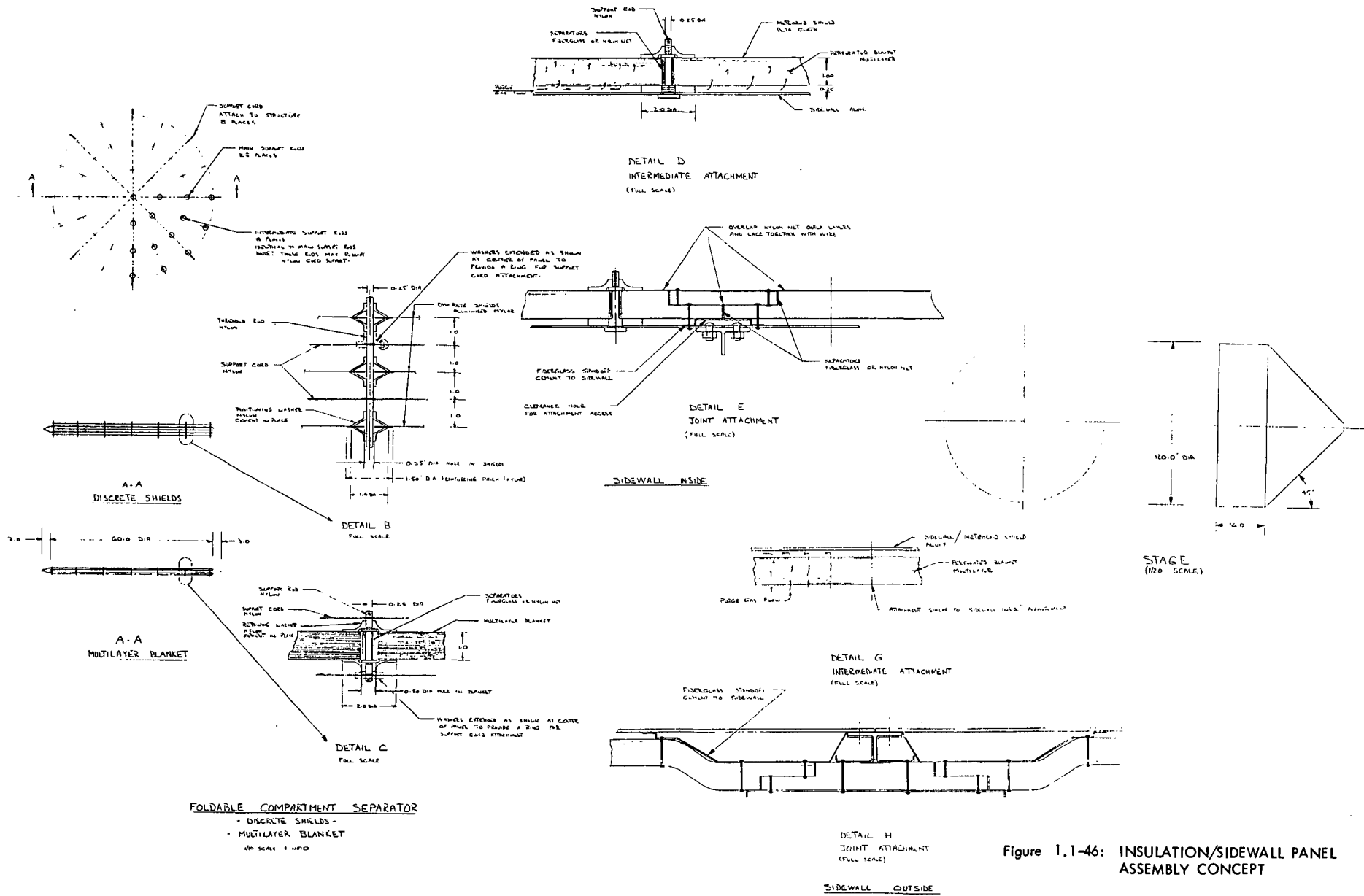


Figure 1.1-46: INSULATION/SIDEWALL PANEL ASSEMBLY CONCEPT

Accessibility for packing the voids along the steps with separators was limited in this design. Two alternate configurations were apparent. One configuration would mount the MLI to the structural panel at a distance which was constant with the fiberglass standoff along the edge. A narrow uniform gap between the structural panel and insulation could be provided by attaching the panels to the inside leg of an "I" section longeron or beam.

A foldable compartment separator is also shown in Figure 1.1-46. This blanket arrangement could be used with a MLI blanket or with widely spaced discrete shields. Detail B shows the discrete shields supported from nylon rods with positioning washers. The radially located nylon rods would be linked together with two nylon tension cords. Tensioning of these cords at the periphery of the separator and attaching to the vehicle structure provided the necessary support (Section A-A). Detail C is a similar arrangement for supporting a MLI blanket.

A preliminary estimate of the weights of sub-structure, fasteners, edge members and other details required to mount the thermal/meteoroid protection system was made for several of the design concepts. The weight data is presented parametrically in Figures 1.1-47 through 1.1-50. Each figure represents a portion of the vehicle such as the sidewall, conical portion, etc. In these curves the weight of the thermal/meteoroid protection installation for each design drawing is plotted vs. MLI thickness. The basic MLI is shown for comparison. The total weight lines are nearly parallel to the MLI lines because the installation features and meteoroid protection were necessary regardless of MLI thickness.

One complete vehicle insulation installation is represented by Figure 1.1-41. Another complete vehicle installation is represented by Figures 1.1-36, 1.1-37, 1.1-38 and 1.1-39. The installation features represent 28.8% and 27.2% of the total thermal/meteoroid protection system weight of these two vehicles respectively. This is somewhat surprising because the design features of each concept are quite different. Total weights should not be considered correct because a constant multilayer thickness and type was assumed to allow comparisons between the various mounting approaches.

Evaluation of Figures 1.1-47 through 1.1-50 shows that MLI mounting features, such as honeycomb sandwich platforms or fiberglass support members, e.g. Figures 1.1-37 and 1.1-39 (Concept 1), constitute a significant weight penalty to the vehicle designs.

Some design concepts proposed the use of discrete shields for radiation baffles between the payload and the tanks. An analytical appraisal of their value for the top deck insulation was made. Assuming only radiation, the heat flow is

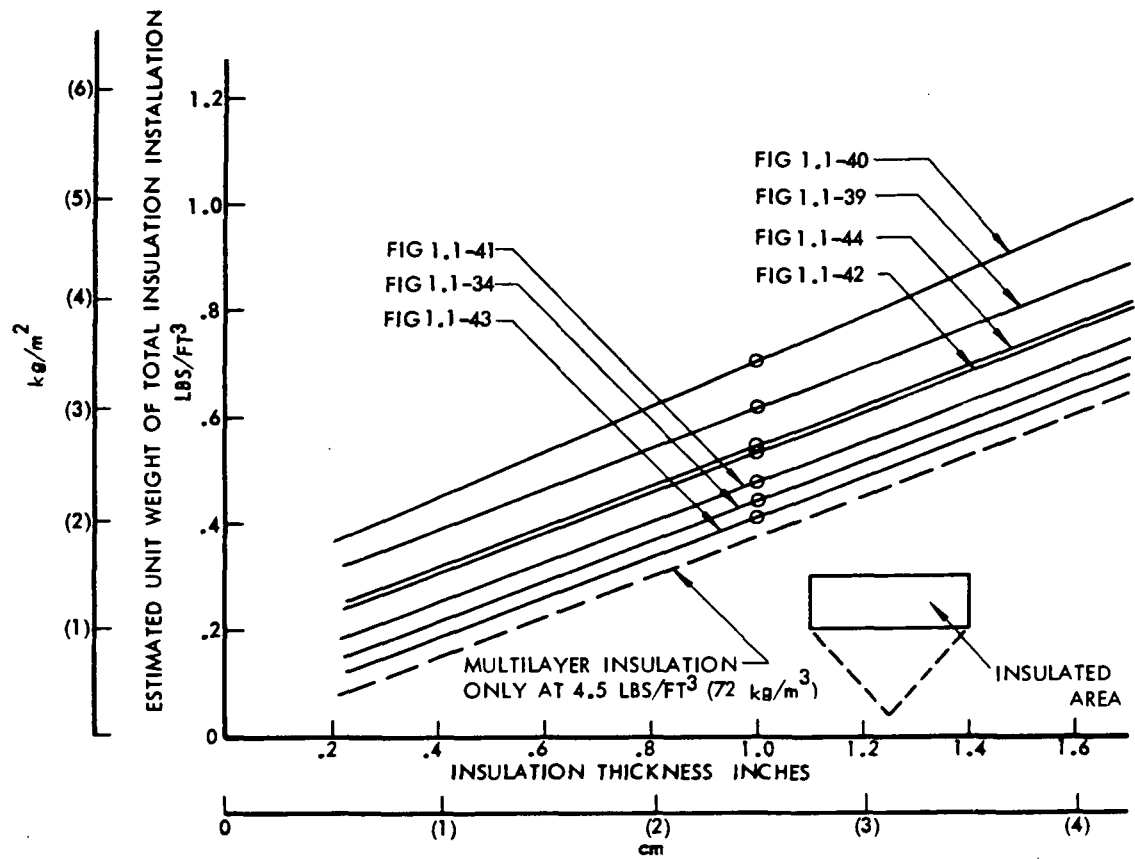


Figure 1.1-47: INSULATION INSTALLATION WEIGHT VS INSULATION THICKNESS

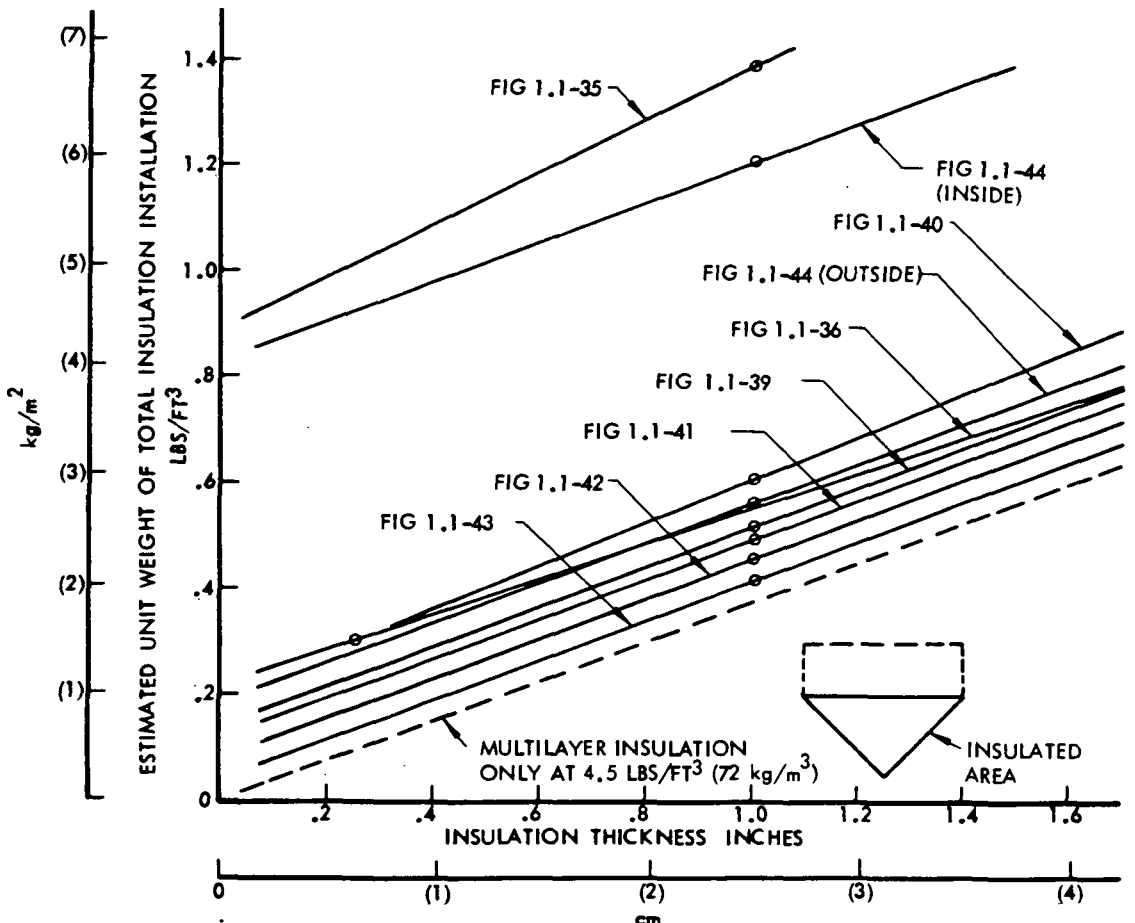


Figure 1.1-48: INSULATION INSTALLATION WEIGHT VS INSULATION THICKNESS

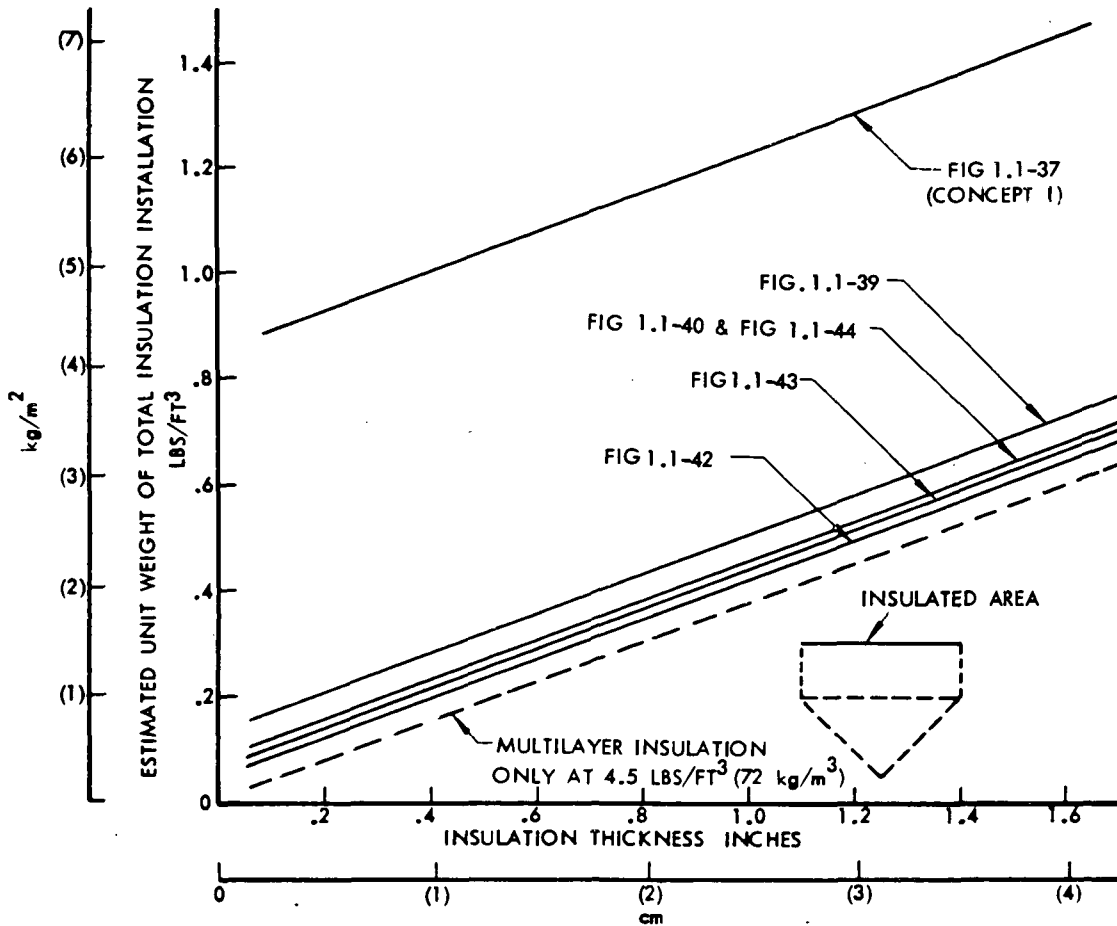


Figure 1.1-49: INSULATION INSTALLATION WEIGHT VS INSULATION THICKNESS

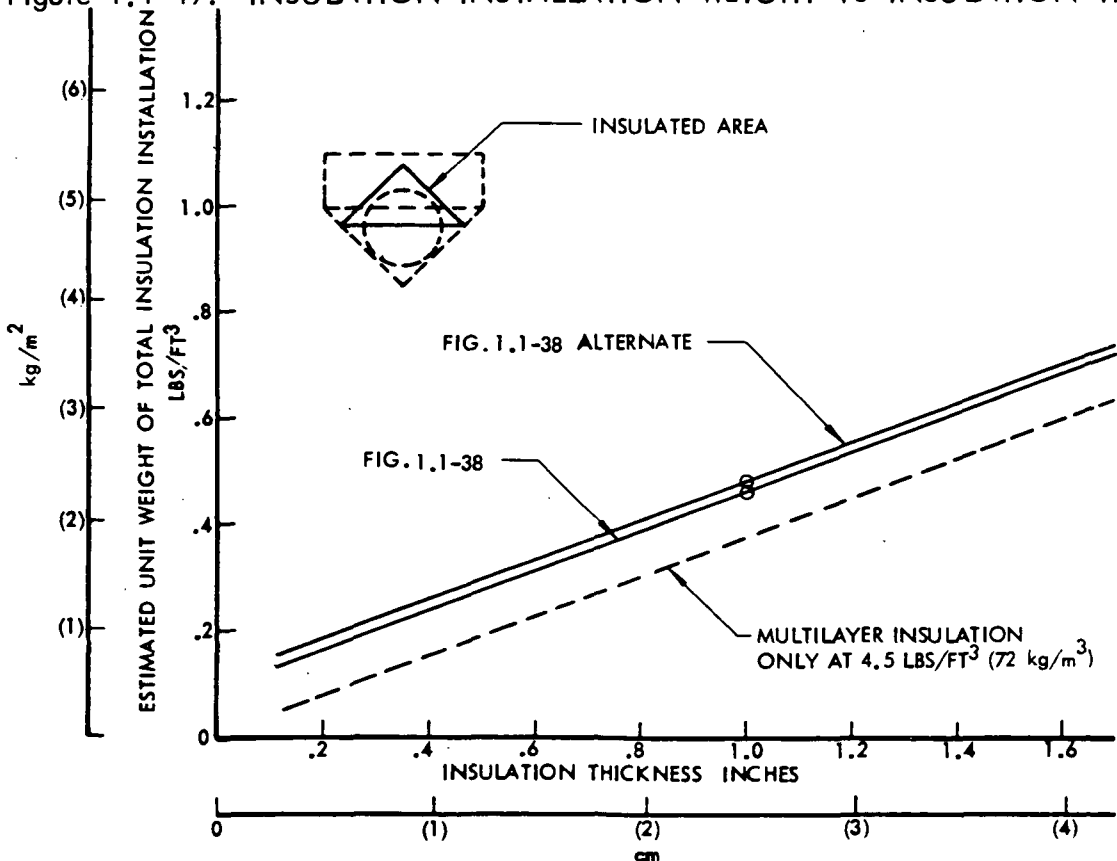


Figure 1.1-50: INSULATION INSTALLATION WEIGHT VS INSULATION THICKNESS

$$q = \frac{\sigma (T_1^4 - T_N^4)}{(N-1) \left( \frac{1}{\epsilon_1} + \frac{1}{\epsilon_2} - 1 \right)}$$

where  $N =$  number of discrete shields.

Using  $\epsilon_1 = \epsilon_2 = .025$  (same as assumption for insulation), the temperature of the outer shield,  $T_1 = 520^\circ\text{R}$  ( $289^\circ\text{K}$ ), and the temperature of the innermost shield,  $T_N = 150^\circ\text{R}$  ( $83.5^\circ\text{K}$ ) the heat flow was:

$$q = \frac{0.171 (5.2)^4 - (1.5)^4}{(N-1) (79)} = \frac{1.57}{N-1} \text{ Btu/Ft}^2 \text{ - Hr}$$

Heat flow of the optimized aluminized mylar/nylon net thickness ( $f_{nn}$ ) was

$$k_{nn} = 3.0 \times 10^{-13} (T_1^2 + T_2^2) (T_1 + T_2) + 0.63 \times 10^{-7} (T_1 + T_2)$$

$$q_{nn} = \frac{1}{\delta_{nn}} \left[ 3.0 \times 10^{-13} (T_1^4 - T_2^4) + 0.63 \times 10^{-7} (T_1^2 - T_2^2) \right]$$

$$= \frac{1}{\delta_{nn}} \left[ 3 \times 10^{-5} (725) + 0.63 \times 10^{-3} (24.79) \right]$$

$$= \frac{1}{\delta_{nn}} \left[ .03175 + .0156 \right] = \frac{.0474}{\delta_{nn}}$$

And, relating the heat flow of discrete shields and aluminized mylar/nylon net;

$$\frac{.0474}{\delta_{nn}} = \frac{1.57}{N-1}$$

$$N = 1 + 33.2 \delta_{nn}$$

$\delta_{nn}$  for the vehicle configurations studied ranged from:

$$.383'' < \delta_{nn} < .904''$$

and the average was:

$$\delta_{nn_{avg}} = 0.5''$$

Therefore, the range in number of discrete shields would be:

$$14 < N < 31$$

and the average number of discrete shields would be

$$N_{average} = 18$$

The number of discrete shields indicated from this study was considered excessive and impractical for the proposed application.

#### Ground Hold Protection

A screening analysis of ground hold heat protection schemes was performed to identify promising approaches for design study. Hydrogen and fluorine were used as study propellants, with fluorine being somewhat thermally representative of the FLOX and methane as well.

Study of ground hold heat transfer was made complex by the predominance of convective heating and its sensitivity to purge gas flow rates, temperatures and vehicle geometry. Because of the many vehicle and thermal protection configurations of interest, a relatively simple approach to the analysis was used, from which generally applicable conclusions on concept performance could be reached. This approach was based on steady state heat transfer through and between vertical walls - the boost shroud, vehicle structure and MLI, and the tank wall in the simplest form. The walls were assumed to be planes, i.e., the change in area of each of the vertical walls with radius was ignored.

Temperature dependent thermophysical properties were used in conduction and convection equations. The external conditions which were used approximated the average annual environment at KSC. A list of the detailed assumptions used in the analysis is given in the following table.

#### Assumptions in Ground Hold Heat Protection Analysis

##### External Environment

Wind velocity = 15 ft/sec (0.05 K/sec)

Ambient temperature = 80°F (300°K)

Sun-to-shroud view factor = 1/2

### Surface Properties

<u>Surface</u>	<u>Emissivity</u>	<u>Solar Absorptivity</u>
Shroud - external	.8	.3
Shroud - internal	.8	
Insulation encapsulant/ vehicle structure		
External	.1	
Internal	.5	
Tank surface	.1	

Convective heating was due to natural or forced turbulent convection, whichever was larger. (Natural convection was larger except at high flow rates, due to low temperatures and large temperature gradients.) Equations used were from Reference 1.1-6. Purge gas conductivity, viscosity and density data were taken primarily from Reference 1.1-7.

Heat transfer to the hydrogen tank with a helium purge in the vehicle and boost shroud is shown in Figure 1.1-51. The purge gas flow rate in this and most other curves following was assumed to be small, with natural convection applying and the heat capacity effect of the gas negligible. As expected with the helium purged system, the hydrogen heating rate was quite high which would require continual venting and top-off of the tank. As shown in Figure 1.1-51, the addition of a divider to create a counterflow heat exchanger did not significantly reduce the heating rate with a low purge gas flow rate.

The addition of foam on the hydrogen tank resulted in considerable reduction in the heating rate as shown in Figure 1.1-52. Placement of the foam directly on the tank wall resulted in the most efficient system since the foam conduction decreased and convective heat transfer increased at lower temperatures. In addition, the area of foam was minimized by placing it on the tank. If the foam could be jettisoned with the boost shroud, the efficiency would be of less importance. Figure 1.1-53 shows the heat flow to the hydrogen tank if the foam was placed outside of the vehicle MLI.

The use of sealed foam on the hydrogen tank introduced the possibility of using nitrogen rather than helium as the purge gas. Figure 1.1-54 shows the heat flow to the hydrogen tank with the nitrogen purge and foam on the tank. The reduction in heat flow compared to Figure 1.1-52 was most dramatic for thin foam and thick multilayer insulation. This was because the static purge gas in the MLI provided the greater share of heat flow resistance for this combination. The static conductivity of nitrogen was about 10% of helium conductivity, while the convective heat transfer coefficient was about 65% of the helium coefficient.

Figure 1.1-51 GROUND HEAT TRANSFER TO H<sub>2</sub> WITH HELIUM PURGE

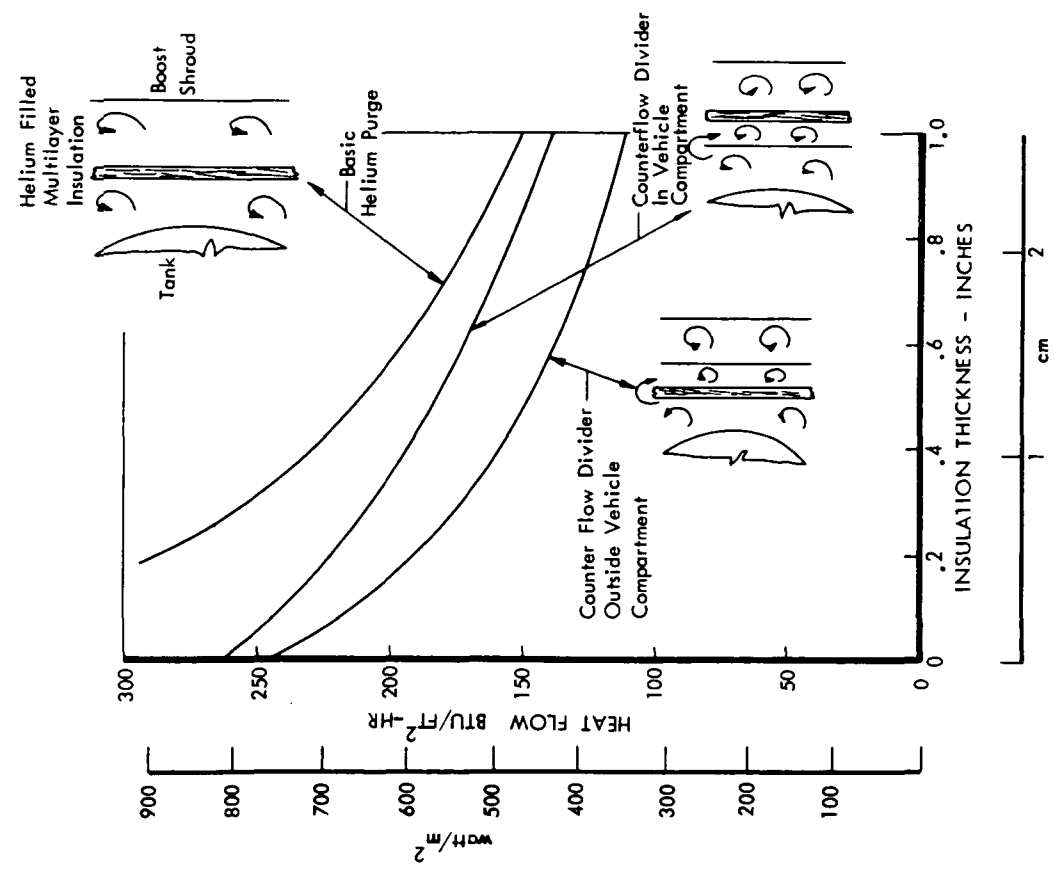
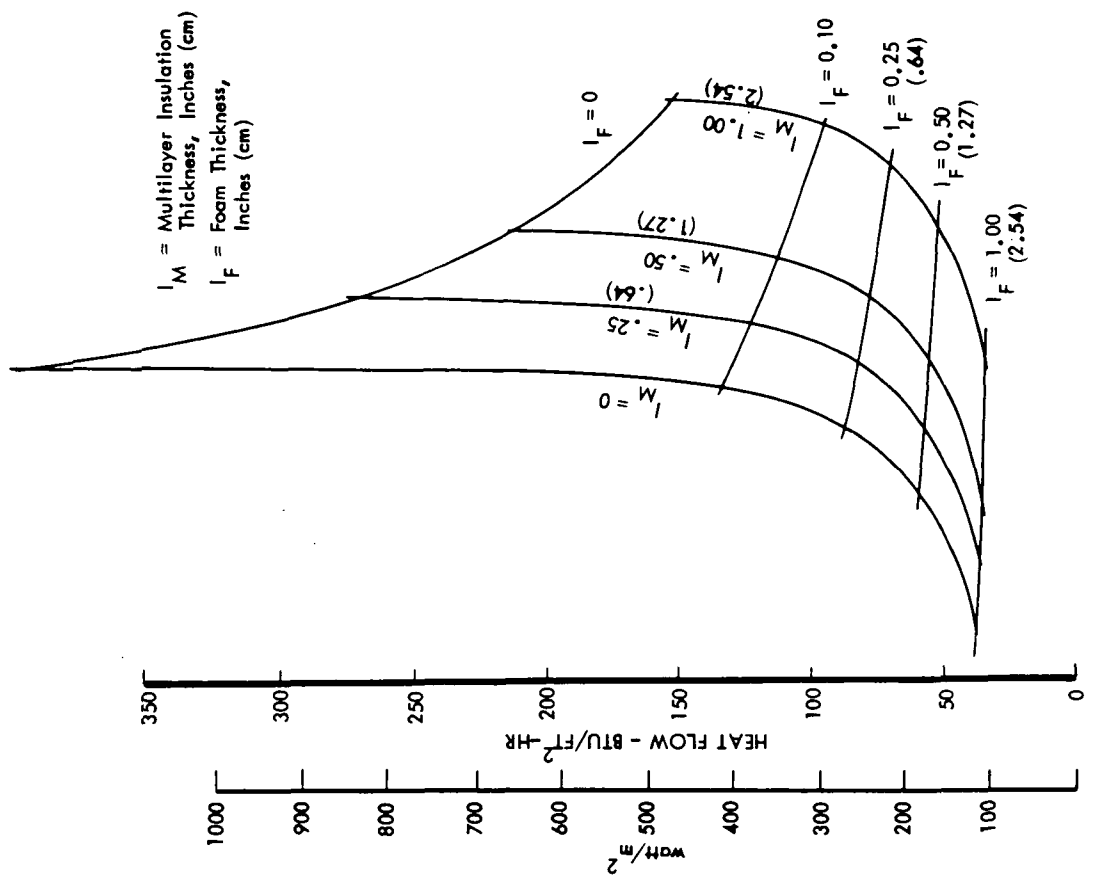


Figure 1.1-52: GROUND HEAT TRANSFER TO H<sub>2</sub> WITH HELIUM PURGE AND FOAM ON TANK<sup>2</sup>



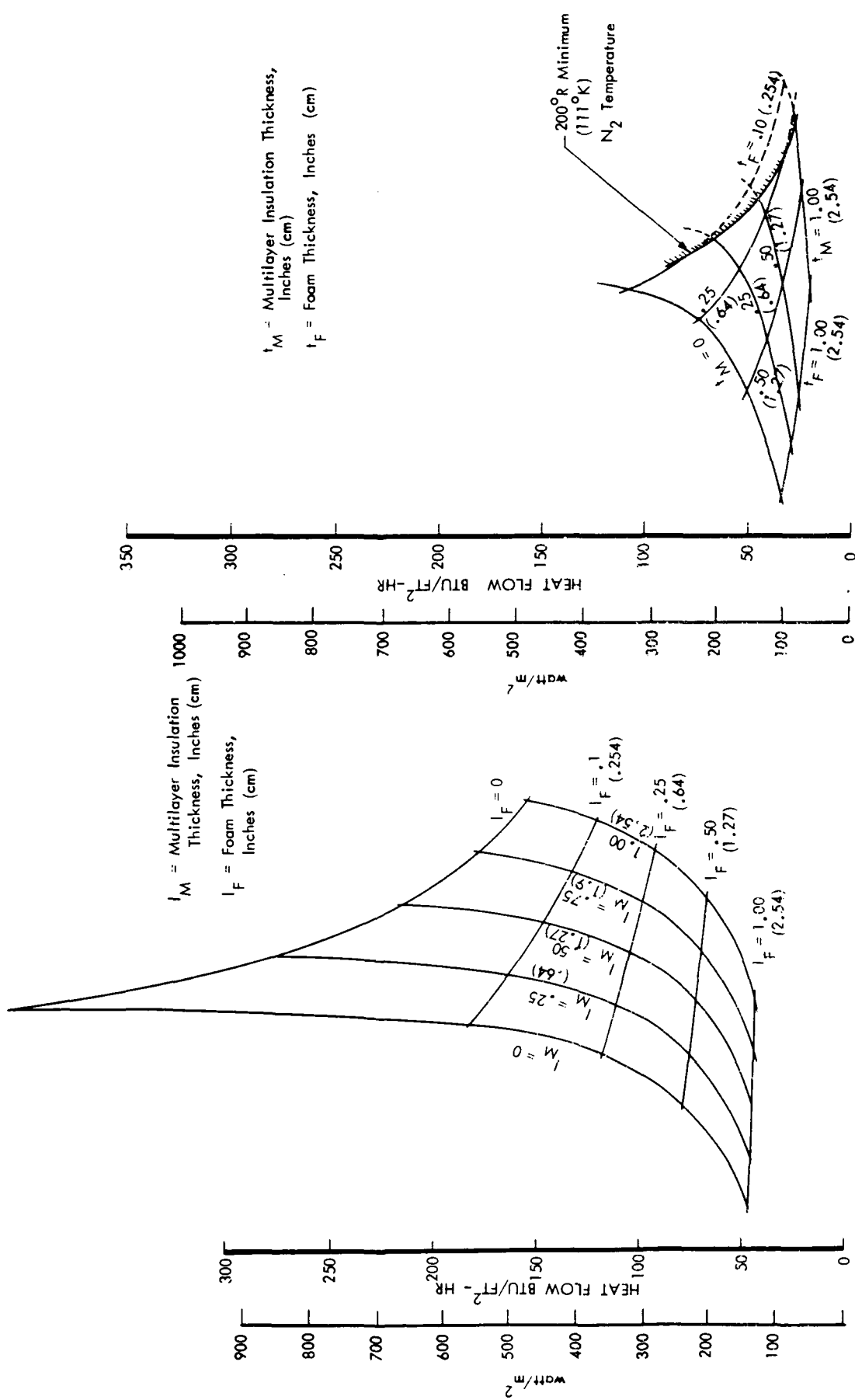


Figure 1.1-53: GROUND HEAT TRANSFER TO H<sub>2</sub> WITH HELIUM PURGE AND FOAM OUTSIDE OF MULTILAYER

Figure 1.1-54: GROUND HEAT TRANSFER TO H<sub>2</sub> WITH NITROGEN PURGE AND FOAM ON TANK

One approach to the evacuation of multilayer insulation after launch would be to evacuate broadside to the panel through many small perforations in the radiation shields. Using these perforations as the cold purge gas exhaust path, the insulation could serve as a heat exchanger to reduce the prelaunch heat transfer. Assuming for simplicity conductivity constant with temperature and purge gas temperature equal to the insulation temperature at any location, solution of the differential equation,

$$\frac{d}{dx} \left( k \frac{dT}{dx} \right) - \dot{m} c_p \frac{dT}{dx} = 0,$$

in terms of heat flow through the internal surface was

$$q_2 = \frac{\dot{m} c_p (T_1 - T_2)}{e \frac{\dot{m} c_p \ell}{k} - 1}$$

where  $x$  = distance from external insulation surface,  
 $\ell$  = insulation thickness,  
 $k$  = insulation conductivity,  
 $T_1$  = external surface temperature,  
 $T_2$  = internal surface temperature,  
 $\dot{m}$  = gas flow rate through unit surface area of insulation,  
 $c_p$  = specific heat of purge gas, and  
 $q_2$  = conduction heat flow through internal insulation surface.

The ratio of heat conduction through the internal surface to that through the external surface was

$$\frac{q_2}{q_1} = e^{-\frac{\dot{m} c_p \ell}{k}}$$

where  $q_1$  = heat flow through external insulation surface.

These relationships were used with the compartment, shroud cavity, and external heating to determine heat flow to the hydrogen tank shown in Figure 1.1-55. It was assumed that the helium entering the tank compartment was at the bulk

temperature of the gas within the compartment, so that the heat storage in the helium occurred only in the insulation. The heat flow reduction was very large for high flow rates and thick insulation blankets. Achieving high flow rates without insulation damage did not appear to be a problem. The maximum cooling condition shown in Figure 1.1-55 resulted in only about  $.045 \text{ lb/ft}^2$  ( $2.15 \text{ N/m}^2$ ) pressure differential. However, the thinner insulations expected for the flight requirements resulted in less efficiency unless the helium flow rate was increased considerably.

Calculated heating rates to the fluorine tank were similar to those on the hydrogen tank. Heat flow with helium and nitrogen purges are shown in Figure 1.1-56. Figure 1.1-57 shows the effect of foam on the tank with a nitrogen purge.

A fiberglass honeycomb structure could be used as a ground hold insulation, and would perform efficiently if it was evacuated. Figure 1.1-58 shows the heat flow to hydrogen and fluorine with a fiberglass structural shell selected from the preliminary structural optimization results. The honeycomb panel was assumed to be filled with  $\text{CO}_2$ , and the radiation, conduction and convection within the cells were varied with temperature and  $\text{CO}_2$  residual pressure. The results show that the structure provided a more efficient insulation if the MLI blankets were mounted outside the structure, resulting in better cryopumping of the  $\text{CO}_2$ .

The use of a cold helium purge was examined to determine the cooling to be derived from the purge gas heat capacity. The model used for this analysis was Vehicle 1-14 (fluorine over hydrogen) with helium at  $\text{LH}_2$  temperature entering at the bottom of the  $\text{LH}_2$  tank, flowing over its surface in a restricted purge envelope, then flowing over the fluorine tank from bottom to top. The compartment and shroud were assumed to be helium filled, but flow rate effects were not included. MLI thicknesses were selected from the tank arrangement thermal efficiency analyses. The results are shown in Figures 1.1-59 and 1.1-60. For the case analyzed, the total heat flow to the hydrogen tank was reduced only about 11%. However, the total heat flow to the fluorine, with the helium much colder than the tank, could be reduced to zero, or even sub-cooled. The flow rate used in the analysis was chosen to obtain a near zero heat leak with the restricted purge. The compartment purge at the same flow rate was somewhat less efficient. The curves showed widely varying heat flow with location on the tank. For the configuration analyzed the fluorine ullage space was still heated at a high rate while the bottom of the tank was being cooled. This would result in severe stratification not removed by convection in the tank, and the ullage pressure would probably rise rapidly. Therefore, the use of a cold purge gas at high flow rates might have to be restricted to configurations where the cooling is more evenly distributed, or where the maximum cooling occurred in the region of the ullage space.

The insulation and purging schemes discussed above offered several promising methods for reducing the propellant heating during ground hold. Basic elements

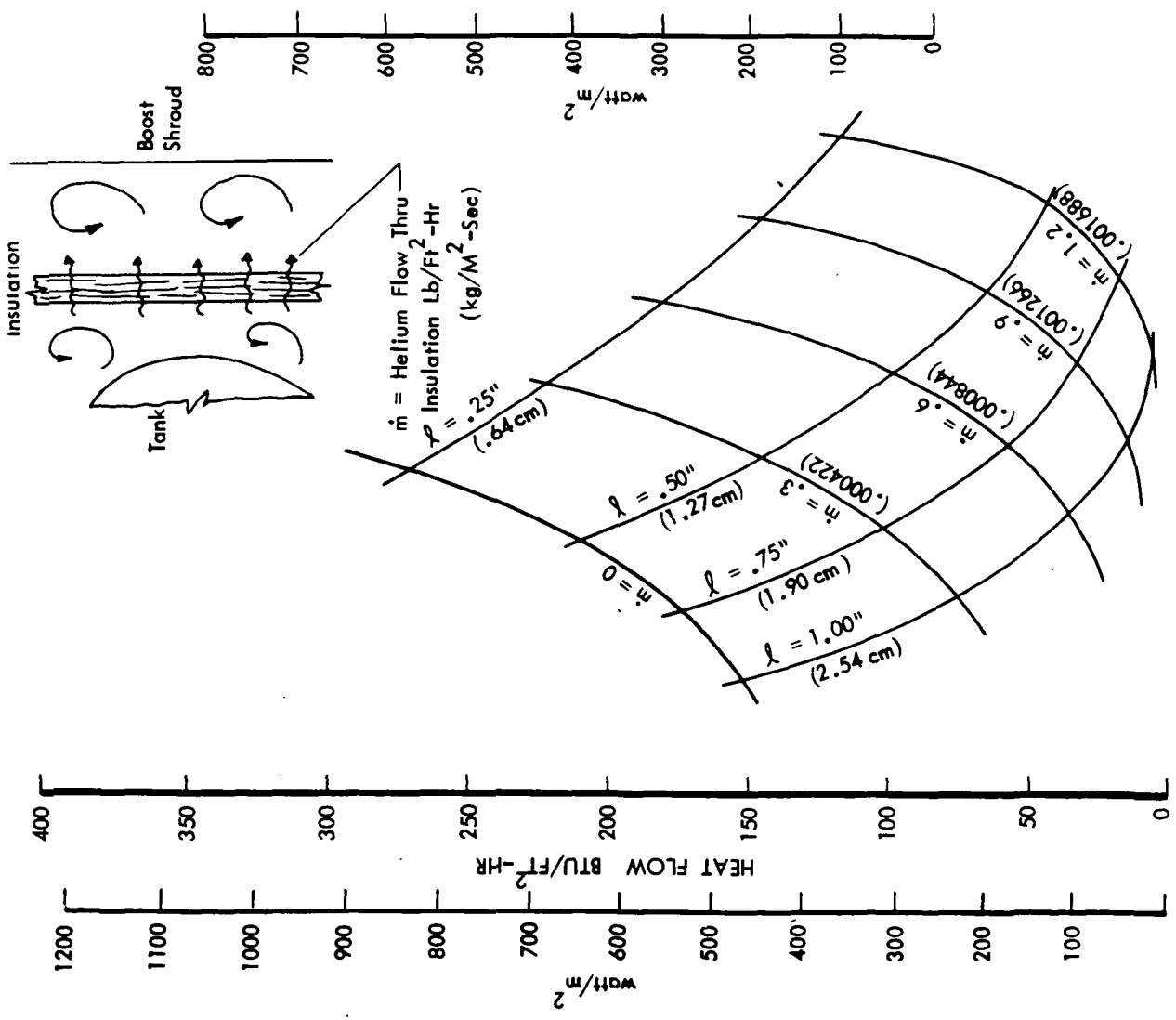


Figure 1.1-55: GROUND HEAT TRANSFER TO  $H_2$  WITH HELIUM FLOW THRU INSULATION

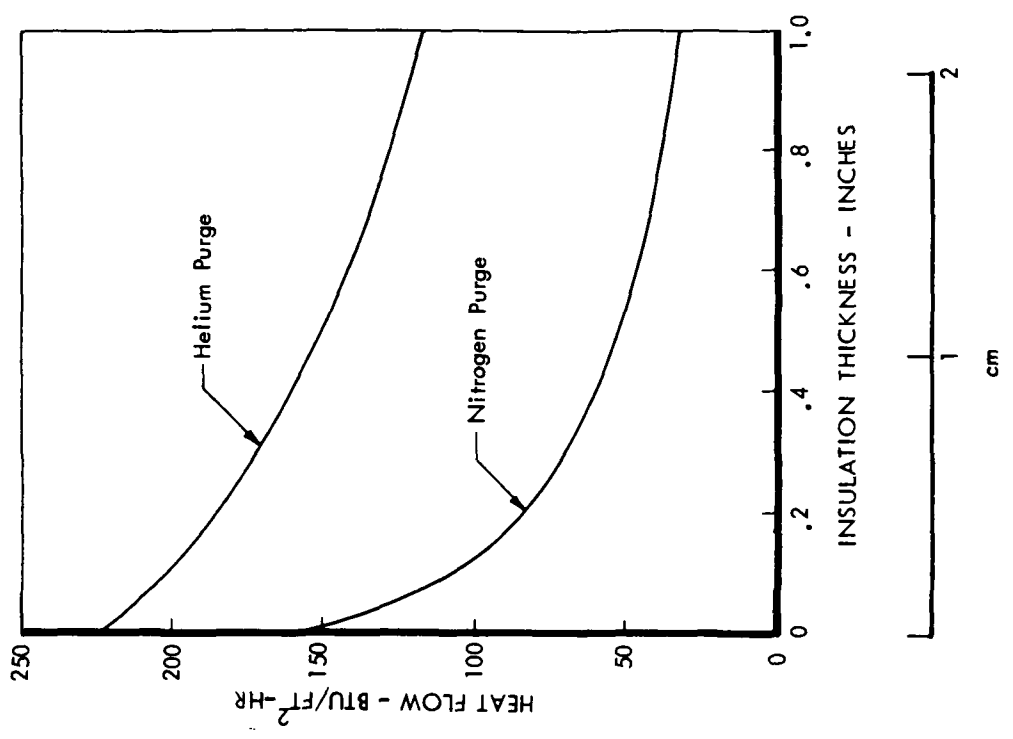


Figure 1.1-56: GROUND HEAT TRANSFER TO  $LF_2$  WITH BASIC HELIUM & NITROGEN PURGES

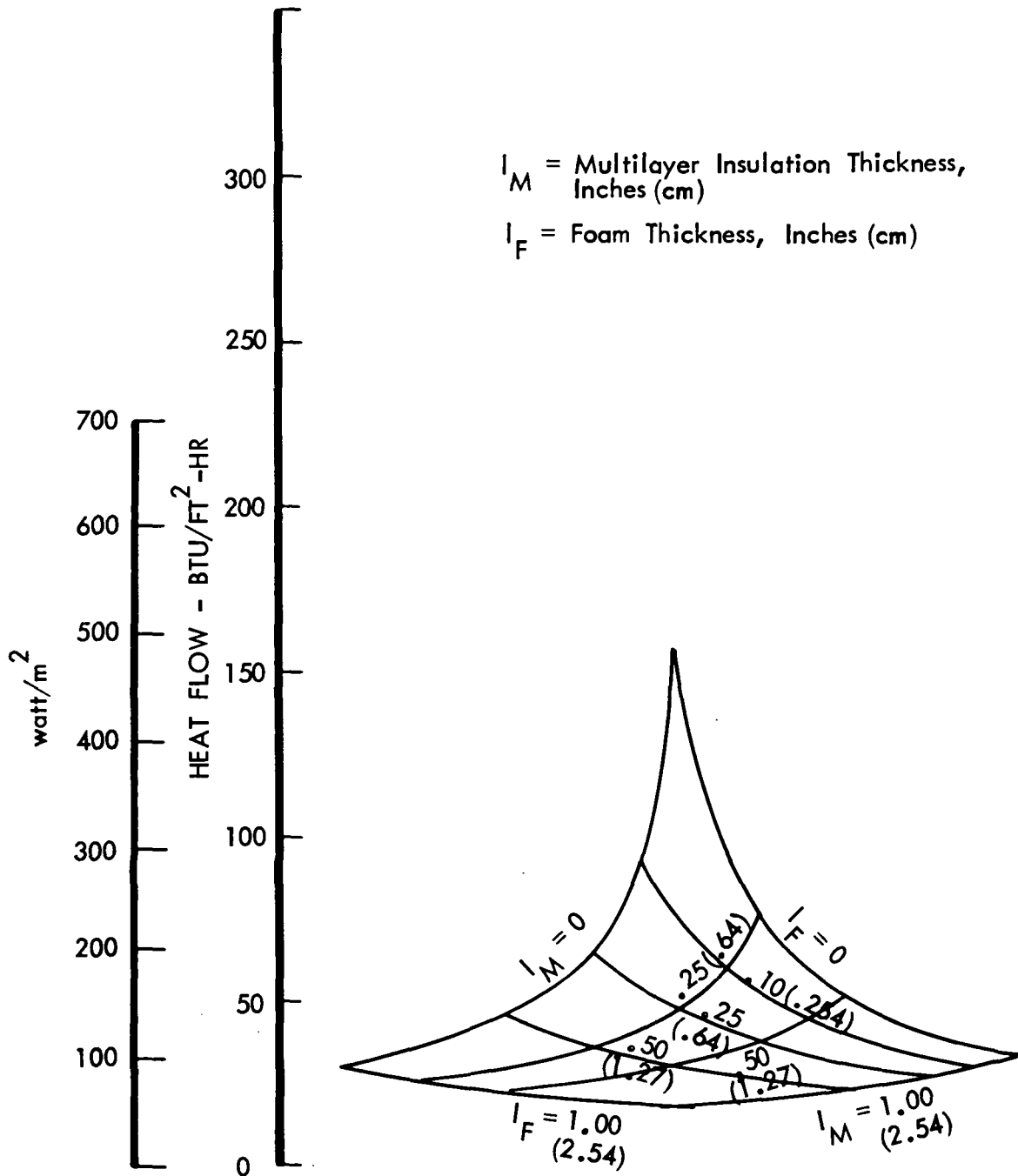


Figure 1.1-57: GROUND HEAT TRANSFER TO F<sub>2</sub> WITH NITROGEN PURGE AND FOAM ON TANK

Structure = 3/4" (1.9 cm) Thick, 3/8" (.95 cm) Cell, .005" (.0127 cm) Ribbon Fiberglass Honeycomb

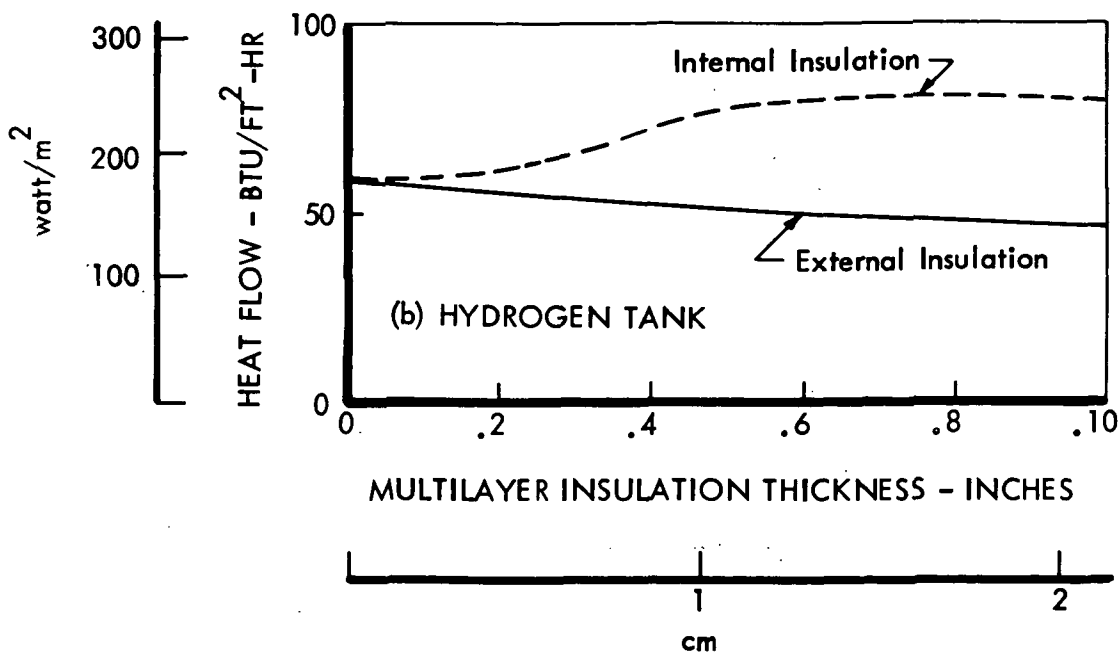
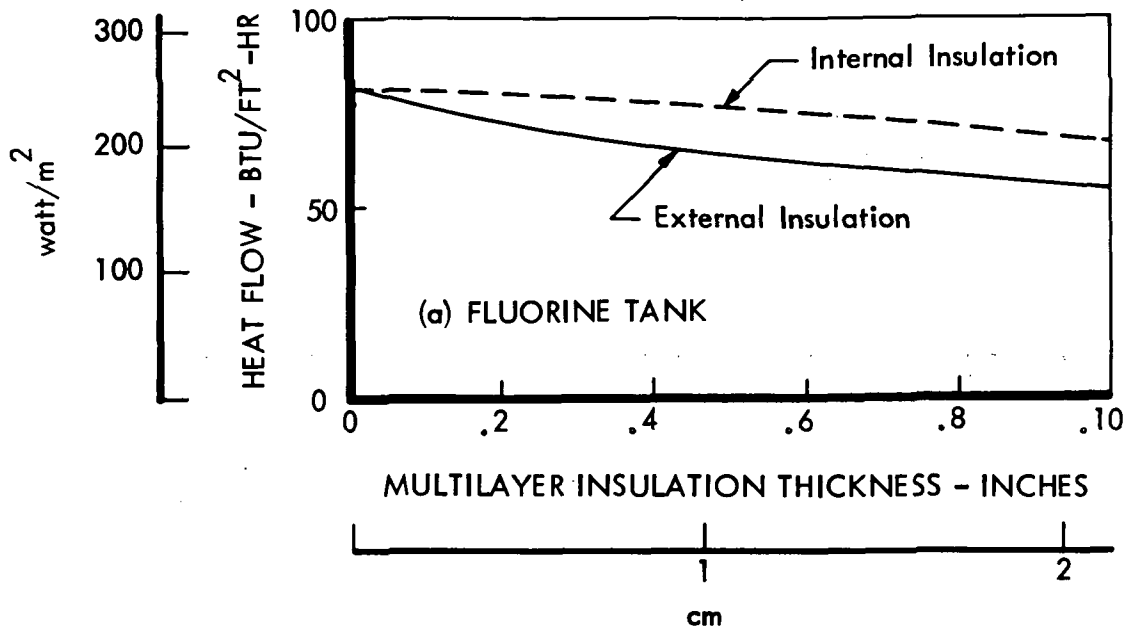


Figure 1.1-58: GROUND HEAT TRANSFER TO  $LF_2$  &  $LH_2$  WITH  $CO_2$  FILLED FIBERGLASS HONEYCOMB STRUCTURE

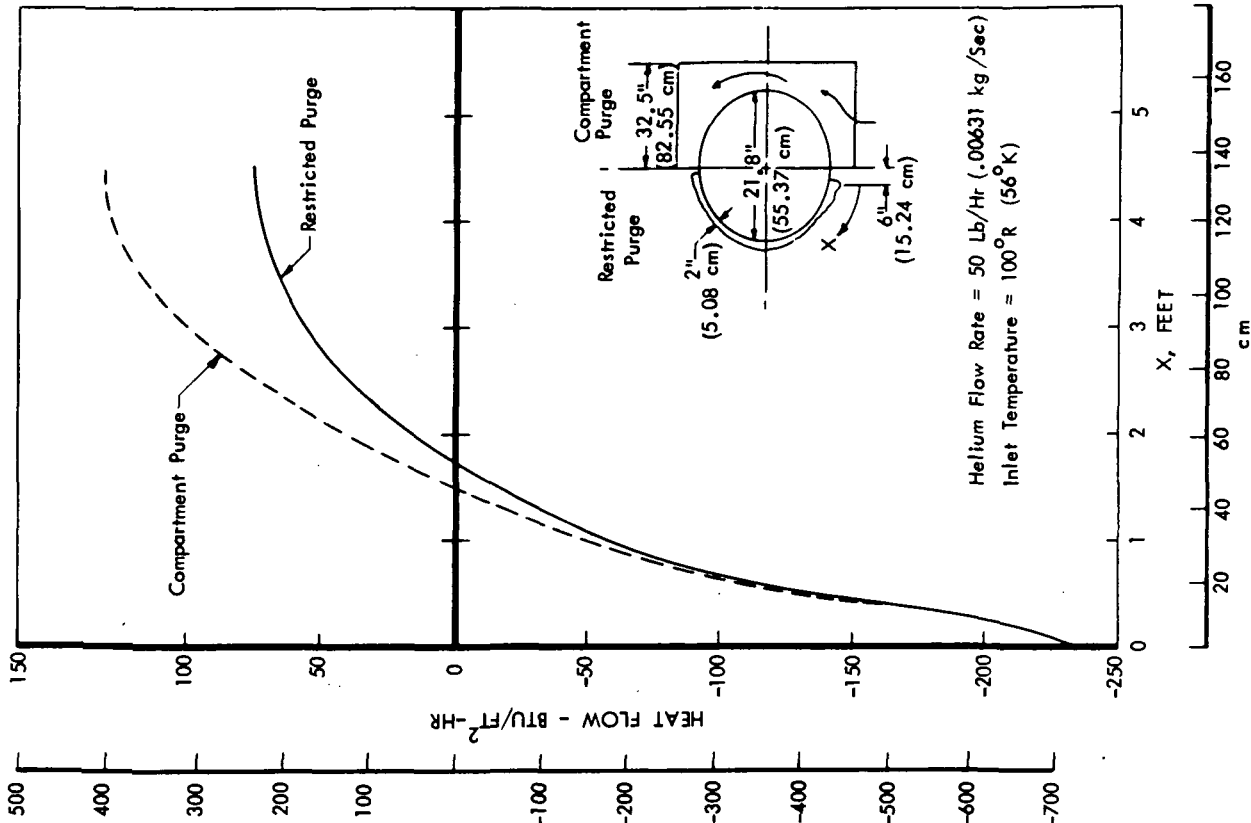


Figure 1.1-60: HEAT TRANSFER DISTRIBUTION ON LF<sub>2</sub> TANK WITH COLD HELIUM PURGE

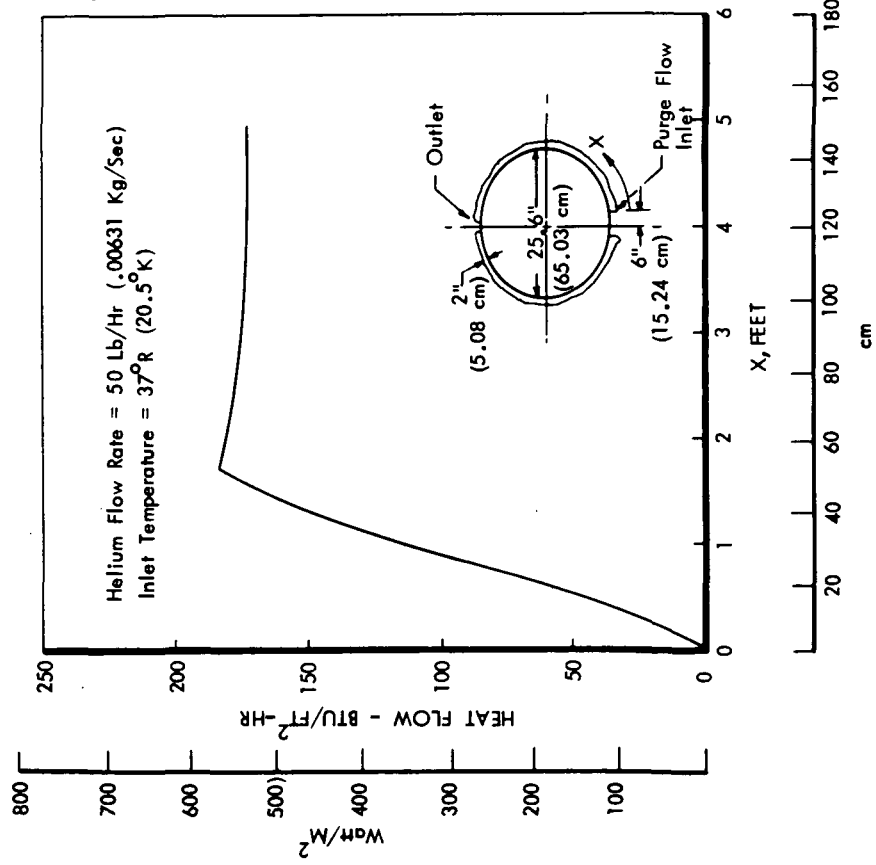


Figure 1.1-59: HEAT TRANSFER DISTRIBUTION ON LH<sub>2</sub> TANK WITH COLD HELIUM PURGE

could be combined in a given design to give further heat leak reductions. However, with the exception of the cold helium purge on the fluorine tank, none of those considered achieved a low enough heat leak for extended non-vented storage. Combinations of the passive insulation systems with the cold helium purge or closed refrigeration systems (such as tank mounted coolant tubes) would be required.

Seven design concepts of ground hold thermal protection systems are described in the following paragraphs. In these it has been assumed that the  $\text{LH}_2$  or  $\text{CH}_4$  tank would be continuously topped-off during ground hold. A heat exchanger to liquify the boil-off from the  $\text{LF}_2$  or FLOX tank was provided on the launch stand for Concepts 1, 2, 3, 4 and 5. Concepts 6 and 7 used  $\text{LN}_2$  in a heat exchanger loop around the  $\text{LF}_2$  or FLOX vent manifold with a subsequent weight penalty to the flight vehicle.

Concept 1 - Figure 1.1-61: Helium purge gas would be delivered at  $154^\circ\text{R}$  ( $85.5^\circ\text{K}$ ) to a distribution disc at the payload deck. This supply would purge the  $\text{LF}_2$  tank compartment and be discharged through the perforated multilayer along the compartment walls. A sealed honeycomb panel would protect the payload from the cold purge gas. Helium at  $\approx 37^\circ\text{R}$  ( $20.6^\circ\text{K}$ ) would be delivered to a distribution dome located between tank compartments. This supply would purge the  $\text{LH}_2$  tank compartment and also be discharged through the walls. The  $\text{LH}_2$  and  $\text{LF}_2$  tanks were not insulated in this concept. A containment cover was wrapped around the vehicle to collect the purge gas exiting the compartments and control gas flow so that all the MLI would be adequately purged. After venting from the outer envelope at the bottom and mid-point of the conical surface, the purge gas would flow between the vehicle and the shroud absorbing additional heat. This same approach could be used for FLOX-Methane propellants with the appropriate adjustments in purge gas temperatures.

Concept 2 - Figure 1.1-62: Helium purge gas would be delivered at  $\approx 154^\circ\text{R}$  ( $85.5^\circ\text{K}$ ) to a distribution disc at the payload deck, and to a plenum chamber around the  $\text{LH}_2$  tank. The purge lines were routed into the vehicle along the  $\text{LH}_2$  vent line. Two layers of foam surrounded the  $\text{LH}_2$  tank with the purge plenum in between. As in Concept 1, the payload was protected by a honeycomb separator panel. A containment cover around the vehicle collected purge gas which had passed through the perforated multilayer and forced the flow downwards towards the exhaust ports at the bottom of the vehicle.

This approach could also be utilized for FLOX-Methane propellants provided the Methane was protected from localized freezing and vessel collapse due to internal pressure drop.

Concept 3 - Figure 1.1-63: Nitrogen purge gas would be delivered at ambient temperature to a line leading to the distribution disc between the payload and

vehicle. This line was wrapped around the LH<sub>2</sub> vent to effect a heat exchange. The LF<sub>2</sub> tanks and manifolds; and the LH<sub>2</sub> tanks and lines were insulated with foam. The vehicle shell provided a gas barrier and a containment envelope for the purge gas which passed through the perforated multilayer. As in Concept 1, venting the purge gas along the outside of the vehicle would intercept some of the heat from the shroud.

Concept 4 - Figure 1.1-64: Liquid nitrogen would be delivered to a shroud mounted heat exchanger. The weight of foam insulation and heat exchanger coils on the shroud would not be chargeable to the vehicle. Boil-off nitrogen gas from the heat exchanger would enter the shroud cavity which was sealed to direct the gas through the side wall and thrust cone perforated insulation, into the vehicle around the tanks. The gas would be vented radially out from the payload deck to atmosphere. The LF<sub>2</sub> tanks and feed manifold system were uninsulated. The LF<sub>2</sub> vent manifold system and the LH<sub>2</sub> tank and lines were foam insulated.

Concept 5 - Figure 1.1-65: Liquid nitrogen would be delivered to a distribution tube around the upper circumference of the vehicle. Boil-off nitrogen gas from this tube would circulate down a plenum on the exterior of the vehicle and into the interior through the side wall and thrust cone perforated insulation. The gas would exit through the payload deck insulation where it would be vented radially to the cavity between the shroud and the vehicle. Some heat from the shroud would be intercepted by this gas before venting to the atmosphere. There was no insulation on the LF<sub>2</sub> tank nor on the feed system. The LF<sub>2</sub> vent manifold system and the LH<sub>2</sub> tank and lines were insulated with foam.

Concept 6 - Figure 1.1-66: Liquid nitrogen would enter the vehicle in a line wrapped around the LF<sub>2</sub> vent manifold system. The vaporized nitrogen gas or liquid would be distributed to a plenum around each LF<sub>2</sub> tank, and from there to the compartment. The shroud was sealed so that venting to atmosphere occurred at the top only. The purge gas would be allowed to move randomly throughout the vehicle and through the insulation. The LH<sub>2</sub> tank and lines were insulated in foam.

Concept 7 - Figure 1.1-67: This concept was similar to Concept 6, except that the feed and vent lines for each tank were concentric tubes at the top of the tanks. The liquid nitrogen heat exchanger was wrapped around these lines. Vaporized or liquid nitrogen exited at the bottom of the LF<sub>2</sub> tank into the compartment. A deflector plate could be necessary if LN<sub>2</sub> was discharged. The LH<sub>2</sub> tank and lines were insulated with foam.

Preliminary weight estimates were made of the seven design concepts. These are summarized in Table 1.1-7. The weights are significant, especially for the more sophisticated systems.



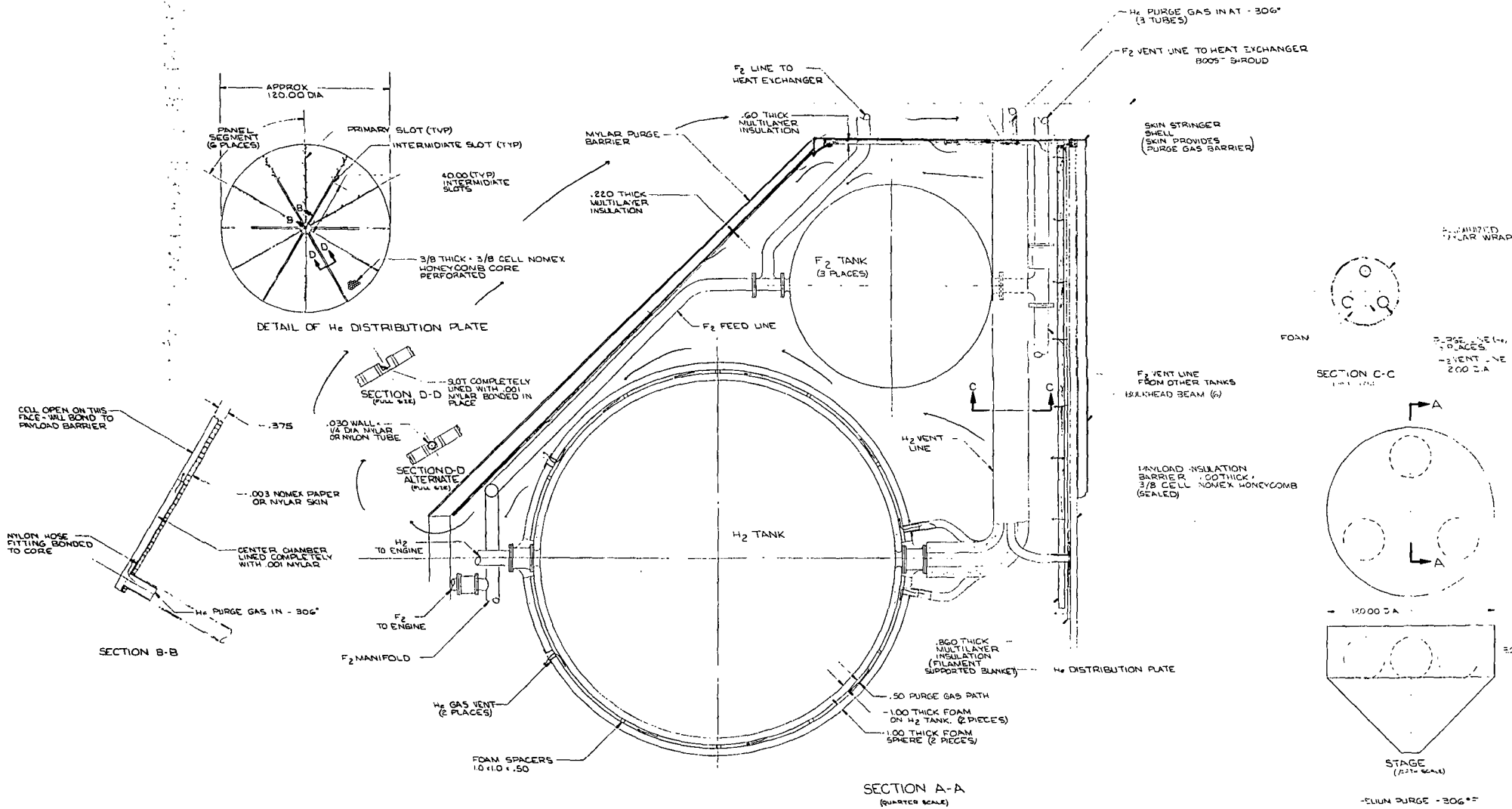


Figure 1.1-62: GROUND HOLD DESIGN CONCEPT #2

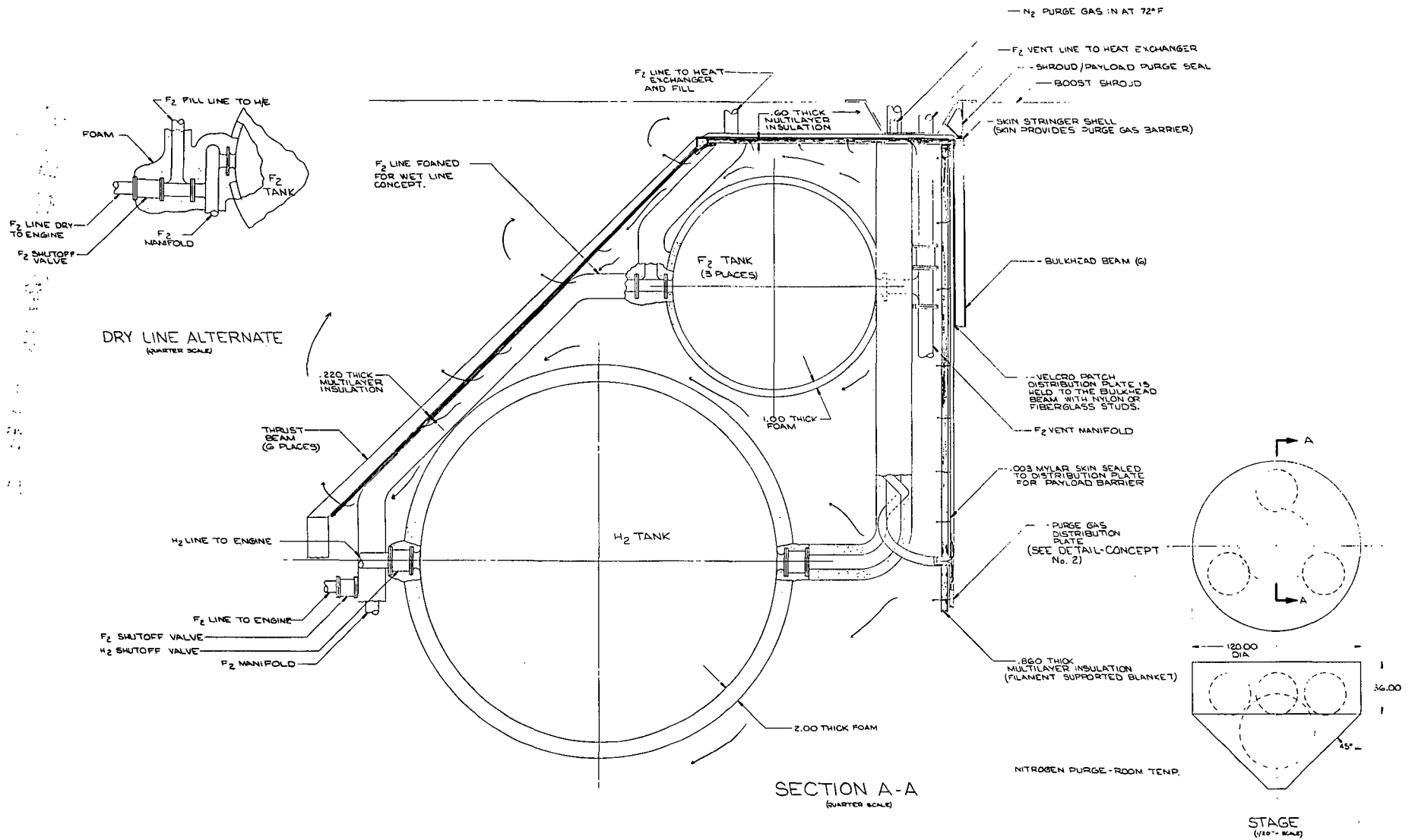


Figure 1.1-63: GROUND HOLD DESIGN CONCEPT #3

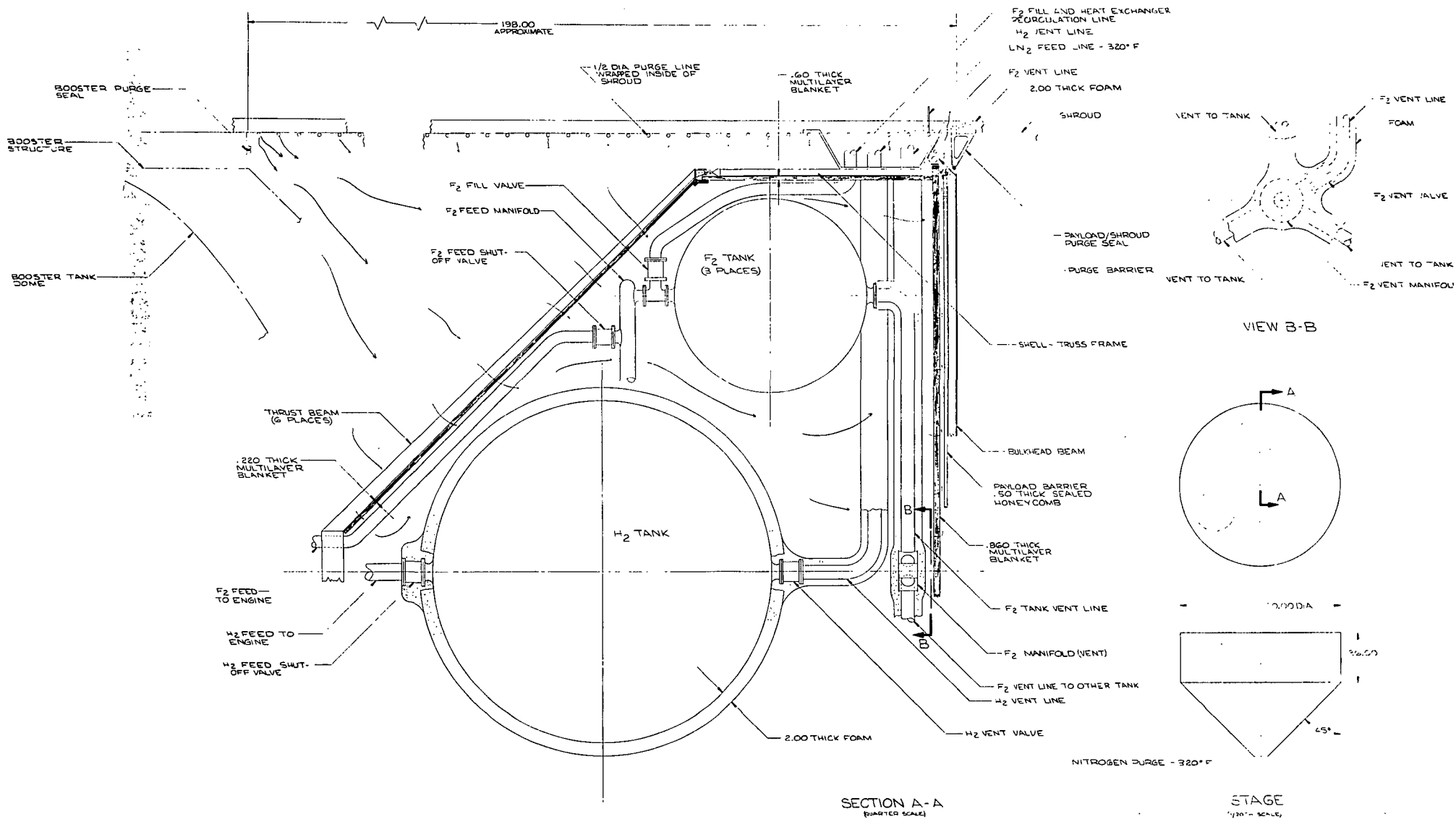


Figure 1.1-64: GROUND HOLD DESIGN CONCEPT #4

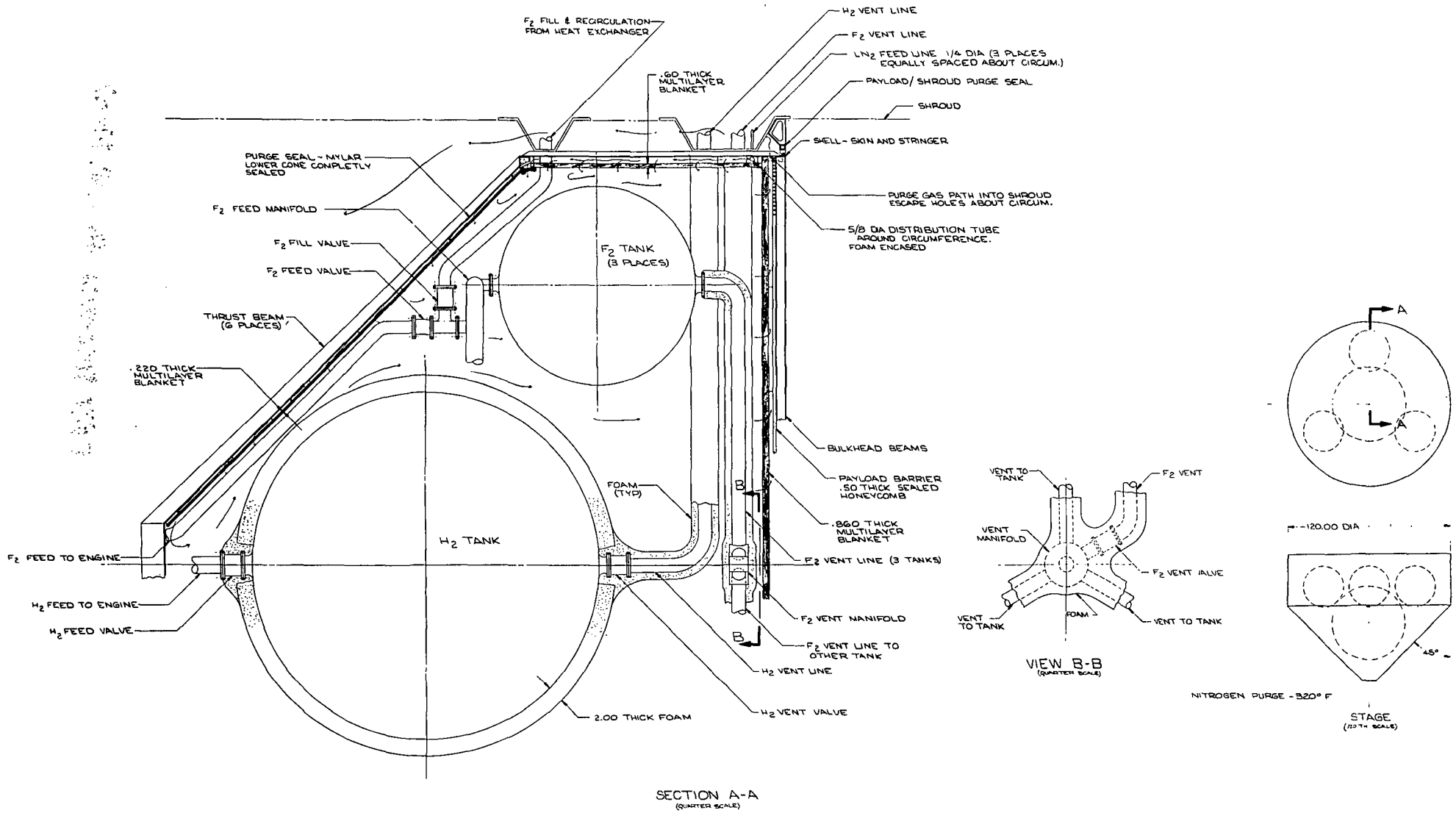


Figure 1.1-65: GROUND HOLD DESIGN CONCEPT #5

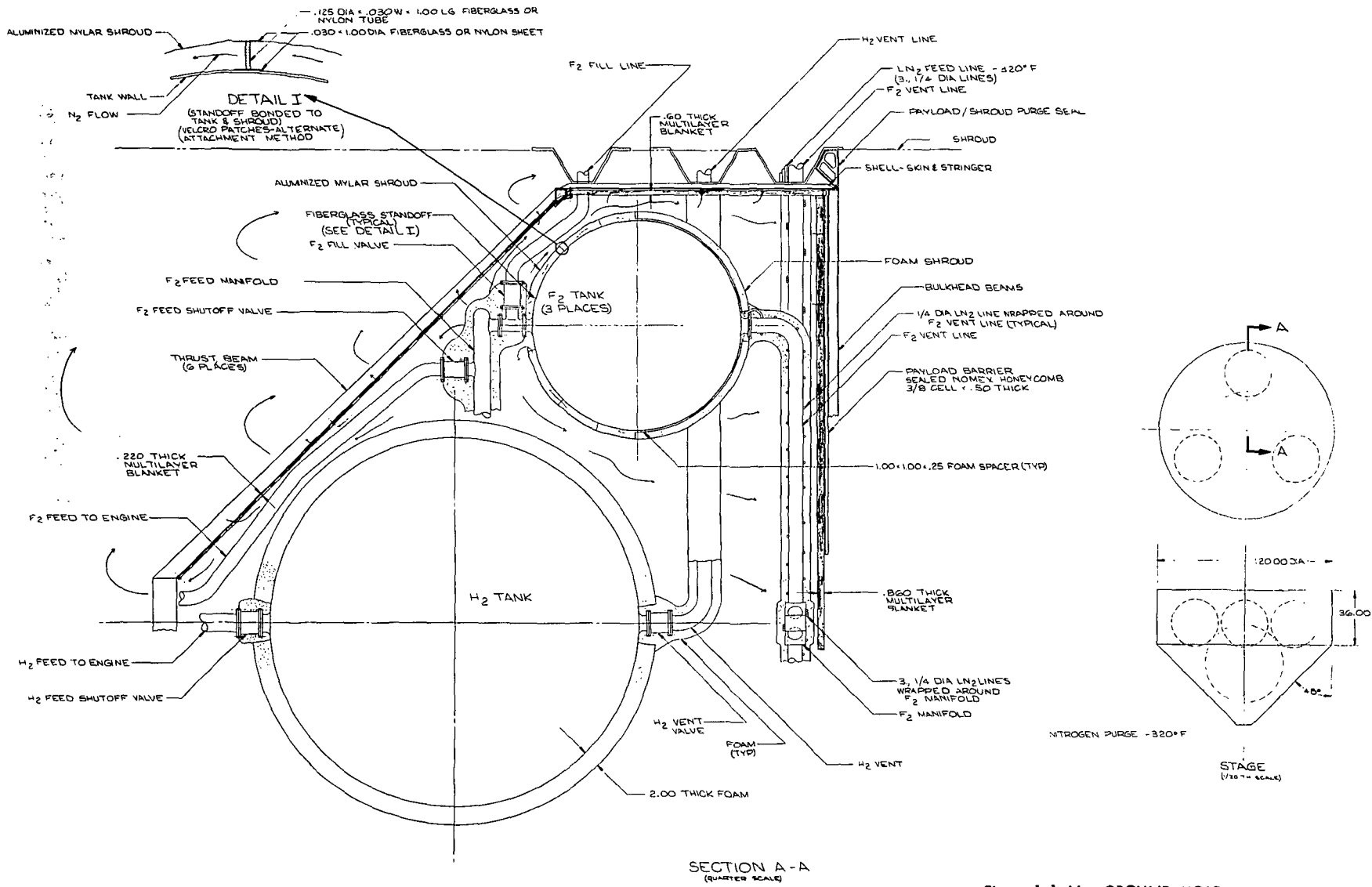


Figure 1.1-66: GROUND HOLD DESIGN CONCEPT #6

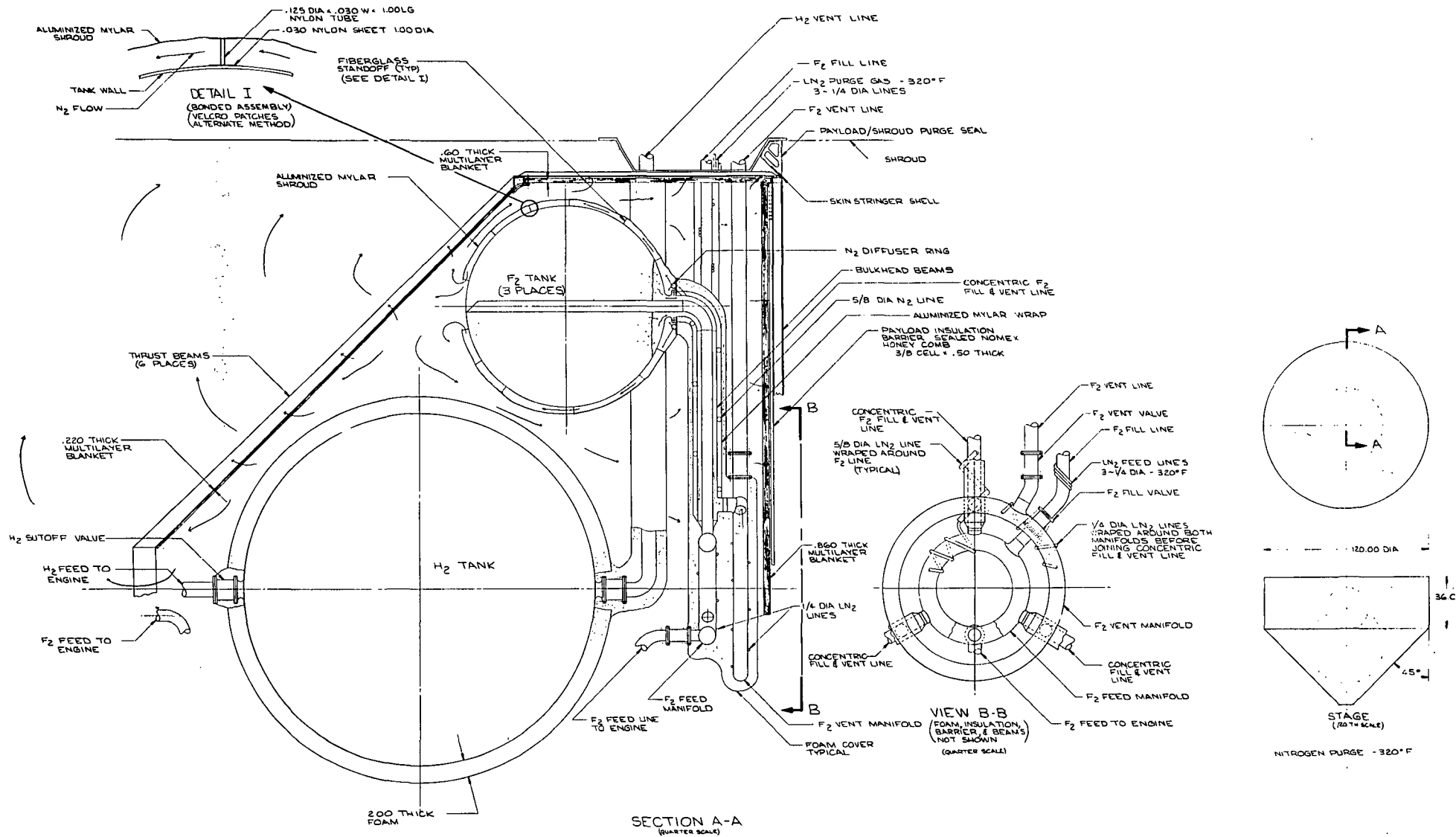


Figure 1.1-67: GROUND HOLD DESIGN CONCEPT #7

**Table 1.1-7**  
**GROUND HOLD PROTECTION WEIGHTS**

ITEM	CONCEPT NUMBER						
	1	2	3	4	5	6	7
H <sub>2</sub> SYSTEM INSULATION	-TOTAL--	48.4 (21.97)	47.3 (21.47)	46.7 (21.20)	46.7 (21.20)	46.9 (21.29)	47.3 (21.47)
TANK		47.0 (21.34)	45.9 (20.84)	45.9 (20.84)	45.9 (20.84)	45.9 (20.84)	45.9 (20.84)
DELIVERY LINE FOAM FILL & VENT FOAM		1.4 (.64)	1.4 (.64)	0.8 (.36)	0.8 (.36)	1.0 (.454)	1.4 (.64)
F <sub>2</sub> SYSTEM INSULATION	-TOTAL--		12.0 (5.45)	2.3 (1.04)	2.3 (1.04)	13.0 (5.9)	7.0 (3.18)
TANKS			9.8 (4.45)			5.9 (2.68)	1.7 (.77)
FILL LINE FOAM			0.6 (.27)				0.5 (.23)
VENT LINE FOAM				2.3 (1.04)	2.3 (1.04)	2.3 (1.04)	2.1 (.95)
DELIVERY LINE FOAM			1.6 (.73)			4.8 (2.18)	2.7 (1.23)
PURGE SYSTEM- TOTAL	38.4 (17.4)	46.7 (21.20)	38.8 (17.62)	324.5 (147.32)	23.1 (10.5)	20.9 (9.5)	21.6 (9.8)
DISTRIBUTION PLATES	38.4 (17.4)	17.7 (8.04)	17.7 (8.04)				
PAYLOAD INSUL. BARRIER		26.7 (12.12)	20.1 (9.1)	20.1 (9.1)	20.1 (9.1)	20.1 (9.1)	20.1 (9.1)
FOAM				191.4 (86.89)	1.0 (.454)		
ALUMINUM TUBING		2.3 (1.04)	1.0 (.454)	113.0 (51.3)	2.0 (.908)	0.8 (.36)	1.5 (.68)
MISC. 5%	1.9 (.86)	4.8 (2.2)	4.9 (2.3)	18.7 (8.49)	3.6 (1.6)	4.0 (1.8)	3.8 (1.73)
TOTAL WT. LBS (Kg)	40.3 (18.3)	99.9 (45.35)	103.0 (46.76)	392.2 (178.06)	75.7 (34.37)	84.8 (38.5)	79.7 (36.18)

WEIGHT IN LBS (Kg)

*3-1-80 10:00 AM*

**Page Intentionally Left Blank**

## Tank Mounted Insulation

Conceptual designs of tank mounted MLI systems were prepared for an initial comparison with the shell mounted concepts discussed previously.

Figure 1.1-68 shows two types of tank mounted multilayer. The oblate spheroid tank was insulated in the conventional gore and polar cap fashion, using pressure sensitive tape to secure the layers. Joints in the radiation shields were staggered and overlapped to prevent radiation windows. Insulation supports were not used in this concept, instead the curvature of the panels and the tape made each a continuous shell which was supported by the tank or preceding layers. Perforated radiation shields were believed necessary.

The cylindrical tank was insulated with one single curvature blanket and two flat blankets. These were assembled on an epoxy/fiberglass grid which in turn was suspended from the tank with webbing. This approach provided close control of shield spacing and permitted fabrication of tapered joints. The curved panel was attached to the fiberglass grid with rigid supports. Threads and buttons were used for the top and bottom panels where the major loads were aligned with the thread ties. The top and bottom panels were attached to sidewall insulation with Velcro tape, which permitted removal for access to the tank outlet. A single layer of 6.3 oz/yd<sup>2</sup> Beta fiber cloth was installed over the exterior of the vehicle for meteoroid protection.

Figure 1.1-69 shows several methods for thermally isolating individual tanks. One approach utilized a foam substrate for extending ground hold capability with a bonded fiberglass stand-off lattice for multilayer support. Another approach made use of an insulated cage (several configurations are shown) which fit closely over the tank and was supported either from the vehicle structure or tank supports. Meteoroid protection was provided either by the corrugated skin panels or Beta fiber cloth over the truss structure. Additional thermal isolation from the payload was provided with a shadow shield or MLI blanket spanning across the top of the vehicle.

Figure 1.1-70 shows combined tank and vehicle mounted protection systems for truss structure and stiffened shell concepts. For the truss structure approach, MLI was applied to each tank individually. The multilayer was layed up in gores over fiberglass support rings and standoffs to form a cage encapsulating the tank. Meteoroid protection for the truss structure approach was Beta fiber cloth mounted on the trusswork.

For the stiffened skin structural concept, the smaller LF<sub>2</sub> tank was mounted on a support stand which was free of any upper stage contact. The support stand was attached to a structural ring. This approach was intended to minimize the heat conducted from the payload.

Heat flow by conduction from the payload would follow a path which was through the external stiffened skin surface down to the support stand base before it could enter the system.

The weight penalty imposed by the  $LF_2$  tank support stand was a potential detriment to this configuration. By mounting the lighter  $LH_2$  tank on the stand, this penalty would be significantly reduced.

The weights of tank mounted protection system designs for Figures 1.1-68 and 1.1-69 are summarized in Table 1.1-8. The bulkhead insulation for the vehicle design of Figure 1.1-69 in Table 1.1-8 was intended to serve as a buffer between payload and tank, and could be unnecessary, or it could be more weight effective to allow thicker insulation on the tank.

A comparison of tank mounted and vehicle mounted protection systems at this stage of the study showed that the tank mounted approaches were considerably lighter weight. However, it should be recognized that these were only preliminary figures and that meteoroid protection requirements had not been fully identified. Installation features and meteoroid protection represent 19.6% and 18.5% of total weight for the designs of Figures 1.1-68 and 1.1-69, respectively, ignoring the weight associated with the bulkhead installation. This was a somewhat smaller percentage than for the shell mounted concepts discussed previously.

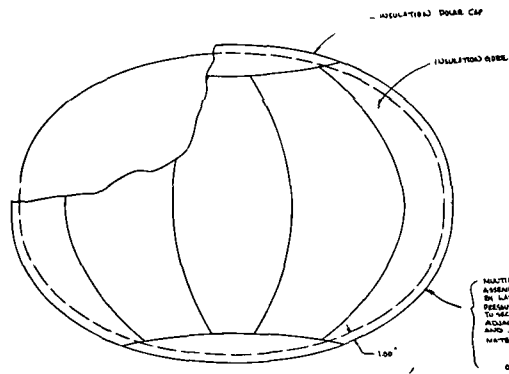
#### Insulation Evacuation and Materials Assessments

Analyses were necessary to determine MLI blanket thermal performance in terms of expected venting behavior of the design concepts. Both edge evacuation and broadside pumping (perforated radiation shields) were considered.

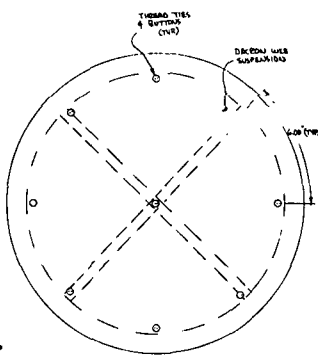
The complete insulation evacuation analysis problem involved coupled mass transfer, heat transfer, gas desorption from the insulation materials, and cryosorption or evaporation at the tank wall. Such an analysis would have been extremely complex and was not possible within the scope of this study. The analysis performed for this study was simplified to include only single gas mass transfer and the gas desorption, essentially equivalent to evacuation of MLI at room temperature. For a single gas, the transient unidirectional flow was described by

$$\frac{dp}{dt} = \frac{d}{dx} \left( B \frac{dp}{dx} \right)$$

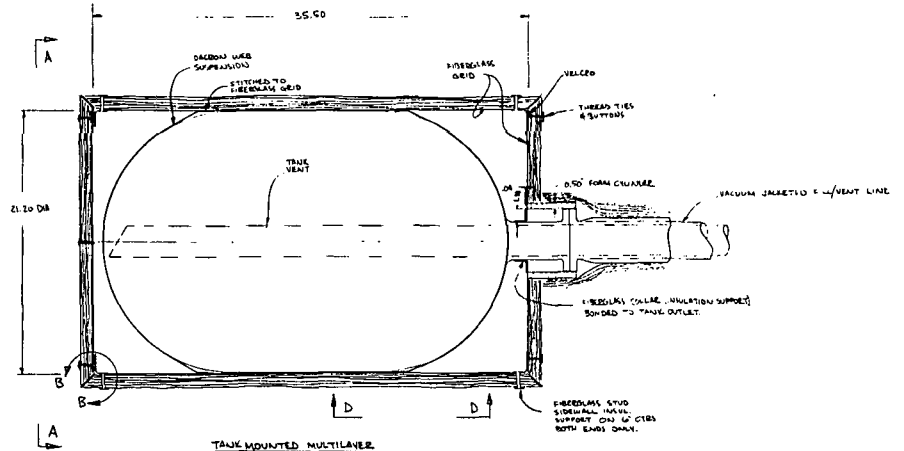
where  $p$  was pressure and  $x$  was distance along the flow path. The coefficient  $B$  was proportional to pressure in the high pressure viscous flow regime and was a constant at  $p = 0$ . The transition region from viscous flow through slip flow to molecular diffusion was not well defined. It was convenient to write the equation as the sum of the viscous and diffusion flow. This was possible since each term dominated the equation in its applicable pressure regime,



MULTILAYER INSULATION ASSEMBLY IN GORE PATTERN BY LAYERS. PRESSURE SENSITIVE TAPE USED TO SEAL LAYERS. ADJUSTMENT GORES OBSOLETE. 1.0\"/>

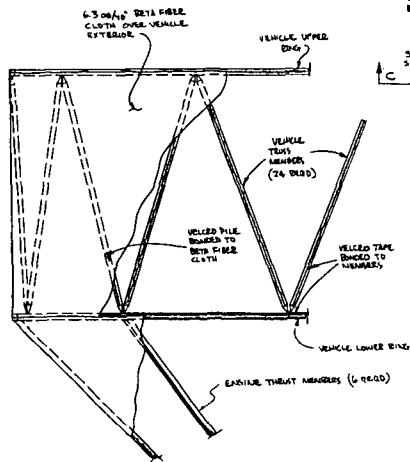


SECTION A-A

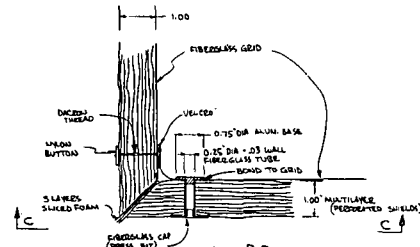


TANK MOUNTED MULTILAYER L/R TANK SCALE 1/2

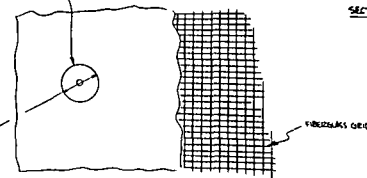
TANK MOUNTED MULTILAYER L/R TANK SCALE 1/2



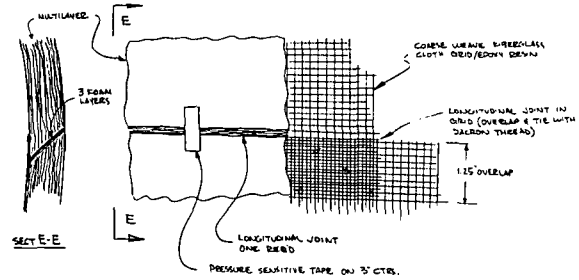
DETAIL I SCALE 1/2



SECTION B-B (FULL SIZE)

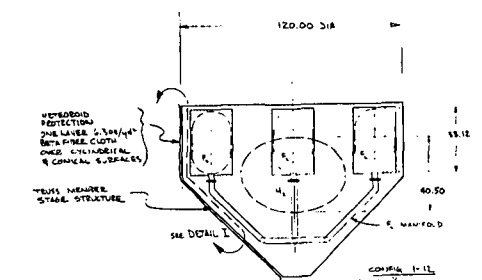
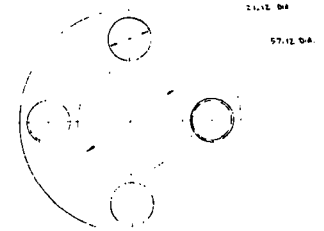


SECTION C-C (FULL SIZE)



SECTION D-D (FULL SIZE)

SECTION E-E



SECTION E-E SCALE 1/10

NOTE: GROUND HOLD THERMAL PROTECTION ASSIGNED EXTERNAL TO VEHICLE (E.G. REFRIGERATED F<sub>2</sub> VENT LINE)

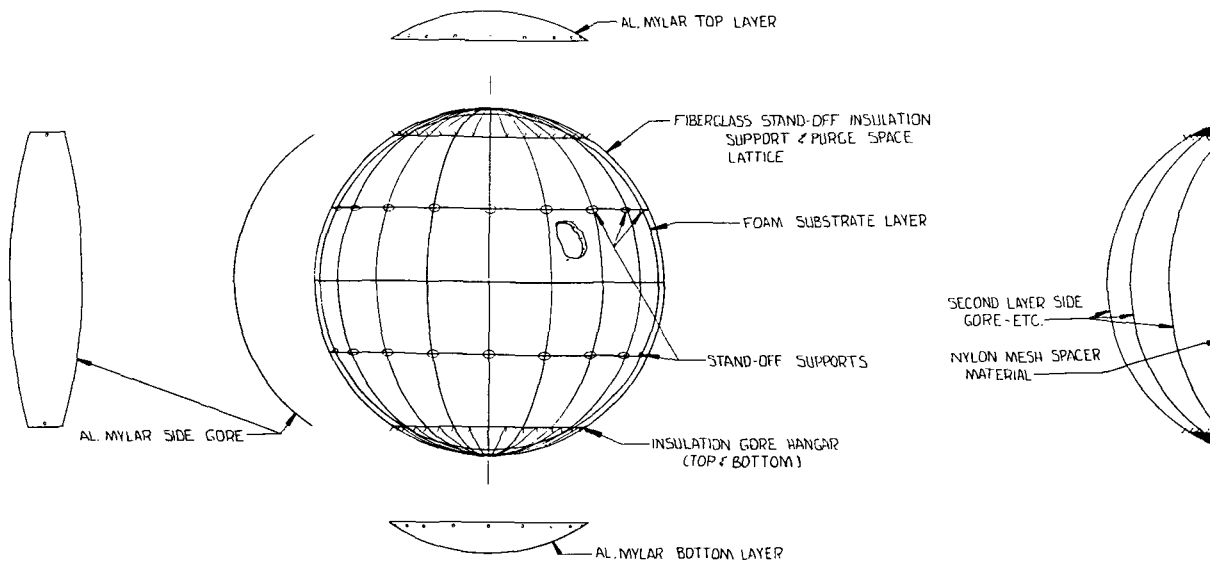
Figure 1.1-68: TANK MOUNTED INSULATION CONCEPT



WCE

### INDIVIDUAL GORE LAYUP

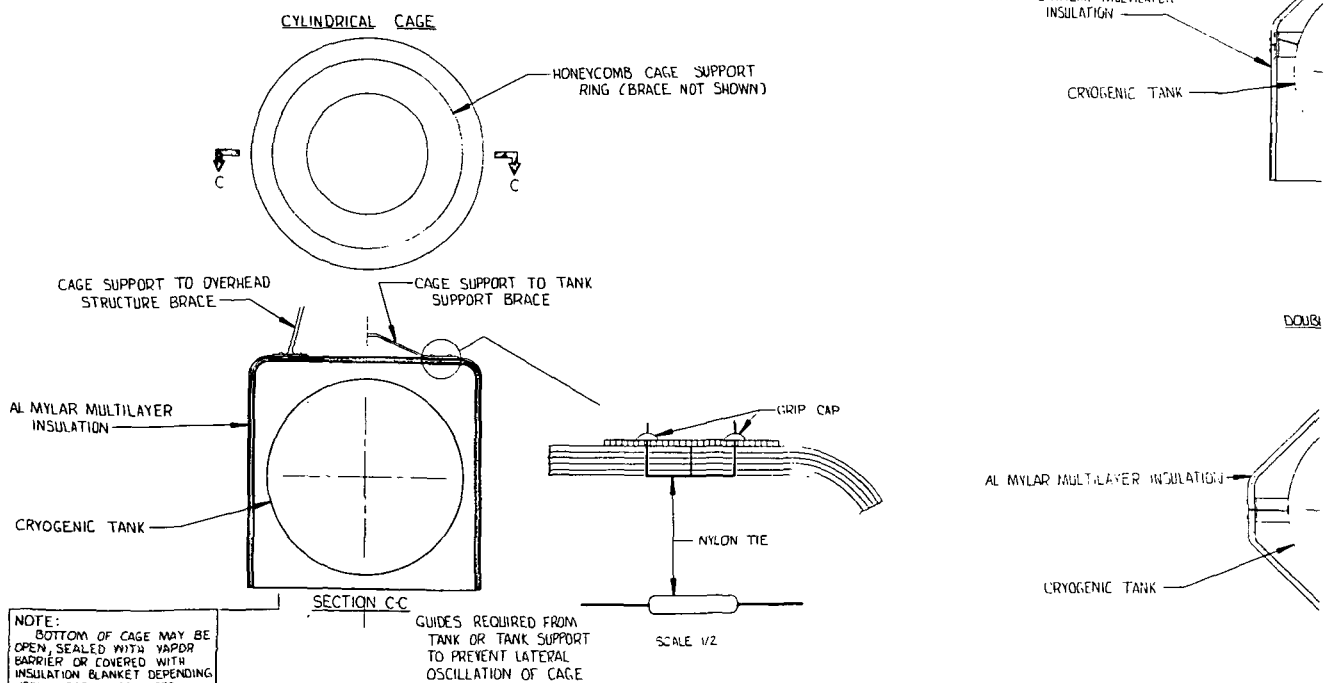
SCALE 1/10



CORRUGATED PANELS NOT SHOWN

### REFLECTOR CAGE

SCALE 1/10



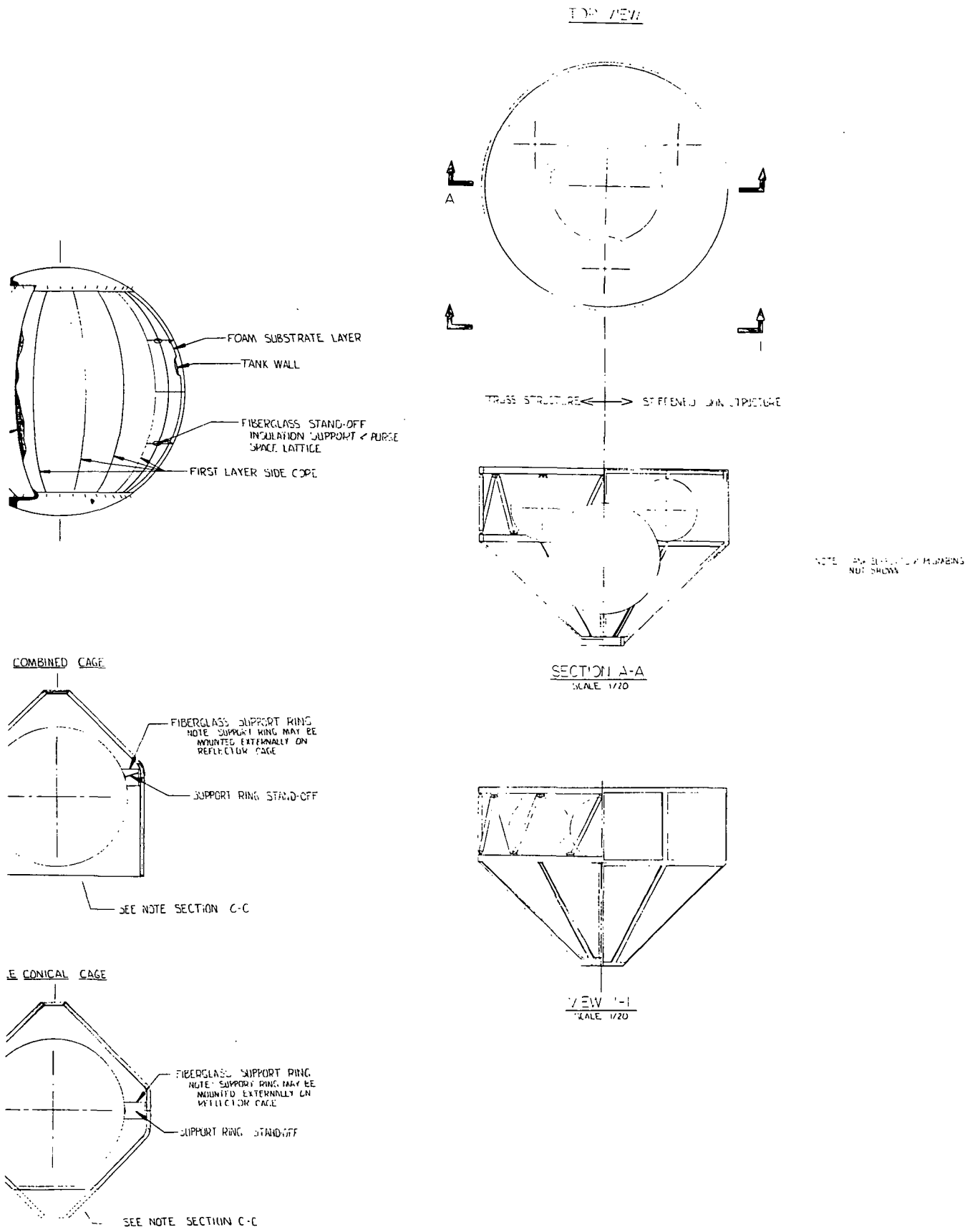


**Figure 1.1-69: TANK MOUNTED INSULATION CONCEPT**

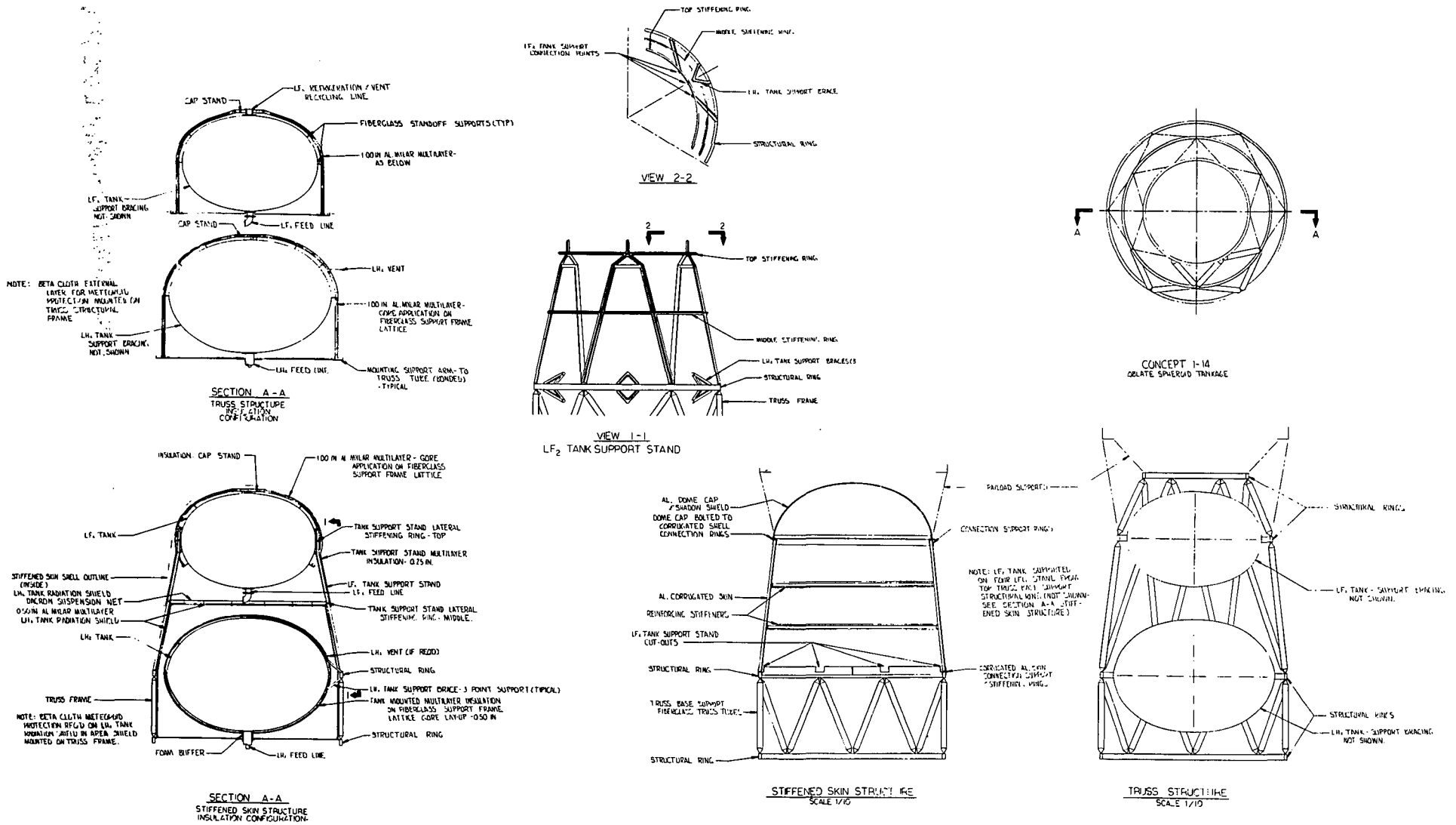


Figure 1.1-70: TANK MOUNTED INSULATION CONCEPT

Table 1.1-8: TANK MOUNTED INSULATION WEIGHTS

ITEM	WEIGHT							
	Bulkhead		Meteoroid Protection		Tanks		Total	
	lb	kg	lb	kg	lb	kg	lb	kg
Insulation Materials	(6.5)	(2.95)			(66.3)	(30.1)	(72.8)	(33.1)
Multilayer	6.5	2.95			63.9	29.0	70.4	32.0
Foam					2.4	1.08	2.4	1.08
Insulation Installation	(10.0)	(4.54)			(10.2)	(4.63)	(20.2)	(9.17)
Alum. Corrugated Panel	10.0	4.54					10.0	4.54
F.G. Standoffs & Hangers					0.3	.13	0.3	.13
F.G. Lattice Insulation Cages					9.9	4.5	9.9	4.5
Meteoroid Protection			(1.8)	(4.4)			(2.8)	(4.4)
Beta Fiber Cloth			8.9	4.0			8.9	4.0
Attachments			0.9	.40			0.9	4.0
Misc. 5%	0.8	.36	0.5	.227	3.8	1.73	5.1	2.32
<b>TOTAL</b>	<b>17.3</b>	<b>7.8</b>	<b>10.3</b>	<b>4.67</b>	<b>80.3</b>	<b>36.5</b>	<b>107.9</b>	<b>49.0</b>

VEHICLE DESIGN - Figure 1.1-69:

ITEM	WEIGHT					
	Meteoroid Protection		Tanks		Total	
	lb	kg	lb	kg	lb	kg
Insulation Materials			(62.4)	(28.3)	(62.4)	(28.3)
Multilayer			62.2	28.2	62.2	28.2
Foam			0.2	.091	0.2	.091
Insulation Installation			(5.0)	(.227)	(5.0)	(.227)
F.G. Cloth			4.2	1.91	4.2	1.91
Foam			0.1	.045	0.1	.045
Velcro			0.2	.091	0.2	.091
Dacron Web			0.1	.045	0.1	.045
Nylon Buttons			0.1	.045	0.1	.045
F.G. Studs			0.3	.136	0.3	.136
Meteoroid Protection	(11.2)	(5.08)			(11.2)	(5.08)
Beta Fiber Cloth	9.0	4.09			9.0	4.08
Velcro	2.2	.99			2.2	.99
Misc. 5%	0.5	.227	3.4	1.54	3.9	1.77
<b>TOTAL</b>	<b>11.7</b>	<b>5.3</b>	<b>70.8</b>	<b>32.1</b>	<b>82.5</b>	<b>37.5</b>

VEHICLE DESIGN - Figure 1.1-68:

and the result gave a fair approximation of the transition region. With this change and the addition of a desorption term, the basic differential equation was

$$\epsilon \frac{dp}{dt} = \frac{gK}{\eta} \frac{d^2 p^2}{dx^2} + D \frac{d^2 p}{dx^2} + NRT \frac{dC}{dt}$$

- where
- C = concentration of absorbed gas, lbm/ft<sup>2</sup>/layer of insulation (Kg/m<sup>2</sup>/layer)
  - D = diffusion coefficient, ft<sup>2</sup>/sec (M<sup>2</sup>/sec)
  - g = acceleration of gravity, ft/sec<sup>2</sup> (M/sec<sup>2</sup>)
  - K = permeability, ft<sup>2</sup> (M<sup>2</sup>)
  - N = insulation layer density, layers/foot (layers/M)
  - p = gas pressure, lbf/ft<sup>2</sup> (N/M<sup>2</sup>)
  - R = gas constant
  - T = temperature, °R(°K)
  - x = distance, ft (M)
  - ε = void fraction in insulation
  - η = viscosity, lb/ft-hr (Kg/M-sec)

The first term on the right side of the equation describes viscous flow at high pressure, and the second term describes diffusion flow at very low pressure. The desorption term used (the third term on the right side of the equation) was an empirical relationship based on insulation material outgassing test data:

$$\frac{dc}{dt} = D_o \left( C - \frac{p}{p_o} C_o \right)$$

where  $D_o$  = a diffusion coefficient for a particular insulation material and absorbed gas.

$p_o$  and  $C_o$  = pressure and concentration at time = 0.

The numerical values of  $D_o$  were obtained from Boeing test data, and K and D estimated from data in Reference 1.1-8. Values of other terms were readily available in the literature. For broadside evacuation of MLI with perforated shields, the values of K and D were adjusted to account for the additional flow resistance of the orifices between each layer.

The differential equation was solved to determine the transient pressure history using a computer program written for this purpose. The Crank-Nicholson finite difference approximations were employed because of their stability and their apparent success (Reference 1.1-9) in dealing with the viscous flow equation.

An analysis was made with the evacuation computer program to compare to a rapid evacuation test from Reference 1.1-10. The results are shown in Figure 1.1-71. The test consisted of a helium purge through the perforated MLI for one hour followed by rapid pumpdown. The analysis was started at 1 minute into the pumpdown at a pressure of  $1 \times 10^{-3}$  torr throughout the sample. The reduced concentration of absorbed water in the nylon net due to the one hour purge was accounted for in the initial concentration selected. Considering the uncertainty in the numerical values of some of the parameters involved, the degree of correlation was reasonable.

The computer program was used to predict the residual gas pressure profiles for aluminized mylar/nylon net and NRC-2, vented both broadside (through 2% perforations) and at panel edges. Results for the perforated insulations at room temperature are shown in Figure 1.1-72. At a temperature of  $300^{\circ}\text{R}$  ( $167^{\circ}\text{K}$ ) the curves were about a decade lower at 180 seconds, but the rate of pressure decay past 180 seconds was much less. Based on available test results, the  $300^{\circ}\text{R}$  ( $167^{\circ}\text{K}$ ) results were probably very conservative.

Interest in aluminized mylar-double silk net MLI prompted an evaluation of its evacuation performance. Silk was known to lose about 7.5% of its weight in a vacuum, compared to about 3% for nylon net. However, the outgassing rate of silk net was initially much higher so it was anticipated that the MLI pressure would be affected for only a short time. The analysis results, shown in Figure 1.1-73, verifies this. In the steeper portion of the curves between 2 and 25 minutes, the pressures were being controlled by silk outgassing. Beyond 25 minutes the pressure was governed by outgassing of the aluminized mylar. The result was less total heat flow during ascent and evacuation than with aluminized mylar/nylon net.

Ascent evacuation and heating analytical results were combined with the coast phase heating to provide a comparison of the MLI systems studied. Figures 1.1-74 and 1.1-75 present the total mission heat leak per unit area versus the MLI weight per unit area for three combinations of materials. The lower and upper weights plotted for NRC-2 and aluminized mylar/nylon net represent the 1/4 to 1 inch (0.64 to 2.54 cm) thickness range for which the ascent heating analysis was performed. Figure 1.1-74 represents the vehicle sidewall and 1.1-75 represents the top deck between the payload and the vehicle.

For purposes of this analysis, it was assumed that the top deck MLI boundary temperatures remained constant at  $520^{\circ}\text{R}$  ( $289^{\circ}\text{K}$ ) and  $40^{\circ}\text{R}$  ( $22.2^{\circ}\text{K}$ ) throughout the mission. Hence, the ascent heating for the top deck reflected only the

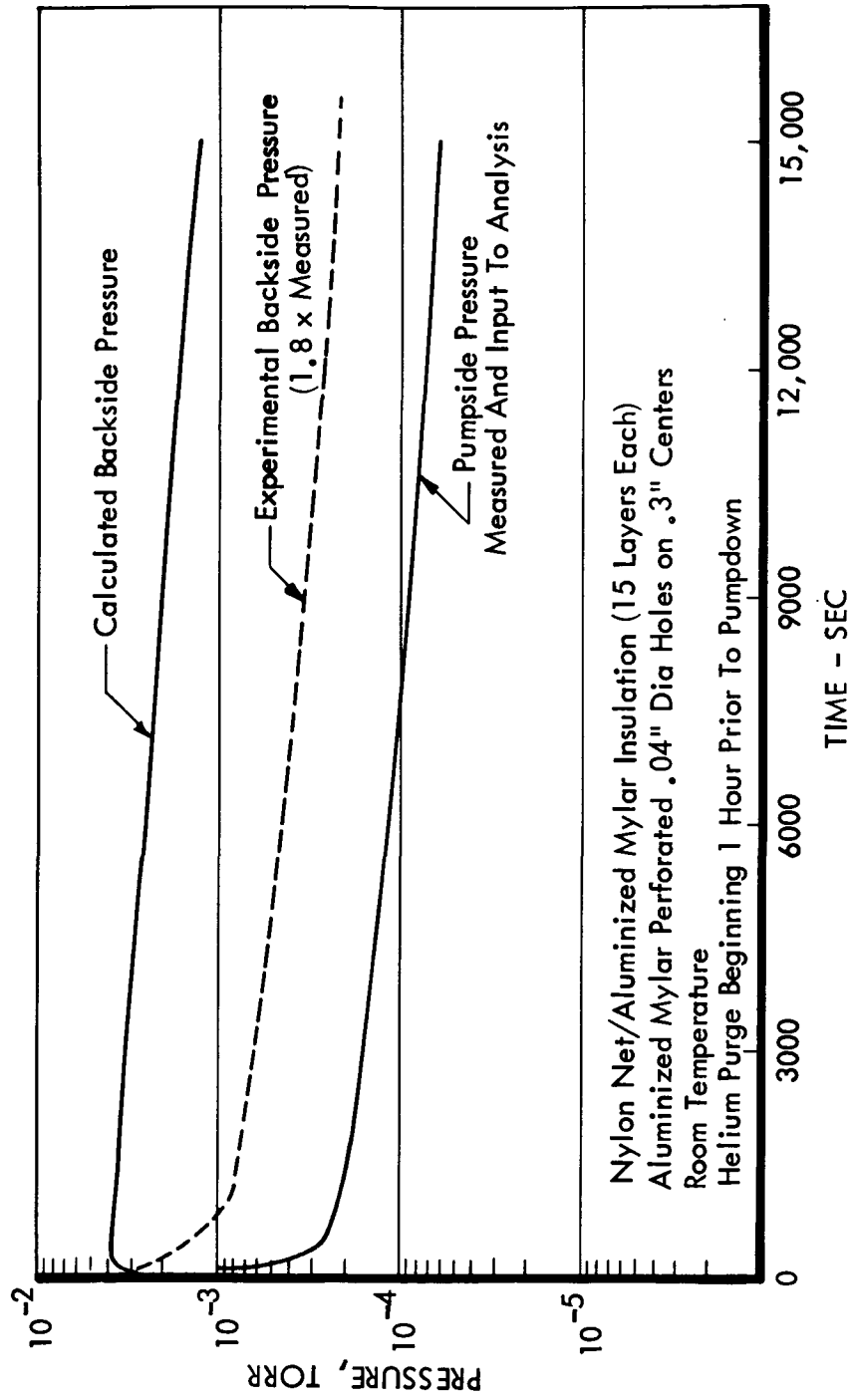


Figure 1.1-71: COMPARISON OF ANALYSIS TO EVACUATION TEST

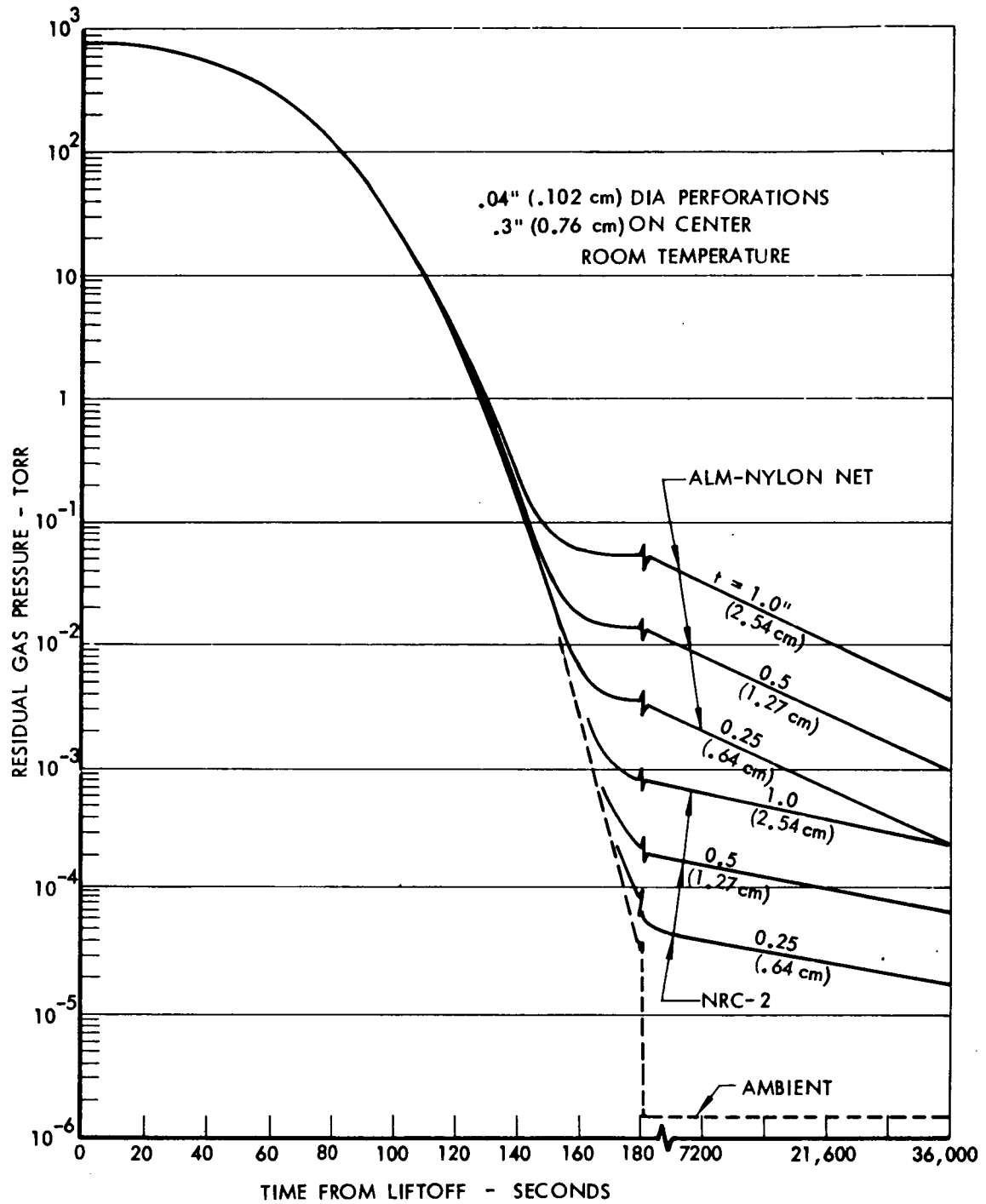


Figure 1.1-72: RESIDUAL GAS PRESSURE IN PERFORATED NRC-2 AND ALUMINIZED MYLAR -NYLON NET

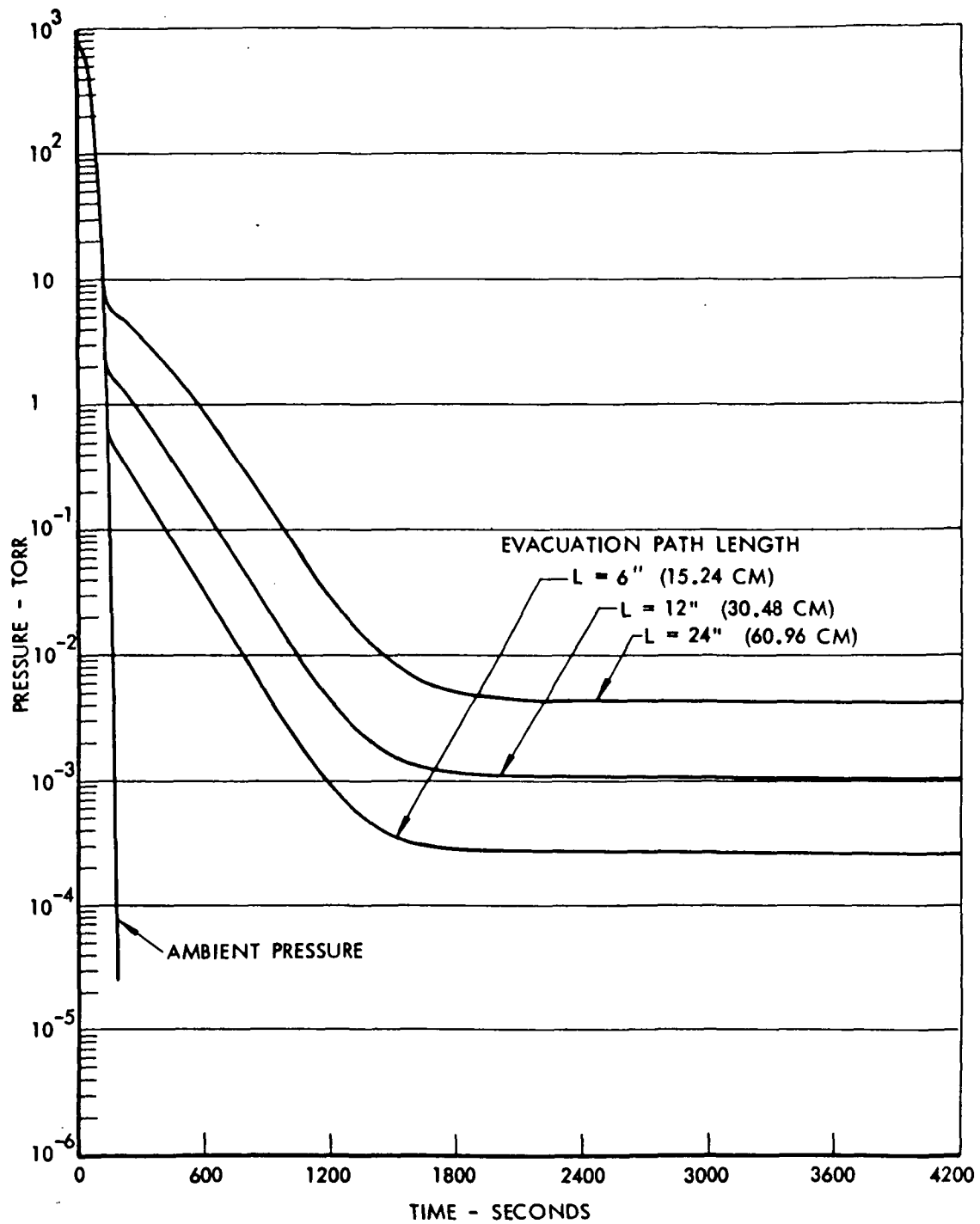


Figure 1.1-73: CALCULATED PRESSURE HISTORY FOR ALUMINIZED MYLAR-2 SILK NET INSULATION EVACUATED ALONG LAYERS, HELIUM PURGE, ROOM TEMPERATURE

Coast Phase Temperatures

$$T_H = 250^{\circ}\text{R} (139^{\circ}\text{K})$$

$$T_C = 40^{\circ}\text{R} (22.2^{\circ}\text{K})$$

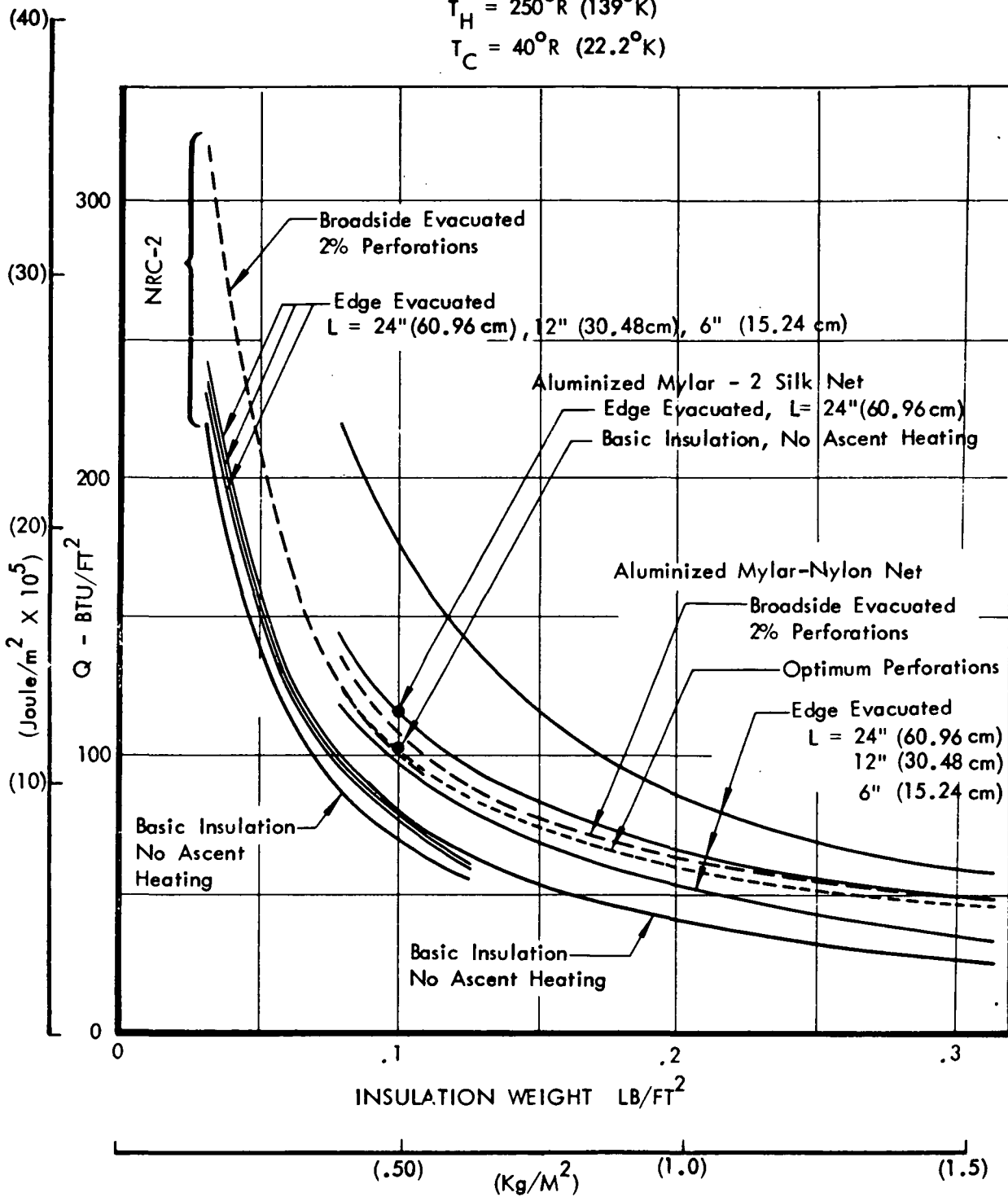


Figure 1.1-74: EFFECT OF ASCENT HEATING AND EVACUATION METHOD ON TOTAL MISSION HEATING - SIDEWALL

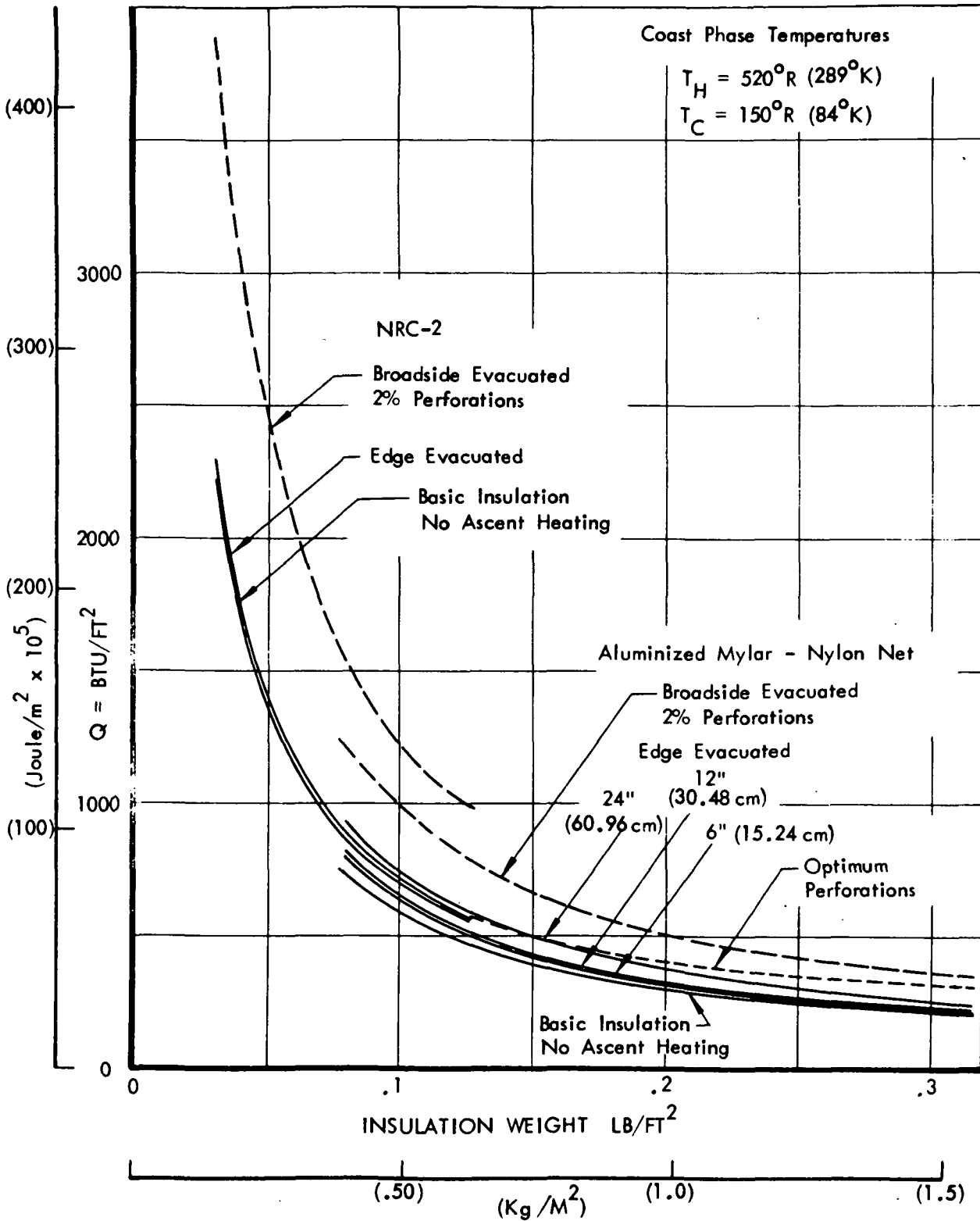


Figure 1.1-75: EFFECT OF ASCENT HEATING AND EVACUATION METHOD ON TOTAL MISSION HEATING - TOP DECK

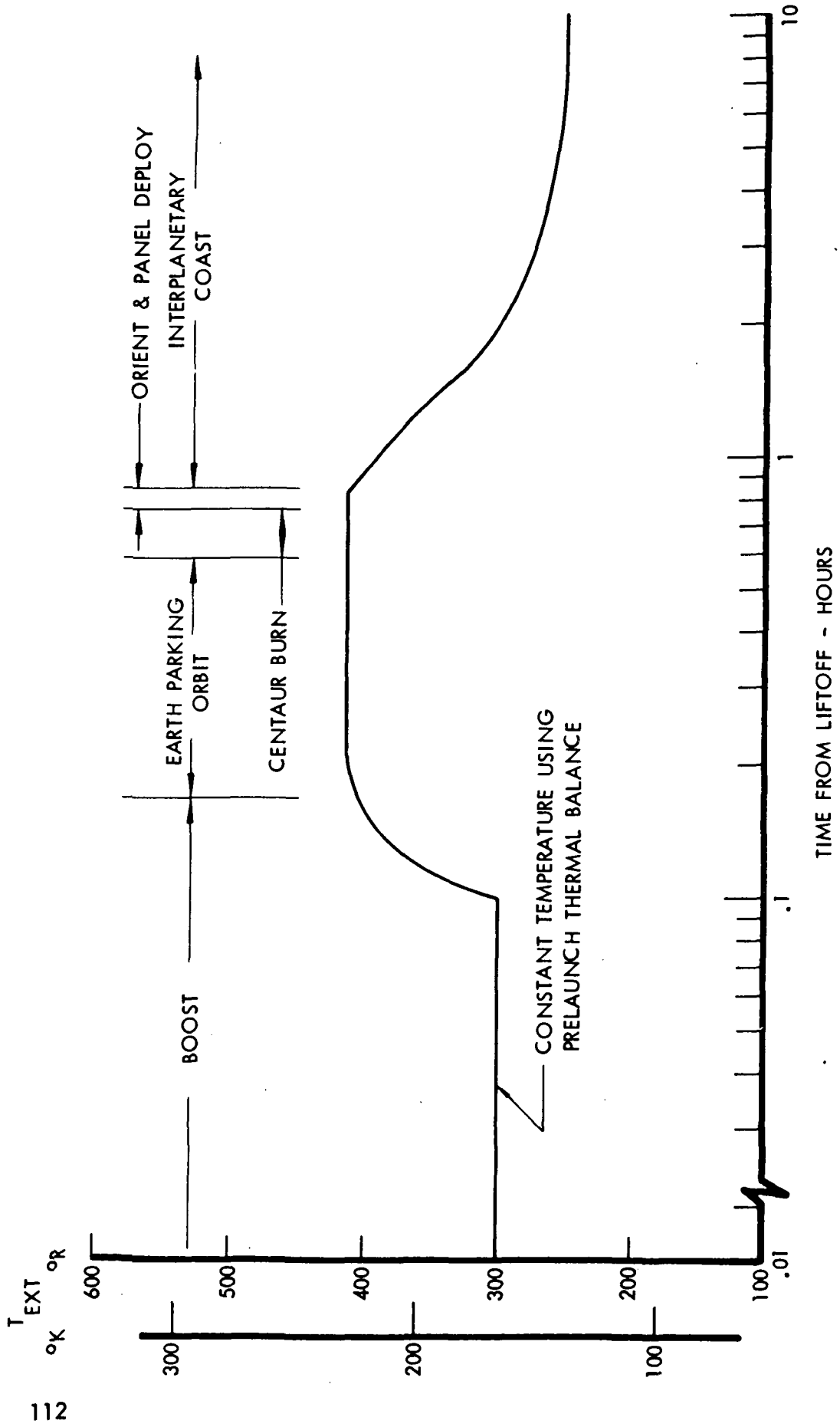


Figure 1.1.-76: MISSION TIME/TEMPERATURE PHASING

increased conductivity due to helium gas pressure. Since the sidewall MLI was subject to considerable variation in environment from launch to earth orbit to coast phase, the boundary temperature was varied with time. Initial temperatures were based on steady state thermal analysis of a helium purged system during ground hold. The external temperature was assumed to rise to  $410^{\circ}\text{R}$  ( $228^{\circ}\text{K}$ ) between boost shroud jettison and earth orbit injection. Following earth orbit, Centaur burn, separation and solar orientation, the sidewall external temperature decayed to  $250^{\circ}\text{R}$  ( $139^{\circ}\text{K}$ ) as the view factor to earth decreased. The time phasing is shown in Figure 1.1-76. Quasisteady heat flow through the MLI was calculated using the residual gas pressure and boundary temperature histories. The sidewall MLI ascent heating therefore reflected both additional gas pressure in the MLI and higher temperatures.

The lowest curve for each insulation gives the total coast phase heating through the basic MLI. The curves for edge evacuated MLI are the sum of the ascent phase heating and basic coast phase heating. These do not include additional heating due to joints required to obtain the assumed vent path length. It is expected that the venting length  $L$  would be at least 24 in (0.61 m), and with some possible exceptions, the evacuation edges would correspond to panel joints and edges dictated by the configuration. The curves for broadside evacuation through perforations include the ascent phase heating for perforated MLI and the coast phase heating. The coast phase heating for the perforated MLI was based on conductivity equations where the radiation term had been increased to account for the perforations.

For aluminized mylar-nylon net, the curves for optimum perforations were obtained by minimizing the total mission heat leak as a function of the percent area perforated. This was done using approximate equations for the ascent heat leak based on correlation of heat leak from previous pressure decay computer solutions with thickness and percent perforation area, and the MLI conductivity equation modified to include percent perforation. The optimum percentage of perforations was found to be linear with MLI thickness;

$$a = 0.8\delta \text{ for the top deck}$$

$$a = 2.7\delta \text{ for the sidewall}$$

where  $a$  = percent area perforated, and  $\delta$  = MLI thickness.

Comparison of the curves in Figures 1.1-74 and 1.1-75 showed that, for NRC-2, edge evacuation was considerably more efficient than broadside evacuation. The choice of evacuation method for the aluminized mylar/nylon net depended on the location and thickness. On the sidewall, edge evacuation was the better choice only for pumping lengths less than 6 to 12 in (15.2 to 30.4 cm). Since these lengths were unrealistically low for most configurations, perforations would be the better choice. On the top deck, optimum perforations were somewhat more efficient than the 24 in (60.8 cm) edge evacuated blanket below  $.15 \text{ lb/ft}^2$

( $0.73 \text{ kg/m}^2$ ), but these reversed in relative efficiency for thicker blankets. The evacuation method for the top deck would depend on the MLI thickness required and the ability to achieve the edge evacuation required without additional joint heat leaks. Comparison of the two insulations in Figure 1.1-74 showed that NRC-2 was considerably more efficient than aluminized mylar/nylon net for the sidewall. On the top deck they were of nearly equal efficiency. The data for the silk net showed that the total heat flow would be less than with nylon net, but that NRC-2 remained the most efficient for the sidewall location on the vehicle.

Comparison of the basic thermal conductivity-density product of several of the more promising insulations was made to aid in selection of materials for preliminary design. Also, equations describing the thermal conductivity parallel to the layers were derived for use in MLI material trades considering effects of penetrations. The basic conductivity equation, applicable for heat transfer either through the layers or along the layers, is given in Table 1.1-9. The equation for  $k_r$  applies only to heat transfer through the layers. The coefficients  $k_r$  and  $k_c$  are given in the table, along with the assumed shields per inch, and density for two mylar thicknesses.

The coefficients for heat transfer through the layers were either obtained by fitting to test data or were taken from Reference 1.1-11. For aluminized mylar/nylon net, curve fitting was done using test data with hot face temperatures from  $360^\circ\text{R}$  ( $200^\circ\text{K}$ ) to  $610^\circ\text{R}$  ( $340^\circ\text{K}$ ). With the silk net and polyurethane foam, test data at only one set of boundary temperatures were available. For these insulations,  $k_r$  was calculated and  $k_c$  determined at the test point with minimum layer density. For heat transfer parallel to the layers,  $k_r$  was determined by curve fitting to the analytical results of Reference 1.1-12. The conduction term,  $k_c (T_1 + T_2)$ , was based on the linear variation with temperature from Reference 1.1-13, and the room temperature values used in Reference 1.1-11.

Several graphical comparisons of these equations are shown in Figures 1.1-77, 1.1-78 and 1.1-79. In Figure 1.1-77,  $k\rho$  versus hot face temperature is shown for .25 mil mylar. Figure 1.1-78 presents a similar comparison for .15 mil mylar. Conductivity parallel to the layers is shown in Figure 1.1-79. The curves showed crinkled aluminized one side mylar most efficient, based on  $k\rho$ , at the low temperatures representative of the sidewall. This MLI gained impressively by using 0.15 mil mylar, and became most efficient for all temperatures. It should be noted that its conductivity would also be most affected by reduced mylar thickness. This was not accounted for here, since no conductivity data on the .15 mil material was available for comparison. The foam spacer appeared attractive at low temperatures using the equation of Reference 1.1-11, but rather poor based on a Boeing data point. Nylon net and the double silk nets were competitive though less efficient than the NRC-2 type of MLI.

Table 1.1-9: INSULATION CONDUCTIVITY EQUATIONS

$$k = k_r (T_1^2 + T_2^2) (T_1 + T_2) + k_c (T_1 + T_2), \text{ BTU/FT-HR-}^\circ\text{R (Joule/meter-sec-}^\circ\text{K)}$$

where  $T_1$  and  $T_2$  are the boundary temperatures

$$k_r = \frac{\sigma}{12n \left( \frac{2}{\epsilon} - 1 \right)} \quad (\text{unless taken directly from reference 1.1-11})$$

(Through layers only)

$\sigma$  = Stefan-Boltzmann Constant  
 $n$  = layers/inch  
 $\epsilon$  = .025

$k_c$  = constant selected to fit test data

INSULATION	n	$\rho$ LB/FT <sup>3</sup> (Kg/m <sup>3</sup> )		THROUGH LAYERS		Ref.	ALONG LAYERS	
		.25 Mil*	.15 Mil*	$k_r$	$k_c$		$k_r$	$k_c$
NRC-2	70	1.55 (24.8)	0.94 (15.04)	$9.6 \times 10^{-14}$ ( $96.8 \times 10^{-14}$ )	$0.89 \times 10^{-8}$ ( $1.54 \times 10^{-8}$ )	1.1-11	$1.19 \times 10^{-10}$ ( $11.99 \times 10^{-10}$ )	$8.4 \times 10^{-6}$ ( $14.5 \times 10^{-6}$ )
Aluminized Mylar-Nylon Net	70	3.84 (61.5)	3.25 (52.0)	$2.5 \times 10^{-14}$ ( $25.2 \times 10^{-14}$ )	$0.53 \times 10^{-8}$ ( $.92 \times 10^{-8}$ )	**	$0.75 \times 10^{-10}$ ( $7.56 \times 10^{-10}$ )	$16.8 \times 10^{-6}$ ( $29.1 \times 10^{-6}$ )
Aluminized Mylar-2 Silk Net	23	1.18 (18.8)	0.90 (15.68)	$7.8 \times 10^{-14}$ ( $78.6 \times 10^{-14}$ )	$2.20 \times 10^{-8}$ ( $3.80 \times 10^{-8}$ )	1.1-14	$0.66 \times 10^{-10}$ ( $6.53 \times 10^{-10}$ )	$6.4 \times 10^{-6}$ ( $11.1 \times 10^{-6}$ )
Aluminized mylar-polyurethane foam	29.5	1.82 (29.3)	1.57 (25.1)	$6.1 \times 10^{-14}$ ( $61.5 \times 10^{-14}$ )	$2.00 \times 10^{-8}$ ( $3.46 \times 10^{-8}$ )	**	$0.26 \times 10^{-10}$ ( $2.62 \times 10^{-10}$ )	$8.3 \times 10^{-6}$ ( $14.4 \times 10^{-6}$ )
	21.7	1.93 (30.9)	1.72 (27.5)	$8.3 \times 10^{-14}$ ( $83.7 \times 10^{-14}$ )	$5.80 \times 10^{-8}$ ( $10.03 \times 10^{-8}$ )	1.1-11		
Aluminized mylar-tissuglas	82	2.82 (45.1)	2.11 (33.8)	$3.7 \times 10^{-14}$ ( $37.3 \times 10^{-14}$ )	$3.10 \times 10^{-8}$ ( $5.36 \times 10^{-8}$ )	1.1-11	$0.26 \times 10^{-10}$ ( $2.62 \times 10^{-10}$ )	$23.0 \times 10^{-6}$ ( $39.8 \times 10^{-6}$ )

\* Mylar Thickness    \*\* Boeing Data

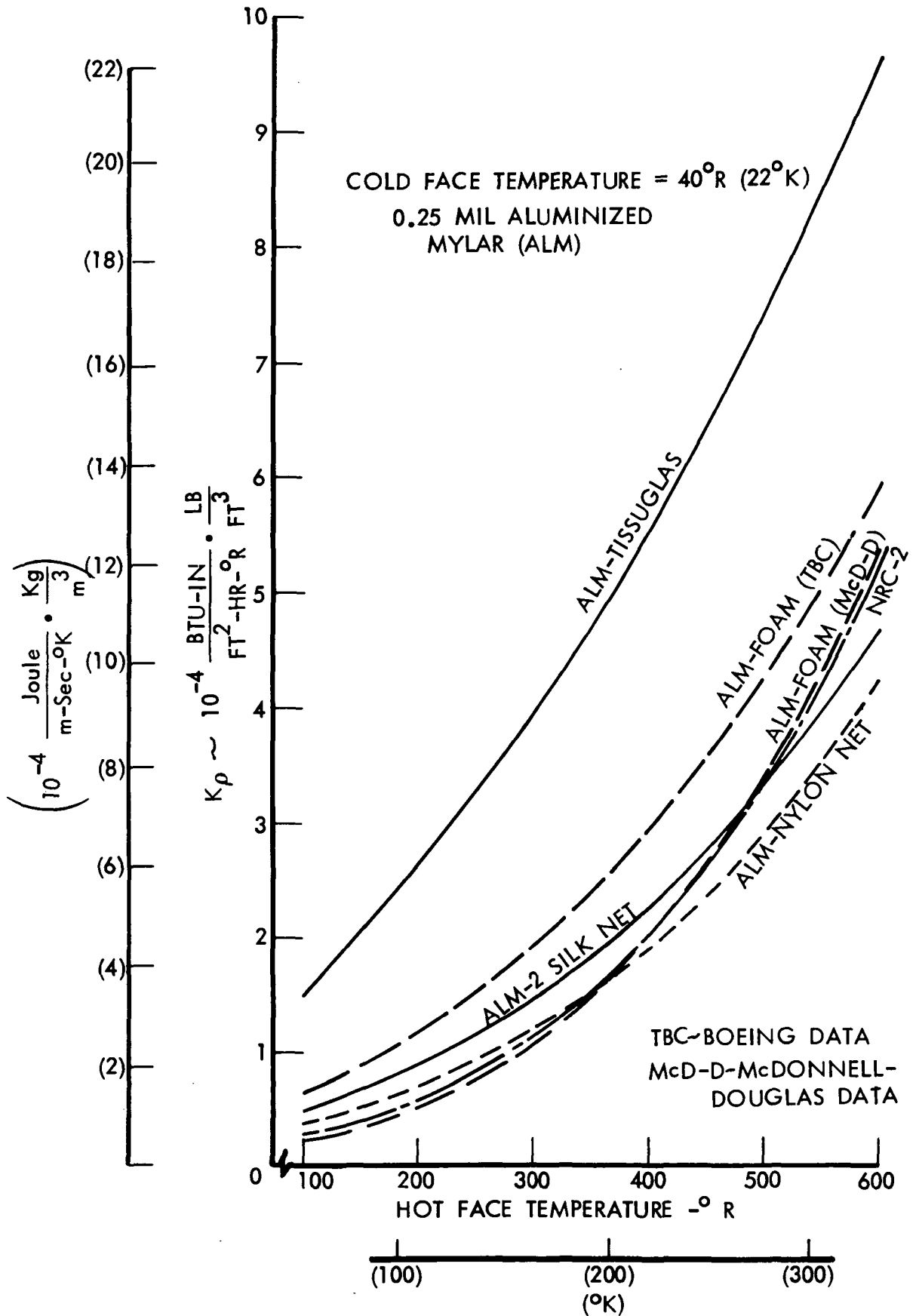


Figure 1.1-77: CONDUCTIVITY-DENSITY PRODUCT FOR SEVERAL MULTILAYER INSULATIONS

COLD FACE TEMPERATURE - 40°R (22°K)  
 0.15 MIL ALUMINIZED MYLAR (ALM)

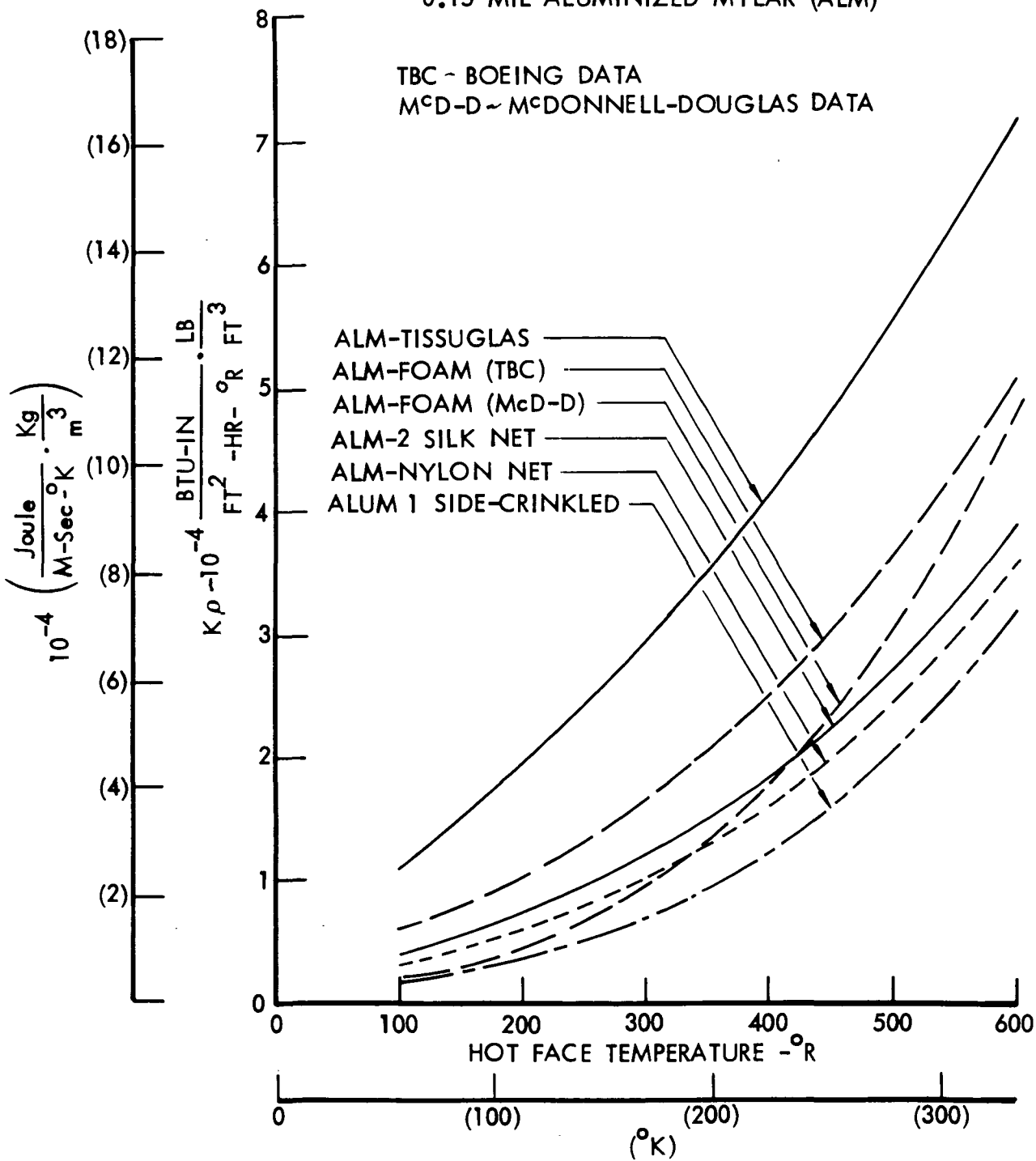


Figure 1.1-78: CONDUCTIVITY - DENSITY PRODUCT FOR SEVERAL MULTILAYER INSULATIONS

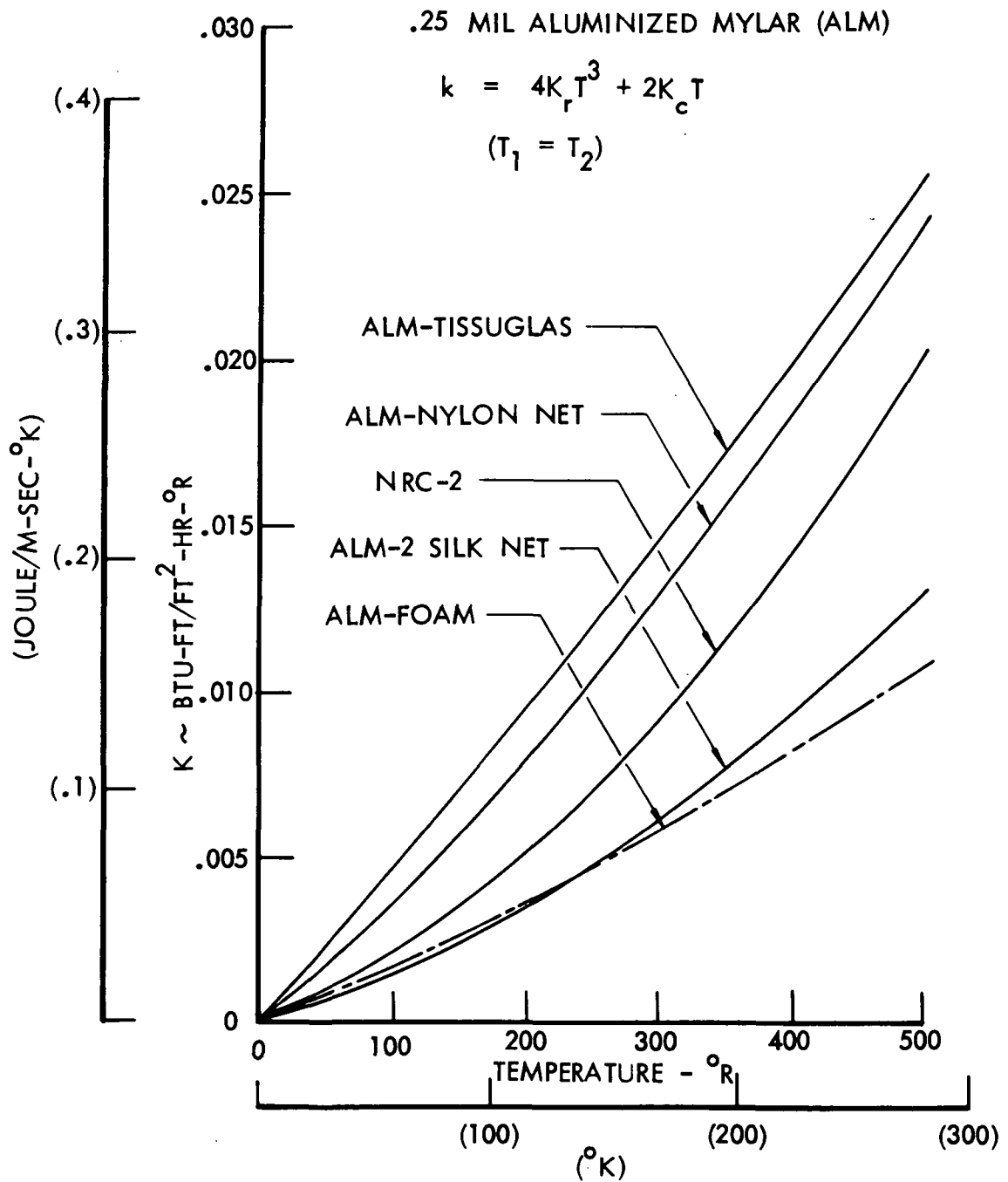


Figure 1.1-79: CONDUCTIVITY PARALLEL TO LAYERS FOR SEVERAL MULTILAYER INSULATIONS

Figure 1.1-79 showed that more dense insulations had higher conductivity parallel to the layers, with double silk nets and foam giving the lowest conductivity. The conductivity parallel to the layers could not be used directly in material selection. Relative thicknesses, conductivity through the layers, and geometry of the penetrations would influence the choice.

Gold coated and aluminized mylar were compared on the basis of conductivity-density product for various coating thicknesses. Two typical vehicle MLI blankets were considered, the top deck with boundary temperatures of 500°R (278°K) and 40°R (22.2°K), and the sidewall with boundary temperatures of 250°R (139°K) and 40°R (22.2°K). Previously, it had been concluded that NRC-2 was best suited to the sidewall location and either aluminized mylar/nylon net or NRC-2 for the top deck. Therefore, this study considered metallized (gold or aluminum) mylar with nylon net spacers and metallized-one-side mylar crinkled to simulate NRC-2.

The thermal conductivity for the metallized mylar/nylon net materials was calculated from the equation:

$$k = \frac{\sigma (T_h^2 + T_c^2) (T_h + T_c)}{\left(\frac{N}{t}\right) \left(\frac{2}{\epsilon} - 1\right)} + 0.63 \times 10^{-7} (T_h + T_c) \frac{\text{BTU-IN}}{\text{FT}^2 \text{-HR-}^\circ\text{R}}$$

or

$$k = \frac{\sigma (T_h^2 + T_c^2) (T_h + T_c)}{\left(\frac{N}{t}\right) \left(\frac{2}{\epsilon} - 1\right)} + 0.16 \times 10^{-7} (T_h + T_c) \frac{\text{W}}{\text{m-}^\circ\text{K}}$$

where N = number of radiation shields  
t = insulation thickness ~ inches  
ε = emittance of the metallized surface as derived from Figure 1.1-80 (Reference 1.1-14)

The equation was developed from test data using curve fitting techniques.

The thermal conductivity for crinkled metallized mylar was calculated from the Reference 1.1-11 report. The equation was:

$$K_e = \frac{1.64\sigma(T_h^2 + T_c^2)(T_h + T_c)}{\left(\frac{N-1}{t}\right)\left(\frac{1}{\epsilon_1} + \frac{1}{\epsilon_2} - 1\right)} + 1.87 \times 10^{-13} (\bar{N})^{2.7} T_m', \frac{\text{BTU-FT}}{\text{FT}^2 \text{-HR-}^\circ\text{R}}$$

or

$$K_e = \frac{1.64\sigma(T_h^2 + T_c^2)(T_h + T_c)}{\left(\frac{N-1}{t}\right)\left(\frac{1}{\epsilon_1} + \frac{1}{\epsilon_2} - 1\right)} + 5.82 \times 10^{-13} (\bar{N})^{2.7} T_m', \frac{W}{m \text{-}^\circ\text{K}}$$

The value of  $\epsilon_1$  was derived from Figure 1.1-80 and  $\epsilon_2$  from Reference 1.1-11. Note that  $(N-1)$  is used here, as given in the reference, whereas in the previous equations, the approximation  $(N-1) \approx N$  was made.

The weights of mylar film and metal coating were calculated using  $\rho$  mylar = 0.0502 lb/in<sup>3</sup> (1390 kg/m<sup>3</sup>),  $\rho$  gold = 0.697 lb/in<sup>3</sup> (19250 kg/m<sup>3</sup>), and  $\rho$  aluminum = 0.102 lb/in<sup>3</sup> (2820 kg/m<sup>3</sup>). The weight of nylon net was obtained from ADL and Boeing test data.

The results of the evaluation are presented in Figure 1.1-81. The aluminum coating was the best choice for both types of MLI, in terms of least conductivity-density product. One additional point was added to these curves, representing Lockheed-National Metallizing data on sputtered gold coated 1/4 mil mylar. The data, supplied by NASA/LeRC consisted of a gold coating thickness of 500 to 700 Å per side, and an emittance of 0.0215. The 1/4 mil mylar had been converted to 0.15 mil for comparison purposes. The slightly higher emittance of this material as compared to Figure 1.1-80 made it less competitive with the aluminum especially at the higher hot face temperature.

Further study was directed towards identification of the most promising MLI by evaluating the influence of blanket fasteners. An analysis of three materials with one type of fastener was made. Table 1.1-10 shows the fastener geometry. The analytical model for computer solution consisted of an axisymmetric arrangement of nodes about the fastener centerline, with 6 nodes through the thickness at 8 different radii from the fastener. As shown, one boundary was at a specified temperature while the other received radiation from a source at a different temperature. The equations of Table 1.1-9 were used for this purpose, and were also used in the computer analysis.

Results of the analysis are summarized in Table 1.1-10. The data showed that fastener heat leak differed significantly with the type of MLI. The heat leak through the fastener decreased with thicker MLI, and the different thicknesses and conductivity parallel to the layers affected the amount of change in the MLI heat flow.

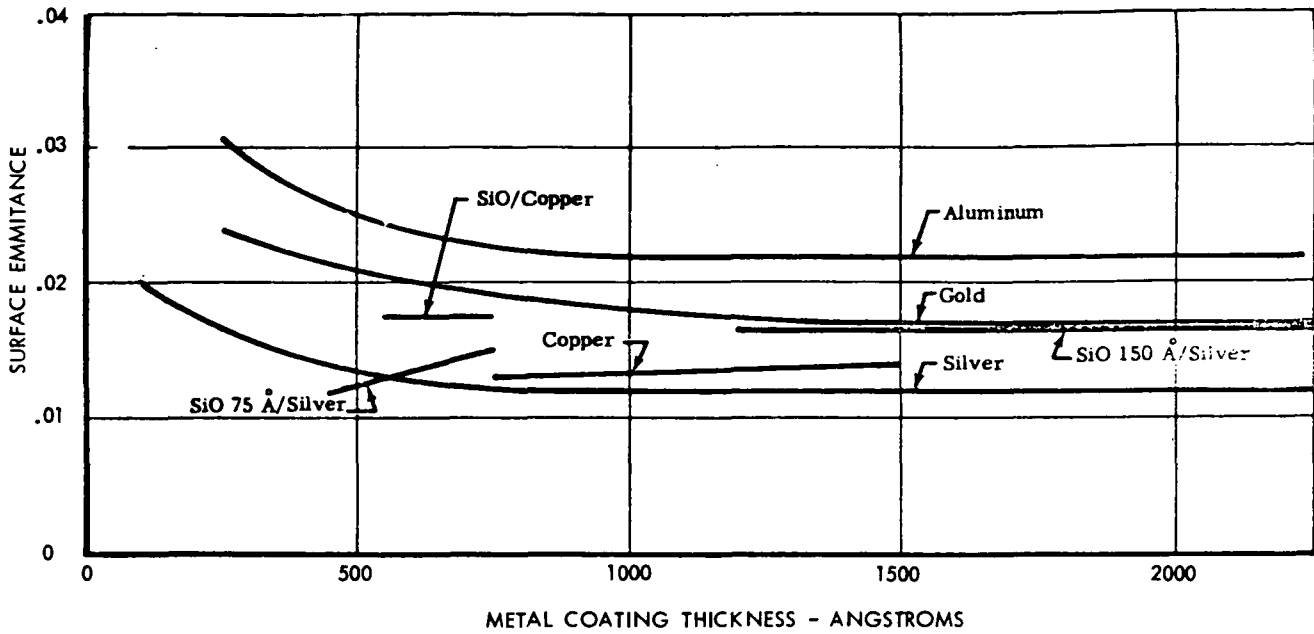


Figure 1.1-80: EMITTANCE OF VACUUM METALLIZED POLYESTER FILM AT  $553^{\circ}\text{R}$  ( $307^{\circ}\text{K}$ ) FOR VARIOUS COATING MATERIALS AND THICKNESSES

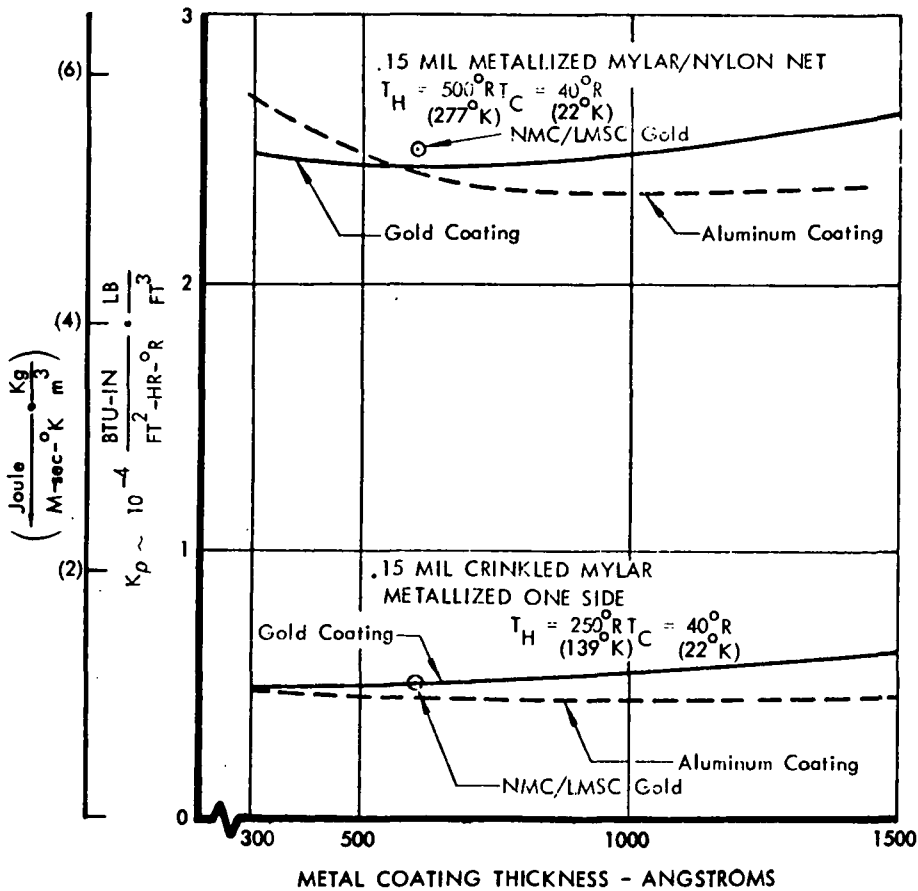
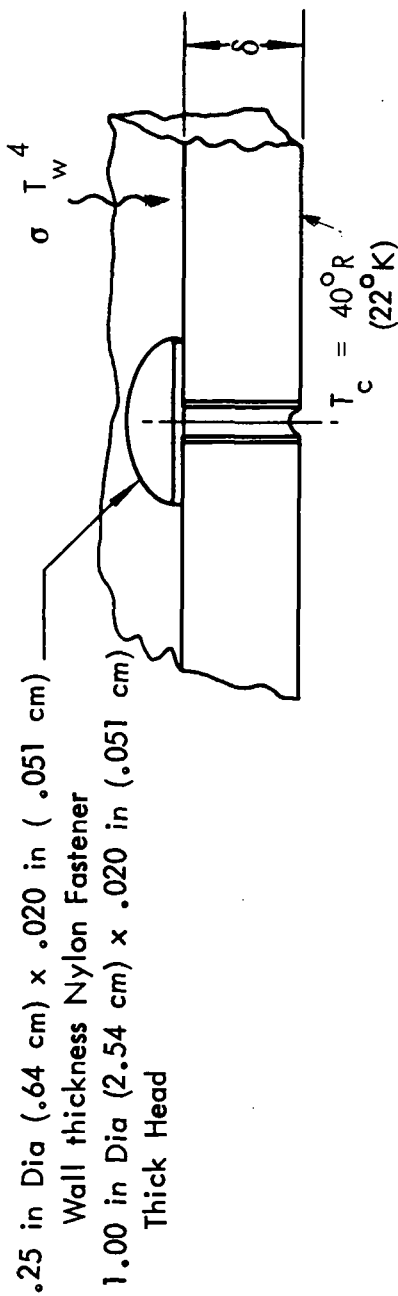


Figure 1.1-81: EFFECT OF METALLIZING ON CONDUCTIVITY/DENSITY PRODUCT

Table 1.1-10: EFFECT OF INSULATION ON FASTENER HEAT LEAK



INSULATION	$T_w = 500^{\circ}R (277^{\circ}K)$				$T_w = 200^{\circ}R (111^{\circ}K)$			
	$\delta$ Inches (CM)	Q Fastener BTU/HR (WATT)	$\Delta Q$ Insulation BTU/HR (WATT)	$\Sigma Q$ BTU/HR (WATT)	$\delta$ Inches (CM)	Q Fastener BTU/HR (WATT)	$\Delta Q$ Insulation BTU/HR (WATT)	$\Sigma Q$ BTU/HR (WATT)
Aluminized Mylar-Nylon Net	0.50 (1.27)	.15085 (.0443)	*-.04279 (-.012537)	.10806 (.03166)	0.20 (.51)	.033866 (.00992)	-.002822 (-.000827)	.031045 (.009096)
NRC-2	1.44 (3.66)	.09798 (.02871)	-.07181 (-.02040)	.02616 (.00766)	0.41 (1.04)	.029100 (.008526)	-.005183 (-.00152)	.023917 (.007007)
Aluminized Mylar - 2 Silk Net	1.85 (4.7)	.06694 (.01962)	-.05676 (-.01663)	.01019 (.00299)	0.84 (2.13)	.019779 (.005795)	-.009376 (-.00272)	.010404 (.00305)

\*The negative insulation  $\Delta Q$  indicates a reduction in insulation heat flow due to (1) reduced surface temperature near the fastener head, and (2) shorting to the fastener shank within the insulation.

The choice of MLI depended, among other considerations, on both the heat leak through the fasteners to be used and the basic  $k\rho$  of the insulation. An efficiency comparison that combined these two properties is shown in Figure 1.1-82 for .25 mil mylar shields and in Figure 1.1-83 for .15 mil mylar shields. The curves represent the sum of heat leak through the undisturbed MLI and the change in heat leak due to the fasteners, multiplied by the MLI weight. This was equivalent to an "effective"  $k\rho$ , but was dependent on thickness because the fastener heat leak was not exactly proportional to thickness. The conclusions thus applied only to thicknesses close to those analyzed. The thicknesses, densities and heat leaks came from Tables 1.1-9 and 1.1-10. With .25 mil mylar and 500°R (277°K), the aluminized mylar/silk net was most efficient, even though aluminized mylar/nylon net was best on a  $k\rho$  basis. At 200°R (111°K) warm face temperature, NRC-2 was best both with and without fasteners. With .15 mil mylar, the crinkled-aluminized one side material (i.e., NRC-2 with thin mylar) was most efficient with or without fasteners at both warm face temperatures. As mentioned previously, there was some uncertainty in the performance of the thinner crinkled mylar. Also, its use on the top deck was questionable due to potential compaction.

Additional analyses of the effect of MLI material on fastener heat leak were made. The analyses were similar to those discussed previously, but with the MLI inside the structure, and a smaller fastener for the top deck. Table 1.1-11 shows the results for the 1/4 in fasteners for the sidewall. As shown, most of the heat leak occurred through the MLI due to conduction from the fastener to the insulation layers. For MLI outside the structure (Table 1.1-10), the heat flow was reduced slightly. The results in Table 1.1-11 indicated little difference between the three materials. However, the estimated errors in the total heat leaks were 8%, 20%, and 33%, respectively, for the insulations as listed. This potential error was due to difficulty in obtaining converged solutions at the very low heat leaks involved. The total blanket performance is shown in Figure 1.1-84 for these insulations and the 1/4 in fastener. The difference in performance in this case was due primarily to the basic conductivity of the MLI.

An analysis was performed of small fasteners for the top deck. The smaller fasteners were suggested for use in areas where shear loads were minimal, their main purpose being to maintain blanket shape and improve handling characteristics. Unlike the results for the vehicle sidewall, the heat leak was clearly affected by MLI thickness and to some extent by lateral conductivity (see Table 1.1-12). Accuracy of these results was considerably better than for the sidewall case. Figure 1.1-85 shows the total blanket performance for the small fasteners. The fasteners had much less influence on material choice than was shown previously for large fasteners in external top deck MLI. The silk net became better than the nylon net for less than 0.8 ft<sup>2</sup> per fastener (0.074 m<sup>2</sup>/fastener).

With internal MLI (i.e., inside the structure), there would be several penetrations due to the tank supports. One penetration design from Figure 1.1-86 was

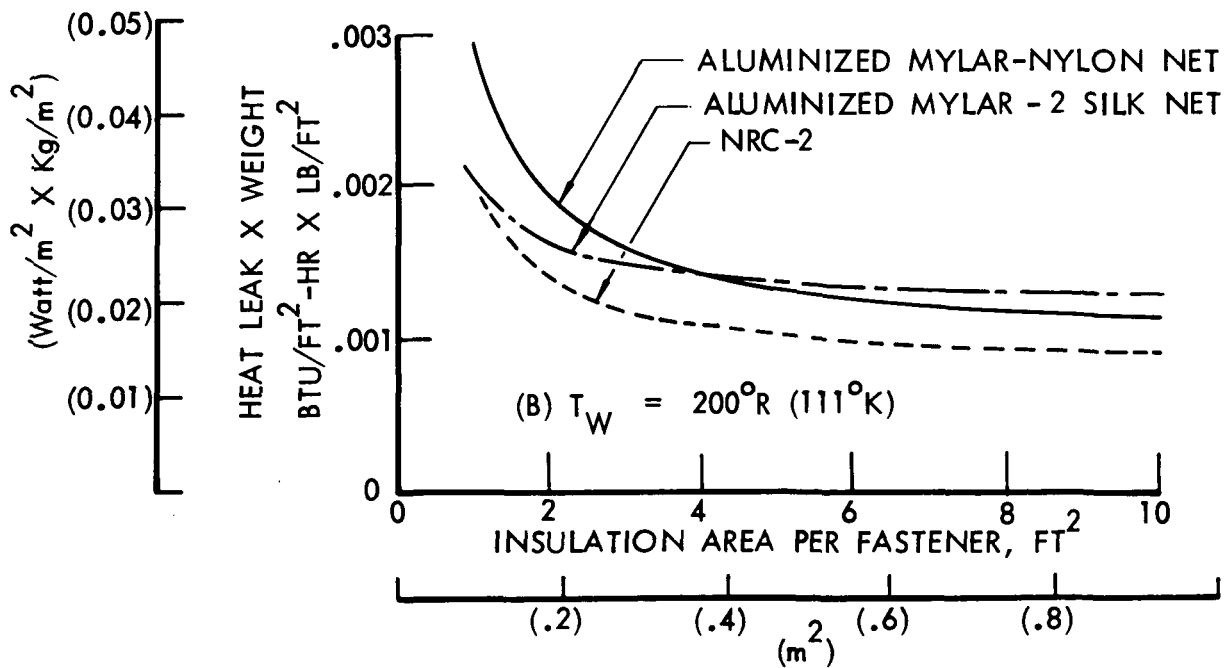
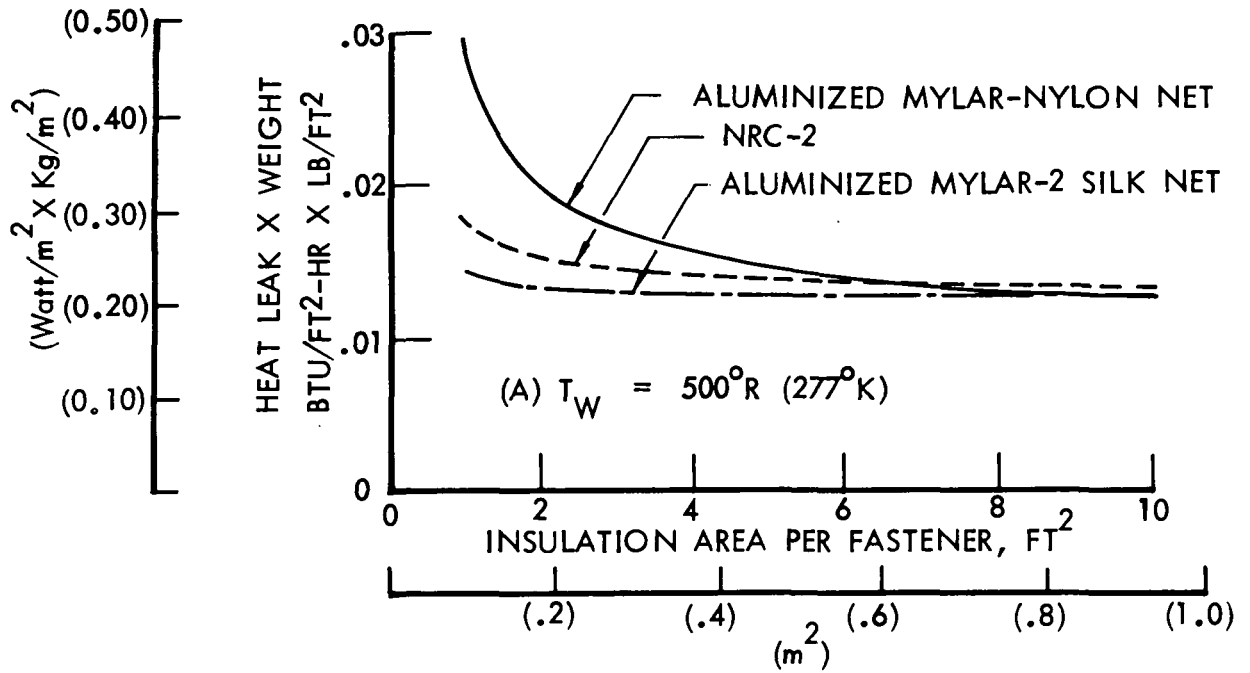


Figure 1.1-82: EFFECT OF FASTENERS ON INSULATION MATERIAL CHOICE - .25 MIL MYLAR

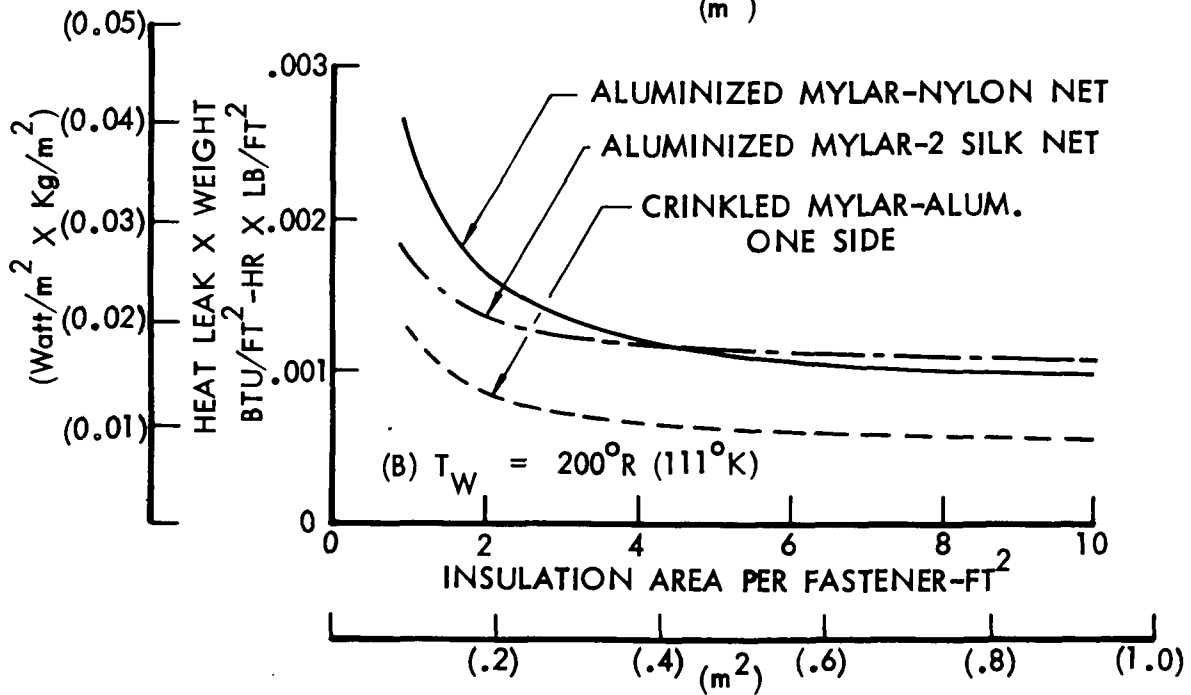
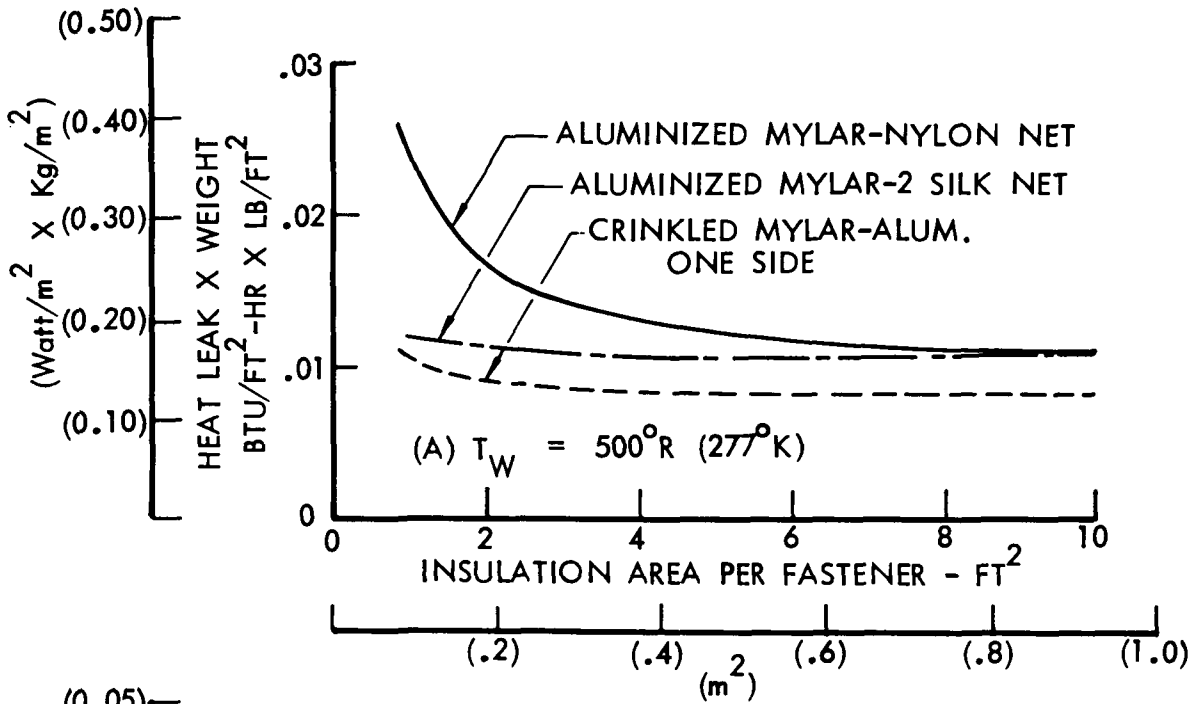
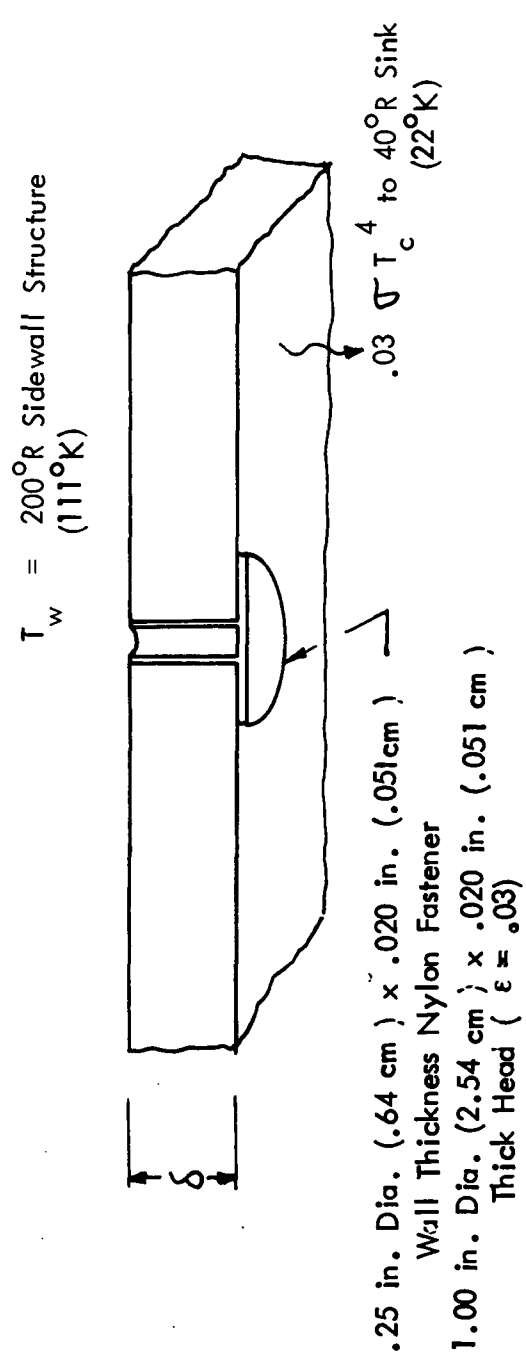


Figure 1.1-83: EFFECT OF FASTENERS ON INSULATION MATERIAL CHOICE - 0.15 MIL MYLAR

Table 1.1-11: EFFECT OF INSULATION ON FASTENER HEAT LEAK - INTERNAL INSULATION, SIDEWALL, LARGE FASTENERS



INSULATION	$\delta$ (inches) (CM)	Fastener $Q$ (BTU/Hr) (WATT)	$\Delta Q$ Insulation (BTU/Hr) (WATT)	$\Sigma Q$ (BTU/Hr) (WATT)
Aluminized Mylar - Nylon Net	0.20 (.54)	.00037 (.0001084)	*.00443 (.001298)	.00480 (.00140)
NRC-2	0.41 (1.04)	.00028 (.000082)	.00513 (.001503)	.00541 (.00159)
Aluminized Mylar - 2 Silk Net	0.84 (2.13)	.00017 (.0000498)	.00461 (.00135)	.00478 (.00141)

\*The positive insulation  $\Delta Q$  indicates an increase in insulation heat flow due to shorting from the warmer fastener shank to the insulation.

.25 in. Dia. (.64 cm) x .02 in. (.051 cm) Wall Thickness Fasteners

$$T_W = 200^{\circ}\text{R} (111^{\circ}\text{K})$$

INSULATION INSIDE STRUCTURE

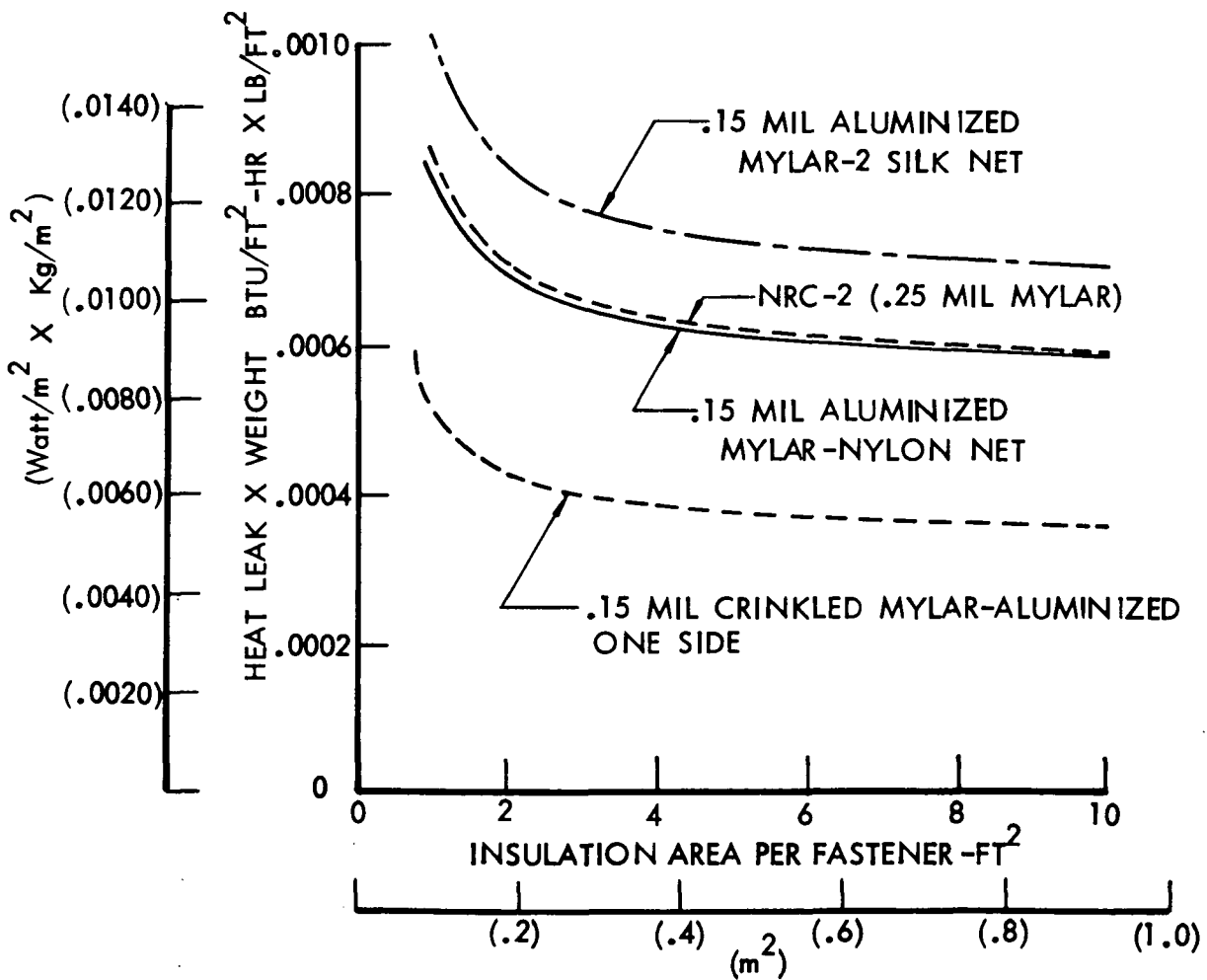
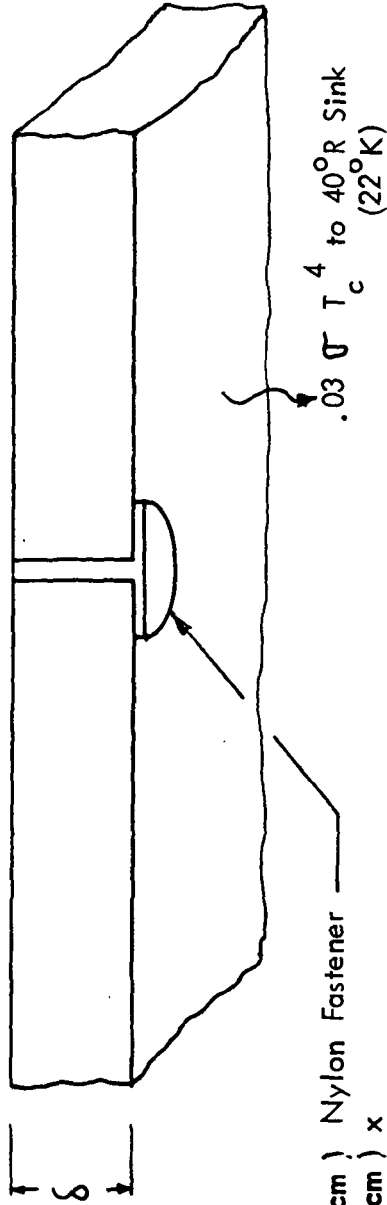


Figure 1.1-84: EFFECT OF FASTENERS ON INSULATION MATERIAL CHOICE - LARGE FASTENERS

Table 1.1-12:

EFFECT OF INSULATION ON FASTENER HEAT LEAK - INTERNAL INSULATION, TOP DECK, SMALL FASTENERS

$T_w = 500^{\circ}\text{R}$  Top Deck Structure  
 $(277^{\circ}\text{K})$



.04 in. Dia. (.102 cm) Nylon Fastener  
 .50 in. Dia. (1.27 cm) x  
 .01 in. (.025 cm) Thick Head ( $\epsilon = .03$ )

INSULATION	$\delta$ (inches) (CM)	Q Fastener (BTU/Hr) (WATT)	$\Delta Q$ Insulation (BTU/Hr) (WATT)	$\Sigma Q$ (BTU/Hr) (WATT)
Aluminized Mylar - Nylon Net	0.50 (1.27)	.00022 (.000064)	.00513 (.0015)	.00535 (.0016)
NRC-2	1.44 (3.66)	.00014 (.000041)	.00219 (.00064)	.00233 (.00068)
Aluminized Mylar - 2 Silk Net	1.85 (4.7)	.00012 (.000035)	.00115 (.00034)	.00127 (.00037)

.04 INCH DIA (0.102 cm ) FASTENERS  
 $T_W = 500^{\circ}R (277^{\circ}K)$   
 INSULATION INSIDE STRUCTURE

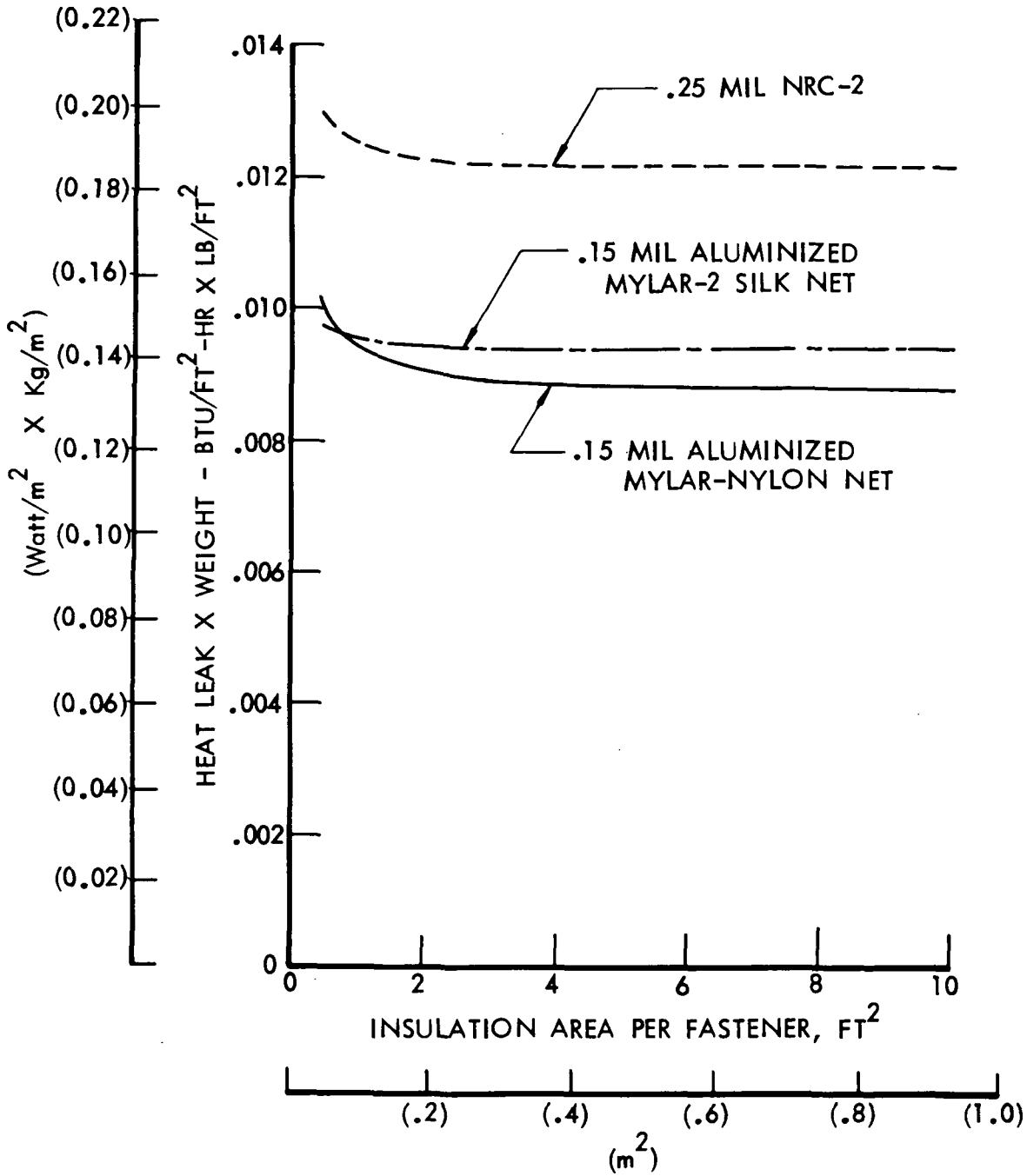


Figure 1.1-85: EFFECT OF FASTENERS ON INSULATION MATERIAL CHOICE - SMALL FASTENERS

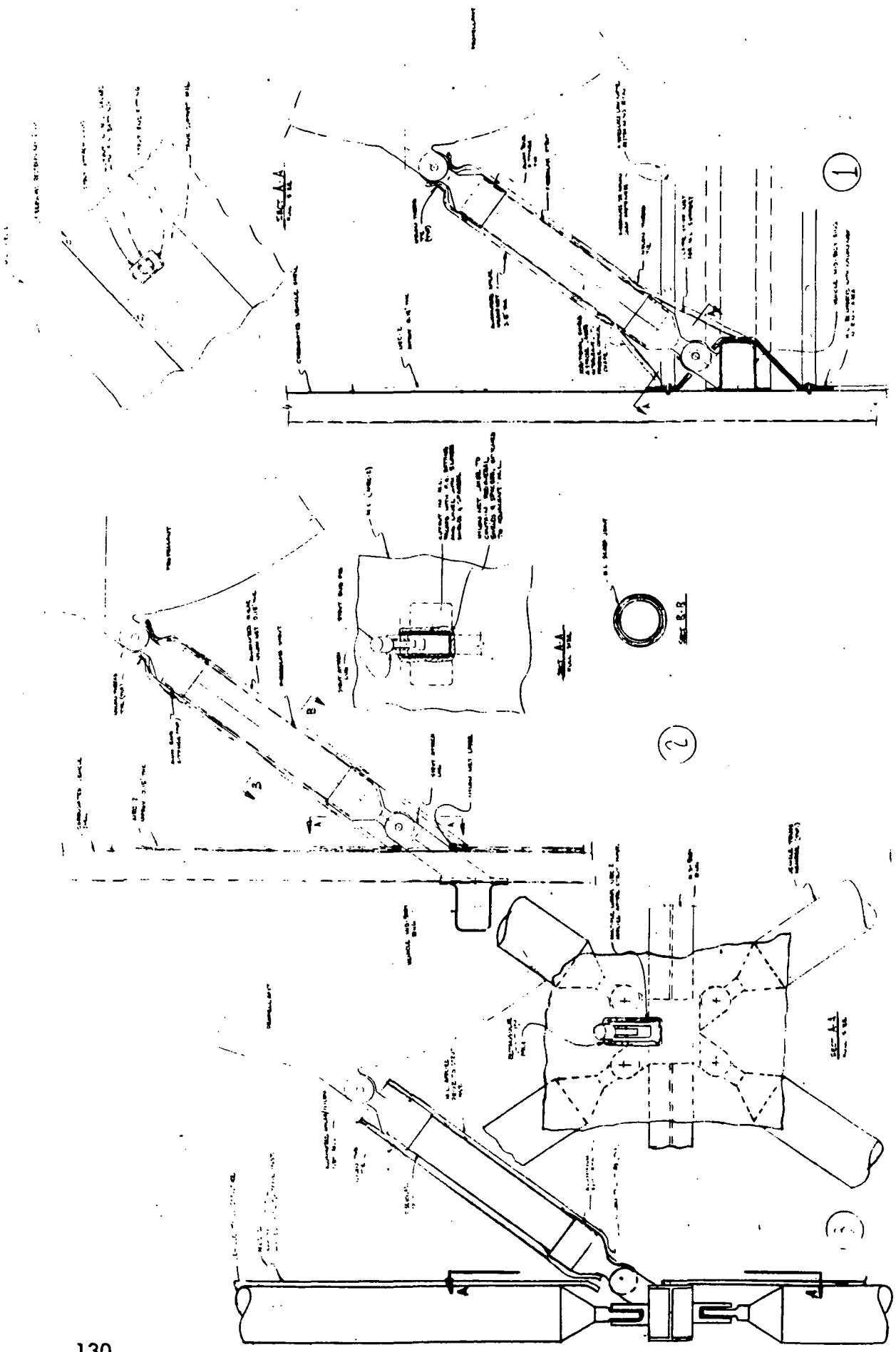


Figure 1.1-86: TANK SUPPORT -MULTILAYER PENETRATION CONCEPTS

selected for analysis to determine the effect on the sidewall MLI. The design was idealized and modelled as shown in Figure 1.1-87, which also shows temperature results for one of the cases analyzed. The idealization consisted primarily of assuming the support perpendicular to the sidewall so that the penetration was axisymmetric. To avoid the very complex radiation interchange problem in the cavity, the view factors were approximated assuming no local radiation interaction between the support and sidewall MLI, and providing radiation from the support MLI to a large area MLI node representing the majority of the cavity wall, and to the tank. Internal radiation within the support was not included because this was not considered important to the MLI performance.

The heat leak results of the analysis are shown in Table 1.1-13. There was little difference in total heat leak between the two cases with different sidewall MLI (Case I and II), even though the relative difference in sidewall heat leak increase was large. A third case was run to evaluate the influence of another support insulation thickness on sidewall MLI. Comparison of Cases I and III showed that the effect on sidewall MLI was insignificant. However, the reduction of total heat flow in Case III was significant, and suggested the need to optimize the support insulation for the final designs.

#### 1.1.5 Combined Systems Evaluation

The objective of the conceptual design and screening phases was to conduct an evaluation which would identify promising combinations of tank/structure/thermal protection for further evaluation in the preliminary design studies. Obvious optimum arrangements of these combinations did not result from the studies, however, several important details were identified. The decisions which were made as a result of the studies are discussed in the following sections.

Two insulation systems were chosen for the preliminary design studies. These were aluminized mylar/nylon net and NRC-2. Silk and dacron net were also retained as alternate spacer materials in the event that these might offer significant advantages. Sliced foam was dropped from the study because of suspected high outgassing and deterioration. All tank supports and fluid lines were to be insulated with MLI, and a minimum number and diameter of nylon retainers were to be used in MLI blankets.

The types of vehicle construction were also narrowed. Shell structures were either honeycomb sandwich or ring stiffened corrugations. The materials for both shell and truss construction were limited to aluminum, fiberglass and carbon composite. It was decided that the Centaur adaptor would be a truss structure of advanced composite (carbon/epoxy) to minimize inert weight.

Two additional ground rules were established for further design studies. These were: (1) FLOX-CH<sub>4</sub> vehicles would have no insulation or compartment separation devices between fuel and oxidizer and (2) there was no weight penalty



Table 1.1-13: TANK SUPPORT - INSULATION INTERACTION ANALYSIS

200°R (111°K) Sidewall Structure  
 40°R (22°K) Tank

Heat Leak Description	Heat Leak Amount - BTU/Hr (WATT)		
	Case I .15" Alum. Mylar-Nylon Net on Sidewall and Support	Case II .31" NRC-2 on Sidewall, .15" Alum. Mylar-Nylon Net on Support	Case III .15" Alum. Mylar-Nylon Net on Sidewall .075" Alum. Mylar-Nylon Net on Support
Increase in Heat Leak through sidewall insulation to tank	.00283 (.000826)	.00404 (.00118)	.00282 (.00083)
Radiation from surface of support insulation to tank	.00210 (.000615)	.00207 (.00061)	.00210 (.000615)
Radiation from cold end of Support insulation to tank	.00053 (.00016)	.00053 (.00016)	.00006 (.0000176)
Conduction from support insulation to cold support end fitting	.00417 (.00122)	.00417 (.00122)	.00226 (.00066)
Conduction through support	.02565 (.007515)	.02565 (.007515)	.02539 (.00744)
TOTAL HEAT LEAK	.03528 (.01034)	.03646 (.01068)	.03263 (.00956)

chargeable to the vehicle for extending ground hold capability. This approach presumed on site refrigeration and/or disposal of toxic propellants.

Selection of the ten design configurations for further investigation in the preliminary evaluation phase of Task I was made based on a review of vehicle structure and thermal system weights. The concept rating system described in Section 1.1.1 formed the basis for selections. Figures 1.1-88 and 1.1-89 show weight estimates for the five  $\text{LH}_2/\text{LF}_2$  and five FLOX/ $\text{CH}_4$  vehicles. The weights of tanks, insulation, helium, helium bottle and propellant vapor have been combined with structure weights for the comparison. Some vehicles utilized truss structure and others continuous shell structures. The weights of vehicle truss structure were factored to an equivalent shell structure to allow the comparison.

The final selections are shown in Figures 1.1-90, 1.1-91 and 1.1-92. The complexity ratings from Table 1.1-4 have been repeated here as an aid to developing the overall concept rating. For the  $\text{LH}_2/\text{LF}_2$  vehicles, 1-14 was still obviously the best choice. The specific tank arrangement, i.e.,  $\text{LF}_2$  forward or aft was the subject of a separate study, described in the next section. Vehicle 1-3 had nearly the same weight as 1-14, but was considered more complex than Vehicle 1-7, therefore it was rated third after Vehicle 1-7. Vehicle 1-20 was both heaviest and most complex and was dropped from the study. Vehicle 1-1 was nearly identical to 1-2 except the latter had one less spherical tank. It was assumed the weights were comparable and thus the less complex, four sphere configuration of 1-2 could be substituted. Two arrangements of this vehicle were retained because there were significant configuration differences.

For the FLOX/ $\text{CH}_4$ , Vehicles 2-18 and 2-19 were the obvious best choices. Vehicle 2-14 was still a candidate although somewhat heavier. Vehicle 2-2 was substituted for 2-1 for the same reasons as described for like vehicles with  $\text{LH}_2/\text{LF}_2$  propellants. Vehicle 2-3 was chosen instead of 2-7 because of its weight reduction potential and the favorable rating of its counterpart, 1-3.

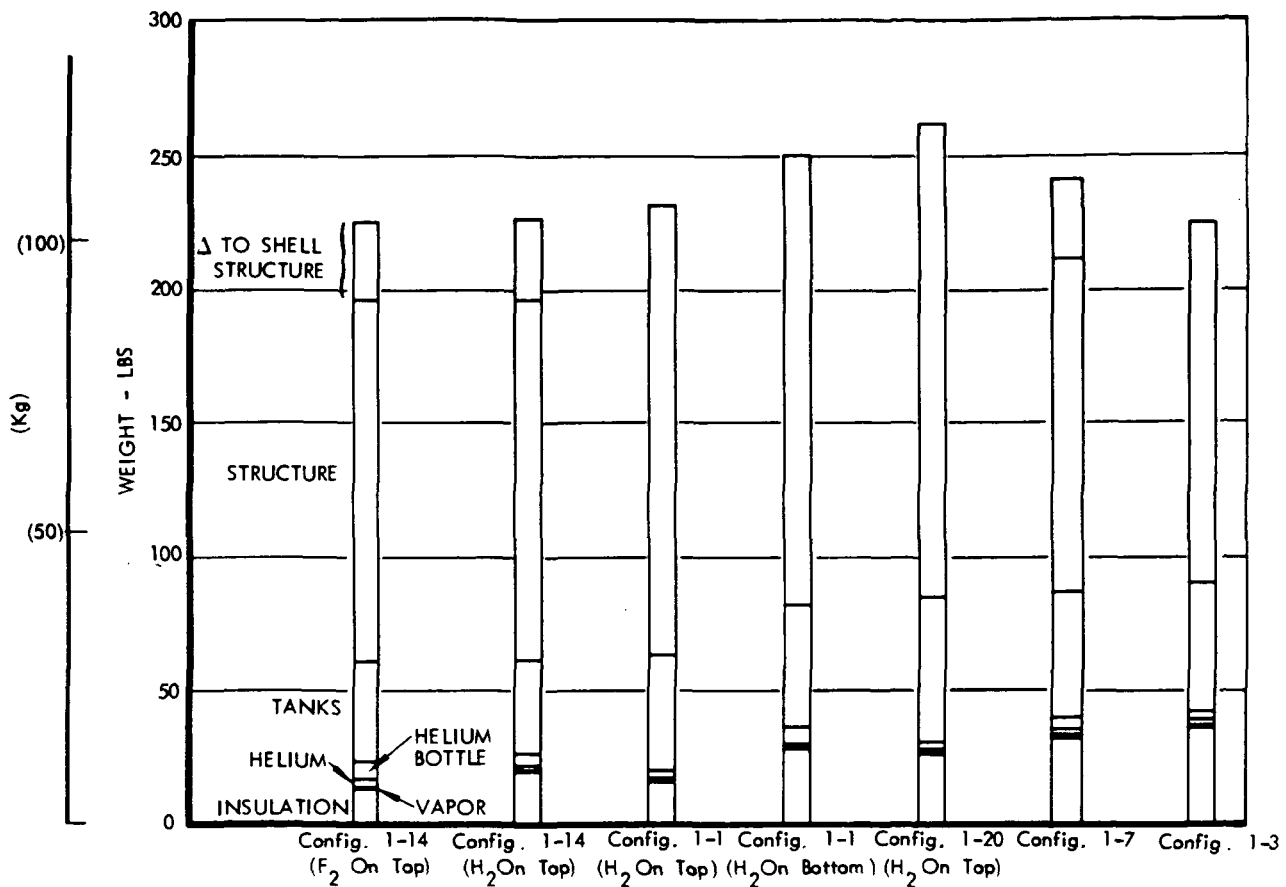


Figure 1.1-88: WEIGHT COMPARISON - LF<sub>2</sub>/LH<sub>2</sub> VEHICLES

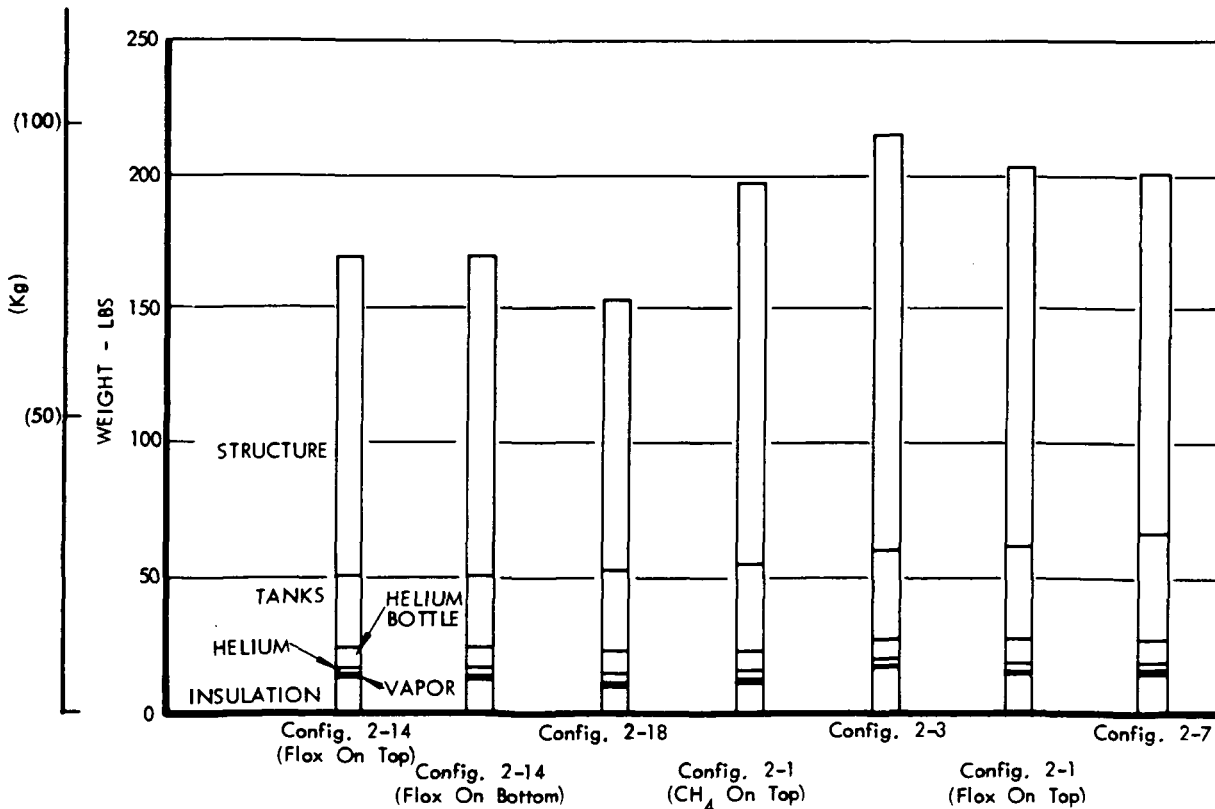


Figure 1.1-89: WEIGHT COMPARISON - FLOX/CH<sub>4</sub> VEHICLES

	CONFIGURATION				
	1-14	1-3	1-2A	1-2B	1-7
TANK ARRANGEMENT	2 Obl. Sph. F <sub>2</sub> on Top	2 Sph. F <sub>2</sub> 2 Sph. H <sub>2</sub>	1 Sph. H <sub>2</sub> on Top 3 Sph. F <sub>2</sub>	3 Sph. F <sub>2</sub> on Top 1 Sph. H <sub>2</sub>	1 Cyl. F <sub>2</sub> 2 Cyl. H <sub>2</sub>
STRUCTURE + THERMAL SYSTEM WEIGHT - LBS (Kg)	225 (102.2)	226 (102.6)	237 (From 1-1) (105.33)	250 (From 1-1) (113.5)	242 (109.9)
COMPLEXITY RATING	1	5	7	7	2
OVERALL CONCEPT RATING	1	3	4	4	2
OTHER FACTORS	Highest Overall Rating Colder H <sub>2</sub> to AFT	Shortest Vehicle Height		Potential For Improved Pay - load Isolation	

Figure 1.1-90 : VEHICLE EVALUATION LH<sub>2</sub>/LF<sub>2</sub> PROPELLANTS

	CONFIGURATION				
	2-18	2-19	2-14	2-2	2-3
TANK ARRANGEMENT	Common Bulk'd Obl. Heads	Common Bulk'd Conical Lower Head	2 Obl. Sph. CH <sub>4</sub> on Top	1 Obl. Sph. Flox on Top 3 Sph. CH <sub>4</sub>	2 Sph. Flox 2 Sph. CH <sub>4</sub>
STRUCTURE + THERMAL SYSTEM WEIGHT - LBS (Kg)	153 (69.5)	153 (From 2-18) (69.5)	170 (77.2)	204 (From 2-1) (92.6)	216 (98.1)
COMPLEXITY RATING	1	2	(2)	3	6 (From 2-8)
OVERALL CONCEPT RATING	1	1	2	3	4
OTHER FACTORS	<ul style="list-style-type: none"> <li>• Most Compact</li> <li>• Least Common Blkh'd Problem</li> </ul>	<ul style="list-style-type: none"> <li>• Similar to 2-18</li> <li>• Potential Reduction Of Engine Support Weight</li> </ul>	<ul style="list-style-type: none"> <li>• Flox On Bottom To Reduce Loads</li> </ul>	<ul style="list-style-type: none"> <li>• Potential For Improved Pay - load Isolation</li> </ul>	<ul style="list-style-type: none"> <li>• Shortest Stage Height</li> <li>• Struct. Weight Can Be Reduced Based On 1-3</li> <li>• Provides Different Shape</li> </ul>

Figure 1.1-91: VEHICLE EVALUATION FLOX/METHANE PROPELLANTS

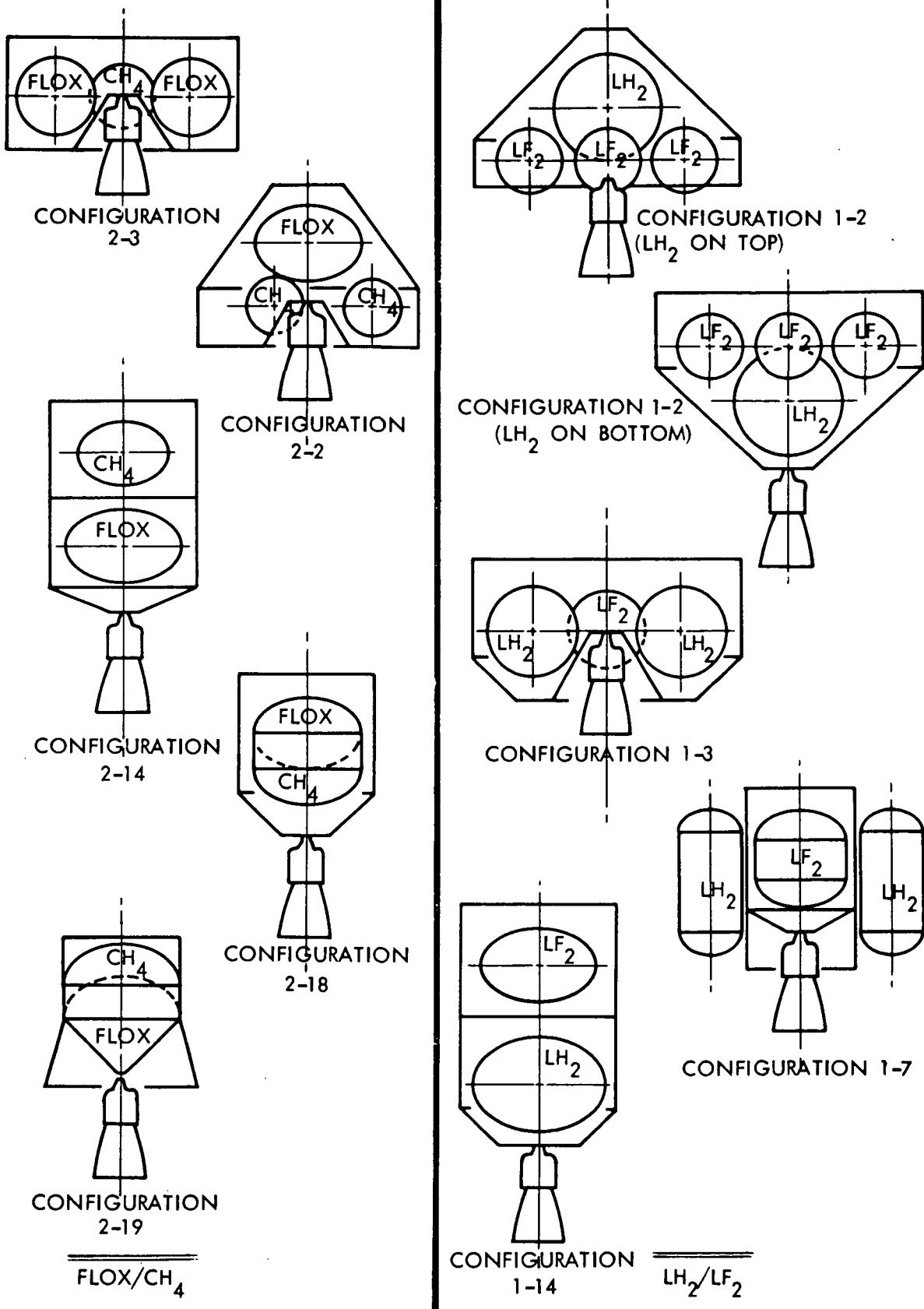


Figure 1.1-92: SCREENING AND CONCEPTUAL DESIGN INVESTIGATION - VEHICLE SELECTIONS

## 1.2 Preliminary Evaluation

This phase of the program involved design definition of the ten vehicle concepts selected in the preceding section. The evaluation included (1) vehicle structural analysis, (2) thermal analysis, (3) meteoroid protection analysis, (4) operational complexity analysis, and (5) weight analysis. The goal was to develop vehicle designs with maximum payload capability and minimum operational complexity.

### 1.2.1 Solar Panel Emittance Study

A study was conducted to determine the effect of solar panel lower surface emittance on the performance of the solar cells. It was desired to use a lower emittance in the vehicle design studies to reduce radiation to the vehicle sidewall.

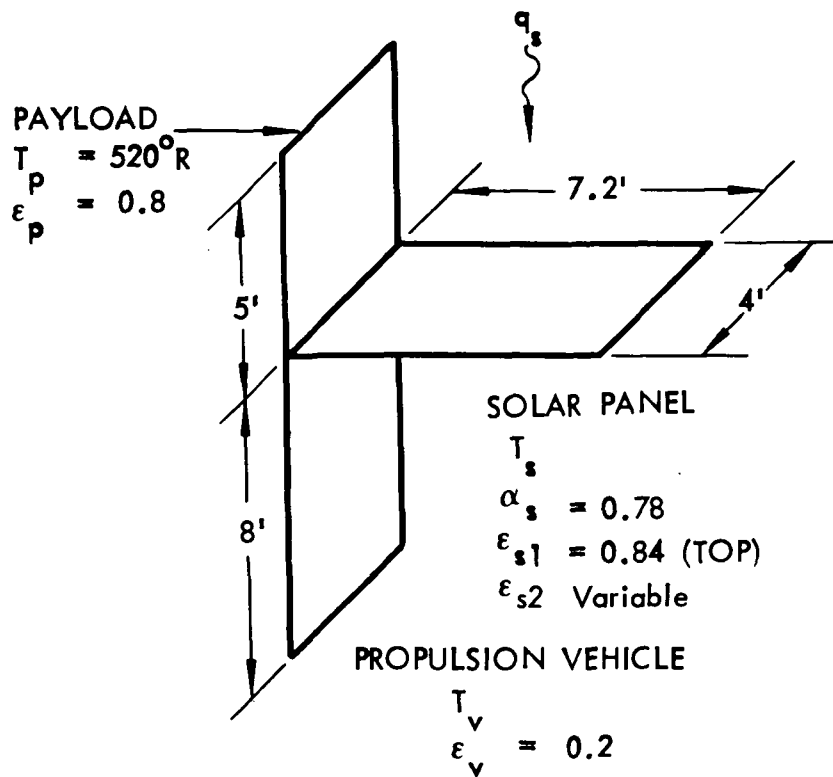
A simplified model of the payload, solar panel, and vehicle, as shown in Figure 1.2-1, was used in the analysis. This model considered only radiation from the sun and between adiabatic surfaces. Surface properties used and the heat balance equations are also shown in the figure. The resulting temperatures are shown in Figure 1.2-2, where the average temperatures were calculated using view factors based on the total areas shown in Figure 1.2-1, and the maximum temperatures based on view factors at the root of the solar panel. The maximum solar panel temperatures shown are not expected to cause damage to the solar cells.

The average panel temperatures are converted to solar cell output in Figure 1.2-3. Solar cell voltage and current at maximum power point versus temperature based on Reference 1.2-1 were used to obtain the power output per cell. Assuming a constant power requirement, the conditions near Mars governed the number of solar cells required. Assuming the solar panel area was directly proportional to the number of solar cells required, the required panel area varied with lower surface emittance as shown at the top of Figure 1.2-3.

Based on these results it was decided to change from the 48 x 86 in (1.2 x 2.2 m) solar panel with lower surface emittance of 1.0, to a panel 48 x 103 in (1.2 x 2.6 m) with a lower surface emittance of .05. From Figure 1.2-2 this would reduce the propulsion vehicle sidewall temperature by approximately 100°R (56°K). An emittance of less than .05 could be achieved with a layer of aluminized mylar. A conservative value was used because the propulsion vehicle sidewall temperature was very sensitive to change in emittance in this range, as shown in Figure 1.2-2. The solar panel temperature used in the propulsion vehicle thermal analysis had to be increased also, and 620°R (345°K) was chosen as an average temperature for the total mission.

### 1.2.2 Selection of Vehicle 1-14 Tank Arrangement

An additional study was required to select the final version of Vehicle 1-14. The purpose of the study was to determine whether the location of the LF<sub>2</sub> tank



$$(1) \quad \alpha_s A_s q_s + A_s \zeta_{sp} \sigma (T_p^4 - T_s^4) - \epsilon_{s1} A_s (1 - F_{sp}) \sigma T_s^4 + A_s \zeta_{sv} \sigma (T_v^4 - T_s^4) - \epsilon_{s2} A_s (1 - F_{sv}) \sigma T_s^4 = 0$$

$$(2) \quad A_s \zeta_{sv} \sigma (T_v^4 - T_s^4) + A_v (1 - F_{vs}) \sigma T_v^4 = 0$$

$$\text{FROM (2)} \quad T_v^4 = \frac{T_s^4}{1 + \frac{A_v (1 - F_{vs})}{A_s \zeta_{sv}}} = \frac{T_s^4}{1 + \frac{(A_v/A_s - F_{sv})}{\zeta_{sv}}}$$

$$\text{FROM (1)} \quad T_s^4 = \frac{\alpha_s q_s / \sigma + \zeta_{sp} T_p^4}{\zeta_{sp} + \epsilon_{s1} (1 - F_{sp}) + \zeta_{sv} \left[ 1 - \frac{1}{1 + \frac{(A_v/A_s - F_{sv})}{\zeta_{sv}}} \right] + \epsilon_{s2} (1 - F_{sv})}$$

WHERE

$$\zeta_{12} \approx \epsilon_1 \epsilon_2 F_{12}$$

$$\left. \begin{aligned} q_s &= 443 \text{ NEAR EARTH} \\ &= 155 \text{ NEAR MARS} \end{aligned} \right\} \text{BTU/FT}^2 \text{-HR}$$

FIGURE 1.2-1 - ANALYTICAL MODEL FOR SOLAR PANEL TEMPERATURE ANALYSIS

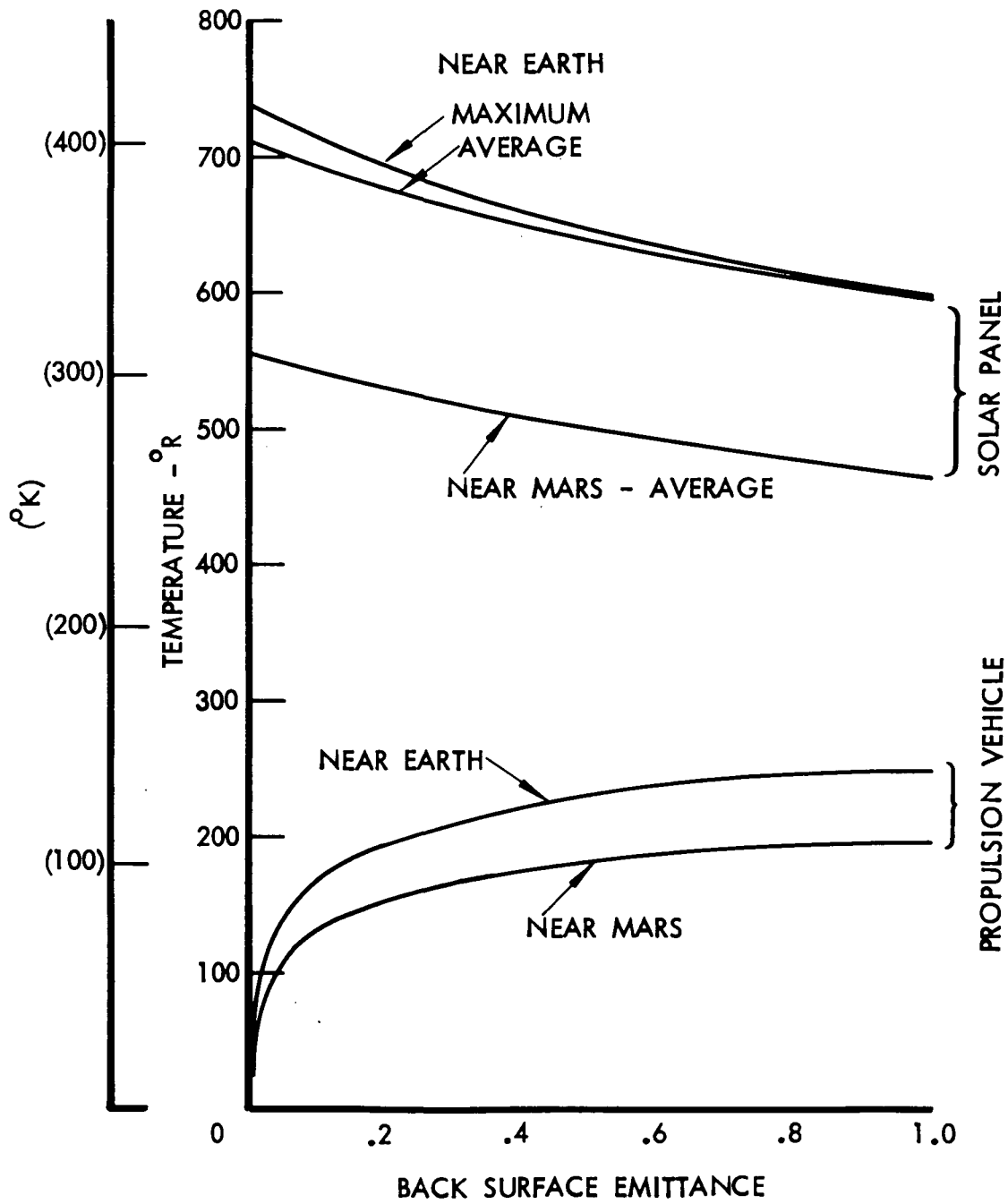


FIGURE 1.2-2 EFFECT OF SOLAR PANEL LOWER SURFACE EMITTANCE ON TEMPERATURES

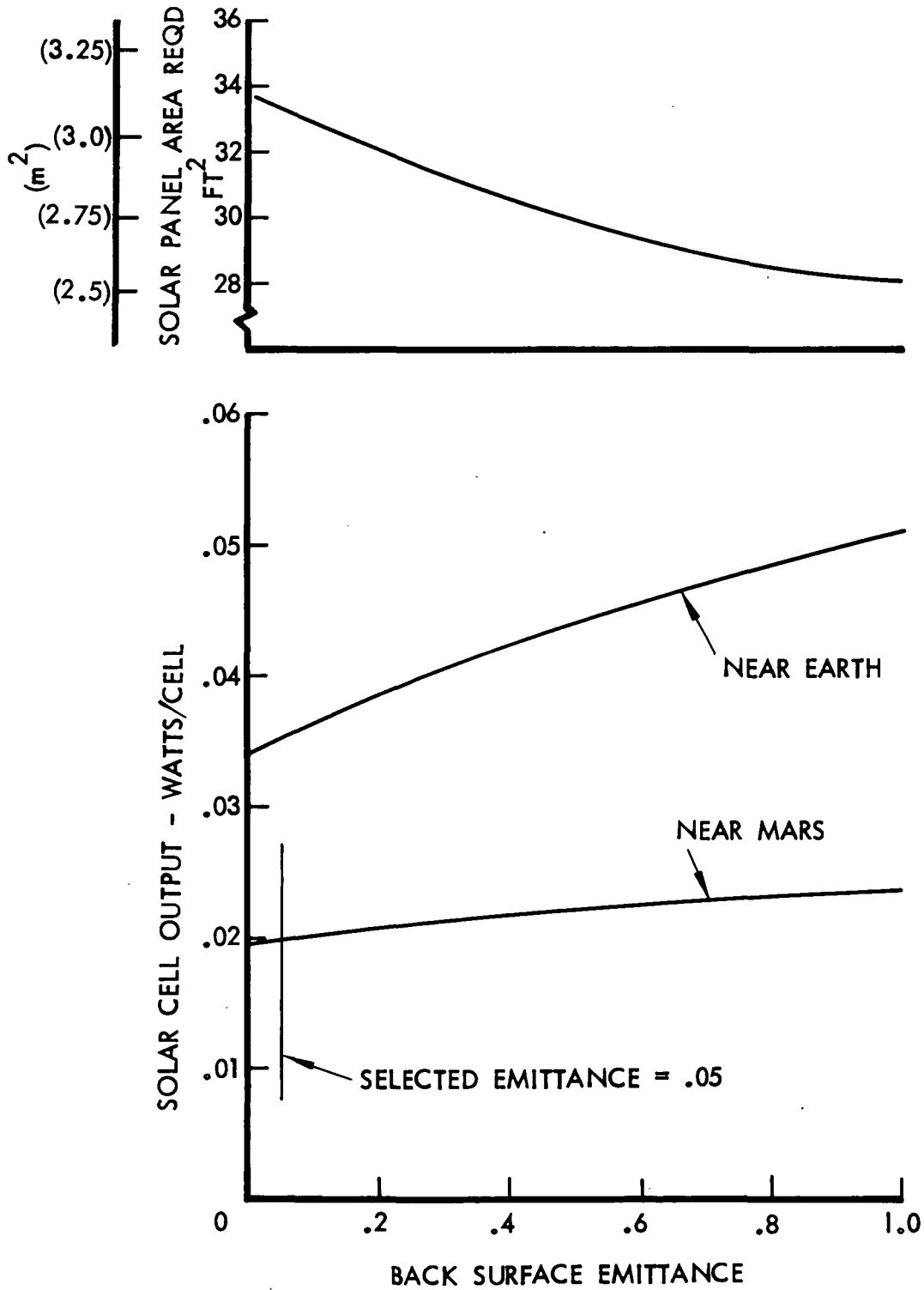


FIGURE 1.2-3 - EFFECT OF SOLAR PANEL LOWER SURFACE EMITTANCE ON SOLAR CELL OUTPUT AND REQUIRED PANEL SIZE

forward or aft provided the least overall weight. The data from Figure 1.1-26 showed a slight weight advantage for LF<sub>2</sub> forward, however, the effect on vehicle structure weight had not been evaluated.

The study described here was directed towards determining vehicle and adaptor weight differences with the LF<sub>2</sub> tank in the forward and aft positions. Continuous shell structures and truss structures were evaluated. The materials and construction methods were:

#### Shell Structures

Aluminum, fiberglass and carbon composite honeycomb sandwich (aluminum core with aluminum and carbon face skins, HRP core with fiberglass face skins).

Ring stiffened corrugations of aluminum, fiberglass and carbon composite. (Aluminum rings)

#### Truss Structures

Tubular struts of aluminum, fiberglass and carbon composite.

Two positions of the payload were evaluated in this study also. In one, the payload c.g. was 20 in (50.8 cm) above the vehicle top deck, and in the other, payload was 51 in (129.5 cm) above the top deck. The weight effects due to raising the payload were of importance because the radiant heat exchange between payload and tanks could be reduced using this approach.

Two programs were utilized to obtain minimum weight designs. One was the computer aided random search method used for the Vehicle Structure Evaluation discussed in Section 1.1.3. A minimum weight design would be selected from a large number of randomly generated designs which satisfied all pertinent failure mode constraints for each of the two loading conditions. The other program was the random search method used in the TATE (Tank Arrangement Thermal Efficiency) evaluation discussed in Section 1.1.2. This program randomly selected insulation thicknesses and calculated heat flow to the propellants, tank pressure rise, tank weight and size, insulation weight, helium and helium tank weight and residual propellant vapor weight. The program was modified to add the conductance of tank supports and fluid lines and to account for the higher ascent heating rates caused by residual gasses within the multilayer.

The study vehicles are shown in Figure 1.2-4. A distance of 16 in (40.6 cm) between payload base and c.g. was assumed. The figure shows estimated component weights used in determining shell and truss member loads. The loads, acceleration load factors and factors of safety were obtained as described in Section 1.1.3. The weight of tanks, ground hold insulation, feed system

plumbing and valves was applied to the vehicle body at the point of tank support attachment, thus the upper vehicle body supported only the payload, meteoroid protection and insulation.

Figure 1.2-5 shows the thermal environment used in the TATE program to obtain insulation and propellant system weights. Significant reductions in external surface temperatures were apparent when the payload was elevated. The enlarged solar panels discussed in Section 1.2.1 were used in the study. It was assumed that each tank was supported with six fiberglass struts, located aft as shown in the figure. Feedline conductances were calculated based on the configurations presented in subsequent sections. The multilayer assumed for this study consisted of unperforated aluminized mylar/nylon net.

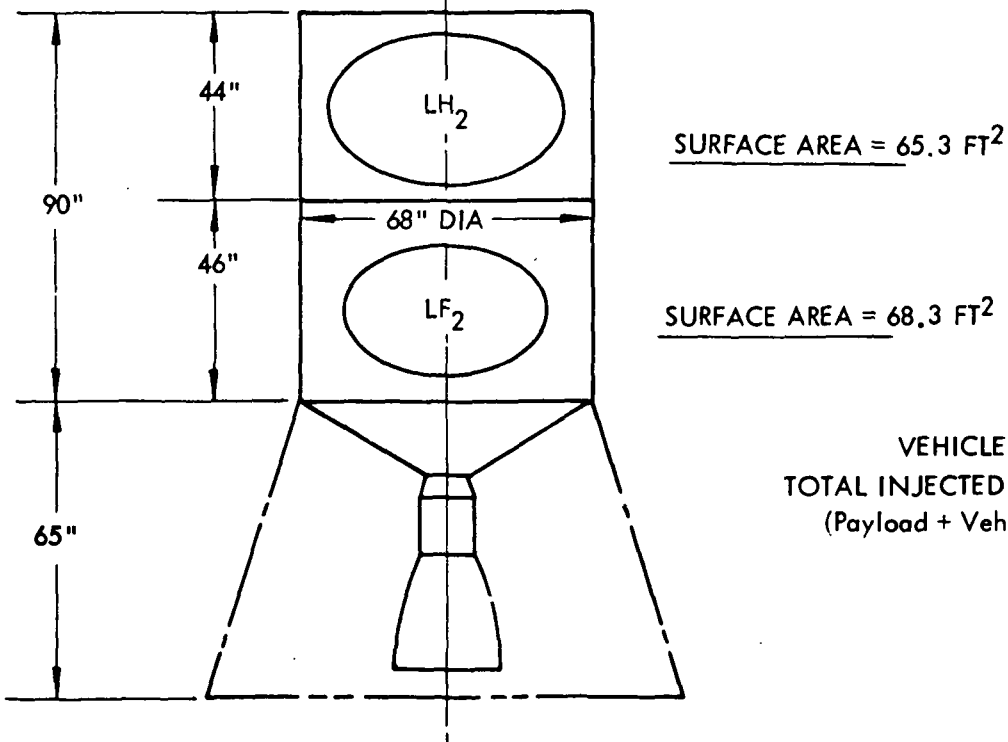
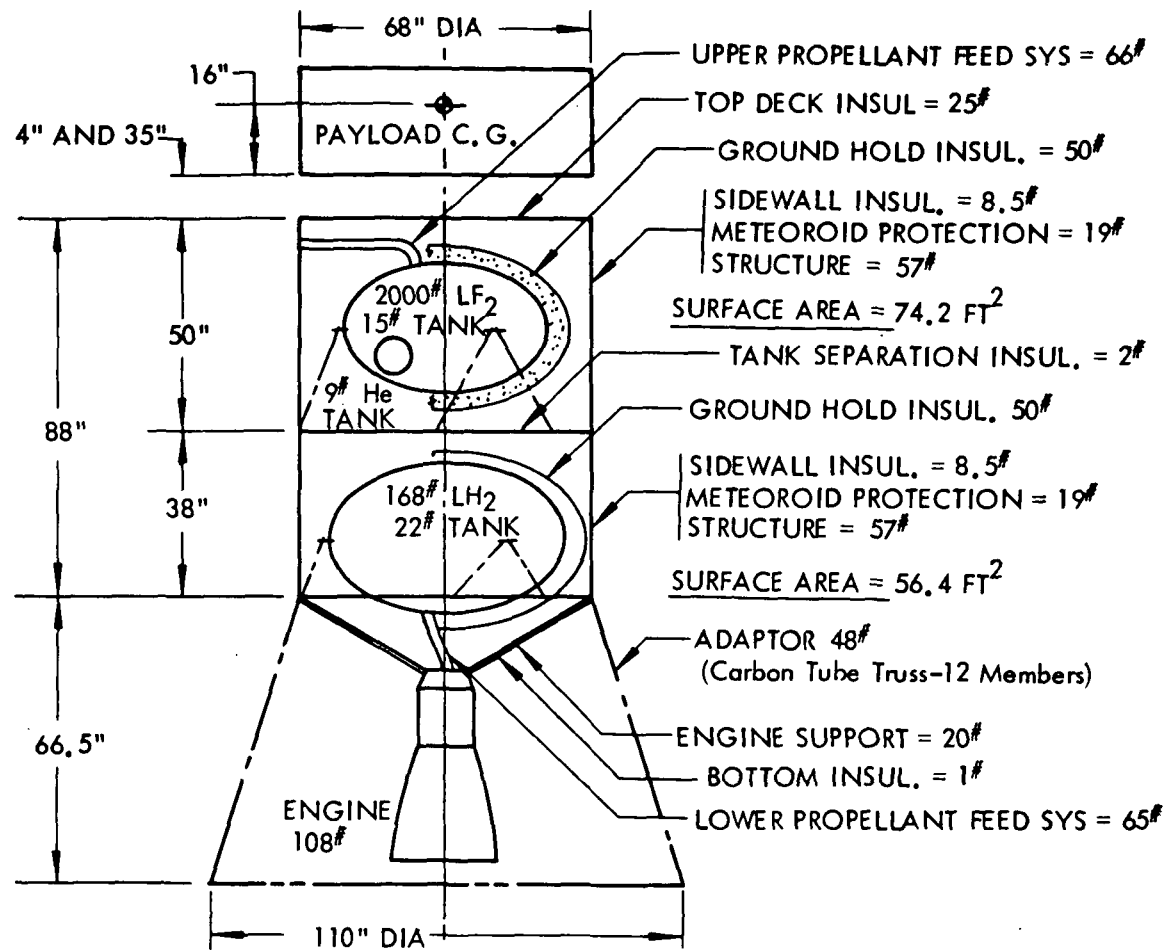
The TATE program randomly selected insulation thicknesses and calculated heat flow to the propellants, tank pressure and size, and the weights of insulation, tanks, propellant vapor, helium and helium tank. Only the five least weight cases were saved. The program also incorporated tank support and fluid line heat leak and the higher ascent heating rates caused by residual gases within the multilayer. The results of the study are presented in Table 1.2-1. The least weight approach occurred when the payload was elevated to 35 in (89.0 cm) and the  $LF_2$  was located forward. The forward location of  $LF_2$  resulted in minimum weights for both payload heights. In these cases, near minimum tank gages were obtained.

Ascent heating was the most predominant mode with the tank support heat leak being almost negligible. Locating the  $LH_2$  tank forward allowed heat to be rejected from the oxidizer feedlines, thus resulting in a net heat loss due to the plumbing.

The structural analysis considered cylindrical shells and truss structures for the vehicle body and truss structure for the vehicle adaptor.

The random search "Vehicle Structure Evaluation Program" discussed in Section 1.1.3 was used to generate designs which satisfied all pertinent failure mode constraints for the given loading conditions and select the minimum weight approaches. The output from this program (least weight cases) is shown in Tables 1.2-2, 1.2-3 and 1.2-4. The dimensions of each design are shown as well as the design limits. The case numbers 1, 2, 3 and 4 refer to specific vehicle configurations which are identified in Table 1.2-1. The continuous shell constructions, i.e., honeycomb sandwich and corrugations tended to optimize at minimum gages due to the low shell loading. For this reason truss structure was more efficient.

Weight totals were obtained using the surface areas of Figure 1.2-4 for shells, and assigning 12 truss members each to the upper body, lower body and adaptor. These totals were then adjusted to account for end attachments, fasteners and



VEHICLE 1-14  
 TOTAL INJECTED WEIGHT = 7500#  
 (Payload + Vehicle + Adaptor)

Figure 1.2-4: VEHICLE 1-14 CONFIGURATION OPTIONS.

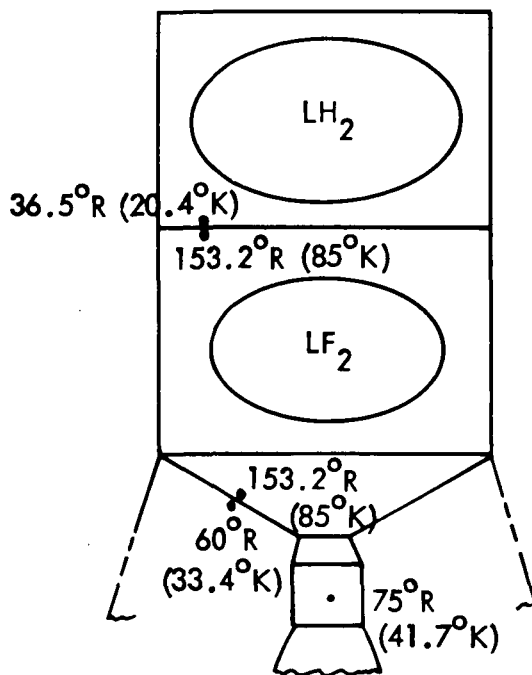
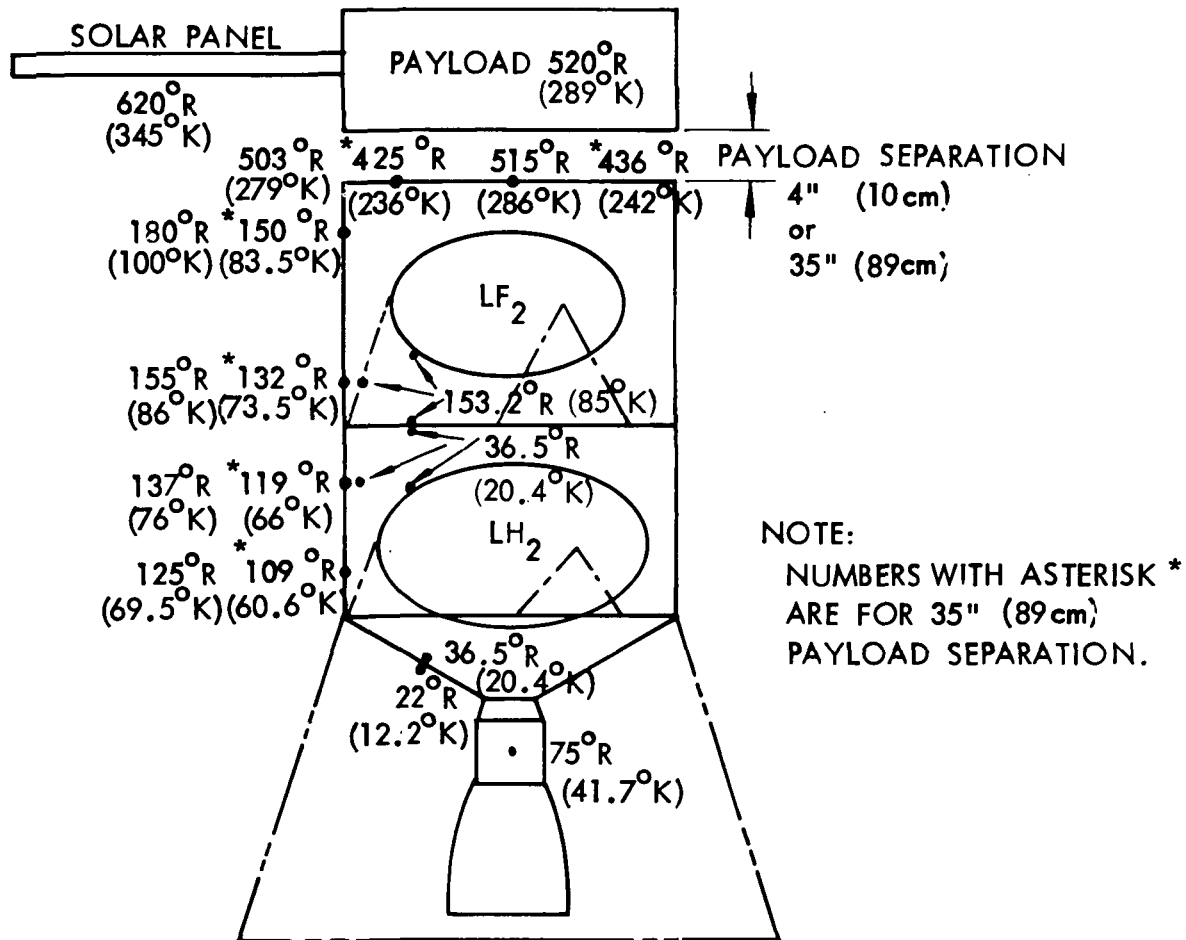


Figure 1.2-5: VEHICLE 1-14 THERMAL ENVIRONMENT

Table 1.2-1:

TANK ARRANGEMENT THERMAL EFFICIENCY STUDY RESULTS

ITEM	PAYLOAD BASE 35" (0.89 m) ABOVE TOP DECK		PAYLOAD BASE 4"(0.102 m) ABOVE TOP DECK	
	LH <sub>2</sub> FORWARD CASE 4	LF <sub>2</sub> FORWARD CASE 3	LH <sub>2</sub> FORWARD CASE 2	LF <sub>2</sub> FORWARD CASE 1
Oxidizer Tank Dimensions – Inches (cm) (a = Major Diameter b = Minor Diameter)	a = 48.2 (122.43) b = 34.1 (86.36)	a = 48.2 (122.43) b = 34.1 (86.36)	a = 48.2 (122.43) b = 34.1 (86.36)	a = 48.2 (122.43) b = 34.1 (86.36)
Fuel Tank Dimensions – Inches (cm)	a = 59.3 (150.62) b = 41.9 (106.43)	a = 58.6 (148.84) b = 41.4 (105.16)	a = 59.5 (151.13) b = 42.1 (106.93)	a = 58.6 (148.84) b = 41.4 (105.16)
Oxidizer Tank Gage – Inches (cm)	0.0191 (0.049) 0.0250 Min. Ga. (0.064)	0.0239 (0.0607) 0.0250 Min. Ga. (0.064)	0.0190 (0.0483) 0.0250 Min. Ga. (0.064)	0.0250 (0.064)
Fuel Tank Gage – Inches (cm)	0.0336 (0.085)	0.026 (0.066)	0.0361 (0.0917)	0.0262 (0.0665)
Insulation Heat Leak – Coast Phase – BTU* (Joule)	3464 (3,651,065)	7212 (7,601,448)	6202 (6,536,908)	10948 (11,539,192)
Insulation Heat Leak – Ascent Phase – BTU* (Joule)	24667 (25,999,018)	19945 (21,022,030)	23653 (24,930,262)	16651 (17,550,154)
Tank Support Heat Leak – BTU (Joule)*	-58 (-61,132)	-13 (-13,720)	-5 (-5,270)	53 (55,862)
Plumbing Heat Leak – BTU (Joule)*	-1432 (-1,509,328)	887 (934,898)	-823 (-867,442)	1602 (1,688,508)
Insulation Weight – Lbs (Kg)	27.94 (12.68)	22.41 (10.17)	31.27 (14.20)	25.93 (11.77)
Fuel Vapor – Lbs (Kg)	0.69 (0.313)	0.50 (0.227)	0.75 (0.340)	0.50 (0.227)
Oxidizer Vapor – Lbs (Kg)	1.22 (0.554)	1.18 (0.536)	1.22 (0.554)	1.26 (0.572)
Helium Gas – Lbs (Kg)	1.90 (0.863)	2.45 (1.112)	1.96 (0.889)	2.56 (1.162)
Helium Tank – Lbs (Kg)	5.20 (2.36)	6.72 (3.05)	5.36 (2.43)	7.01 (3.18)
Fuel Tank – Lbs (Kg)	30.69 (13.93)	23.17 (10.52)	33.15 (15.05)	23.33 (10.59)
Oxidizer Tank – Lbs (Kg)	15.07 (6.84)	15.07 (6.84)	15.07 (6.84)	15.07 (6.84)
Total Weight – Lbs (Kg)	82.71 (37.55)	71.50 (32.46)	88.78 (40.31)	75.71 (34.37)

\* FUEL & OXIDIZER COMBINED

Table 1.2-2: RING STIFFENED CORRUGATED SHELL DATA

MATERIAL	CASE	LOCATION	SHELL HEIGHT (in.)	ULT. LOAD $N_x$ (lb/in.)	CORRUGATIONS										RINGS										WEIGHT (lb/ft <sup>2</sup> )				
					DEPTH (in.)		SKIN THICKNESS (in.)		WIDTH (in.)		ANGLE (deg)		NO.	SPAC-ING (in.)	THICK-NESS (in.)	RING HEIGHT (in.)		REINFORCEMENT THICKNESS (in.)		WIDTH (in.)									
					MAX.	MIN.	DES.	MAX.	MIN.	DES.	MAX.	MIN.				DES.	MAX.	MIN.	DES.		MAX.	MIN.	DES.						
ALUMINUM	1	UPPER BODY	50	293	3.00	0.500	0.683	0.200	0.020	0.020	3.00	0.500	1.01	90	45	47	1	25	0.03	5.00	1.00	1.01	0.250	0	0.009	1/4 H	0.392		
		LOWER BODY	38	523			0.648		0.020			0.880				62	1	19				1.17				0.017		0.469	
		UPPER BODY	44	275			1.22		0.024			1.46				53	0											0.426	
		LOWER BODY	46	421			0.801		0.020			0.944				52	1	23					1.05				0.038		0.432
		UPPER BODY	50	370			0.856		0.021			0.860				49	1	25					1.10				0.021		0.437
		LOWER BODY	38	606			0.696		0.021			0.833				61	1	19					1.03				0.045		0.475
		UPPER BODY	44	351			0.623		0.021			0.876				58	1	22					1.06				0.009		0.440
		LOWER BODY	46	498			0.639		0.020			0.814				49	2	15.3					1.09				0.011		0.443
CARBON/EPOXY	1	UPPER BODY	50	293			1.31		0.022		1.43				68	0												0.250	
		LOWER BODY	38	523			1.29		0.029		1.46				54	0												0.289	
		UPPER BODY	44	275			1.23		0.021		1.34				61	0												0.225	
		LOWER BODY	46	421			0.704		0.020		0.921				55	1	23						1.04				0.012		0.260
		UPPER BODY	50	370			1.42		0.027		1.63				55	0												0.276	
		LOWER BODY	38	606			1.31		0.031		1.52				52	0												0.310	
		UPPER BODY	44	351			1.27		0.026		1.26				65	0												0.255	
		LOWER BODY	46	498			1.45		0.031		1.68				54	0												0.309	
FIBERGLASS	1	UPPER BODY	50	293			0.705		0.030		1.03				48	2	16.7					1.00				0.024		0.412	
		LOWER BODY	38	523			0.580		0.026		0.568				55	3	9.5						1.11				0.002		0.469
		UPPER BODY	44	275			0.696		0.025		0.818				54	2	14.7						1.07				0.025		0.394
		LOWER BODY	46	421			0.631		0.026		0.629				52	3	11.5						1.02				0.072		0.456
		UPPER BODY	50	370			0.634		0.025		0.777				54	3	12.5						1.17				0.069		0.447
		LOWER BODY	38	606			0.621		0.028		0.531				54	3	9.5						1.22				0.033		0.529
		UPPER BODY	44	351			0.613		0.026		0.824				49	3	11.0						1.01				0.083		0.448
		LOWER BODY	46	498			0.647		0.020		0.500				76	3	11.5						1.00				0.046		0.481

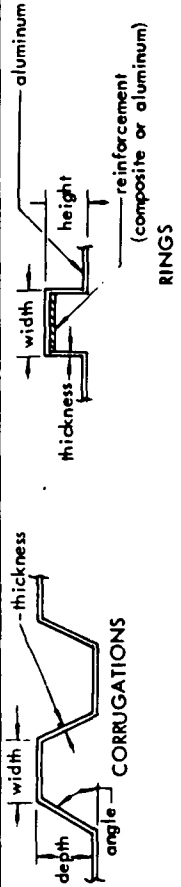


Table 1.2-2: RING STIFFENED CORRUGATED SHELL DATA

MATERIAL	CASE	LOCATION	SHELL HEIGHT (cm)	ULT LOAD N <sub>x</sub> (N/m)	CORRUGATIONS												RINGS								WEIGHT (Kg/m <sup>2</sup> )								
					DEPTH (cm)			SKIN THICKNESS (cm)			WIDTH (cm)			ANGLE (rad)			NO.	SPAC. ING (cm)	THICKNESS (cm)	RING HEIGHT (cm)			REINFORCEMENT THICKNESS (cm)										
					MAX.	MIN.	DES.	MAX.	MIN.	DES.	MAX.	MIN.	DES.	MAX.	MIN.	DES.				MAX.	MIN.	DES.	MAX.	MIN.		DES.							
ALUMINUM	1	UPPER BODY	127	5,128	7.62	1.27	1.74	0.508	0.051	0.051	7.62	1.27	2.57	1.58	0.79	0.82	1	64	0.076	12.7	2.54	2.56	0.635	0	0.023	0.042	2.97	2.56	0.023	0.023	1.913		
		LOWER BODY	96.52	9,153	↑	↑	1.65	↑	↑	0.051	↑	2.24	↑	↑	1.09	1.09	1	48	↑	↑	↑	↑	↑	↑	↑	↑	↑	↑	↑	2.288			
	2	UPPER BODY	111.76	4,813			3.10			0.061		3.71			0.93	0.93	0														2.078		
		LOWER BODY	116.84	7,368			2.03			0.051		2.40			0.91	0.91	1	58														2.108	
	3	UPPER BODY	127	6,475			2.17			0.053		2.18			0.86	0.86	1	64														2.133	
		LOWER BODY	96.52	10,605			1.77			0.053		2.12			1.07	1.07	1	48														2.318	
	4	UPPER BODY	111.76	6,143			1.58			0.053		2.23			1.02	1.02	1	56														2.147	
		LOWER BODY	116.84	8,715			1.62			0.051		2.07			0.86	0.86	2	39														2.162	
CARBON/EPOXY	1	UPPER BODY	127	5,128			3.33		0.056		3.63			1.19	1.19	0															1.220		
		LOWER BODY	96.52	9,153			3.28		0.074		3.71			0.95	0.95	0																1.410	
	2	UPPER BODY	111.76	4,813			3.12		0.053		3.40			1.07	1.07	0																1.088	
		LOWER BODY	116.84	7,368			1.79		0.051		2.34			0.96	0.96	1	58																1.269
	3	UPPER BODY	127	6,475			3.61		0.069		4.14			0.96	0.96	0																	1.347
		LOWER BODY	96.52	10,605			3.33		0.088		3.86			0.91	0.91	0																	1.513
	4	UPPER BODY	111.76	6,143			3.23		0.066		3.20			1.14	1.14	0																	1.244
		LOWER BODY	116.84	8,715			3.68		0.088		4.27			0.95	0.95	0																	1.508
FIBERGLASS	1	UPPER BODY	127	5,128			1.79		0.076		2.62			0.84	0.84	2	43															2.011	
		LOWER BODY	96.52	9,153			1.47		0.066		1.44			0.96	0.96	3	24																2.288
	2	UPPER BODY	111.76	4,813			1.77		0.064		2.08			0.95	0.95	2	37																1.923
		LOWER BODY	116.84	7,368			1.60		0.066		1.60			0.91	0.91	3	29																2.225
	3	UPPER BODY	127	6,475			1.61		0.064		1.97			0.95	0.95	3	32																2.181
		LOWER BODY	96.52	10,605			1.58		0.071		1.35			0.95	0.95	3	24																2.582
	4	UPPER BODY	111.76	6,143			1.58		0.066		2.09			0.86	0.86	3	28																2.186
		LOWER BODY	116.84	8,715			1.64		0.058		7.62	1.27	1.60	1.58	0.79	1.33	3	29	0.076	12.7	2.54	2.56	0.635	0	1.17	2.11	2.56	2.56	0.061	0.061	2.347		

Table 1.2-3: HONEYCOMB SANDWICH DATA

CASE	LOCATION	SHELL HEIGHT (in.)	ULT LOAD N <sub>x</sub> (lb/in.)	CORE DENSITY (lb/ft <sup>3</sup> )*	CORE DEPTH (in.)		FACE SKIN THICKNESS (in.)		RIBBON THICKNESS (in.)		CELL SIZE (in.)		WEIGHT (lb/ft <sup>2</sup> )	
					MAX.	MIN.	DES.	MAX.	MIN.	DES.	MAX.	MIN.		DES.
1	UPPER BODY	50	293	1.59	0.500	0.250	0.100	0.020	0.020	0.005	0.001	0.250	0.343	0.607
	LOWER BODY	38	523	1.44	↑	0.258	↑	↑	↑	↑	↑	↑	0.368	0.602
	UPPER BODY	44	275	1.43		0.260							0.373	0.603
	LOWER BODY	46	421	1.51		0.252							0.369	0.603
2	UPPER BODY	50	370	1.48		0.251							0.363	0.602
	LOWER BODY	38	606	1.43		0.256							0.370	0.602
	UPPER BODY	44	351	1.55	↓	0.251	↓				↑		0.355	0.603
	LOWER BODY	46	498	1.74	0.500	0.252	0.100				0.001	0.250	0.306	0.607
3	UPPER BODY	50	293	4.31	1.00	0.252	0.050				0.003	0.200	0.371	0.393
	LOWER BODY	38	523	4.27	↑	0.253	↑				↑	↑	0.374	0.393
	UPPER BODY	44	275	4.50		0.250							0.370	0.396
	LOWER BODY	46	421	4.41		0.251							0.371	0.395
4	UPPER BODY	50	370	4.45		0.251							0.364	0.398
	LOWER BODY	38	606	4.75		0.251							0.352	0.404
	UPPER BODY	44	351	4.53		0.252							0.375	0.398
	LOWER BODY	46	498	4.32		0.252							0.372	0.393
1	UPPER BODY	50	293	2.85		0.253							0.373	0.432
	LOWER BODY	38	523	3.08		0.272							0.354	0.440
	UPPER BODY	44	275	2.90		0.251							0.373	0.431
	LOWER BODY	46	421	3.06		0.252			↓				0.369	0.436
3	UPPER BODY	50	370	2.94		0.256			0.021				0.370	0.434
	LOWER BODY	38	606	2.93		0.299			0.020				0.374	0.453
	UPPER BODY	44	351	2.91	↓	0.252	↓		0.020		↓	↓	0.374	0.432
	LOWER BODY	46	498	2.90	1.00	0.250	0.050	0.020	0.020	0.005	0.003	0.200	0.370	0.437

\*ALUM CORE WITH ALUM AND CARBON FACES  
HRP (F.G.) CORE WITH F.G. FACES

Table 1.2-3: HONEYCOMB SANDWICH DATA

CASE	LOCATION	SHELL HEIGHT (cm)	ULT LOAD $N_x$ (N/m)	CORE DENSITY (Kg/m <sup>3</sup> )*	CORE DEPTH (cm)			FACE SKIN THICKNESS (cm)			RIBBON THICKNESS (cm)			CELL SIZE (cm)			WEIGHT (Kg/m <sup>2</sup> )	
					MAX	MIN	DES	MAX	MIN	DES	MAX	MIN	DES	MAX	MIN	DES		
1	UPPER BODY	127	5,128	25.47	1.27	0.635	0.635	0.254	0.051	0.051	0.003	0.013	0.003	0.003	0.953	0.635	0.871	29.62
	LOWER BODY	96.52	9,153	23.07	↑	↑	↑	↑	↑	↑	↑	↑	↑	↑	↑	↑	0.935	29.38
	UPPER BODY	111.76	4,813	22.91													0.947	29.43
	LOWER BODY	116.84	7,368	24.19			0.640										0.937	29.43
2	UPPER BODY	127	6,475	23.71			0.638										0.922	29.38
	LOWER BODY	96.52	10,605	22.91			0.650										0.940	29.38
	UPPER BODY	111.76	6,143	24.83	↑		0.638	↓									0.902	29.43
	LOWER BODY	116.84	8,715	27.88	1.27		0.640	0.254			0.003	0.003	0.003	0.003		0.635	0.777	29.62
3	UPPER BODY	127	5,128	69.05	4.54		0.640	0.127								0.508	0.942	19.18
	LOWER BODY	96.52	9,153	68.41	↑		0.643	↑									0.950	19.18
	UPPER BODY	111.76	4,813	72.09			0.635										0.940	19.32
	LOWER BODY	116.84	7,368	70.65			0.638										0.942	19.28
4	UPPER BODY	127	6,475	71.29			0.638										0.925	19.42
	LOWER BODY	96.52	10,605	76.09			0.638										0.894	19.72
	UPPER BODY	111.76	6,143	72.57			0.640										0.953	19.42
	LOWER BODY	116.84	8,715	69.21			0.640										0.945	19.18
1	UPPER BODY	127	5,128	45.66			0.643										0.947	21.08
	LOWER BODY	96.52	9,153	49.34			0.691										0.899	21.47
	UPPER BODY	111.76	4,813	46.46			0.638										0.947	21.03
	LOWER BODY	116.84	7,368	49.02			0.640			↓							0.937	21.28
2	UPPER BODY	127	6,475	47.10			0.650			0.051							0.940	21.18
	LOWER BODY	96.52	10,605	46.94			0.760			0.052							0.950	22.11
	UPPER BODY	111.76	6,143	46.62	↑		0.640	↑		0.051							0.950	21.08
	LOWER BODY	116.84	8,715	46.46	4.54	0.635	0.688	0.127	0.051	0.051	0.008	0.013	0.008	0.008	0.953	0.508	0.940	21.33

\*ALUM CORE WITH ALUM AND CARBON FACES  
HRP (F.G.) CORE WITH F.G. FACES

Table 1.2-4: TRUSS STRUCTURE DATA

	CASE	LOCATION	MEMBER LENGTH (in.)	LOAD (lb)	TUBE THICKNESS (in.)			TUBE RADIUS (in.)			WT. PER MEMBER (lb)
					MAX.	MIN.	DESIGN	MAX.	MIN.	DESIGN	
ALUMINUM	1	UPPER BODY	55	6,575	0.200	0.020	0.020	4.00	0.500	1.44	1.012
		LOWER BODY	44	9,235	↑	↑	0.022	↑	↑	1.39	0.827
	2	UPPER BODY	48	6,035	↑	↑	0.020	↑	↑	1.29	0.787
		LOWER BODY	52	7,325	↑	↑	0.021	↑	↑	1.43	0.988
	3	UPPER BODY	55	6,610	↑	↑	0.021	↑	↑	1.43	1.046
		LOWER BODY	44	10,020	↑	↑	0.023	↑	↑	1.40	0.888
	4	UPPER BODY	48	6,225	↓	↓	0.021	↑	↑	1.31	0.815
		LOWER BODY	52	8,080	0.200	0.020	0.021	↑	↑	1.48	1.014
CARBON/EPOXY	1	UPPER BODY	55	6,575	0.100	0.028	0.028	↑	↑	1.20	0.674
		LOWER BODY	44	9,235	↑	↑	0.028	↑	↑	0.93	0.623
	2	UPPER BODY	48	6,035	↑	↑	0.028	↑	↑	1.07	0.525
		LOWER BODY	52	7,325	↑	↑	0.028	↑	↑	1.20	0.636
	3	UPPER BODY	55	6,610	↑	↑	0.028	↑	↑	1.20	0.676
		LOWER BODY	44	10,020	↑	↓	0.042	↑	↑	0.95	0.640
	4	UPPER BODY	48	6,225	↑	↓	0.028	↑	↑	1.08	0.529
		LOWER BODY	52	8,080	↑	0.028	0.028	↑	↑	1.24	0.658
FIBERGLASS	1	UPPER BODY	55	6,575	↑	0.018	0.036	↑	↑	1.45	1.195
		LOWER BODY	44	9,235	↑	↑	0.042	↑	↑	1.36	1.041
	2	UPPER BODY	48	6,035	↑	↑	0.036	↑	↑	1.30	0.935
		LOWER BODY	52	7,325	↑	↑	0.036	↑	↑	1.40	1.150
	3	UPPER BODY	55	6,610	↑	↑	0.036	↑	↑	1.46	1.202
		LOWER BODY	44	10,020	↑	↑	0.042	↑	↑	1.38	1.055
	4	UPPER BODY	48	6,225	↓	↓	0.036	↑	↑	1.31	0.939
		LOWER BODY	52	8,080	0.100	0.018	0.036	↑	↑	1.57	1.215
ALUMINUM	1	ADAPTOR	73	14,010	0.200	0.020	0.027	↑	↑	2.08	2.589
	2	↑	72	13,220	0.200	0.020	0.026	↑	↑	2.01	2.379
	3	↑	73	15,360	0.200	0.020	0.029	↑	↑	2.07	2.710
	4	↑	72	14,540	0.200	0.020	0.028	↑	↑	2.05	2.564
CARBON/EPOXY	1	↑	73	14,010	0.100	0.028	0.042	↑	↑	1.49	1.665
	2	↑	72	13,220	↑	0.028	0.042	↑	↑	1.45	1.595
	3	↑	73	15,360	↑	0.028	0.042	↑	↑	1.54	1.717
	4	↑	72	14,540	↑	0.028	0.042	↑	↑	1.49	1.647
FIBERGLASS	1	↑	73	14,010	↑	0.018	0.048	↑	↑	2.11	3.061
	2	↑	72	13,220	↑	0.018	0.048	↑	↑	1.96	2.804
	3	↓	73	15,360	↓	0.018	0.048	↓	↓	2.28	3.311
	4	ADAPTOR	72	14,540	0.100	0.018	0.048	4.00	0.500	2.03	2.906

Table 1.2-4: TRUSS STRUCTURE DATA

	CASE	LOCATION	MEMBER LENGTH (cm)	LOAD (N)	TUBE THICKNESS (cm)			TUBE RADIUS (cm)			WT PER MEMBER (Kg)
					MAX	MIN	DESIGN	MAX	MIN	DESIGN	
ALUMINUM	1	UPPER BODY	13.97	29,246	0.508	0.0508	0.0508	10.16	1.27	3.67	0.459
		LOWER BODY	11.18	41,077	↑	↑	0.0559	↑	↑	3.53	0.375
	2	UPPER BODY	12.19	26,844	↑	↑	0.0508	↑	↑	3.28	0.357
		LOWER BODY	13.21	32,582	↑	↑	0.0533	↑	↑	3.63	0.449
	3	UPPER BODY	13.97	29,401	↑	↑	0.0533	↑	↑	3.63	0.475
		LOWER BODY	11.18	44,569	↑	↑	0.0584	↑	↑	3.56	0.403
	4	UPPER BODY	12.19	27,689	↓	↓	0.0533	↑	↑	3.33	0.370
		LOWER BODY	13.21	35,940	0.508	0.0508	0.0533	↑	↑	3.76	0.460
CARBON/EPOXY	1	UPPER BODY	13.97	29,246	0.254	0.071	0.0711	↑	↑	3.05	0.306
		LOWER BODY	11.18	41,077	↑	↑	↑	↑	↑	2.36	0.283
	2	UPPER BODY	12.19	26,844	↑	↑	↑	↑	↑	2.72	0.238
		LOWER BODY	13.21	32,582	↑	↑	↓	↑	↑	3.05	0.288
	3	UPPER BODY	13.97	29,401	↑	↑	0.0711	↑	↑	3.05	0.307
		LOWER BODY	11.18	44,569	↑	↑	0.1066	↑	↑	2.41	0.290
	4	UPPER BODY	12.19	27,689	↑	↓	0.0711	↑	↑	2.74	0.240
		LOWER BODY	13.21	35,940	↑	0.071	0.0711	↑	↑	3.15	0.299
FIBERGLASS	1	UPPER BODY	13.97	29,246	↑	0.046	0.0914	↑	↑	3.68	0.543
		LOWER BODY	11.18	41,077	↑	↑	0.1066	↑	↑	3.45	0.473
	2	UPPER BODY	12.19	26,844	↑	↑	0.0914	↑	↑	3.30	0.424
		LOWER BODY	13.21	32,582	↑	↑	0.0914	↑	↑	3.56	0.522
	3	UPPER BODY	13.97	29,401	↑	↑	0.0914	↑	↑	3.71	0.546
		LOWER BODY	11.18	44,569	↑	↑	0.1066	↑	↑	3.51	0.479
	4	UPPER BODY	12.19	27,689	↓	↓	0.0914	↑	↑	3.33	0.426
		LOWER BODY	13.21	35,940	0.254	0.046	0.0914	↑	↑	3.99	0.552
ALUMINUM	1	ADAPTOR	18.54	62,316	0.508	0.0508	0.0686	↑	↑	5.28	1.175
	2	↑	18.29	58,803	↑	↑	0.0660	↑	↑	5.11	1.080
	3	↑	18.54	68,321	↓	↓	0.0737	↑	↑	5.26	1.230
	4	↑	18.29	64,500	0.508	0.0508	0.0711	↑	↑	5.21	1.164
CARBON/EPOXY	1	↑	18.54	62,316	0.254	0.071	0.1066	↑	↑	3.78	0.756
	2	↑	18.29	58,803	↑	↑	0.1066	↑	↑	3.68	0.724
	3	↑	18.54	68,321	↑	↓	0.1066	↑	↑	3.91	0.780
	4	↑	18.29	64,500	↑	0.071	0.1066	↑	↑	3.78	0.748
FIBERGLASS	1	↑	18.54	62,316	↑	0.046	0.1219	↑	↑	5.36	1.390
	2	↑	18.29	58,803	↑	↑	0.1219	↑	↑	4.98	1.273
	3	↓	18.54	68,321	↓	↓	0.1219	↓	↓	5.79	1.503
	4	ADAPTOR	18.29	64,500	0.254	0.046	0.1219	10.16	1.27	5.16	1.320

reinforcements. Rings at the ends and middle of the cylindrical body were omitted from the comparisons because they were required for payload and tank support loads, and thus were common to either continuous shells or truss structures.

A design study was conducted to obtain truss member and attachment weights. Representative truss member sizes were selected from Table 1.2-4 and the curve of Figure 1.2-6 was constructed from designs of typical end fittings shown in the figure. Bonded joints were assumed for carbon and fiberglass composite members and welded joints for aluminum members. Attachment brackets were designed for several truss members to prepare the curve of Figure 1.2-7. The figure shows a typical bracket for truss members intersecting a structural ring.

End attachment  $\Delta$  weights for shell structures were obtained from data generated in the Reference 1.2-2 program. In that study, detailed designs and weight summaries were prepared for shell structures consisting of corrugations, stiffened skin and honeycomb sandwich. Metallic and composite materials had been included in the designs. Figures 1.2-8 and 1.2-9 show the end attachment details for honeycomb sandwich and corrugated shells respectively. The shell structures of that study were short; thus end attachments constituted a major portion of total shell weight. To utilize that data for this study the weight of end attachments, i.e., reinforcements, rings, doublers, splice plates and fasteners, was determined in terms of pounds per inch of circumference for the specific design load. The weight was then ratioed to the design load of Vehicle 1-14 for equivalent types of shell construction.

Table 1.2-5 summarizes the combined weights of vehicle structure and attachments. Carbon/epoxy composite provided the least weight structural concept and tubular truss construction was more efficient than cylindrical shells. Honeycomb sandwich was generally less efficient than corrugations with the exception of fiberglass construction.

Placement of the  $LF_2$  tank in the forward position resulted in heavier structure, however, the weight differences were small in the case of truss structure. The corrugated composite shell constructions appeared to be the most sensitive to tank location.

Comparing the data of Table 1.2-1 and Table 1.2-5 led to the conclusion that placement of the  $LF_2$  tank forward produced the most weight efficient configuration; however, weight differences between either arrangement were small in the majority of cases. The use of a fiberglass truss adaptor with some of the shell constructions would result in a heavier vehicle when the  $LF_2$  tank was forward; however, there were no specific reasons to select fiberglass for this particular structure. The  $LF_2$  tank forward configuration was retained for further investigation.

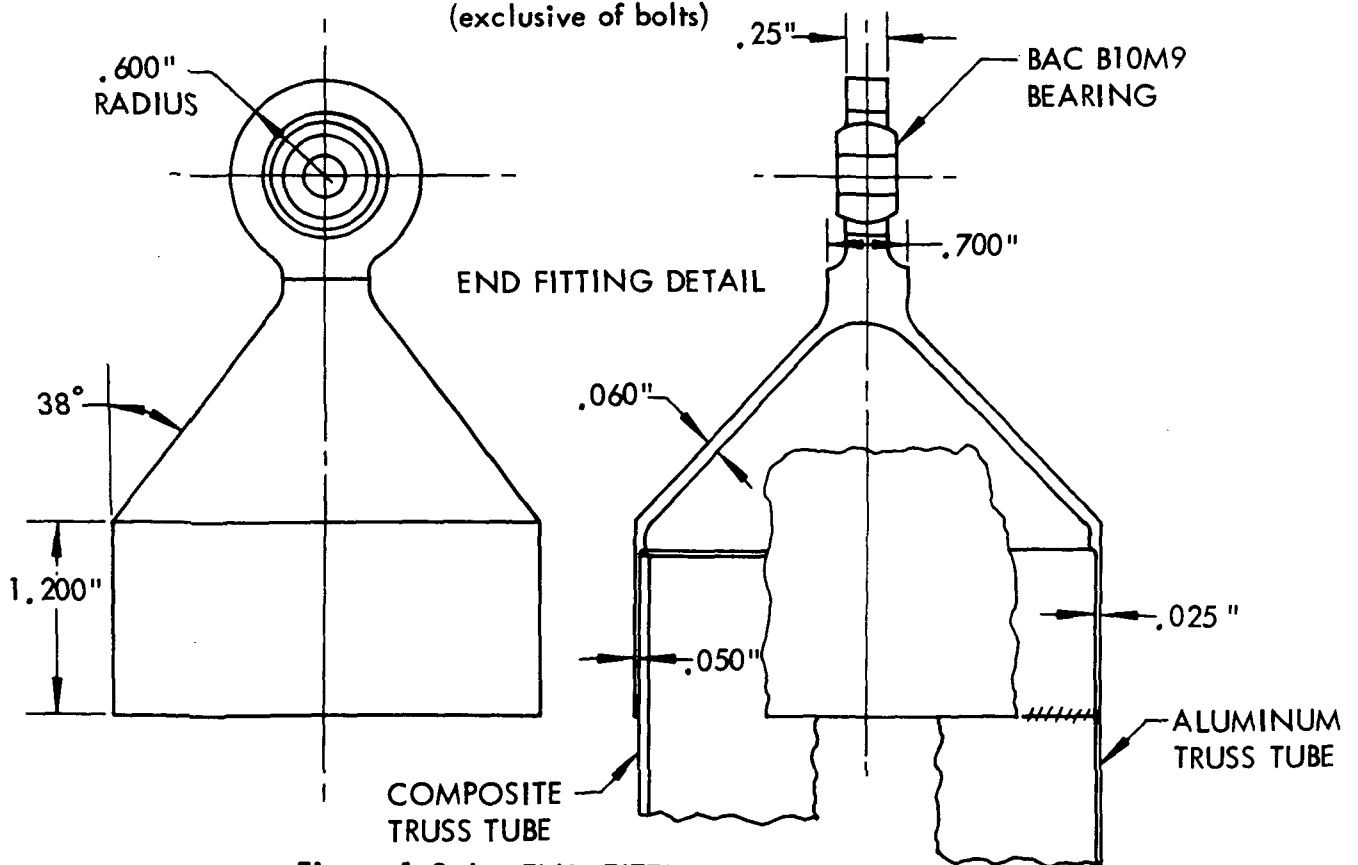
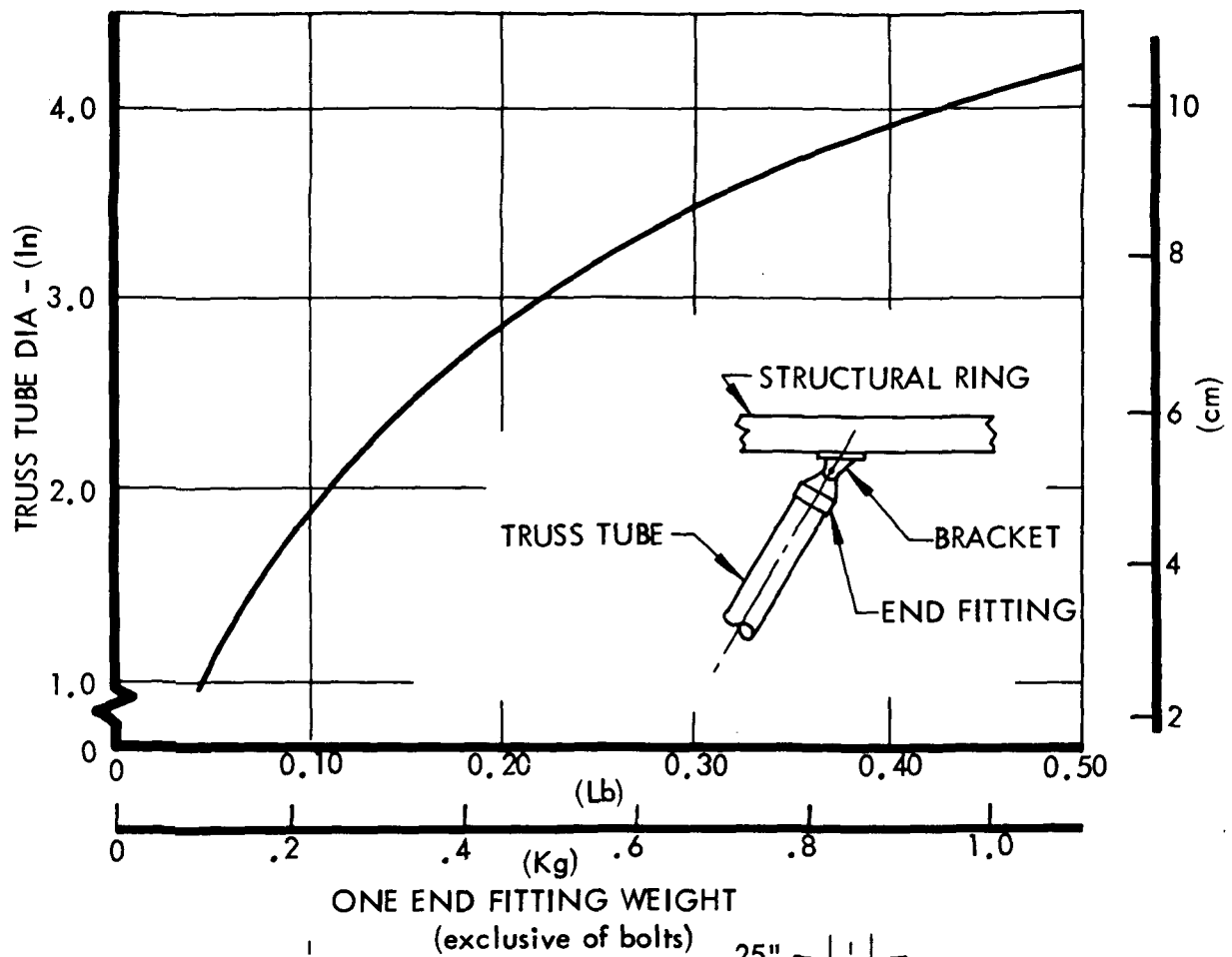


Figure 1.2-6: END FITTING WEIGHT DATA

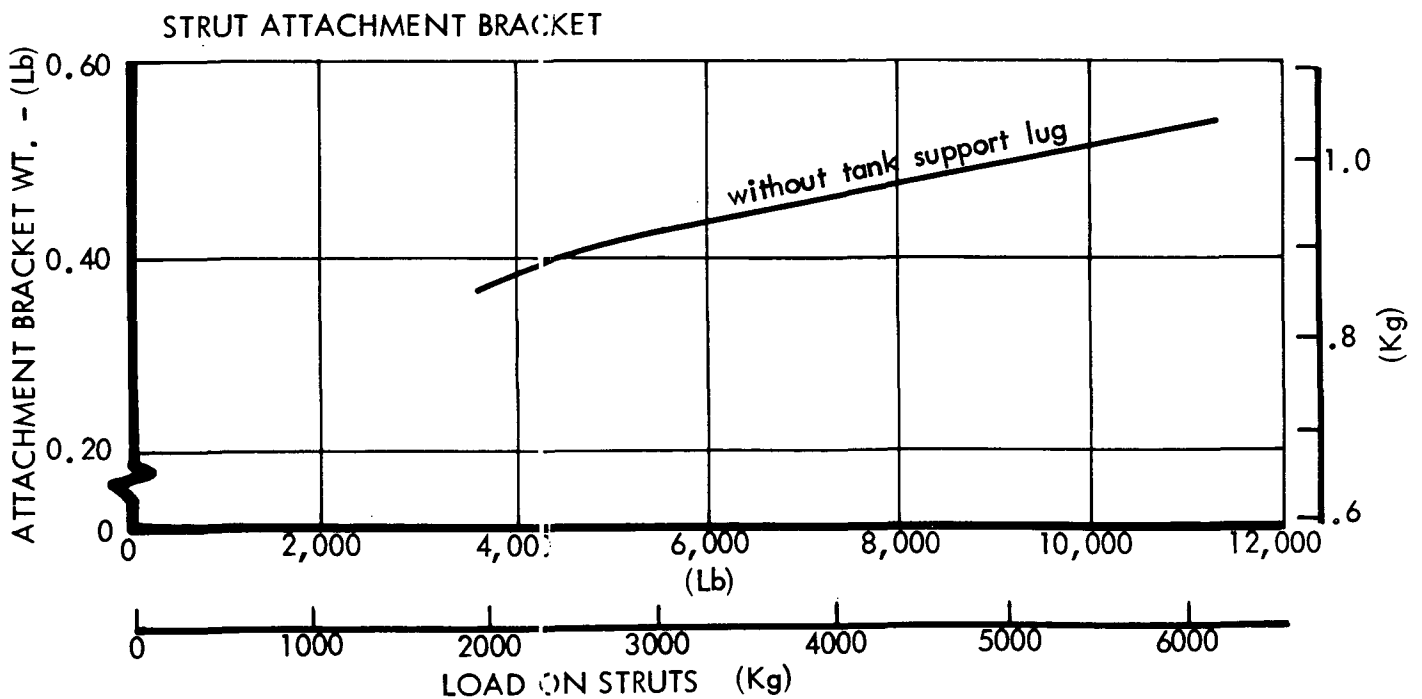
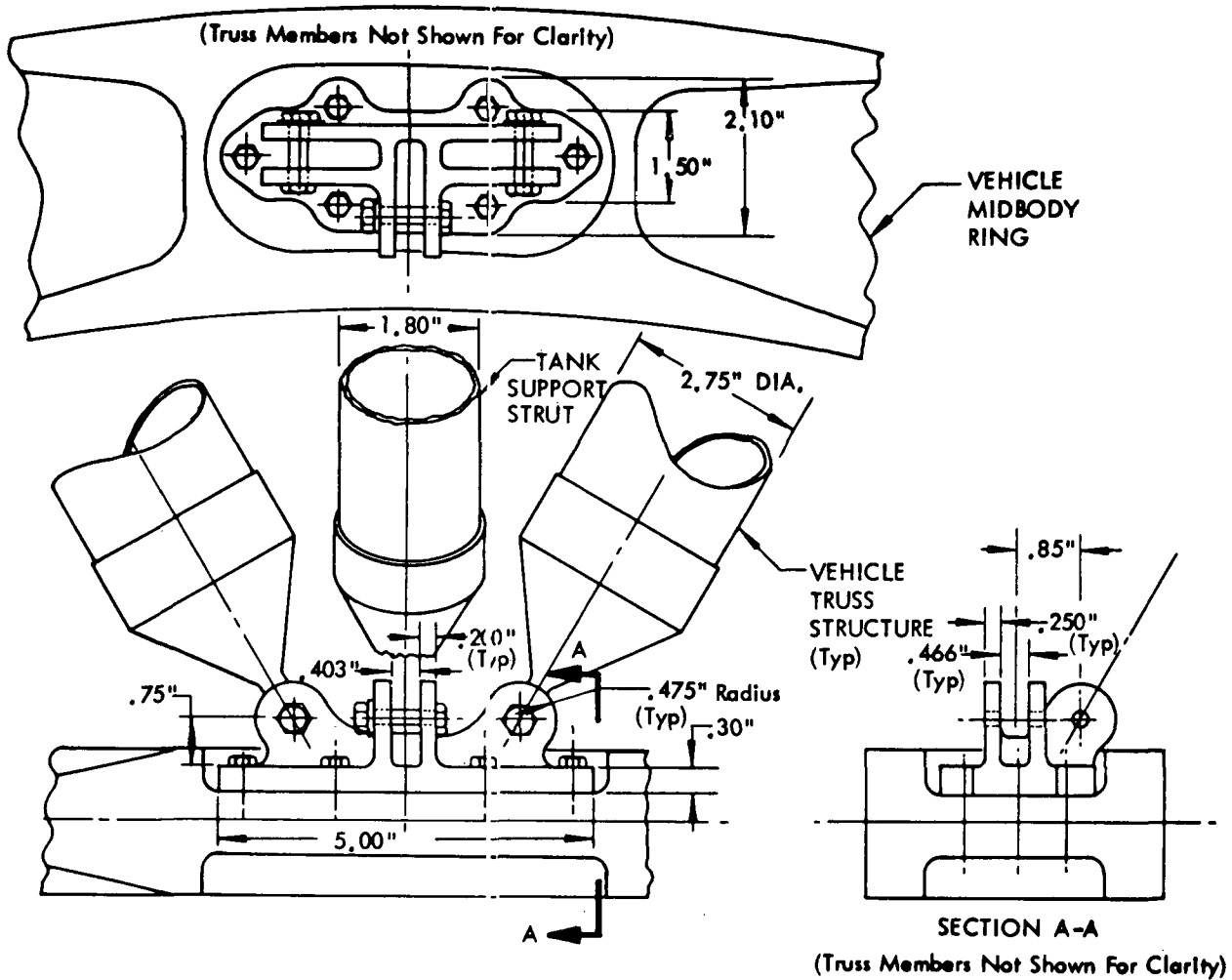
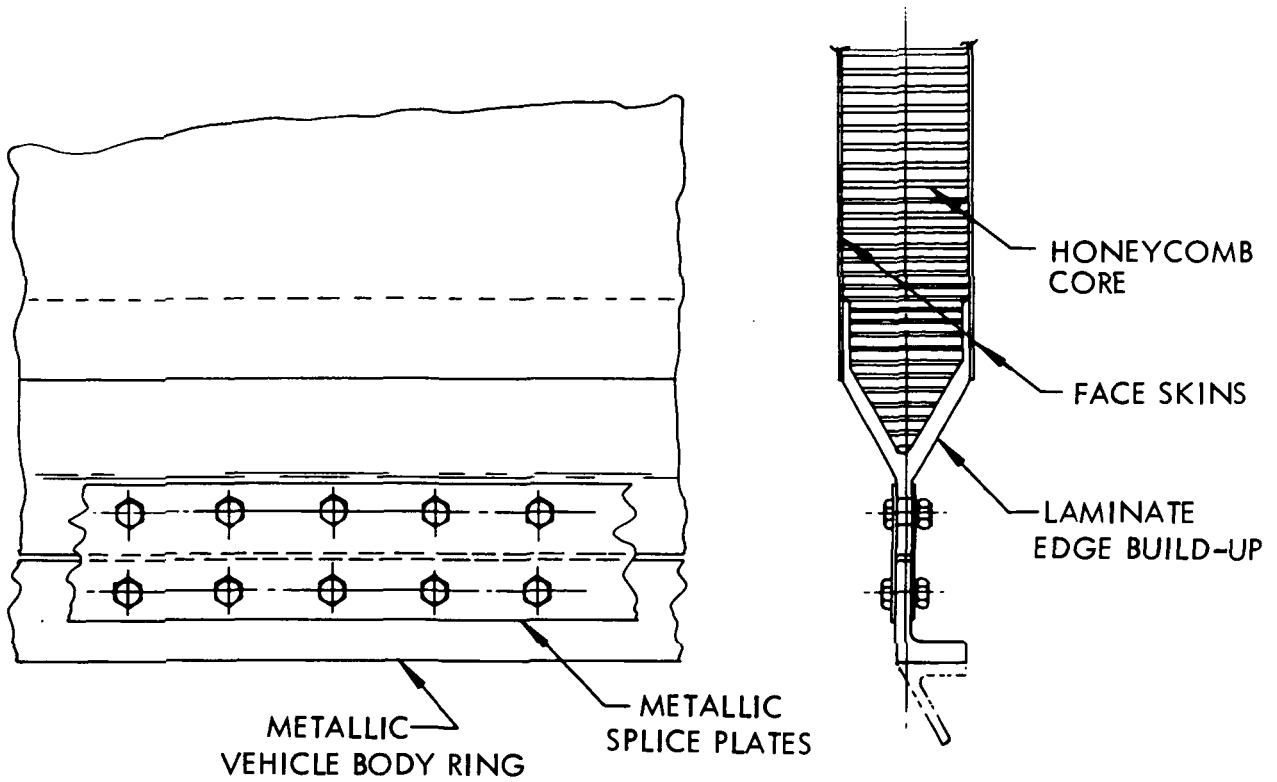
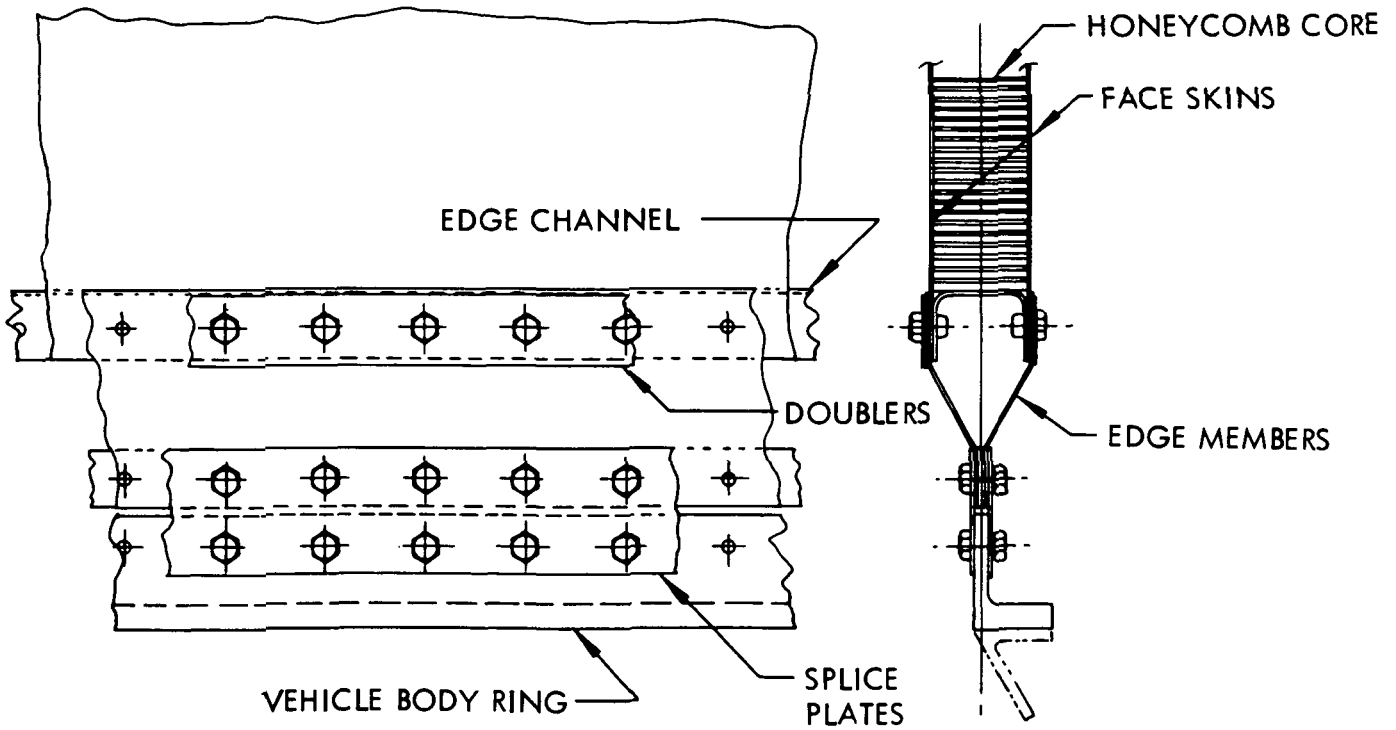


Figure 1.2-7: ATTACHMENT BRACKET WEIGHT DATA



COMPOSITE HONEYCOMB SANDWICH SHELL STRUCTURE



METALLIC HONEYCOMB SANDWICH SHELL STRUCTURE

Figure 1.2-8: HONEYCOMB SANDWICH EDGE ATTACHMENT DETAILS

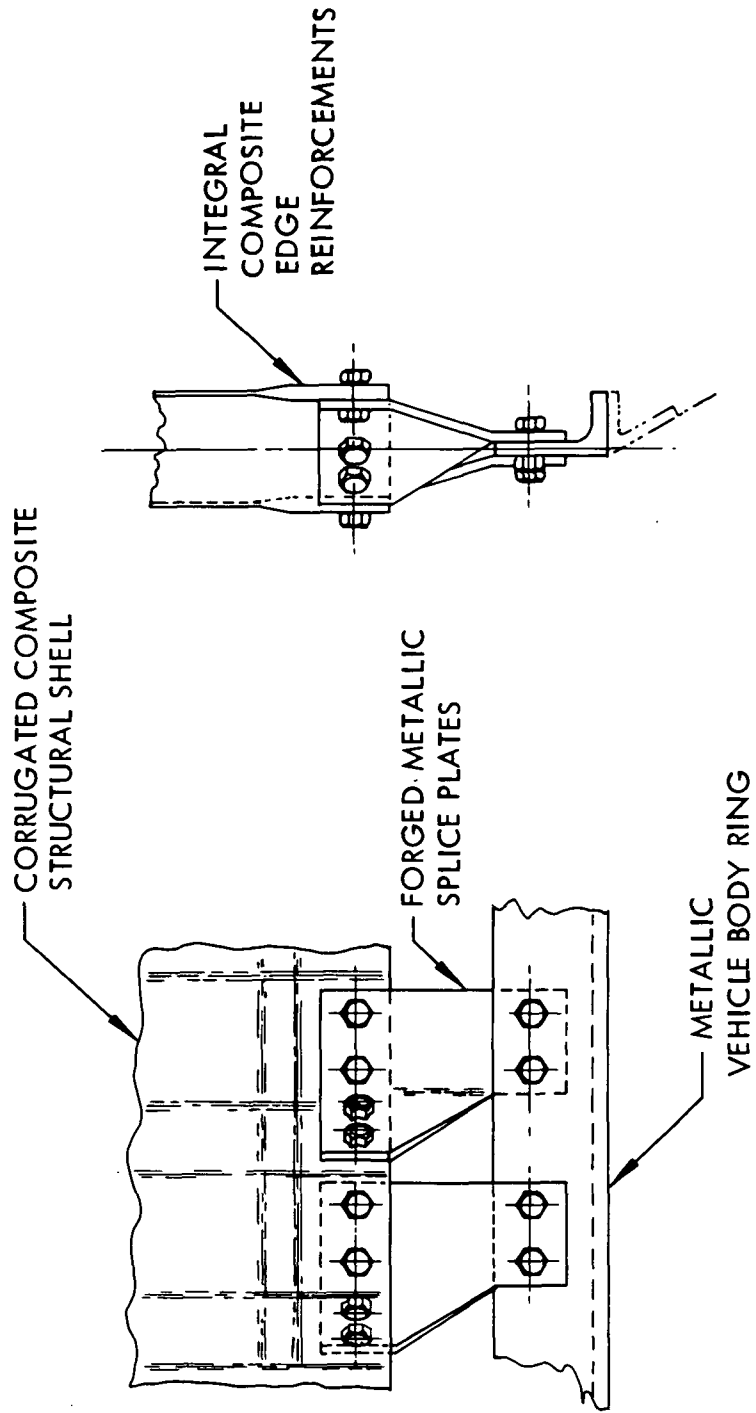


Figure 1.2-9: CORRUGATED CONSTRUCTION EDGE ATTACHMENT DETAILS

Table 1.2-5: VEHICLE AND ADAPTOR WEIGHTS

		VEHICLE CONFIGURATION I-14 STRUCTURAL WEIGHTS* - LBS (Kg)				
		PAYLOAD C.G. 51" (129.5 cm) ABOVE TOP DECK		PAYLOAD C.G. 20" (50.8 cm) ABOVE TOP DECK		
		LH <sub>2</sub> FORWARD - CASE 4	LF <sub>2</sub> FORWARD - CASE 3	LH <sub>2</sub> FORWARD - CASE 2	LF <sub>2</sub> FORWARD - CASE 1	
		CONSTRUCTION METHOD				
	CORRUGATED SHELL	ALUMINUM	79.6 (36.14)	84.2 (38.23)	74.7 (33.92)	77.0 (34.96)
		CARBON/EPOXY	76.8 (34.87)	85.5 (38.82)	65.3 (29.65)	75.6 (34.32)
		FIBERGLASS/ EPOXY	101.1 (45.90)	110.5 (50.17)	89.7 (40.72)	97.7 (44.36)
	HONEYCOMB SANDWICH SHELL	ALUMINUM	126.5 (57.43)	134.1 (60.88)	119.3 (54.16)	127.0 (57.66)
		CARBON/EPOXY	88.2 (40.04)	95.4 (43.31)	82.7 (37.55)	88.5 (40.18)
		FIBERGLASS/ EPOXY	93.4 (42.40)	100.8 (45.76)	87.7 (39.82)	94.0 (42.68)
	TUBE TRUSS	ALUMINUM	40.1 (18.21)	42.0 (19.07)	38.8 (17.62)	40.3 (18.30)
		CARBON/EPOXY	31.0 (14.07)	32.2 (14.62)	29.9 (13.57)	31.7 (14.39)
		FIBERGLASS/ EPOXY	44.2 (20.06)	45.5 (20.66)	42.9 (19.48)	44.7 (20.29)

		VEHICLE I-14 ADAPTOR STRUCTURAL WEIGHTS* - LBS (Kg)				
		PAYLOAD C.G. 51" (129.5 cm) ABOVE TOP DECK		PAYLOAD C.G. 20" (50.8 cm) ABOVE TOP DECK		
		LH <sub>2</sub> FORWARD - CASE 4	LF <sub>2</sub> FORWARD - CASE 3	LH <sub>2</sub> FORWARD - CASE 2	LF <sub>2</sub> FORWARD - CASE 1	
		CONSTRUCTION METHOD				
	TUBE TRUSS	ALUMINUM	46.7 (21.20)	48.8 (22.16)	43.8 (19.89)	46.3 (21.02)
		CARBON/EPOXY	30.9 (14.03)	32.6 (14.80)	29.9 (13.57)	31.0 (14.07)
		FIBERGLASS/ EPOXY	50.2 (22.79)	60.1 (27.29)	47.5 (21.57)	52.8 (23.97)

\*Including End Attachment Weights

### 1.2.3 Preliminary Design Development

Table 1.2-6 is a flow diagram showing major study elements in this phase of the program. The vehicle structure evaluation and tank arrangement thermal efficiency analyses were conducted first. A thermal math model of each vehicle was constructed for the latter study. The structural evaluation involved a re-appraisal of vehicle dimensions, assignment of major component weights, calculation of loads and optimization of various structural concepts.

Vehicle details such as payload height, type of structure, and insulation location were evaluated to determine least-weight trends preparatory to conducting the detailed meteoroid protection assessment. The meteoroid protection capability of the selected details was determined and then if additional protection was necessary, several alternative methods were evaluated.

Preliminary design drawings were prepared for the ten vehicles. Internal structure, engine mounts and tank supports were included. A detailed weight analysis was made from these drawings.

The study was concluded by determining, in a qualitative sense, the operational complexity of each configuration. The complexity ratings and weights were then compared and recommendations made for selection of two designs for the final evaluation phase.

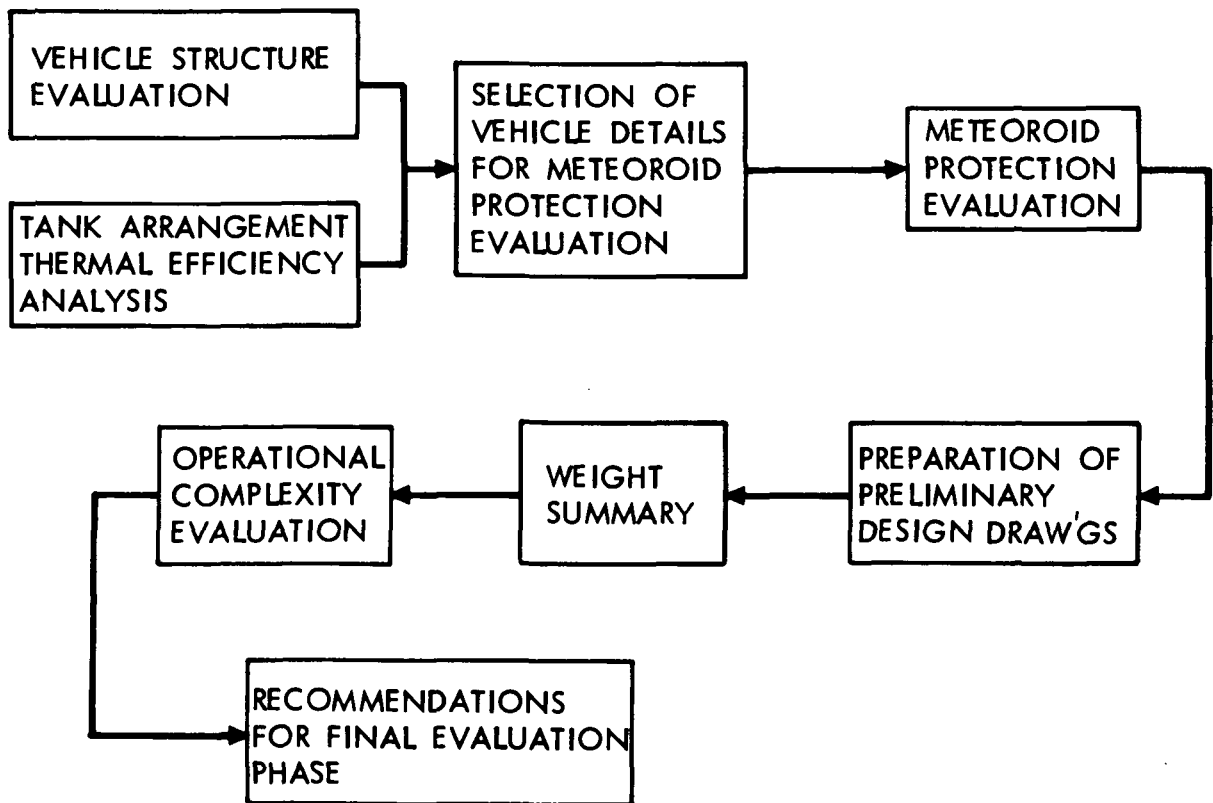
#### Vehicle Structure Evaluation

The "Vehicle Structure Evaluation Computer Program" described in Section 1.1.3 was used to determine the weights of shell and truss structure concepts for the body of the study vehicles and for trusswork Centaur adaptors. Three payload heights were evaluated. These heights were approximately 1/2 and 1/5 the vehicle diameter and a minimum case of 4 inches (10.2 cm) above the top deck insulation. Two continuous shell construction methods, and truss structures were investigated in combination with three materials. The shells consisted of honeycomb sandwich and ring stiffened corrugations. The materials were aluminum, carbon/epoxy, and fiberglass/epoxy composites.

Sketches of the vehicle configurations with the dimensions and weights used for the study are included in Appendix B of the Volume II document, NASA CR-121104. Loads were calculated for each study vehicle in the manner described in Section 1.1.3. The ultimate design loads for all methods of construction are included with the study results.

The detailed results of the analysis are presented in Appendix B. This data consists of tabulated weights and member dimensions for all vehicles and construction methods. These weights are for the main body structure and do not include end attachments or other structural members such as payload supports, tank supports,

Table 1.2-6: PRELIMINARY DESIGN STUDY FLOW DIAGRAM



or internal bracing. An analysis of this data indicated that; (1) truss structure was the least weight approach, regardless of material choice, with carbon/epoxy being the lightest; (2) the least weight shell structures were carbon/epoxy; (3) aluminum and carbon/epoxy corrugated shells were consistently lower weight than aluminum and carbon/epoxy honeycomb sandwich; (4) fiberglass honeycomb sandwich was more weight efficient than fiberglass corrugations for vehicles with long bodies (i.e., 1-14, 2-14) due to higher shell loading; but less efficient for vehicles with short bodies.

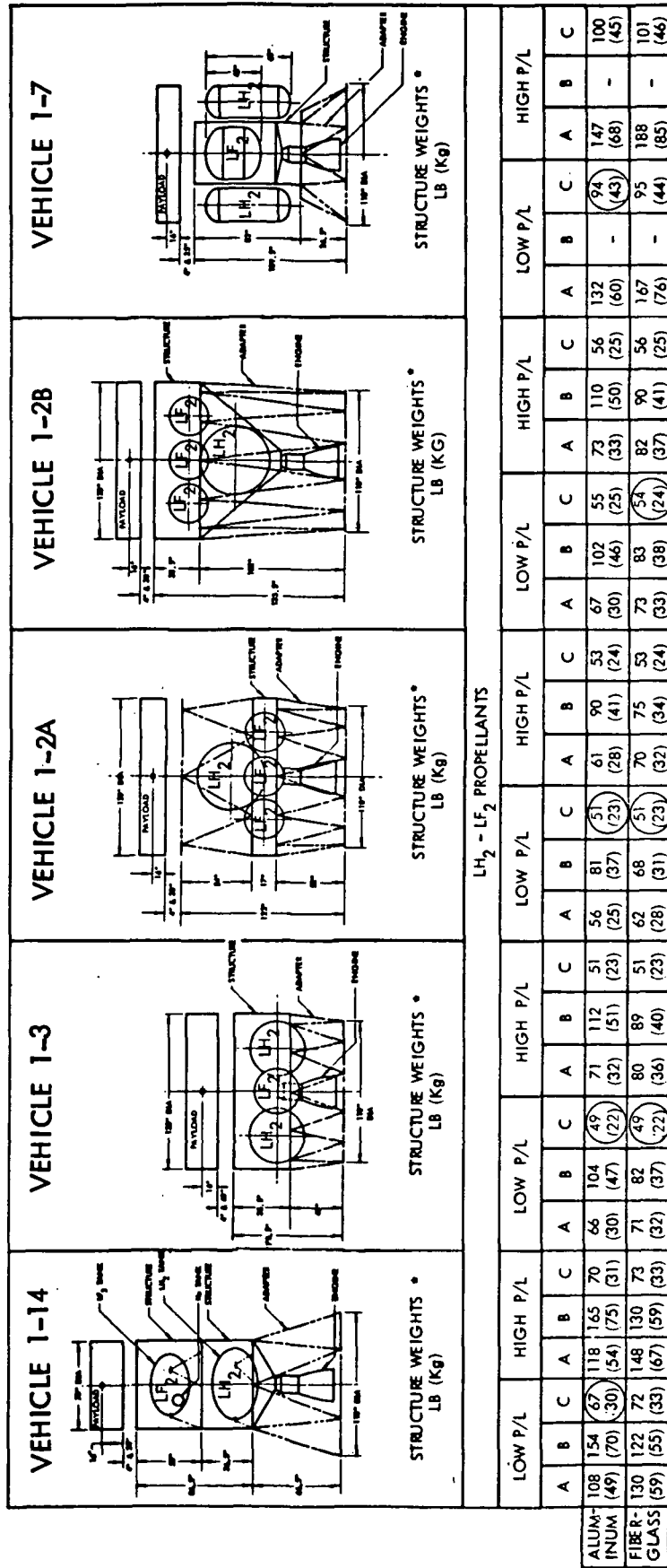
This phase of the study was concluded by calculating end fitting and attachment bracket weights for all of the vehicle bodies and adaptors using the curves of Figures 1.2-6 and 1.2-7, and the methods described in Section 1.2.2. The final results are presented in Figures 1.2-10 and 1.2-11. The least weight case is circled in the figures. Carbon/epoxy composite and median payload height designs were omitted from the figures. In all cases truss structure with a low payload height gave the least weight. Aluminum truss members were also least weight in a great number of cases. The final structure weights were compared with weight estimates used in deriving the loads and it was found that the error was only 1.5 to 3.5%, thus a second iteration was unnecessary. The end fittings and attachments contributed significantly to the weights of tubular truss members, particularly for the carbon/epoxy construction.

#### Tank Arrangement Thermal Efficiency

The thermal efficiency analyses were conducted as preliminary designs were being developed. Thus, design information such as the type and location of internal structural members, tank supports and fluid lines was available for construction of the thermal models.

Fluid line arrangements developed for the study vehicles are presented in Figures 1.2-12 through 1.2-21. Particular attention was given to routing of lines which were attached to external structure. Wherever convenient, these external attachments were located on aft facing surfaces; however, with the reduced solar panel emittance discussed previously, vehicle external surface temperatures would be lower and the importance of external connection location would be lessened. Connections to surfaces which faced the payload were avoided. Line sizes for  $\text{LF}_2/\text{LH}_2$  propellants were selected based on experience. The line sizes for  $\text{FLOX}/\text{CH}_4$  propellants were derived from the Pratt and Whitney report, Reference 1.1-1.

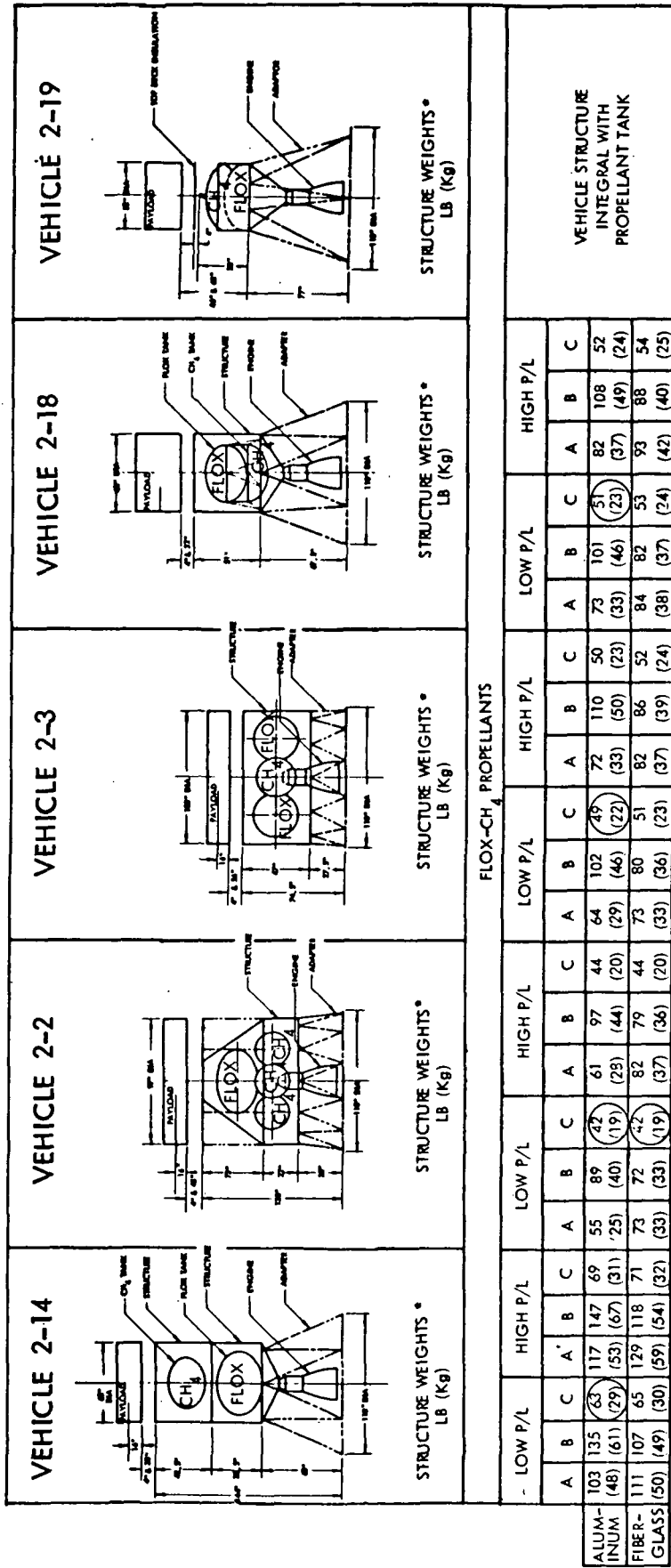
A tank support arrangement employing six fiberglass tubular struts was selected for spherical and oblate spheroid tanks. The supports were connected to the tank at three discrete locations and were angled aft so that they could be attached to cooler structure. Connections were made at vehicle "hard" points. Member lengths were derived from layouts and loads were calculated for critical combinations of axial and lateral accelerations. The fiberglass tube sizes were optimized



A - CORRUGATED SHELL  
 B - HONEYCOMB SANDWICH  
 C - TRUSS STRUCTURE

\* INCLUDING VEHICLE ADAPTER AND END FITTING WEIGHTS

Figure 1.2 - 10: PRELIMINARY DESIGN VEHICLE STRUCTURE EVALUATION RESULTS



A - CORRUGATED  
 B - HONEYCOMB SANDWICH SHELL  
 C - TRUSS STRUCTURE

\* INCLUDING VEHICLE ADAPTOR AND END FITTING WEIGHTS

Figure 1.2 -11: VEHICLE STRUCTURE EVALUATION RESULTS

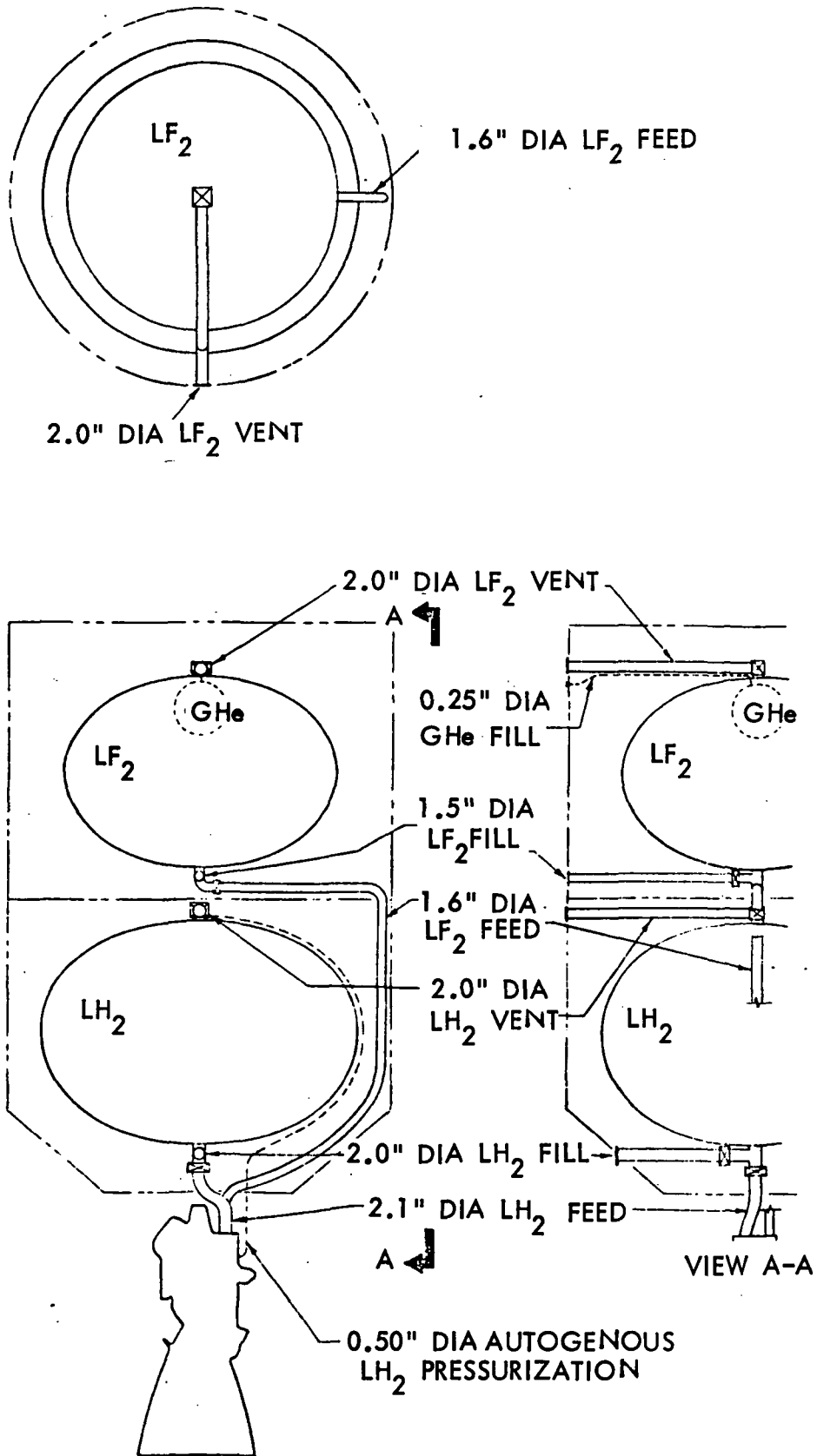


Figure 1.2-12: VEHICLE 1-14 FLUID LINE ARRANGEMENT

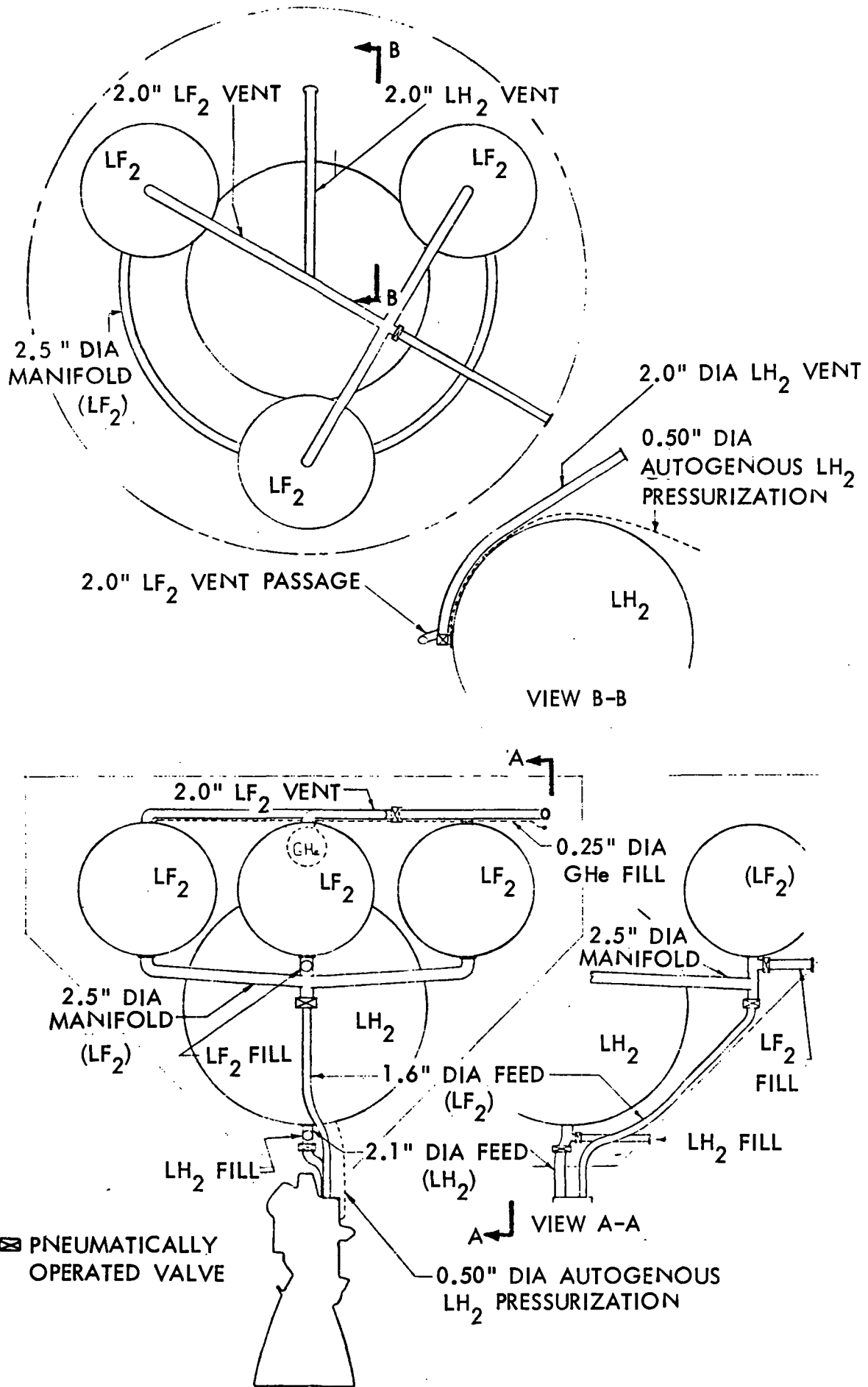


Figure 1.2-13: VEHICLE 1-2B FLUID LINE ARRANGEMENT

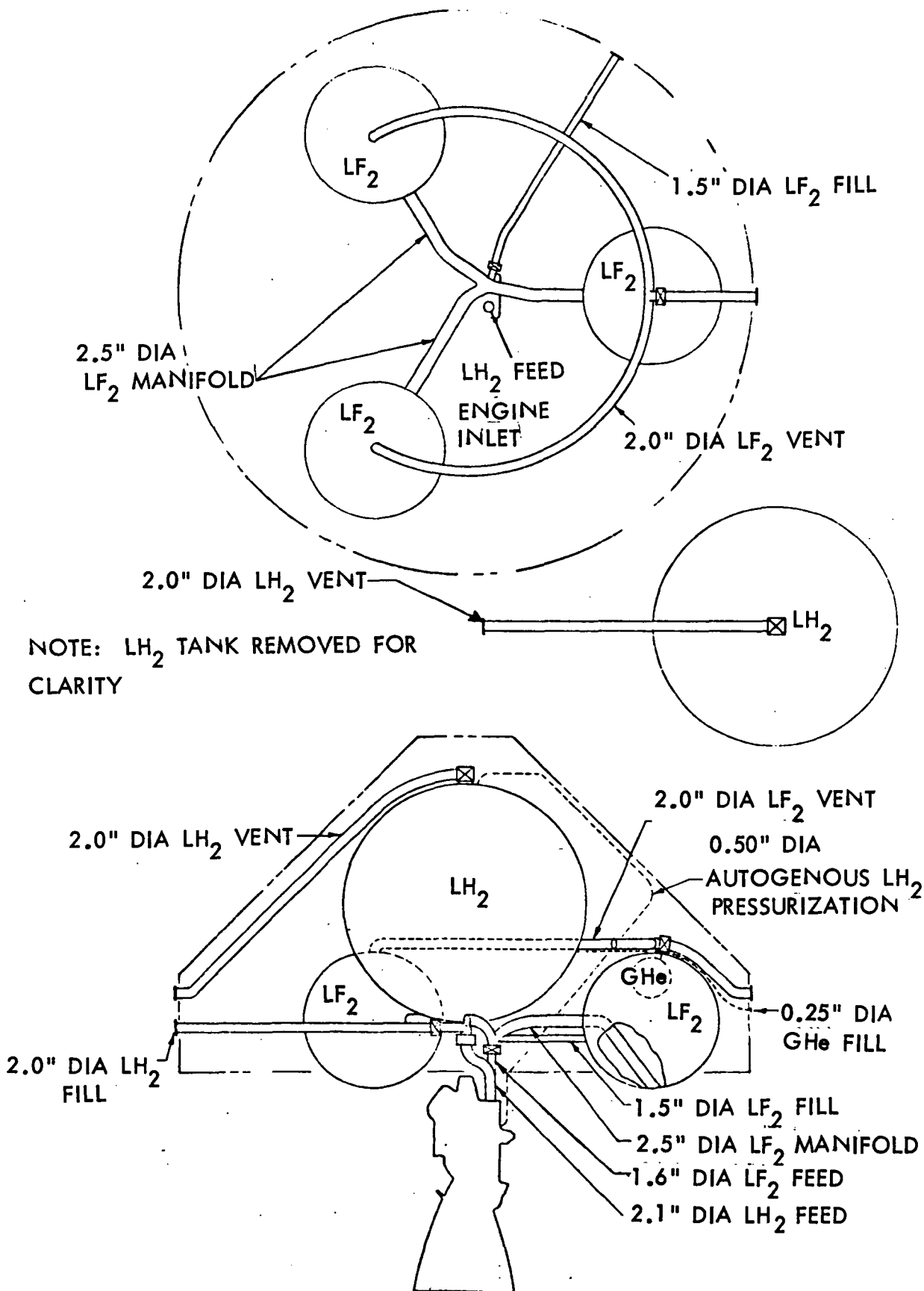


Figure 1.2-14: VEHICLE 1-2A FLUID LINE ARRANGEMENT

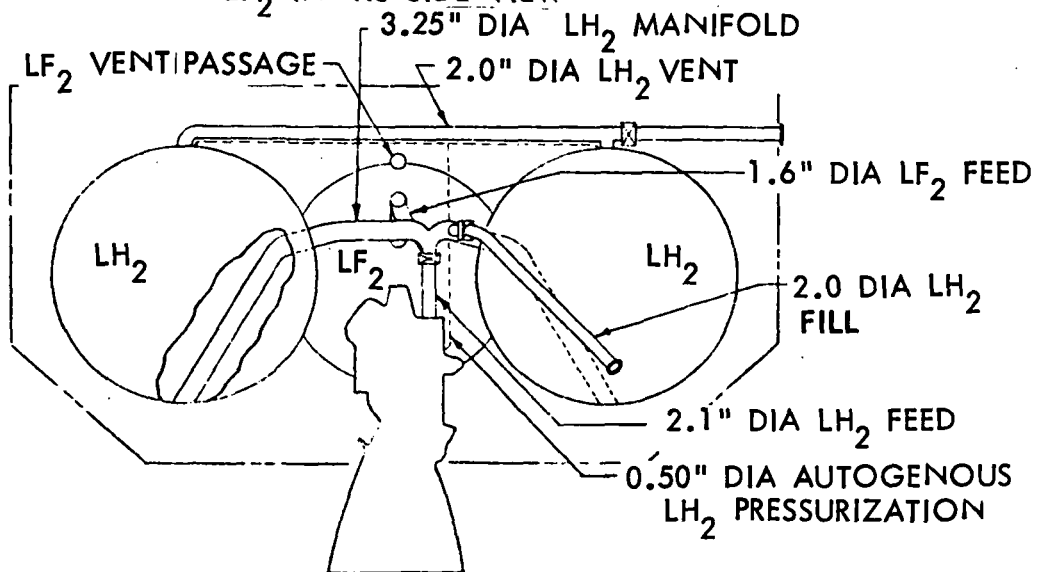
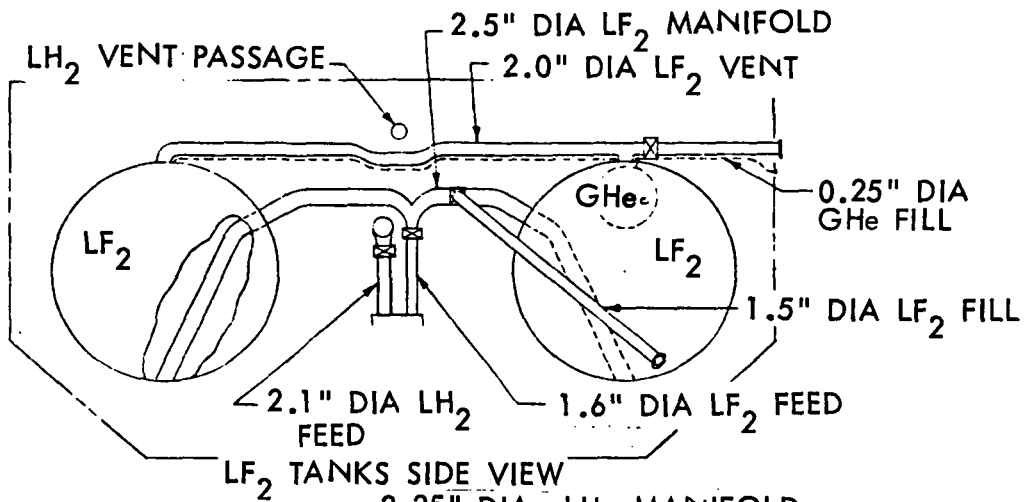
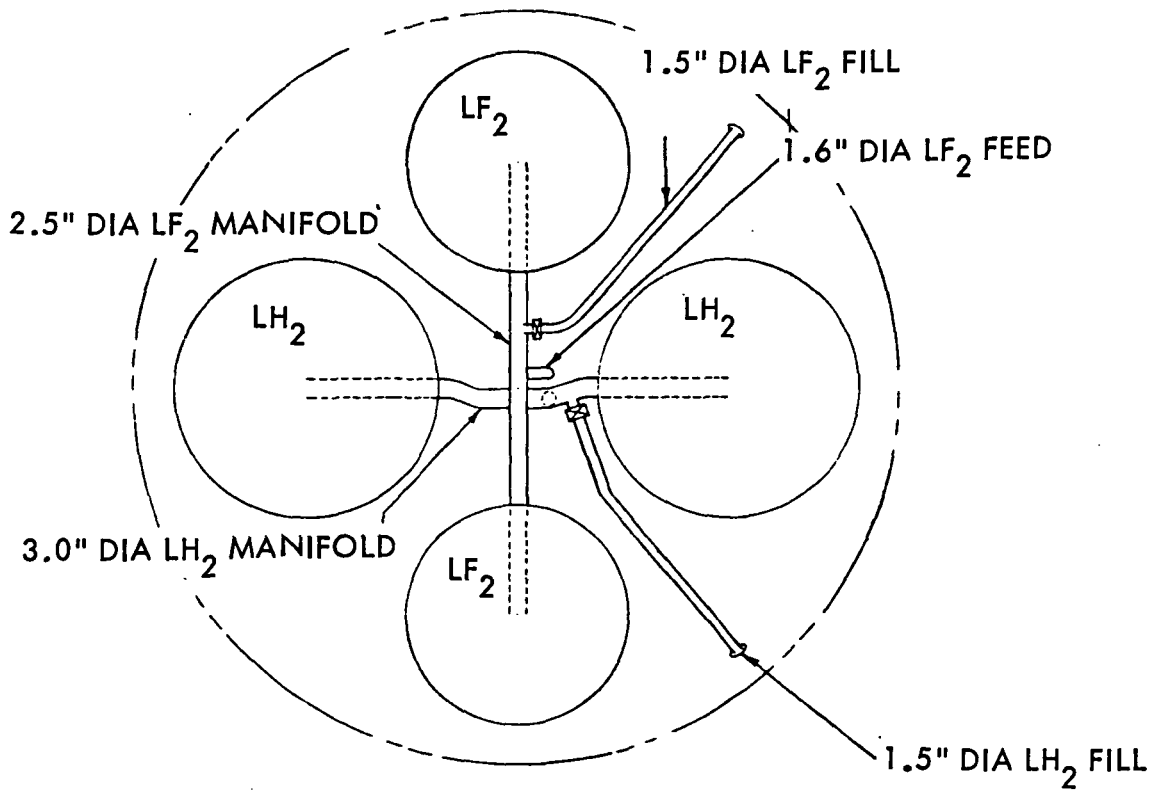


Figure 1.2-15: VEHICLE 1-3 FLUID LINE ARRANGEMENT

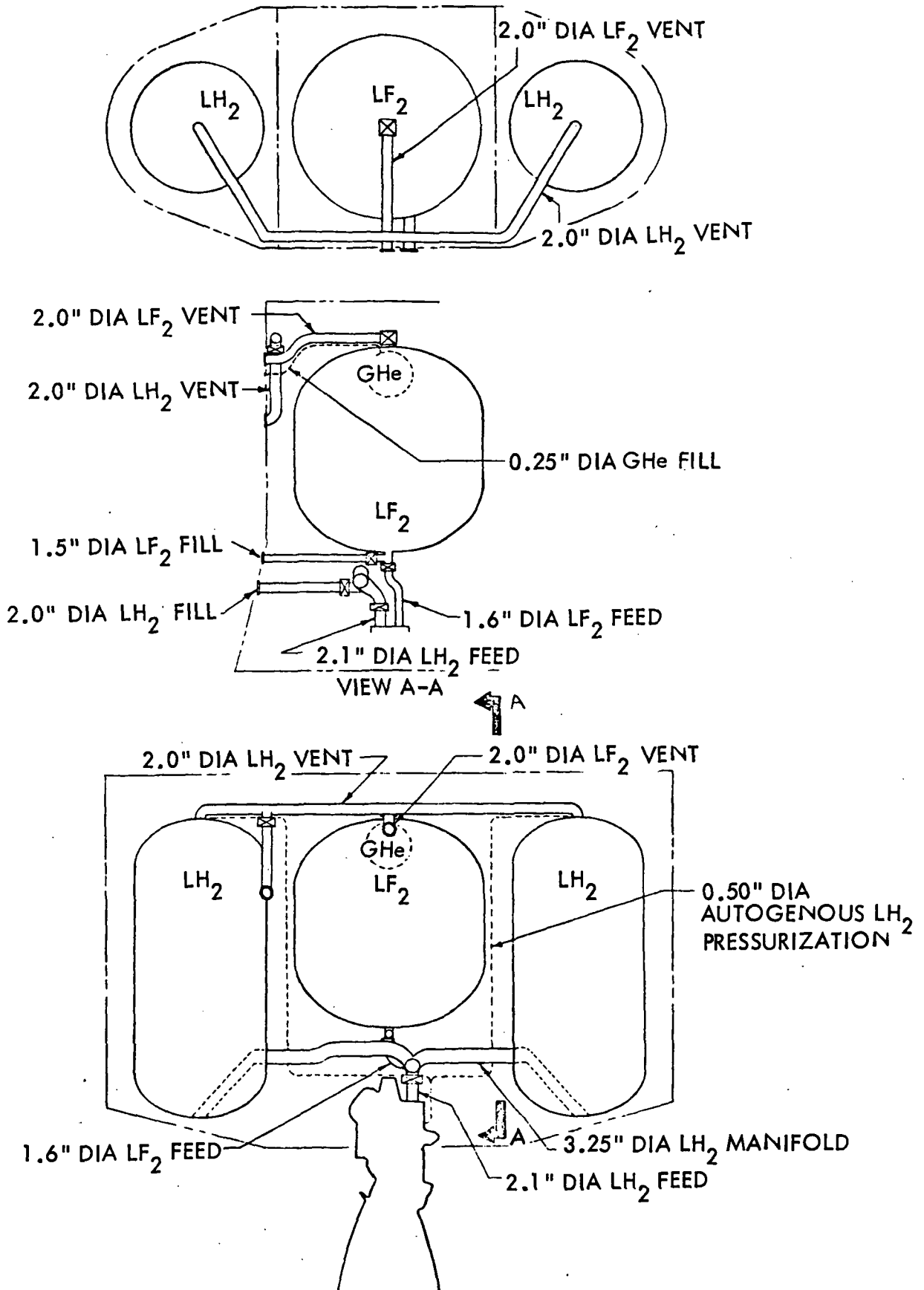


Figure 1.2-16: VEHICLE 1-7 FLUID LINE ARRANGEMENT

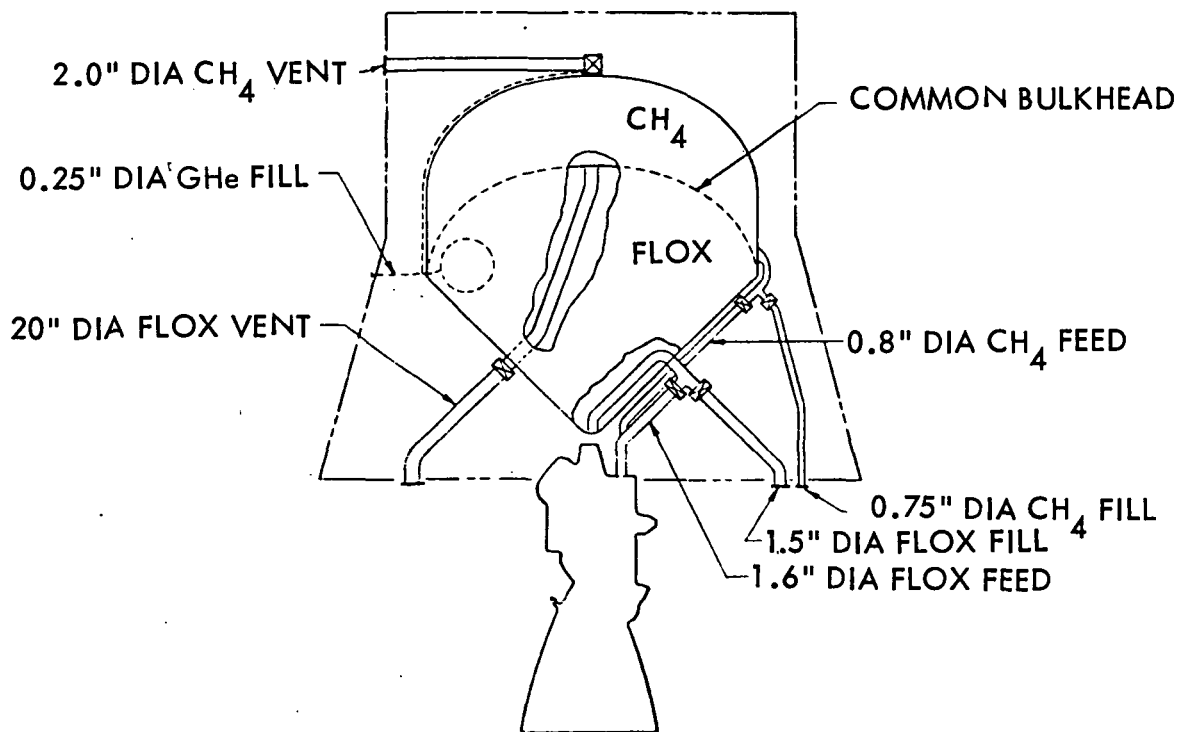
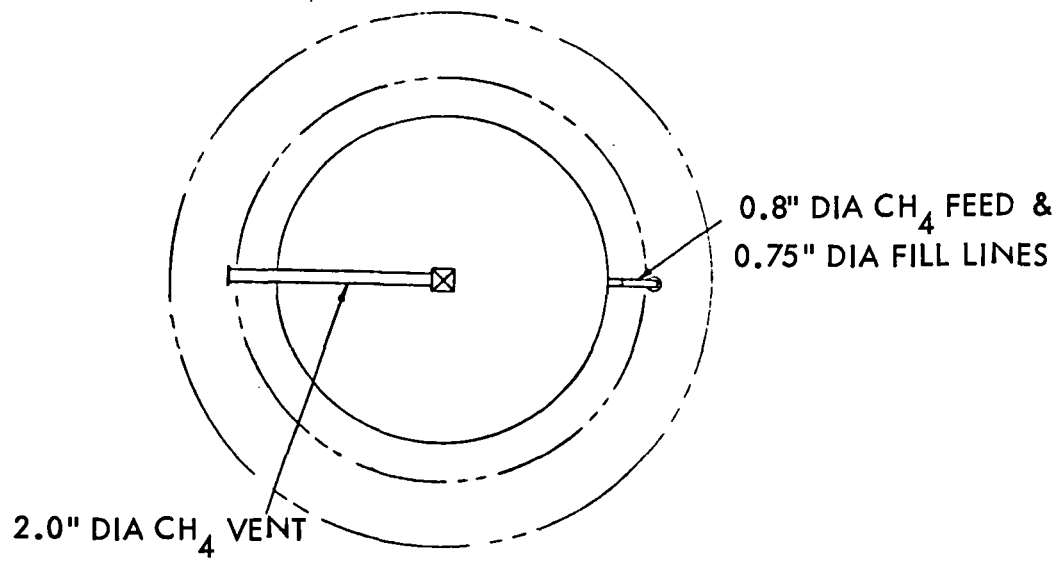


Figure 1.2-17: VEHICLE 2-19 FLUID LINE ARRANGEMENT

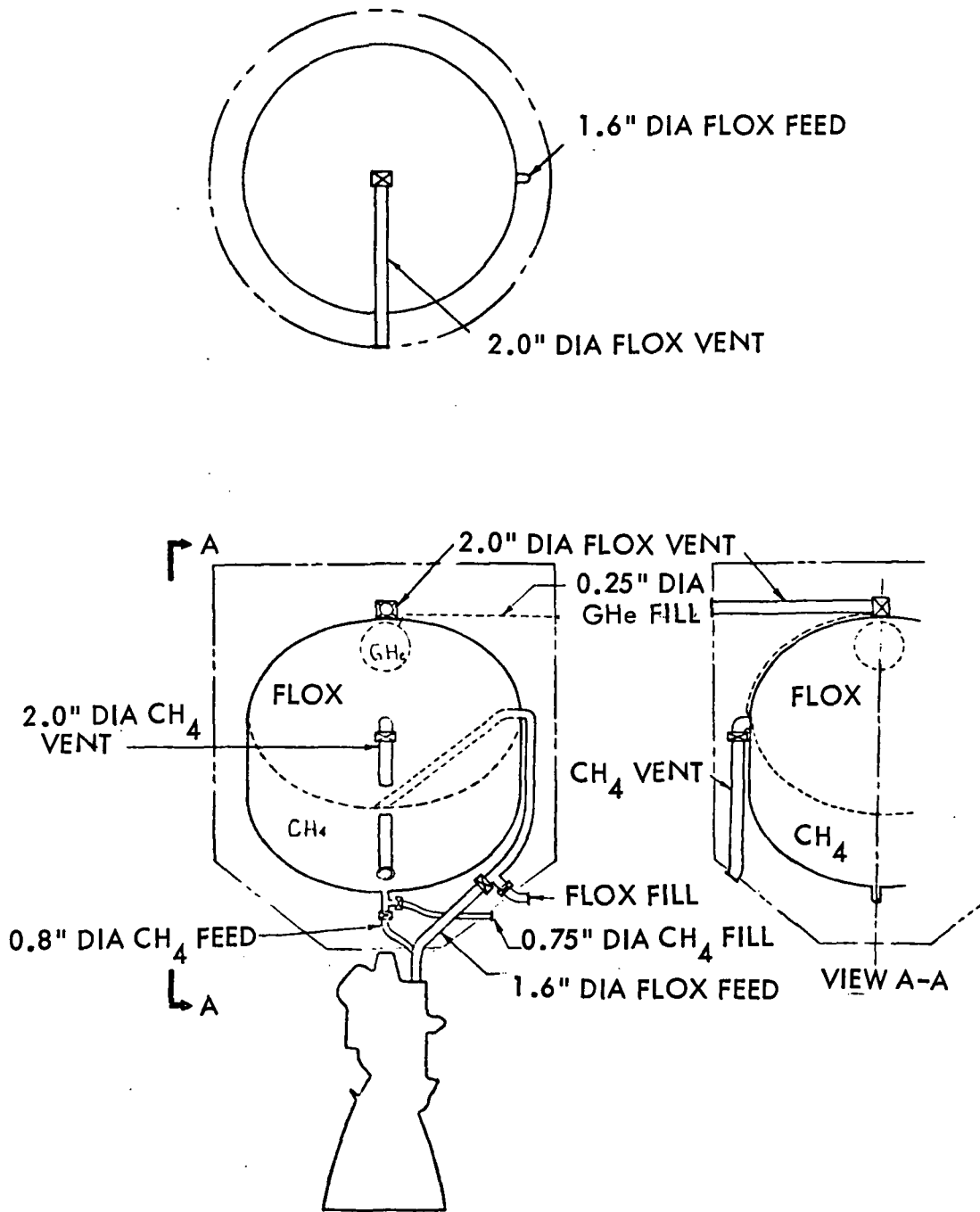


Figure 1.2-18: VEHICLE 2-18 FLUID LINE ARRANGEMENT

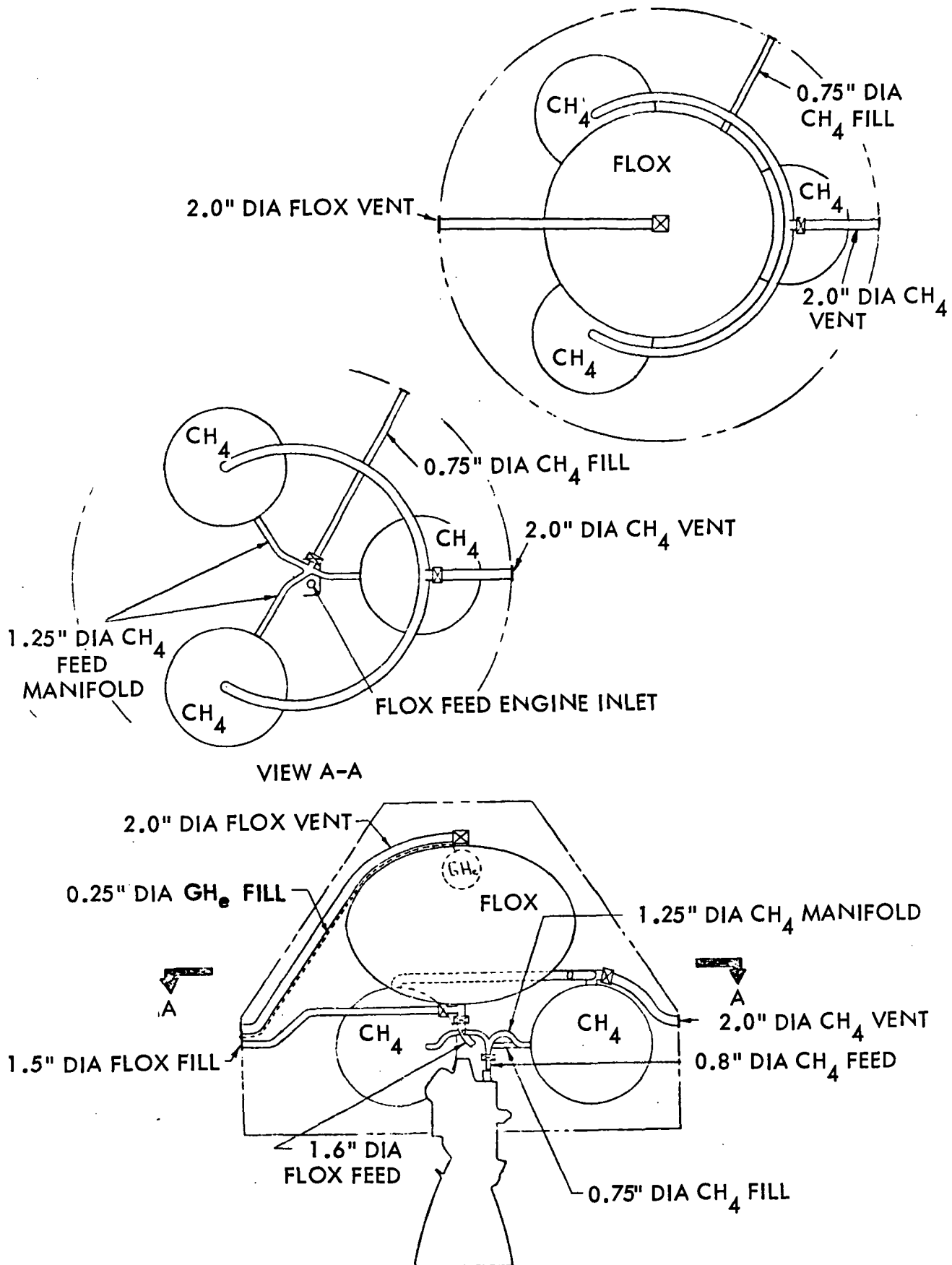
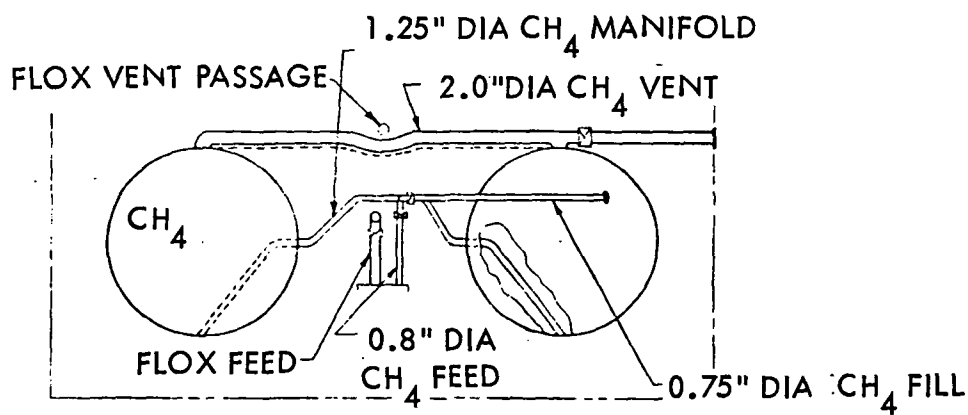
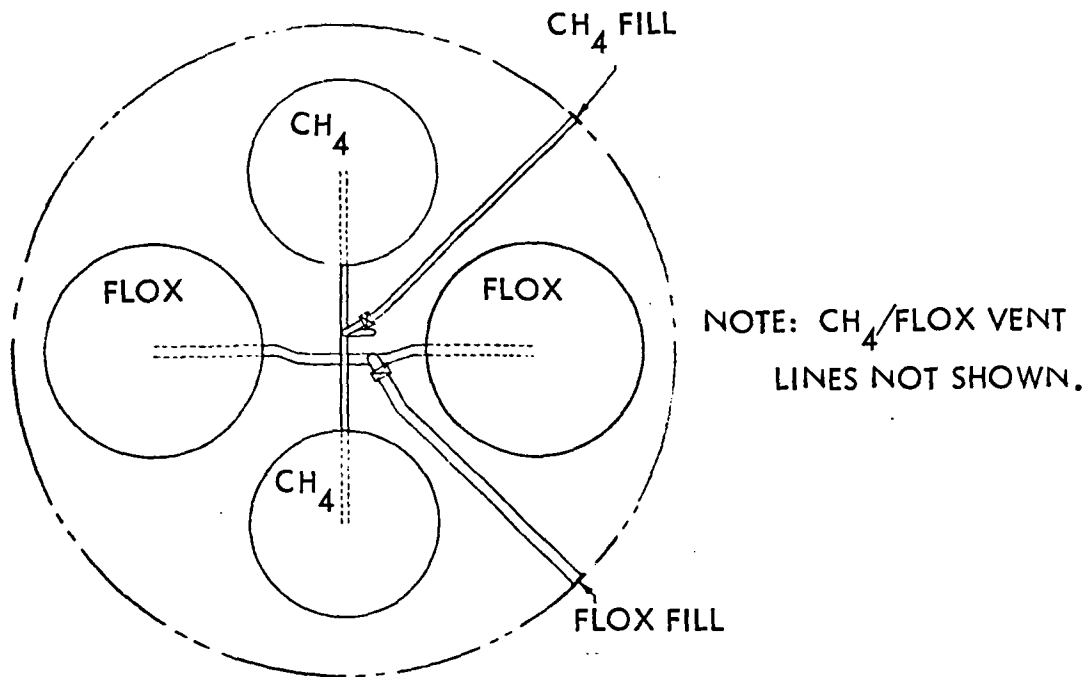


Figure 1.2-19: VEHICLE 2-2 FLUID LINE ARRANGEMENT



CH<sub>4</sub> TANKS SIDE VIEW

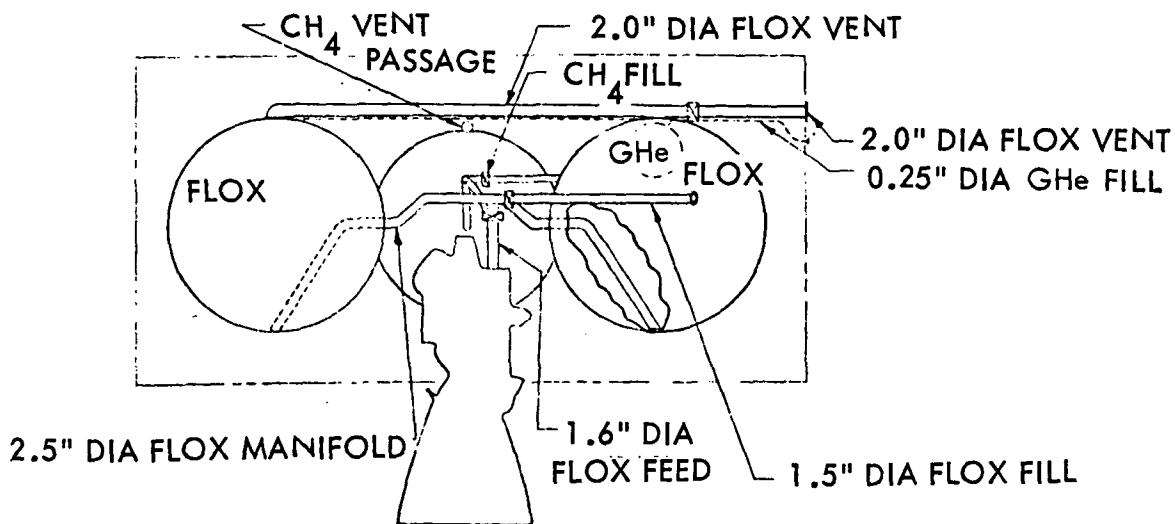
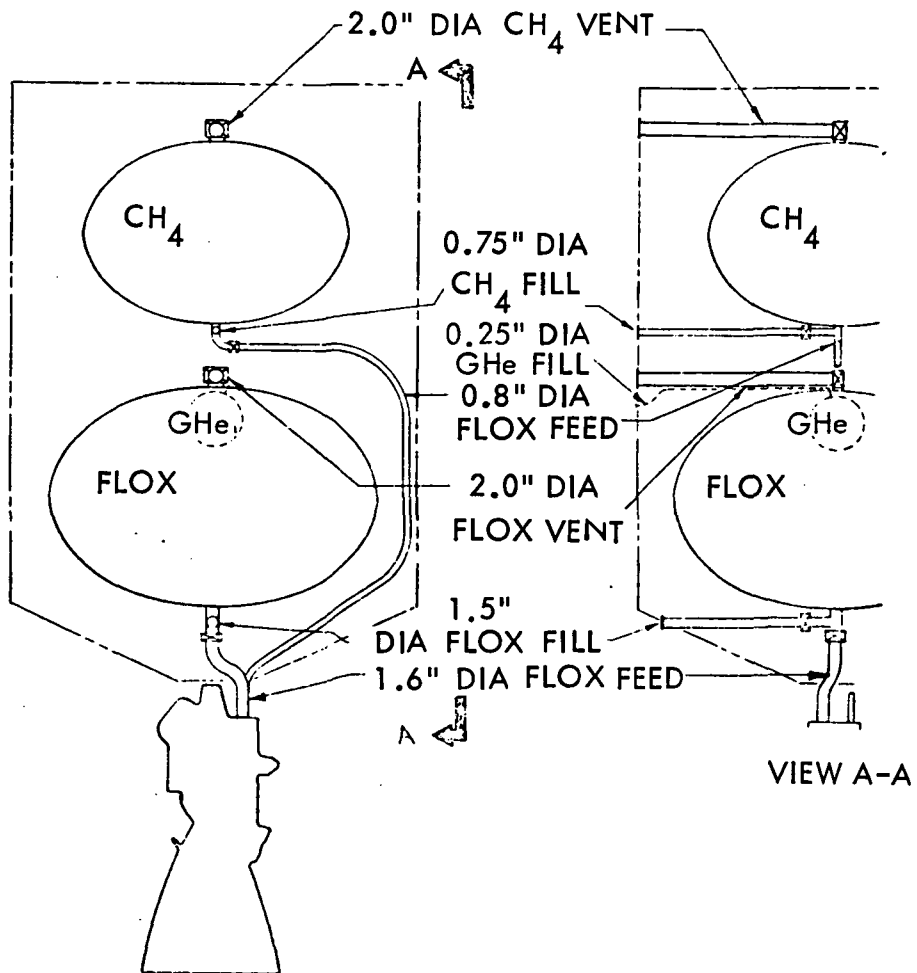
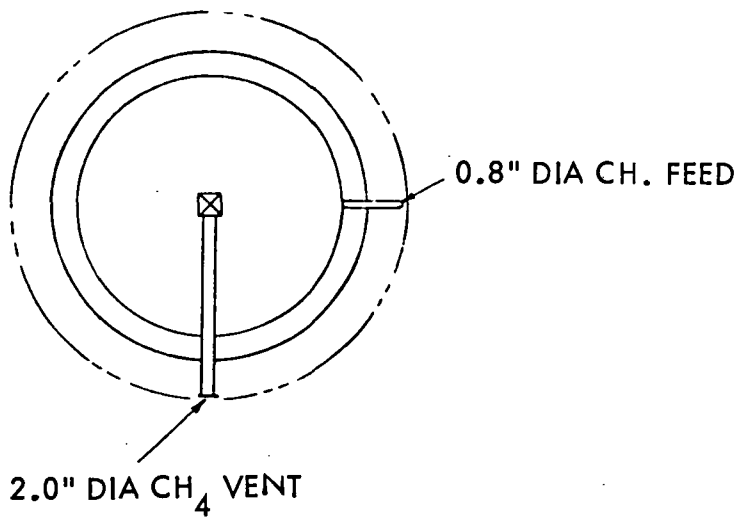


Figure 1.2-20: VEHICLE 2-3 FLUID LINE ARRANGEMENT



by equating the Euler buckling stress to the local crippling stress with the material ultimate strength as a design constraint. The tubes were hollow and without internal radiation baffles.

The analyses to determine vehicle temperatures and to perform the propellant and insulation system weight optimization were performed in the following sequence.

Input Data - The plumbing and structural arrangements established for a given vehicle concept, and the structural analysis and optimization provided conduction path geometry.

Previous optimization using the TATE (Tank Arrangement Thermal Efficiency) program provided estimates of insulation thicknesses.

With the established vehicle geometry and selected surface radiation properties, the geometric view factors and radiative interchange factors were generated using a thermal radiative interchange factor computer program. The surface properties used were as follows:

<u>Location</u>	<u>Emittance</u>	<u>Solar Absorptance</u>
1) Payload lower surface	1.0	-
2) Solar panel lower surface	0.05	-
3) Vehicle upper exterior surface	0.05	-
4) Vehicle sidewall and bottom exterior surface	0.4	0.16
5) Vehicle interior compartment surfaces	0.03	-
6) Tank surfaces	0.2	-

The fourth item shown assumes that a silicon monoxide coating (Reference 1.2-3) is applied to exterior surfaces.

Thermal Analysis - The above input data was used to build a thermal math model for each vehicle concept. Variations in the model accounted for the differences in the vehicle such as structural configuration, payload separation distance, structural material, insulation inside or outside, type of insulation, etc.

A steady state thermal analysis of each variation of each vehicle concept was performed on the BETA (Boeing Engineering Thermal Analyzer) program to determine temperatures for the coast phase (payload toward the sun).

Optimization - The temperatures and structural and plumbing conductances resulting from the thermal analysis were used as input to the TATE program. This represented a refinement from previous applications of this program in the screening phase, where temperatures were based on radiation equilibrium temperatures, the compartment internal wall was set at the tank temperature, and no structural or plumbing heat leaks were included.

An additional input was the ascent heating as a function of the type of insulation, location on the vehicle, and insulation thickness. The ascent heating data was taken from the analysis described in Section 1.1.4, using edge evacuation with a two-foot evacuation path length and a helium purge. Maximum tank pressure could occur prior to the end of the mission because propellant cooling was possible due to low temperatures during the coast phase and the  $\text{CH}_4$  could be cooled by the FLOX. Therefore, the TATE program checked tank pressure at launch, end of ascent heating and at the end of the mission, and used the maximum value in calculating tank wall thickness.

The conductance of insulation fasteners was approximated from previous analyses discussed in Section 1.1.4 and was added to the basic temperature-dependent insulation conductance.

Each variation of each vehicle concept was optimized to the insulation thicknesses for minimum weight, using the TATE program.

The TATE program printed out the five least-weight cases, including component weights, insulation thicknesses, the total heat leak through each element, and the critical design condition (i.e., launch, end of ascent heating, or end of mission).

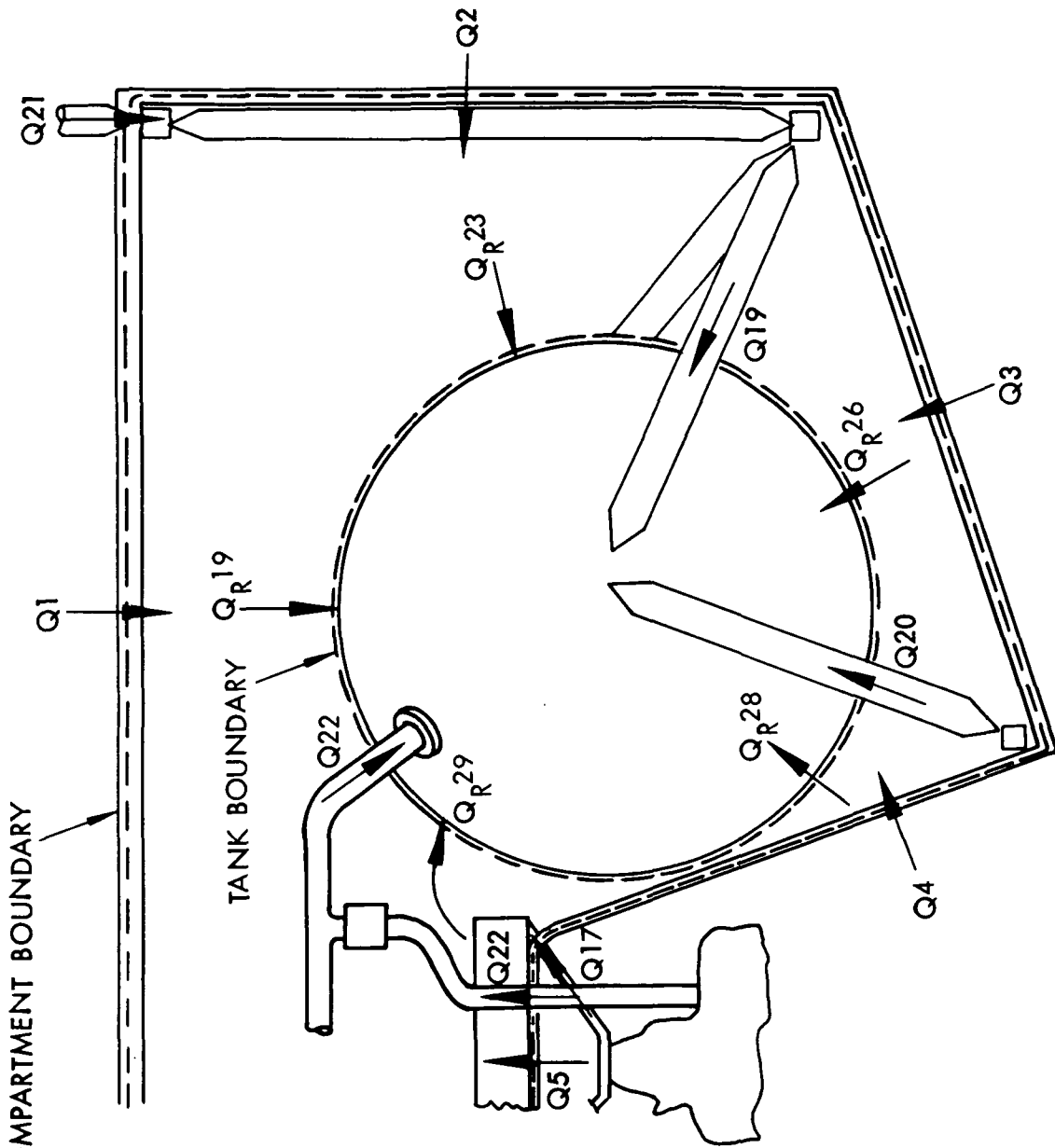
The results obtained are discussed in the following paragraphs:

A preliminary study was made on Vehicle 2-3 to validate the approach. One matter of concern was that the heat leak through individual elements in a surface bounding a propellant compartment was not directly equal to the heat leak reaching the tank from each element. Some of the heat could flow by conduction and radiation to other elements in the surface. However, the total heat flow to the tank had to equal the heat entering the compartment, since the tank was the only heat sink in the system. The TATE program calculated the amount of heat entering the compartment rather than the actual elemental heat leaks conducted or radiated to the tank. A numerical check was made to verify that these two approaches would result in the same total heat flow to the tank. Figure 1.2-22 shows the results. The total heat leak, as expected, was equal within a small amount attributable to cut-off on the thermal convergence to steady state. The plumbing heat leaks, such as Q22 shown, were not included because they would be the same in both summations.

Another concern was the use of constant boundary temperatures with varying insulation thickness in the TATE program. The surface temperatures varied somewhat with insulation thickness. For example, the steady state temperatures from the BETA program, for the nodal arrangement in Figure 1.2-23 are given in Table 1.2-7. All nodes except the constant value used for propellant temperature (Node 11) showed some variation with insulation thickness, with the strongest influence at Nodes 3 and 6. Figure 1.2-24 shows the heat transfer through the insulation, as calculated by the BETA program, compared to the TATE program method, where heat flow was inversely proportional to thickness because the boundary temperatures were not changed. Figure 1.2-25 shows a comparison for heat leaks which were constants in the TATE program. The reasonably good agreement justified the constant boundary temperature approach in the TATE program.

The temperatures used were generated by the BETA program based on a set of estimated insulation thicknesses. Since the optimum thicknesses could differ significantly, it was expected that a second iteration through the BETA and TATE programs could be necessary in some cases. This was done only for the selected configuration of structure, insulation, and meteoroid protection, for a given vehicle concept.

A further trade that was necessary before beginning the analysis and optimization of each vehicle was to select the insulation(s) to be used. Optimum system weights were generated with three insulation material combinations on Vehicle 1-14 to aid in the selection. The Vehicle 1-14 configuration included an aluminum truss, insulation inside the structure, and 4 in (10.2 cm) payload separation. The insulation candidates and the optimized weights are given in Table 1.2-8. The first case used aluminized mylar/nylon net insulation with room temperature outgassing data, which had served as a baseline previously. The second case was a "low-outgassing" aluminized mylar/nylon net. Some IRAD test data showed that the amount of outgassing from nylon net was extremely sensitive to temperature. Extrapolation of this data to temperatures representative of the bulk of the insulation indicated that the outgassing could be as low as aluminized mylar at room temperature. The aluminized mylar outgassing data was used in the analysis for the "low-outgassing" net insulation. Other test data showed that dacron net (Style B2A, Apex Mills) had very low outgassing. However, since available thermal conductivity data was for aluminized mylar/nylon net, this was selected with the assumption that a like netting of dacron could be substituted without changing thermal performance significantly. The third case was the same as the second case, except NRC-2 was substituted for the net-type insulation on the vertical sidewall. The NRC-2 was used only on the vertical surface to avoid compaction of the layers due to gravity and flight loads. A potential fourth candidate was aluminized mylar/silk net. However, the ascent heating analysis for this insulation was not done for the full range of thicknesses and outgassing path lengths. Also, the thermal conductivity appeared to be somewhat higher than with the nylon net spacer, and the weight was expected to be greater than Case 2.



THRU TANK BOUNDARY:

	BTU/HR	WATTS
$Q_{R19}$	+2.732	.800
$Q_{R23}$	+2.153	.631
$Q_{R26}$	+0.391	.115
$Q_{R28}$	+0.245	.072
$Q_{R29}$	+0.017	.005
$Q_{19}$	+0.029	.008
$Q_{20}$	+0.012	.003
$\Sigma Q$	+5.579	1.634

THRU COMPARTMENT BOUNDARY:

	BTU/HR	WATTS
$Q_1$	+3.237	.948
$Q_2$	-0.346	-.101
$Q_3$	-0.358	-.105
$Q_4$	-0.130	-.038
$Q_5$	-0.006	-.002
$Q_{17}$	-0.565	-.165
$Q_{21}$	+3.740	1.095
$\Sigma Q$	+5.572	1.632

Figure 1.2-22: COMPARISON OF HEAT LEAKS THRU COMPARTMENT WALL TO HEAT LEAKS TO TANK

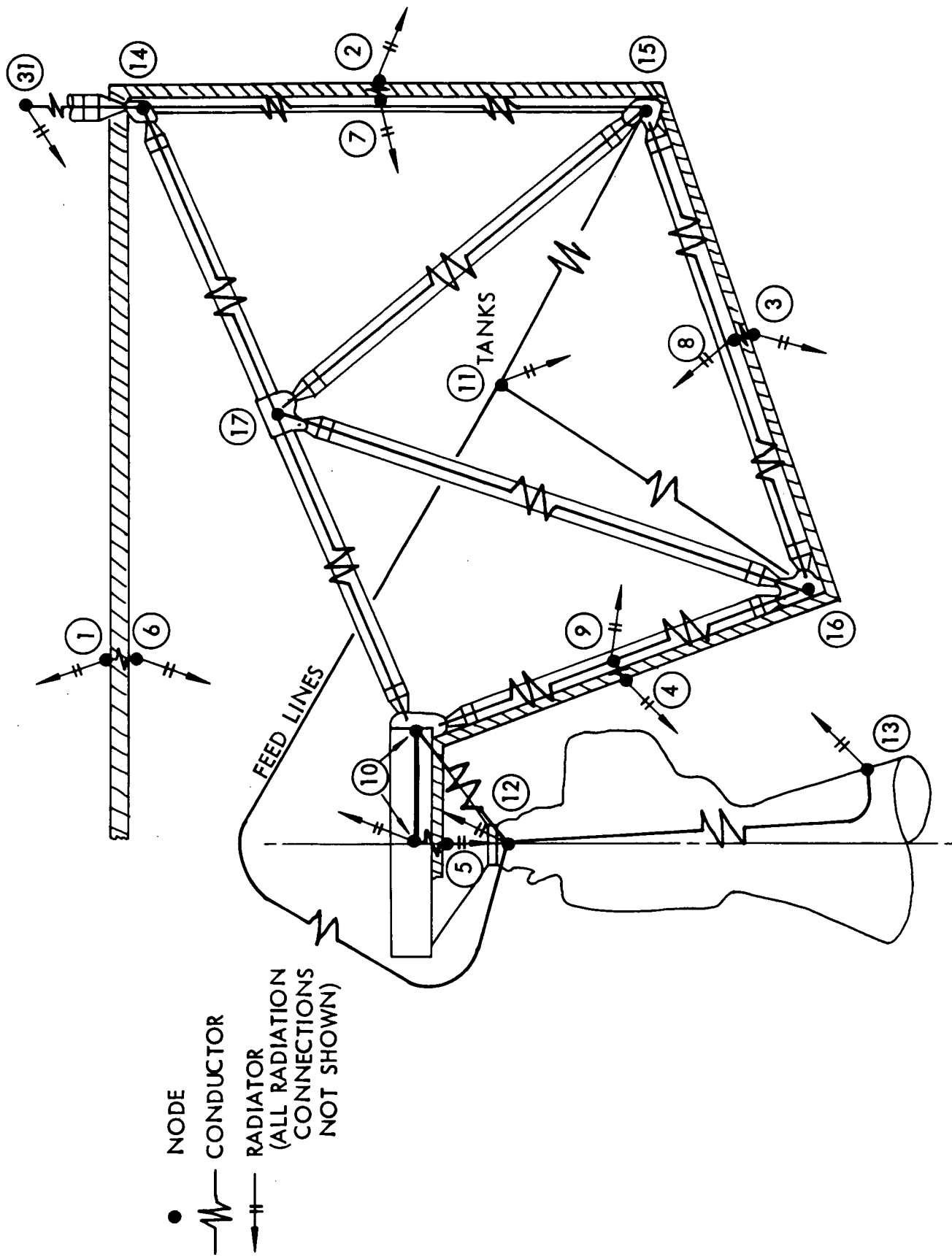


Figure 1.2-23: VEHICLE 2-3 NODAL NETWORK (INSULATION OUTSIDE)

Table 1.2-7: TEMPERATURES FOR SEVERAL INSULATION THICKNESS - VEHICLE 2-3

NODE NO.	TEMPERATURES																			
	ALUMINUM TRUSS STRUCTURE, *D = 4", (10cm) INSULATION OUTSIDE																			
	** D1 →	0.6	1.2	0.3	0.3	D2 →	0.3	0.6	0.15	0.3	D3 →	0.3	0.6	0.15	0.3	D4 →	0.3	0.6	0.15	0.3
		°R	°K	°R	°K	°R	°K	°R	°K	°R	°K	°R	°K	°R	°K	°R	°K	°R	°K	
1		511.8	284.3	512.4	284.7	510.6	283.7	510.6	283.7											
2		159.8	88.8	159.6	88.7	160.0	88.9	159.8	88.8											
3		59.9	33.3	52.1	28.9	69.5	38.6	60.5	33.6											
4		86.8	48.2	83.4	46.3	92.2	51.2	87.6	48.7											
5		133.2	74.0	132.3	73.5	134.8	74.9	134.7	74.8											
6		214.0	118.9	197.8	109.9	237.2	131.8	237.6	132.0											
7		191.1	106.2	191.2	106.2	190.8	106.0	194.1	107.8											
8		186.2	103.4	186.8	103.8	185.1	102.8	189.4	105.2											
9		184.9	102.7	185.3	102.9	184.0	102.2	187.9	104.4											
10		185.0	102.7	185.4	103.0	184.3	102.4	187.9	104.4											
11		170.0	94.4	170.0	94.4	170.0	94.4	170.0	94.4											
12		136.0	75.6	135.7	75.4	136.6	75.9	137.6	76.4											
13		85.1	47.3	84.1	46.7	87.0	48.3	85.8	47.7											
14		195.3	108.5	195.5	108.6	195.0	108.3	198.2	110.1											
15		190.2	105.7	190.4	105.8	189.7	105.4	193.2	107.3											
16		186.4	103.6	186.9	103.8	185.6	103.1	189.5	105.3											
17		189.3	105.2	189.6	105.3	188.7	104.8	192.3	106.8											

\* Payload Separation

\*\* Insulation Thickness at Locations Shown in Figure 1.2-23

Table 1.2-8: VEHICLE 1-14 SYSTEM WEIGHTS WITH THREE INSULATION COMBINATIONS, ALUMINUM TRUSS STRUCTURE, INSULATION INSIDE, 4" (10 cm) PAYLOAD SEPARATION.

	COMPONENT WEIGHT					
	CASE 1		CASE 2		CASE 3	
	lb	kg	lb	kg	lb	kg
Insulation	23.51	10.66	10.31	4.68	9.62	4.36
Fuel Vapor	.48	.22	.47	.21	.47	.21
Oxidizer Vapor	1.27	.58	1.04	.47	.89	.40
Helium (Oxidizer Only)	2.57	1.17	2.27	1.03	2.08	.94
Helium Tank	7.05	3.20	6.23	2.83	5.70	2.59
Fuel Tank	22.41	10.17	22.21	10.07	22.21	10.07
Oxidizer Tank	15.21	6.90	14.99	6.80	14.90	6.76
<b>TOTAL</b>	<b>72.50</b>	<b>32.90</b>	<b>57.52</b>	<b>26.09</b>	<b>55.87</b>	<b>25.33</b>

Case 1 - 0.15 Mil Aluminized Mylar/Nylon Net

Case 2 - Same as 1 But With Outgassing Comparable To NRC-2 At Room Temperature

Case 3 - Same As 2 But With .25 Mil NRC-2 On The Vertical Sidewall

Optimization Program Heat  
Flow With Run No.  
C 1016-1 as Data Base

RUN NO.	SYM.	INSUL. THICK.			
		$\delta 1$		$\delta 2$ THRU $\delta 5$	
		In	cm	In	cm
C1016-1	○	0.6	1.5	0.3	.8
-4	◇	1.2	3.0	0.6	1.5
-5	▽	0.3	.8	0.15	.4
-6	□	0.3	.8	0.3	.8

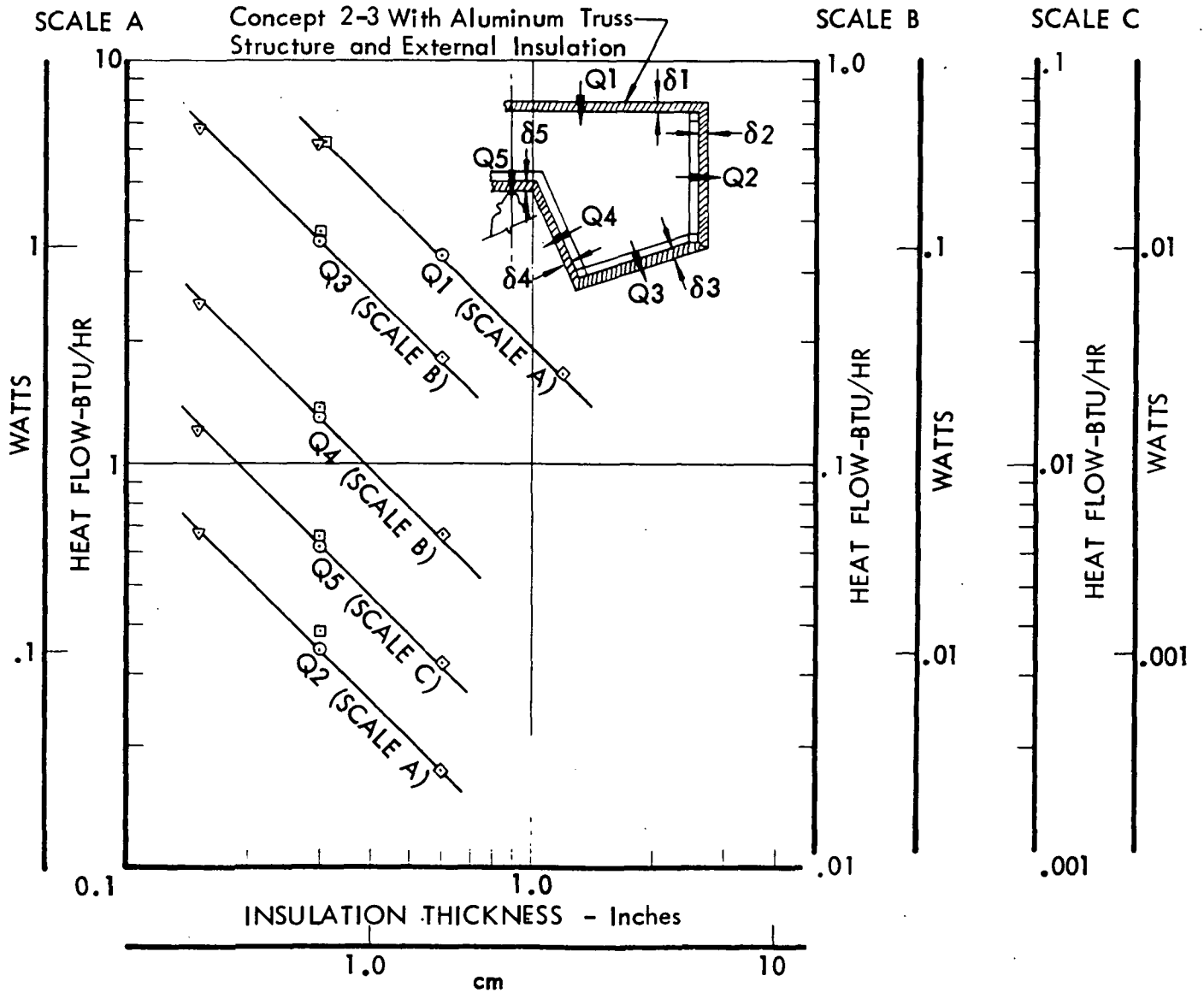


Figure 1.2-24: COMPARISON OF OPTIMIZATION PROGRAM HEAT TRANSFER ANALYSIS METHOD TO THERMAL ANALYZER RESULTS - INSULATION THICKNESS DEPENDENT HEAT TRANSFER

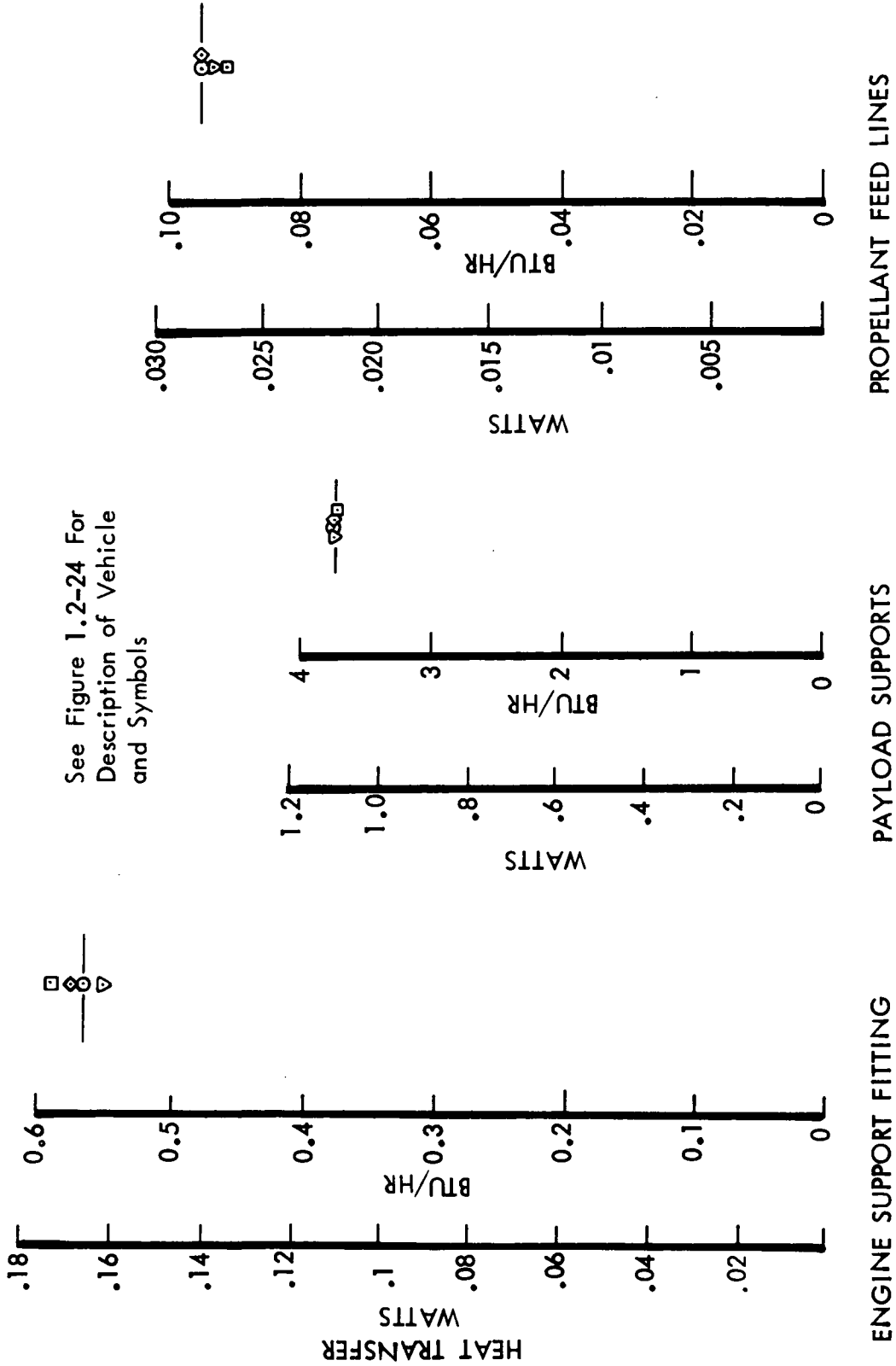


Figure 1.2-25: COMPARISON OF OPTIMIZATION PROGRAM HEAT TRANSFER ANALYSIS METHOD TO THERMAL ANALYZER RESULTS - HEAT LEAKS "INDEPENDENT" OF INSULATION THICKNESS

The optimum weights in Table 1.2-8 showed that the room temperature nylon net outgassing (Case 1) caused a significant weight penalty. The use of NRC-2 on the vertical sidewall gave the lightest result but the weight saving compared to Case 2 was small.

It was concluded from this study that the "low outgassing" aluminized mylar/nylon net insulation would be used for the preliminary design analyses and optimizations.

Vehicle 1-14 Results: The thermal model configuration for this vehicle is shown in Figure 1.2-26. The top deck and compartment separation blankets in the figure combine MLI and secondary structure to support the MLI, derived from the layouts. The penetration conductances for fluid lines and tank supports are given in Table 1.2-9. Fluid lines were stainless steel and tank supports were fiberglass. Vehicle structural conductances for three types of construction materials and three payload heights are shown in Table 1.2-10.

The temperatures calculated for the 19 nodes of Figure 1.2-26 are listed in Tables 1.2-11 through 1.2-16. Six different configurations are represented. These are (1) corrugated shell with MLI inside, (2) corrugated shell with MLI outside, (3) truss structure with MLI inside, (4) truss structure with MLI outside, (5) truss structure with MLI inside and one shadow shield on the top deck, and (6) truss structure with MLI outside on the top deck and inside elsewhere. Each of these configurations was evaluated for three structural materials; aluminum, fiberglass/epoxy and carbon/epoxy.

Elevating the payload tended to reduce the top deck temperature. The use of fiberglass structure with internal insulation also reduced temperatures aft along the vehicle because of the low conductivity. All configurations experienced a large reduction in structure temperatures on aft facing surfaces because of their ability to radiate to space. The use of one shadow shield halfway between the payload and the top deck blanket reduced temperatures on the top deck significantly.

The system weight (tanks, insulation, helium, helium tank and propellant vapor) optimization data for Vehicle 1-14 is listed in Table 1.2-17 and shown graphically in Figure 1.2-27. The entry in Table 1.2-17 identified as " $T_{MIN}F$ " was a case which was run using the minimum insulation thickness required for meteoroid protection on external surfaces. Therefore, the system weight for this case is not directly comparable to the other weights shown. The table shows insulation thicknesses and tank gages. The insulation thicknesses are converted to layer quantity by using the layer ratios of Table 1.1-9. The table also shows the weight of each MLI blanket and the weights of fuel and oxidizer tanks. Weights not shown but included in the total are for the helium, helium tank and propellant vapor.

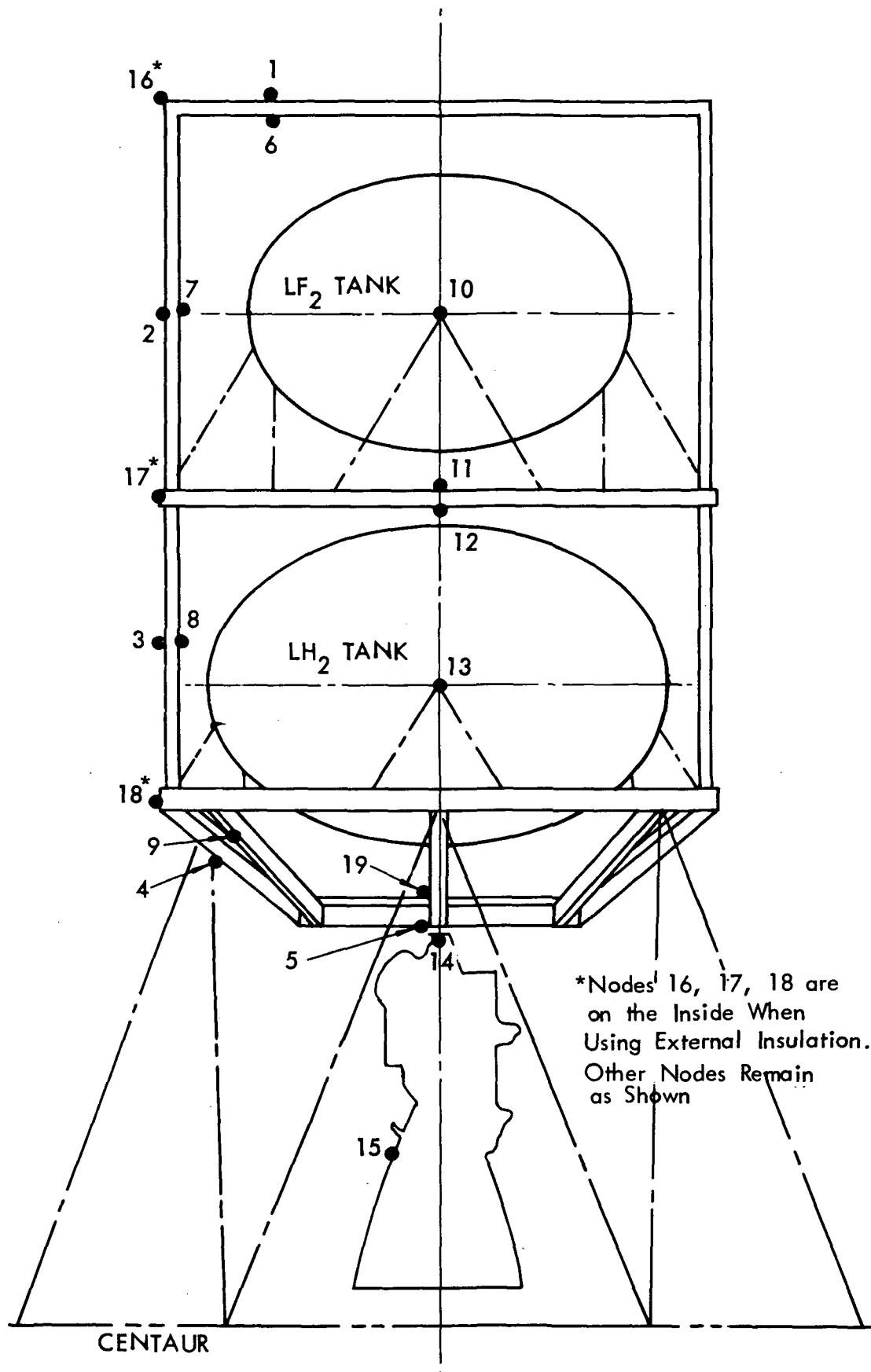


Figure 1.2-26: VEHICLE 1-14 NODE NUMBERS

Table 1.2-9: PENETRATION CONDUCTANCES CONFIGURATION 1-14

PENETRATION	LENGTH		DIAMETER		AREA		CONDUCTANCE		TANK NODE NO.	VEHICLE NODE NO.	
	in	cm	in.	cm	in <sup>2</sup>	cm <sup>2</sup>	Btu/hr-°R Watts/K	°K		INSULATION INSIDE	INSULATION OUTSIDE
Oxidizer Tank Supports	10.50	26.7	2.00	5.08	6 x 0.200 = 1.20	(7.74)	.00144	.000243	10	17	17
Fuel Tank Supports	16.50	41.9	2.00	5.08	6 x .094 = 0.564	(3.64)	.00029	.000047	13	18	18
Oxidizer Vent	27	68.6	2.0	5.08	0.2199	1.419	.00189	.000308	10	2	7
Oxidizer Fill	28	71.1	1.5	3.8	0.0942	.6077	.00073	.000119	10	17	17
Oxidizer Feed	42	107.0	1.6	4.1	0.1759	1.135	.00057	.000093	10	13	13
Oxidizer Pressurant	40	102.0	0.25	0.64	0.0385	.2484	.00022	.000036	10	2	7
Fuel Vent	26	66.0	2.0	5.1	0.2199	1.419	.00012	.000020	13	17	17
Fuel Fill	31	78.0	2.0	5.1	0.2199	1.419	.00077	.000013	13	18	18
Fuel Feed	45	114.0	1.6	4.1	0.1759	1.135	.00152	.000247	13	14	14
Fuel Pressurant	23	58.0	2.1	5.3	0.2309	1.490	.00010	.000016	13	14	14
Fuel Pressurant	23	58.0	0.5	1.27	0.0314	.2026	.00010	.000016	13	14	14

Table 1.2-10: VEHICLE STRUCTURE CONDUCTANCES CONFIGURATION I-14  
INSULATION OUTSIDE ONLY

LOCATION	STRUCTURE CONFIGURATION	STRUCTURE MATERIAL	EXTERNAL NODE	INTERNAL NODE	CONDUCTANCE Btu/Hr-R/Watts/°K
Sidewall - Oxidizer Compartment	Corrugated Shell Payload Separation 4" (10cm)	Aluminum	17	7	.7321
		Glass		8	.9526
	Corrugated Shell Payload Separation 14" (36cm)	Aluminum		7	.00530
		Carbon		8	.00380
	Corrugated Shell Payload Separation 35" (89cm)	Aluminum		7	.04230
		Carbon		8	.05656
	Corrugated Shell Payload Separation	Aluminum		7	.6823
		Glass		8	.8916
	Corrugated Shell Payload Separation	Aluminum		7	.00314
		Carbon		8	.00371
	Corrugated Shell Payload Separation	Aluminum		7	.03643
		Carbon		8	.04984
Corrugated Shell Payload Separation	Aluminum		7	.6504	
	Carbon		8	.8504	
Corrugated Shell Payload Separation	Aluminum		7	.00306	
	Carbon		8	.00363	
Corrugated Shell Payload Separation	Aluminum		7	.03451	
	Carbon		8	.04766	
Sidewall - Fuel Compartment	Corrugated Shell 4" (10cm) Payload Separation	Aluminum	14	19	.09669
		Glass			.04318
	Corrugated Shell 14" (36cm) Payload Separation	Aluminum			.05121
		Carbon			.08859
	Corrugated Shell 35" (89cm) Payload Separation	Aluminum			.03926
		Carbon			.04736
	Corrugated Shell 4" (10cm) Payload Separation	Aluminum			.08257
		Carbon			.01343
	Corrugated Shell 14" (36cm) Payload Separation	Aluminum			.03596
		Carbon			.00771
	Corrugated Shell 35" (89cm) Payload Separation	Aluminum			.04304
		Carbon			.00700
Corrugated Shell 4" (10cm) Payload Separation	Aluminum	31	16	.01139	
	Glass			.01424	
Corrugated Shell 14" (36cm) Payload Separation	Aluminum			.01211	
	Carbon			.00197	
Corrugated Shell 35" (89cm) Payload Separation	Aluminum			.00184	
	Carbon			.00206	
Corrugated Shell Payload Separation	Aluminum			.00336	
	Carbon			.00189	
Corrugated Shell Payload Separation	Aluminum			.00062	
	Carbon			.00102	
Corrugated Shell Payload Separation	Aluminum			.00067	
	Carbon			.00109	
Corrugated Shell Payload Separation	Aluminum	31	16	.00064	
	Carbon			.00105	
Engine Support Fitting Payload Support Struts (To Oxidizer Compartment)	Corrugated Shell 4" (10cm) Payload Separation	Aluminum	14	19	.09669
		Glass			.04318
	Corrugated Shell 14" (36cm) Payload Separation	Aluminum			.05121
		Carbon			.08859
	Corrugated Shell 35" (89cm) Payload Separation	Aluminum			.03926
		Carbon			.04736
	Corrugated Shell 4" (10cm) Payload Separation	Aluminum			.08257
		Carbon			.01343
	Corrugated Shell 14" (36cm) Payload Separation	Aluminum			.03596
		Carbon			.00771
	Corrugated Shell 35" (89cm) Payload Separation	Aluminum			.04304
		Carbon			.00700
Corrugated Shell 4" (10cm) Payload Separation	Aluminum	31	16	.01139	
	Glass			.01424	
Corrugated Shell 14" (36cm) Payload Separation	Aluminum			.01211	
	Carbon			.00197	
Corrugated Shell 35" (89cm) Payload Separation	Aluminum			.00184	
	Carbon			.00206	
Corrugated Shell Payload Separation	Aluminum			.00336	
	Carbon			.00189	
Corrugated Shell Payload Separation	Aluminum			.00062	
	Carbon			.00102	
Corrugated Shell Payload Separation	Aluminum			.00067	
	Carbon			.00109	
Corrugated Shell Payload Separation	Aluminum	31	16	.00064	
	Carbon			.00105	
Payload Support Struts (To Oxidizer Compartment)	Corrugated Shell 4" (10cm) Payload Separation	Aluminum	14	19	.09669
		Glass			.04318
	Corrugated Shell 14" (36cm) Payload Separation	Aluminum			.05121
		Carbon			.08859
	Corrugated Shell 35" (89cm) Payload Separation	Aluminum			.03926
		Carbon			.04736
	Corrugated Shell 4" (10cm) Payload Separation	Aluminum			.08257
		Carbon			.01343
	Corrugated Shell 14" (36cm) Payload Separation	Aluminum			.03596
		Carbon			.00771
	Corrugated Shell 35" (89cm) Payload Separation	Aluminum			.04304
		Carbon			.00700
Corrugated Shell 4" (10cm) Payload Separation	Aluminum	31	16	.01139	
	Glass			.01424	
Corrugated Shell 14" (36cm) Payload Separation	Aluminum			.01211	
	Carbon			.00197	
Corrugated Shell 35" (89cm) Payload Separation	Aluminum			.00184	
	Carbon			.00206	
Corrugated Shell Payload Separation	Aluminum			.00336	
	Carbon			.00189	
Corrugated Shell Payload Separation	Aluminum			.00062	
	Carbon			.00102	
Corrugated Shell Payload Separation	Aluminum			.00067	
	Carbon			.00109	
Corrugated Shell Payload Separation	Aluminum	31	16	.00064	
	Carbon			.00105	





Table 1.2-15: COAST PHASE TEMPERATURES, VEHICLE 1-14

NODE NO.	TEMPERATURES											
	TRUSS SIDEWALL STRUCTURE, INSULATION INSIDE, ONE SHADOW SHIELD											
	14" PAYLOAD SEPARATION (36 cm)						35" PAYLOAD SEPARATION (89 cm)					
	ALUMINUM		FIBERGLASS		CARBON/ EPOXY		ALUMINUM		FIBERGLASS		CARBON/ EPOXY	
°R	°K	°R	°K	°R	°K	°R	°K	°R	°K	°R	°K	
1	193.6	107.6	345.4	191.9	316.0	175.6	166.6	92.6	269.9	149.9	252.3	140.2
2	161.0	89.4	159.0	88.3	161.1	89.5	143.2	79.6	142.2	77.6	143.7	79.8
3	130.2	72.3	125.3	69.6	125.4	69.7	118.5	65.8	113.8	63.2	113.9	63.3
4	97.1	53.9	46.1	25.6	58.9	32.7	91.3	50.7	41.6	23.1	54.2	30.1
5	94.9	52.7	65.5	36.4	64.7	35.9	89.0	49.4	56.2	31.2	56.9	31.6
6	166.0	92.2	180.2	100.1	176.7	98.2	164.0	91.1	171.3	95.2	169.8	94.3
7	164.0	91.1	164.8	91.6	164.9	91.6	161.1	89.5	161.5	89.7	161.6	89.8
8	90.7	50.5	88.8	49.3	88.8	49.3	86.0	47.8	84.1	46.7	84.1	46.7
9	69.5	38.6	44.6	24.8	51.3	28.5	66.8	37.1	42.1	23.4	48.7	27.1
10	165.0	91.7	165.0	91.7	165.0	91.7	165.0	91.7	165.0	91.7	165.0	91.7
11	159.0	88.3	160.1	88.9	159.8	88.8	158.3	87.9	158.8	88.2	158.8	88.2
12	93.8	52.1	93.9	52.2	93.8	52.1	93.0	51.7	92.9	51.6	92.8	51.6
13	40.0	22.2	40.0	22.2	40.0	22.2	40.0	22.2	40.0	22.2	40.0	22.2
14	92.3	51.3	66.0	36.7	65.3	36.3	86.3	47.9	56.6	31.4	57.3	31.8
15	81.8	45.4	73.5	40.8	73.9	41.1	72.9	40.5	62.0	34.4	62.6	34.8
16	183.7	102.1	365.3	197.9	273.0	151.7	159.3	88.4	288.6	160.3	222.5	123.6
17	144.7	80.4	144.3	80.2	142.5	79.2	129.7	72.1	132.3	73.5	128.4	71.3
18	121.1	67.3	95.3	52.9	105.2	58.4	111.3	61.8	87.0	48.3	95.1	52.8
19	66.1	36.7	52.6	29.2	52.6	29.2	63.6	35.3	48.3	26.8	48.9	27.2

Table 1.2-16: COAST PHASE TEMPERATURES, VEHICLE 1-14

NODE NO.	TEMPERATURES											
	TRUSS STRUCTURE SIDEWALL, INSULATION OUTSIDE ON TOP, INSIDE ELSEWHERE											
	4" (10 cm) PAYLOAD SEPARATION				14" (36 cm) PAYLOAD SEPARATION				35" (89 cm) PAYLOAD SEPARATION			
	ALUMINUM		FIBERGLASS/ EPOXY		ALUMINUM		FIBERGLASS/ EPOXY		ALUMINUM		FIBERGLASS/ EPOXY	
°R	°K	°R	°K	°R	°K	°R	°K	°R	°K	°R	°K	
1	509.4	283.0	509.4	283.0	486.3	270.2	486.3	270.2	435.9	242.2	436.0	242.2
2	170.8	94.9	169.0	93.9	156.6	87.0	158.9	88.3	139.8	77.7	142.2	79.0
3	136.1	75.6	130.7	72.6	129.0	71.7	125.3	69.6	117.5	65.3	113.8	63.2
4	100.0	55.6	48.6	27.0	96.5	53.6	46.1	25.6	90.7	50.4	41.6	23.1
5	97.9	54.4	70.6	39.2	94.4	52.4	65.5	36.4	88.6	49.2	56.2	31.2
6	197.7	109.8	223.6	124.2	167.4	93.0	209.7	116.5	149.6	83.1	197.8	109.9
7	168.4	93.6	171.4	95.2	163.4	90.8	167.9	93.3	159.7	88.7	164.0	91.1
8	93.2	51.8	91.3	50.7	90.3	50.2	89.0	49.4	85.5	47.5	84.3	46.8
9	70.9	39.4	46.1	25.6	69.3	38.5	44.7	24.8	66.6	37.0	42.2	23.4
10	165.0	91.7	165.0	91.7	165.0	91.7	165.0	91.7	165.0	91.7	165.0	91.7
11	162.3	90.2	165.8	92.1	159.0	88.3	163.4	90.8	157.3	87.4	161.5	89.7
12	95.3	52.9	96.1	53.4	93.8	52.1	95.0	52.8	92.6	51.4	93.8	52.1
13	40.0	22.2	40.0	22.2	40.0	22.2	40.0	22.2	40.0	22.2	40.0	22.2
14	95.5	53.1	71.1	39.5	91.8	51.0	65.9	36.6	85.8	47.7	56.6	31.4
15	87.1	48.4	79.9	44.4	81.7	45.4	73.5	40.8	72.7	40.4	62.0	34.4
16	196.8	109.3	460.0	255.6	164.9	91.6	313.0	173.9	146.9	81.6	261.3	145.2
17	152.4	84.6	151.0	83.9	141.9	78.8	144.2	80.1	127.6	70.9	132.3	73.5
18	126.2	70.1	98.8	54.9	120.1	66.7	95.3	52.9	110.3	61.3	87.0	48.3
19	67.4	37.4	54.9	30.5	65.9	36.6	52.6	29.2	63.4	35.2	48.3	26.8

Table 1.2-17: OPTIMUM SYSTEM WEIGHTS VEHICLE 1-14

STRUCTURE	MATERIAL	PAYLOAD SEPARATION		INSULATION THICKNESS						INSULATION WEIGHT		TANK GAGE		TANK WEIGHT		SYSTEM WEIGHT		REMARKS					
		in	cm	TOP	SIDE		INSIDE	SIDE RUEL	BOTTOM	lb	kg	RUEL	OXIDIZER	in	cm	FUEL	OXIDIZER		lb	kg			
					OXIDIZER	RUEL															in	cm	lb
Corrugated Shell	Aluminum	4	10	.49	1.24	.08	.20	.08	.20	.01	.03	8.54	3.88	.025	.064	22.39	10.16	14.97	6.79	55.8	25.3	Insulation Outside	
	Fiberglass	4	10	.52	1.32	.06	.15	.04	.10	.12	.30	9.92	4.51	.025	.064	22.21	10.07	15.08	6.84	58.2	26.4		
	Aluminum	14	36	.42	1.07	.08	.20	.13	.33	.10	.25	8.79	3.99	.025	.064	22.23	10.08	14.66	6.65	53.3	24.2		
	Fiberglass	14	36	.47	1.19	.07	.18	.04	.10	.09	.23	9.15	4.15	.025	.064	22.33	10.13	14.85	6.74	55.1	25.0		
	Aluminum	35	89	.36	.91	.07	.18	.08	.20	.06	.15	.03	7.02	3.19	.025	.064	22.21	10.07	14.54	6.60	50.6		23.0
	Fiberglass	35	89	.34	.86	.06	.15	.03	.08	.10	.25	7.63	3.46	.025	.064	22.32	10.13	14.70	6.67	52.5	23.8		
Truss	Aluminum	4	10	.52	1.32	.06	.15	.04	.10	.12	.30	9.92	4.50	.025	.064	22.20	10.07	15.10	6.83	58.4	26.5	Insulation Outside	
	Fiberglass	4	10	.47	1.19	.07	.18	.11	.28	.09	.23	8.84	4.01	.025	.064	22.30	10.12	14.73	6.68	53.9	24.4		
	Aluminum	14	36	.48	1.22	.08	.20	.04	.10	.11	.28	9.41	4.27	.025	.064	22.20	10.07	14.86	6.74	55.3	25.1		
	Fiberglass	35	89	.37	.94	.07	.18	.07	.18	.05	.13	7.60	3.45	.025	.064	22.25	10.09	14.54	6.60	51.2	23.3		
	Aluminum	35	89	.36	.91	.05	.08	.04	.10	.09	.23	7.36	3.34	.025	.064	22.20	10.07	14.77	6.70	52.7	23.9		
	Fiberglass	4	10	.43	1.09	.09	.23	.05	.13	.10	.25	11.28	5.13	.025	.064	22.28	10.11	14.88	6.75	55.7	25.3		
Truss	Aluminum	4	10	.51	1.30	.09	.23	.04	.10	.12	.30	10.35	4.70	.025	.064	22.21	10.07	14.97	6.79	57.4	26.0	Insulation On Top Outside Elsewhere	
	Fiberglass	4	10	.40	1.02	.07	.18	.06	.15	.09	.23	8.25	3.75	.025	.064	22.21	10.07	14.45	6.55	51.2	23.2		
	Aluminum	35	89	.33	.84	.05	.13	.04	.10	.10	.25	7.21	3.27	.025	.064	22.23	10.08	14.79	6.71	52.6	23.9		
	Fiberglass	14	36	.33	.86	.15	.04	.05	.13	.10	.25	6.21	2.82	.025	.064	22.18	10.06	14.75	6.69	52.1	23.6		
	Aluminum	35	89	.33	.86	.15	.04	.05	.13	.10	.25	5.96	2.71	.025	.064	22.21	10.07	14.48	6.57	49.1	22.3		
	Fiberglass	35	89	.19	.48	.06	.15	.04	.10	.10	.25	6.33	2.87	.025	.064	22.19	10.07	14.53	6.59	49.8	22.6		
Corrugated Shell	Aluminum	4	10	.41	1.04	.12	.30	.06	.15	.14	.36	11.30	5.13	.025	.064	22.23	10.08	14.93	6.77	57.9	26.3	Insulation Inside	
	Fiberglass	4	10	.45	1.14	.09	.23	.04	.10	.11	.28	9.77	4.44	.025	.064	22.26	10.10	14.88	6.75	55.9	25.4		
	Aluminum	14	36	.34	.86	.11	.28	.06	.15	.14	.36	9.94	4.51	.025	.064	22.20	10.07	14.91	6.76	56.3	25.5		
	Fiberglass	14	36	.42	1.07	.06	.15	.04	.10	.11	.28	8.50	3.86	.025	.064	22.21	10.07	14.88	6.75	54.6	24.8		
	Aluminum	35	89	.25	.64	.08	.20	.05	.13	.12	.30	8.10	3.68	.025	.064	22.21	10.07	14.80	6.71	53.6	24.3		
	Fiberglass	35	89	.32	.81	.05	.13	.04	.10	.09	.23	7.08	3.21	.025	.064	22.21	10.07	14.78	6.70	52.4	23.8		
Truss	Aluminum	4	10	.39	.99	.12	.30	.06	.15	.12	.30	10.23	4.64	.025	.064	22.23	10.08	14.99	6.80	57.5	26.1	Insulation Inside	
	Fiberglass	4	10	.46	1.17	.08	.20	.04	.10	.11	.28	9.38	4.26	.025	.064	22.20	10.07	14.92	6.77	55.8	25.3		
	Aluminum	14	36	.36	.91	.08	.20	.04	.10	.13	.33	9.35	4.25	.025	.064	22.20	10.07	14.95	6.78	56.2	25.5		
	Fiberglass	14	36	.42	1.07	.07	.18	.05	.13	.10	.25	8.49	3.85	.025	.064	22.21	10.07	14.88	6.75	54.6	24.8		
	Aluminum	35	89	.27	.69	.08	.20	.06	.15	.10	.25	7.66	3.48	.025	.064	22.21	10.07	14.85	6.74	53.5	24.3		
	Fiberglass	35	89	.33	.84	.07	.18	.05	.13	.08	.20	7.43	3.37	.025	.064	22.22	10.08	14.75	6.69	52.6	23.9		
Truss	Aluminum	14	36	.36	.91	.19	.48	.05	.13	.20	.51	10.25	4.64	.025	.064	22.23	10.08	14.99	6.80	57.5	26.1	Insulation Inside NRC-2 On Side ALUM/Silk Net ALUM/Silicaed Foam NRC-2 on Side + ALUM/Silk Net + ALUM/Silicaed Foam +	
	Fiberglass	14	36	.55	1.40	.15	.38	.08	.20	.17	.43	14.36	6.44	.025	.064	22.23	10.08	14.99	6.80	57.5	26.1		
	Aluminum	14	36	.92	2.34	.23	.58	.15	.33	.27	.69	21.53	9.74	.025	.064	22.23	10.08	14.99	6.80	57.5	26.1		
	Fiberglass	14	36	.32	.81	.76	1.93	.02	.05	.77	1.96	33.84	15.33	.025	.064	22.23	10.08	14.99	6.80	57.5	26.1		
	Aluminum	14	36	.46	1.17	.77	1.96	.04	.10	.77	1.96	33.84	15.33	.025	.064	22.23	10.08	14.99	6.80	57.5	26.1		
	Fiberglass	14	36	.86	2.18	.58	1.47	.08	.20	.58	1.47	60.13	27.23	.025	.064	22.23	10.08	14.99	6.80	57.5	26.1		

↑ Designed by Minimum Gage    + Minimum Thickness Fixed    ↓ Insulation Inside, T<sub>min</sub>



Table 1.2-18: OPTIMUM SYSTEM WEIGHTS, VEHICLE 1-2B

STRUCTURE	MATERIAL	PAYLOAD SEPARATION		INSULATION THICKNESS						TANK GAGE			SYSTEM WEIGHT							
		in	cm	TOP OXID.	SIDE OXID.	INSIDE		SIDE FUEL	BOT FUEL	FUEL	OXIDIZER		lb	kg						
						in	cm				in	cm				in	cm			
Truss	Aluminum	4	10	.57	1.45	.16	.41	.08	.12	.30	.14	.36	.075	.064	.025*	.064*	79.3	36.0	Insulation Inside	
	Fiberglass	4	10	.44	1.12	.09	.23	.05	.07	.18	.14	.36	.025*	.064*	.025*	.064*	68.2	30.9		
	Aluminum	60	152	.35	.89	.09	.23	.02	.05	.10	.25	.13	.025*	.064*	.025*	.064*	67.3	30.5		
Corrugated Shell	Aluminum	4	10	.55	1.40	.16	.41	.08	.13	.33	.16	.40	.025*	.064*	.025*	.064*	81.6	37.0	Insulation Inside	
	Fiberglass	4	10	.48	1.22	.09	.23	.05	.08	.20	.24	.61	.025*	.064*	.025*	.064*	68.9	31.5		
	Aluminum	60	152	.33	.84	.10	.25	.02	.05	.09	.23	.14	.36	.025*	.064*	.025*	.064*	68.6		31.1
Truss	Aluminum	4	10	.52	1.32	.05	.13	.02	.05	.13	.16	.41	.025*	.064*	.025*	.064*	61.2	27.8	Insulation Outside	
	Fiberglass	4	10	.47	1.19	.08	.20	.03	.08	.05	.13	.06	.15	.025*	.064*	.025*	.064*	66.1		30.0
	Aluminum	60	152	.30	.76	.05	.13	.02	.05	.13	.03	.08	.025*	.064*	.025*	.064*	72.9	33.1		
Corrugated Shell	Aluminum	4	10	.35	.89	.05	.13	.01	.03	.01	.03	.11	.28	.025*	.064*	.025*	.064*	66.6	30.2	Insulation Outside
	Fiberglass	4	10	.51	1.30	.07	.18	.03	.08	.05	.13	.52	1.32	.025*	.064*	.025*	.064*	62.0	28.1	
	Aluminum	60	152	.28	.71	.05	.13	.02	.05	.13	.07	.18	.025*	.064*	.025*	.064*	72.2	32.7		
Truss	Aluminum	4	10	.44	1.12	.08	.20	.04	.07	.18	.04	.10	.23	.025*	.064*	.025*	.064*	68.0	30.8	Insulation Outside on Top, Inside Elsewhere
	Fiberglass	4	10	.48	1.22	.08	.20	.03	.08	.07	.18	.09	.23	.025*	.064*	.025*	.064*	69.7	31.6	
	Aluminum	60	152	.28	.71	.05	.13	.04	.05	.13	.92	2.34	.025*	.064*	.025*	.064*	60.7	27.5		
Truss	Aluminum	4	10	.71	1.80	.33	.84	.31	.79	.34	.86	.86	.86	.025*	.064*	.025*	.064*	105.5	47.9	Insulation Inside
	Fiberglass	24	61	.16	.41	.07	.18	.05	.13	.07	.18	.07	.18	.025*	.064*	.025*	.064*	61.5	27.9	
	Aluminum	24	61	.22	.56	.07	.18	.03	.08	.02	.06	.15	.07	.18	.025*	.064*	.025*	.064*	59.8	
Shell	Aluminum	24	61	.26	.66	.08	.20	.01	.03	.03	.03	.02	.05	.025*	.064*	.025*	.064*	60.1	27.3	Insulation Outside
	Fiberglass	24	61	.26	.66	.07	.18	.01	.03	.02	.05	.13	.28	.025*	.064*	.025*	.064*	61.4	27.9	
	Aluminum	24	61	.20	.51	.06	.15	.02	.05	.03	.23	.58	.025*	.064*	.025*	.064*	57.9	26.3		
Shell	Aluminum	24	61	.24	.61	.06	.15	.01	.03	.02	.05	.13	.15	.025*	.064*	.025*	.064*	60.6	27.5	One Shadow Shield
	Fiberglass	24	61	.24	.61	.06	.15	.01	.03	.02	.05	.13	.15	.025*	.064*	.025*	.064*	60.6	27.5	
	Fiberglass	24	61	.24	.61	.06	.15	.01	.03	.02	.05	.13	.15	.025*	.064*	.025*	.064*	60.6	27.5	

\* Designed By Minimum Gauge

The data of Figure 1.2-27 shows a relatively small variation in system weight for the different approaches examined. The optimizations were performed using centerline dimensions to calculate insulation areas. Due to the small weight differences obtained the actual insulation areas (including the difference between insulation inside and outside the structure) would have some effect on the comparisons. Approximately 0.5 lb (.23 kg) of insulation would be added to the cases with insulation outside, and about the same amount subtracted from the cases with insulation inside. The lightest weight cases were obtained using a shadow shield. The weight of the shield and mounting provisions are not included in the graph.

The payload separation in the graph refers to the distance between top deck insulation and the bottom of the payload.

The thermal system analysis provided a convenient means for further evaluation of MLI material choices. In this case, the influence on system weight was obtained for Vehicle 1-14. The medium payload height was chosen and the multi-layer concepts were; (1) NRC-2 on the sidewall with aluminized mylar/nylon net on the top deck, inside and on the bottom, (2) aluminized mylar/two silk nets, and (3) aluminized mylar/sliced foam. The data points for the 14 in (35.5 cm) payload separation are shown on the graph. None of these approaches were as efficient as the combination of aluminized mylar/nylon net with a shadow shield on the top deck. The sliced foam spacer gave the highest weight, however, total weight differences were slight.

**Vehicle 1-2B Results:** The optimum system weights and dimensions from these analyses are presented in Table 1.2-18. The weights are shown graphically in Figure 1.2-28. The intermediate payload height was omitted in this evaluation to reduce computer run time with the exception of several cases where use of a shadow shield was studied.

The results show that minimum tank gages were obtained in all cases. The least weights were obtained with the high payload position which increased the view to space. The addition of one shadow shield to both truss and corrugated construction was efficient, however, the weight difference ( $\approx 3$  lb (1.4 kg)) was slight and would probably be consumed by the shield and installation weight. Overall, the system weights for this vehicle were greater than for Vehicle 1-14.

**Vehicle 1-2A Results:** This was the inverted version of the preceding vehicle. The large view to space along the conical surface of the top deck was reflected in the lower system weights of Figure 1.2-29. Raising the payload height had a lesser effect in this case.

The optimization data is included in Table 1.2-19.

Vehicle 1-3 Results: The system weight plots are presented in Figure 1.2-30. The data used to construct the plots is included in Table 1.2-20. System weights were significantly greater for this vehicle. Insulation thicknesses on the top deck were over 0.80 in (2.04 cm) in several cases. With the insulation inside there was little difference in system weights between aluminum and fiberglass structure, either for corrugated or truss construction.

Vehicle 1-7 Results: The results are presented in Table 1.2-21 and Figure 1.2-31. This vehicle was only suited for truss construction because of its rectangular configuration. Thick MLI blankets were obtained on the top deck for the low payload case.

Vehicle 2-2 Results: Table 1.2-22 and Figure 1.2-32 show study results. Large insulation thicknesses were derived for the top deck with insulation inside the structure. In these cases the FLOX tank gages also exceeded the minimum design limit. The least weight approach indicated by the graph was with insulation outside of the structure.

Vehicle 2-3 Results: Truss structure was the only method of construction evaluated for the remaining FLOX/CH<sub>4</sub> vehicles. This was because least system weights were obtained for truss structures in the LH<sub>2</sub>/LF<sub>2</sub> vehicle studies and because continuous shells were not weight efficient in the "Vehicle Structure Evaluation". The results for this vehicle are shown in Figure 1.2-33 and Table 1.2-23. System weights were greater than any of the other FLOX/CH<sub>4</sub> vehicles.

Vehicle 2-18 Results: Fiberglass struts were the only structural arrangement evaluated. The design configuration allowed the payload support struts to extend to a ring which also served to support the tank and the engine, thus the main body members were the payload supports. Fiberglass was selected to minimize heat conduction from the payload. The results are presented in Figure 1.2-34 and Table 1.2-24. The last entry in the table was an evaluation of system weights where the MLI thickness was limited to the minimum required for meteoroid protection. The least weight case employed one shadow shield, however the weight advantage was only about 2 lbs (0.9 kg).

Vehicle 2-14 Results: The data for this vehicle is presented in Figure 1.2-35 and Table 1.2-25. Weight differences were small for the various construction methods, however, the use of a shadow shield was least weight. Fiberglass truss members also produced least weights.

Vehicle 2-19 Results: The data is presented in Figure 1.2-36 and Table 1.2-26. In this configuration the truss members were actually payload supports as described for Vehicle 2-18. The loads were introduced into the tank cylindrical shell at the top and the weights in the figure do not reflect additional shell stiffening for compressive loading. These weights were given in the discussion

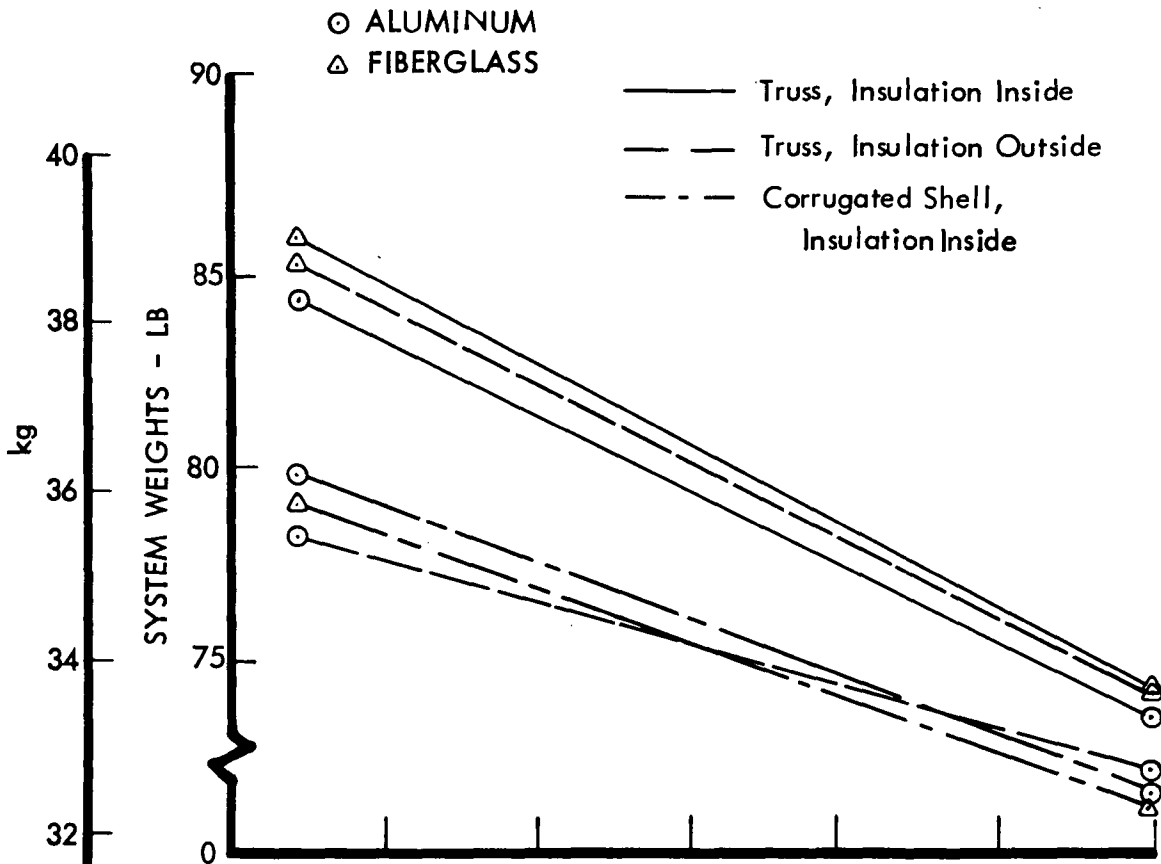


Figure 1.2-30: SYSTEM WEIGHTS, VEHICLE 1-3

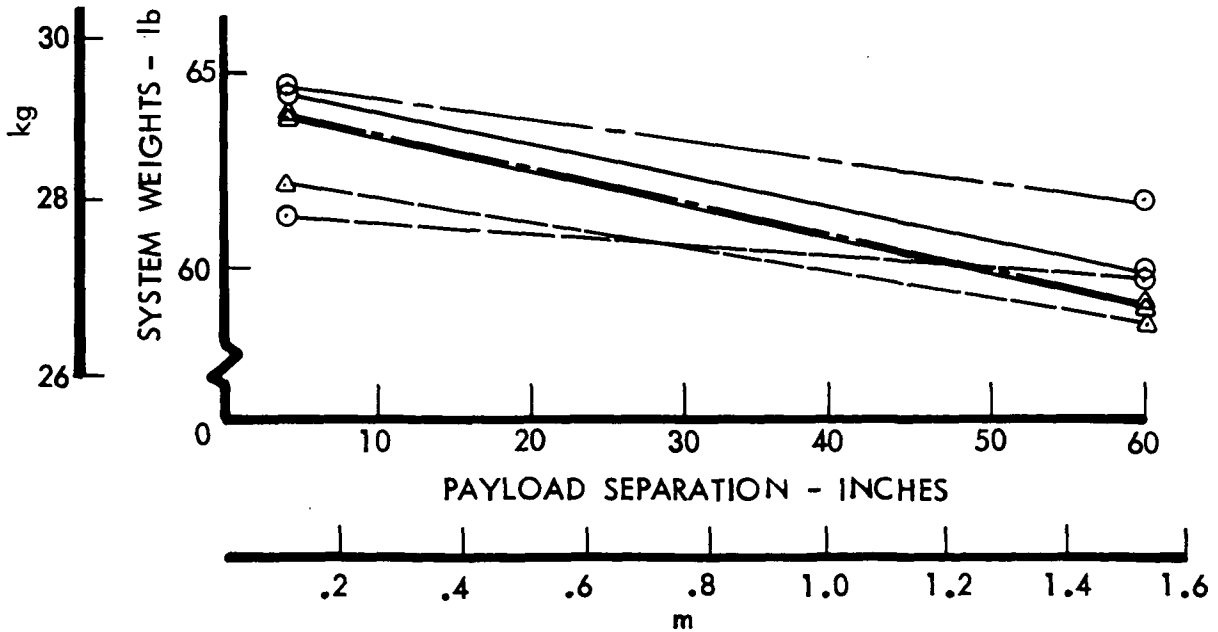


Figure 1.2-29: SYSTEM WEIGHTS, VEHICLE 1-2A

Table 1.2-19: OPTIMUM SYSTEM WEIGHTS, VEHICLE 1-2A

STRUCTURE	MATERIAL	PAYLOAD SEPARATION		INSULATION THICKNESS										TANK GAGE				SYSTEM WEIGHT		
		in	cm	TOP	UPPER SIDE		INSIDE	CYLINDER SIDE		BOTTOM		FUEL	OXIDIZER		lb	kg				
					in	cm		in	cm	in	cm		in	cm			in	cm		
Truss	Aluminum	4	10	.30	.76	.30	.76	.18	.46	.05	.13	.02	.05	.025*	.064	.025*	.064	61.4	27.9	★
	Aluminum	60	152	.15	.38	.15	.38	.16	.41	.13	.33	.02	.05	.025*	.064	.025*	.064	59.8	27.1	★
	Fiberglass	4	10	.29	.74	.29	.74	.22	.56	.06	.15	.02	.05	.025*	.064	.025*	.064	62.3	28.2	★
	Fiberglass	60	152	.21	.53	.21	.53	.15	.38	.04	.10	.03	.08	.025*	.064	.025*	.064	58.7	26.6	★
Truss	Aluminum	4	10	.27	.69	.27	.69	.18	.46	.05	.13	.08	.20	.025*	.064	.025*	.064	64.6	29.3	★
	Aluminum	60	152	.24	.61	.24	.61	.15	.38	.03	.08	.04	.10	.025*	.064	.025*	.064	60.0	27.2	★
	Fiberglass	4	10	.32	.81	.32	.81	.22	.56	.04	.10	.03	.08	.025*	.064	.025*	.064	63.9	29.0	★
	Fiberglass	60	152	.22	.56	.22	.56	.16	.41	.03	.08	.03	.08	.025*	.064	.025*	.064	59.1	26.8	★
Corrugated Shell	Aluminum	4	10	.28	.71	.28	.71	.18	.46	.05	.13	.07	.18	.025*	.064	.025*	.064	64.7	29.3	★
	Aluminum	60	152	.23	.58	.23	.58	.16	.41	.03	.08	.12	.30	.025*	.064	.025*	.064	61.8	28.0	★
	Fiberglass	4	10	.30	.76	.30	.76	.24	.61	.04	.10	.03	.08	.025*	.064	.025*	.064	64.0	29.0	★
	Fiberglass	60	152	.21	.53	.21	.53	.16	.41	.03	.08	.03	.08	.025*	.064	.025*	.064	59.1	26.8	★

\* Rounded To Minimum Gage    ✦ Insulation Outside    ★ Insulation Inside

Table 1.2-20: OPTIMUM SYSTEM WEIGHTS, VEHICLE 1-3

STRUCTURE	MATERIAL	PAYLOAD SEPARATION		INSULATION THICKNESS										TANK GAGE				SYSTEM WEIGHT				
		in	cm	TOP FUEL	SIDE FUEL	BOTTOM FUEL		INSIDE	TOP OXIDIZER	SIDE OXIDIZER	BOTTOM OXIDIZER	FUEL		OXIDIZER		lb	kg					
						in	cm					in	cm	in	cm			in	cm	in	cm	
Truss	Aluminum	4	10	.81	2.06	.20	.51	.10	.25	.14	.36	.46	1.17	.07	.08	.02	.05	.025	.064	84.5	38.3	★
	Aluminum	60	152	.51	1.30	.13	.33	.09	.23	.07	.18	.30	.76	.05	.13	.03	.08	.025	.064	73.4	33.3	★
	Fiberglass	4	10	.84	2.13	.21	.53	.12	.30	.20	.51	.45	1.14	.09	.23	.01	.03	.025	.064	86.1	39.1	★
	Fiberglass	60	152	.47	1.19	.14	.36	.10	.25	.11	.28	.30	.76	.06	.15	.04	.10	.025	.064	74.1	33.6	★
Corrugated Shell	Aluminum	4	10	.69	1.75	.15	.38	.12	.30	.04	.10	.42	1.07	.08	.20	.02	.05	.025	.064	79.8	36.2	★
	Aluminum	60	152	.43	1.09	.11	.28	.07	.18	.04	.10	.33	.84	.06	.15	.03	.08	.025	.064	71.4	32.4	★
	Fiberglass	4	10	.68	1.73	.17	.43	.11	.28	.04	.10	.44	1.12	.06	.15	.02	.05	.025	.064	79.0	35.8	★
	Fiberglass	60	152	.43	1.09	.12	.30	.09	.23	.03	.08	.33	.84	.05	.13	.03	.08	.025	.064	70.9	32.2	★
Truss	Aluminum	4	10	.70	1.78	.09	.23	.13	.33	.10	.25	.50	1.27	.05	.13	.01	.03	.025	.064	78.2	35.5	★
	Aluminum	60	152	.52	1.32	.07	.18	.09	.23	.06	.15	.35	.89	.05	.13	.04	.10	.025	.064	71.9	32.6	★
	Fiberglass	4	10	.85	2.16	.18	.46	.11	.28	.21	.53	.44	1.12	.07	.08	.01	.03	.025	.064	85.4	38.7	★
	Fiberglass	60	152	.47	1.19	.15	.38	.09	.23	.10	.25	.28	.71	.06	.15	.03	.08	.025	.064	73.9	33.5	★
Truss	Aluminum	4	10	.65	1.65	.30	.76	.30	.76	.09	.23	.38	.97	.31	.79	.30	.76	.025	.064	94.0	42.6	★

x T F  
min

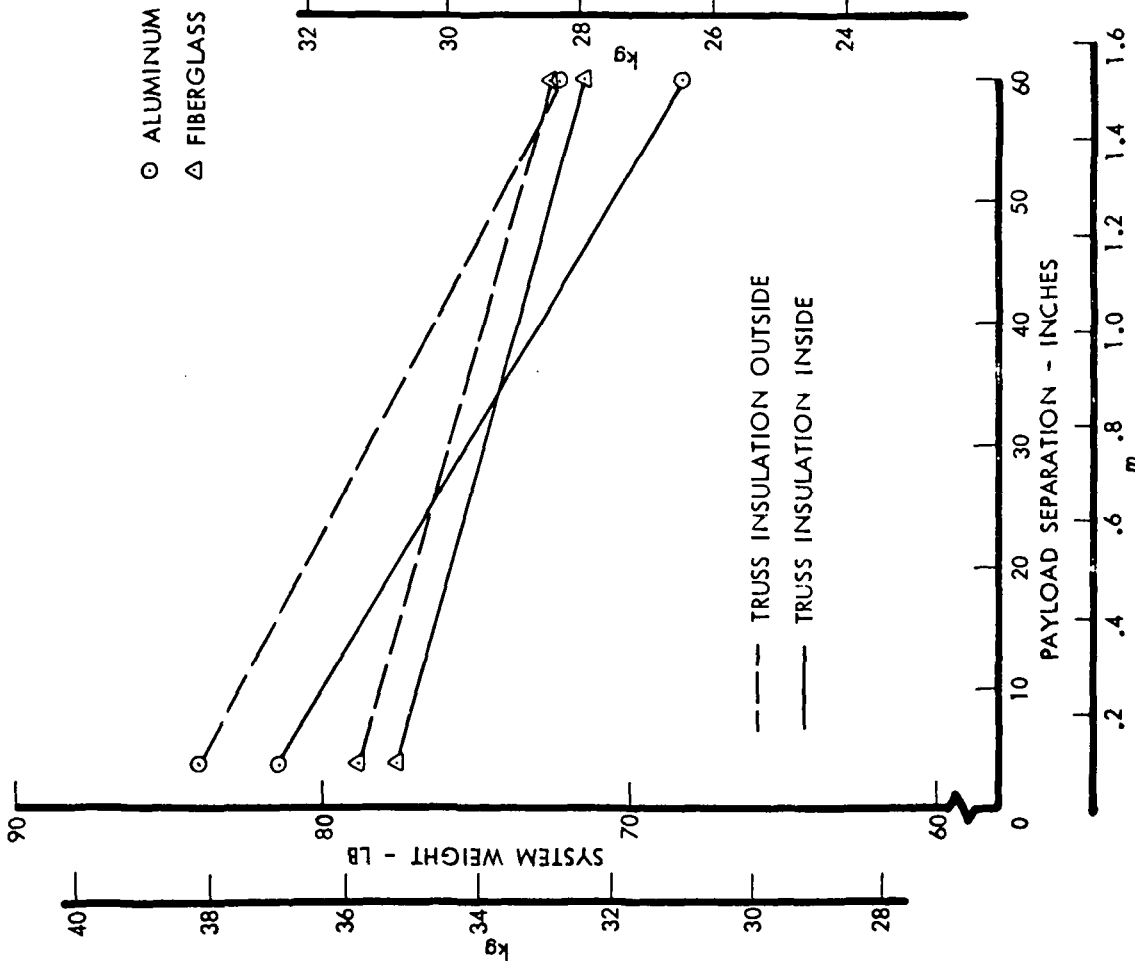


Figure 1.2-31: SYSTEM WEIGHTS, VEHICLE 1-7

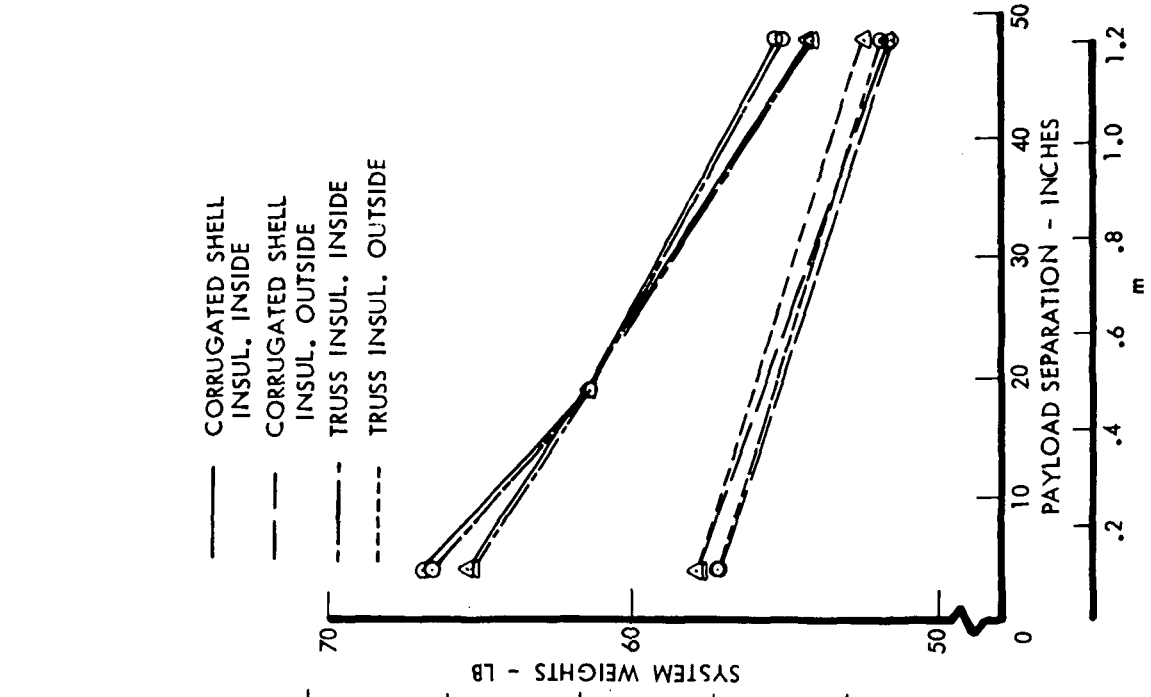


Figure 1.2-32: SYSTEM WEIGHTS, VEHICLE 2-2



○ ALUMINUM  
 △ FIBERGLASS

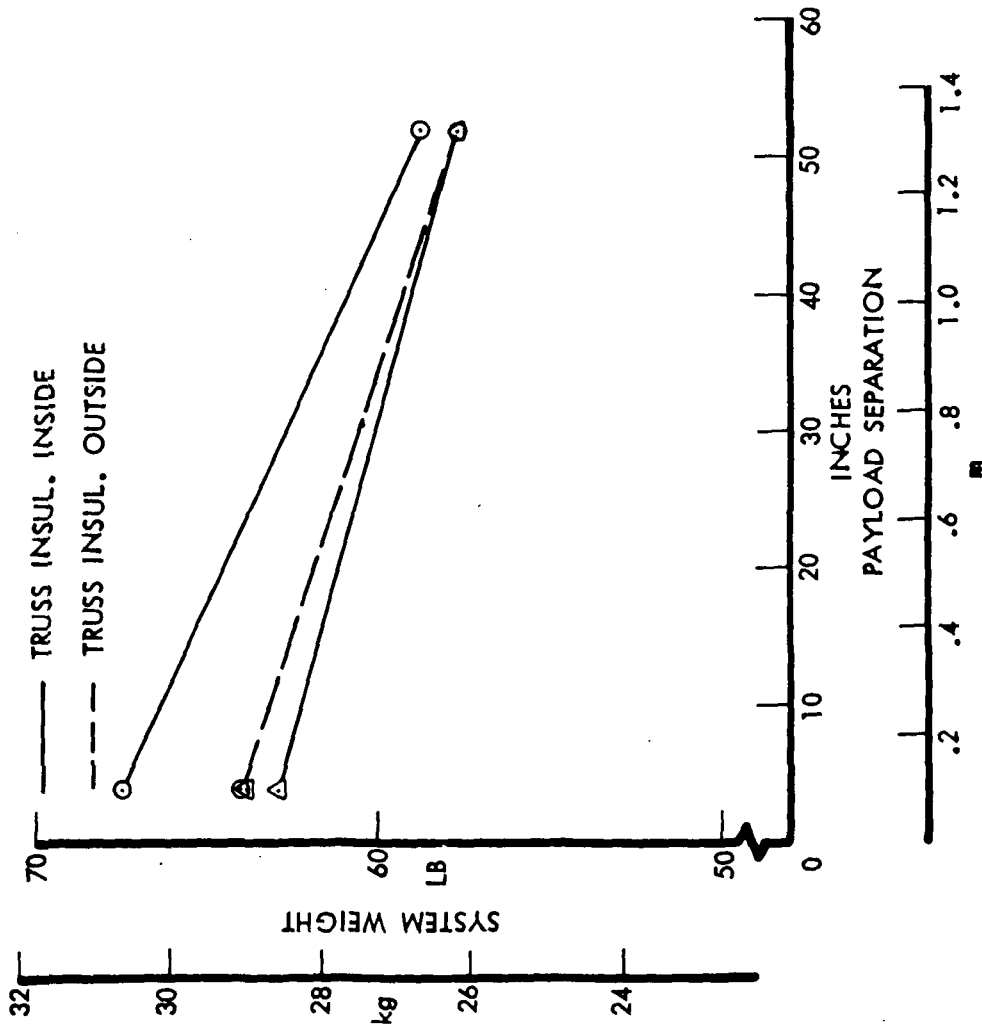


Figure 1.2-33: SYSTEMS WEIGHTS, VEHICLE 2-3

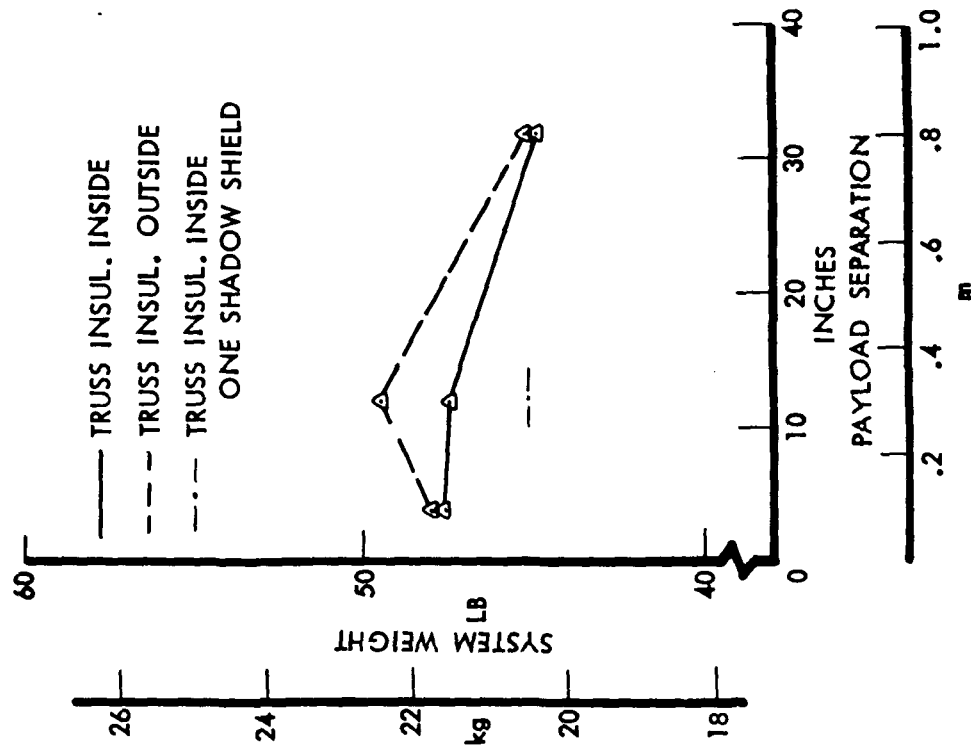


Figure 1.2-34: SYSTEM WEIGHTS, VEHICLE 2-18



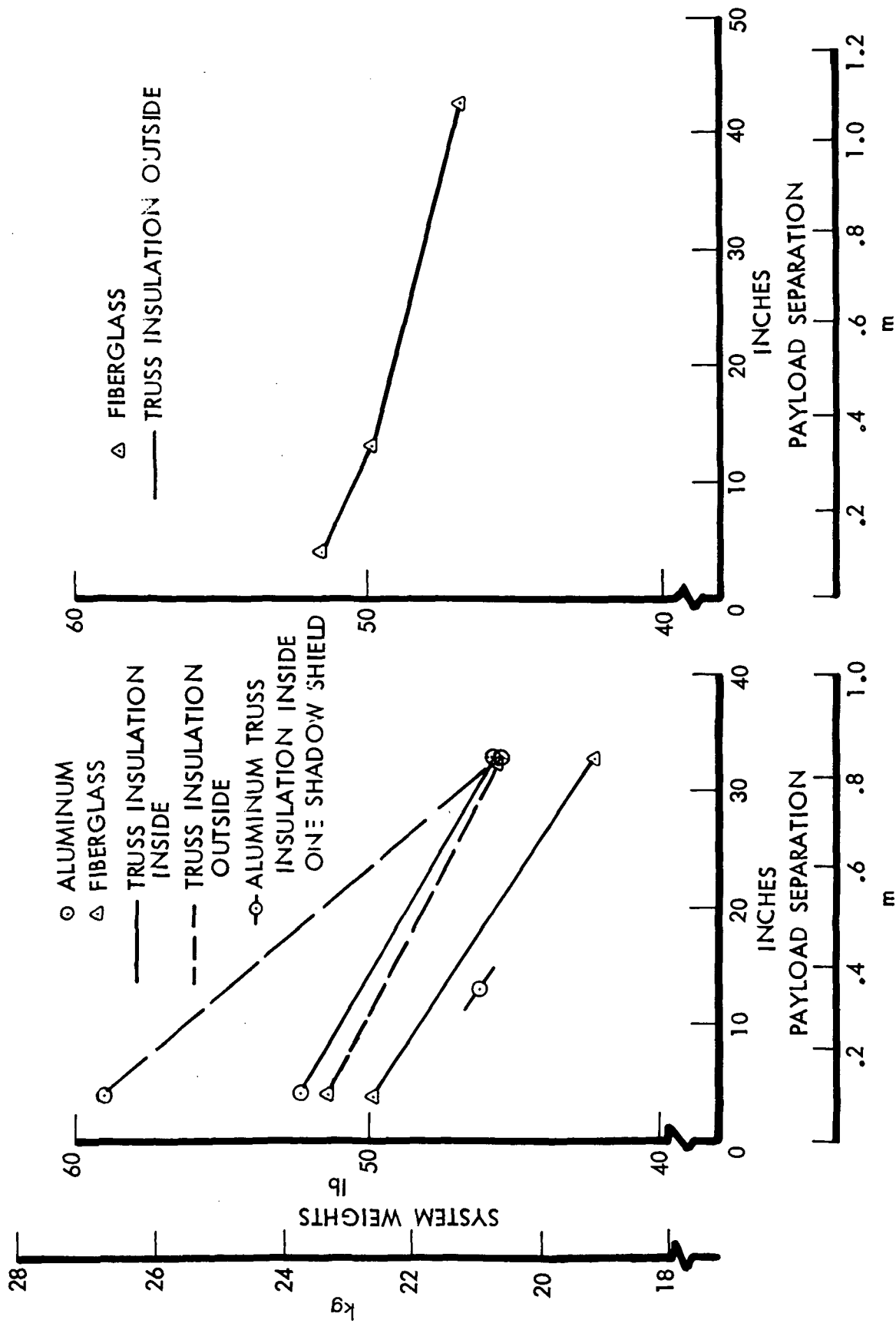


Figure 1.2-35: SYSTEM WEIGHTS, VEHICLE 2-14

Figure 1.2-36: SYSTEM WEIGHTS, VEHICLE 2-19



of the "Vehicle Structure Evaluation". The system weights were greater than Vehicle 2-18, partly because of the inefficiency of the conical portion of the tank as a pressure vessel.

### Meteoroid Protection Evaluation

An experimental program was conducted to obtain simulated meteoroid impact data. The experiments were performed with a light gas gun which shot cylindrical polyethylene projectiles at velocities ranging from 23,000 to 27,000 fps, (7.0 to 8.2 km/sec).

The propellant tanks were the vehicle components which were protected. An aluminum witness plate was used to record projectile damage. This plate was located behind the meteoroid protection system and represented the propellant tank wall. A 50% penetration of the tank wall was established as a maximum limit.

Meteoroid protection systems evaluated consisted of (1) aluminum single sheets, (2) Beta fiber fabric, (3) fiberglass/epoxy laminate, (4) metallic and non-metallic honeycomb sandwich, (5) several types of MLI with different spacer materials, and (6) combinations of MLI with Items 1 through 4.

The experimental results were developed in terms of an equivalent thickness of aluminum protection system ( $T_1$ ) necessary to protect a certain aluminum tank wall thickness ( $T_2$ ). Both thicknesses ( $T_1$  and  $T_2$ ) were normalized to meteoroid diameter ( $D$ ) so the data could be used to evaluate protection systems for various vehicles and probabilities of mission success. Design curves were prepared for all of the protection concepts tested.

Design meteoroid sizes for each vehicle were determined from an assessment of the predicted environment, considering the vehicle size, mission duration and a probability of no failure of 0.999.

A discussion of the meteoroid protection test program, derivation of the Earth/Mars trajectory, derivation of the 50% maximum penetration criteria, development of design curves and design meteoroid diameters is contained in Section 2.0, Task II, "Experimental Evaluation" and in Appendix C of the companion Volume II, NASA CR-121104.

An initial screening process was employed to select vehicle details for the meteoroid protection study. The parameter of primary importance was payload height. A low payload position tended to reduce vehicle structure weight, increase heat transfer to the propellants, reduce payload support weight and reduce top deck meteoroid protection weight due to the decreased view factor. Conversely, a high payload position increased payload support and vehicle structure weights, reduced heat transfer to the propellants because of the enlarged radiation window and afforded less meteoroid protection for the top deck.

The approach used in the initial screening was to: (1) determine payload support weights as a function of payload height, (2) determine the top deck meteoroid protection required as a function of payload height, (3) summarize vehicle weights including body and adaptor structure, and thermal systems as derived by the "TATE" program in terms of payload height, and (4) select the least-weight, practical design concept for the meteoroid protection study.

Payload supports were fiberglass tubular struts except for the low payload case where a molded fiberglass bracket was assumed. The payload support weights were determined from Figure 1.2-37 and a computer program which calculated support strut length and load for each payload height. Twelve payload support struts were employed in each vehicle except 1-7 where eight members were used. The length and load of payload supports were used to calculate  $P/L^2$  and derive a wall stress from the first curve of Figure 1.2-37. The member area was then obtained by dividing wall stress by member load. Member weight was calculated using a material density of  $0.066 \text{ lb/in}^3$  ( $1890 \text{ kg/m}^3$ ). End fitting weights were obtained by means of the second curve of Figure 1.2-37. This curve was constructed from the data of Figures 1.2-6 and 1.2-7. The end fitting weights were added to member weights to obtain the values entered in tables such as 1.2-27.

Top deck meteoroid protection was obtained by adding MLI to the basic blanket required for thermal protection. The meteoroid protection weights shown in the following tables represent the  $\Delta$  weight of MLI necessary to obtain adequate protection. The basic top deck blanket weight is included in the system weight column. This additional material would utilize non-aluminized radiation shields to maintain the thermal balance derived by the TATE program. MLI was selected for meteoroid protection because it was the most weight-efficient concept.

The initial screening results for the ten study vehicles are shown in Tables 1.2-27 through 1.2-36. Table 1.2-27 presents the data used in making a selection for Vehicle 1-14. Four MLI locations were considered. The insulation material represented in this chart is aluminized mylar (.15 mil)/nylon net. In the majority of cases the top deck MLI was adequately thick for meteoroid protection. Blanket thickness data for this vehicle was from Table 1.2-17. It should be noted that the weights do not include internal structural members, engine supports and various clips, brackets, and miscellaneous hardware.

There were several least weight choices. In the medium payload height, for an aluminum truss structure, these included (1) MLI inside with a shadow shield on the top deck, (2) MLI outside, and (3) MLI inside. Of these, the latter was chosen because it had the thickest MLI blankets in other areas of the vehicle and thus would require the least additional protection. A fiberglass truss structure in this same payload height, combined with a shadow shield, offered low weight, however, the shield weight was absent and the fiberglass members had

no particular advantage over aluminum. Another low weight combination was MLI outside on the top deck and inside on the sidewall. Obtaining a low heat leak payload support penetration through the MLI would be difficult, therefore, this approach was abandoned.

Table 1.2-28 presents data used to make a selection for Vehicle 1-2B. The shadow shield approach combined with aluminum or fiberglass truss structure was least weight, however, the weight of a shield and installation hardware would make these concepts about on a par with an aluminum truss structure - low payload position - MLI outside. This latter concept was selected for the meteoroid protection analysis.

Table 1.2-29 indicated that the least weight approach for Vehicle 1-2A was an aluminum truss structure with a low payload and MLI outside the structure. This concept was chosen for further evaluation.

The best initial selection for Vehicle 1-3 was an aluminum truss structure with a low payload position and MLI on the outside. Table 1.2-30 summarizes the weights of the various approaches considered.

The concept selected for Vehicle 1-7 consisted of fiberglass truss structure with a low payload and MLI on the inside. The weight data is shown in Table 1.2-31.

Results for the LH<sub>2</sub>/LF<sub>2</sub> vehicles are summarized below. These selections became baseline vehicles for the detailed meteoroid protection study.

<u>Vehicle</u>	<u>Payload Height</u>	<u>Structure &amp; Material</u>	<u>Insulation Location</u>
1-14	Medium (14")	Aluminum Truss	Inside Structure
1-3	Low (4")	Aluminum Truss	Outside Structure
1-2A	Low (4")	Aluminum Truss	Outside Structure
1-2B	Low (4")	Aluminum Truss	Outside Structure
1-7	Low (4")	Fiberglass Truss	Inside Structure

Data for Vehicle 2-14 is provided in Table 1.2-32. Both low and high payload positions produced least-weight cases. A vehicle with an aluminum truss structure, low payload and MLI on the inside was chosen because it was nearly least-weight and had the thickest MLI in areas other than the top deck.

In Table 1.2-33 it can be seen that the top deck MLI required for thermal protection of Vehicle 2-3 was also adequate for meteoroid protection. There are several low weight approaches apparent in the table. The combination of low payload position and aluminum truss structure was best and was selected for further study. The continuous shell structure concepts were not analyzed for

meteoroid protection. The table shows a significant structural weight penalty for corrugated construction and experience with Vehicles 1-14 and 1-2B indicated that it was impossible to offset a penalty that large.

The low payload case, using fiberglass payload supports for the body structure and with MLI inside, was the least-weight concept for Vehicle 2-18. The data is shown in Table 1.2-34.

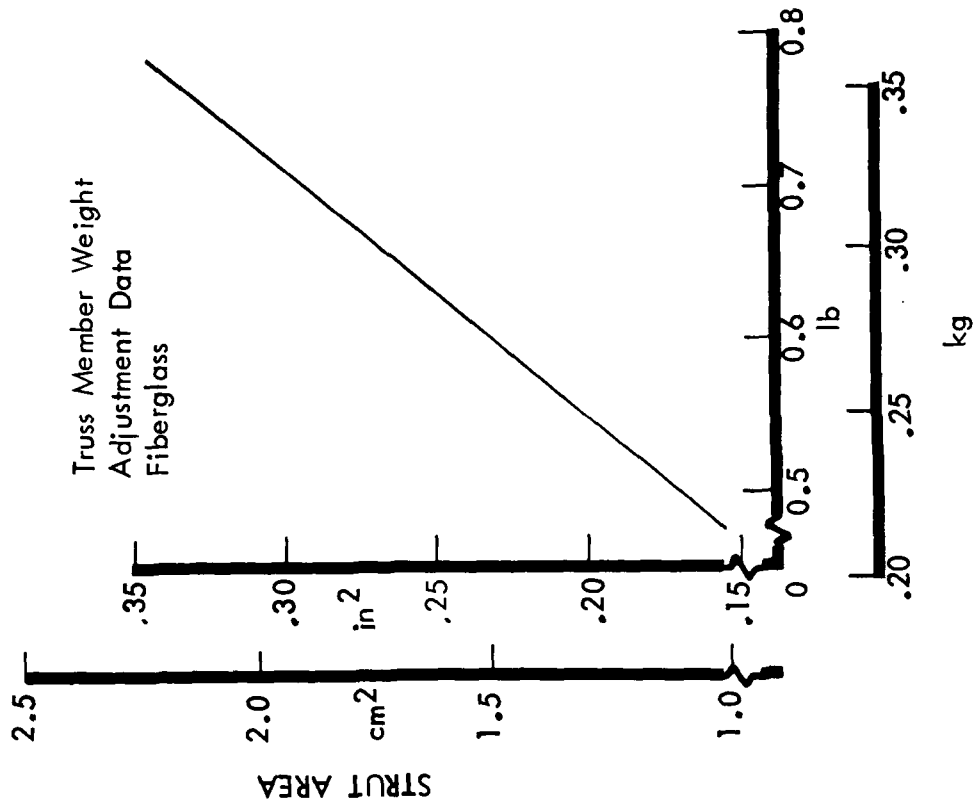
Table 1.2-35 presents data for Vehicle 2-19. The low payload position was the best approach. In this case the MLI on the top deck provided adequate meteoroid protection. An evaluation of sidewall and bottom cone showed that meteoroid protection could be obtained with minimal additions of MLI. The sidewall and conical portions of the tankage were considerably thicker than the minimum gage encountered in other vehicles.

Table 1.2-36 shows data for Vehicle 2-2. In the cases evaluated there was no requirement for additional MLI on the top deck for meteoroid protection. Therefore, the selection was made based on structure and thermal systems weight. A low payload position, aluminum truss structure, with MLI outside offered the least-weight and was selected for further study. A fiberglass truss structure was about equal.

Results for the FLOX-CH<sub>4</sub> vehicles are summarized below.

<u>Vehicle</u>	<u>Payload Height</u>	<u>Structure &amp; Material</u>	<u>Insulation Location</u>
2-18	Low (4")	Fiberglass Truss	Inside Structure
2-19	Low (4")	Fiberglass Truss	Outside Structure
2-14	Low (4")	Aluminum Truss	Inside Structure
2-2	Low (4")	Aluminum Truss	Outside Structure
2-3	Low (4")	Aluminum Truss	Outside Structure

The approach for selecting the overall meteoroid protection concept was to determine if the structure, MLI and tank gages were adequate in all areas of the vehicle, without additional protection. If sufficient protection was available, then a least-weight design had been obtained. However, in all cases there was insufficient protection. Several alternatives were then considered to find the least-weight approach. The alternatives included (1) increasing the tank gage, (2) adding metallic or glass fabric bumper sheets, (3) increasing the MLI thickness, (4) use of continuous structural shells in place of truss structure, and (5) combinations of these approaches.



END FITTING & BRACKET WEIGHT PER STRUT

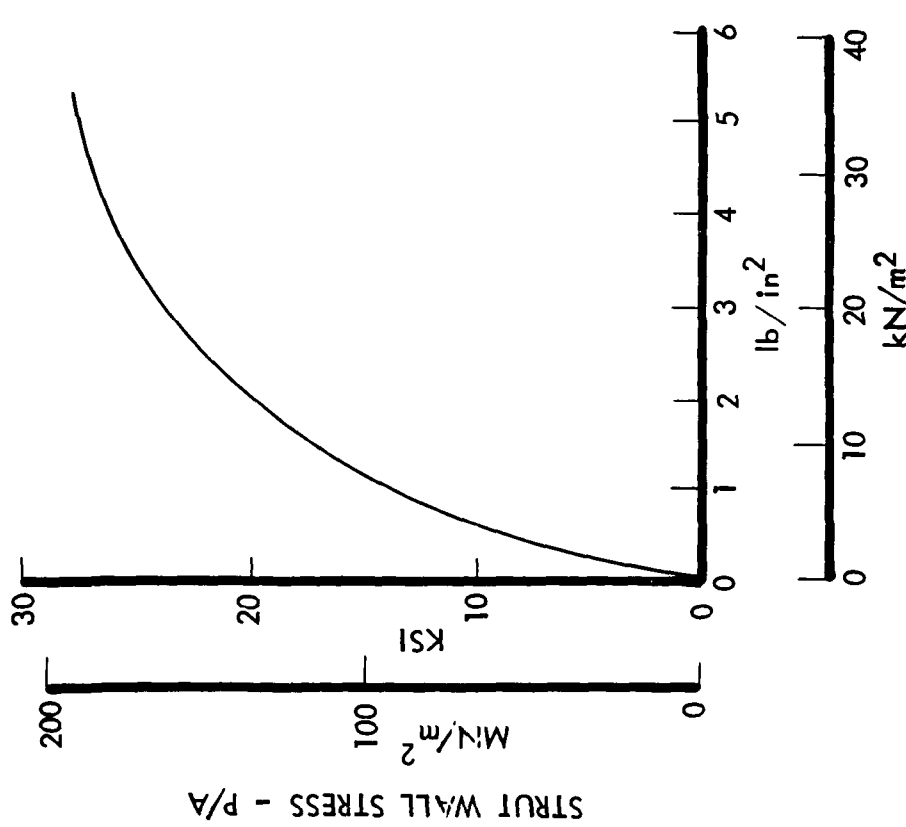


Figure 1.2-37: PAYLOAD SUPPORT DATA

Table 1.2-27: METEOROID PROTECTION INITIAL SCREENING RESULTS, VEHICLE 1-14

PAYLOAD HEIGHTS	CONSTRUCTION	-SYSTEM WEIGHT						TOP DECK METEOROID PROTECTION						TOTAL WEIGHT							
		Insulation Inside		Insulation Outside		Insulation Inside - Shadow Shield		Insulation Inside		Insulation Inside - Shadow Shield		Insulation Inside		Insulation Outside		Insulation Inside - Shadow Shield		Insulation Outside Top-Inside Remainder			
		lb	kg	lb	kg	lb	kg	lb	kg	lb	kg	lb	kg	lb	kg	lb	kg	lb	kg		
4" (10cm) Low	Aluminum Truss	57.5	26.1	65.3	29.6	-	-	55.7	25.3	66.9	30.3	10.9	4.9	-	-	135.3	61.4	143.1	64.9	133.5	60.6
	Fiberglass Truss	55.8	25.3	58.4	26.5	-	-	57.4	26.0	71.9	32.6	10.9	4.9	-	-	138.6	62.9	141.2	64.0	140.2	63.6
	Aluminum Corrugation	57.9	26.3	55.8	25.3	-	-	-	-	108.4	46.9	10.9	4.9	-	-	177.2	80.4	175.1	79.4	-	-
	Fiberglass Corrugation	55.9	25.4	58.2	26.4	-	-	-	-	130.0	59.0	10.9	4.9	-	-	196.8	89.3	199.1	90.3	-	-
14" (36cm) Medium	Aluminum Truss	56.2	25.5	53.9	24.4	50.6	23.0	-	-	67.7	30.7	9.1	4.1	-	-	133.0	60.3	130.7	59.3	128.9	58.5
	Fiberglass Truss	54.6	24.8	55.3	25.1	52.1	23.6	-	-	71.9	32.6	9.1	4.1	-	-	135.6	61.5	136.3	61.8	133.5	60.6
	Aluminum Corrugation	56.3	25.5	53.3	24.2	-	-	-	-	113.1	51.3	9.1	4.1	-	-	178.5	81.0	175.5	79.6	-	-
	Fiberglass Corrugation	54.6	24.8	55.1	25.0	-	-	-	-	135.0	61.2	9.1	4.1	-	-	198.7	90.1	199.2	90.4	-	-
35" (89cm) High	Aluminum Truss	53.5	24.3	51.2	23.2	49.1	22.3	51.2	23.2	69.7	31.6	13.8	6.3	0.4	0.2	137.4	62.3	134.7	61.1	134.1	60.8
	Fiberglass Truss	52.5	23.8	52.7	23.9	49.8	22.6	52.6	23.9	73.0	33.1	13.8	6.3	-	-	139.3	63.2	139.5	63.3	137.7	62.5
	Aluminum Corrugation	53.6	24.3	50.6	23.0	-	-	-	-	118.0	53.5	13.8	6.3	0.6	0.3	186.0	84.4	182.4	82.7	-	-
	Fiberglass Corrugation	52.4	23.8	52.5	23.8	-	-	-	-	148.2	67.2	13.8	6.3	0.1	0.0	214.5	97.3	214.5	97.3	-	-

Table 1.2-28: METEOROID PROTECTION INITIAL SCREENING RESULTS, VEHICLE 1-2B

PAYLOAD HEIGHTS	CONSTRUCTION	SYSTEM WEIGHT				STRUCTURE WEIGHT				PAYLOAD SUPPORT WEIGHT				TOP DECK METEOROID PROTECTION				TOTAL WEIGHT			
		INSULATION		INSULATION		INSULATION		INSULATION		INSULATION		INSULATION		INSULATION		INSULATION		INSULATION		INSULATION	
		INSIDE	OUTSIDE	INSIDE	OUTSIDE	INSIDE	OUTSIDE	INSIDE	OUTSIDE	INSIDE	OUTSIDE	INSIDE	OUTSIDE	INSIDE	OUTSIDE	INSIDE	OUTSIDE	INSIDE	OUTSIDE	INSIDE	OUTSIDE
lb	kg	lb	kg	lb	kg	lb	kg	lb	kg	lb	kg	lb	kg	lb	kg	lb	kg	lb	kg	lb	kg
4" (10cm) Low	Aluminum Corrugation	81.6	37.0	63.1	28.6	67.8	30.8	10.9	4.9	-	-	-	-	160.3	72.7	141.8	64.3	-	-	-	-
	Aluminum Truss	79.3	36.0	66.1	30.0	54.7	24.8	10.9	4.9	-	-	-	-	144.9	65.7	131.7	59.7	-	-	-	-
	Fiberglass Truss	68.2	30.9	72.9	33.1	54.4	24.7	10.9	4.9	-	-	-	-	133.5	60.6	138.2	62.7	-	-	-	-
24" (61cm) Medium	Alum.Truss,Shadow Shield	61.5	27.9	60.1	27.3	55.5	25.2	12.9	5.9	3.5	1.6	1.3	0.6	133.4	60.5	129.8	58.9	-	-	-	-
	Fiberglass Truss,Shadow Shield	59.8	27.1	61.4	27.9	55.3	25.1	12.9	5.9	2.1	1.0	1.3	0.6	130.1	59.0	130.9	59.4	-	-	-	-
	Alum.Corrug,Shadow Shield	-	-	57.9	26.3	69.8	31.7	12.9	5.9	-	-	-	-	2.5	1.1	-	-	-	-	-	-
	FiberglassCorrug,Shadow Shield	-	-	60.6	27.5	76.8	34.8	12.9	5.9	-	-	-	-	1.8	0.8	-	-	-	-	-	-
60" (152cm) High	Aluminum Corrugation	68.6	31.1	59.5	27.0	72.7	33.0	26.5	12.0	-	-	-	-	1.0	0.5	168.8	76.6	159.7	72.4	-	-
	Aluminum Truss	67.3	30.5	59.9	27.2	56.2	25.5	26.5	12.0	-	-	-	-	0.4	0.2	150.5	68.2	143.0	64.9	-	-

Table 1.2-29: METEOROID PROTECTION INITIAL SCREENING RESULTS, VEHICLE 1-2A

4" (10cm) Low	Aluminum Truss	64.6	29.3	61.4	27.9	51.3	23.3	30.8	14.0	-	-	-	-	146.7	66.5	143.5	65.1	-	-	-	-
	Aluminum Corrugation	64.7	29.3	-	-	56.0	25.4	30.8	14.0	-	-	-	-	151.5	68.7	-	-	-	-	-	-
	Fiberglass Truss	63.9	29.0	62.3	28.3	51.4	23.3	30.8	14.0	-	-	-	-	146.1	66.3	144.5	65.1	-	-	-	-
	Fiberglass Corrugation	64.0	29.0	-	-	61.6	27.9	30.8	14.0	-	-	-	-	156.4	70.9	-	-	-	-	-	-
60" (152cm) High	Aluminum Truss	60.0	27.2	59.8	27.1	53.3	24.2	108.8	49.4	0.1	-	-	0.1	222.2	100.8	222.0	100.7	-	-	-	-
	Aluminum Corrugation	61.7	28.0	-	-	60.7	27.5	108.8	49.4	0.1	-	-	-	231.3	104.9	-	-	-	-	-	-
	Fiberglass Truss	59.1	26.8	58.7	26.6	53.4	24.2	108.8	49.4	0.1	-	-	0.1	221.4	100.4	221.0	100.2	-	-	-	-
	Fiberglass Corrugation	59.1	26.8	-	-	70.4	31.9	108.8	49.4	0.1	-	-	-	238.4	108.1	-	-	-	-	-	-

Table 1.2-30: METEOROID PROTECTION INITIAL SCREENING RESULTS, VEHICLE 1-3

4" (10cm) Low	Aluminum Truss	84.5	38.3	78.2	35.5	49.3	22.4	10.9	4.9	-	-	-	-	144.7	65.6	138.4	63.8	-	-	-	-
	Fiberglass Truss	86.1	39.1	85.4	38.7	49.3	22.4	10.9	4.9	-	-	-	-	146.3	66.4	145.6	66.0	-	-	-	-
	Aluminum Corrugation	79.8	36.2	-	-	65.8	29.8	10.9	4.9	-	-	-	-	156.5	71.0	-	-	-	-	-	-
	Fiberglass Corrugation	79.0	35.8	-	-	71.1	32.3	10.9	4.9	-	-	-	-	161.0	73.0	-	-	-	-	-	-
60" (152cm) High	Aluminum Truss	73.4	33.3	71.9	32.6	50.9	23.1	26.5	12.0	0.2	0.1	-	-	151.0	68.5	149.3	67.7	-	-	-	-
	Fiberglass Truss	74.1	33.6	73.9	33.5	50.8	23.0	26.5	12.0	0.1	-	-	0.3	0.1	151.5	68.7	151.5	68.7	-	-	-
	Aluminum Corrugation	71.4	32.4	-	-	70.7	32.1	26.5	12.0	-	-	-	-	168.6	76.5	-	-	-	-	-	-
	Fiberglass Corrugation	70.9	32.2	-	-	79.9	36.2	26.5	12.0	-	-	-	-	177.3	80.4	-	-	-	-	-	-

Table 1.2-31: METEOROID PROTECTION INITIAL SCREENING RESULTS, VEHICLE 1-7

4" (10cm) Low	Aluminum Truss	81.6	37.0	84.1	38.1	94.1	42.7	7.3	3.3	-	-	-	-	183.0	83.0	185.5	84.1	-	-	-	-
	Fiberglass Truss	77.6	35.2	78.9	35.8	95.4	43.3	7.3	3.3	-	-	-	-	180.3	81.8	181.6	82.4	-	-	-	-
35" (89cm) High	Aluminum Truss	68.2	30.9	72.3	32.8	100.2	45.4	14.3	6.5	-	-	-	-	182.7	82.9	186.8	84.7	-	-	-	-
	Fiberglass Truss	71.4	32.4	72.5	32.9	100.9	45.8	14.3	6.5	-	-	-	-	186.6	84.6	187.7	85.1	-	-	-	-

Table 1-2-32: METEOROID PROTECTION INITIAL SCREENING RESULTS, VEHICLE 2-14

PAYLOAD HEIGHT	CONSTRUCTION	STRUCTURE WEIGHT		SYSTEM WEIGHT				FIBERGLASS PAYLOAD SUPPORTS		TOP DECK METEOROID PROTECTION				TOTAL WEIGHT			
		lb	kg	INSULATION OUTSIDE		INSULATION INSIDE		lb	kg	INSULATION OUTSIDE		INSULATION INSIDE		lb	kg		
				lb	kg	lb	kg			lb	kg	lb	kg				
4" (10cm) Low	Aluminum Truss	62.6	28.4	59.2	26.9	52.4	23.8	10.9	4.9					132.7	60.2	125.9	57.1
	Fiberglass Truss	65.4	29.7	51.4	23.3	49.8	22.6	10.9	4.9					127.7	57.9	126.1	57.2
33" (84cm) High	Aluminum Truss	68.6	31.1	45.5	20.6	45.7	20.7	11.9	5.4					126.0	57.2	126.2	57.2
	Fiberglass Truss	70.6	32.0	45.5	20.6	42.3	19.2	11.9	5.4					128.0	58.1	124.8	56.6

Table 1.2-33: METEOROID PROTECTION INITIAL SCREENING RESULTS, VEHICLE 2-3

4" (10cm) Low	Aluminum Corrugations	63.8	28.9	-	-	-	-	10.9	4.9								
	Aluminum Truss	49.1	22.3	64.0	29.0	67.5	30.6	10.9	4.9					124.0	56.2	127.5	57.8
	Fiberglass Truss	50.8	23.0	64.0	29.0	62.9	28.5	10.9	4.9					125.7	57.0	124.6	56.5
	Fiberglass Corrugations	72.9	33.1	-	-	-	-	10.9	4.9								
52" (132cm) High	Aluminum Corrugations	71.5	32.4	-	-	-	-	20.2	9.2								
	Aluminum Truss	50.3	22.8	57.6	26.1	58.8	26.7	20.2	9.2					128.1	58.1	129.3	58.6
	Fiberglass Truss	51.8	23.5	57.6	26.1	57.7	26.2	20.2	9.2					129.6	58.8	129.7	58.8
	Fiberglass Corrugations	81.9	37.1	-	-	-	-	20.2	9.2								

Table 1.2-34: METEOROID PROTECTION INITIAL SCREENING RESULTS, VEHICLE 2-18

4" (10cm) Low	Fiberglass Truss			48.0	21.8	47.6	21.6	28.6	13.0					76.6	34.7	76.2	34.6
12" (30cm) Medium	Fiberglass Truss			49.5	22.5	47.5	21.5	35.2	16.0					84.7	38.4	82.7	37.5
	Fiberglass Truss/Shadow Shield			-	-	45.2	20.5	35.2	16.0								36.5
32" (81cm) High	Fiberglass Truss			45.2	20.5	44.9	20.4	57.0	25.9					102.2	46.4	101.9	46.2

\*Not Including Adaptor Weight

Table 1.2-35: METEOROID PROTECTION INITIAL SCREENING RESULTS, VEHICLE 2-19

PAYLOAD HEIGHTS	PAYLOAD SUPPORTS WEIGHT		SYSTEM WEIGHT		ADAPTER MEMBERS WEIGHT		ADAPTER END FITTINGS WEIGHT		TANK Δ WEIGHTS			TOP DECK METEOROID PROTECTION WEIGHT		TOTAL WEIGHT			
	lb	kg	lb	kg	lb	kg	lb	kg	SKIRT	SHELL	LOWER RING	lb	kg	lb	kg		
4" (10cm) Low	9.0	4.1	51.8	23.5	23.9	10.8	10.7	4.9	10.9	4.9	6.3	2.9	4.3	2.0	-	116.9	53.0
13" (33cm) Medium	11.7	5.3	50.1	22.7	24.2	11.0	10.7	4.9	11.8	5.4	7.5	3.4	4.3	2.0	-	120.3	54.6
43" (109cm) High	30.8	14.0	47.0	21.3	24.7	11.2	11.2	5.1	12.9	5.9	8.7	3.9	4.3	2.0	0.2	139.8	63.4

Table 1.2-36: METEOROID PROTECTION INITIAL SCREENING RESULTS, VEHICLE 2-2

CONSTRUCTION	SYSTEM WEIGHT		STRUCTURE WEIGHT		PAYLOAD SUPPORT WEIGHT		TOP DECK METEOROID PROTECTION WEIGHT			TOTAL WEIGHT					
	INSULATION INSIDE	INSULATION OUTSIDE	INSULATION INSIDE	INSULATION OUTSIDE	INSULATION INSIDE	INSULATION OUTSIDE	INSULATION INSIDE	INSULATION OUTSIDE	INSULATION INSIDE	INSULATION OUTSIDE	INSULATION OUTSIDE				
	lb	kg	lb	kg	lb	kg	lb	kg	lb	kg	lb	kg			
4" (10cm) Low	Aluminum Truss	66.6	30.2	57.2	25.9	41.6	18.9	47.5	21.5	-	-	155.7	70.6	146.3	66.4
	Fiberglass Truss	65.2	29.6	57.8	26.2	41.6	18.9	47.5	21.5	-	-	154.3	70.0	146.9	66.6
	Aluminum Corrugation	66.8	30.3	57.1	25.9	55.2	25.0	47.5	21.5	-	-	169.5	76.9	159.8	72.5
	Fiberglass Corrugation	65.4	29.7	57.9	26.3	73.4	33.3	47.5	21.5	-	-	186.3	84.5	178.8	81.1
19" (48cm) Medium	Aluminum Corrugation	61.4	27.9	-	-	56.7	25.7	67.0	30.4	-	-	185.1	84.0	-	-
48" (122cm) High	Aluminum Truss	55.0	24.9	51.9	23.5	44.0	20.0	124.3	56.4	-	-	223.3	101.3	220.2	99.9
	Fiberglass Truss	54.2	24.6	52.5	23.8	44.0	20.0	124.3	56.4	-	-	222.5	100.9	220.8	100.2
	Aluminum Corrugation	55.3	25.1	51.6	23.4	60.6	27.5	124.3	56.4	-	-	240.2	109.0	236.5	107.3
	Fiberglass Corrugation	54.3	24.6	51.7	23.5	82.1	37.2	124.3	56.4	-	-	260.7	118.3	258.1	117.1

The order in which the alternative meteoroid protection approaches were evaluated was:

- (1) increase tank gage,
- (2) increase tank gage and add Beta fiber cloth to the MLI,
- (3) add multiple layers of Beta fiber cloth, ignoring protection afforded by the MLI,
- (4) add Beta fiber cloth and increase MLI thickness,
- (5) increase MLI thickness, with aluminized or non-aluminized radiation shields,
- (6) evaluate alternate MLI materials,
- (7) replace truss structure with continuous shell structure, and
- (8) evaluate other competitive arrangements, e.g., alternate structural concepts, insulation locations or shadow shields.

Vehicle 1-14: The design meteoroid diameter for this vehicle with a medium height payload was 0.065 in (0.17 cm), and tank gages were  $\approx$  .025 in (0.064 cm). Using the design curve of Figure 1.2-38, where tank gage/design meteoroid diameter ( $T_2/D$ ) = 0.385, a value for the normalized MLI thickness ( $T_1/D$ ) in terms of equivalent aluminum thickness was obtained. This value was 0.099 and was converted to the correct number of aluminized mylar/nylon net layers by:

$$\frac{T_1/D \times D \times \rho_{\text{alum.}}}{W_{\text{MLI}}} = 23 \text{ shield/spacer pairs}$$

where  $\rho_{\text{alum}}$  = density of aluminum and  $W_{\text{MLI}}$  = weight of a shield/spacer pair.

Using 70 shields per inch (28 shields/cm), the thickness of MLI required to give adequate protection was 0.33 in (0.84 cm). Referring to Table 1.2-17, the MLI thickness on the top deck was 0.36 in (0.92 cm), the upper sidewall was 0.08 in (0.20 cm), the lower sidewall was 0.13 in (0.33 cm), and the vehicle base was 0.11 in (0.28 cm). MLI by itself provided adequate protection only for the top deck. The first entry in Table 1.2-37 indicates this fact. System weights are those derived from the TATE (Tank Arrangement Thermal Efficiency) program and include tanks, insulation, propellant vapor, helium and helium tank. Structure weights are those obtained from the "Vehicle Structure Evaluation". The protection  $\Delta$  weights are those additional quantities of multilayer, Beta fiber cloth or tank material necessary to obtain protection for the baseline vehicle.

Increasing tank gage to obtain adequate protection resulted in prohibitive weights. For example, in the LF<sub>2</sub> tank bay the sidewall MLI was 0.08 in (0.20 cm) thick and using the curve of Figure 1.2-38 it was impossible to derive an adequate tank gage.

The MLI thickness on the sidewall was converted to 6 shield and spacer layers, and using the equation described previously, a value of 0.024 was obtained for T<sub>1</sub>/D. Entering the graph at T<sub>1</sub>/D = 0.024 an intercept with the MLI protection curve could not be obtained, therefore, the normalized tank gage (T<sub>2</sub>/D) was considerably greater than 2.6. This value of T<sub>2</sub>/D would result in a tank gage of 0.17 in (0.43 cm) or a factor of 6.8 on tank weight. The resultant weight penalty was >87 lb (39.5 kg) for the LF<sub>2</sub> tank alone.

The curves of Figure 1.2-39 identified as T<sub>β</sub>/D = 0.0273, 0.046 and 0.092 represent protection systems consisting of combinations of MLI and Beta fiber cloth. The first curve mentioned used one layer of Style 8116 cloth, the second used one layer of Style 15035 cloth and the third used two layers of Style 15035 cloth. Beta fiber cloth combined with the MLI and an increase in tank gage was found to give the required protection. Using the upper sidewall as an example, the combined protection system thickness T<sub>1</sub>/D was

$$T_1/D = T_{ML}/D + T_{\beta}/D = 0.051$$

where T<sub>ML</sub> was the MLI thickness and T<sub>β</sub> was the Beta fiber cloth thickness.

For the sidewall, T<sub>ML</sub>/D was 0.024 as described previously. Using one layer of Style 8116 Beta fiber cloth:

$$T_{\beta}/D = \frac{W_{\beta}}{\rho_{alum} \times D} = 0.0273$$

where W<sub>β</sub> = weight of one layer of Beta fiber cloth.

The curve T<sub>β</sub>/D = 0.0273 of Figure 1.2-39 was used to obtain a value of T<sub>2</sub>/D. Converting to wall thickness resulted in a tank gage of 0.098 in (0.25 cm). Item 2 in Table 1.2-37 represents the weights for this approach. The tank Δ weight represents the increase from 0.025 in (0.064 cm) to 0.098 in (0.25 cm). The weight of an 0.025 in (0.064 cm) tank is included in the systems weights.

Entries for one and two layers of Style 15035 cloth are identified as Items 3 and 4 in Table 1.2-37. It can be seen that increasing Beta fiber cloth weight

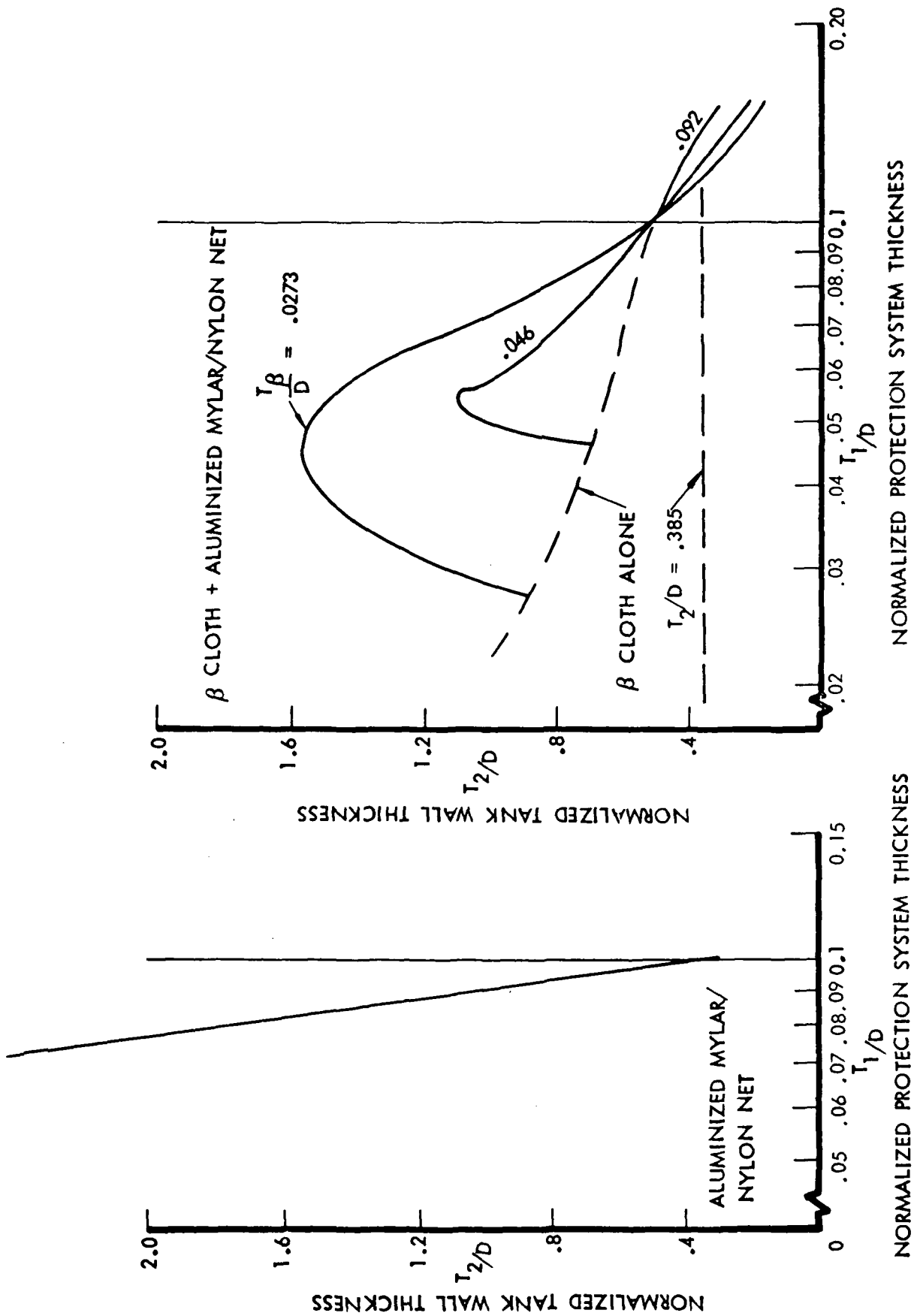


Figure 1.2-38: METEOROID PROTECTION DESIGN DATA - MLI

Figure 1.2-39: METEOROID PROTECTION DESIGN DATA - β CLOTH & MLI

Table 1.2-37: METEOROID PROTECTION EVALUATION 4" (10 cm) PAYLOAD HEIGHT, VEHICLE 1-14

	PROTECTION	STRUCTURE WEIGHT		SYSTEMS WEIGHT		PROTECTION ΔWT				TOTAL WEIGHT		
		lb	kg	lb	kg	β CLOTH		TANK		lb	kg	
						lb	kg	lb	kg			
1. Baseline Vehicle-Aluminum Truss, ALM/Nylon Net MLI Inside Structure	Inadequate	67.7	30.7	56.2	25.5	-	-	-	-	-	-	(123.9) (56.2)
2. Baseline Vehicle Plus Low Weight β Cloth & Increased Tank Gage	Adequate	67.7	30.7	56.2	25.5	4.3	2.0	109.0	49.4	-	-	237.2 (107.6)
3. Baseline Vehicle Plus One β Cloth* & Increased Tank Gage		67.7	30.7	56.2	25.5	7.3	3.3	37.3	16.9	-	-	168.5 (76.4)
4. Baseline Vehicle Plus Two β Cloth* & Increased Tank Gage		67.7	30.7	56.2	25.5	14.4	6.5	3.0	1.4	-	-	141.3 (64.1)
5. Baseline Vehicle Plus Multiple Layers β Cloth*		67.7	30.7	56.2	25.5	37.0	16.8	-	-	-	-	160.9 (73.0)
6. Baseline Vehicle Plus Low Weight β Cloth & Increased MLI**		67.7	30.7	56.2	25.5	4.3	2.0	-	-	8.4	3.8	136.6 (62.0)
7. Baseline Vehicle Plus One β Cloth* & Increased MLI**		67.7	30.7	56.2	25.5	7.4	3.4	-	-	6.5	2.9	137.8 (62.6)
8. Baseline Vehicle Plus Two β Cloth* & Increased MLI**		67.7	30.7	56.2	25.5	14.8	6.7	-	-	10.4	4.7	134.3 (61.0)
9. Baseline Vehicle Plus Increased MLI**		67.7	30.7	56.2	25.5	-	-	-	-	12.9	5.9	135.2 (61.4)
10. Baseline Vehicle Plus Increased MLI (Aluminized Shields)		67.7	30.7	64.8	29.4	-	-	-	-	10.0	4.5	135.8 (61.6)
11. Baseline Vehicle Except NRC-2 On Sidewall Plus Increased MLI**		67.7	30.7	54.6	24.8	-	-	-	-	13.2	6.0	136.0 (61.7)
12. Baseline Vehicle Except NRC-2 On Sidewall Plus Increased MLI (Aluminized Shields)		67.7	30.7	65.6	29.8	3.5	1.6	-	-	9.3	4.2	131.2 (59.6)
13. Baseline Vehicle Except NRC-2 On Sidewall Plus Low Weight β Cloth & Increased MLI**		67.7	30.7	54.6	24.8	-	-	-	-	2.2	1.0	131.2 (59.6)
14. Baseline Vehicle Except ALM/2 Silk Net Plus Increased MLI**		67.7	30.7	57.1	25.9	-	-	-	-	12.1	5.5	133.7 (60.6)
15. Baseline Vehicle Except ALM/2 Silk Net Plus Increased MLI (Aluminized Shields)		67.7	30.7	73.7	33.4	-	-	-	-	13.0	5.9	131.3 (59.6)
16. Baseline Vehicle Except ALM/Sliced Foam Plus Increased MLI**		67.7	30.7	57.1	25.9	-	-	-	-	-	-	-
17. Baseline Vehicle Except ALM/Sliced Foam Plus Increased MLI (Aluminized Shields)		67.7	30.7	63.5	28.8	-	-	-	-	-	-	-
18. Fiberglass Corrugated Shell (.029") Plus Increased MLI On Bottom		135.0	61.2	54.6	24.8	-	-	-	-	-	-	-
19. Baseline Vehicle Except Insulation Outside Plus Increased MLI**		67.7	30.7	53.9	24.4	-	-	-	-	-	-	-
20. Baseline Vehicle Except Shadow Shield Plus Increased MLI**	Adequate	67.7	30.7	50.6	23.0	-	-	-	-	-	-	-

\* Selected For Preliminary Design  
 □ Not Including Shadow Shield Weight  
 • J. P. Stevens Co., Style 15035.  
 \*\* Non-Aluminized Shields  
 † System Weights Include Insulation, Tanks, Prop. Vapor, Helium & Helium Tank  
 • J. P. Stevens Co., Style 8116

Table 1.2-38: METEOROID PROTECTION EVALUATION 4" (10 cm) PAYLOAD HEIGHT, VEHICLE 1-2B, LF<sub>2</sub> ON TOP

	PROTECTION	STRUCTURE WEIGHT		SYSTEMS WEIGHT		PROTECTION ΔWT				TOTAL WEIGHT		
		lb	kg	lb	kg	β CLOTH		TANK		lb	kg	
						lb	kg	lb	kg			
1. Baseline Vehicle-Aluminum Truss, ALM/Nylon Net MLI Outside Vehicle	Inadequate	54.7	24.8	66.1	30.0	-	-	-	-	-	-	(120.8) (54.8)
2. Baseline Vehicle Plus Low Weight β Cloth* & Increased Tank Gage	Adequate	54.7	24.8	66.1	30.0	4.7	2.1	108.2	49.1	-	-	233.7 (106.0)
3. Baseline Vehicle Plus One β Cloth* & Increased Tank Gage		54.7	24.8	66.1	30.0	8.7	3.9	66.7	30.3	-	-	196.2 (89.0)
4. Baseline Vehicle Plus Two β Cloth* & Increased Tank Gage		54.7	24.8	66.1	30.0	17.5	7.9	12.6	5.7	-	-	150.9 (68.4)
5. Baseline Vehicle Plus Multiple Layers β Cloth*		54.7	24.8	66.1	30.0	34.8	15.8	-	-	-	-	155.6 (70.6)
6. Fiberglass Corrugated Shell (.023") Plus Increased Multilayer**		73.1	33.2	72.3	32.8	-	-	-	-	9.8	4.4	155.2 (70.4)
7. Baseline Vehicle Plus Low Weight β Cloth* & Increased Multilayer**		54.7	24.8	66.1	30.0	4.8	2.2	-	-	13.6	6.2	139.2 (63.1)
8. Baseline Vehicle Plus One β Cloth* & Increased Multilayer**		54.7	24.8	66.1	30.0	8.8	4.0	-	-	10.7	4.9	140.3 (63.6)
9. Baseline Vehicle Plus Two β Cloth* & Increased Multilayer**		54.7	24.8	66.1	30.0	17.5	7.9	-	-	4.1	1.9	142.4 (64.6)
10. Baseline Vehicle Plus Increased Multilayer**		54.7	24.8	66.1	30.0	-	-	-	-	16.5	7.5	137.3 (62.3)
11. Baseline Vehicle Plus Increased Multilayer (Aluminized Shields)		54.7	24.8	105.5	47.9	-	-	-	-	160.2	72.7	-
12. Baseline Vehicle Except Insulation Inside & Increased Multilayer**		54.7	24.8	79.3	36.0	-	-	-	-	11.9	5.4	145.9 (66.2)
13. Fiberglass Truss-Insulation Inside Plus Increased Multilayer**		54.4	24.7	68.2	30.9	-	-	-	-	15.1	6.8	137.7 (62.5)
14. Baseline Vehicle Except Insulation Inside, Shadow Shield & 24" Payload Height Plus Increased MLI**		55.5	25.2	61.5	27.9	-	-	-	-	15.9	7.2	132.9 (60.3)
15. Baseline Vehicle Except Shadow Shield & 24" Payload Height Plus Increased MLI**		55.5	25.2	60.1	27.3	-	-	-	-	17.1	7.8	132.7 (60.2)
16. Fiberglass Truss-Insulation Inside, 24" Payload Height, & Shadow Shield Plus Increased MLI**		55.3	25.1	59.8	27.1	-	-	-	-	16.2	7.3	131.3 (59.6)
17. Fiberglass Truss-Insulation Outside, 24" Payload Height, & Shadow Shield Plus Increased MLI**	Adequate	55.3	25.1	61.4	27.9	-	-	-	-	16.3	7.4	133.0 (60.3)

with a fixed thickness of MLI reduced tank gage requirements considerably. This led to an investigation of multiple layers of Beta fiber cloth alone, shown as Item 5 in the table. The MLI was ignored in this case and an 0.025 in (0.064 cm) tank gage was retained. This was not an efficient approach.

Figure 1.2-39 was also used to evaluate the combination of Beta fiber cloth and increased MLI thickness. In this case the 0.025 in (0.064 cm) tank gage was retained, thus  $T_2/D = 0.385$  and values of  $T_1/D$  were obtained for the three Beta fiber cloth thicknesses. Solving  $T_1/D = T_{ML}/D + T_{\beta}/D$  for  $T_{ML}$ , minimum thicknesses of MLI necessary for meteoroid protection were obtained. The thicknesses of MLI on the sidewall, lower sidewall and base were then increased to these values and the weights are reflected in Items 6, 7 and 8 of Table 1.2-37. The results of this investigation indicated that MLI by itself would be an efficient protection system.

Figure 1.2-38 was used to determine MLI thicknesses necessary to protect the 0.025 in (0.064 cm) tanks. Item 9 in the table shows that this was the least-weight approach investigated at that point. It was assumed that the additional MLI would contain non-aluminized mylar sheets so that the thermal balance obtained in the TATE analysis would be retained.

The influence of aluminized mylar sheets throughout the MLI/meteoroid protection blanket was investigated by means of the TATE program. The minimum MLI thickness on exterior surfaces was set at 0.33 in (0.84 cm). The program selected a new optimum weight design, Item 10 of Table 1.2-37, which proved to be slightly less weight than the approach using non-aluminized shields.

Several other types of MLI were investigated, Items 11 through 17 in the table, and nearly equivalent weights were obtained. The sliced foam spacer material offered slightly less weight, but was rejected because of uncertainties in predicting the thermal conductivity. Item 13 represents a check on the conclusion that increased MLI was the most efficient meteoroid protection. The analysis was made with NRC-2 MLI and the second most efficient approach, i.e., Beta fiber cloth combined with MLI. The original conclusion was proven correct.

An aluminum corrugated shell was evaluated for protection characteristics. Figure 1.2-40 shows curves for aluminum skin and combinations of skin and aluminized mylar/nylon net MLI. The aluminum skin alone did not provide sufficient protection for the 0.025 in (0.064 cm) tank wall. That curve showed the characteristic decrease in protection as aluminum thickness was increased above  $T_1/D = 0.1$  due to the acceleration of particles fragmented from the skin. A combination of thin aluminum sheet and MLI was investigated using the curve entitled  $T_{AL}/D = 0.027$ . Solving  $T_1/D = T_{AL}/D + T_{ML}/D$  for  $T_{ML}$  and  $T_{AL}$ , it was found that the thickness of MLI required was 0.26 in (0.66 cm) and the thickness of aluminum was 0.002 in (0.005 cm). The aluminum was equivalent to about 0.10 in (0.25 cm) of MLI which resulted in greater blanket thicknesses than were obtained by using just the MLI as the meteoroid protection system.

A fiberglass laminate corrugated shell was also evaluated. Using the fiberglass laminate curve of Figure 1.2-41, a value of  $T_1/D = 0.163$  was obtained for  $T_2/D = 0.385$ . The equivalent fiberglass laminate thickness for this case is 0.017 in (0.043 cm). The corrugated skin thickness for this design case was 0.029 in (0.074 cm). Therefore, the laminate alone provided sufficient protection. The continuous shell structures resulted in significant weight penalties due to the basic structure weight.

Two approaches which also appeared promising in the initial vehicle selection (Table 1.2-27) were variations of the baseline vehicle of Table 1.2-37 with insulation outside the structure and with one shadow shield between payload and top deck. These were evaluated for total weight, using increased MLI thickness to provide meteoroid protection. The results are shown as Items 19 and 20 in the table. The shadow shield approach provided the least weight, however, the weight of the shield and attachments was not included.

The concept selected for preliminary design development was Item 10 in the table. This approach was chosen because it was practical to construct and was one of the least-weight cases.

Vehicle 1-2B: A similar meteoroid protection evaluation was conducted for this vehicle. The results are presented in Table 1.2-38. All of the alternatives used in the analysis of Vehicle 1-14 were investigated with essentially the same results, i.e., the least overall weight approach to providing meteoroid protection was to add MLI. However, unlike Vehicle 1-14, it was found very inefficient to use aluminized shields in the extra MLI. System weights increased significantly using aluminized shields, largely due to the additional insulation, helium and helium bottle weight. The helium and bottle weight increases were attributed to a higher operating pressure in the oxidizer tank. In addition to the baseline vehicle alternatives, fiberglass corrugated shell and fiberglass truss structure concepts were evaluated. The fiberglass corrugated construction was not competitive because of high structure and system weights. An aluminum corrugated shell was rejected because of poor protection characteristics and higher structure weights. The fiberglass truss structure with insulation inside and additional non-aluminized MLI for meteoroid protection was also a least weight approach; however, since aluminum tubular structure was more commonly used, the latter approach appeared to be the best choice.

The last four entries in the table show the effects of a shadow shield, exclusive of the shield weight. The least-weight approach is Item 16, however, when considering the additional weight of payload supports and shadow shield, Item 10 was the most practical selection.

Vehicle 1-2A: Table 1.2-39 presents meteoroid protection evaluation results. Since additional MLI was the most efficient means of providing protection, the study was limited to this approach. MLI inside the structure (Item 3) and a

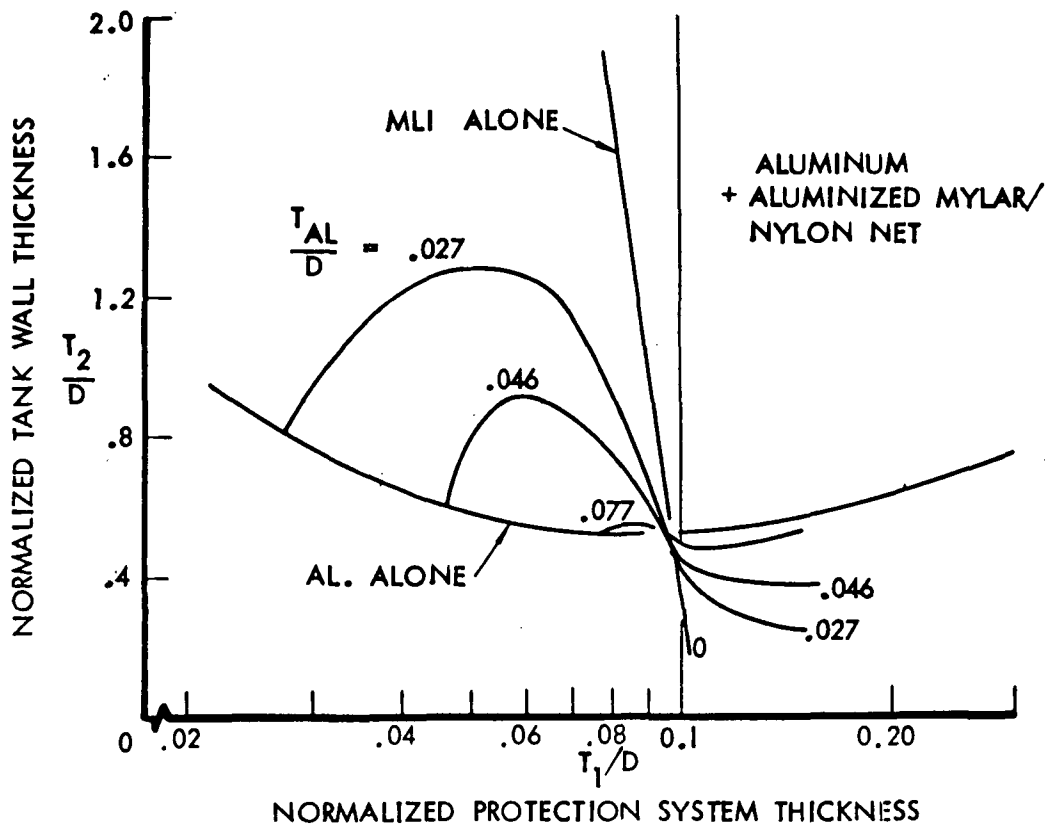


Figure 1.2-40: METEOROID PROTECTION DESIGN DATA - ALUMINUM & MLI

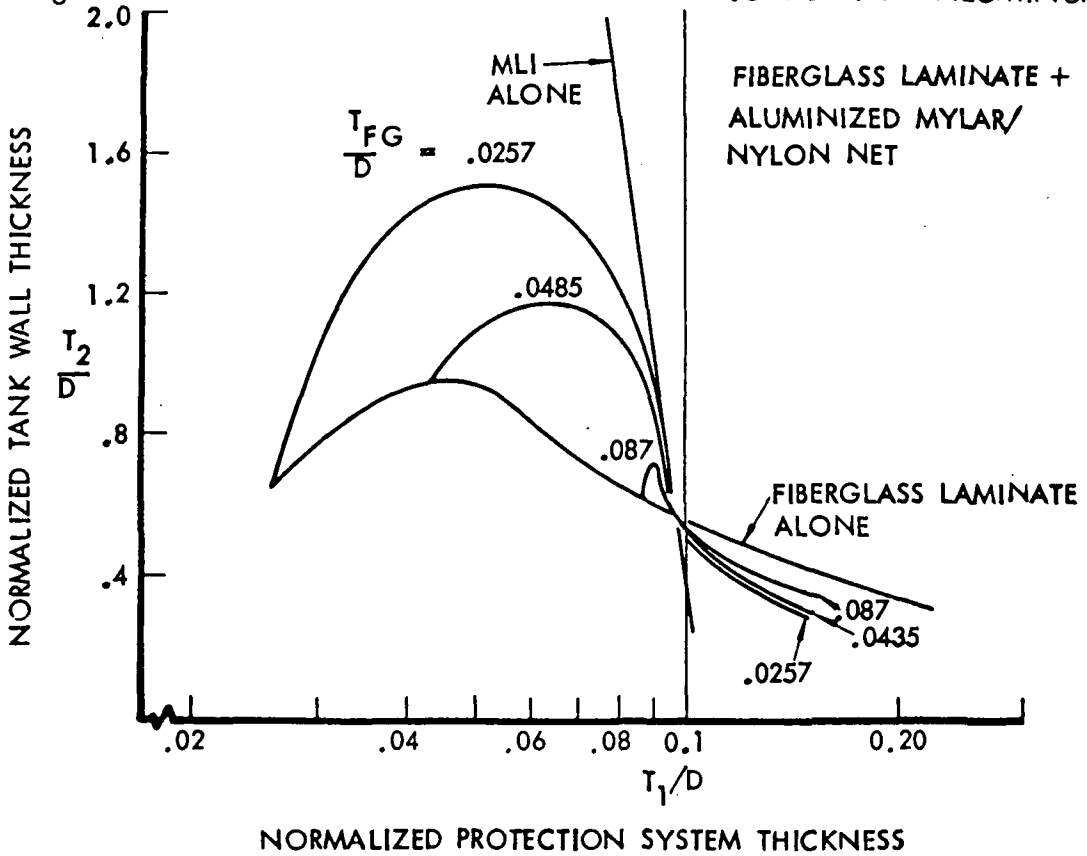


Figure 1.2-41: METEOROID PROTECTION DESIGN DATA - FIBERGLASS & MLI

fiberglass truss with MLI both inside and outside were evaluated. The concept chosen was an aluminum truss structure with MLI outside and aluminized shields in the meteoroid protection blanket.

Vehicle 1-3: Table 1.2-40 shows that the least-weight design was obtained with the baseline vehicle and additional MLI containing non-aluminized shields. The concept with MLI inside the structure was competitive, however, the compartment separation structure was expected to complicate that design.

Vehicle 1-7: The best design in Table 1.2-41 used aluminized radiation shields. A more comprehensive study of this vehicle was not undertaken because of excessive total weight.

Vehicle 2-3: The MLI on the sidewall and base of this vehicle was less than that required for meteoroid protection; therefore, alternative protection approaches were evaluated. These included: (1) adding Beta fiber cloth and increasing tank gages; (2) adding multiple layers of Beta fiber cloth, ignoring the MLI; (3) adding Beta fiber cloth and increasing MLI thickness; and (4) increasing MLI thickness alone. The same general trends observed for Vehicles 1-14 and 1-2B were obtained in this analysis. These were; for (1) above, it was more efficient to increase Beta fiber cloth weight than tank gage; for (2), multiple layers of Beta fiber cloth were not as efficient as the combination of cloth and increased tank gage; for (3), minimum cloth thickness with maximum MLI thickness was more optimum; and for (4), increased MLI thickness was the best approach evaluated. The analysis results are summarized in Table 1.2-42. Payload support weights were omitted since they were common to all approaches.

In the initial evaluation of Table 1.2-33 a fiberglass truss structure with insulation inside also appeared attractive for Vehicle 2-3. Multilayer thicknesses were increased on this vehicle to provide meteoroid protection and the weight is included in Table 1.2-42. This approach was competitive with the baseline vehicle, however, the more conventional aluminum structure would be the logical choice. The baseline vehicle with insulation on the inside was also evaluated and found to be only slightly heavier. The least-weight case incorporated the use of additional MLI with non-aluminized shields. This approach was chosen for preliminary design.

Vehicle 2-14: An appraisal of meteoroid protection approaches similar to the one described for Vehicle 2-3 was conducted. The results are shown in Table 1.2-43. The trends indicated are the same as described for Vehicle 2-3 and the least-weight approach consisted of additional MLI. A fiberglass truss structure with a high payload position was also evaluated. This approach was only slightly more efficient than the baseline.

Vehicle 2-18: Results are shown in Table 1.2-44. The least-weight case was obtained with additional MLI with non-aluminized shields. This approach was selected for design.

Vehicle 2-19: The addition of MLI was the only approach considered for this and Vehicle 2-2. The results are included in Table 1.2-45. Non-aluminized shields provided the least-weight.

Table 1.2-39: METEOROID PROTECTION EVALUATION 4" (10 cm) PAYLOAD HEIGHT, VEHICLE 1-2A

	PROTECTION	STRUCTURE WEIGHT		SYSTEMS WEIGHT		METEOROID PROTECTION ΔWT						TOTAL WEIGHT			
		WEIGHT		WEIGHT		β CLOTH		TANK		MLI		WEIGHT			
		lb	kg	lb	kg	lb	kg	lb	kg	lb	kg	lb	kg		
1.	Baseline Vehicle-Aluminum Truss, MLI Outside, ALM/Nylon Net	51.3	23.3	61.4	27.9	-	-	-	-	-	-	-	-	112.7	(51.1)
2.	Baseline Vehicle Plus Increased MLI**	51.3	23.3	61.4	27.9	-	-	-	-	14.4	6.5	-	-	127.1	57.7
3.	Baseline Vehicle Plus Increased MLI** Except Insulation Inside	51.3	23.3	64.6	29.3	-	-	-	-	12.8	5.8	-	-	128.7	58.4
4.	Baseline Vehicle Plus Increased MLI (Aluminized Shields)	51.3	23.3	75.2	34.1	-	-	-	-	-	-	-	-	126.5	57.4
5.	Fiberglass Truss, Insulation Outside Plus Increased MLI**	51.4	23.3	62.3	28.3	-	-	-	-	13.4	6.1	-	-	127.1	57.7
6.	Fiberglass Truss, Insulation Inside Plus Increased MLI**	51.4	23.3	63.9	29.0	-	-	-	-	12.9	5.9	-	-	128.2	58.2

Table 1.2-40: METEOROID PROTECTION EVALUATION 4" (10 cm) PAYLOAD HEIGHT, VEHICLE 1-3

1.	Baseline Vehicle-Aluminum Truss, MLI Outside, ALM/Nylon Net	49.3	22.4	78.2	35.5	-	-	-	-	-	-	-	-	127.5	(57.8)
2.	Baseline Vehicle Except Insulation Inside Plus Increased MLI**	49.3	22.4	84.5	38.3	-	-	-	-	11.8	5.4	-	-	145.6	66.0
3.	Baseline Vehicle Plus Increased MLI**	49.3	22.4	78.2	35.5	-	-	-	-	13.6	6.2	-	-	141.1	64.0
4.	Baseline Vehicle Plus Increased MLI (Aluminized Shields)	49.3	22.4	94.0	42.6	-	-	-	-	-	-	-	-	143.3	65.0

Table 1.2-41: METEOROID PROTECTION EVALUATION 4" (10 cm) PAYLOAD HEIGHT, VEHICLE 1-7

1.	Baseline Vehicle-Fiberglass Truss, ALM/Nylon Net, MLI Inside	95.4	43.3	77.6	35.2	-	-	-	-	-	-	-	-	173.0	(78.5)
2.	Baseline Vehicle Plus Increased MLI**	95.4	43.3	77.6	35.2	-	-	-	-	12.3	5.6	-	-	185.3	84.1
3.	Baseline Vehicle Plus Increased MLI (Aluminized Shields)	95.4	43.3	88.4	40.1	-	-	-	-	-	-	-	-	183.8	83.4

Table 1.2-42: METEOROID PROTECTION EVALUATION 4" (10 cm) PAYLOAD HEIGHT, VEHICLE 2-3

1.	Baseline Vehicle-Aluminum Truss, ALM/Nylon Net, MLI Outside	49.1	22.3	64.0	29.0	-	-	-	-	-	-	-	-	113.1	(51.3)
2.	Baseline Vehicle Plus Low Weight β Cloth & Increased Tank Gage	49.1	22.3	64.0	29.0	3.9	1.8	81.5	37.0	-	-	-	-	198.5	90.0
3.	Baseline Vehicle Plus One β Cloth* & Increased Tank Gage	49.1	22.3	64.0	29.0	6.6	3.0	41.3	18.7	-	-	-	-	161.0	73.0
4.	Baseline Vehicle Plus Two β Cloth* & Increased Tank Gage	49.1	22.3	64.0	29.0	13.1	5.9	4.1	1.9	-	-	-	-	130.3	59.1
5.	Baseline Vehicle Plus Multiple Layers β Cloth*	49.1	22.3	64.0	29.0	24.2	11.0	-	-	-	-	-	-	137.3	62.3
6.	Baseline Vehicle Plus Low Weight β Cloth & Increased MLI**	49.1	22.3	64.0	29.0	3.9	1.8	-	-	8.1	3.7	125.1	56.7	125.1	56.7
7.	Baseline Vehicle Plus One β Cloth* & Increased MLI**	49.1	22.3	64.0	29.0	8.1	3.7	-	-	5.4	2.4	126.6	57.4	126.6	57.4
8.	Baseline Vehicle Plus Increased MLI**	49.1	22.3	64.0	29.0	-	-	-	-	10.9	4.9	124.0	56.2	124.0	56.2
9.	Baseline Vehicle Plus Increased MLI** Insulation Inside	49.1	22.3	67.5	30.6	-	-	-	-	10.6	4.8	127.2	57.7	127.2	57.7
10.	Fiberglass Truss, 4" Payload Height, Insulation Inside, Plus Increased MLI**	50.8	23.0	62.9	28.5	-	-	-	-	10.8	4.9	124.5	56.5	124.5	56.5
11.	Baseline Vehicle Plus Increased MLI (Aluminized Shields)	49.1	22.3	105.5	47.9	-	-	-	-	-	-	154.6	70.1	154.6	70.1

● Included in System Weight  
 \* J. P. Stevens Co., Style 15035  
 \* J. P. Stevens Co., Style 8116  
 \* Selected For Preliminary Design  
 \*\* Non-Aluminized Shields  
 † Systems Weight Includes Insulation, Tanks, Prop. Vapor, Helium & Helium Tank

Table 1.2-43: METEOROID PROTECTION EVALUATION 4" (10 cm) PAYLOAD HEIGHT, VEHICLE 2-14

PROTECTION	SYSTEM WEIGHT*		ADAPTER WEIGHT†		METEOROID PROTECTION Δ WT		TANK SKIRT RING		STRUCTURE WEIGHT		TOTAL WEIGHT	
	lb	kg	lb	kg	lb	kg	lb	kg	lb	kg	lb	kg
1. Baseline Vehicle - Aluminum Truss, ALUM/Nylon Net, MLI Inside	52.4	23.8	-	-	-	-	-	-	-	-	62.6	28.4 (115.0) (52.2)
2. Baseline Vehicle Plus One B* Cloth & Increased Tank Gauge	52.4	23.8	5.8	2.6	24.8	11.2	-	-	-	-	62.6	28.4 145.6 66.0
3. Baseline Vehicle Plus Two B* Cloth & Increased Tank Gauge	52.4	23.8	11.6	5.3	1.1	0.5	-	-	-	-	62.6	28.4 127.7 57.9
4. Baseline Vehicle Plus Multiple Layers B* Cloth	52.4	23.8	25.5	11.6	-	-	-	-	-	-	62.6	28.4 140.5 63.7
5. Baseline Vehicle Plus Low Wt. B* Cloth & Increased MLI**	52.4	23.8	3.5	1.6	-	-	6.4	2.9	-	-	62.6	28.4 124.9 56.7
6. Baseline Vehicle Plus One B* Cloth & Increased MLI**	52.4	23.8	5.8	2.6	-	-	4.6	2.1	-	-	62.6	28.4 125.4 56.9
7. Baseline Vehicle Plus Increased MLI**	52.4	23.8	-	-	-	-	8.5	3.9	-	-	62.6	28.4 123.5 56.0
8. Fiberglass Truss, High Payload, Insulation Inside Plus Increased MLI**	42.3	19.2	-	-	-	-	10.1	4.6	-	-	62.6	28.4 121.9 55.3*
9. Baseline Vehicle Plus Increased MLI (Aluminized Shields)	59.3	26.9	-	-	-	-	-	-	-	-	66.6	30.2 122.4 55.5
10. Baseline Vehicle Except 13" Payload Height, Shadow Shield & Incr. MLI**	46.2	21.0	-	-	-	-	-	-	-	-	66.6	30.2 122.4 55.5

Table 1.2-44: METEOROID PROTECTION EVALUATION 4" (10 cm) PAYLOAD HEIGHT, VEHICLE 2-18

1. Baseline Vehicle - Fiberglass Payload Supports, MLI Inside, ALUM/Nylon Net	47.6	21.6	-	-	-	-	-	-	-	-	28.6	13.0 (74.2) (34.6)
2. Baseline Vehicle Plus One B* Cloth & Increased Tank Gauge	47.6	21.6	3.3	1.5	37.0	16.8	-	-	-	-	28.6	13.0 116.5 52.8
3. Baseline Vehicle Plus Two B* Cloth & Increased Tank Gauge	47.6	21.6	6.5	2.9	3.5	1.6	-	-	-	-	28.6	13.0 88.2 39.1
4. Baseline Vehicle Plus Multiple Layers B* Cloth	47.6	21.6	12.1	5.5	-	-	-	-	-	-	28.6	13.0 86.3 40.1
5. Baseline Vehicle Plus Low Wt. B* Cloth & Increased MLI**	47.6	21.6	2.0	0.9	-	-	2.6	1.2	-	-	28.6	13.0 80.8 36.7
6. Baseline Vehicle Plus One B* Cloth & Increased MLI**	47.6	21.6	3.3	1.5	-	-	1.4	0.6	-	-	28.6	13.0 80.9 36.7
7. Baseline Vehicle Plus Increased MLI**	47.6	21.6	-	-	-	-	4.1	1.9	-	-	28.6	13.0 80.3 36.4*
8. Baseline Vehicle Except Insulation Outside Plus Increased MLI**	48.0	21.8	-	-	-	-	4.8	2.2	-	-	28.6	13.0 81.4 36.9
9. Baseline Vehicle Except 12" Payload Ht. & Shadow Shield Plus Incr. MLI**	45.2	20.5	-	-	-	-	5.5	2.5	-	-	35.2	16.0 85.9 39.0
10. Baseline Vehicle Plus Increased MLI (Aluminized Shields)	53.4	24.2	-	-	-	-	-	-	-	-	28.6	13.0 82.0 37.2

Table 1.2-45: METEOROID PROTECTION EVALUATION 4" (10 cm) PAYLOAD HEIGHT, VEHICLE 2-19

PROTECTION	SYSTEM WEIGHT*		ADAPTER WEIGHT†		METEOROID PROTECTION Δ WT		TANK SKIRT RING		STRUCTURE WEIGHT		TOTAL WEIGHT	
	lb	kg	lb	kg	lb	kg	lb	kg	lb	kg	lb	kg
1. Baseline Vehicle - Fiberglass Payload Supports, ALUM/Nylon Net, MLI	51.8	23.5	34.6	15.7	-	-	-	-	-	-	116.9	53.0
2. Baseline Vehicle Plus Increased MLI**	51.8	23.5	34.6	15.7	9.0	4.1	3.6	1.6	10.9	4.9	120.5	54.7*
3. Baseline Vehicle Plus Increased MLI (Aluminized Shields)	56.9	25.8	34.6	15.7	9.0	4.1	•	•	10.9	4.9	122.0	55.3

Table 1.2-46: METEOROID PROTECTION EVALUATION 4" (10 cm) PAYLOAD HEIGHT, VEHICLE 2-2

1. Baseline Vehicle - Aluminum Truss, MLI Outside, ALUM/Nylon Net	57.2	25.9	-	-	-	-	-	-	-	-	41.6	18.9 (98.8) (44.8)
2. Baseline Vehicle Plus Increased MLI**	57.2	25.9	-	-	-	-	-	-	-	-	41.6	18.9 105.1 47.7*
3. Baseline Vehicle Plus Increased MLI (Aluminized Shields)	69.2	31.4	-	-	-	-	-	-	-	-	41.6	18.9 110.8 50.3

\* Selected For Preliminary Design  
 □ Not Including Shadow Shield Weight  
 \*\* Non-Aluminized Shields  
 • J. P. Stevens Co., Style 15035  
 † Payload Supports & End Attachments Only  
 ‡ Including End Attachment Weights  
 • Systems Wts. Include Insulation, Tanks, Prop. Vapor, Helium & Helium Tank  
 • Included in System Weights  
 • J. P. Stevens Co., Style 8116

Vehicle 2-2: Results of the evaluation are shown in Table 1.2-46. The case with non-aluminized shields was chosen for preliminary design.

### Preliminary Design & Weights

Preliminary design drawings were developed which combined the results of the vehicle structure and meteoroid protection evaluation with; (1) the selection and arrangement of internal structural members, (2) tank, engine and plumbing supports, and (3) configuration of thermal/meteoroid protection blankets, joints and attachments. Stress analyses were conducted to define member sizes.

The design drawings and discussion of important features are contained in Appendix D of Volume II, NASA CR-121104. The detailed weight statement for each vehicle is also contained in the appendix.

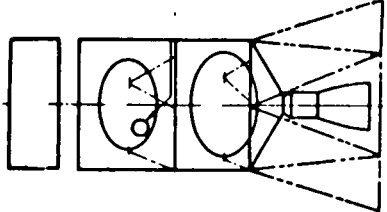
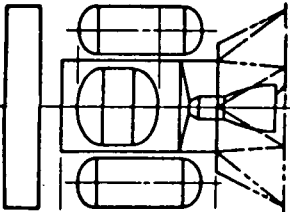
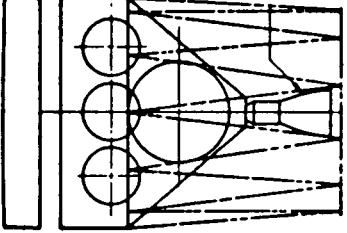
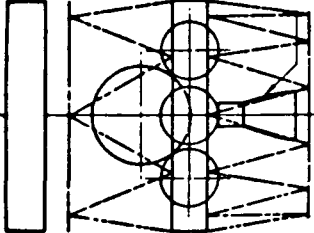
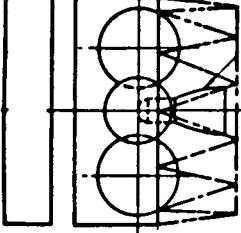
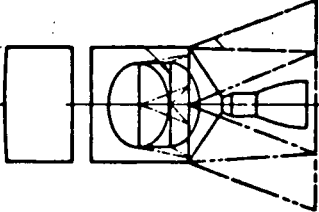
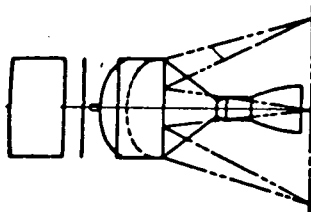
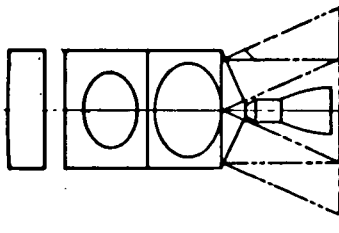
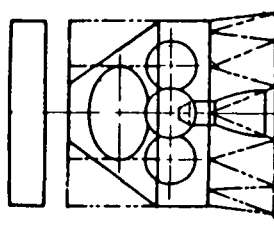
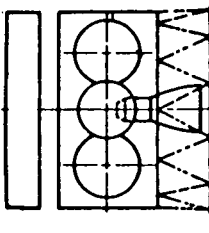
The chart of Figure 1.2-42 summarizes the weight data for the ten vehicle preliminary designs. The weights represented the entire vehicle and were obtained from the detailed analysis of the preliminary design drawings described in the appendix. The most efficient vehicles in terms of maximum payload were 1-14 for  $\text{LH}_2\text{-LF}_2$  propellants and 2-18 for  $\text{FLOX-CH}_4$  propellants.

### Operational Complexity

The ten preliminary designs were evaluated for their operational complexity, their sensitivity to accurate prediction of thermal performance, and the degree of confidence in the structural concept chosen. The evaluations were qualitative in nature.

Operational complexity was considered for prelaunch and flight operations, fabrication and assembly, and operational checkout. The charts of Figures 1.2-43 and 1.2-44 show the results for  $\text{FLOX-CH}_4$  vehicles. Only those features which were considered disadvantages were mentioned, thus the vehicle with the least comments appeared best. No attempt was made to weigh the disadvantages.

In general, vehicles with multiple tanks rated poorly. Problems of an operational nature (e.g., propellant management) as well as the increased complexity of manufacture, assembly and functional checkout were anticipated. The configuration of multiple tank vehicles tended to complicate the insulation design, increasing the number of MLI panel joints and penetrations. As a result, there was less confidence in making an accurate estimate of thermal performance. The comments on structural integrity pertained to the impact of a stiffness design criteria on structure weight. The structure for the vehicle designs was selected on the basis of steady state loads and no consideration was given to dynamic excitation or coupling. Vehicles such as those in this study could be expected to meet certain stiffness requirements and as a result, those with a more complex structural system would be penalized more than those vehicles with simple structural arrangements such as 2-18, 2-19 and 2-14.

	1-14	1-7	1-2B	1-2A	1-3
VEHICLE					
	Lb   kg	Lb   kg	Lb   kg	Lb   kg	Lb   kg
HARDWARE	506   230	563   255	611   277	644   292	652   296
PROPELLANT	2170   984	2170   984	2170   984	2170   984	2170   984
TOTAL*	2676   1214	2733   1240	2781   1261	2814   1276	2822   1280
PAYLOAD	4824   2188	4767   2162	4719   2141	4686   2126	4678   2122
MASS FRACTION X	0.82	0.80	0.79	0.78	0.78
	2-18	2-19	2-14	2-2	2-3
VEHICLE					
	Lb   kg	Lb   kg	Lb   kg	Lb   kg	Lb   kg
HARDWARE	399   181	400   181	432   196	515   234	516   234
PROPELLANT	2440   1107	2440   1107	2440   1107	2440   1107	2440   1107
TOTAL*	2839   1288	2840   1288	2872   1307	2955   1340	2956   1341
PAYLOAD	4661   2114	4660   2114	4628   2099	4545   2062	4544   2061
MASS FRACTION X	0.87	0.87	0.86	0.83	0.83

X EXCLUDING ADAPTOR WEIGHT \* INCLUDES VEHICLE ADAPTOR & PAYLOAD SUPPORTS  
 Figure 1.2-42: VEHICLE PRELIMINARY DESIGN, WEIGHT SUMMARY

RATING PARAMETER	VEHICLE			
	2-18	2-19	2-14	2-3
OPERATIONAL COMPLEXITY	PROPELLANT LOADING & PRESSURE MANAGEMENT TO AVOID COMMON BULKHEAD COLLAPSE.  POSSIBLE NEED FOR PRESSURE STABILIZATION OF COMMON BULKHEAD WHILE HANDLING & INSTALLING. STABILIZING RING REQUIRED FOR PAYLOAD SUPPORTS DURING STACKING OPERATIONS.	PROPELLANT LOADING & PRESSURE MANAGEMENT TO AVOID COMMON BULKHEAD COLLAPSE.	THERMAL STABILIZATION PERIOD IS EXTENDED BY TANK SEPARATION.	PROPELLANT ULLAGE MANAGEMENT DIFFICULTIES. MULTIPLE COMPARTMENT PURGING DIFFICULTIES.
PRELAUNCH OPERATIONS				FUEL ULLAGE MANAGEMENT DIFFICULTIES. MULTIPLE COMPARTMENT PURGING DIFFICULTIES.  USE OF HEAT EXCHANGERS TO EXTEND GROUND HOLD INCURS WEIGHT & OPERATIONAL PENALTIES. MULTIPLE TANKS INCREASE TOPPING & VENT RATES. THERMAL STABILIZATION PERIOD IS EXTENDED BY TANK SEPARATION.
FLIGHT OPERATIONS	NARROW VEHICLE MORE SENSITIVE TO ADAPTOR STAGING ALIGNMENT.	VEHICLE IS SENSITIVE TO SOLAR POINTING TOLERANCE BECAUSE OF TANKAGE CONFIG. NARROW VEHICLE MORE SENSITIVE TO ADAPTOR STAGING ALIGNMENT.	LONG VEHICLE MORE SENSITIVE TO SOLAR POINTING TOLERANCE. NARROW VEHICLE MORE SENSITIVE TO ADAPTOR STAGING ALIGNMENT.	MULTIPLE TANKS COMPLICATE ACQUISITION & TELEMETRY OF PROPELLANT CONDITION DATA. ADAPTOR SEPARATION COMPLICATED BY NUMEROUS MEMBERS. PROPELLANT UTILIZATION COMPLICATED BY MULTIPLE TANKS.  LONG VEHICLE MORE SENSITIVE TO SOLAR POINTING TOLERANCE.  PROPELLANT SETTLING TIME EXTENDED BY MULTIPLE TANKS, MANIFOLDS & FEED LINES. HIGH RESIDUAL LOSSES, TANKS, LINES & MANIFOLDS.
FABRICATION AND ASSEMBLY	COMMON BULKHEAD TANK ASSEMBLY MORE COMPLICATED THAN CONVENTIONAL TANKS .  TOP DECK INSULATION ASSEMBLY REQUIRES HAND FITTING AROUND PAYLOAD SUPPORT PENETRATIONS.		FLOX TANK REPLACEMENT WILL NECESSITATE REMOVAL OF CH <sub>4</sub> TANK. VEHICLE HEIGHT NECESSITATES INSULATION PANEL MID-BODY JOINT.	MULTIPLE TANKS & MANIFOLDS COMPLICATE LEAK CHECKING & REPAIR. FLOX TANK REPLACEMENT WILL NECESSITATE REMOVAL OF INSUL. SUPPORT CONE.  MORE COMPLEX STRUCTURAL ARRANGEMENT. MORE TANK SUPPORT ATTACHMENT POINTS COMPLICATE ASSEMBLY. TOP DECK INSULATION ASSEMBLY REQUIRES HAND FITTING AROUND PAYLOAD SUPPORT PENETRATIONS. MULTIPLE INSULATION PANELS & PANEL JOINTS COMPLICATES CONSTRUCTION ENGINE RECESS INSULATION INSTALLATION. REQUIRES HAND FITTING. COMPARTMENT PURGE SYSTEM COMPLICATED BY MULTIPLE TANKS.

Figure 1.2-43: OPERATIONAL COMPLEXITY EVALUATION - FLOX/CH<sub>4</sub> VEHICLES

VEHICLE				
RATING PARAMETER	2-18	2-19	2-14	2-3
OPERATIONAL COMPLEXITY (CONT'D) OPERATIONAL CHECKOUT (e.g. SYSTEM FUNCTION & LEAK CHECK)	2-2 ACCESS TO FLOX TANK COMPARTMENT FOR LEAK CHECKS & ADJUSTMENTS REQUIRES EXTENSIVE INSULATION PANEL REMOVAL.	TOP DECK ACCESS REQUIRES REPLACEMENT OF HAND FIT INSULATION JOINTS AROUND PAYLOAD SUPPORTS.  SYSTEM OPERATION CHECKS REQUIRE PRESSURE MANAGEMENT IN COMMON BLKHD. TANKS TO AVOID COLLAPSE.	TOP DECK ACCESS REQUIRES REPLACEMENT OF HAND FIT INSULATION JOINTS AROUND PAYLOAD SUPPORTS.  DEMONSTRATION OF PURGE SYSTEM ADEQUACY COMPLICATED IN MULTIPLE TANK CONFIGURATION.	MULTIPLE FLOX TANKS COMPLICATE NO-VENT REFRIGERATION (TANK MOUNTED) CONCEPTS.
THERMAL PERFORMANCE TOLERANCE PRELAUNCH THERMAL PROTECTION	TWO SIDEWALL INSULATION PLUMBING PENETRATIONS. SIX SIDEWALL INSULATION TANK SUPPORT PENETRATIONS.	PURGING COMPLICATED BY PROXIMITY OF INSULATION & TANK.  TWELVE PAYLOAD SUPPORTS PENETRATE TOP DECK INSUL. SIX ADAPTOR STUBS PENETRATE INSUL. ENGINE MOUNTED DIRECTLY TO FLOX TANK.	ONE MID-BODY INSULATION PANEL JOINT. FOUR SIDEWALL INSULATION PLUMBING PENETRATIONS. TWELVE SIDEWALL INSULATION TANK SUPPORT PENETRATIONS.	MULTIPLE FLOX TANKS COMPLICATE NO-VENT REFRIGERATION (TANK MOUNTED) CONCEPTS.
DESIGN DETAILS	TWO SIDEWALL INSULATION PLUMBING PENETRATIONS. SIX SIDEWALL INSULATION TANK SUPPORT PENETRATIONS.	TWELVE PAYLOAD SUPPORTS PENETRATE TOP DECK INSUL. SIX ADAPTOR STUBS PENETRATE INSUL. ENGINE MOUNTED DIRECTLY TO FLOX TANK.	ONE MID-BODY INSULATION PANEL JOINT. FOUR SIDEWALL INSULATION PLUMBING PENETRATIONS. TWELVE SIDEWALL INSULATION TANK SUPPORT PENETRATIONS.	MULTIPLE FLOX TANKS COMPLICATE NO-VENT REFRIGERATION (TANK MOUNTED) CONCEPTS.
STRUCTURAL INTEGRITY CONFIDENCE EFFECT OF STIFFNESS DESIGN CRITERIA ON STRUCTURE WEIGHTS (TANK SUPPORTS & GENERAL STRUCTURE)				

\* Propellant Heating Via The Engine During Ascent and Earth Orbit (Prior to Vehicle Orientation) Was Not Included in the Analysis and Could Have a Significant Effect on Vehicle Weight

Figure 1.2-44: OPERATIONAL COMPLEXITY EVALUATION - FLOX/CH<sub>4</sub> VEHICLES

RATING PARAMETER	VEHICLE		
	1-14	1-7	1-2B 1-2A 1-3
OPERATIONAL COMPLEXITY		FUEL ULLAGE MANAGEMENT DIFFICULTIES. MULTIPLE COMPARTMENT PURGING DIFFICULTIES. MULTIPLE FUEL TANKS INCREASE TOPPING AND VENT RATES.	OXIDIZER ULLAGE MANAGEMENT DIFFICULTIES. OXIDIZER TANK SEPARATION COMPLICATES PURGE FUNCTIONS.  USE OF TANK MOUNTED HEAT EXCHANGERS TO EXTEND OXIDIZER GROUND HOLD INCURS WEIGHT & OPERATIONAL PENALTIES.  MULTIPLE TANKS INCREASE TOPPING AND VENT RATES.
PRELAUNCH OPERATIONS			PROPELLANT ULLAGE MANAGEMENT DIFFICULTIES. TANK SEPARATION COMPLICATES PURGE FUNCTIONS.
FLIGHT OPERATIONS	NARROW VEHICLE MORE SENSITIVE TO ADAPTOR STAGING ALIGNMENT. LONG VEHICLE MORE SENSITIVE TO SOLAR POINTING TOLERANCE.	VEHICLE CONFIGURATION WITH EXTERNAL FUEL TANKS IS SENSITIVE TO SOLAR POINTING TOLERANCE. UNUSUAL PAYLOAD CONFIGURATION.  ADAPTOR SEPARATION COMPLICATED BY NUMEROUS MEMBERS. MULTIPLE TANKS COMPLICATE ACQUISITION & TELEMETRY OF PROPELLANT CONDITION DATA. PROPELLANT UTILIZATION COMPLICATED BY MULTIPLE TANKS. PROPELLANT SETTLING TIME EXTENDED BY MULTIPLE TANKS MANIFOLDS AND FEED LINES.  HIGH RESIDUAL LOSSES IN TANKS, LINES, AND MANIFOLDS.	STABILIZING RING REQUIRED FOR PAYLOAD SUPPORTS DURING STACKING OPERATIONS.
FABRICATION & ASSEMBLY	LH <sub>2</sub> TANK REPLACEMENT WILL NECESSITATE REMOVAL OF LF <sub>2</sub> TANK. VEHICLE HEIGHT NECESSITATES INSULATION PANEL MID-BODY JOINT.	INSULATION BLANKET EDGE JOINTS ARE EXTREMELY COMPLICATED. INSTALLATION OF COMPARTMENT SEPARATION BLANKET IS DIFFICULT.  MULTIPLE TANKS AND MANIFOLDS COMPLICATE ASSEMBLY, LEAK CHECKING AND REPAIR.	ACCESS FOR INSTALLATION OF COMPARTMENT SEPARATION BLANKET IS LIMITED.  ENGINE RECESS INSULATION INSTALLATION WILL NECESSITATE REMOVAL OF INSULATION SUPPORT CONE.  ENGINE RECESS INSULATION INSTALLATION REQUIRES HAND FITTING.

Figure 1.2-45: OPERATIONAL COMPLEXITY EVALUATION - LH<sub>2</sub>/LF<sub>2</sub> VEHICLES

RATING PARAMETER	VEHICLE		
	1-14	1-7	1-2A 1-3
OPERATIONAL COMPLEXITY (Cont'd) FABRICATION & ASSEMBLY		COMPARTMENT PURGE SYSTEM COMPLICATED BY FUEL TANK SEPARATION.	MORE COMPLEX STRUCTURAL ARRANGEMENT. MORE TANK SUPPORT ATTACHMENT POINTS COMPLICATE ASSEMBLY. TOP DECK OR UPPER SURFACE INSULATION ASSEMBLY REQUIRES HAND FITTING AROUND PAYLOAD SUPPORT PENETRATIONS. MULTIPLE INSULATION PANELS & PANEL JOINTS COMPLICATE CONSTRUCTION. COMPARTMENT PURGE SYSTEM COMPLICATED BY MULTIPLE TANKS AND SEPARATION DISTANCE.
OPERATIONAL CHECKOUT (e.g. System Function & Leak Check)			TOP DECK ACCESS REQUIRES REPLACEMENT OF HAND FIT INSULATION JOINTS AROUND PAYLOAD SUPPORTS. ACCESS TO LH <sub>2</sub> TANK COMPARTMENT FOR LEAK CHECKS & ADJUSTMENTS REQUIRES EXTENSIVE INSULATION PANEL REMOVAL. DEMONSTRATION OF PURGE SYSTEM ADEQUACY COMPLICATED IN MULTIPLE TANK CONFIGURATIONS.
THERMAL PERFORMANCE PRELAUNCH THERMAL PROTECTION		———— MULTIPLE TANKS COMPLICATE PURGE DISTRIBUTION.	MULTIPLE LF <sub>2</sub> TANKS COMPLICATE NO-VENT REFRIGERATION (TANK MOUNTED) CONCEPTS.
DESIGN DETAILS	FOUR SIDEWALL INSULATION PLUMBING PENETRATIONS, TANK SUPPORTS PENETRATE SIDEWALL INSULATION.  COMPARTMENT SEPARATION INSULATION BLANKET PENETRATED BY FLUID LINES.	FOUR SIDEWALL INSULATION PLUMBING PENETRATIONS, MANY INSULATION PANEL JOINTS AND SEVERE ALIGNMENT PROBLEMS.	SIX PAYLOAD SUPPORTS PENETRATE TOP DECK INSUL, TWELVE ADAPTOR STUBS PENETRATE BASE INSUL, COMPARTMENT SEPARATION BLANKET PENETRATED BY PRIMARY STRUCTURE & FLUID LINES.  TWO SIDEWALL & TWO BOTTOM CONE PLUMBING PENETRATIONS. SIX JOINTS IN BASE INSULATION.  STRUCTURE INSIDE OF INSULATION COMPLICATES PERFORMANCE PREDICTION.
STRUCTURAL INTEGRITY CONFIDENCE EFFECT OF STIFFNESS DESIGN CRITERIA ON STRUCTURE WEIGHTS (TANK SUPPORTS & GENERAL STRUCTURE).		EXPECT SOME WEIGHT INCREASE DUE TO LOW STIFFNESS OF FIBERGLASS.	EXPECT LARGE STRUCTURE AND INSULATION SUPPORT WEIGHT INCREASES.  EXPECT LARGE STRUCTURE WEIGHT INCREASE.

Figure 1.2-46: OPERATIONAL COMPLEXITY EVALUATION - LH<sub>2</sub>/LF<sub>2</sub> VEHICLES

The charts of Figures 1.2-45 and 1.2-46 show results for LH<sub>2</sub>-LF<sub>2</sub> vehicles. Those configurations with multiple tanks received the most unfavorable comments, a fact that was apparent in the evaluation of FLOX-CH<sub>4</sub> vehicles. The necessity for isolating fuel and oxidizer compartments with MLI added complexity to the LH<sub>2</sub>-LF<sub>2</sub> vehicles because fluid lines and in some cases structure penetrated these blankets. The blanket penetration problem was the most severe in vehicles with multiple tanks and MLI located outside of the structure. Vehicles with a more complex structural system, such as 1-2B, 1-2A and 1-3, were expected to suffer more of a weight penalty if a stiffness design criteria were imposed.

Vehicles 2-18 and 1-14 offered the most promise of achieving the "minimum operational complexity" objectives of the program.

### Vehicle Selection

The tabulation below summarizes the weight and operational complexity ratings of the ten vehicles.

<u>Vehicle</u>	<u>Weight Rating</u>	<u>Operational Complexity</u>
1-14	1	Least Complex
1-7	2	↓
1-2B	3	
1-2A	4	
1-3	5	
2-18	1	Least Complex
2-14	2	↓
2-19	1	
2-2	3	
2-3	4	

For LH<sub>2</sub>-LF<sub>2</sub> propellants, the least-weight approach was Vehicle 1-14 and this was also the least complex. Complexity increased with increasing weight.

The FLOX-CH<sub>4</sub> vehicles followed the same order with the exception of Vehicle 2-19 which was as weight efficient as 2-18, although more complex. Vehicle 2-18 was more representative of a structure-mounted thermal/meteoroid protection system.

It was concluded that Vehicles 1-14 and 2-18 most nearly met program goals of maximum payload weight with minimum operational complexity and these were selected for final design evaluation.

### 1.3 Final Evaluation

This phase of the program involved final design definition of LH<sub>2</sub>-LF<sub>2</sub> and FLOX-CH<sub>4</sub> Vehicles 1-14 and 2-18. Design refinements included minor structural changes and a more detailed thermal analysis. A weight summary was prepared. In addition, two analyses were performed to investigate (1) possible design changes due to variations of the meteoroid velocity function or flux, and (2) the sensitivity of vehicle weight to variations in the mean apparent thermal conductivity of MLI. A tank mounted MLI design was also prepared and comparisons were made with Vehicles 1-14 and 2-18.

#### 1.3.1 Final Design Development

Vehicle 1-14: The finalized design drawings for this vehicle are shown in Figures 1.3-1 and 1.3-2. The structural detail drawing, Figure 1.3-1, reflects changes to the upper bay structure. The truss members were changed to connect directly from the mid-body ring to the payload. Fiberglass was selected for these members, typical of all payload supports, and new sizes were determined based on the increased length and material properties. The upper body ring of the preliminary vehicle design was eliminated.

The primary electrical leads were added in Figure 1.3-1, as well as the valve actuation pressurant lines. A wiring diagram of the NASA/LeRC Research Propulsion Module was used as a guide in determining the type, quantity and location of electrical leads for a flight vehicle.

Some insulating details were changed in preparation of the final designs. These were the longitudinal panel joint, the junction of sidewall and compartment separation blankets and the conical base blanket. Details of fluid line and tank support penetrations were also added in Figure 1.3-2.

Several panel lace joint specimens were fabricated to aid in selection of the final configuration of longitudinal splice joint. Two types of joints, scarf and shiplap, were investigated. The shiplap joint was found to give the best closure. Diagonal lacing as shown in the preliminary design was unnecessary, instead a tie across the joint at 4-inch intervals was adequate. The joint was held in alignment by the X-850 film laminate. The laminate overlapped the joint on both sides and served as a guide during assembly. An external gap of 0.10 in (0.25 cm) indicated that the shiplap joint was in the correct position.

The final design of this vehicle removed the plumbing support members which were located in the compartment separation plane. This in turn eliminated the means of supporting the compartment separation MLI blanket. It was decided to add an attachment ring to the mid-body structural ring which necessitated splitting the upper sidewall insulation blanket at several locations to effect a lap joint.

The conical portion of the base blanket was changed to a laced joint rather than the Velcro fastened scarf joint of the preliminary design. The flat base blanket was then split at the edge in two locations to accommodate the propellant feed lines. This cut would be closed by hand stitching after the blanket was installed. This same technique would be employed for the upper sidewall blanket to allow installation around the  $LF_2$  vent line.

Vehicle 2-18: A slight increase in vehicle diameters, 2.20 in (5.6 cm), was necessary to improve the clearance between the truss mounted MLI and the tank. The FLOX feedline outlet was also moved from the sidewall of the tank to the bottom to eliminate MLI and payload support interference. Figures 1.3-3 and 1.3-4 present the final design drawings.

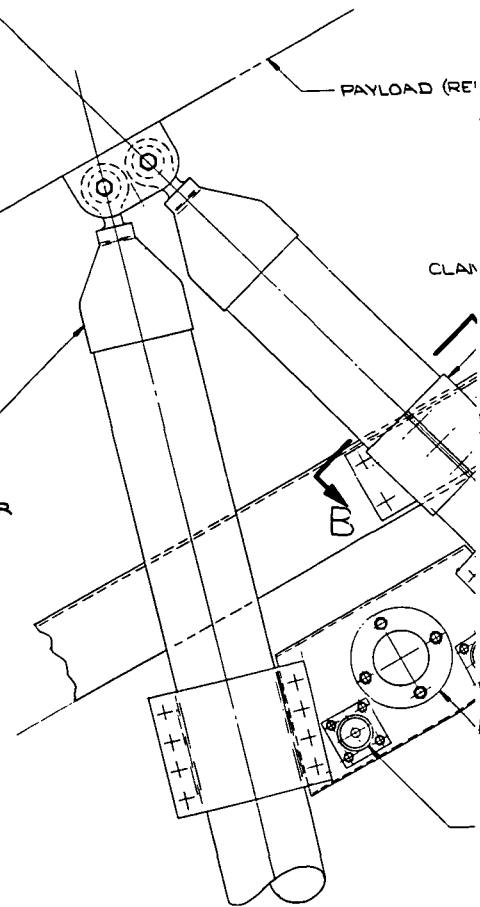
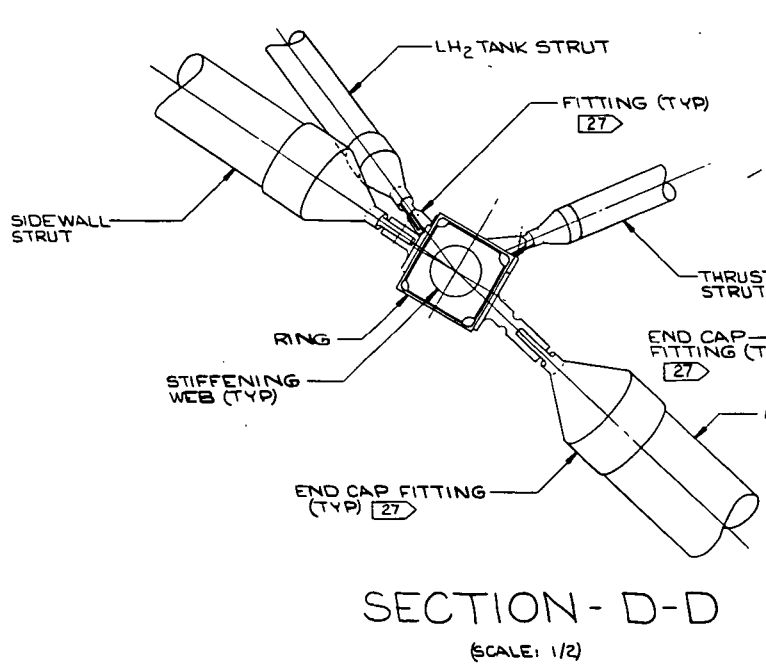
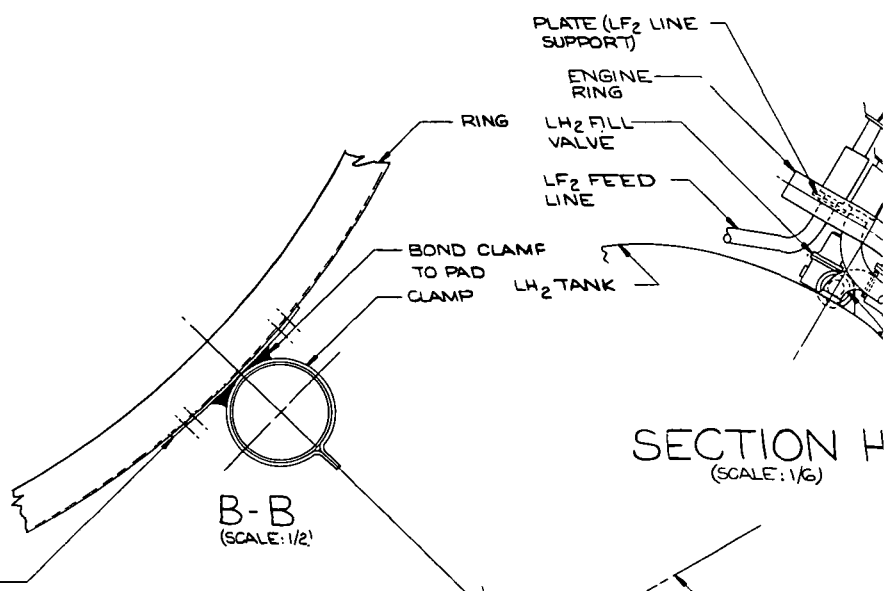
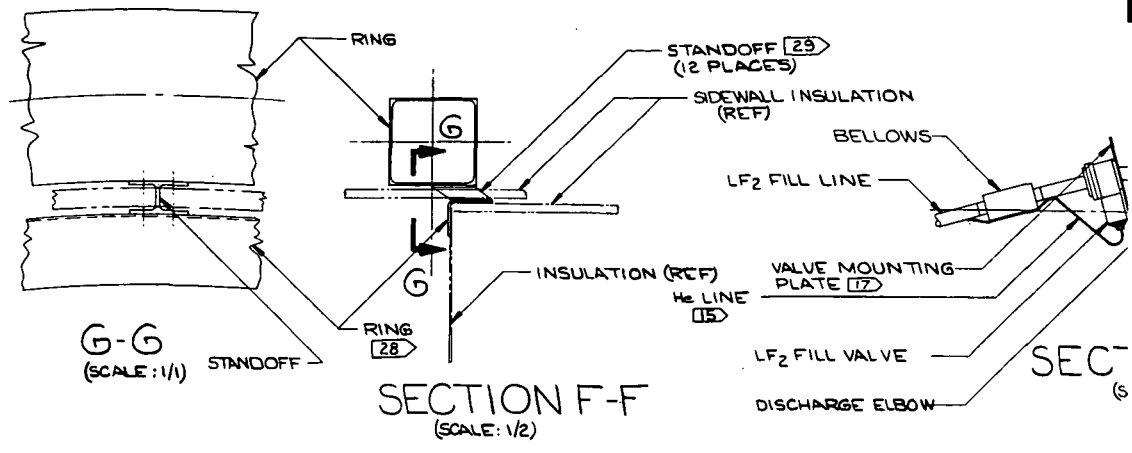
Insulating details remained essentially the same as the preliminary design concept for the conical base blanket. This was changed to two blankets, one conical and one flat, with a joint at the engine mount ring. The base portion would be installed around the propellant feedlines by reaching through the conical engine thrust structure. The conical blanket would be applied last. The zipper joint in the conical portion would provide access to the interior for final fit-up. Figure 1.3-4 incorporated MLI penetration details at tank supports and fluid lines.

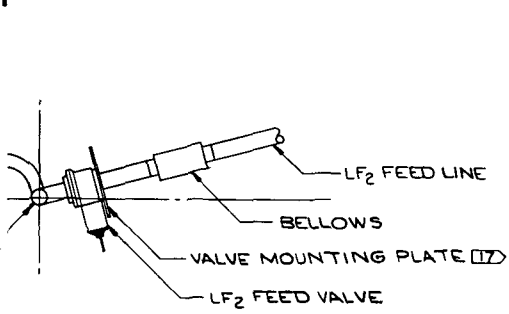
### 1.3.2 Thermal Analysis

The final design analyses were relatively complex compared to the preliminary design analyses. Each of the struts in the vehicle truss and engine support structure were modelled, accounting for conduction and radiation to surrounding surfaces. These struts were "smeared" into a shell for the preliminary design analysis. Additional refinements in the final design analysis were wiring conductors, MLI lateral conductors, and circumferential heat transfer in the structure. Approximately 80 nodes and 150 conductors were used to analyze the 2-18 vehicle and 135 nodes and 235 conductors to analyze the 1-14 vehicle.

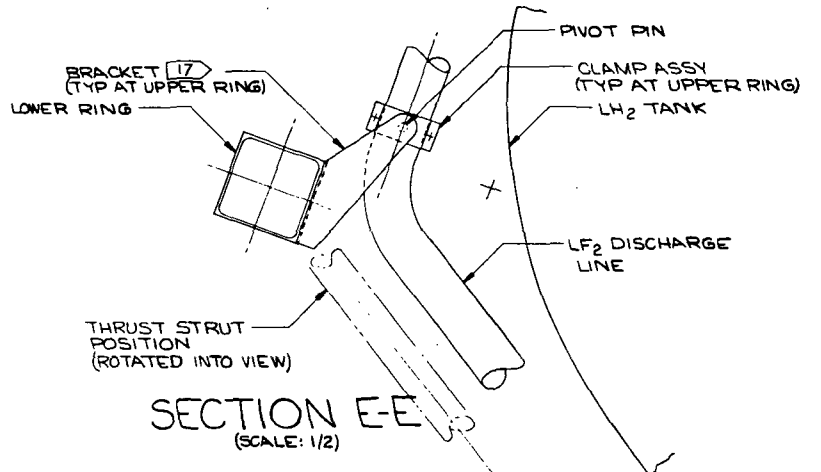
The thermal analysis node and conduction networks for the 1-14 design are shown in Figures 1.3-5 and 1.3-6. Figure 1.3-5 shows the structure, plumbing and wiring conductors, and Figure 1.3-6 shows the MLI conductors. In addition to the conduction network, 531 radiators were used to model the radiation from the solar panels and payload to the propulsion vehicle, between nodes on the vehicle (both externally and internally), and reradiation to space.

As shown by Figure 1.3-5, the structure was modelled to permit radiation and conduction in the circumferential direction, as well as in the longitudinal direction. The MLI nodes were assumed to be full  $360^\circ$  segments, so that circumferential temperature gradients in the insulation were suppressed. The results showed that, with a few exceptions, the circumferential gradients in the structure were small. For instance, the mid-body ring temperature varied from a minimum of  $154.8^\circ R$  ( $86^\circ K$ ) to a maximum of  $156.7^\circ R$  ( $87^\circ K$ ), with the extremes

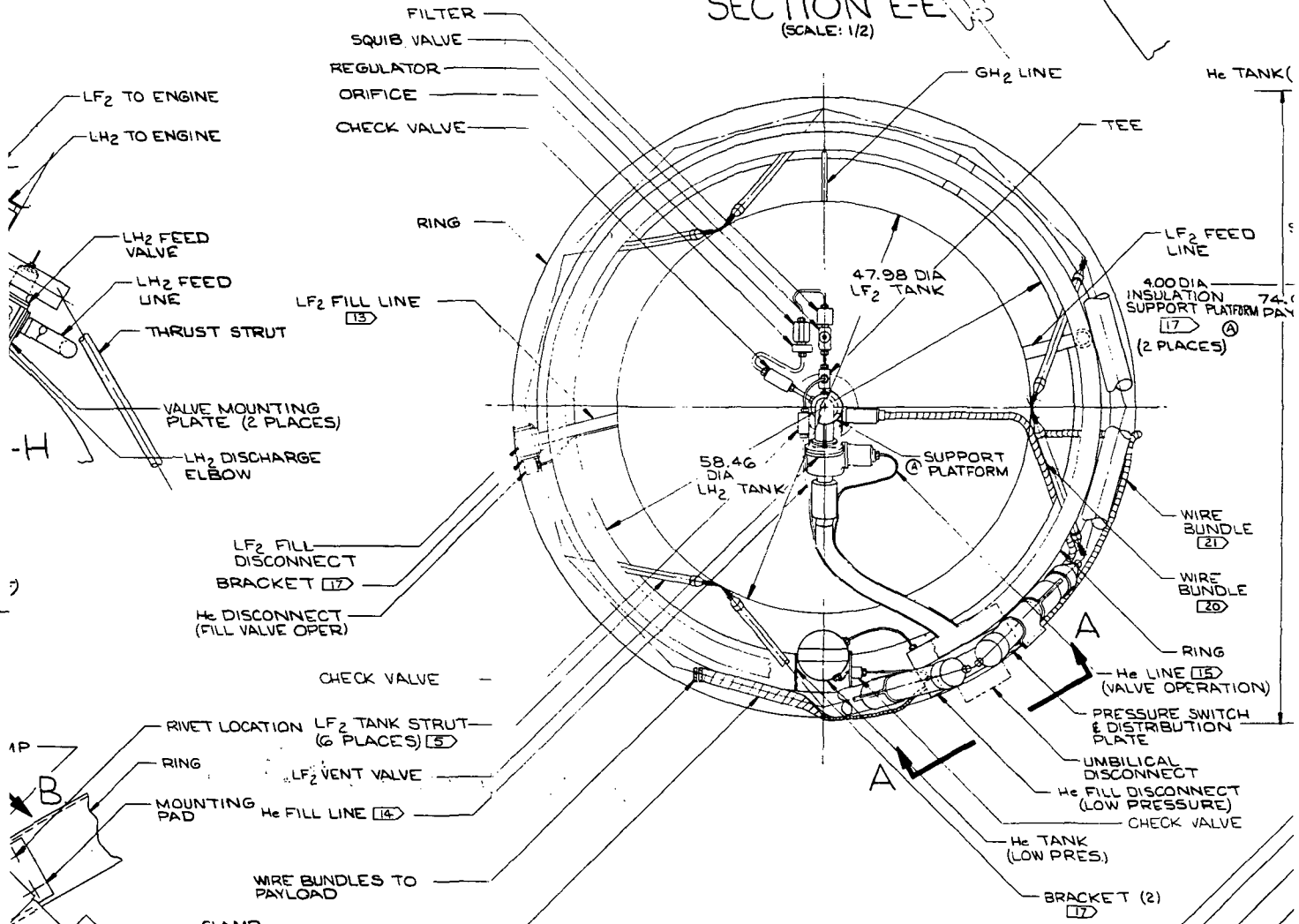




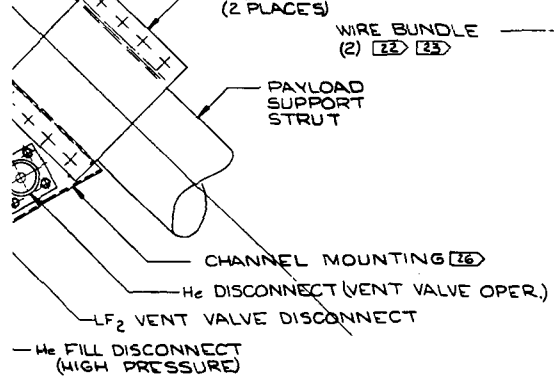
SECTION C-C  
SCALE: 1/6



SECTION E-E  
SCALE: 1/2

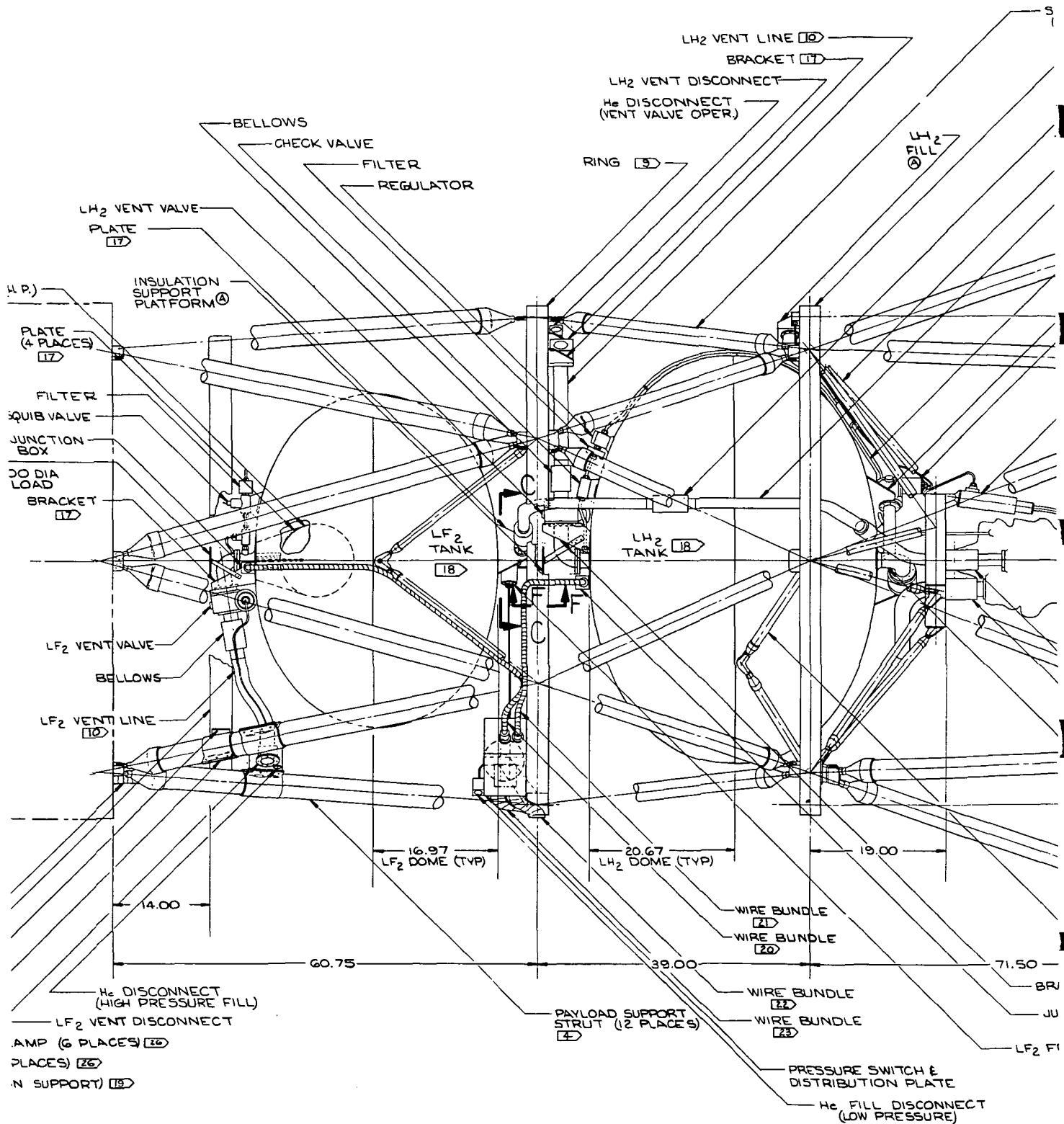


TOP VIEW  
SCALE: 1/6



VIEW A-A  
SCALE: 1/2





SIDE VIEW  
(SCALE: 1/6)

- [25] NYLON & CO
- [26] FIB
- [27] 2215 FIT 1.50 FIB
- [28] .06 STI
- [29] X-E CO. .06 FIB
- [30] HOOK & PILE FASTENER, VELCRO OR EQUIV.
- [31] .040 x 1.00 x 1.00 DIA REQD, FIBERGLASS LAMINATE COLLAR
- [32] MOLDED NYLON
- [33] EXTERNAL SHIELD ON ALL INSULATION BLANKETS WILL BE COATED WITH SCHJELDAHL GT 1015

IDE WALL STRUT  
(2 PLACES) (3)

RING (8)

BELLOWS (3 PLACES)

THRUST STRUT

LF<sub>2</sub> FEED LINE (12)

GH<sub>2</sub> LINE (16)

VALVE MOUNTING PLATE (17)

LH<sub>2</sub> FILL VALVE

ACTUATOR  
(2 PLACES)

70.00  
DIA

ENGINE

110.00 DIA  
CENTAUR  
INTERFACE

LH<sub>2</sub> TANK STRUT  
(6 PLACES) (6)

LF<sub>2</sub> GIMBAL BELLOWS

LH<sub>2</sub> GIMBAL BELLOWS

BRACKET (17)

FUNCTION BOX

SEED VALVE

ADAPTOR STRUT  
(2 PLACES)  
(19)

(19)

H<sub>2</sub> LINES (15) (3)  
(ACTUATORS & VALVE OPERATION)

LF<sub>2</sub> FEED LINE

BELLOWS

GH<sub>2</sub> LINE  
(FROM ENGINE)

BRACKET  
(2 PLACES)  
(17)

PLATE  
(17)

LF<sub>2</sub> TO  
ENGINE

LH<sub>2</sub> TO  
ENGINE

ADAPTOR  
STRUT

BOTTOM

(SCALE: 1/6)

ON NET, SEARS, ROEBUCK  
WT. .37 oz / yd<sup>2</sup>, .007 AVG T.

ERGLASS LAMINATE.

1-T6 ALUMINUM MACHINED  
TING,  
1.125 x .060 x 65.90 DIA  
ERGLASS RING.

0 FIBERGLASS LAMINATE  
INDOFF.

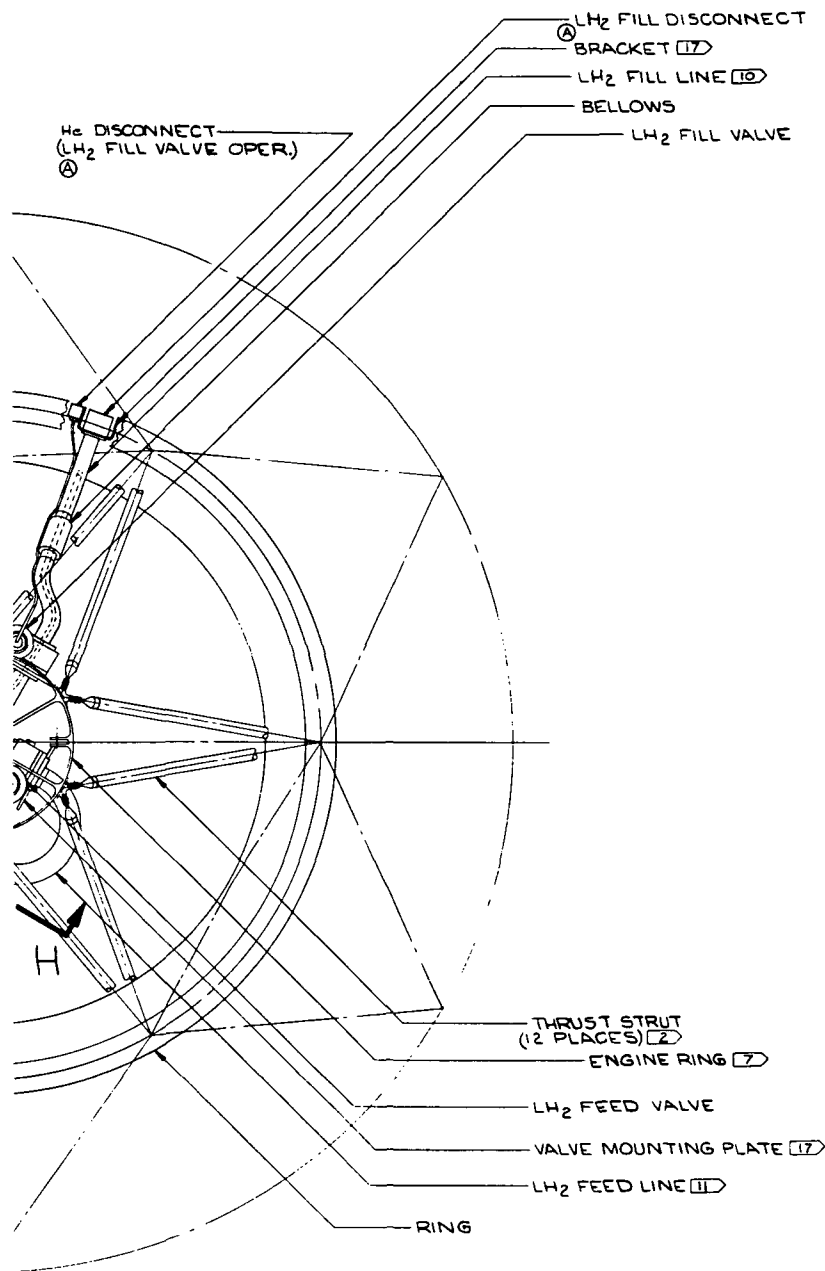
150 FILM SCHJELDAHL

0 x 1.00 x 1.00 \* LENGTH REQD.  
ERGLASS LAMINATE ANGLE

- (20) 11-.032 MN (MANGANIN) CONDUCTORS  
2-.080 CN (CONSTANTAN)
- (21) 13-.032 MN CONDUCTORS  
2-.064 MN  
2-.013 CN  
2-.013 CR (CHROMEL) CONDUCTORS
- (22) 11-.032 MN CONDUCTORS  
6-.080 CN
- (23) 13-.032 MN CONDUCTORS  
2-.064 MN  
4-.080 CN
- (24) ALUMINIZED MYLAR FILM.  
.15 MIL THICK

- (11) 2.10 DIA x .035 WALL, CRES.
- (12) 1.62 DIA x .035 WALL, CRES.
- (13) 1.50 DIA x .020 WALL, CRES.
- (14) .25 DIA x .049 WALL, CRES.
- (15) .25 DIA x .020 WALL, CRES.
- (16) .50 DIA x .049 WALL, CRES.
- (17) .250 CRES PLATE
- (18) 2219-T6E46 ALUM, t: .025
- (19) 3.00 x 1.50 x .060 x 64.60 DIA, FIB

REVISION				
NO.	DATE	DESCRIPTION	BY	APPROV.
A		RELOCATED LH <sub>2</sub> FILL LINE TO TOP OF LOWER RING. ADDED PLATFORM TO SUPPORT BLANKETS. SEE TOP & PLAN VIEW.		



GENERAL NOTES:

- 1) 3.00 DIA x .042 WALL, CARBON EPOXY COMPOS. TE.
- 2) 1.25 DIA x .035 WALL, 2219-T4 ALUM.
- 3) 2.58 DIA x .021 WALL, 7075-T6 ALUM.
- 4) 3.44 DIA x .036 WALL, FIBERGLASS
- 5) 1.35 DIA x .025 WALL, FIBERGLASS
- 6) 1.00 DIA x .015 WALL FIBERGLASS
- 7) 19.00 DIA x 2.00 x .250 WALL, 2219-T4 ALUM.
- 8) 73.00 DIA x 3.00 SQ x .095 WALL, 2219-T4 ALUM.
- 9) 73.00 DIA x 3.00 SQ x .083 WALL, 2219-T4 ALUM.
- 10) 2.00 DIA x .035 WALL, CRES.

VIEW

a)

STRUCTURAL DEVELOPMENT (2-5525)

A

REVISION A

2-2676-7 1-2-71

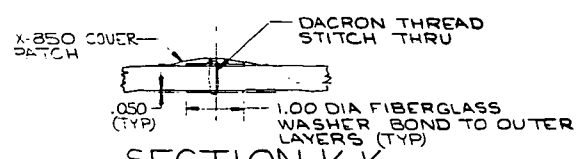
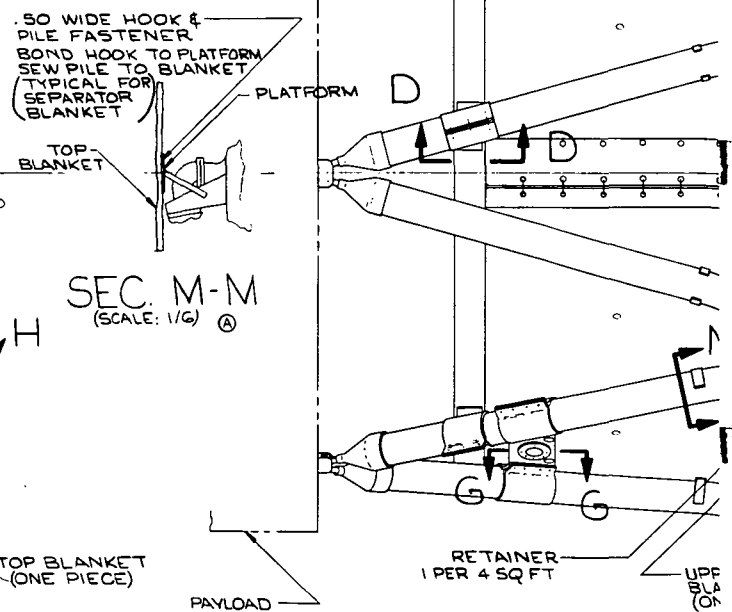
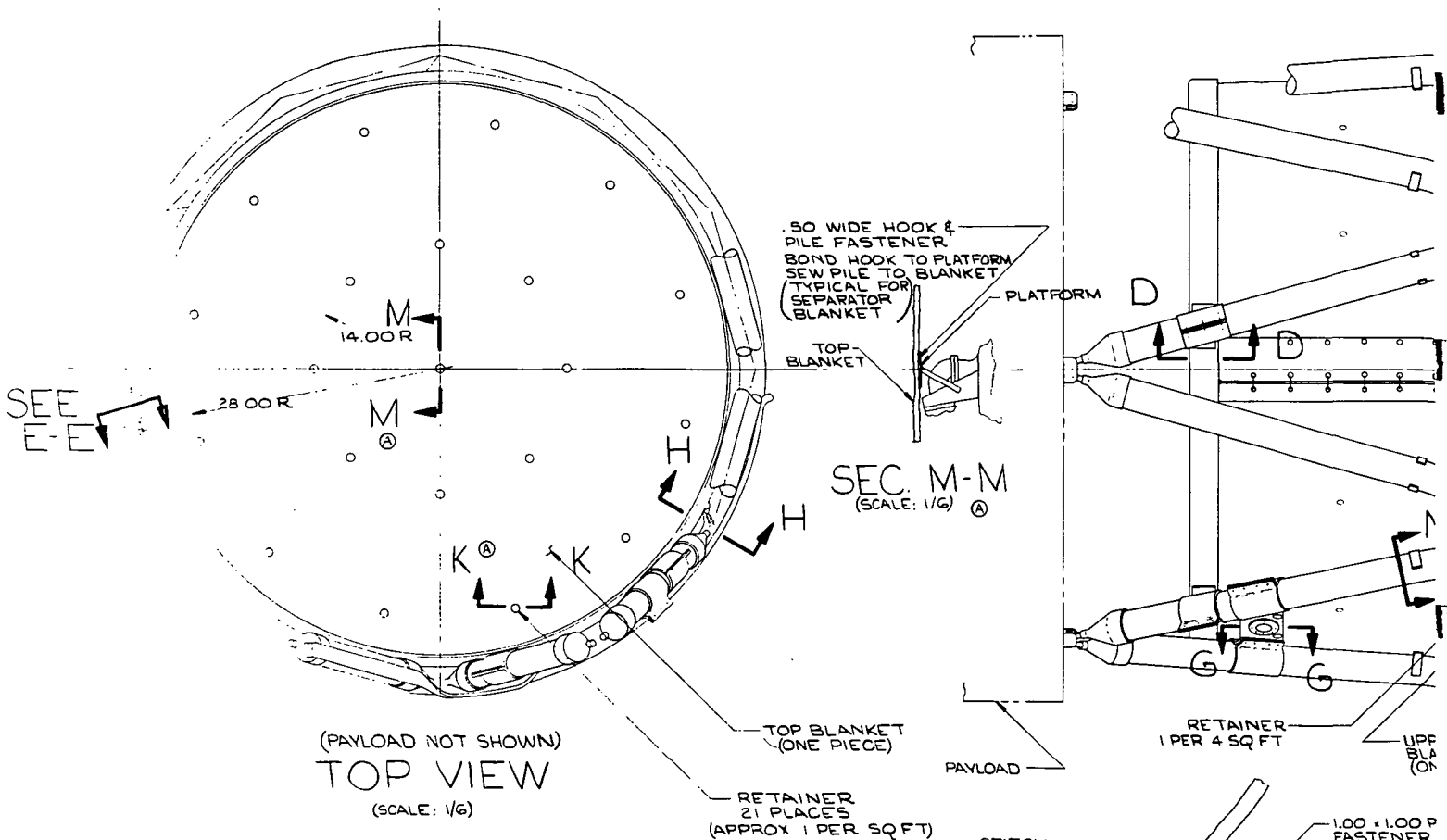
LF<sub>2</sub>-LH<sub>2</sub> PROPELLANTS THERMAL/METEOROID PROTECTION SYSTEM VEHICLE 1-14

SK-11-043145

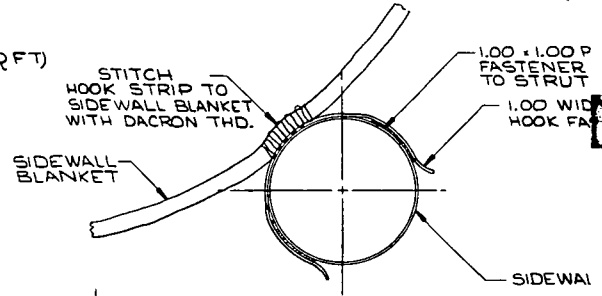
NOTED

Figure 1.3-1: STRUCTURAL DESIGN - VEHICLE 1-14

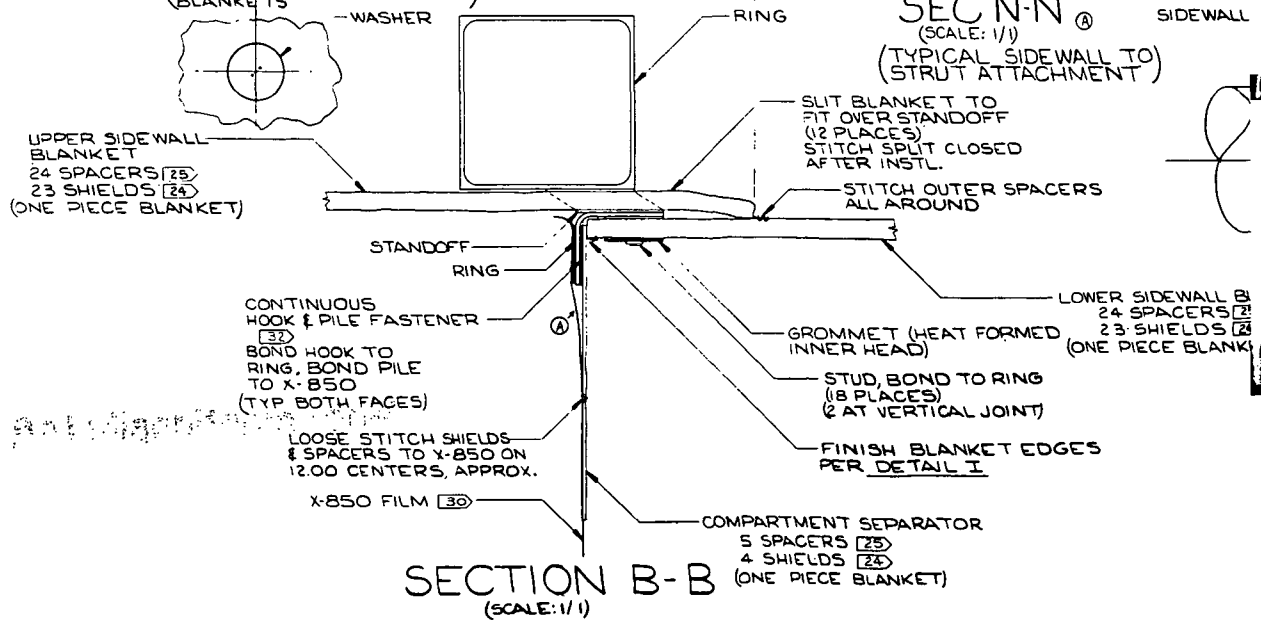
IR@GLASS



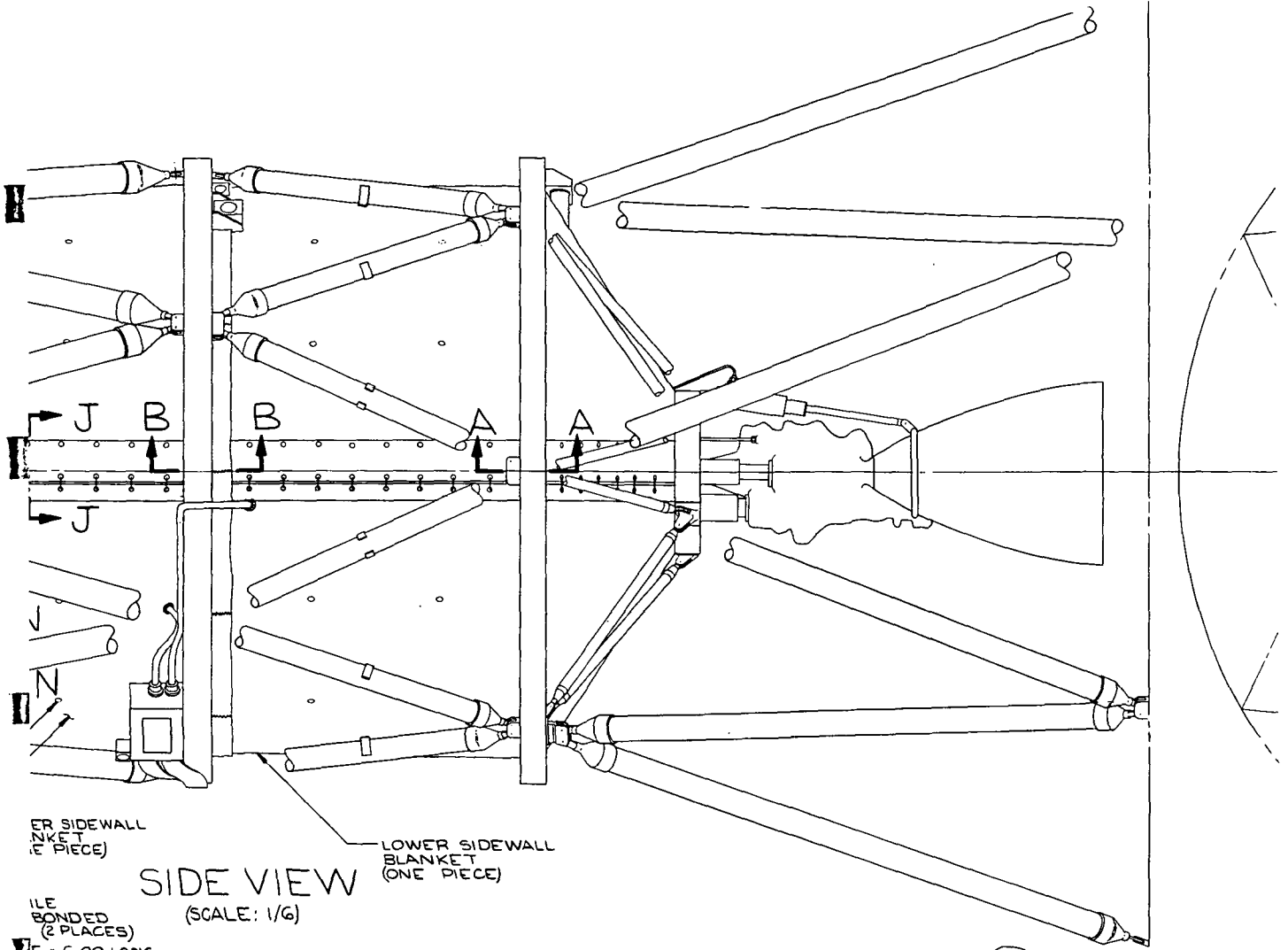
SECTION K-K (SCALE: 1/1) (TYPICAL TOP & SEPARATOR BLANKETS)



SECTION N-N (SCALE: 1/1) (TYPICAL SIDEWALL TO STRUT ATTACHMENT)



SECTION B-B (SCALE: 1/1)



**SIDE VIEW**

(SCALE: 1/6)

UPPER SIDEWALL  
BLANKET  
(ONE PIECE)

LOWER SIDEWALL  
BLANKET  
(ONE PIECE)

PILE  
BONDED  
(2 PLACES)  
PIE x 6.00 LONG  
FASTENER STRIP

ADAPTOR STRUT

THRUST STRUT

RING

1.00 WIDE CONTINUOUS HOOK  
& PILE FASTENER (32)  
BOND HOOK TO RING AND  
SEW PILE TO X-850 (30)

CONICAL BLANKET

ADAPTOR STRUT

SEPARATION SYSTEM

RETAINER (TYP)  
(HEAT FORMED HEAD)  
THRUST STRUT

SECT  
(SCALE)

SHIELDS

SPACERS

BLANKET

1.00 x 1.00 HOOK & PILE  
(32) PATCHES  
SEW HOOK, AT 4.00 SPACING, TO BASE  
BLANKET X-850  
SEW PILE, TO MATCH, TO OUTER  
SPACER AROUND BLANKET.

SCARF BLANKET  
EDGES, FINISH PER  
DETAIL J

CONICAL BASE BLANKET  
24 SPACERS (25)  
23 SHIELDS (26)

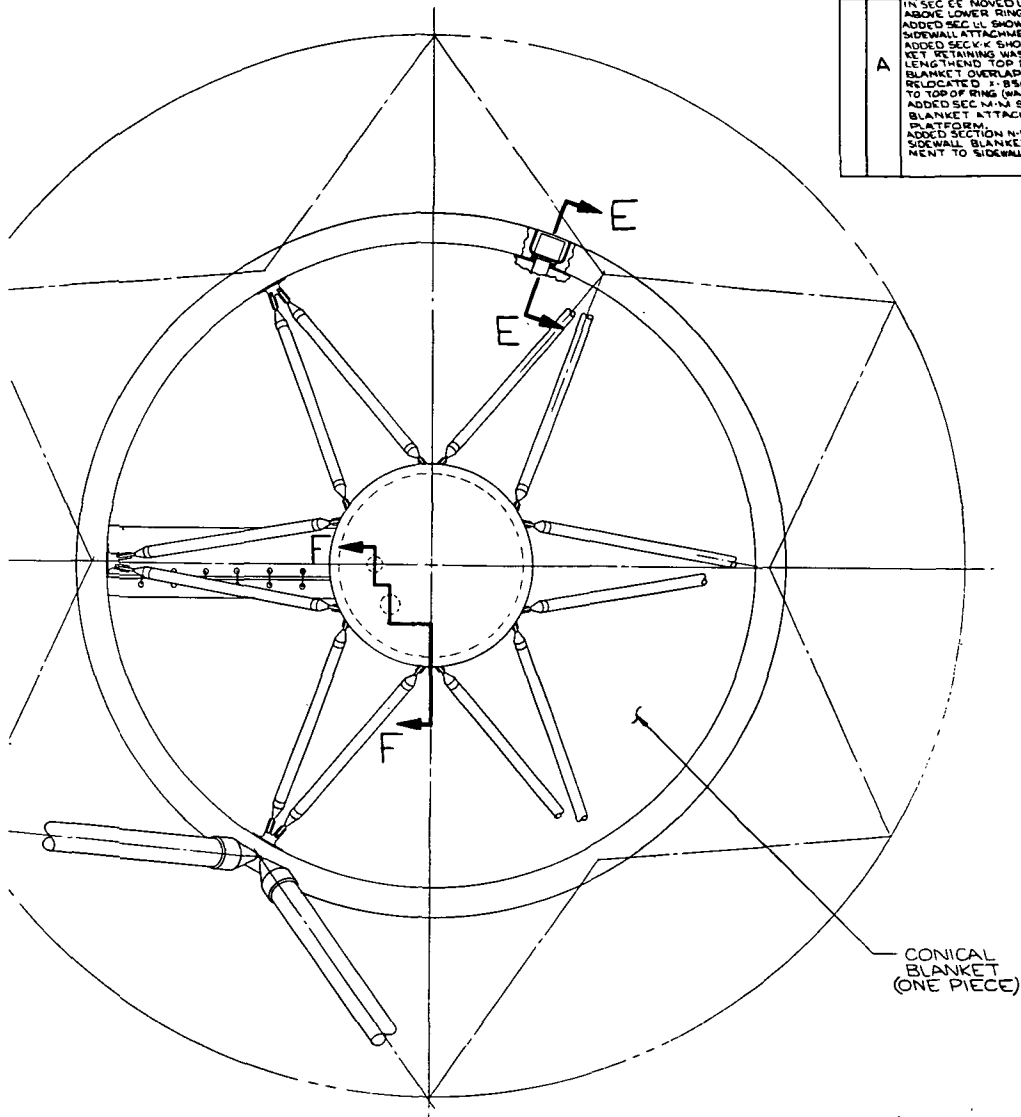
1.00 x .50 HOOK & PILE FASTENER (32)  
PATCH (3 PER STRUT)  
BOND HOOK TO STRUT  
SEW PILE TO X-850

DETAIL J  
(NO SCALE)

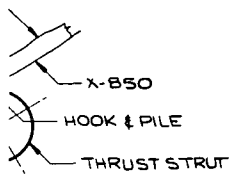
**SECTION A-A**

(SCALE: 1/1)

REVISION			
NO.	DATE	DESCRIPTION	BY
A		IN SEC EE MOVED L/R FILL LINE ABOVE LOWER RING. ADDED SEC U, SHOWING TYP SIDEWALL ATTACHMENT. ADDED SEC V, SHOWING BLANKET RETAINING WASHER. LENGTHENED TOP DECK BLANKET OVERLAP IN SEC D-D. RELOCATED F-B50 IN SEC B8 TO TOP OF RING (WAS UNDER). ADDED SEC W-N SHOWING BLANKET ATTACHMENT TO PLATFORM. ADDED SECTION N-N SHOWING SIDEWALL BLANKET ATTACHMENT TO SIDEWALL STRUTS.	

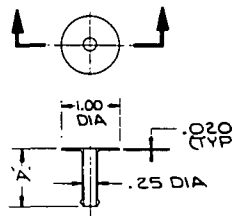


TOP VIEW  
(SCALE: 1/6)

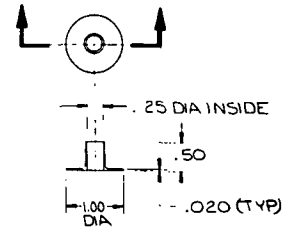


ION C-C  
(SCALE: 1/1)

ERS



STUD 34  
(SCALE: 1/1)

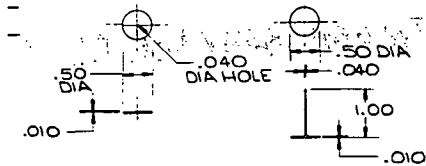


GROMMET 34  
(SCALE: 1/1)

DIM	NO
.40	18
.75	18

SEE SHEET ONE FOR NOTES AND STRUCTURAL ARRANGEMENT

SPACER LOOPED AROUND BLANKET END  
STITCH OUTER SPACERS ALL AROUND



RETAINER WASHER 34  
(SCALE: 1/1)

RETAINER STEM 34  
(SCALE: 1/1)

2-5085

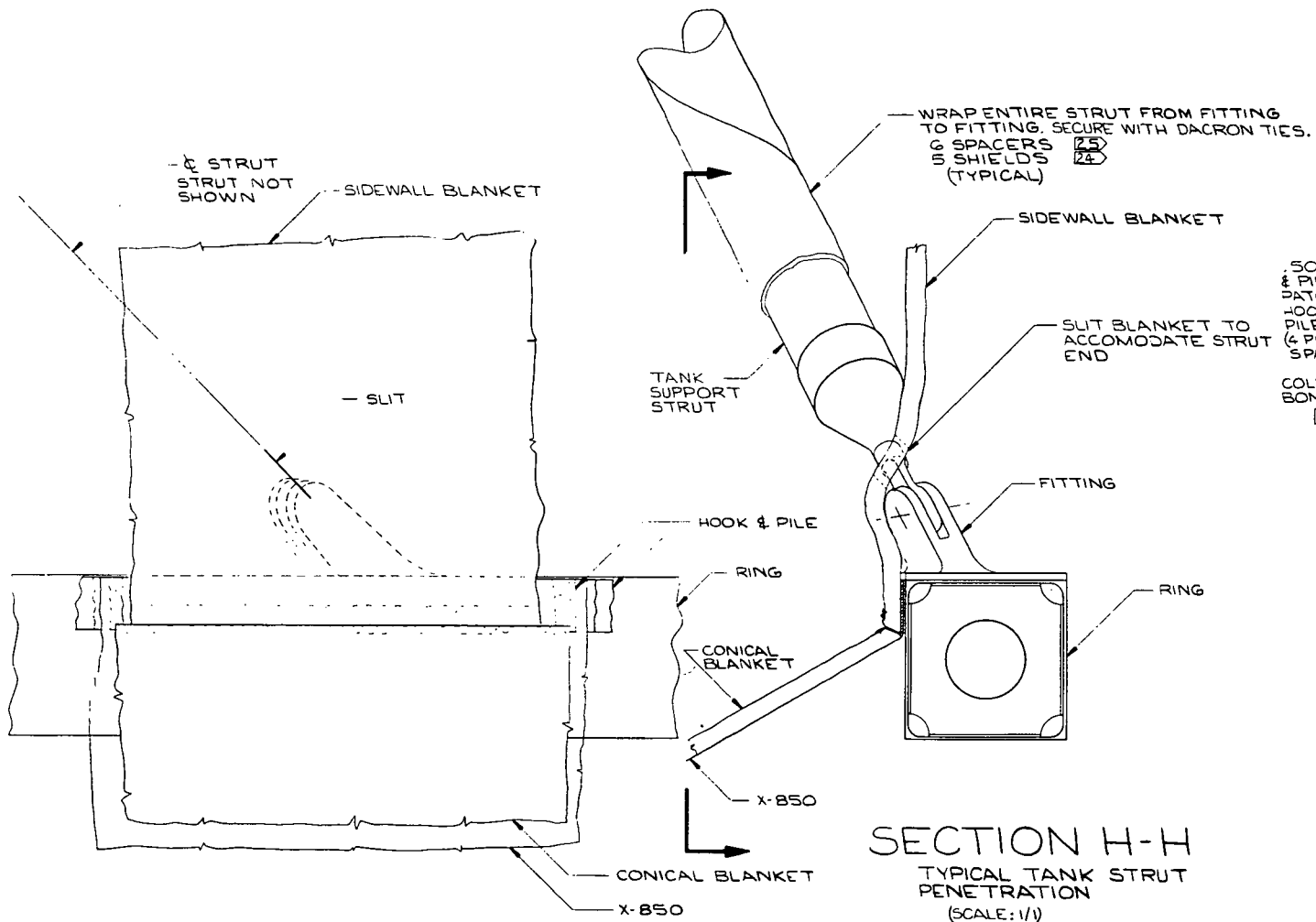
REVISION A

K.W. OSBORNE 1971

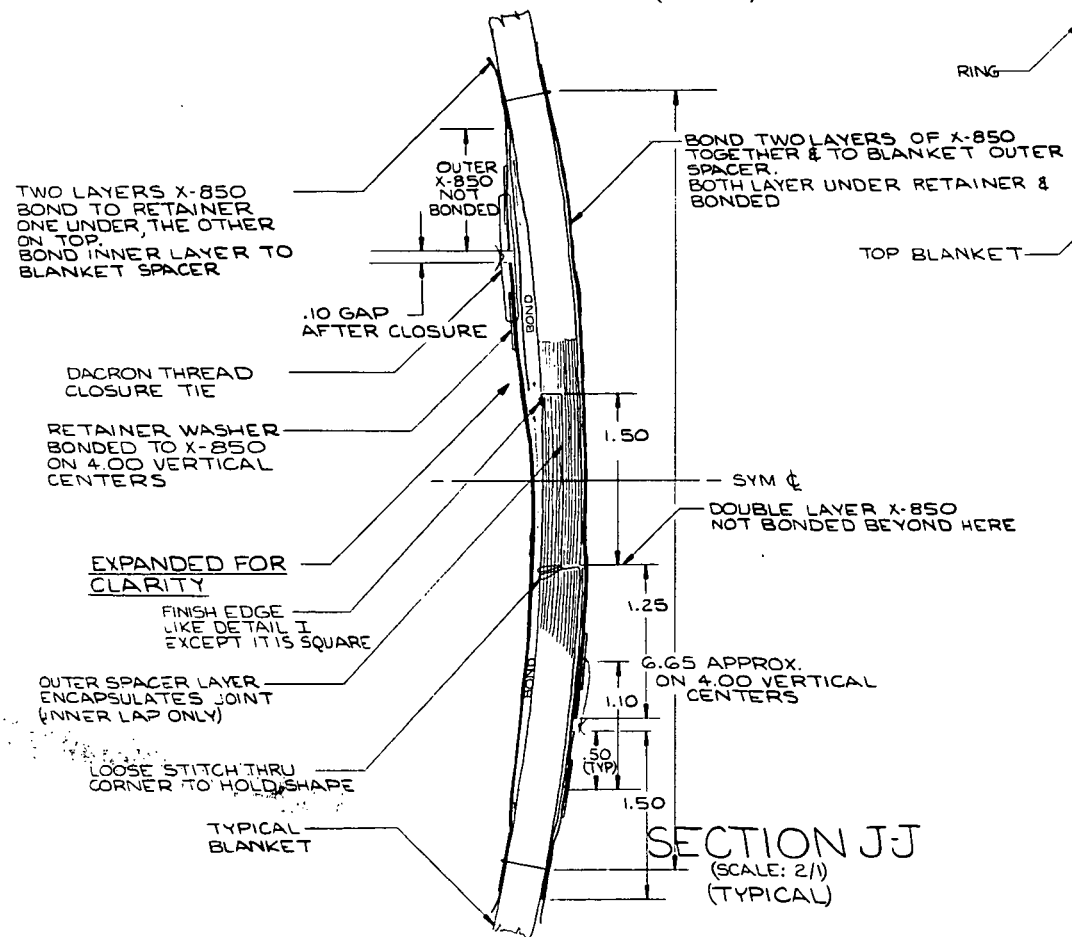
LF<sub>2</sub>-LH<sub>2</sub> PROPELLANTS THERMAL/METEOROID PROTECTION SYSTEM VEHICLE 1-14

SK11-043145

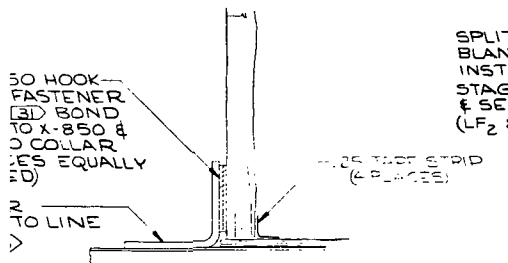
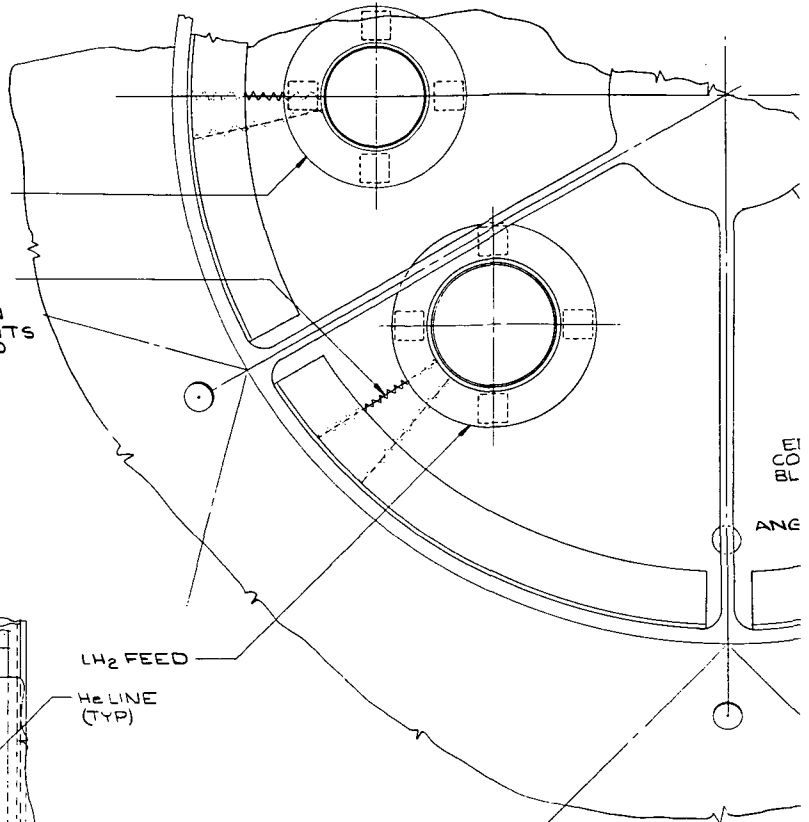
Figure 1.3-2: INSULATION DETAILS - VEHICLE 1-14



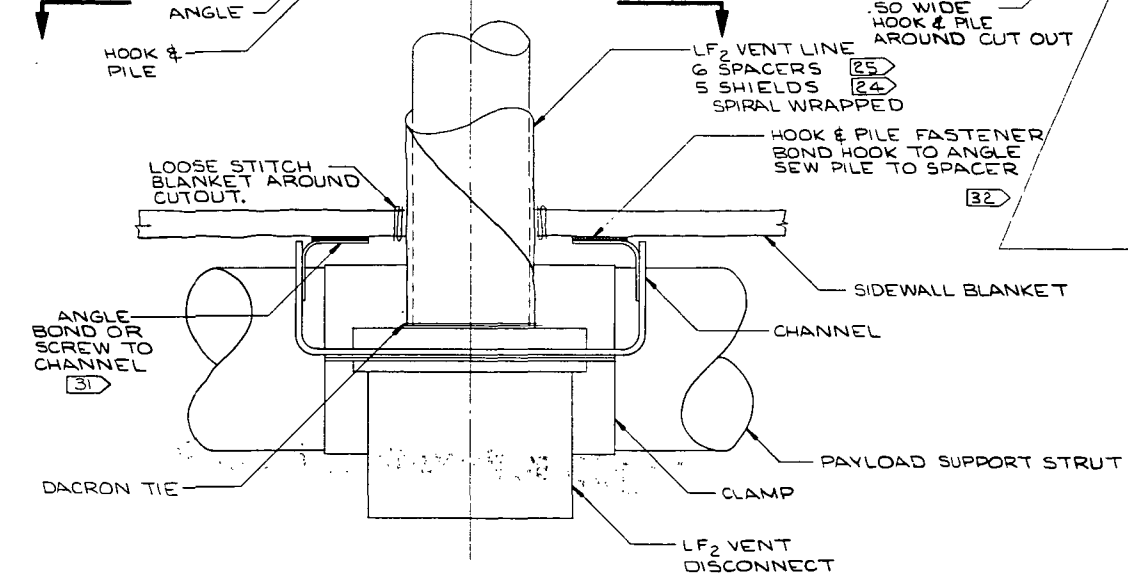
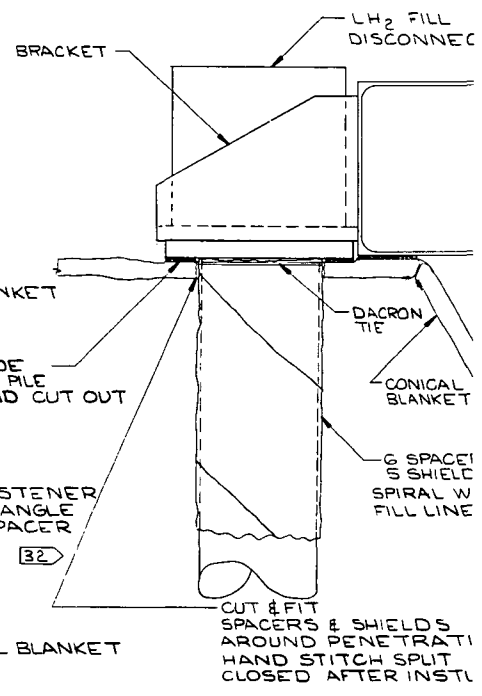
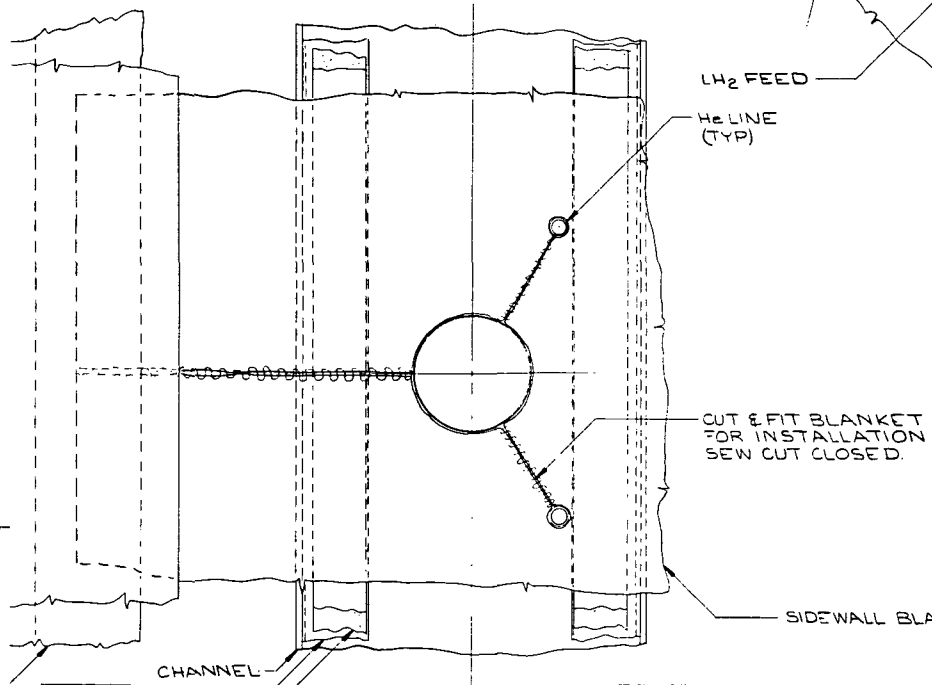
SECTION H-H  
TYPICAL TANK STRUT PENETRATION  
(SCALE: 1/1)



SECTION J-J  
(SCALE: 2/1)  
(TYPICAL)

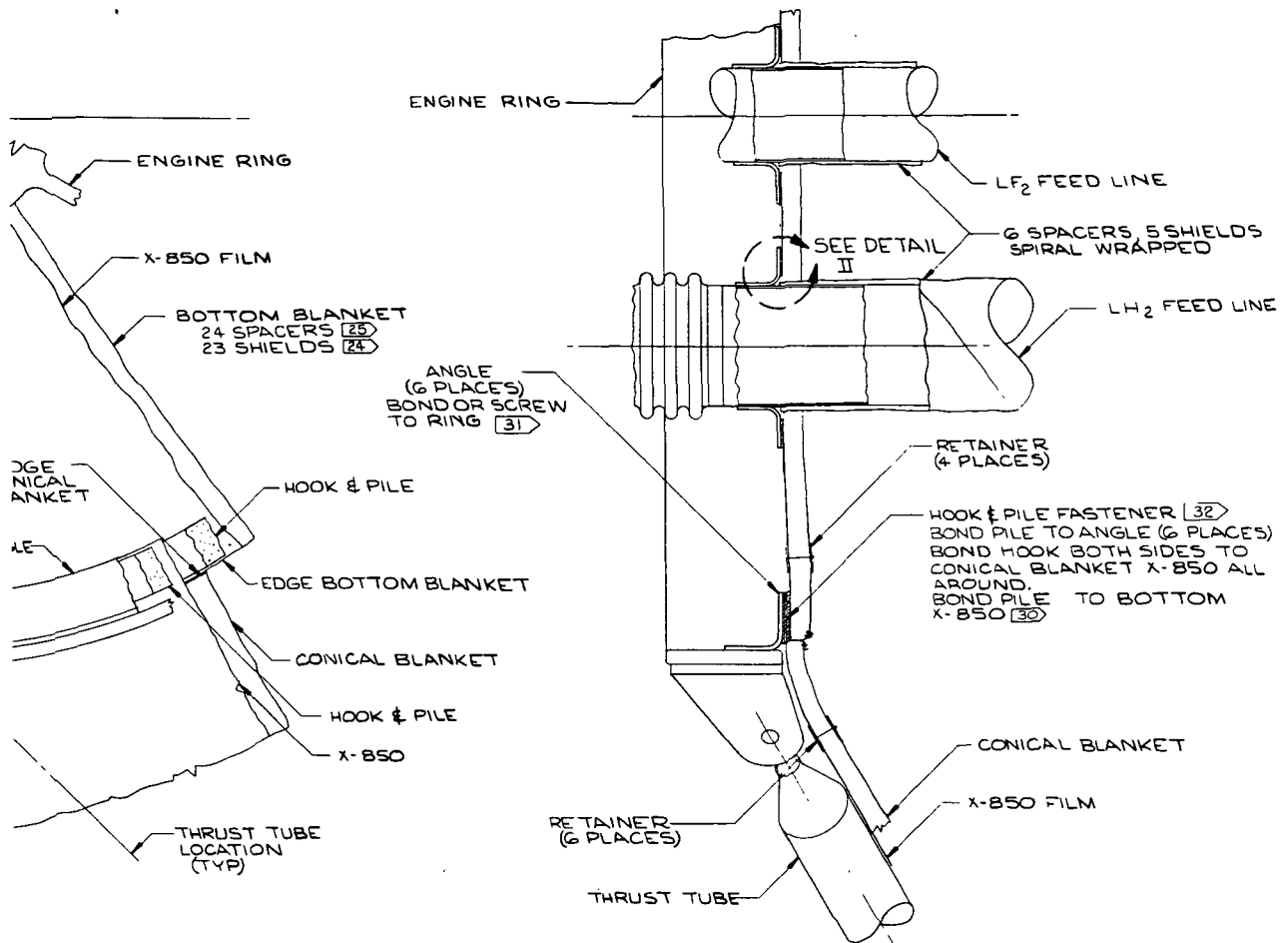


DETAIL II TYPICAL PENETRATION  
(NO SCALE)

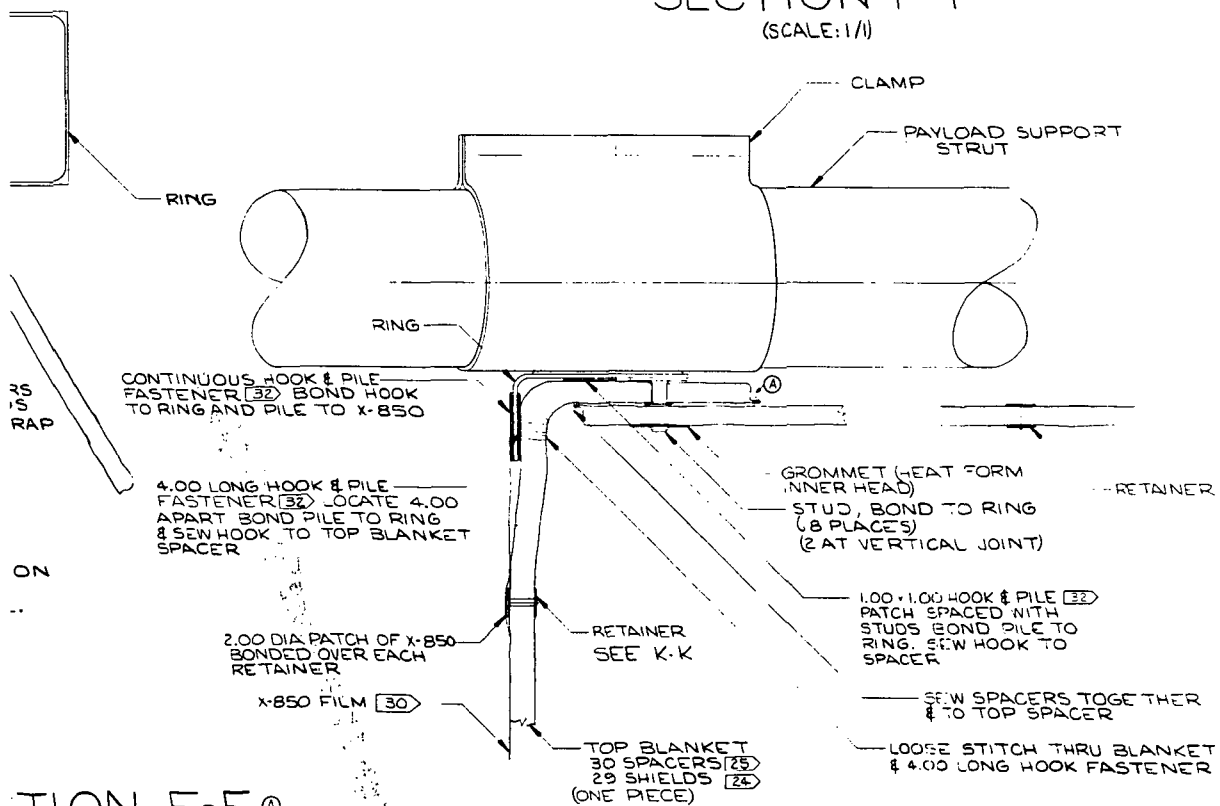


SECTION G-G  
(SCALE: 1/1)

SEC  
(T)



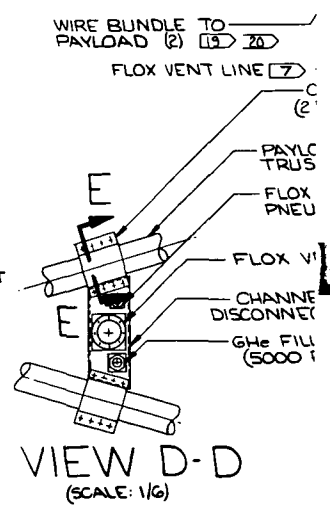
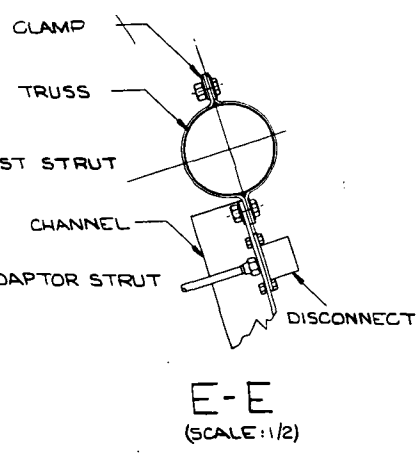
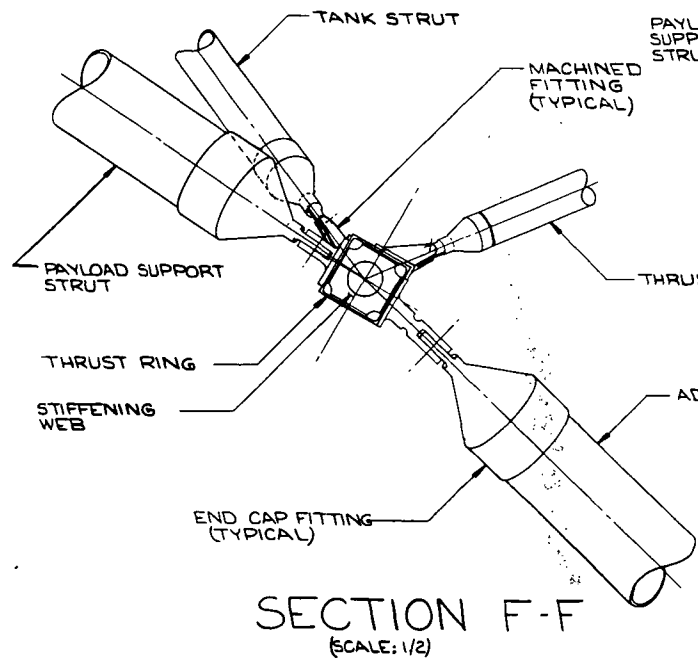
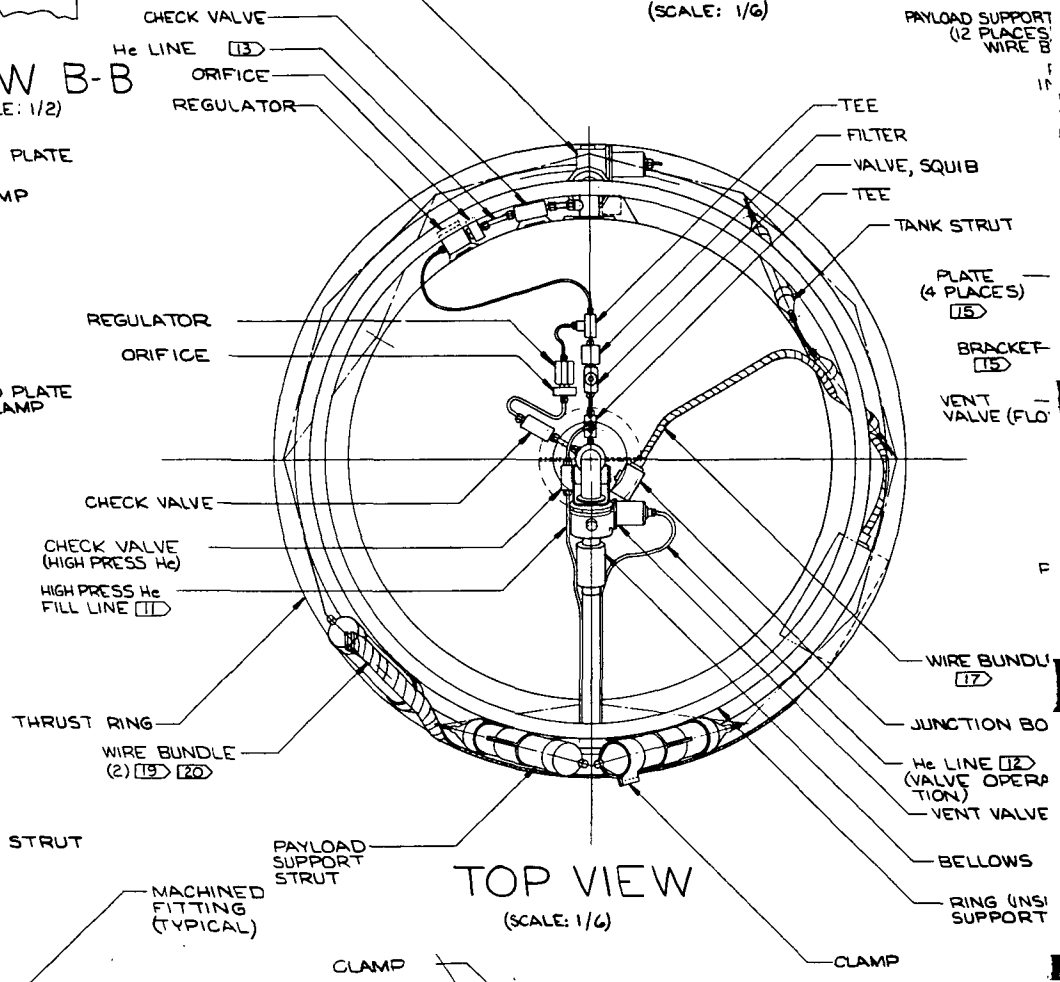
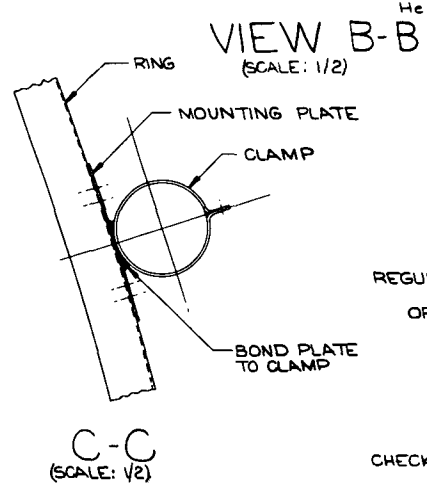
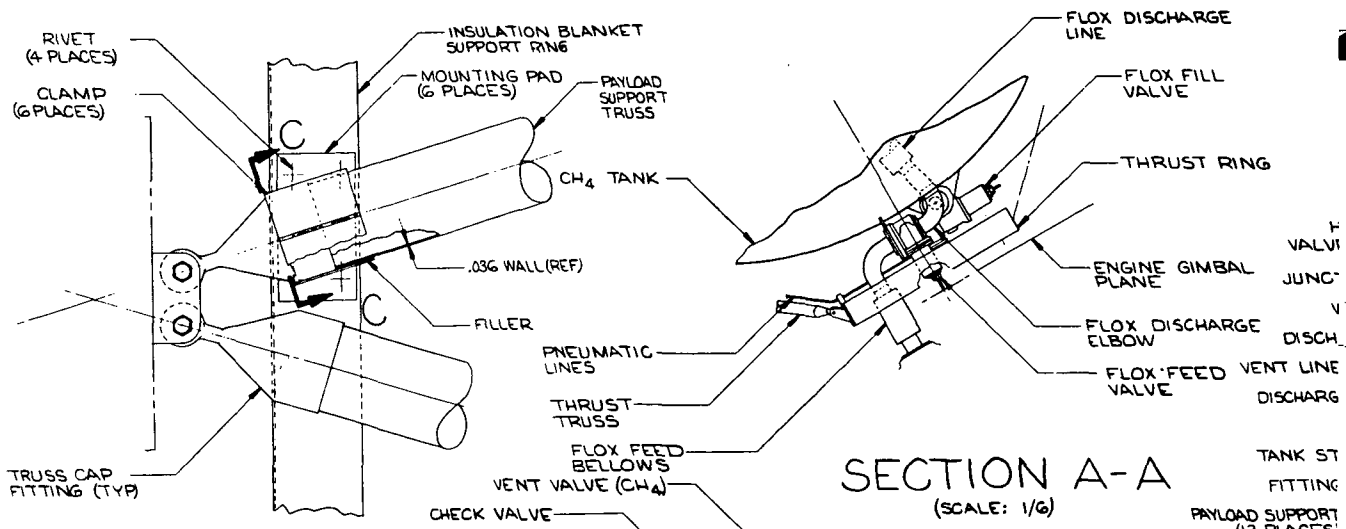
SECTION F-F  
(SCALE: 1/1)

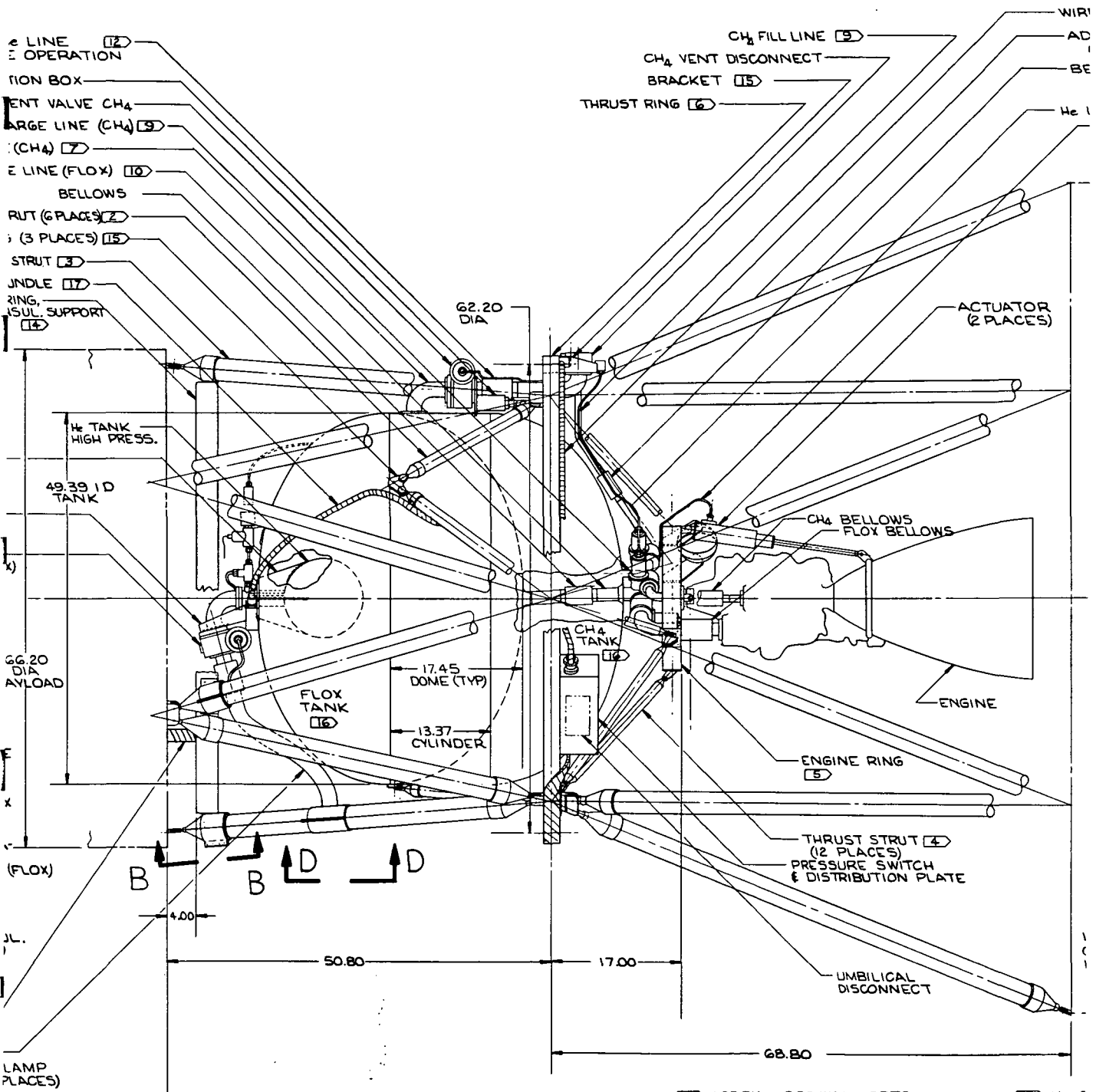


SECTION E-E @  
(SCALE: 1/1)  
(CONICAL PENETRATION)

SECTION D-D  
(SCALE: 1/1)

Figure 1.3-2: Continued INSULATION DETAILS - VEHICLE 1-14





SIDE VIEW  
(SCALE: 1/6)

GENERAL NOTES:

- 1 2.90 DIA x .042 WALL, CARBON/EPOXY COMPOSITE
- 2 1.70 DIA x .028 WALL, FIBERGLASS
- 3 3.15 DIA x .036 WALL, FIBERGLASS
- 4 1.25 DIA x .035 WALL, 2219-T4 ALUM.
- 5 19.00 DIA x 2.00 x .250 WALL, 2219-T4 ALUM.
- 6 68.45 DIA x 2.25 SO x .058 WALL 2219-T4 ALUM
- 7 2.00 DIA x .035 WALL, CRES

- 8 1.25 DIA x .020 WALL, CRES.
- 9 .80 DIA x .020 WALL, CRES.
- 10 1.60 DIA x .035 WALL, CRES.
- 11 .25 DIA x .049 WALL, CRES.
- 12 .25 DIA x .020 WALL, CRES.
- 13 .50 DIA x .020 WALL, CRES.
- 14 3.00 x 1.50 x .060 THICK, FIBERGLASS.
- 15 .250 CRES
- 16 2219-T6E4G ALUM t=.025
- 17 11-.032 MW (MANGANAN) CONDUCTORS  
2-.080 CW (CONSTANTAN) "
- 18 13-.032 MW CONDUCTORS  
2-.064 MW "  
2-.013 CW CONDUCTORS  
2-.013 CA (CHROME) CONDUCTORS
- 19 11-C  
6-C
- 20 13-C  
2-C  
4-C
- 21 MYL
- 22 NYL  
WT=
- 23 .04C  
FIBE
- 24 .06C  
FIBE
- 25 ALUM  
.15 N
- 26 MOL
- 27 X-8E

2 LINE OPERATION  
ION BOX  
VENT VALVE CH4  
ARGE LINE (CH4)  
(CH4)  
E LINE (FLOX)  
BELLWS  
RUT (6 PLACES)  
(3 PLACES)  
STRUT  
UNDLE  
RING,  
SUL. SUPPORT

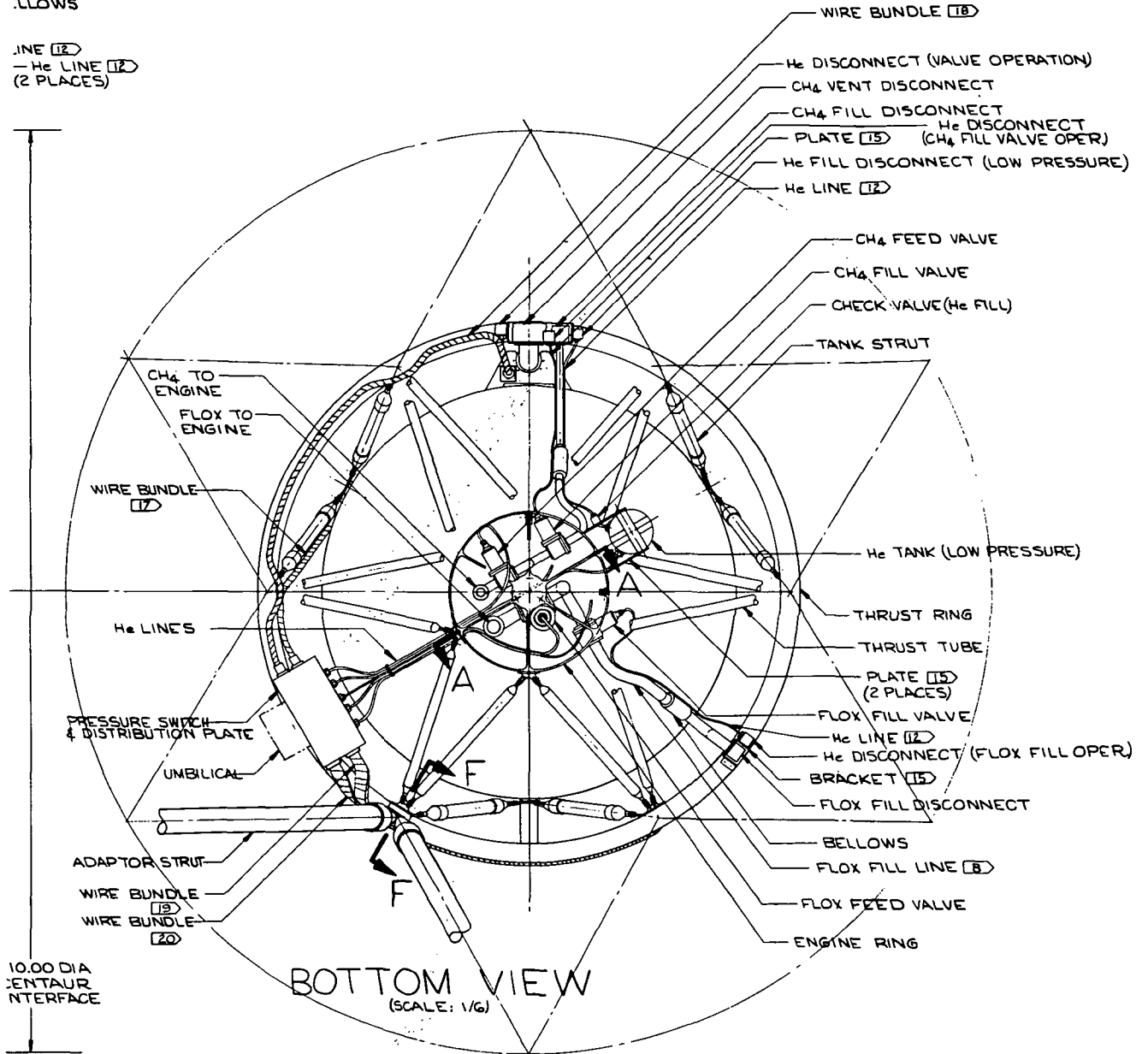
He TANK HIGH PRESS.  
49.39 I.D. TANK  
66.20 DIA. AYLOAD  
FLOX TANK  
17.45 DOME (TYP)  
13.37 CYLINDER  
CH4 TANK  
CH4 BELLWS FLOX BELLWS  
ENGINE  
ENGINE RING  
THRUST STRUT (12 PLACES)  
PRESSURE SWITCH & DISTRIBUTION PLATE  
UMBILICAL DISCONNECT

LAMP PLACES)  
AD SUPPORT  
VENT VALVE  
MATIC DISCONNECT  
ENT DISCONNECT  
T MOUNTING  
DISCONNECT  
SIG)

WIRI  
AD  
BE  
He I  
ACTUATOR (2 PLACES)  
CH4 FILL LINE  
CH4 VENT DISCONNECT  
BRACKET  
THRUST RING  
62.20 DIA  
68.80  
17.00  
50.80  
4.00

E BUNDLE (18)  
 ADPTOR STRUT (19)  
 (2 PLACES)  
 FLOWS

LINE (12)  
 - He LINE (12)  
 (2 PLACES)



(28) HOOK & PILE FASTENER, VELCRO OR EQUIV.

(29) EXTERNAL SHIELD ON ALL INSULATION BLANKETS WILL BE COATED WITH SCHJELDAHL GT1015

32 Mx CONDUCTORS  
 180 Cx " "  
 32 Mx CONDUCTORS  
 264 Mx " "  
 80 Cx " "  
 AR FILM. .15 MIL THICK

ON NET, SEARS ROEBUCK Co.,  
 .37 oz 1/4", .007 AVE THICKNESS

1.00x1.00x.100 DIA REQ'D,  
 GLASS LAMINATE COLLAR

1.00x1.25x.125 LENGTH REQ'D,  
 GLASS LAMINATE ANGLE.

MINIIZED MYLAR FILM.  
 .011 THICK.

DED NYLON

50 FILM SCHJELDAHL CO.

STRUCT. TECH. 2-5525	E.W. OSBORNE MAR 71	THE <b>BOEING</b> COMPANY AEROSPACE GROUP SEATTLE WASHINGTON
FLOX-CH <sub>4</sub> PROPELLANTS, THERMAL/METEOROID PROTECTION SYSTEM VEHICLE 2-18		CODE IDENT NO. 81705 SK-11-043144

Figure 1.3-3: STRUCTURAL DESIGN - VEHICLE 2-18

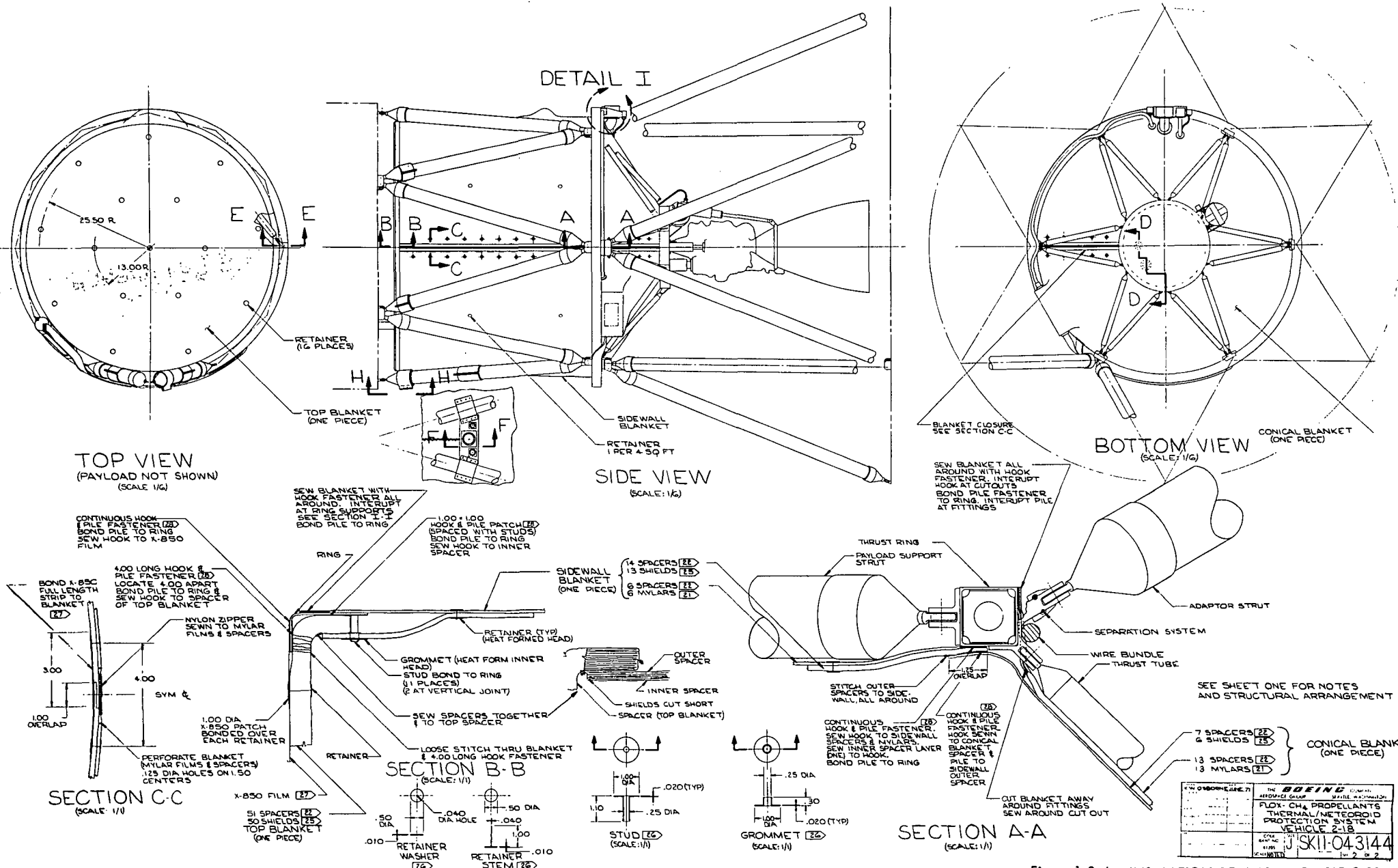
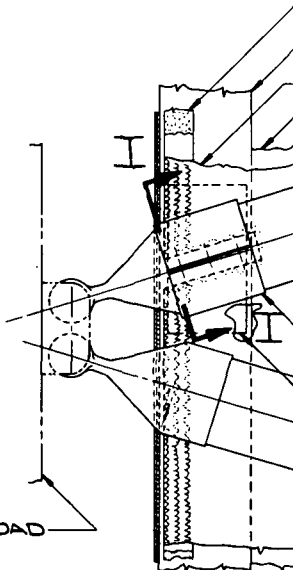
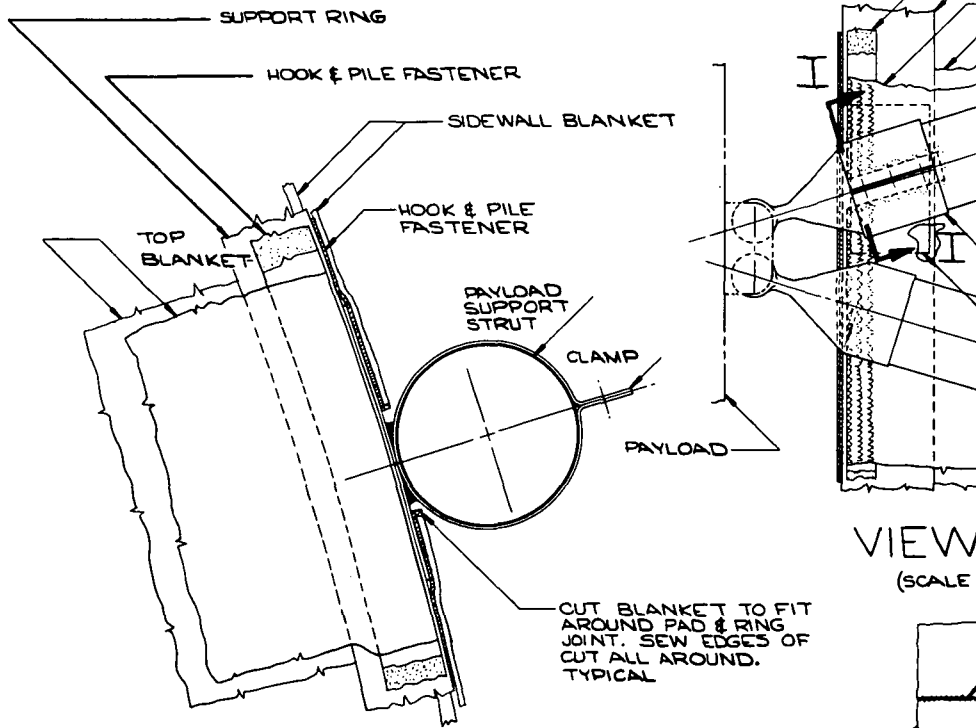
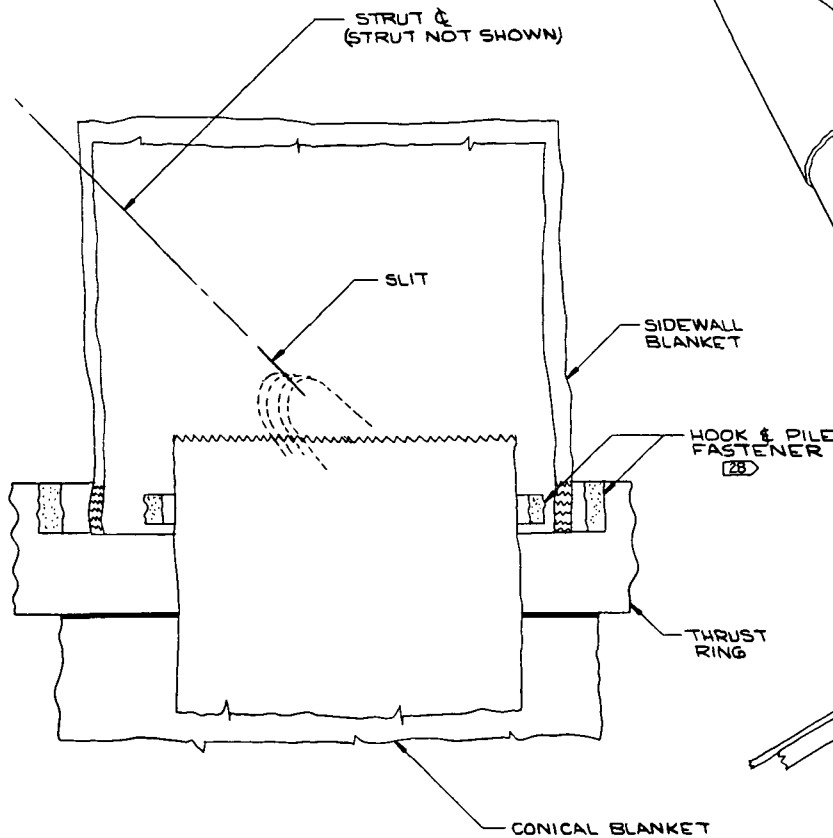


Figure 1.3-4: INSULATION DETAILS - VEHICLE 2-18

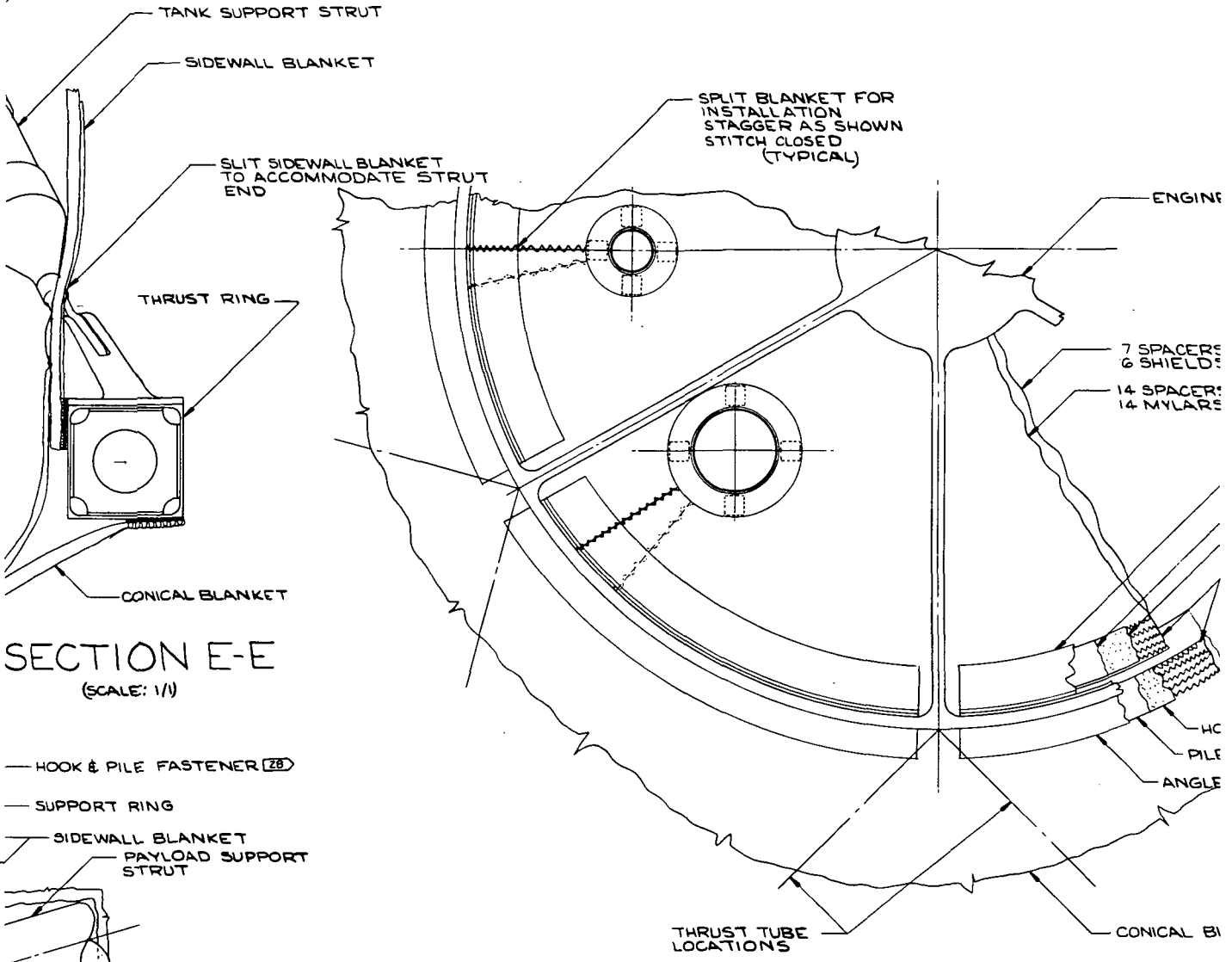


SECTION I - I  
(SCALE: 1/1)

TOP EDGE OF SIDEWALL BLANKET

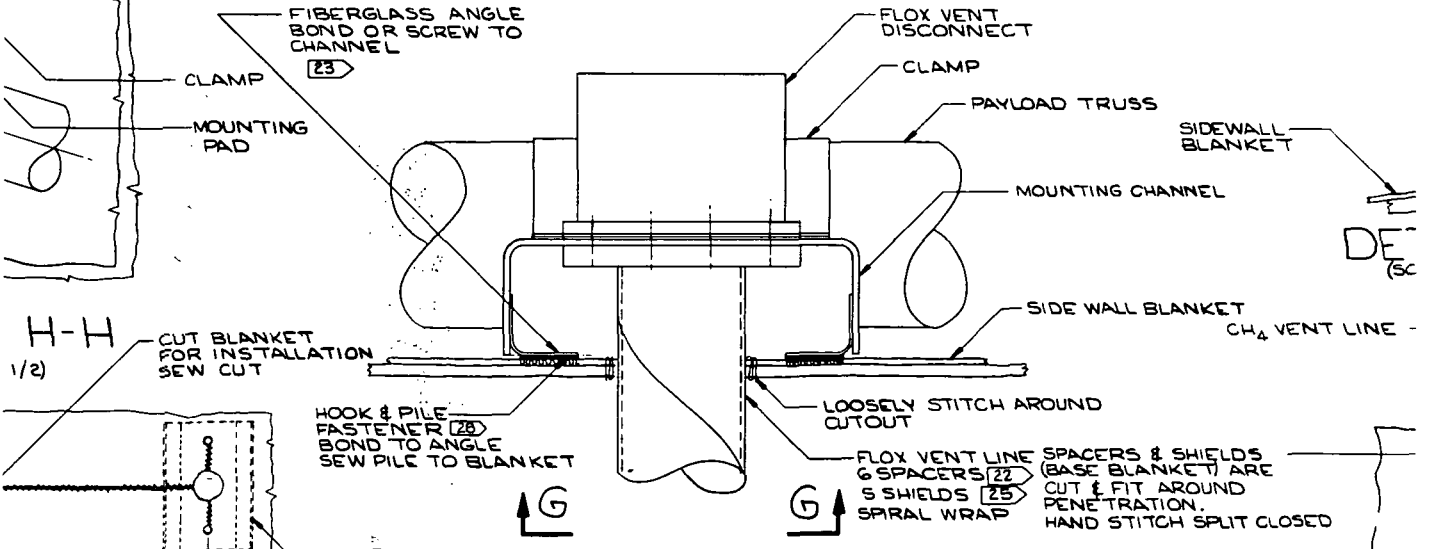
**Page Intentionally Left Blank**

6 SPACERS (22) WRAP ENTIRE STRUT  
5 SHIELDS (25) DOWN TO FITTING  
SPIRAL WRAP TIE WITH DACRON THD.  
(TYP)



SECTION E-E  
(SCALE: 1/1)

HOOK & PILE FASTENER (28)  
SUPPORT RING  
SIDEWALL BLANKET  
PAYLOAD SUPPORT STRUT



SECTION F-F  
(SCALE: 1/1)

W G-G NO STRUCTURE SHOWN EXCEPT CHANNEL & ANGLE  
(SCALE: 1/4)

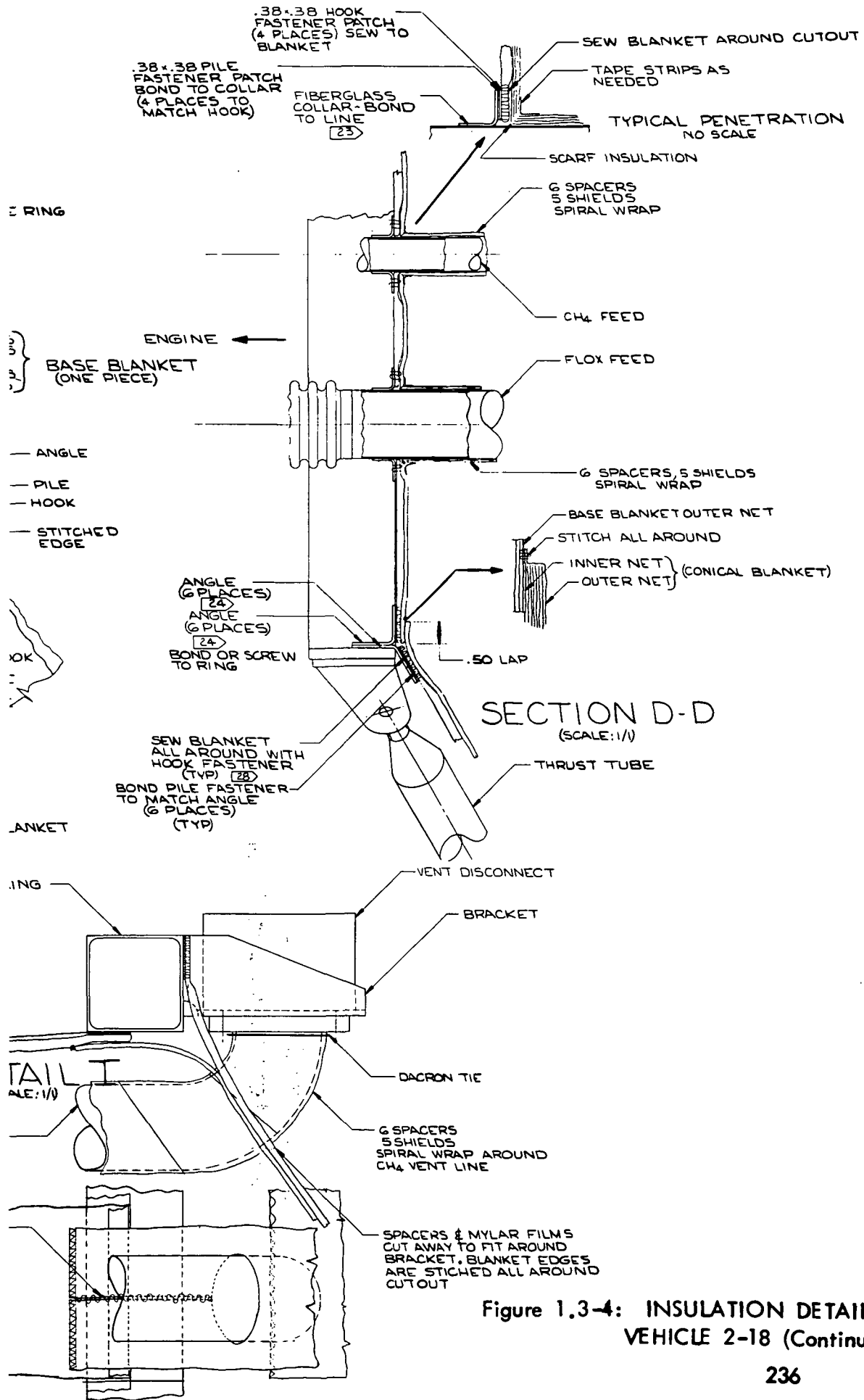


Figure 1.3-4: INSULATION DETAILS -  
VEHICLE 2-18 (Continued)



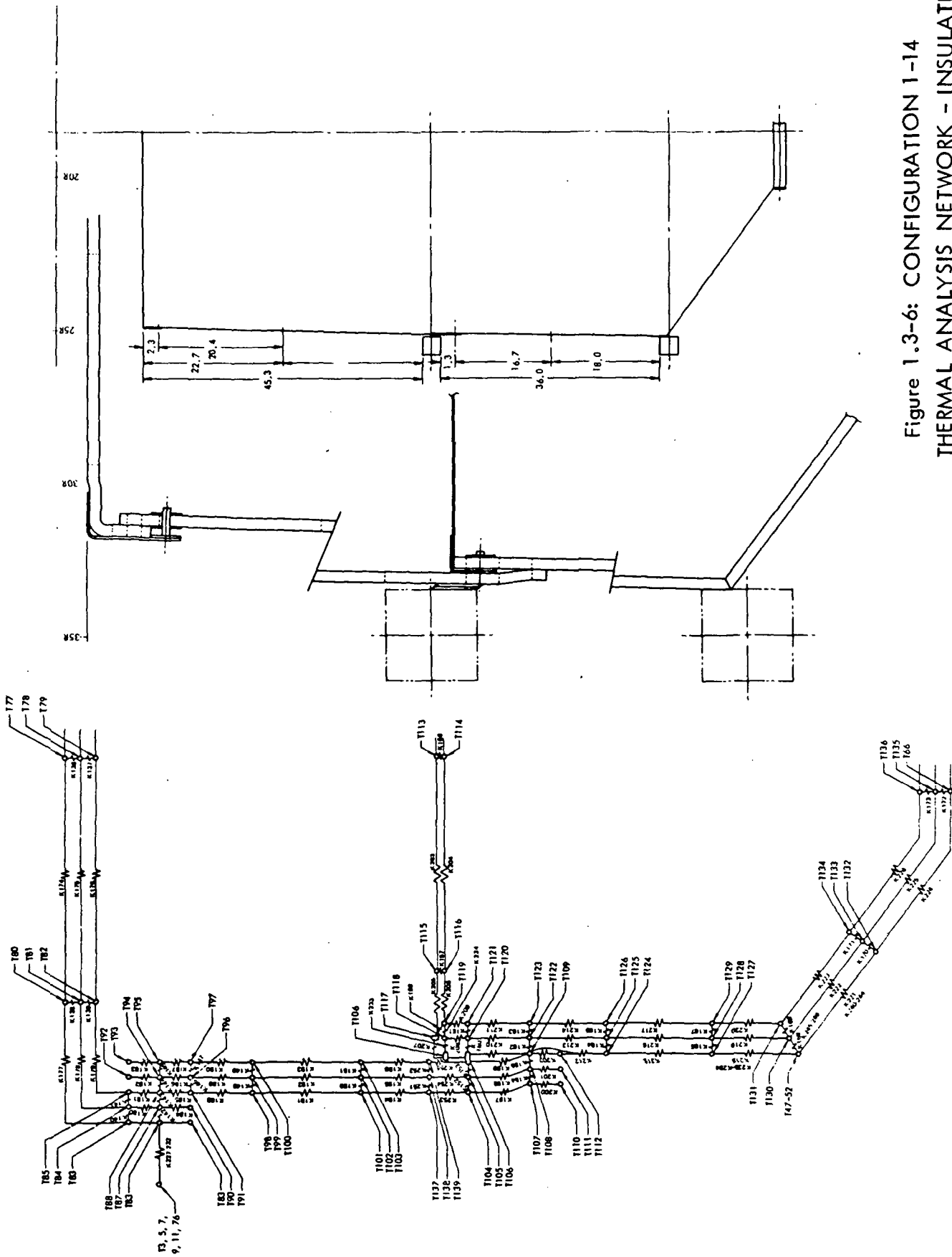


Figure 1.3-6: CONFIGURATION 1-14  
THERMAL ANALYSIS NETWORK - INSULATION

180°R (100°K) apart. The upper fiberglass struts varied about 6°R (3.3°K) except near the fluorine vent which was 40°R (22°K) cooler than other nodes with similar location. The relatively small circumferential gradients in the structure were believed to justify the approach used for the MLI.

Figure 1.3-7 shows the temperature distribution on the MLI surfaces and compares the results to the temperatures obtained in the preliminary design analysis. The sidewall MLI temperatures showed a step change at the lap joints. The preliminary design analysis temperatures were reasonable approximations of the more detailed analysis, except for the upper sidewall. Conduction from the warmer MLI on the top deck was the probable reason for the discrepancy on the upper sidewall. This conduction was not included in the preliminary design analysis.

The results of these analyses were used in the TATE (Tank Arrangement Thermal Efficiency) program to derive system weights for tanks, MLI, propellant vapor, helium and helium tank for the final designs. The output is presented in Table 1.3-1. For Vehicle 2-18 additional MLI with non-aluminized shields, up to a thickness of 0.27 in (0.69 cm), would be necessary to obtain meteoroid protection. This additional MLI would be on the sidewall and bottom of the vehicle.

The table also shows the system weights for those two vehicles prior to the final thermal analysis. The weight differences between the preliminary and final analyses were slight. Actual MLI blanket areas were used in the final analysis as opposed to the preliminary analysis where vehicle centerline dimensions were used to calculate areas. This accounts, in part, for a decrease in Vehicle 1-14 weight, whereas the MLI thicknesses increased.

### 1.3.3 Weights

A weight analysis of the two vehicle final designs was prepared. The results are summarized in Table 1.3-2. In each case the total hardware weight increased slightly from the preliminary design. The increases were due largely to inclusion of the electrical system components and more definition of the pneumatic control system. Tables 1.3-3 through 1.3-7 give the weight breakdown. The final comparisons are shown below:

	FLOX-CH <sub>4</sub> Vehicle 2-18	LH <sub>2</sub> -LF <sub>2</sub> Vehicle 1-14
Mass Fraction $\left( \frac{W_p}{W_i + W_p} \right)$	0.86	0.81
Payload Weight Lb (kg)	4642 (2110)	4791 (2180)

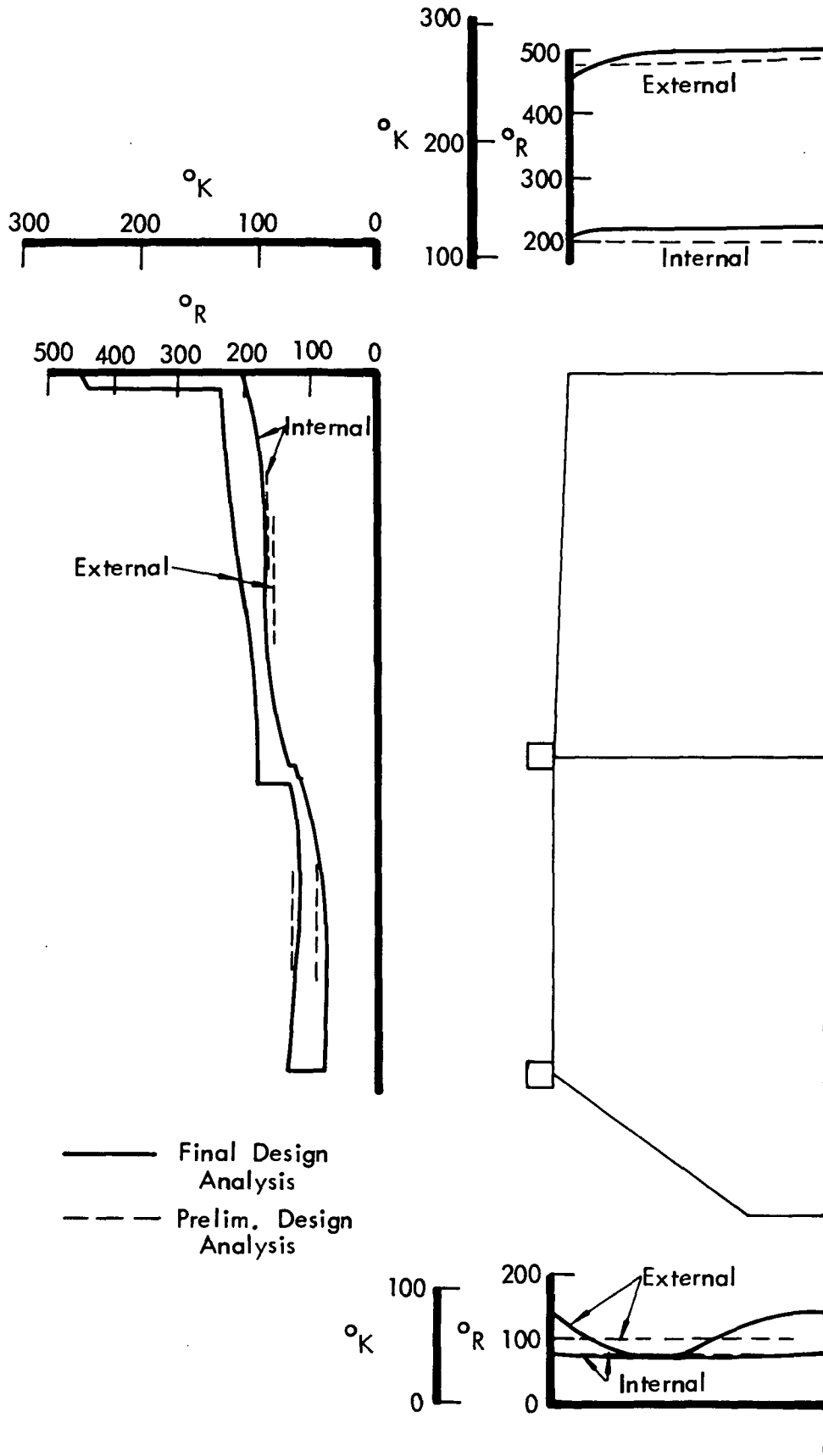


Figure 1.3-7: CONFIGURATION 1-14 INSULATION TEMPERATURES

Table 1.3-1: SYSTEM WEIGHT COMPARISONS

PRELIMINARY DESIGN - SYSTEM WEIGHTS

INSULATION THICKNESS				TANK GAGE						SYSTEM * WEIGHT		INSULATION LOCATION	VEHICLE		
Top		Side		Bottom		Inside		Fuel Head		Fuel Cylinder				Oxid.	
in	cm	in	cm	in	cm	in	cm	in	cm	in	cm	in	cm	lb	kg
0.38	.97	0.14	.36	—	—	0.01	.03	—	—	.025	.064	.025	.064	47.6	21.6
0.32	.81	0.33	.84	0.33	.84	0.02	.05	.025	.064	—	—	.025	.064	64.6	29.3

FINAL DESIGN - SYSTEM WEIGHTS

0.72	1.83	0.18	.46	—	—	0.08	.20	—	—	.025	.064	.025	.064	50.5	22.9
0.49	1.07	0.33	.84	0.40	.84	0.34	.84	0.60	.13	.035	.064	—	—	82.2	28.9

\* System Weight Includes: Tanks, Insulation, Propellant Vapor, Helium, Helium Tank

Table 1.3-2: FINAL EVALUATION VEHICLE WEIGHTS

VEHICLE CONFIGURATION NO.	1-14		2-18	
TYPE PROPELLANT	LF <sub>2</sub> /LH <sub>2</sub>		FLOX/CH <sub>4</sub>	
	lb	kg	lb	kg
STRUCTURES	(147.9)	(67.1)	(86.1)	(39.1)
Primary Structure	47.7	21.6	29.5	13.4
Secondary Structure	69.5	31.5	29.4	13.3
Payload Support	30.7	13.9	27.2	12.3
THERMAL SYSTEM	(94.8)	(34.6)	(62.3)	(28.3)
Primary Components	82.2	28.9	50.5	22.9
Secondary Insulation Δ Weight	12.6	5.7	8.9	4.0
Protection Δ Weight	▷		2.9	1.3
PROPULSION SYSTEM	(284.8)	(129.2)	(257.6)	(116.8)
Engine	108.0	49.0	108.0	49.0
Fuel System	62.5	28.3	44.2	20.0
Oxidizer System	71.8	32.6	71.1	32.3
Pneumatic Control	21.4	9.7	19.3	8.8
Pressurization Δ Weight	21.1	9.6	15.0	6.8
ELECTRICAL	(11.0)	(5.0)	(12.0)	(5.4)
Cable	3.3	1.5	3.9	1.8
Connectors	1.7	.8	2.0	.9
▷ Pressure Switch & Distribution Plate	5.0	2.3	5.0	2.3
Supports	1.0	.5	1.1	.5
TOTAL HARDWARE	539.0	235.9	418.0	189.6
PROPELLANT	2170.0	984.3	2440.0	1106.8
TOTAL SYSTEM	2709.0	1220.2	2858.0	1296.4

▷ Included in Primary Thermal System Components

▷ Weight Allowance Only

Table 1.3-3: WEIGHT DATA - STRUCTURE

	CONFIGURATION					
	1-14			2-18		
	lb	kg	lb	kg	lb	kg
SECONDARY STRUCTURE						
MAIN BODY RINGS		(69.5)	(31.5)		(29.4)	(13.3)
Upper Ring	-	51.16	23.21	-	12.17	5.52
Mid Ring	23.23	10.54	-	-	-	-
Lower Ring	27.93	12.67		12.17	5.52	
TANK SUPPORT STRUCTURE		3.82	1.73		3.13	1.42
THRUST STRUCTURE		14.52	6.59		14.10	6.40
Engine Ring	8.68	3.94		8.68	3.94	
Thrust Ring	Incl. As Lower Ring					
Thrust Strut Assembly	5.84	2.65		5.42	2.46	

Table 1.3-4: WEIGHT DATA - INSULATION

	CONFIGURATION					
	1-14			2-18		
	lb	kg	lb	kg	lb	kg
SECONDARY INSULATION		(12.6)	(5.7)		(8.9)	(4.0)
ADDITIONAL MULTILAYER		.74	.33		.93	.42
Tank Supt. Structure MLI	.17	.08		.14	.06	
Plumbing Insulation	.35	.16		.25	.11	
Misc. Overlaps, Etc.	.22	.10		.54	.24	
MAJOR JOINT ASSEMBLIES		8.77	3.98		5.67	2.57
Sidewall & Base	.13	.06		.12	.05	
At Upper Ring*	4.63	2.10		3.97	1.80	
At Mid Ring*	3.24	1.47				
At Lower Ring	.19	.09		.29	.13	
At Engine & Thrust Ring	.58	.26		1.29	.59	
X-850 FILM		1.11	.50		.73	.10
MISC. ATTACHMENTS ▽		.08	.04		.56	.25
Velcro	.03	.01		.03	.01	
Clamps, Retainers, Etc.	.05	.02		.53	.24	
MISC. INSULATION ITEMS		1.90	.86		1.51	.68

▽ Items Not Accounted For Under Major Joints

\* Including Ring

Table 1.3-5: WEIGHT DATA - FUEL SYSTEM

PROPELLANT CONFIGURATION	LF <sub>2</sub> /LH <sub>2</sub>			FLOX/CH <sub>4</sub>		
	1-14			2-18		
	lb	kg	lb	kg	lb	kg
FUEL SYSTEM		62.5	28.3		44.2	20.0
VENT		22.3	10.1		21.6	9.8
Lines	2.1	1.0		1.2	0.5	
Flanges	0.5	0.2		0.8	0.4	
Valves	8.0	3.6		8.0	3.6	
Bellows	5.0	2.3		5.0	2.3	
Disconnects	3.0	1.4		3.0	1.4	
Supports	3.7	1.7		3.6	1.6	
FEED		17.0	7.7		9.6	4.4
Lines	2.2	1.0		0.3	0.1	
Flanges	0.6	0.3		0.2	0.1	
Bellows	5.2	2.4		2.0	0.9	
Valves	6.2	2.8		5.5	2.5	
Supports	2.8	1.3		1.6	0.7	
FILL		22.4	10.2		12.4	5.6
Lines	2.1	1.0		0.7	0.3	
Flanges	0.6	0.3		0.2	0.1	
Disconnects	3.0	1.4		1.9	0.9	
Valves	8.0	3.6		5.5	2.5	
Bellows	5.0	2.3		2.0	0.9	
Supports	3.7	1.7		2.1	1.0	
TANK OUTLET Δ WT.		0.8	0.4		0.4	0.2
Vent	0.4	0.2		0.4	0.2	
Feed	0.4	0.2		0.2	0.1	

Table 1.3-6: WEIGHT DATA - OXIDIZER SYSTEM

PROPELLANT CONFIGURATION	LF <sub>2</sub> /LH <sub>2</sub>				FLOX/CH <sub>4</sub>			
	1-14		2-18		1-14		2-18	
	lb	kg	lb	kg	lb	kg	lb	kg
OXIDIZER SYSTEM								
VENT								
		71.8	32.6		71.1	32.3		
		20.4	9.3		23.9	10.8		
Lines	2.1	1.0		3.1	1.4			
Flanges	0.8	0.4		0.8	0.4			
Valves	8.0	3.6		8.0	3.6			
Disconnects	3.0	1.4		3.0	1.4			
Bellows	5.0	2.3		5.0	2.3			
Supports	1.5	0.7		4.0	1.8			
FEED								
		33.2	15.1		29.9	13.6		
Lines	5.2	2.4		4.5	2.0			
Flanges	0.9	0.4		0.9	0.4			
Bellows	16.0	7.3		12.0	5.4			
Valves	7.5	3.4		7.5	3.4			
Supports	3.6	1.6		5.0	2.3			
FILL								
		17.3	7.8		16.6	7.5		
Lines	0.9	0.4		0.4	0.2			
Flanges	0.2	0.1		0.2	0.1			
Bellows	3.8	1.7		3.8	1.7			
Valves	7.0	3.2		7.0	3.2			
Disconnects	2.5	1.1		2.5	1.1			
Supports	2.9	1.3		2.7	1.2			
TANK OUTLET								
Δ WT.								
Vent.	0.4	0.2		0.4	0.2		0.7	0.3
Feed	0.5	0.2		0.3	0.1			

Table 1.3-7: WEIGHT DATA - PNEUMATIC SYSTEM

PROPELLANT CONFIGURATION	LF <sub>2</sub> /LH <sub>2</sub>				FLOX/CH <sub>4</sub>			
	1-14		2-18		1-14		2-18	
	lb	kg	lb	kg	lb	kg	lb	kg
PNEUMATIC CONTROLS								
LOW PRESSURE SYSTEM								
		21.4	9.7		19.3	8.8		
		17.0	7.7		15.1	6.8		
Bottle & Installation	10.0	4.5		10.0	4.5			
Helium	1.0	0.5		1.0	0.5			
Lines & Fittings	3.5	1.6		1.6	0.7			
Valves & Disconnects	2.5	1.1		2.5	1.1			
GROUND CONTROLLED SYSTEMS								
		4.4	2.0		4.2	1.9		
Lines & Fittings	1.3	0.6		1.1	0.5			
Disconnects	2.4	1.1		2.4	1.1			
Supports	0.7	0.3		0.7	0.3			
PRESSURIZATION SYSTEM Δ WT.								
		21.1	9.6		15.0	6.8		
HELIUM SYSTEM								
		10.8	4.9		15.0	6.8		
Lines & Fittings	1.2	0.5		1.6	0.7			
Filters	1.0	0.5		1.0	0.5			
Valves	3.5	1.6		4.1	1.9			
Regulators	3.5	1.6		7.0	3.2			
Supports	1.6	0.7		1.3	0.6			
GASEOUS HYDROGEN SYS.								
		10.3	4.7					
Lines & Fittings	2.1	1.0						
Filters	2.0	0.9						
Valves	1.0	0.5						
Regulators	3.5	1.6						
Supports	1.7	0.8						

### 1.3.4 Meteoroid Protection Sensitivity

Vehicle configurations 1-14 and 2-18, were investigated for possible design changes caused by variation of the velocity function or meteoroid flux. Since MLI had been determined the best form of meteoroid protection, the design changes consisted of variations in MLI thickness and thus in vehicle weight.

The discussion in Appendix C explains how meteoroid protection design curves were obtained from laboratory tests using polyethylene projectiles (sp. gr. .95) at velocities about 8 km/sec. These curves related protection system thickness and depth of penetration, but the test parameters did not include projectile density and velocity. Since meteoroids have high velocities, and also are believed to have low density, for instance 0.5 gms/cc, the effect of the parameters was obtained from other sources. The effect of density ( $\rho$ ) was studied by Arenz (Reference 1.3-1) and velocity ( $V$ ) by Nysmith (Reference 1.3-2) and others. The effect of these parameters has been presented as affecting the total material thickness ( $T$ ) normalized to the projectile diameter ( $D$ ). These separate functional dependencies were combined as:

$$\frac{T_{\text{TOTAL}}}{D} \approx F_1(\rho) F_2(V) \quad (1)$$

The procedure related the model meteoroid environment to an equivalent environment consisting of polyethylene particles travelling at 8 km/sec. Since the total thickness of shielding and tank wall were the same for either environment, the diameter of the test projectiles was related to that of the meteoroids by the preceding equation giving:

$$\frac{D_M}{D_T} = \frac{F_1(\rho_T) F_2(V_T)}{F_1(\rho_M) F_2(V_M)} \quad (2)$$

Where subscript M and T refer to the meteoroid and test projectiles respectively.

The masses were related by

$$\frac{M_M}{M_T} = \frac{\rho_M}{\rho_T} \left( \frac{D_M}{D_T} \right)^3 = \frac{\rho_M}{\rho_T} \left( \frac{F_1(\rho_T)}{F_1(\rho_M)} \right)^3 \left( \frac{F_2(V_T)}{F_2(V_M)} \right)^3 \quad (3)$$

The differential flux in the velocity range  $\Delta V$  was

$$\Delta N = N_1 M_M^{-\alpha} f(V_M) \Delta V \quad (4)$$

where  $f(V_M)$  was the velocity distribution of meteoroids in the absence of Earth's field. Using equation (3) and integrating over velocity

$$N = N_1 \left[ \frac{\rho_T}{\rho_M} \left( \frac{F_1(\rho_m)}{F_1(\rho_T)} \right)^3 \right]^\alpha M_T^{-\alpha} \int \left( \frac{F_2(V_M)}{F_2(V_T)} \right)^{3\alpha} f(V_M) dV \quad (5)$$

From Reference 1.3-1, the density function was reduced to

$$F_1(\rho) \approx \rho^{0.6} \quad (6)$$

hence

$$\left[ \frac{\rho_T}{\rho_M} \left( \frac{F_1(\rho_m)}{F_1(\rho_T)} \right)^3 \right]^\alpha = \left( \frac{.5}{.95} \right)^{.968} = .537 \quad (7)$$

where  $\alpha = 1.21$ . From Reference 1.3-2 the velocity dependence for  $V$  greater than 8 km/sec. was:

$$F_2(V) \approx V^\beta \quad (8)$$

where  $\beta = 0.182$ , consequently

$$\left( \frac{F_2(V_M)}{F_2(V_T)} \right)^{3\alpha} = \left( \frac{V_M}{8} \right)^{.661} \quad V_M > 8 \quad (9)$$

$$\left( \frac{F_2(V_M)}{F_2(V_T)} \right)^{3\alpha} = 1 \quad 4 < V_M < 8$$

By numerical integration

$$\int \left( \frac{F_2(V_M)}{F_2(V_T)} \right)^{3\alpha} f(V_M) d_v = 1.449 \quad (10)$$

From equation (5) the equivalent flux adjusted for density and velocity then became for near-earth orbit,

$$N = .778 N_1 M_T^{-\alpha} \quad (11)$$

In addition, the flux and relative velocity of impact varied with distance from the sun as discussed in Appendix C of Volume II, NASA CR-121104. For this study, the flux variation in the Earth-Mars region was selected such that  $\gamma = -2$ . From Figure C-7 of Appendix C the average flux factor was

$$\frac{F(\gamma)}{F(0)} = 0.63 \quad (12)$$

Equation (10) provided an average velocity  $\bar{V}_M$  for impact in shielded structure, since by definition

$$\int \left( \frac{F_2(V_M)}{F_2(V_T)} \right)^{3\alpha} f(V_M) d_v = \left( \frac{\bar{V}_M}{8} \right)^{3\alpha\beta} = 1.449 \quad (13)$$

or

$$\frac{\bar{V}_M}{8} = 1.753 \quad (14)$$

Also from Figure C-7 of Appendix C the average velocity function was

$$\frac{F(\gamma - 1/2)}{F(\gamma)} = .9075 \quad (15)$$

Hence averaged over the mission time

$$\frac{\bar{V}_M}{8} = 1.753 \times .9075 = 1.591 \quad (16)$$

and the quantity in equation (13) became

$$\left(\frac{\bar{V}_M}{8}\right)^{3\alpha\beta} = 1.359 \quad (17)$$

The equivalent flux averaged over the mission using equations (5), (7), (12) and (17) was then

$$N = .46 N_1 M_T^{-\alpha} (\text{Meters})^{-2} (\text{Sec})^{-1} \quad (18)$$

where  $\log N_1 = -14.2$ .

The probability of no failure was

$$P_o = e^{-NA t} \quad (19)$$

where  $t = 1.8 \times 10^7$  sec and A was the effective exposed area of the tanks, taking into consideration the view factors of each region. With  $P_o = .999$  the equivalent test projectile mass  $M_T$  was then computed using equations (18) and (19). Using the density of polyethylene the spherical diameter of the design projectile was computed for each vehicle.

To determine the sensitivity of the design to different models of the environment in the solar system and to the velocity dependence of impact, i.e., to the values of  $\beta$  and  $\gamma$ , the above calculations were repeated for various values of  $\beta$  and  $\gamma$ . For Vehicle 1-14 the results are:

$$P_o = 0.999$$

PROJECTILE DIAMETER

$\gamma \backslash \beta$	0	.182	.667
-2	.0591 in (0.15 cm)	.0644 in (0.16 cm)	.0921 in (0.23 cm)
-.362	.0655 in (0.17 cm)	.0709 in (0.18 cm)	.1008 in (0.26 cm)
+3	.0858 in (0.22 cm)	.0920 in (0.23 cm)	.1273 in (0.32 cm)

For Vehicle 2-18 the results are:

-2	.0405 in (0.10 cm)	.0540 in (0.14 cm)	.0768 in (0.20 cm)
-.362		.0595 in (0.15 cm)	
+3		.0768 in (0.20 cm)	

Conversely, for a given design, that is, a fixed projectile mass  $M_T$  and variable flux  $N$ , equation (19) gave the dependence of  $P_0$  on the values of  $\beta$  and  $\gamma$ . The results of this computation are shown in Figure 1.3-8.

A 0.999 probability of no failure was established for the analyses of this program. Using the meteoroid diameters tabulated above, the weight of multilayer which was added to obtain protection was calculated. These weights were normalized to the final vehicle designs and the results are shown in Figures 1.3-9 and 1.3-10. In the case of Vehicle 1-14, this approach was not exactly correct because the additional multilayer was assumed to have non-aluminized shields. The final vehicle design employed aluminized shields and thicknesses were derived by means of the thermal optimization program. In that program, insulation blanket thicknesses were allowed to optimize above the minimum required for meteoroid protection.

It was concluded that overall weight of both of these vehicles was relatively insensitive to the variations in meteoroid flux and velocity studied. This was particularly evident when it was realized that the meteoroid protection weight represented approximately 1% of the total inert weight of both vehicles.

#### 1.3.5 Thermal Conductivity Sensitivity

An analysis was made to determine the sensitivity of vehicle weight to variations in mean thermal conductivity of the MLI. The insulation conductivity equation of Table 1.1-3 ( $k = k_r (T_1^2 + T_2^2) (T_1 + T_2) + k_c (T_1 + T_2)$ ) was used. The radiation and conduction constants ( $k_r$  and  $k_c$ ) were varied to determine the effect on tank weight for Vehicle 1-14. Tank size, propellant mass and MLI thicknesses were fixed at the values selected for the final design of this vehicle, thus higher heat transfer through the MLI would result in higher final pressure and a greater tank wall thickness.

The results of this evaluation are shown in Table 1.3-8. Fuel tank gages increased slightly when the conduction constant was increased. Changes in the radiation constant had negligible effect on tank gages. Oxidizer tank gages obtained in this study were below the minimum. In the worst case tank weight was increased by 1.8 lb (0.8 kg) which had a negligible effect on vehicle total weight. In all of the study cases there was some ullage space remaining at the end of the mission.

#### 1.3.6 Tank Mounted MLI Comparison

The tank mounted MLI design configuration is shown in Figure 1.3-11. The  $LH_2$  tank of Vehicle 1-14 was used to illustrate the concept. Designs for the  $LF_2$  tank and for Vehicle 2-18 tankage were similar.

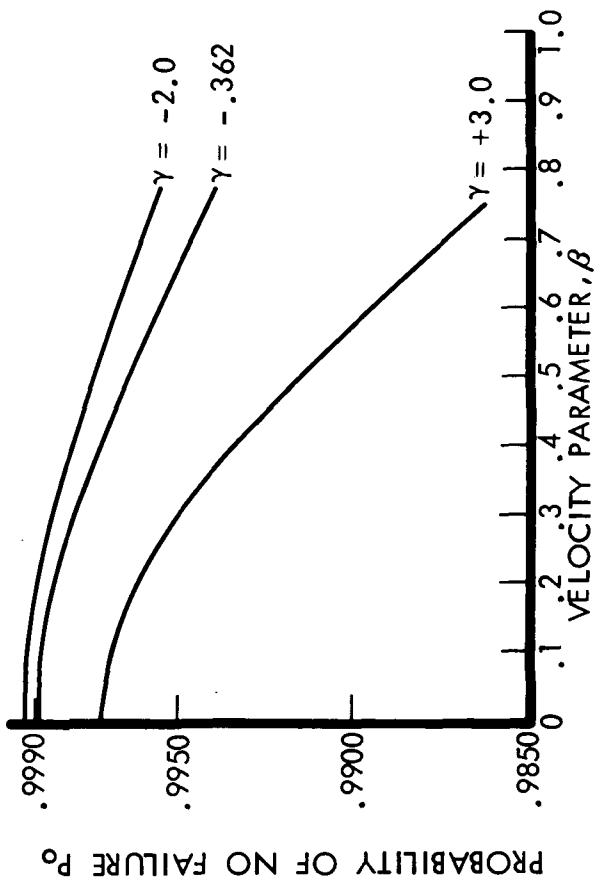


Figure 1.3-8: RELIABILITY OF METEOROID PROTECTION AS A FUNCTION OF THE MODEL OF THE METEOROID FLUX AND OF THE PENETRATION DEPENDENCE OF VELOCITY

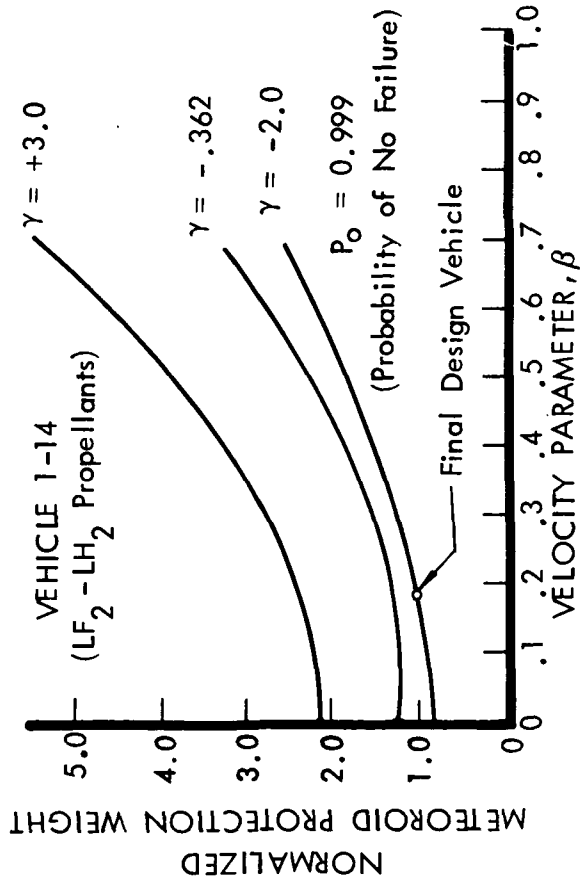


Figure 1.3-9: METEOROID PROTECTION WEIGHT SENSITIVITY - VEHICLE 1-14

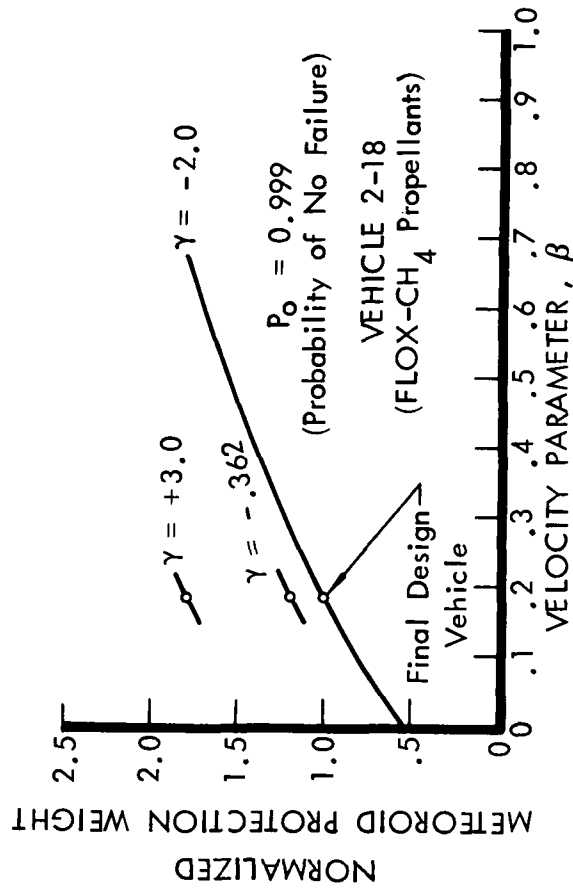


Figure 1.3-10: METEOROID PROTECTION WEIGHT SENSITIVITY - VEHICLE 2-18

Table 1.3-8: EFFECT OF VARIATIONS IN MEAN THERMAL CONDUCTIVITY ON TANK WEIGHT

VEHICLE 1-14	TANK GAGE			TANK WEIGHT			
	LH <sub>2</sub>		LF <sub>2</sub>	LH <sub>2</sub>		LF <sub>2</sub>	
	in	cm	in	lb	kg	lb	kg
$k_r = 2.5 \times 10^{-14}$ Btu/Ft-Hr-°R	.0350	.0890	.0250*	32.06	14.60	14.93	6.77
$k_c = 0.53 \times 10^{-8}$ " " " "							
Final Design Vehicle							
$1.5 \times k_c$	.0360	.0915	.0250*	33.08	15.05	14.93	6.77
$1.0 \times k_r$							
$2.0 \times k_c$	.0367	.0932	.0250*	33.83	15.40	14.93	6.77
$1.0 \times k_r$							
$1.0 \times k_c$	.0351	.0891	.0250*	32.21	14.62	14.93	6.77
$1.25 \times k_r$							
$1.0 \times k_c$	.0350	.0890	.0250*	32.06	14.60	14.93	6.77
$1.5 \times k_r$							

\* Minimum Gage

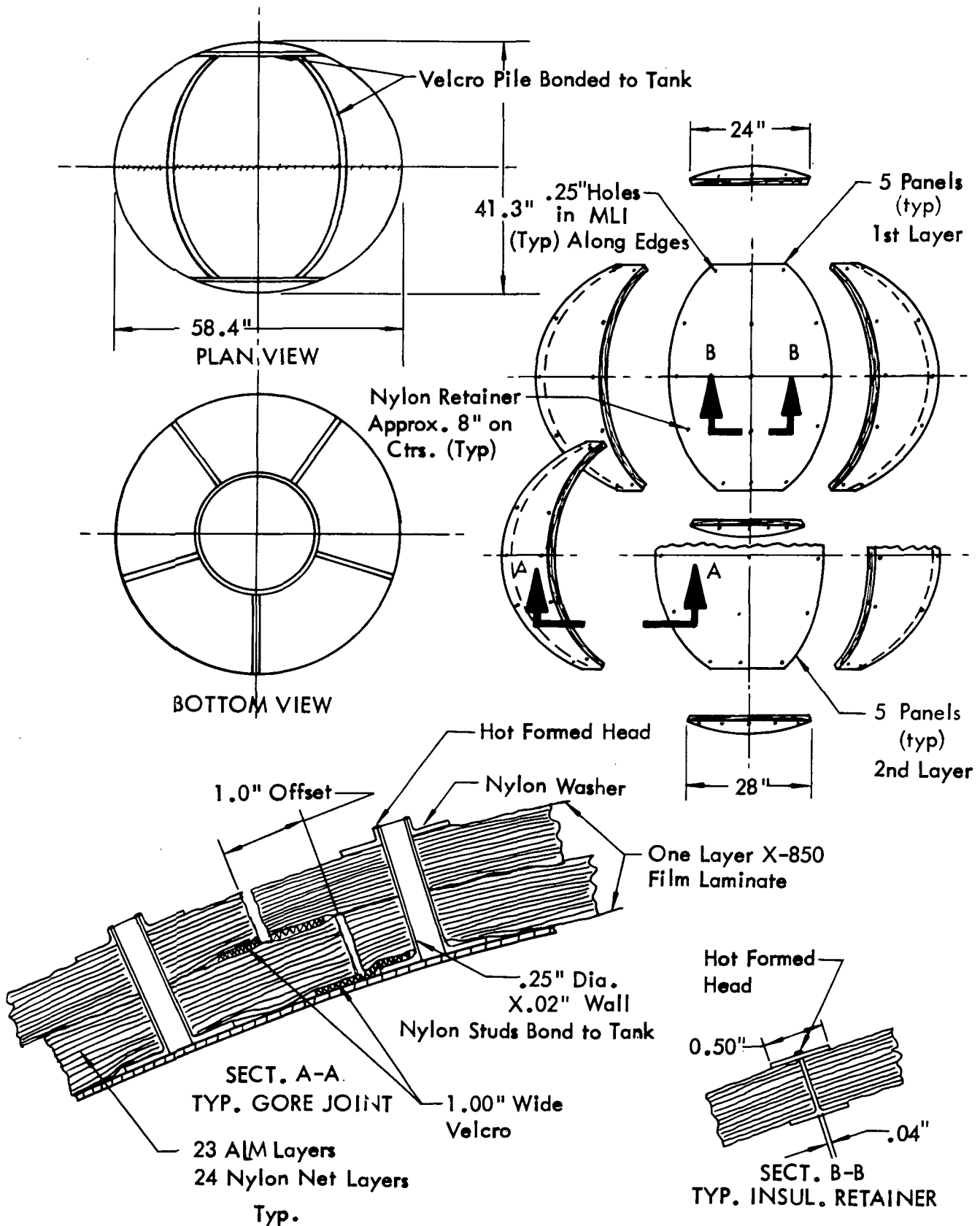


Figure 1.3-11:  
TANK MOUNTED THERMAL/METEOROID PROTECTION DESIGN

The MLI blanket was divided into two thicknesses, each supported by one X-850 layer. Nylon pin retainers were used to fasten the MLI assembly to the X-850 laminate. Net layers would be formed to the tank contour. The radiation shields would be cut and taped along the edges to conform to the tank curvature. The adjoining panels would be butted together and the outer panel layer offset slightly to cover the butt joints.

Hollow nylon studs were used to attach the panels to the tank at discrete points. Nylon washers would hold the outer-most panel in place on the studs. The abutting joints of the inner panel layer would be held to the tank with Velcro tape. The outer panels would be secured to the inner panels along the edges with Velcro tape.

The meteoroid protection system chosen was additional MLI. Meteoroid protection requirements were determined from the design curve of Figure 1.3-12. The technique was described in Section 1.2.3. This curve was developed from impact tests with the MLI directly against the witness plate (spacing = 0). The thickness of 15 gage mylar alternated with nylon net necessary to provide adequate protection for Vehicle 1-14 tankage was 0.64 in (1.63 cm), and for Vehicle 2-18 was 0.52 in (1.32 cm). The insulation blanket would contain some aluminized mylar layers to meet thermal protection requirements. A thermal balance analysis to obtain the exact number of aluminized shields was not performed.

The weights of vehicles with structure mounted and tank mounted thermal/meteoroid protection are compared in Table 1.3-9. There were only slight weight differences between these two approaches.

In Table 1.3-9 the total weights of thermal system components for the tank mounted insulation system are slightly less than for the structure mounted concepts largely due to the elimination of MLI lap joints and fiberglass support rings in the tank mounted system. The MLI was considerably thicker for tank mounted than for structure mounted designs. However, surface areas were less for the tank mounted designs and the net effect was a negligible change in MLI weight. For Vehicle 1-14 a weight reduction of 7 lb (3.2 kg) was obtained for tank mounted MLI. For Vehicle 2-18, tank mounted MLI increased the weight by 0.5 lb (0.23 kg). These insulation weight differences are unimportant in light of total system weights approximating 2700 lb (1225 kg). Although a thermal balance analysis was not performed for the tank mounted designs it is believed that the blanket thicknesses derived for meteoroid protection are more than adequate for thermal protection.

The weight breakdown for the tank mounted design is the same as shown in Tables 1.3-3, 1.3-5, 1.3-6 and 1.3-7 for structure mounted MLI. Table 1.3-10 shows the secondary insulation weights for the tank mounted design.

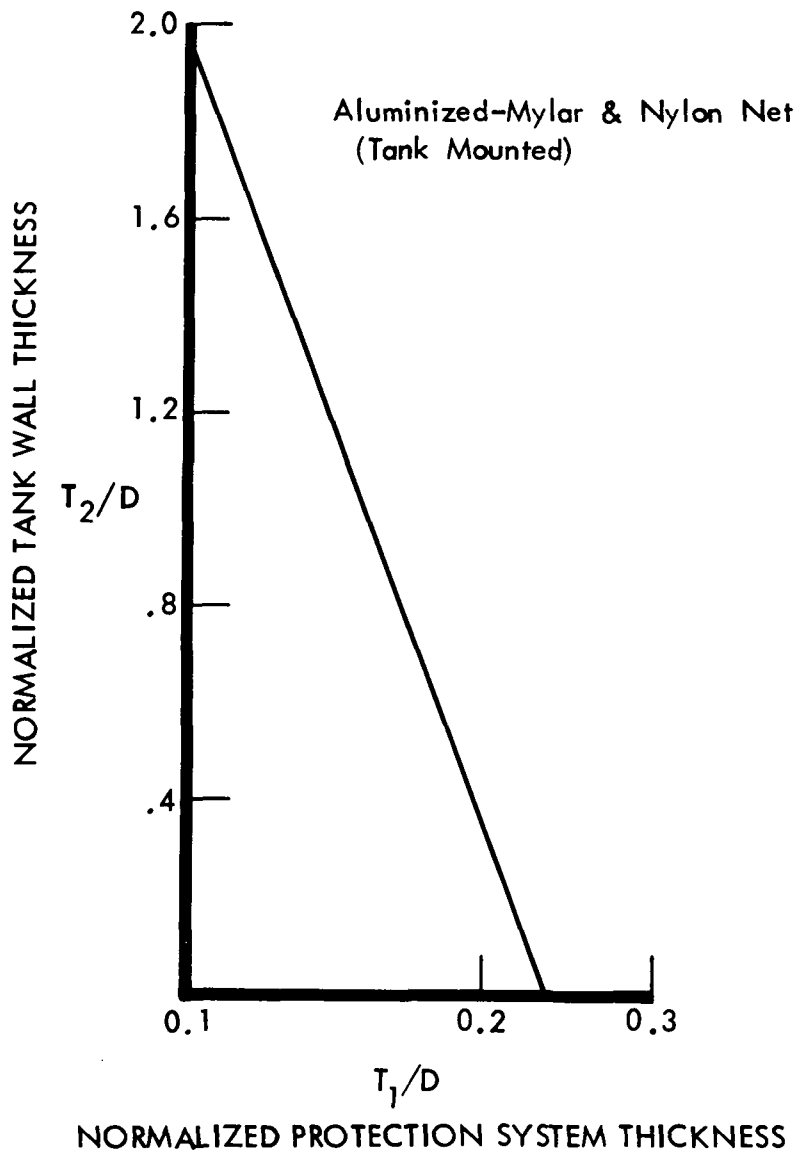


Figure 1.3-12: METEOROID PROTECTION DESIGN DATA - TANK MOUNTED MLI

Table 1.3-9: VEHICLE AND TANK MOUNTED MLI WEIGHT COMPARISONS

VEHICLE CONFIGURATION NO.	VEHICLE MOUNTED INSULATION DESIGN				TANK MOUNTED INSULATION DESIGN			
	1-14		2-18		1-14		2-18	
	LF <sub>2</sub> /LH <sub>2</sub>		FLOX/CH <sub>4</sub>		LF <sub>2</sub> /LH <sub>2</sub>		FLOX/CH <sub>4</sub>	
TYPE PROPELLANT	lb	kg	lb	kg	lb	kg	lb	kg
<b>STRUCTURES</b>	(147.9)	( 67.1)	( 86.1)	( 39.1)	(147.9)	( 67.1)	(86.1)	( 39.1)
Primary Structure	47.7	21.6	29.5	13.4	47.7	21.6	29.5	13.4
Secondary Structure	69.5	31.5	29.4	13.3	69.5	31.5	29.4	13.2
Payload Support	30.7	13.9	27.2	12.3	30.7	13.9	27.2	12.3
<b>THERMAL SYSTEM</b>	(94.8)	(43.0)	( 62.3)	( 28.3)	(82.2)	(37.3)	(55.3)	( 25.1)
Primary Components*	82.3	37.3	50.5	22.9	▷ 56.6	▷ 25.7	▷ 42.3	▷ 19.2
Secondary Insul. Δ Weight	12.6	5.7	8.9	4.0	7.1	3.2	4.3	2.0
Protection Δ Weight	▷	—	2.9	1.3	—	—	—	—
Insulation & Protection	—	—	—	—	18.6	8.4	8.7	3.9
<b>PROPULSION SYSTEM</b>	(284.8)	(129.2)	(257.6)	(116.8)	(284.8)	(129.2)	(257.6)	(116.8)
Engine	108.0	49.0	108.0	49.0	108.0	49.0	108.0	49.0
Fuel System	62.5	28.3	44.2	20.0	62.5	28.3	44.2	20.0
Oxidizer System	71.8	32.6	71.1	32.3	71.8	32.6	71.1	32.3
Pneumatic Control	21.4	9.7	19.3	8.8	21.4	9.7	19.3	8.8
Pressurization Δ Weight	21.1	9.6	15.0	6.8	21.1	9.6	15.0	6.8
<b>ELECTRICAL</b>	( 11.0)	( 5.0)	( 12.0)	( 5.4)	( 11.0)	( 5.0)	(12.0)	( 5.4)
Cable	3.3	1.5	3.9	1.8	3.3	1.5	3.9	1.8
Connectors	1.7	0.8	2.0	0.9	1.7	0.8	2.0	0.9
▷ Pressure Switch & Distr. Plate	5.0	2.3	5.0	2.3	5.0	2.3	5.0	2.3
Supports	1.0	0.5	1.1	0.5	1.0	0.5	1.1	0.5
<b>TOTAL HARDWARE</b>	539.0	245.0	418.0	189.6	526.0	238.6	411.0	186.4
<b>PROPELLANT</b>	2170.0	984.3	2440.0	1106.8	2170.0	984.3	2440.0	1106.8
<b>TOTAL SYSTEM</b>	2709.0	1230.0	2858.0	1296.4	2696.0	1222.0	2851.0	1293.2
<b>MASS FRACTION</b>	0.81		0.86		0.81		0.87	
<b>PAYLOAD</b>	4791	2173	4642	2106	4804	2180	4649	2109

▷ Included in Primary Thermal System Components ▷ Weight Estimate ▷ Excluding MLI  
 \*(including MLI)

Table 1.3-10: WEIGHT DATA - TANK MOUNTED MLI

CONFIGURATION	1-14				2-18			
	lb	kg	lb	kg	lb	kg	lb	kg
SECONDARY INSULATION ADDITIONAL MLI			(7.1)	(3.2)	(4.3)	(2.0)		
Tank Support Struts	0.17	0.08	0.74	0.34	0.14	0.06	0.93	0.42
Plumbing Lines	0.35	0.16			0.25	0.11		
Misc. Overlaps, Etc.	0.22	0.10			0.54	0.24		
X-850 FILM LAMINATE			2.80	1.27			1.61	0.73
MISC. ATTACHMENTS			3.51	1.59			1.80	0.82
Velcro	1.71	0.78			0.80	0.36		
Clamps, Retainers, Etc.	1.80	0.81			1.00	0.45		

## 2.0 TASK II - EXPERIMENTAL EVALUATION

Experimental programs were conducted in three areas. These were: (1) meteoroid impact tests, (2) thermal performance and launch environment tests, and (3) full scale mockup fabrication. The following sections describe the tests, analysis of results, and correlation with analytical predictions.

### 2.1 Meteoroid Impact Testing

Discussion in this section covers the derivation of the penetration criteria, a description of the tests and development of design curves, and the results of the final design proof tests. A description of the meteoroid environment, the earth-mars trajectory used in the study, and the entire quantity of design curves are contained in Appendix C of Volume II, NASA CR-121104.

#### 2.1.1 Tank Wall Penetration Criteria

A threshold of spall criteria was initially adopted for assessing tank wall damage. However, tests indicated that penetrations  $\approx$  50 to 80% of the thickness could occur with no spallation from the witness plate which represents the tank wall. There was concern that the tank would be unable to perform its assigned function after suffering this type of damage.

An experimental investigation was conducted with 0.025 in (0.064 cm) thick 2219-T6E46 aluminum sheet with flaws 30%, 60% and 90% of the thickness. The results are shown in Figure 2.1-1. The data was plotted in terms of initial flaw depth-to-thickness ratio,  $(a/t)$ , versus stress at which the flaw was observed to penetrate the thickness. It was seen from this figure that growth through the thickness occurred at yield strength for an initial flaw approximately 65% deep. The allowable initial flaw would have to be less than this value. If it was conservatively estimated that the effective threshold stress intensity for the applicable tank environments was 85% of critical, and that the line depicted in Figure 2.1-1 represented a critical condition, then safe sustained vessel life up to yield strength was guaranteed if meteoroid damage was limited to 53% deep penetrations. The allowable meteoroid penetration was thus set at 50% maximum.

#### 2.1.2 Design Curve Derivation

The effect of spacing ( $S$ ) between the meteoroid shield and the tank wall on the performance of meteoroid shields had been studied extensively. Boeing has investigated the effect in aluminum and fiberglass cloth meteoroid shield experiments. Another example is given in Reference 1.3-1. A general conclusion was that for relative spacings greater than  $S/D = 30$ , where  $D$  was the spherical meteoroid diameter, there was little increase in performance of aluminum meteoroid shields. With Beta fiber cloth shields there was still some improvement up to about  $S/D = 55$ .

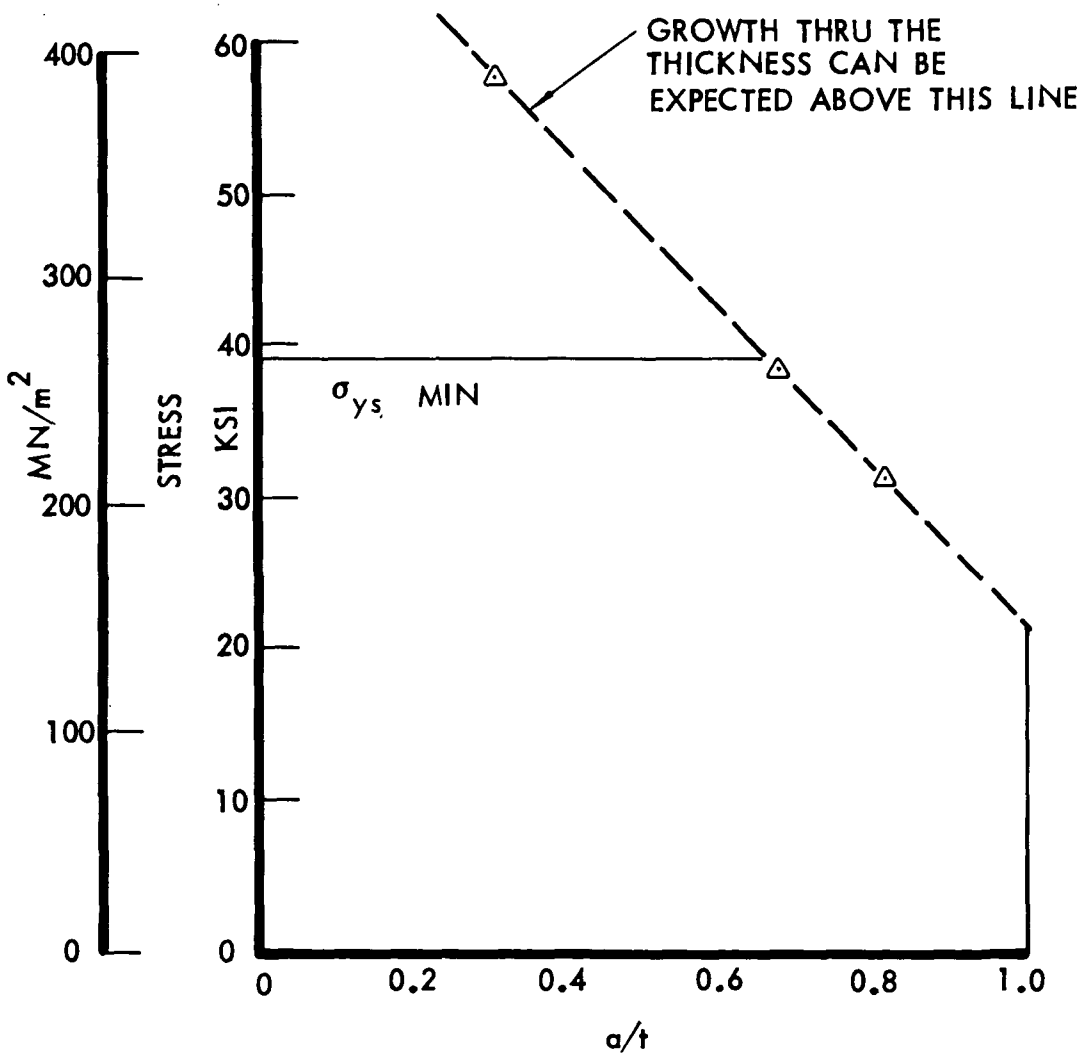


Figure 2.1-1: FLAW GROWTH-THRU-THE-THICKNESS OF 2219T6E46 ALUMINUM

The designs of propulsion vehicles for this study indicated a spacing of about 4 to 6 inches (10.2 to 15.2 cm) between the meteoroid protection system and the propellant tanks. A representative design meteoroid diameter was .06 to .07 in (0.15 to 0.18 cm), therefore a lower limit for the design vehicles was  $S/D \approx 55$ . The projectile used in the tests was a 3/32 in (0.25 cm) diameter by 3/32 in (0.25 cm) long polyethylene cylinder. The equivalent spherical diameter of this projectile was 0.11 in (0.28 cm). To maintain the  $S/D = 55$  relationship for the equivalent test environment of polyethylene projectiles traveling at  $\approx 8$  K/sec, a spacing of 6 in (15.2 cm) was required.

Cylindrical projectiles with random attitudes at impact gave random damage patterns. Cylindrical projectiles were used because they were economical to launch and were believed to produce more representative damage as explained in Appendix C. Random damage required statistical analysis of a large quantity of data. Typically, four to six test shots were made with one thickness of meteoroid protection system,  $T_1$ . The arithmetic mean value was determined and a  $3\sigma$  value, which was a RMS of the deviation from the mean, was calculated. Development of a design curve required testing of two to four thicknesses of meteoroid protection system. The test results were evaluated by measuring penetration depth of the witness plate,  $P$ , and doubling the value to obtain  $T_2$ , the minimum tank wall thickness. The meteoroid protection system thickness,  $T_1$ , was expressed in an equivalent thickness of aluminum and  $T_2$ ,  $P$  and  $T_1$  were normalized to test projectile diameter  $D$  to construct the curve of Figure 2.1-2. The curve labeled  $3\sigma$  was used in the design evaluation described in Section 1.2.3. The meteoroid impact experiments included over 350 valid shots. A valid shot was one which exceeded 23,000 feet/sec (7 km/sec). A total of 74 design curves were developed from the data. These are discussed in Appendix C.

The tank mounted meteoroid protection system which was evaluated was MLI. Twelve data points were obtained to develop the design curves of Figure 2.1-3. The MLI was located directly against the witness plate ( $S/D = 0$ ) in these tests. This curve is displaced to the right of the curve of Figure 2.1-2, resulting in a greater protection system weight per unit area, for equivalent tank wall thickness. For the values of  $T_2/D$  of interest, the required protection system thickness was about double. The  $3\sigma$  curve of this figure yielded a conservative design because it was displaced further to the right than a curve drawn through the exact  $3\sigma$  values at  $T_1/D = 0.102$  and  $0.205$ . The curve was drawn this way because there was limited data and it was believed the shape should resemble that of Figure 2.1-2.

When experimental penetration data for a particular shielding material was normalized to the projectile diameter, the resulting curve could be used directly for a range of projectile sizes and material thicknesses. However, when two materials such as Beta fiber cloth and NRC-2 were combined, a family of curves was required to represent various combinations of thicknesses. To obtain such data directly would have required a prohibitively large experimental program.

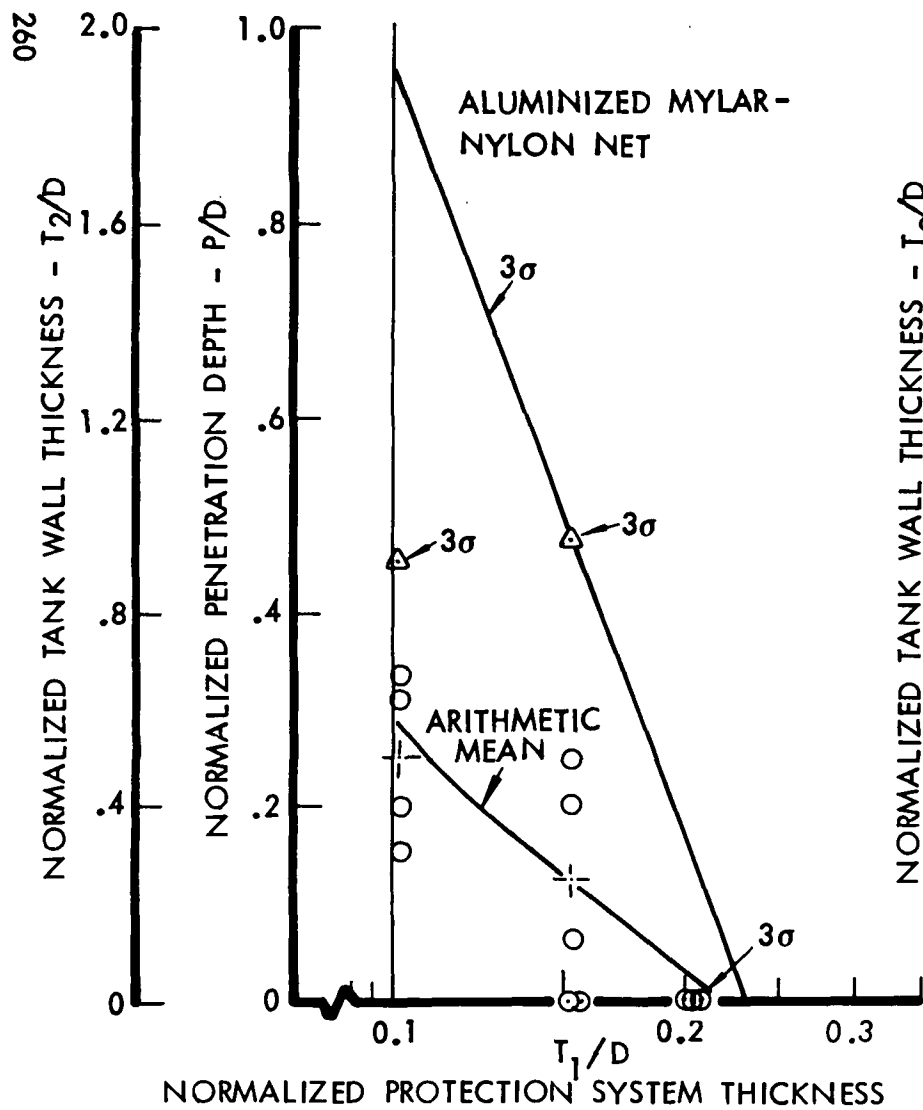


Figure 2.1-2: TANK MOUNTED METEOROID PROTECTION DESIGN DATA

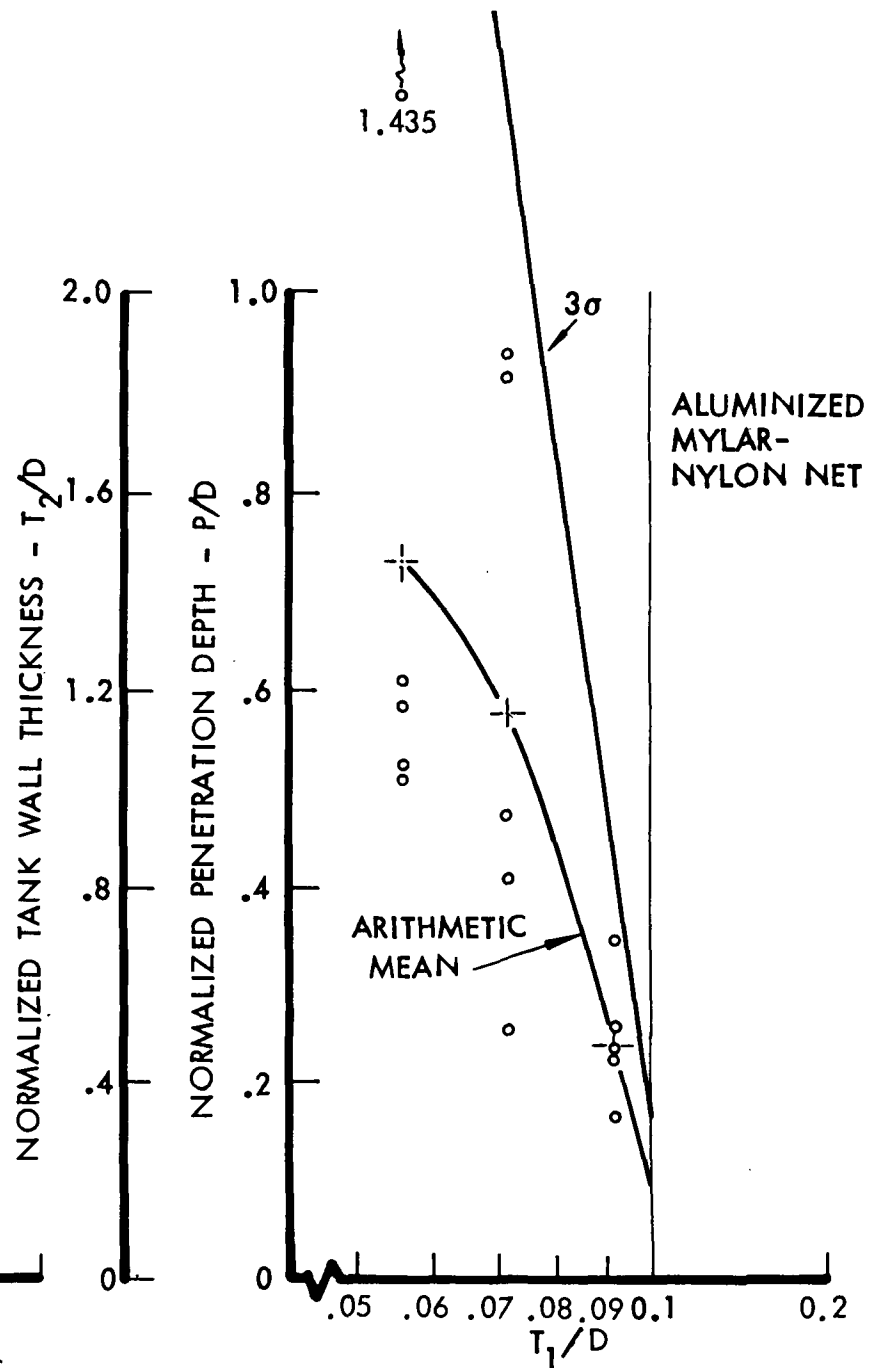


Figure 2.1-3: METEOROID PROTECTION DESIGN DATA - MLI

It had been anticipated that the test projectile and the design meteoroid would be close enough so that test data obtained with, for example, one layer of Beta fiber cloth and various thicknesses of MLI could have been used directly. However, the test projectile was  $\approx 50\%$  larger than the design meteoroid, consequently, scaling was required. In addition, it was desirable to be able to consider a range of combinations. For this purpose a formula was obtained for generating curves for additional combinations as well as for those tested directly.

The formula gave essentially an interpolation. It was not based on the physics of the impact phenomena, but did check the experimental results for those tests which were run with combinations. The curve for a given shielding material was represented by a function

$$T_2/D = f_\alpha (t) \quad (1)$$

where  $t = T_1/D$ , the normalized thickness of the shield. The curve for another material was represented by

$$T_2/D = f_\beta (t) \quad (2)$$

It was desired to combine these in various proportions. The combined thickness of the two was

$$t = t_\alpha + t_\beta \quad (3)$$

The penetration formula for the combined shielding materials was

$$\frac{T_2}{D} = \frac{t_\alpha}{t f_\alpha (t)} + \frac{t_\beta}{t f_\beta (t)} \quad (4)$$

Note that this formula satisfied the necessary end conditions. For instance, if  $t_\beta = 0$ , Equation (4) reverted to the Equation (1) and, if Equations (1) and (2) were identical, then Equation (4) again reverted to Equation (1) or (2).

Figure 2.1-4 shows the arithmetic mean value curves for Beta fiber cloth alone, NRC-2 alone, experimental points for the combination, and a curve obtained by Equation (4). The configuration represented in the figure was for Beta fiber cloth in front of the NRC-2, i.e. the cloth received the initial impact. The agreement was very good in this case. This was also true for other combinations of NRC-2 and single sheet materials. These were well behaved materials. However, nylon net was not so well behaved and the agreement was not so good in Figure 2.1-5. This was probably statistical and further data could have brought closer agreement. For the purpose of generating design curves, the formula was used however, since it gave conservative results.

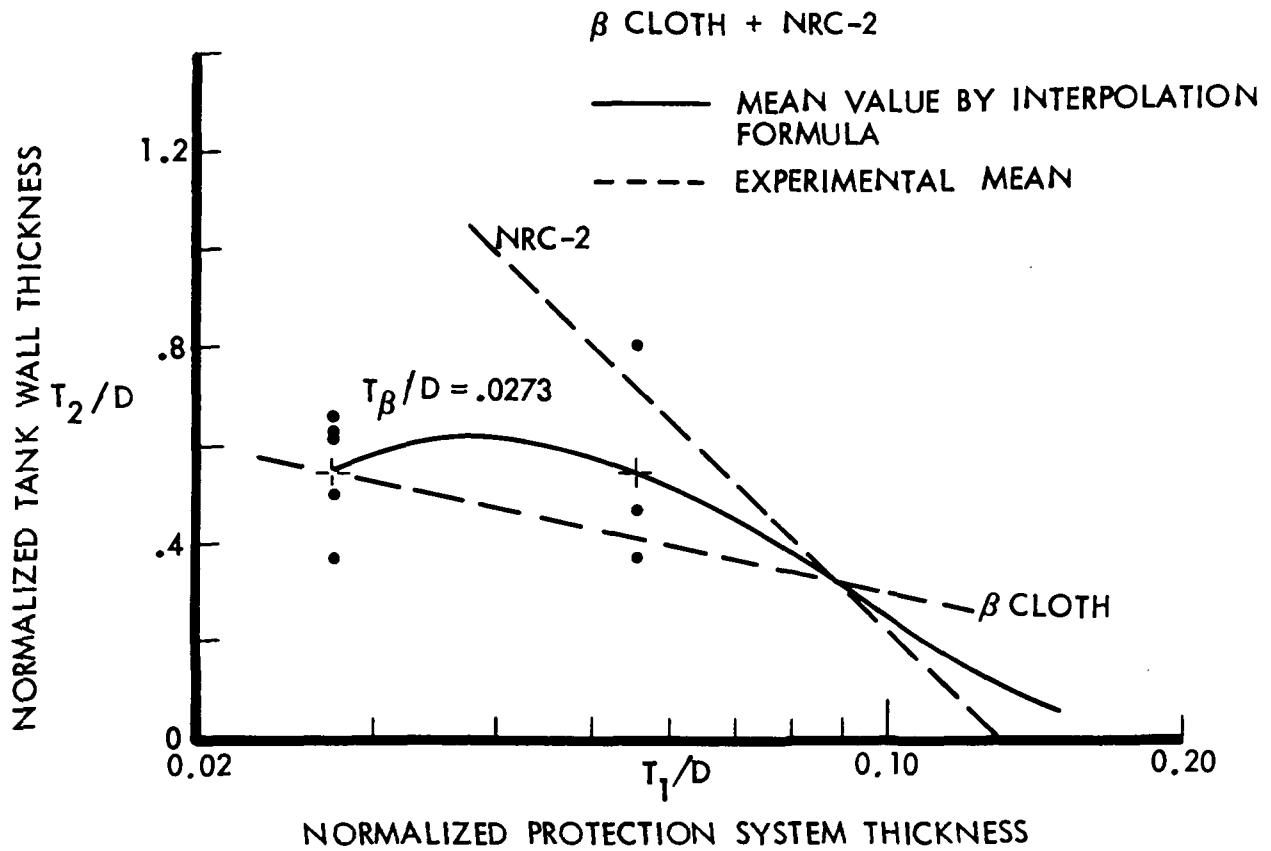


Figure 2.1-4: METEOROID PROTECTION DESIGN DATA -  $\beta$  CLOTH & MLI

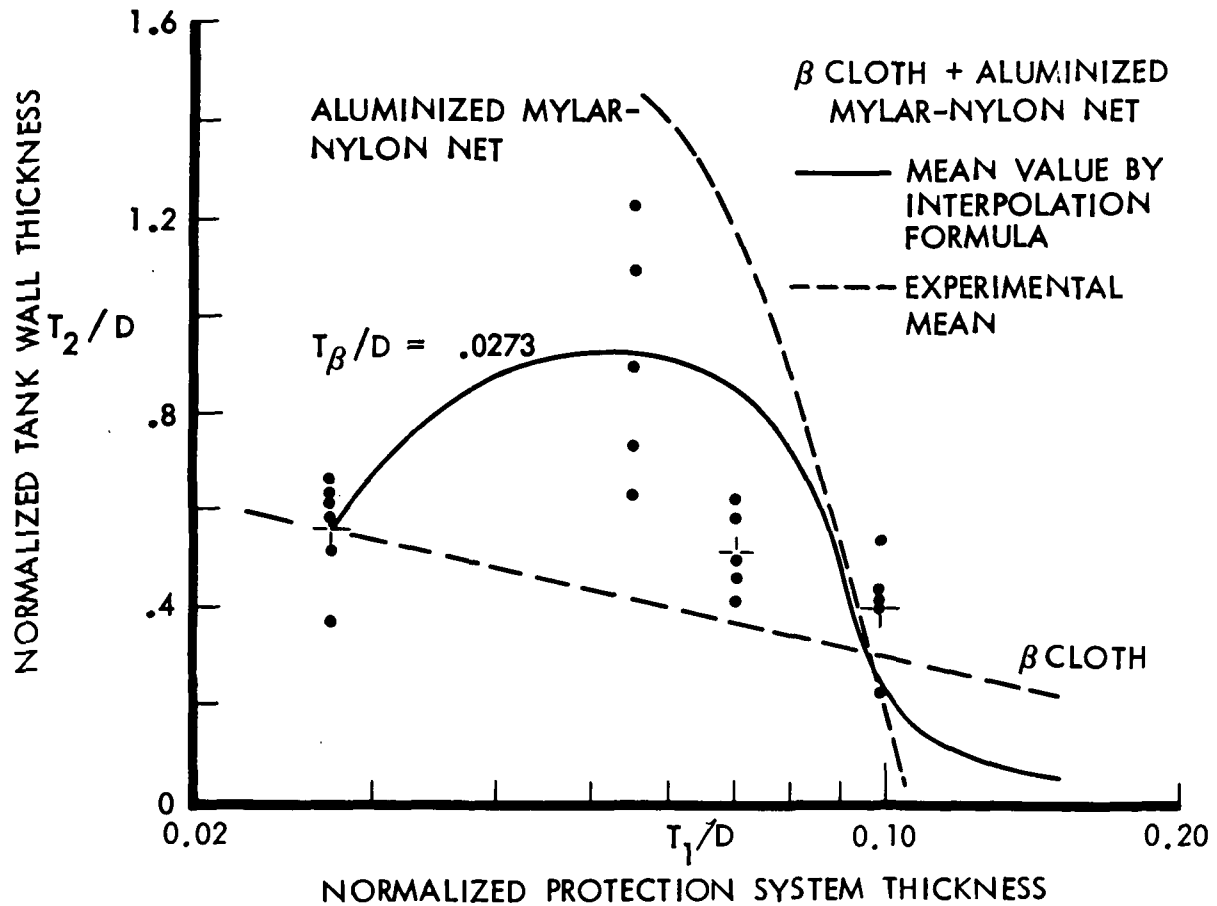


Figure 2.1-5: METEOROID PROTECTION DESIGN DATA -  $\beta$  CLOTH & MLI

Most of the data had considerable scatter, and following a conservative design practice,  $3\sigma$  was added to the mean values. This was straightforward when only one material was being considered. However, when combinations of materials were tested, the resulting scatter (i.e.,  $3\sigma$ ) might not be consistent with that of the separate materials. For those combinations where test results were available,  $3\sigma$  was computed and added to the interpolated mean value as in Figure 2.1-6. Two thicknesses of Beta fiber cloth are shown in that figure. The results fell outside of the  $3\sigma$  curves of the separate materials. This was not a paradox but reflects the fact that the scatter in the test results of the combined materials was larger than that of the separate materials. While this may have been only statistical in some cases, it appeared to have some physical basis in others.

For combinations of materials where the MLI was in front of the structural skin, for example Figure 2.1-7, the curve had to drop to zero with the same final slope as the MLI alone, but displaced to the right by the added thickness of skin. The skin alone point had to start on the skin alone curve. The intermediate portion of the curve was adjusted to conform to combined MLI/skin or bumper/MLI/skin test data.

### 2.1.3 Final Design Proof Tests

The finalized thermal/meteoroid protection systems of Vehicles 1-14 and 2-18 were tested to verify design adequacy. The protection system for both vehicle designs was MLI consisting of .15 mil double aluminized mylar shields and nylon net spacers. The distance between the MLI blanket and the propellant tanks was approximately 4.00 in (10.2 cm). The design meteoroid diameters for Vehicles 1-14 and 2-18 were 0.065 and 0.054 inches (0.17 and 0.14 cm), respectively. The value of normalized tank wall thickness ( $T_2/D$ ) was about the same for both vehicles. Using the  $3\sigma$  curve of Figure 2.1-2 a value of  $T_1/D = 0.098$  was obtained for the typical normalized protection system thickness in terms of aluminum. Solving for the test thickness of MLI as described in Section 1.2.3:

$$T_1 = \frac{T_1/D \times D \times \rho_{ALUM}}{W_{MLI}} = 39 \text{ shield/spacer pairs}$$

where  $D$  was the diameter of the test meteoroid, 0.110 in (0.28 cm).

Spacing between the meteoroid protection system and the witness plate (simulated tank wall) for Vehicles 1-14 and 2-18 was 6.7 in (17.0 cm) and 8.0 in (20.3 cm), respectively. These values were derived from the relationships of  $S/D = 4/.065 = 61$  and  $S/D = 4/.054 = 74$ , where the diameter of the test projectile was used.

A total of 45 valid shots were made. Twenty-four shots were made for Vehicle 1-14 and twenty-one for Vehicle 2-18. The shots were made with the projectile

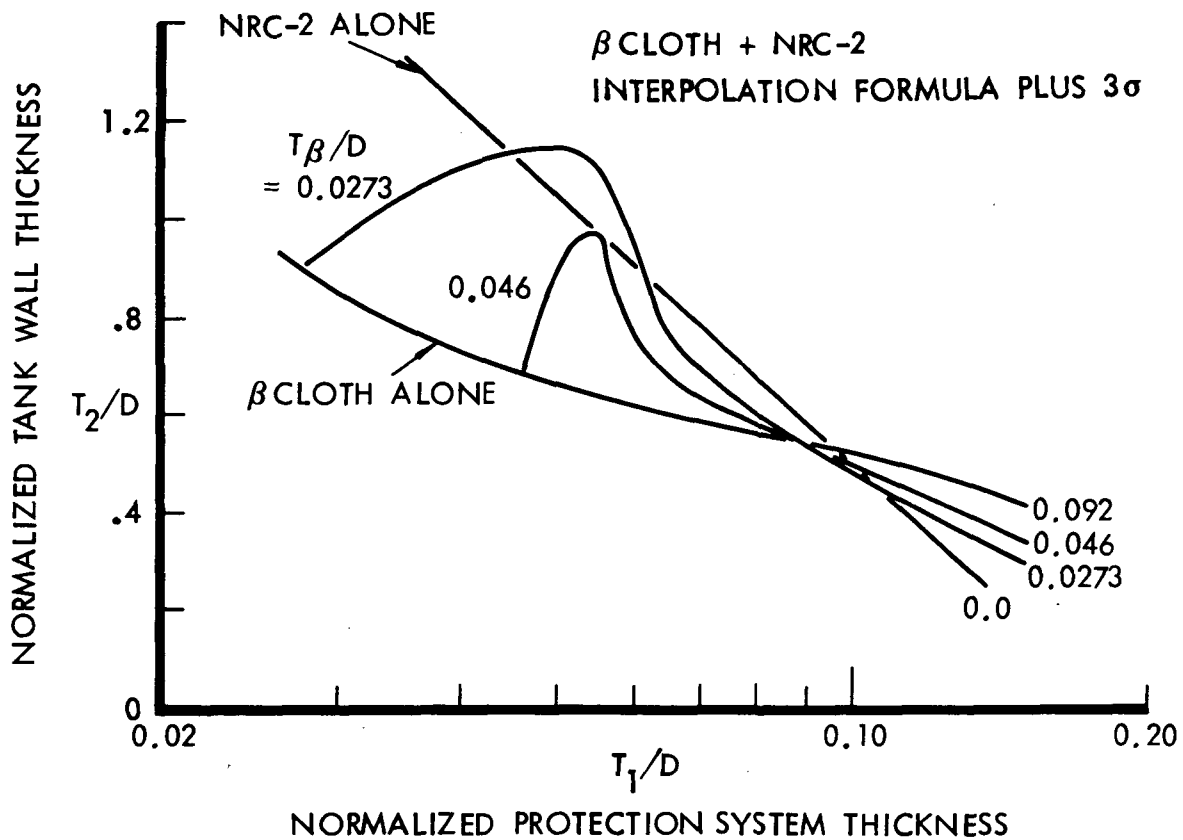


Figure 2.1-6: METEOROID PROTECTION DESIGN DATA -  $\beta$ CLOTH & MLI

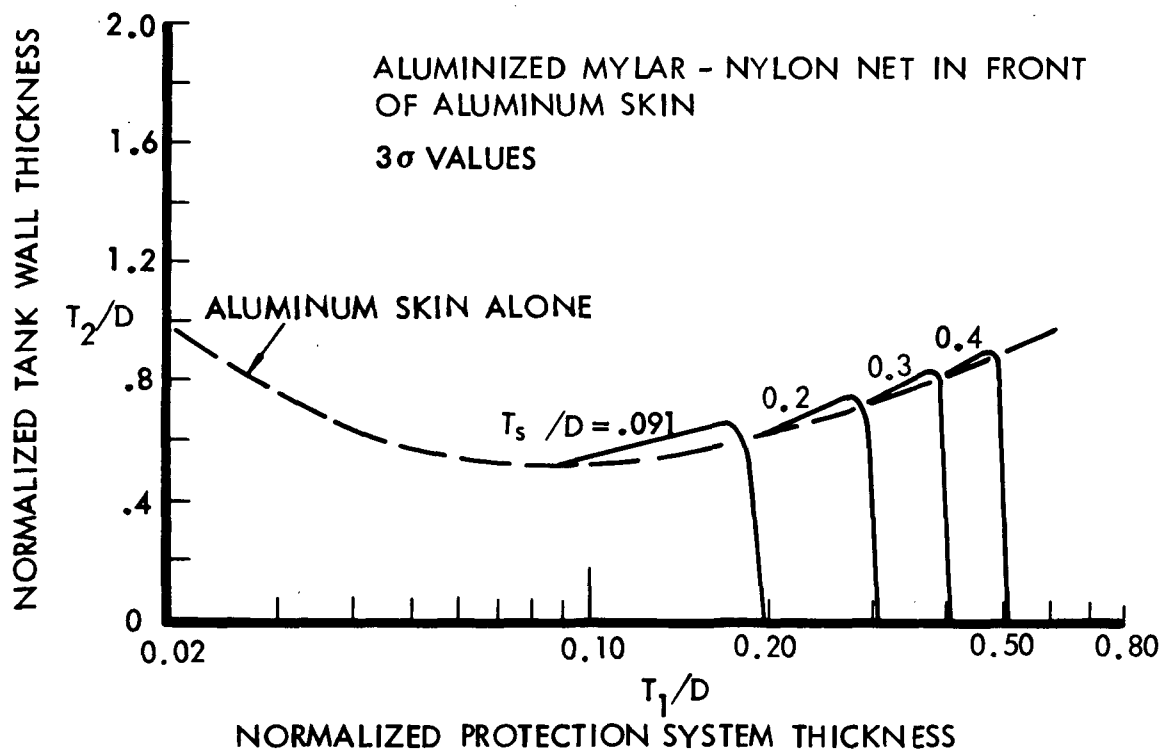
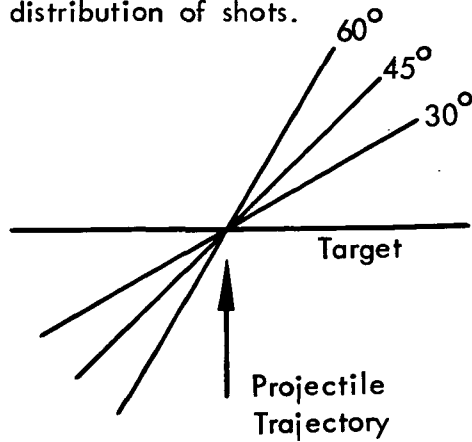


Figure 2.1-7: METEOROID PROTECTION DESIGN DATA - MLI & ALUMINUM

direction of impact normal to the target surface ( $0^\circ$ ) and with the target rotated  $30^\circ$ ,  $45^\circ$  and  $60^\circ$ . The table shows the distribution of shots.

Vehicle 2-18	Vehicle 1-14
7 at $0^\circ$	9 at $0^\circ$
5 at $30^\circ$	5 at $30^\circ$
5 at $45^\circ$	5 at $45^\circ$
4 at $60^\circ$	5 at $60^\circ$
21 Total	24 Total



The test results were analyzed using the 50% maximum tank wall penetration criteria. The most severe damage resulted from the  $0^\circ$  impact angle tests. The data points for these sixteen test shots were plotted on the meteoroid protection design curve of Figure 2.1-8. All of the points fell below the  $3\sigma$  design curve, thus the system provided the necessary degree of protection.

The meteoroid protection design study discussed in Section 1.2-3 had required extrapolation of the Figure 2.1-8 curve to obtain the needed values of  $T_1/D > 0.092$ . This extrapolation is shown as a dashed line on Figure 2.1-8. The proof test data was used to correct the curve between  $T_1/D = .092$  and  $.098$  as shown by the solid line in the figure. There was only a slight change.

Some photographs of typical meteoroid damage are shown in Figures 2.1-9 through 2.1-17. Target angles of  $30^\circ$ ,  $45^\circ$  and  $60^\circ$  are shown in Figures 2.1-9, 2.1-10 and 2.1-11. Three different impacts at  $0^\circ$  target angle are shown in Figures 2.1-12, 2.1-13 and 2.1-14. The witness plate damage, respectively, is shown in Figures 2.1-15, 2.1-16 and 2.1-17. Figures 2.1-15 and 2.1-17 represented the least and greatest damage obtained in the tests and Figure 2.1-16 was an example of median damage.

## 2.2 Thermal Performance and Launch Environment Testing

A series of tests were performed to evaluate the combined thermal/meteoroid protection design concept. The series consisted of boiloff tests with  $LN_2$  and  $LH_2$  and structural tests to simulate the launch environment. The test part was modelled to represent an aluminum truss structure vehicle with MLI mounted on the interior.

### 2.2.1 Test Program

The program schematic is shown in Figure 2.2-1. The first three tests determined heat transfer rates through the modelled MLI system with different sets of boundary

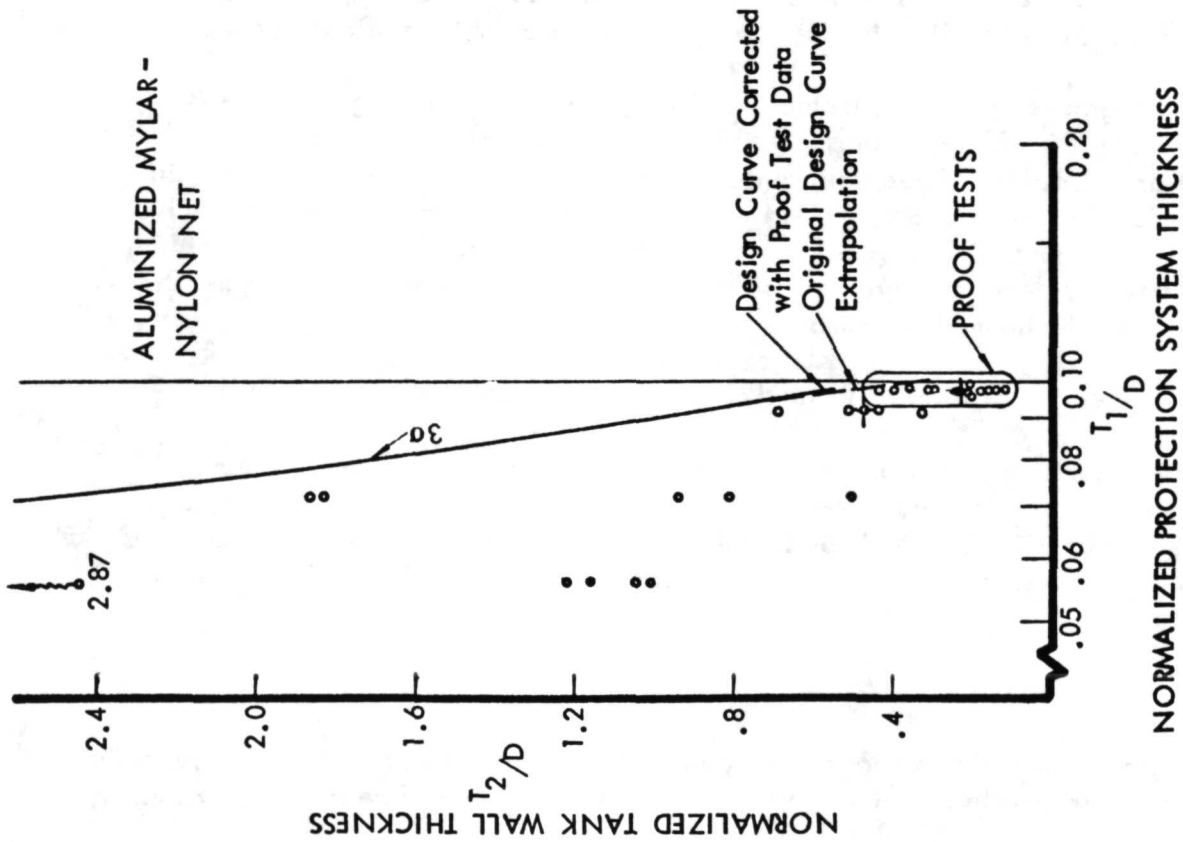


Figure 2.1-8: METEOROID PROTECTION DESIGN DATA - MLI

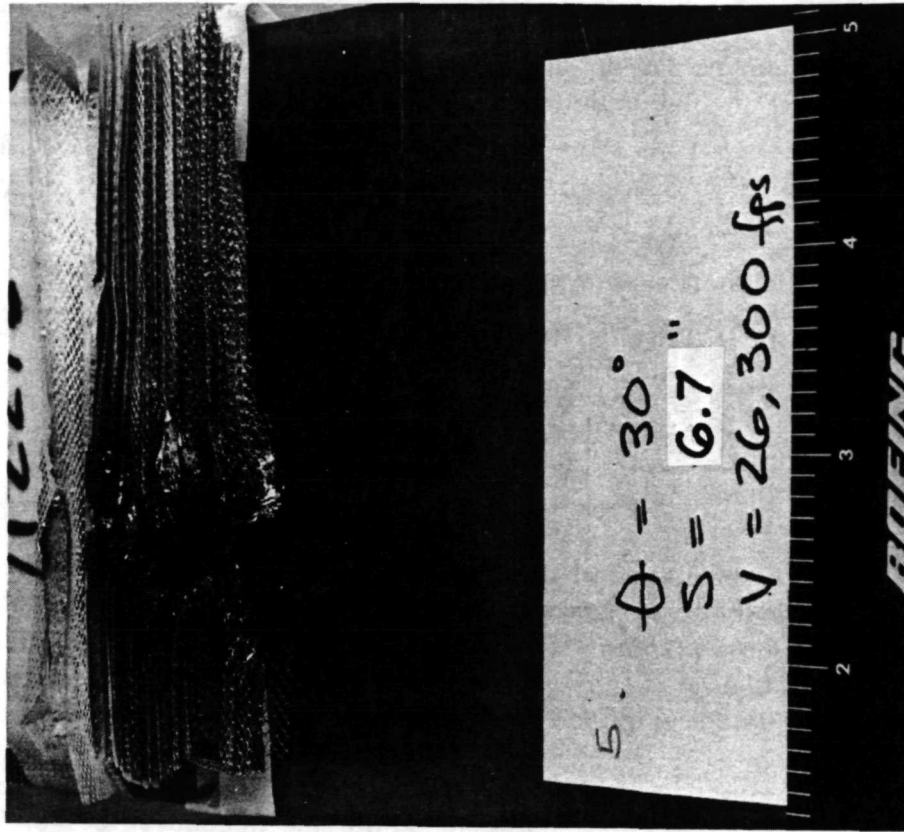


Figure 2.1-9: PROOF TEST SAMPLE - VEHICLE 1-14

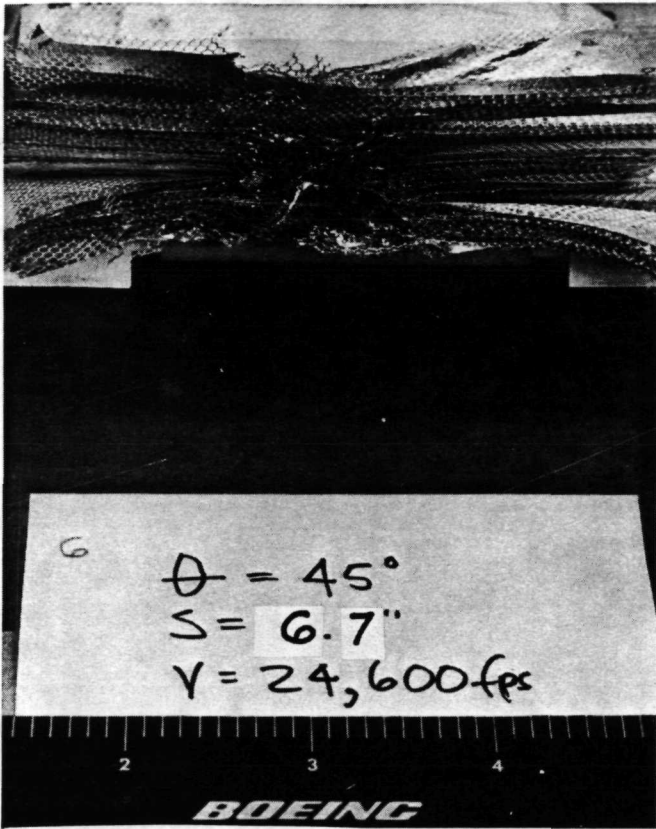


Figure 2.1-10: PROOF TEST SAMPLE, VEHICLE 1-14

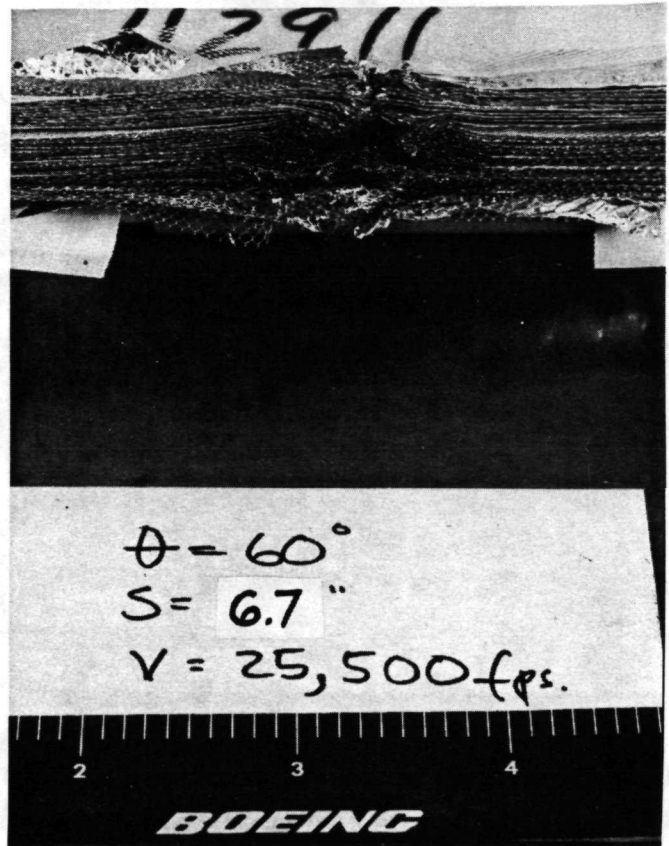


Figure 2.1-11: PROOF TEST SAMPLE, VEHICLE 1-14

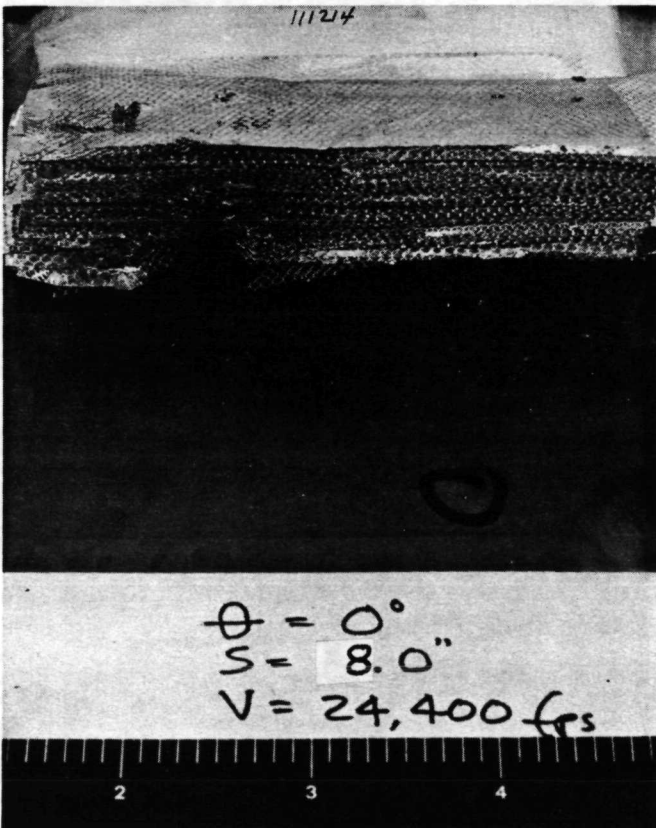


Figure 2.1-12: PROOF TEST SAMPLE, VEHICLE 2-18

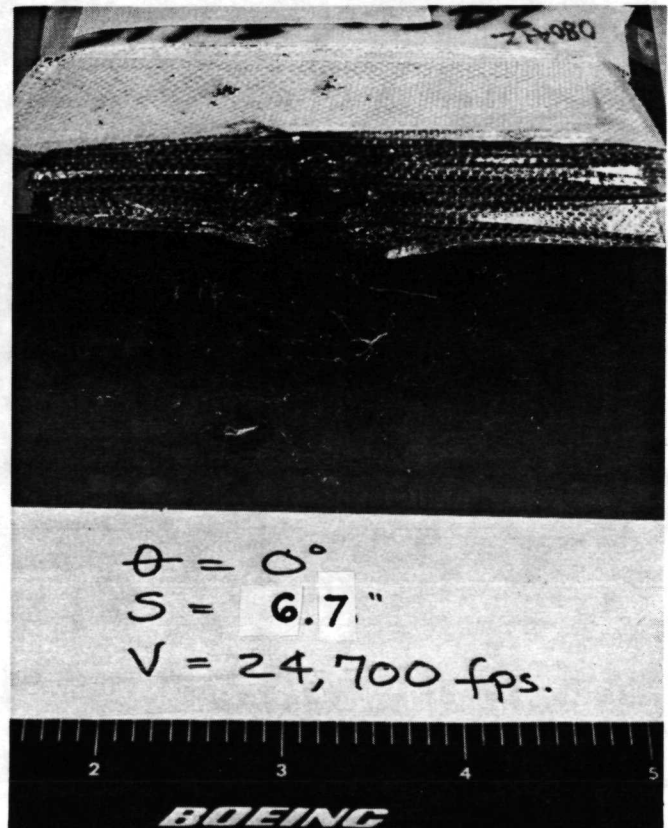


Figure 2.1-13: PROOF TEST SAMPLE, VEHICLE 1-14

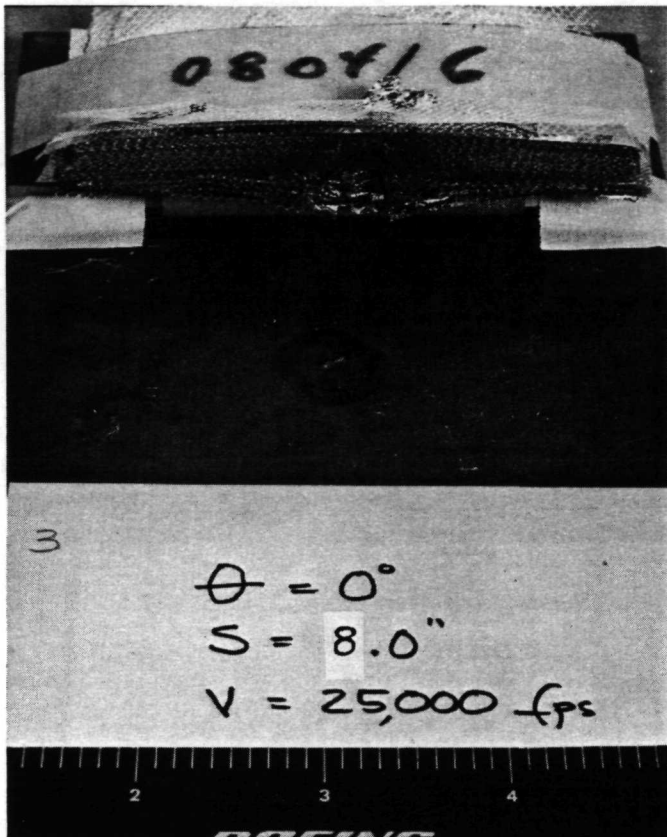


Figure 2.1-14: PROOF TEST SAMPLE, VEHICLE 2-18

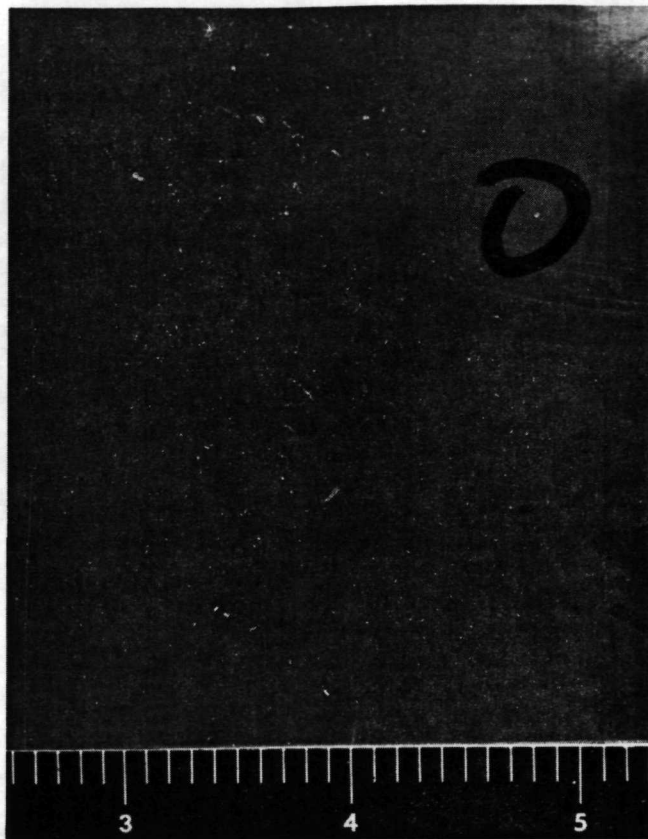


Figure 2.1-15: WITNESS PLATE DAMAGE

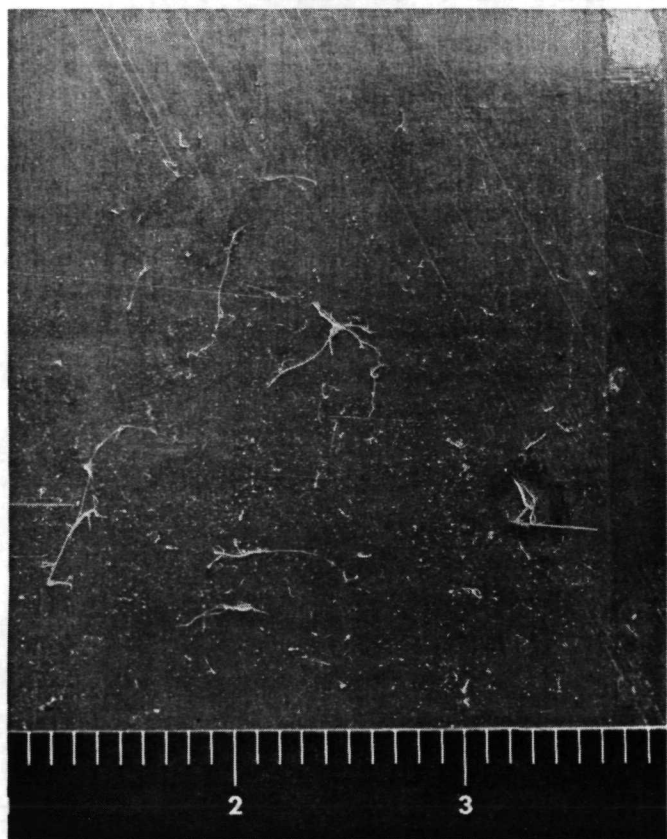


Figure 2.1-16: WITNESS PLATE DAMAGE

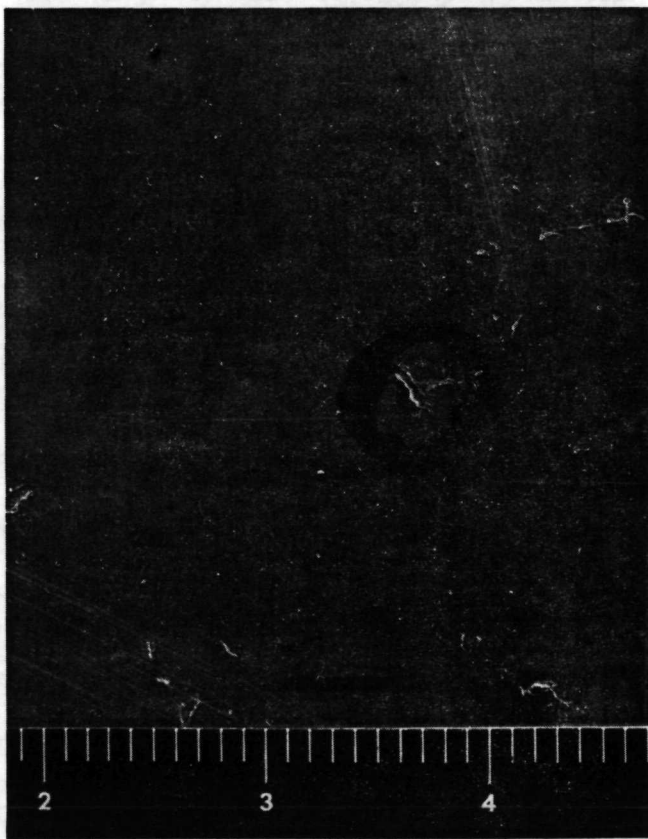


Figure 2.1-17: WITNESS PLATE DAMAGE

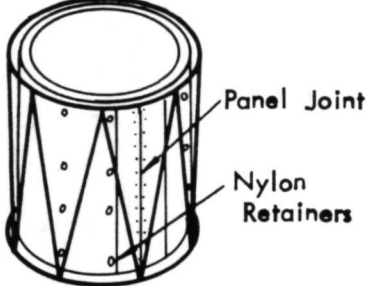
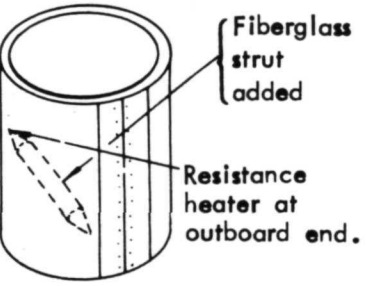
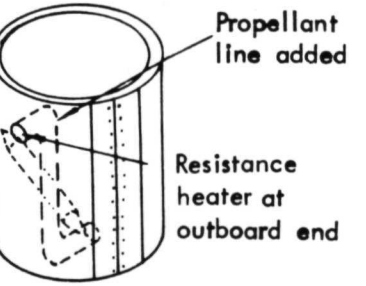
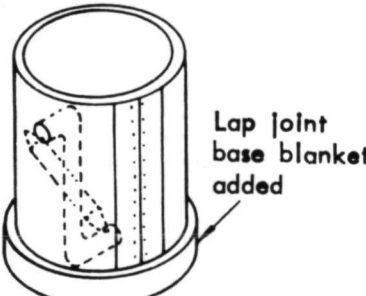
TEST	TEST TYPE	WARM BOUNDARY	TEST FLUID	SIMULATION
T-1 T-2 T-3	HEAT FLOW TESTS 	65°F (292°K) 65°F (292°K) -320°F (77.3°K)	LH <sub>2</sub> LN <sub>2</sub> LH <sub>2</sub>	Heat Transfer to propellants through side walls and top deck
S-1 S-2 S-3	STRUCTURAL TESTS • Vibration • Acoustic • Acceleration	—	—	Titan 3D-centaur launch
T-4	HEAT FLOW TEST Same Config. sample as test T-1	65°F (292°K)	LH <sub>2</sub>	Heat transfer after exposure to launch loads
T-5	HEAT FLOW TEST 	(a) Heater Inactive 65°F (292°K)  (b) Heater Activated 65°F (292°K)	LH <sub>2</sub>  LH <sub>2</sub>	Tank support/multilayer penetration
T-6 T-7	HEAT FLOW TEST 	(a) Heater Inactive 65°F (292°K) (b) Heaters Activated 65°F (292°K)  (a) Heater Inactive 65°F (292°K)	LH <sub>2</sub>  LH <sub>2</sub>  LN <sub>2</sub>	Propellant line multilayer penetration
T-8	HEAT FLOW TEST 	Heaters Inactive  Base 65°F (292°K)  Sidewall -320°F (77.3°K)	LH <sub>2</sub>	

Figure 2.2-1: THERMAL PERFORMANCE AND LAUNCH ENVIRONMENT TEST PROGRAM

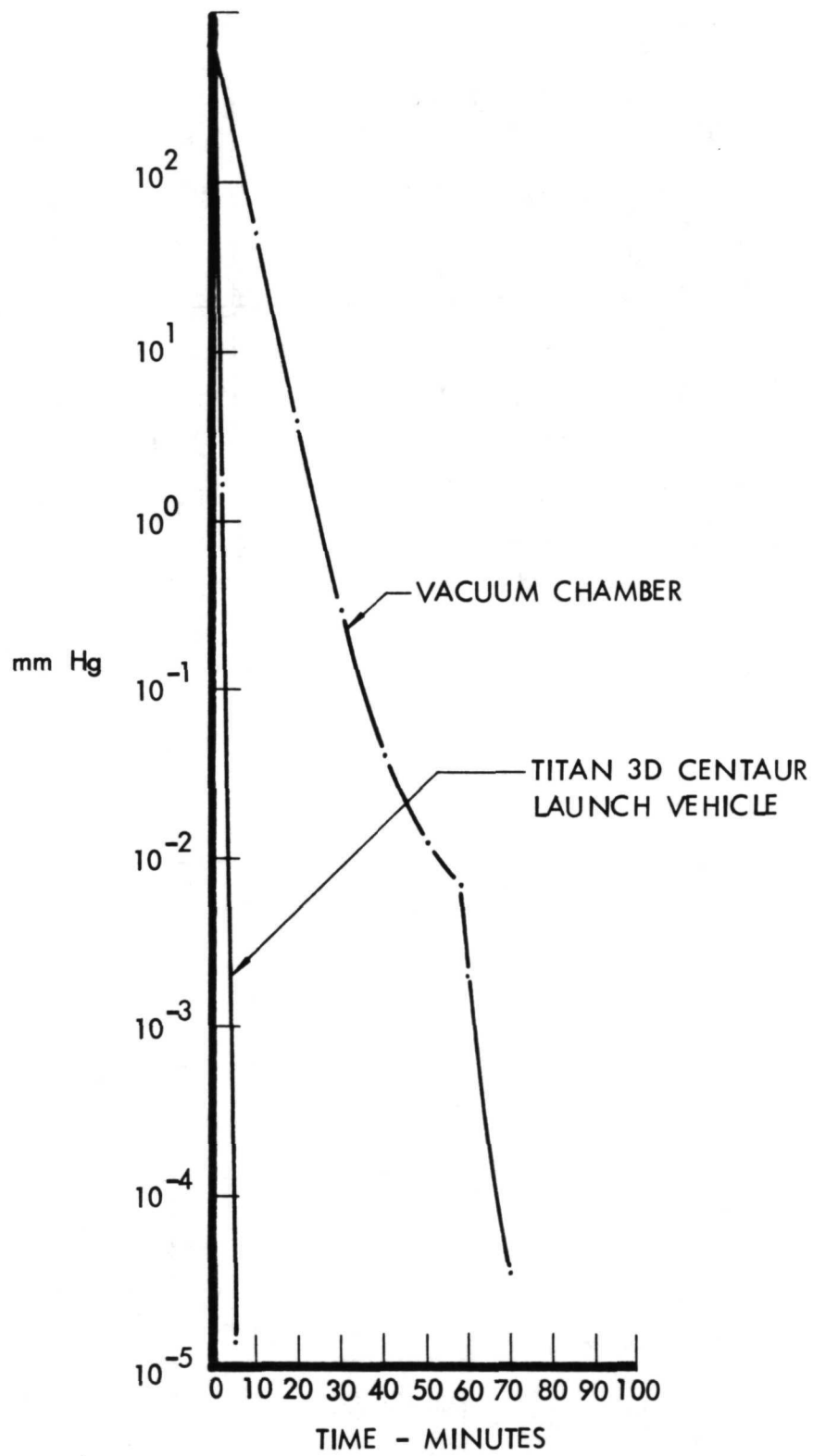


Figure 2.2-2: DEPRESSURIZATION RATES

temperatures. The temperature combinations were selected to represent heat transfer from the payload to the LH<sub>2</sub> tank, from the payload and solar panels to the LF<sub>2</sub> tank, and from the lower vehicle sidewall to the LH<sub>2</sub> tank. The test cryogenics were LH<sub>2</sub> and LN<sub>2</sub>. The latter was used to represent LF<sub>2</sub>. The warm boundary was established with heated water which was circulated through a thermal shroud surrounding the test article.

The purpose of the first three tests was to establish baseline heat flow values which could be used for further assessment of thermal performance as testing progressed.

The next three tests exposed the test article to the vibration, acoustic and acceleration environments typical of a Titan 3D-Centaur launch. These experiments were performed in series so that a visual appraisal of damage and identification of critical test environments could be made. The order of the test series is defined numerically in Figure 2.2-1. The loads were applied to the aluminum framework by attachments at both ends of the cylinder. The test environment was obtained from Martin Titan III study documents, MRC 67-332 and MRC 68-62 and from a Boeing document, D2-116032-4.

The fourth thermal test (T-4) was a repeat of T-1. The purpose was to determine thermal performance degradation, if any, after the launch environment tests. Launch depressurization was simulated as nearly as possible at the beginning of this test by rapid pumpdown of the chamber. Figure 2.2-2 shows a comparison between the empty chamber pumping speed and the depressurization rate typical for the launch vehicle.

The results of the fourth thermal test became the new baseline for further thermal performance comparisons. The quantitative effects of the structural tests were determined by comparison with T-1 test results.

The fifth thermal test was an evaluation of a fiberglass tank support strut and MLI penetration. The test article was modified by adding the fiberglass strut while minimizing disturbance of the adjacent MLI. A resistance heater was installed on the warm end of the strut attachment as an aid to maintaining thermal equilibrium of the aluminum trusswork frame. The heat flow increment due to the strut and penetration was derived by comparison with T-4 test results.

The sixth and seventh tests comprised an evaluation of the fiberglass strut tank support and a stainless steel fluid line and line penetration. The fluid line was added to the test system and a resistance heater installed at the outboard end. Test T-6 was conducted with LH<sub>2</sub> and test T-7 with LN<sub>2</sub>. Comparisons could then be made with tests T-1 and T-2 for determination of the cumulative effects of structural loads and strut and fluid line modifications for two propellants. The results of test T-6 could be compared with test T-5 for an evaluation of the fluid line heat leak.

The eighth test modified the MLI to include a lap joint similar to those used at the top deck to sidewall junction of the final designs. The thermal shroud base was isolated from the sidewall section so that two warm boundary temperatures could be used. The base was controlled to a higher temperature than the sidewall to represent the thermal environment of the flight vehicles. The objective of this test was to evaluate the cumulative effects of line penetrations and MLI joints in a thermal environment approximating the flight environment.

## 2.2.2 Test System Description

### Boiloff Test System

Boiloff tests were conducted at Boeing's Tulalip Test Site, Area 8 - Pad 1. A photograph of the major components at the site is shown in Figure 2.2-3. Figure 2.2-4 is a schematic of the system.

Tests were conducted in a cylindrical, aluminum vacuum chamber 8 ft (2.4 m) in diameter by 7 ft (2.1 m) long. An NRC vacuum pumping system comprised of a rotary gas ballast roughing pump, Type 100S, with a pump speed of 100 CFM ( $2.8 \text{ m}^3/\text{min}$ ) and a 10 in (25.4 cm) diameter oil diffusion pump, Type 0155, with a pump speed of 1200 liters/sec. was connected to the chamber through a 10 in (25.4 cm) line. Thermocouple and ionization gages provided vacuum readout.

The chamber contained a thermal shroud, 28 in (0.71 m) in diameter by 84 in (2.1 m) high, constructed of copper sheet with coolant lines soldered to the inside. The shroud was constructed in two halves like a clam shell to permit installation and removal of the test article. Coolant lines of the two halves were manifolded together. Liquid nitrogen or water was circulated through the coolant tubes depending on the warm boundary requirement.  $\text{LN}_2$  fill was controlled automatically by liquid level sensors. Water was constantly circulated by pumping from a 1000 gallon ( $4.546 \text{ m}^3$ ) reservoir through a heat exchanger to the thermal shroud and back to the reservoir.

The calorimeter assembly consisted of a guard tank mounted above the test tank. Both were made of stainless steel. The test tank was a cylinder with flat ends, 12 in (0.31 m) in diameter by 35 in (0.89 m) high and a capacity of 17 gallons ( $.077 \text{ m}^3$ ). The guard tank was 20 in (0.51 m) in diameter by 8 in (0.20 m) high with a capacity of 11 gallons ( $.05 \text{ m}^3$ ). The guard tank was welded to the test tank vent line to intercept heat leak and a blanket of aluminized mylar/nylon net separated the two tanks. The test tank fill line was located within the vent line. Both tanks had instrumentation probes which incorporated liquid level and temperature sensors. The test article was a cylindrical truss arrangement which was closed at the bottom and open at the top. The test article was designed to fit over the guard tank with a small amount of clearance. A photograph of the guard and test tank assembly mounted on the vacuum chamber

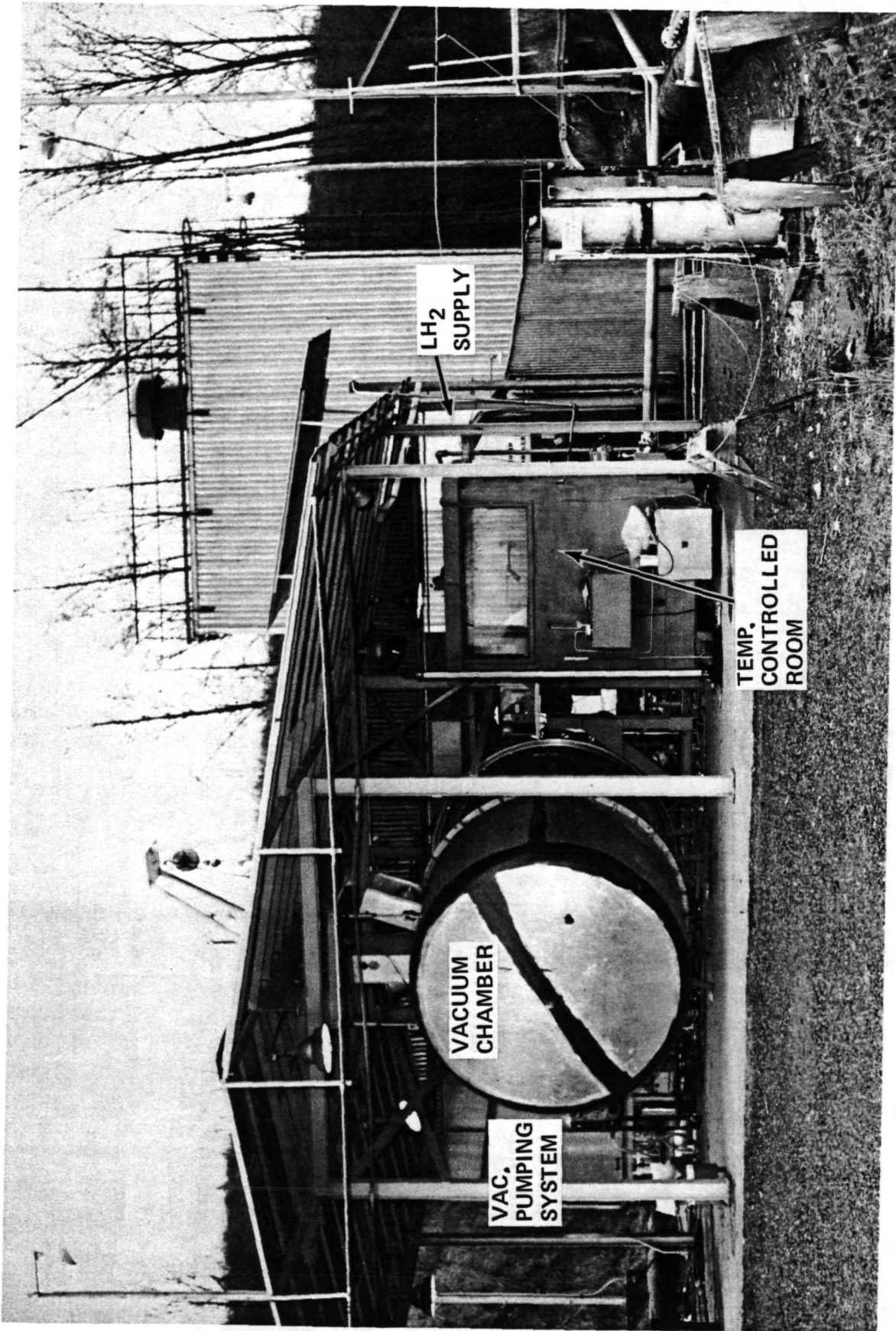


Figure 2.2-3: THERMAL TEST SITE - AREA 8 TULALIP

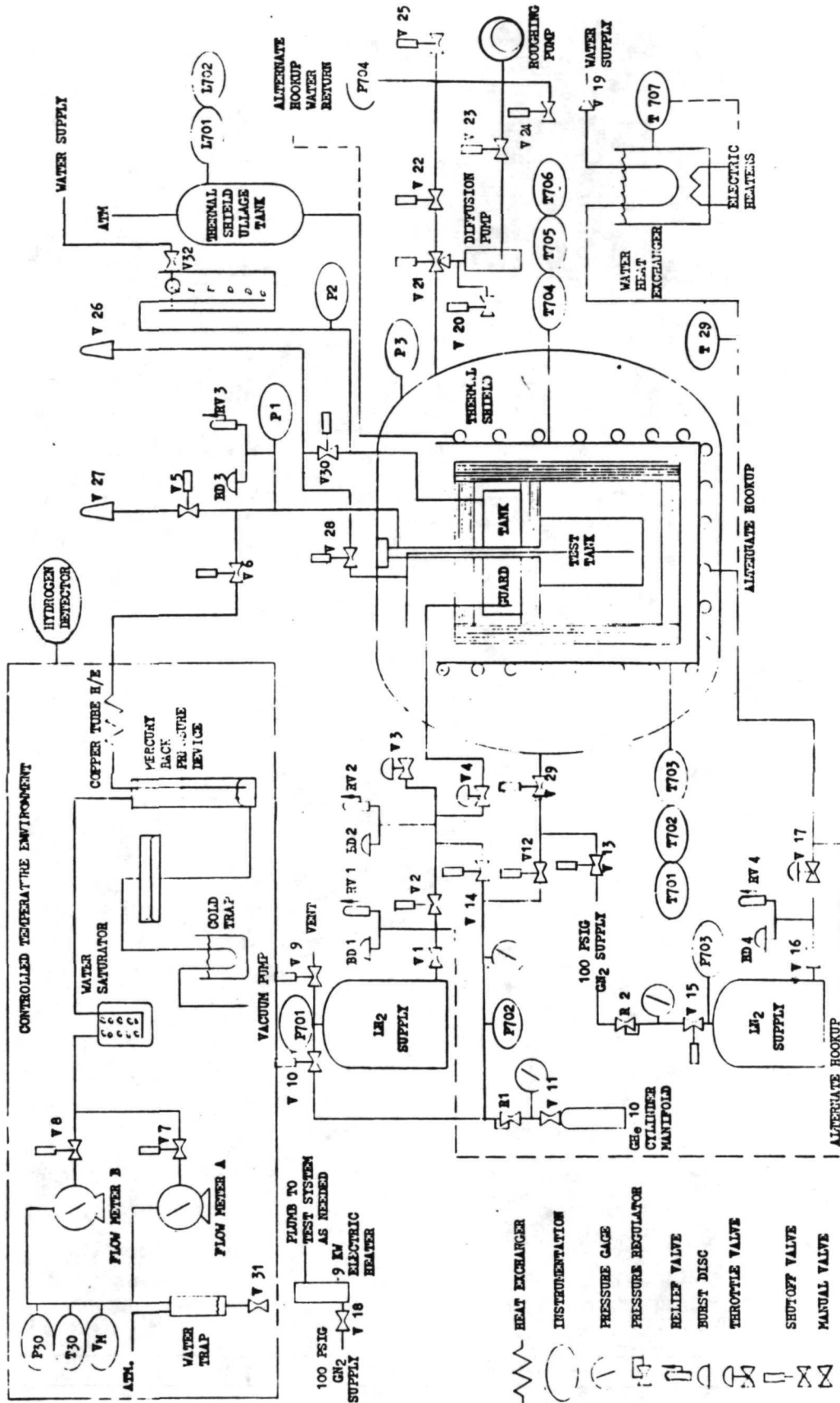


Figure 2.2-4: SCHEMATIC-THERMAL TEST SYSTEM

door is shown in Figure 2.2-5. The test tank was offset from the center of the guard to allow room for the fluid line and tank support strut installation. The design drawing showing calorimeter tank and test article details is presented in Figure 2.2-6.

A wet test meter system was used to measure the volume of boiloff gas from the test tank. Two meters with rated capacities of 10 to 150 cubic ft/hr (0.28 to 4.25 m<sup>3</sup>/hr) and 0.5 to 20 cubic ft/hr (0.01 to 0.56 m<sup>3</sup>/hr) were installed in parallel and valved in as desired. Both meters were manufactured by American Meter Co., the first was a Model AL-20 and the second a Model AL-18. A  $\pm 1\%$  accuracy was quoted over the entire measurement range.

A mercury back pressure device, referenced to vacuum, provided a constant pressure environment to the boiling fluid in the test tank. The essentials of the system were a large area vacuum referenced mercury reservoir connected to a small area mercury pot. The boiloff gas bubbled through the small pot and then was measured. The elevation of the large reservoir mercury level to the gas discharge line in the pot was only changed 1/115th of any atmospheric pressure change due to the area ratios. A trim pot was included in the back pressure system to allow even closer control of elevation.

Pressure in the guard tank was controlled from 1.3 to 1.5 psig (9.0 to 10.3 kN/m<sup>2</sup>) by a water manometer.

The wet test meter measured the gas volume passing through at saturated and at a conditioned temperature (T-30 in Figure 2.2-4). To eliminate errors, corrections were made for dry gas at standard temperature and pressure. The gas as it left the wet test meter was saturated and a temperature slightly above ambient. In order to prevent the water condensed in the vent line from back pressuring the system, a water trap was included.

The corrections to the gas volume being measured assumed saturated gas. In order to assure this without reducing the water level in the wet test meter, the gas was bubbled through distilled water in a closed vessel before reaching the wet test meter.

The measured gas volume did not entirely represent the heat leak. Some of the gas evolved remained in the ullage space to replace the liquid. Therefore, a correction factor was applied to the gas volume measured. The factor was based on the relative densities of the liquid and the saturated vapor. The correction assumed the vapor leaving the tank was saturated. If the vapor was superheated, the actual heat leak would be higher than the measured heat leak. In order to determine the amount of sensible heating, a thermocouple was installed at the junction of the tank and vent outlet.

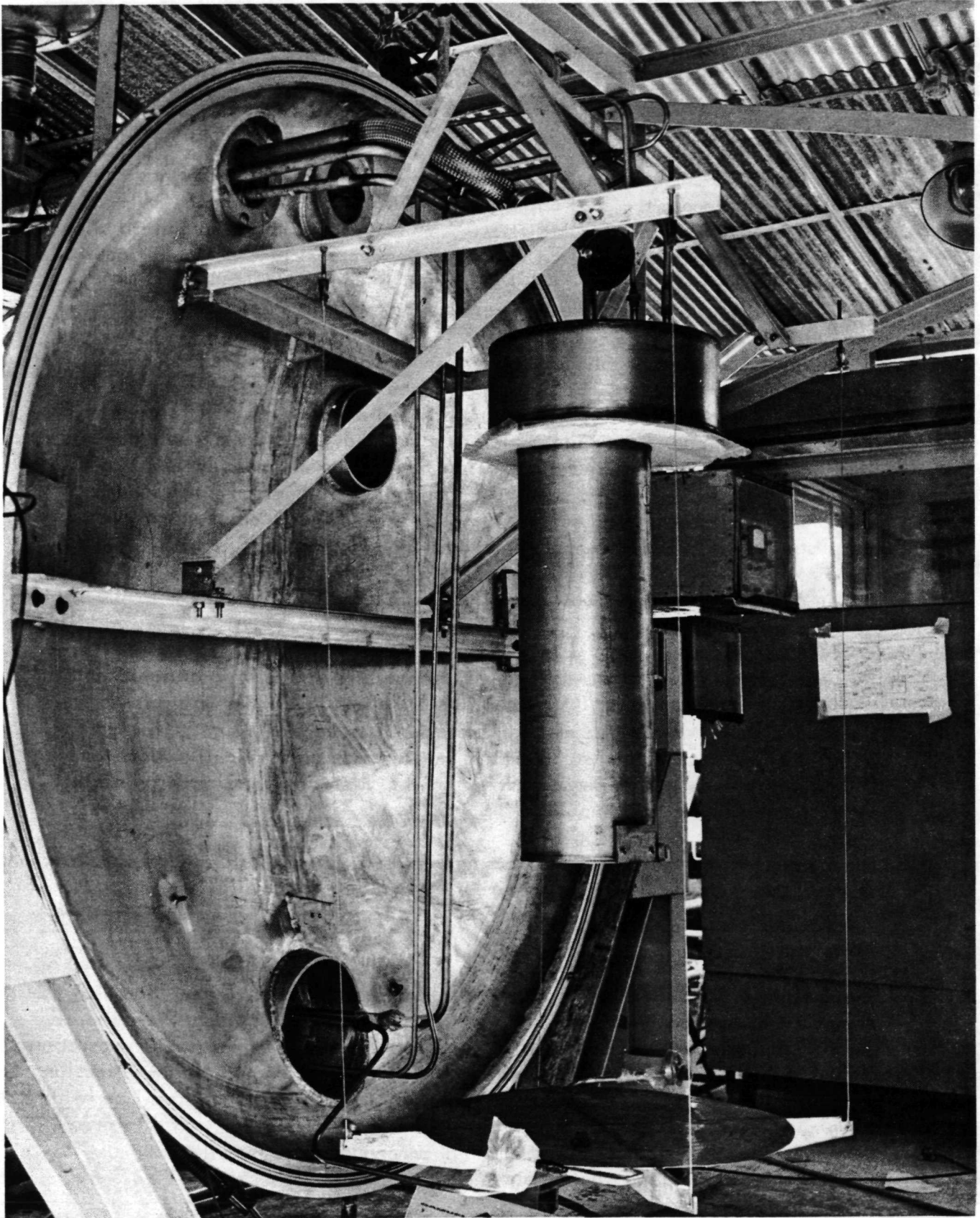
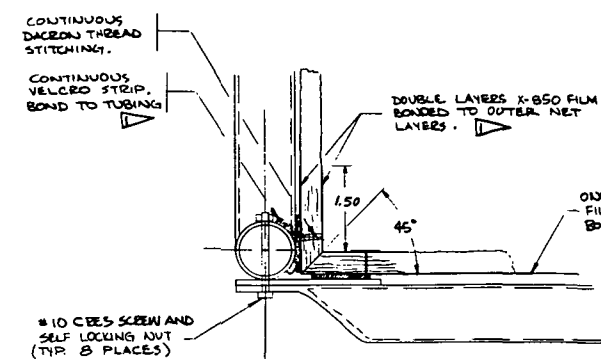
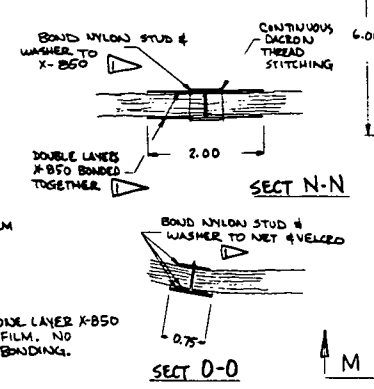


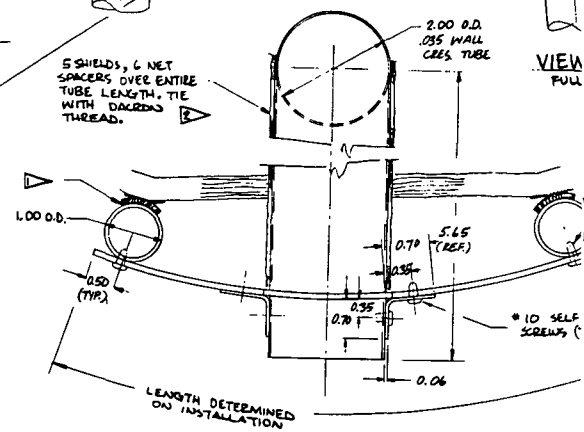
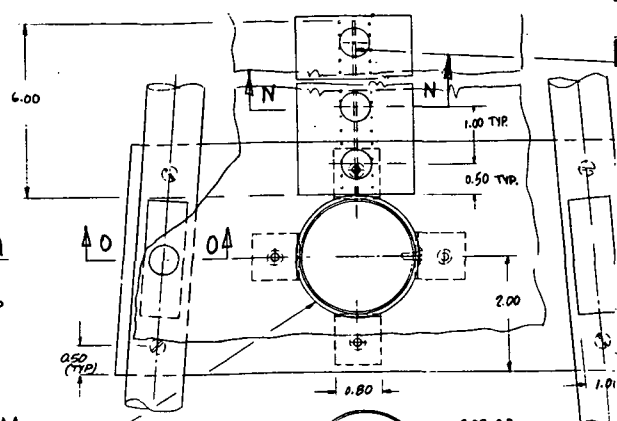
Figure 2.2-5: GUARD AND TEST TANK ASSEMBLY



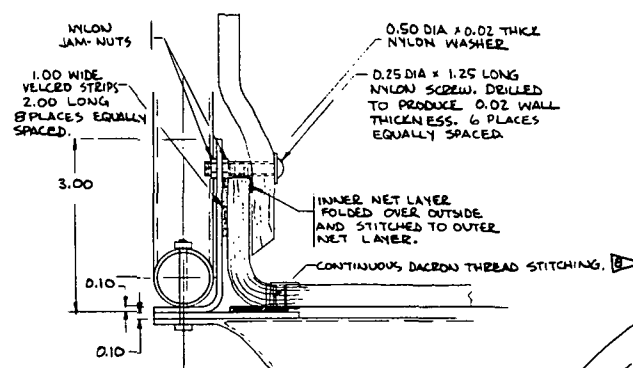
SECT P-P FULL SCALE



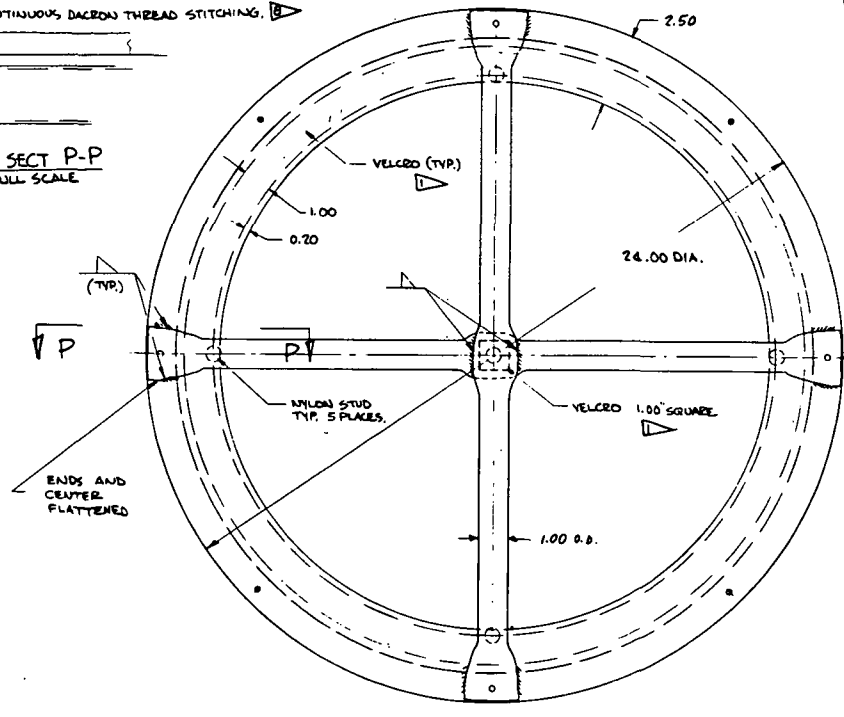
CUTOUT SIDEWALL N.L. TO ACCOMMODATE INSULATED TUBE. NO GAPS PERMITTED.



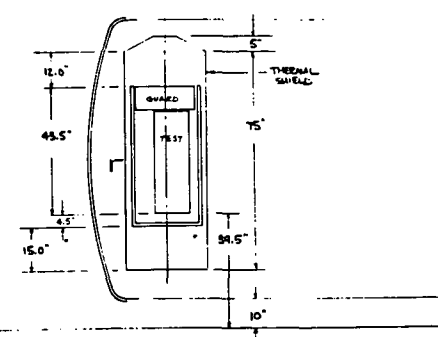
SECT M-M FULL SCALE



ALT. SECT P-P FULL SCALE



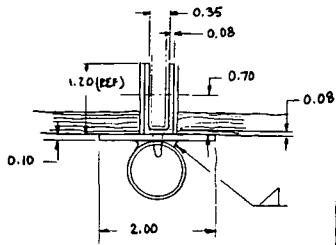
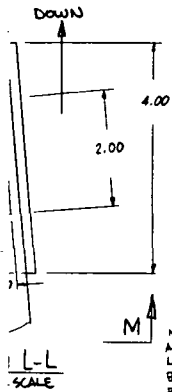
SECT B-B 1/2 SCALE



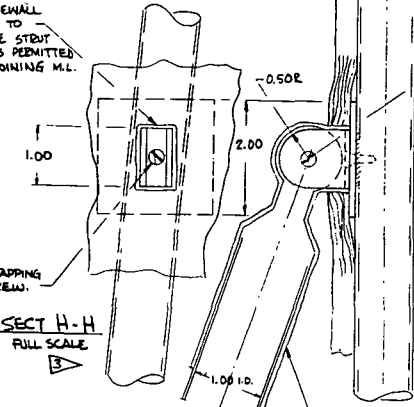
TULIP AREA 8 CHAMBER DIMEN.

- ▶ BOND W/ MULTILAYER NYLON AN LAYERS AT RATIO 1:3
- ▶ LOCATE ALUM. AL ON TEST
- ▶ ALUM. AL ORIENT IN FIBERGLA BETWEEN
- ▶ FUSION WELD COLD SHOE WELDS. LEA 2x10<sup>-10</sup> ST
- ▶ TEST & GLW FROM 321
- ▶ STITCHING BASIC DL

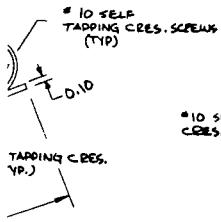
SPLIT M.L. TO REPRESENT ASSEMBLY JOINT. NO GAP PERMITTED.



CUTOUT SIDEWALL MULTILAYER TO ACCOMMODATE STRUT LUG. NO GAPS PERMITTED BETWEEN ADJOINING M.L. BLANKETS.



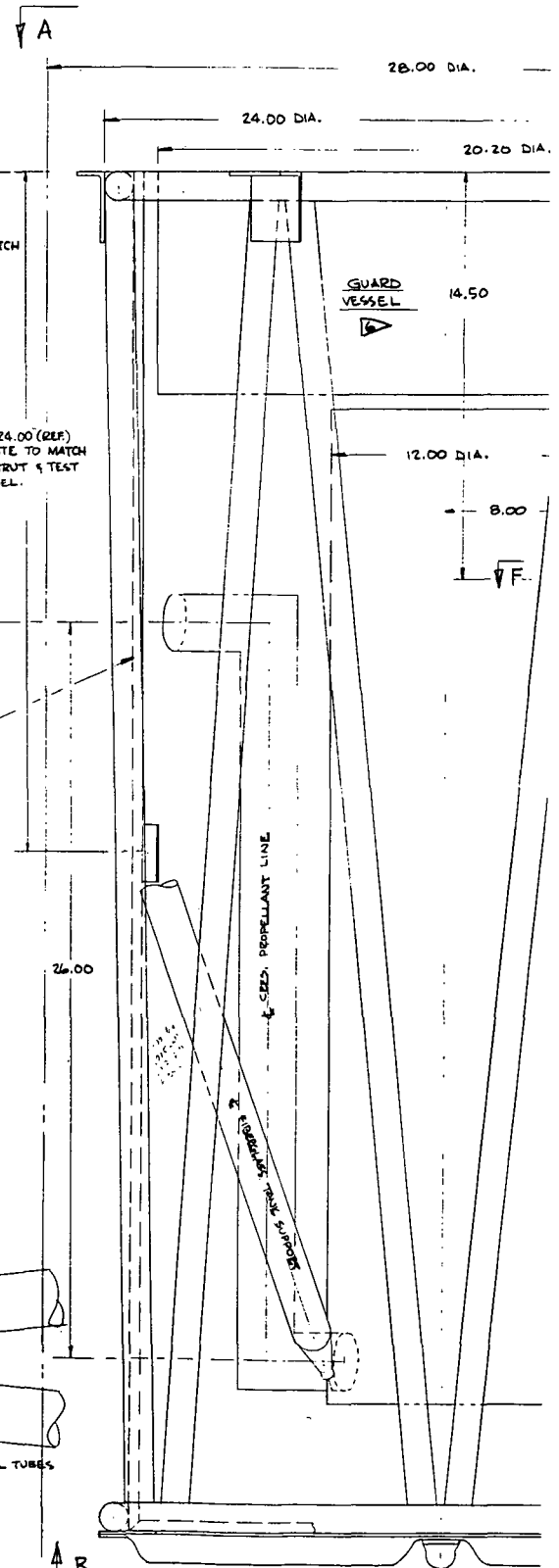
SECT H-H FULL SCALE



10 SELF TAPPING CRES. SCREW

5 SHIELDS, 6 NET SPACERS OVER ENTIRE STRUT AND END FITTING. TIE WITH DACRON THREAD.

MULTILAYER BLANKET (TYP.)



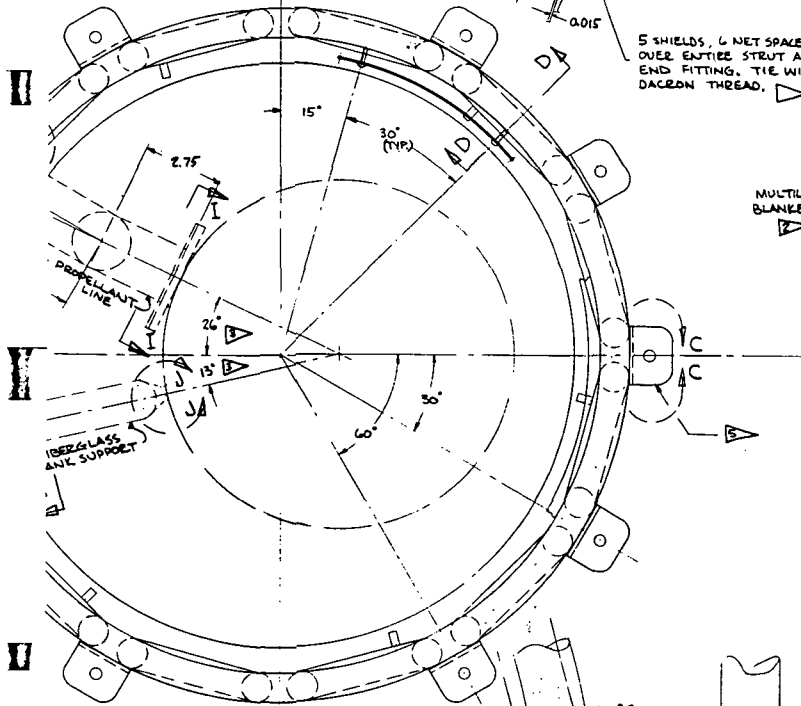
15.90 (REF) LOCATE TO MATCH CRES. TUBE & TEST VESSEL.

24.00 (REF) LOCATE TO MATCH F.G. STRUT & TEST VESSEL.

26.00

PROPPELLANT LINE

SECTION B



SECT. A-A 1/2 SCALE

TH EMS 6-29 ADHESIVE.

CONSISTS OF ALTERNATING LAYERS 0.15 MIL DBL. ARMED 3 SEAMS ROEBUCK .007 FIBER DIA. NYLON NET. NETTING & ON BOTH EXTERNAL SURFACES OF BLANKET. LAYER TO SHIELDS PER INCH.

COMPONENTS TO MATCH PRIOR TO WELDING BRACKETS VESSEL.

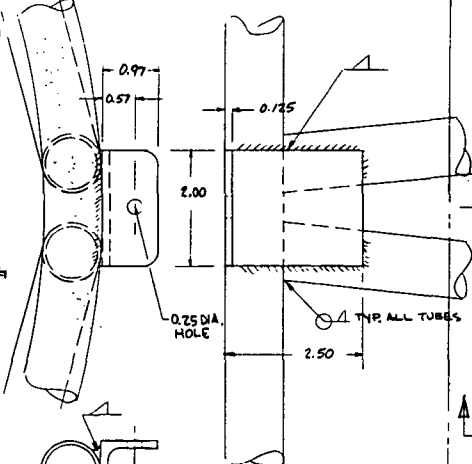
.01 6061 OR 5052 DRAWN TUBE.

INSULATION TEST ASSEMBLY SO THAT THE TWO IS SUPPORT RODS PASS THROUGH THE JOINT THERMAL SHIELD HALVES.

PER BAC 5950 CLASS A. PERVAZANT INSPECT PER BAC 5423. WELDED ASSEMBLY WITH LN<sub>2</sub> THEN VACUUM LEAK CHECK ALL & DETECTOR SHALL BE CALIBRATED TO A SENSITIVITY OF AT LEAST 1 CC HELIUM/SEC. PROOF TEST TO 20 PSIG.

20 VESSEL AND ASSOCIATED TUBING FABRICATED SHALL. MATERIAL.

SHALL NOT DECREASE INSULATION THICKNESS FROM WIRET DIMENSIONS (70 SHIELDS/INCH)



SECT C-C FULL SCALE

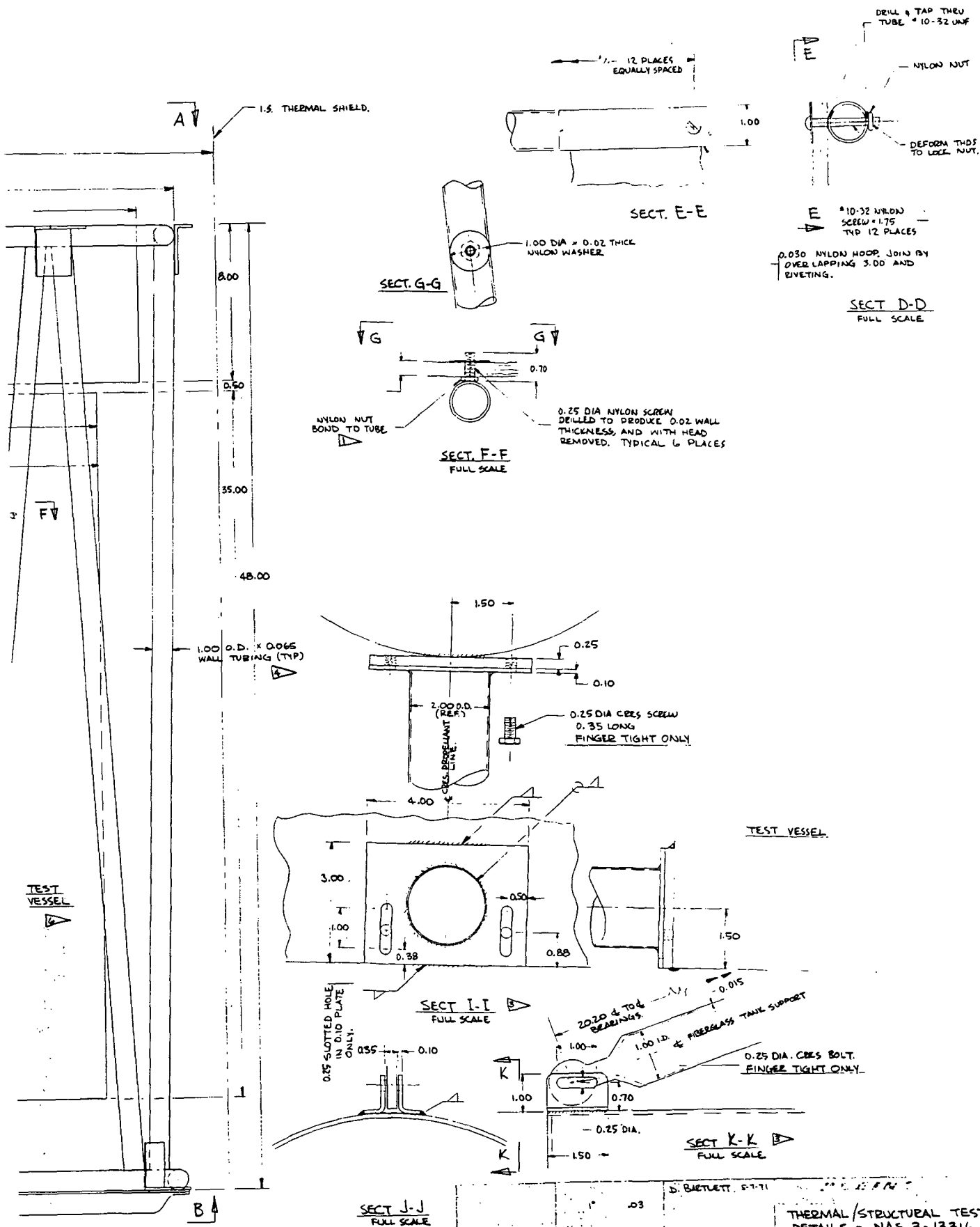
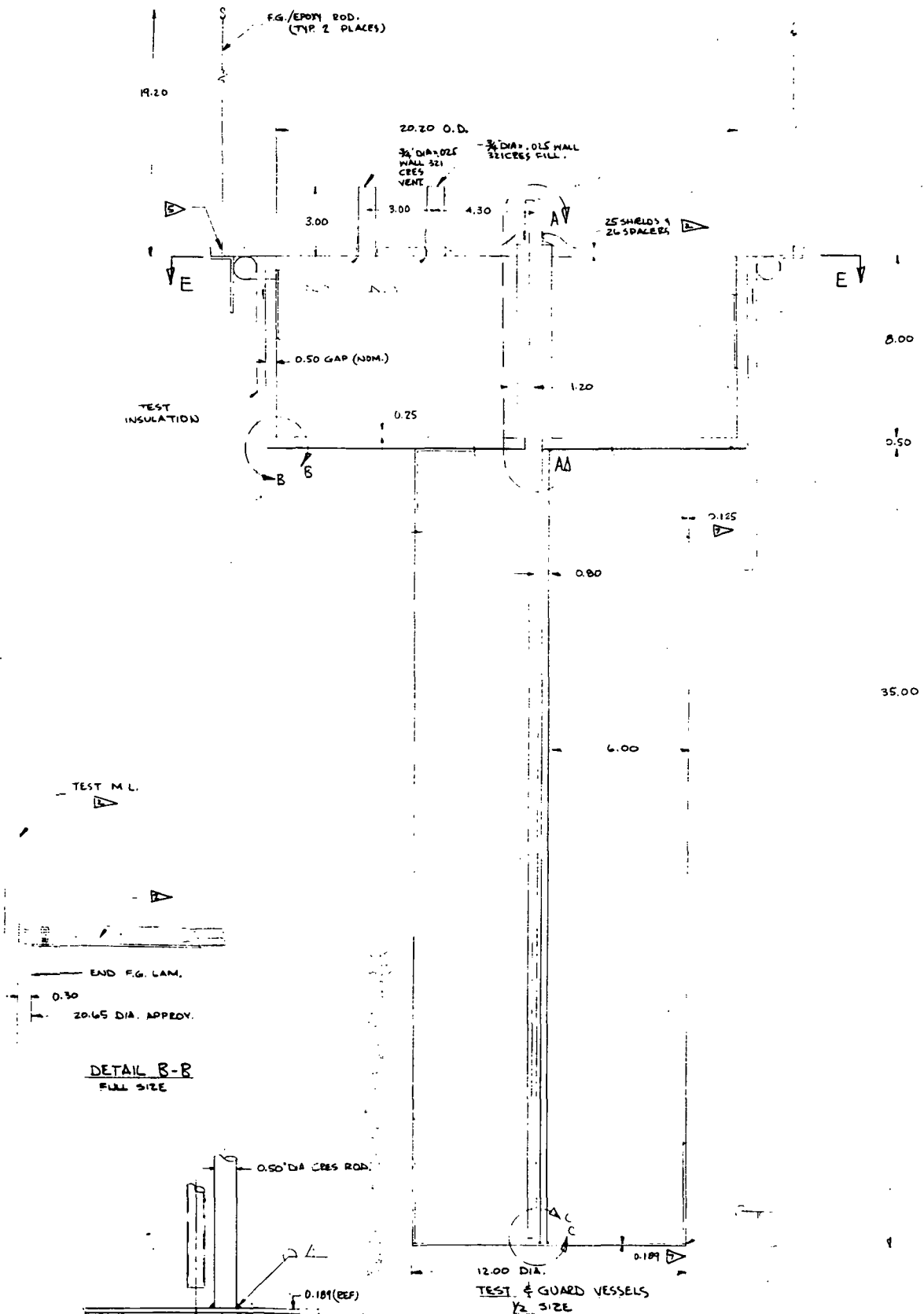


Figure 2.2-6: TEST ARTICLE DETAILS



DETAIL B-B  
FULL SIZE

SECT. C-C  
FULL SIZE

		D. BARTLETT	THE BOEING COMPANY AEROSPACE GROUP
		D. BARTLETT	THERMAL/STRUCTURAL TEST DETAILS - NAS3-13316
			SK11-5771
			REV. 2 3

Figure 2.2-6: TEST ARTICLE DETAILS (Continued)

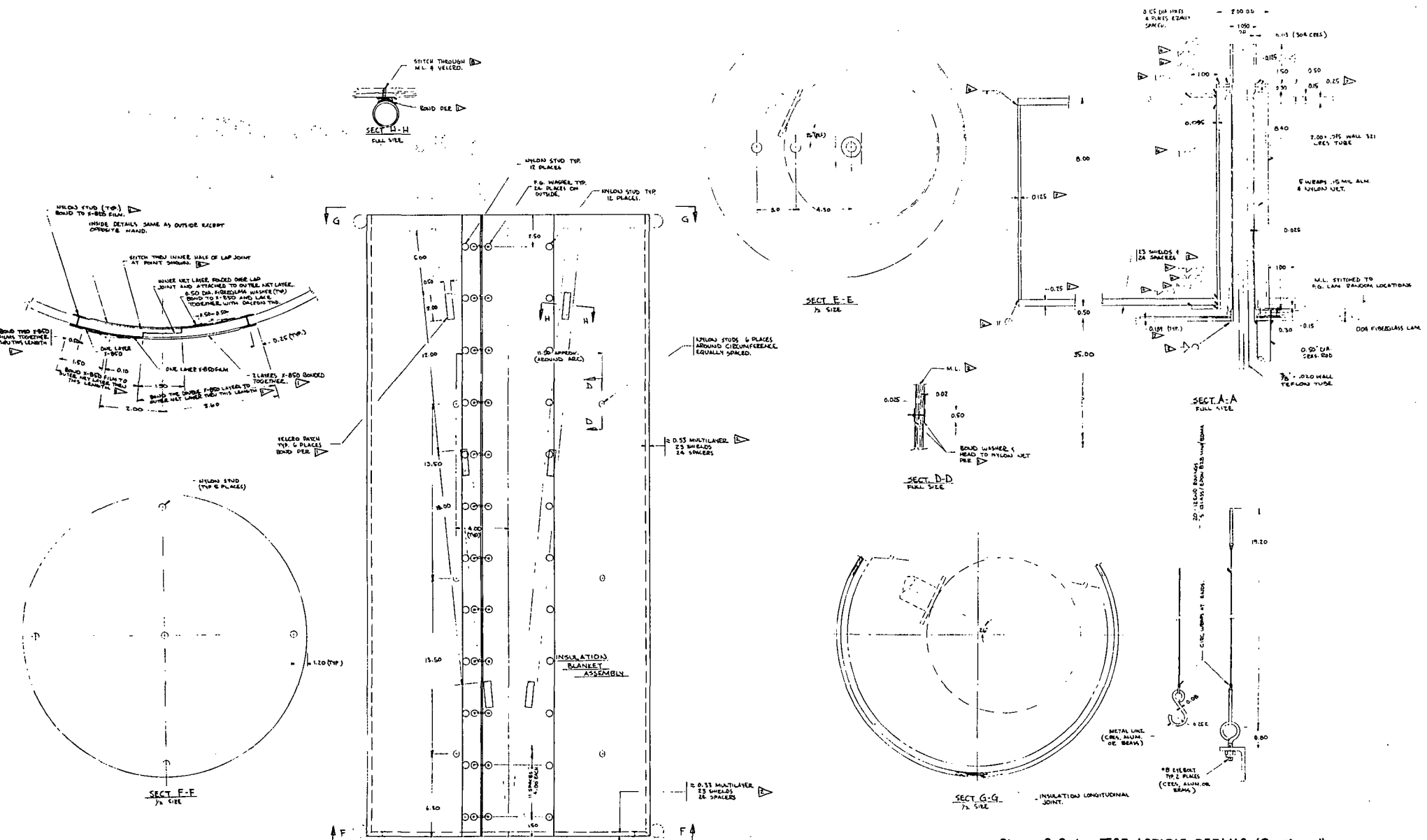
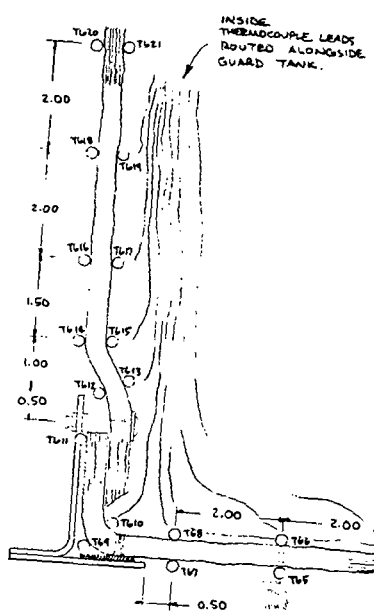
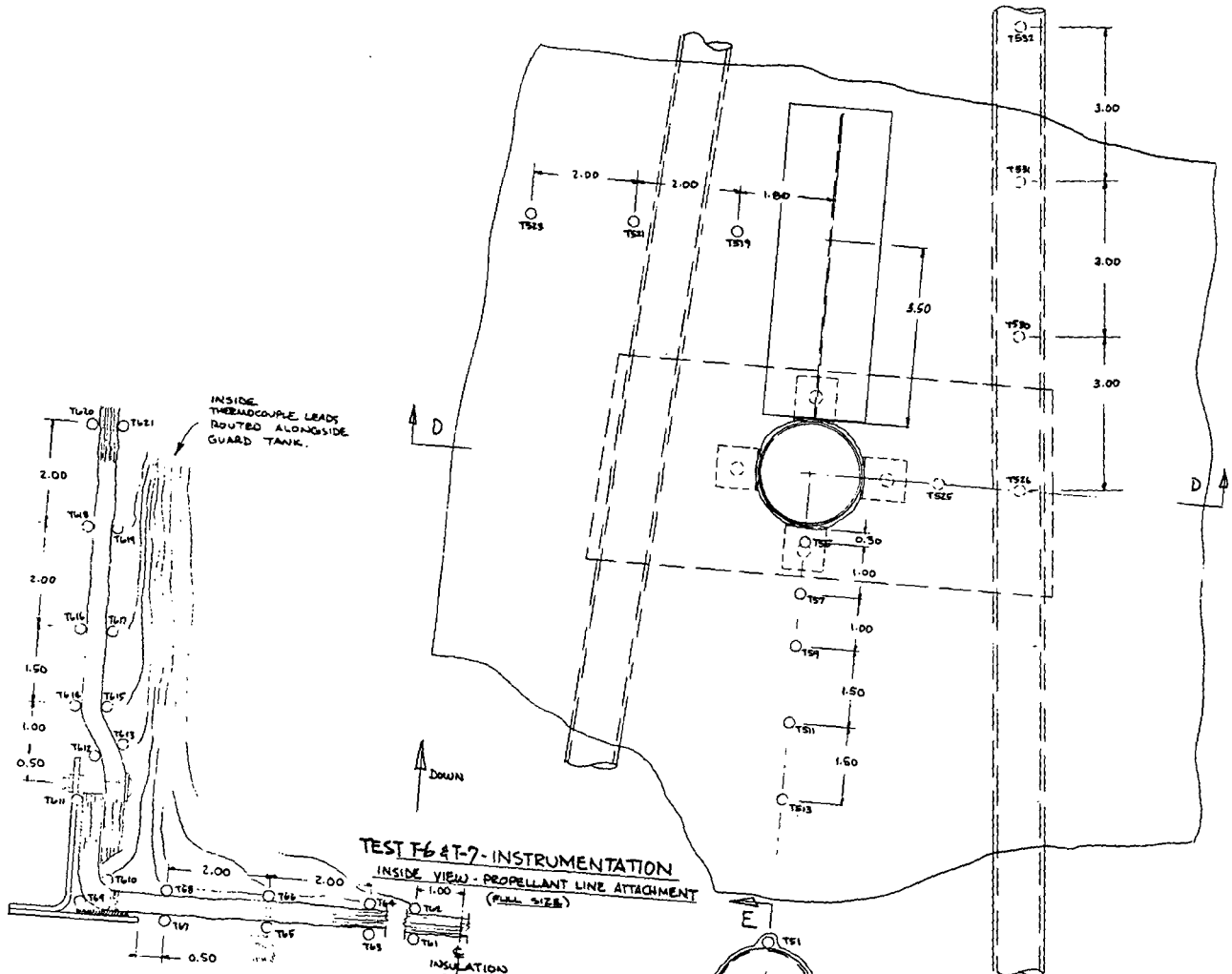
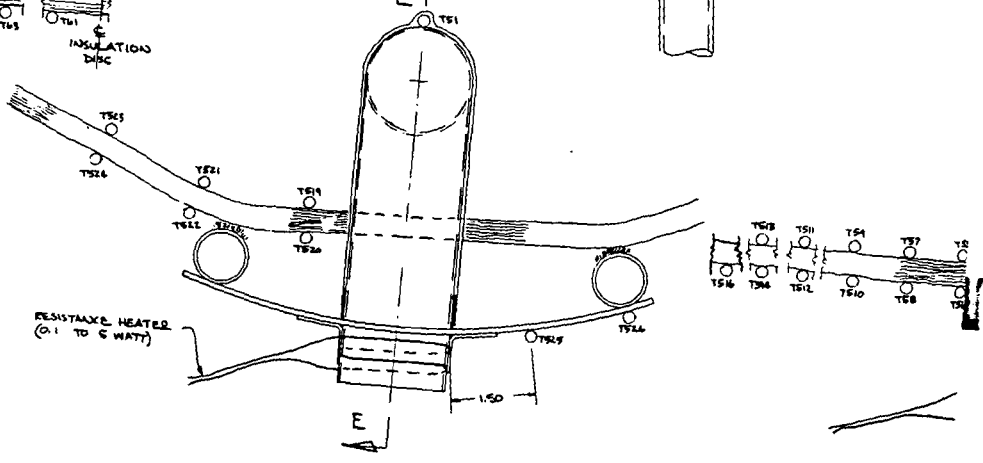


Figure 2.2-6: TEST ARTICLE DETAILS (Continued)

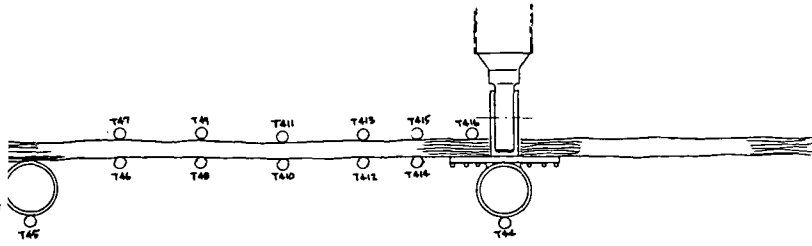


**TEST T-7 INSTRUMENTATION**  
 INSIDE VIEW - PROPELLANT LINE ATTACHMENT  
 (FULL SIZE)  
 INSULATION DISC

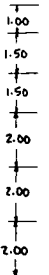
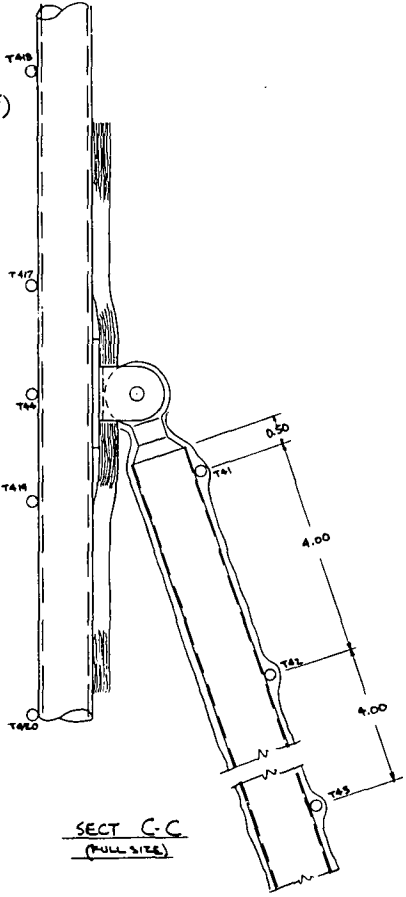
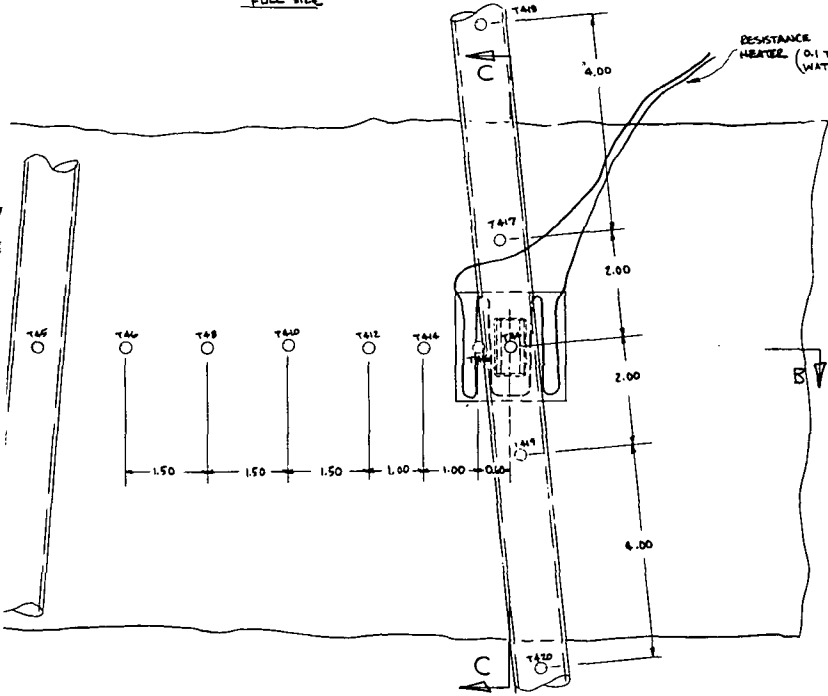
**TEST T-8 INSTRUMENTATION**  
 TOP DECK JOINT SIMULATION TEST  
 (FULL SIZE)



**SECT D-D**

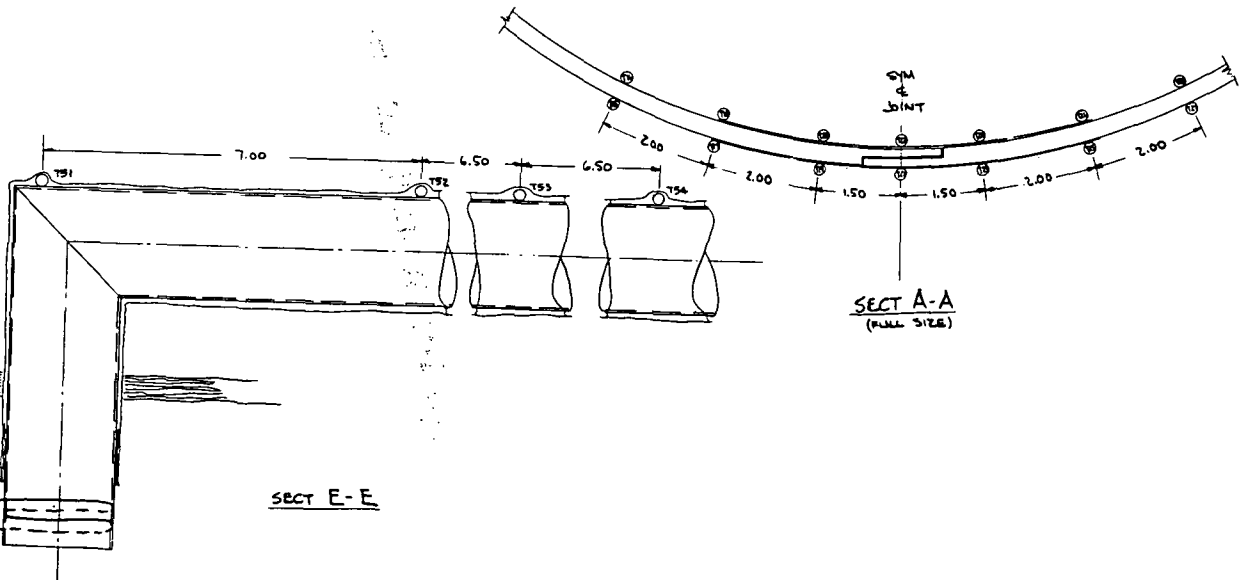


SECT B-B  
FULL SIZE



TEST T-4 & T-5 INSTRUMENTATION  
OUTSIDE VIEW - STUB ATTACHMENT  
(FULL SIZE)

SECT C-C  
(FULL SIZE)



SECT A-A  
(FULL SIZE)

SECT E-E





The conversion factors for heat of vaporization and density for hydrogen were taken from the NBS monograph 94, dated August 1965. The values were 191.67 Btu/lb ( $4.46 \times 10^5$  joule/kilogram) at one atmosphere and  $0.005209 \text{ lb/ft}^3$  ( $0.083 \text{ kg/m}^3$ ) at one atmosphere and  $70^\circ\text{F}$  ( $294^\circ\text{K}$ ). Conversion factors for nitrogen were from NBS technical note 129A, dated February 1963. The values were 85.667 Btu/lb ( $1.99 \times 10^5$  joule/kilogram) and  $0.0724 \text{ lb/ft}^3$  ( $1.16 \text{ kg/m}^3$ ).

Figure 2.2-7 is a photograph showing the interior of the temperature controlled room and the components of the gas measurement system.

Liquid hydrogen was supplied from an 800 gallon ( $3.64 \text{ m}^3$ ) dewar. The transfer line was vacuum jacketed. The fill valve for the guard tank was controlled automatically by liquid level sensors. The test tank fill valve was controlled remotely by the test conductor.

Instrumentation consisted of pressure transducers, copper/constantan thermocouples and carbon resistor liquid level sensors. The pressure transducers were bonded strain gage type calibrated to an overall accuracy of  $\pm 3\%$  of full scale. Thermocouples were calibrated by lot number to achieve an overall accuracy of  $\pm 4\%$  at  $-300^\circ\text{F}$  ( $89^\circ\text{K}$ ). The thermocouple reference junction was in a  $\text{LN}_2$  bath. Carbon resistor level sensors operated a blinker light system on the control panel. These sensors contributed to the sensible heat leak of test tank when in operation. The heat leak was 0.38 Btu/hr (1.3 watt) per sensor when in  $\text{LH}_2$ , and 0.44 Btu/hr (1.5 watt) per sensor when in  $\text{LN}_2$ . A technique was developed wherein only one sensor was operated during a data run.

Wet test meters were modified to provide a 10 count output for each revolution of the rotor. This function was performed remotely with signals being fed to the data collection system.

Data signals were fed through signal conditioning equipment to a Beckman 210 data acquisition system. Raw counts were then tabulated and punched on a paper tape by a typewriter located at the test area. When the test run was completed the paper tape was fed into a PDP-8 computer for data reduction. Test control pressures, liquid level sensors and proportional valve positions were monitored by visual readout on the control panel. A continuous log of all events was maintained for each test.

### Test Article

The test article, shown in Figures 2.2-8, 2.2-9 and 2.2-10, was an aluminum tubing framework consisting of two hoops connected by diagonal bracing. The dimensions were 2 ft (0.6 m) diameter by 4 ft (1.2 m) high. The MLI was attached to the interior with patches of Velcro tape. On the open end (top) the MLI was secured to the frame with thirteen nylon screws. A  $1/16 \times 1.00$  in ( $0.16 \times 2.54$  cm) teflon band was used as an aid in holding the MLI against the hoop. The cylindrical MLI blanket was one piece with a longitudinal shi lap

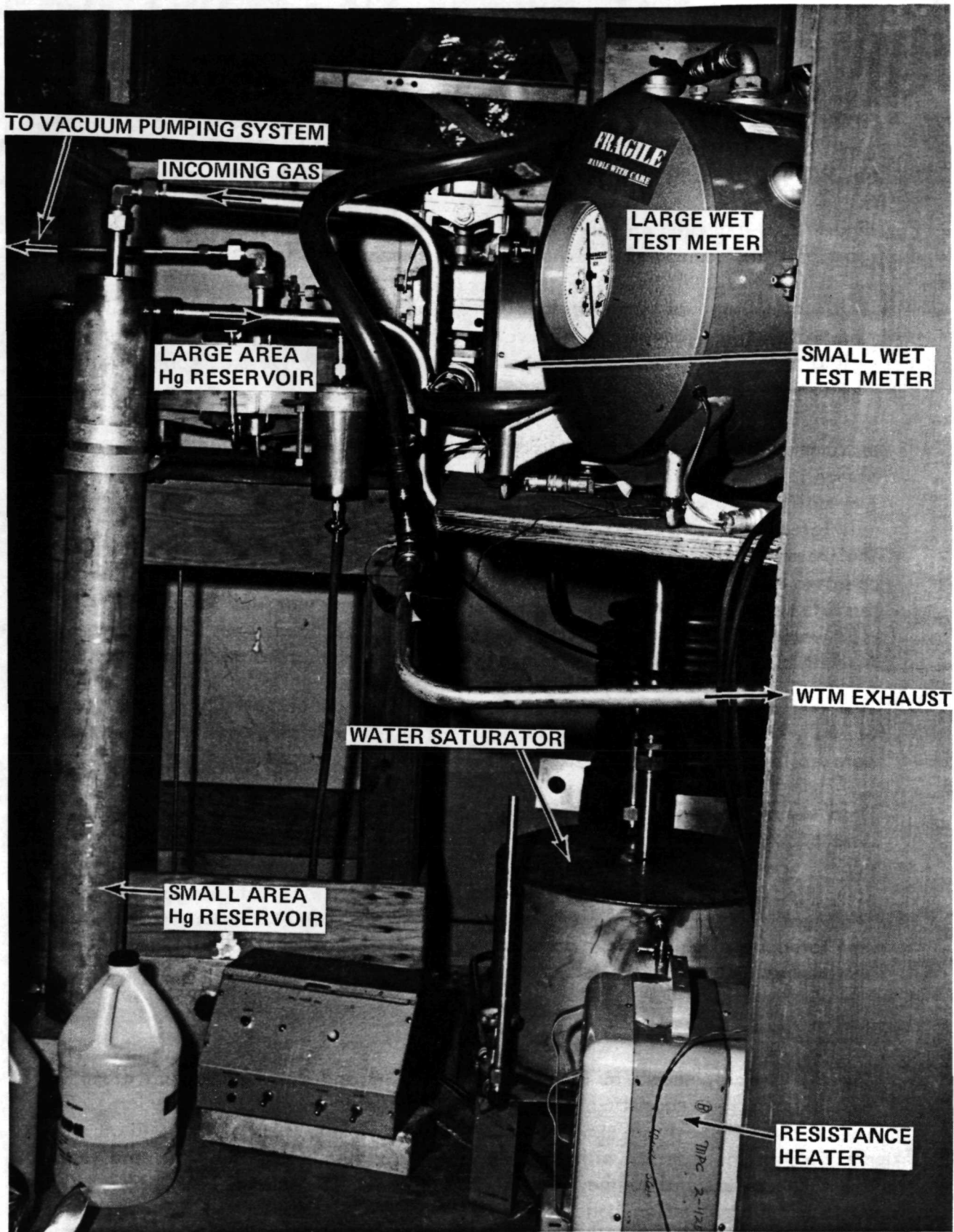


Figure 2.2-7: GAS MEASUREMENT SYSTEM COMPONENTS

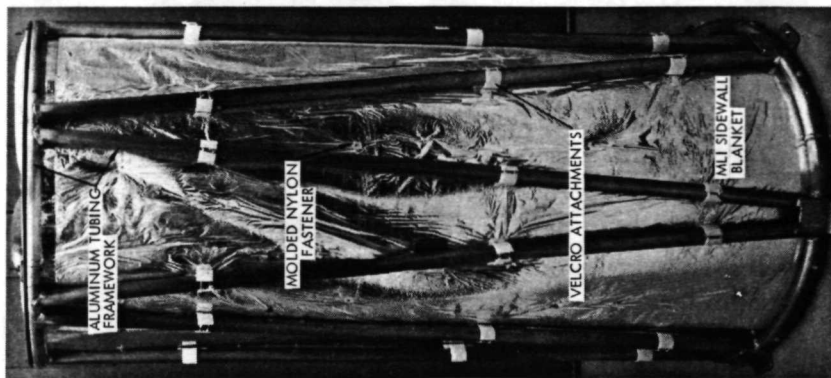


Figure 2.2-8: TEST ARTICLE

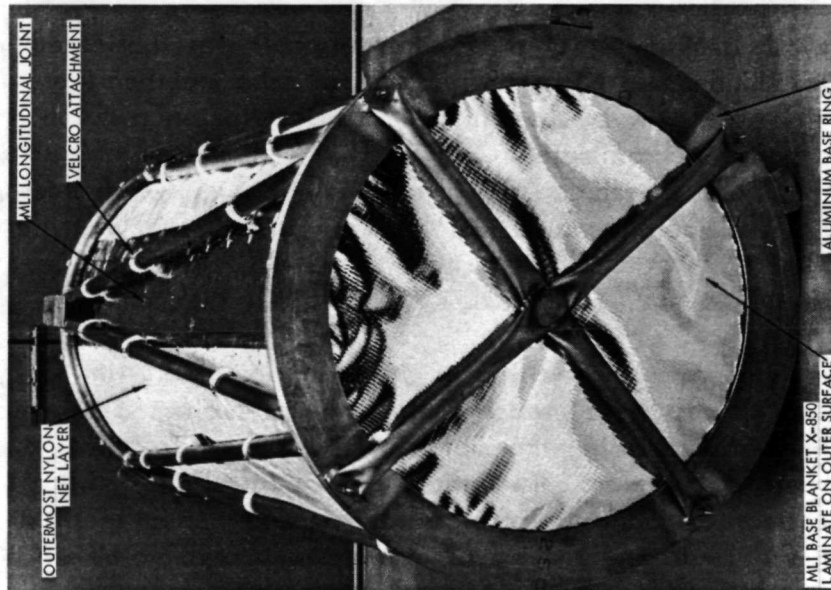


Figure 2.2-9: TEST ARTICLE

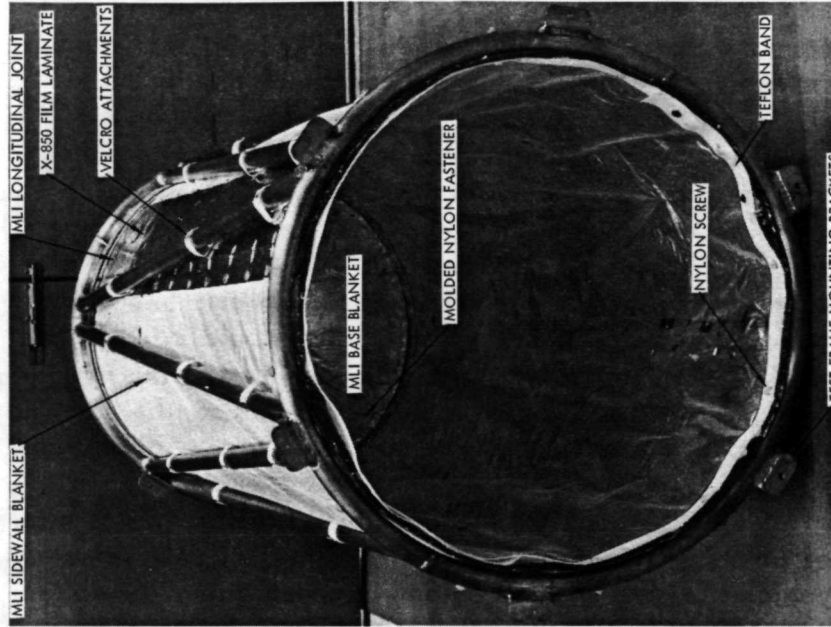


Figure 2.2-10: TEST ARTICLE

splice joint similar to those of the final design. The joint was reinforced with X-850 film laminate as evidenced in the photograph of Figure 2.2-10. The base blanket, visible in Figure 2.2-8, was reinforced on the outside with X-850 laminate as described in the final designs. This blanket was attached to an aluminum ring with Velcro tape. A carefully fitted 45° bevel joint was employed at the junction of the base and sidewall blankets. This joint was made by a cut and try process. It was found that the best bevel resulted when a rotary sanding disc was used while supporting the blanket between two beveled aluminum plates. This technique produced a better bevel than could be obtained by hand cutting the layers, however, there was a slightly scalloped edge on the mylar due to the netting. The base blanket and ring were indexed to the sidewall so that the fit could be reproduced subsequent to removal for test modifications.

The MLI consisted of 23 - 15 gage double aluminized mylar shields alternated with 24 nylon net layers. This was the same thickness of MLI selected for the final design of Vehicle 1-14. Molded nylon fasteners which controlled the blanket thicknesses, visible in Figure 2.2-8, were used in the same proportion as the Vehicle 1-14 design.

A fiberglass/epoxy thermal model of a LH<sub>2</sub> tank support was fabricated. The part had bonded aluminum end fittings with integral spherical bearings. Aluminized mylar radiation shields were suspended in the interior on a nylon thread. The shields were spaced approximately 2.00 in (5.1 cm) apart. The shields were bonded to the thread and the thread/shield assembly in turn was bonded to each aluminum fitting. The fiberglass tube was 1.00 in (2.54 cm) in diameter with an 0.015 in (0.038 cm) thick wall. The part was 20.2 in (51.4 cm) between bearing centerlines.

MLI was spiral wrapped over the outside of the strut and tied with dacron thread. Five shields and six spacers were used. Extra material projected beyond the warm end attachment to permit covering the metallic fitting after installation. Thermocouples were bonded to the tube before the MLI was installed. The MLI blanket modifications necessary to add the fiberglass support and simulated fluid line were confined to localized areas where hand fitting was employed to obtain an efficient joint.

A stainless steel tube was constructed to represent a fluid line. The tube was 2.00 in (5.1 cm) in diameter with an 0.035 in (0.09 cm) wall. The MLI penetration at the warm end was modeled to represent the final design configuration. It was found necessary to cut the MLI from the edge of the blanket inward to the line penetration during mockup fabrication. A similar cut was made in the test article blanket. The cut was covered on the inside and outside with X-850 patches which were stitched in place through the MLI. The patch can be seen in Figure 2.2-11. This is a view from the outside of the test article at the fluid line penetration location.

The tube was insulated with 5 shield and 6 spacer layers, tied in place with dacron thread. Figure 2.2-12 shows an interior view with the fluid line and fiberglass strut installed. The photograph was taken looking upwards from the bottom before the base blanket was replaced. The test tank is to the left. The beveled edge of the sidewall MLI is immediately adjacent to the aluminum tubing hoop. The longitudinal splice joint is also visible as was the MLI blanket at the top which separated the guard and test tanks.

The eighth test defined in Figure 2.2-1 incorporated a new base blanket which was mounted on a fiberglass ring. The ring represented the MLI mounting ring at the top of Vehicles 1-14 and 2-18. The test joint configuration was modeled after the lap joints of those vehicles. Installation of the base blanket required that the sidewall blanket be tucked inside the lap joint and hollow nylon screws inserted through holes in the MLI and fiberglass ring. The holes were made in the MLI with a hand punch. A hand drill was used for making the matching holes in the fiberglass ring. These fasteners represented the nylon studs used to hold sidewall blankets in place in the vehicle final designs. The fasteners were spaced the same as the final design configuration.

Figure 2.2-13 is a view into the inside of the base blanket. The fiberglass ring formed the boundary of the blanket. The upturned leg of the lap joint can be seen in the photograph. The wires are thermocouple leads.

Figure 2.2-14 is a view of the outside of the base blanket. The matching external thermocouples are evident. The lap joint configuration represented the intersection of top deck and sidewall MLI blankets on Vehicles 1-14 and 2-18. For the thermal tests this joint was located below the test tank with the flange of the overlap facing upwards along the vertical sidewall blanket. The base portion of the thermal shroud acted as the payload heat source in this test.

Figure 2.2-15 is an external view at the base of the test article. The fiberglass ring is visible inside the aluminum tubing. The sidewall MLI blanket has been tucked inside the base blanket lap joint and the hollow fasteners have been installed. The Velcro patches which attached the sidewall blanket to the tubing had "ears" which were used to pull the mating pieces together and then were tied together around the tube.

Approximately thirty channels of instrumentation were available. A portion of these were used for monitoring test functions such as the temperature of the thermal shroud, the guard tank temperature and pressure, and the temperature at the test tank outlet. Because of this limitation it was impossible to retain all of the thermocouples as the test series progressed. Instead only those areas of particular interest were instrumented and the data from other locations in earlier tests was utilized.

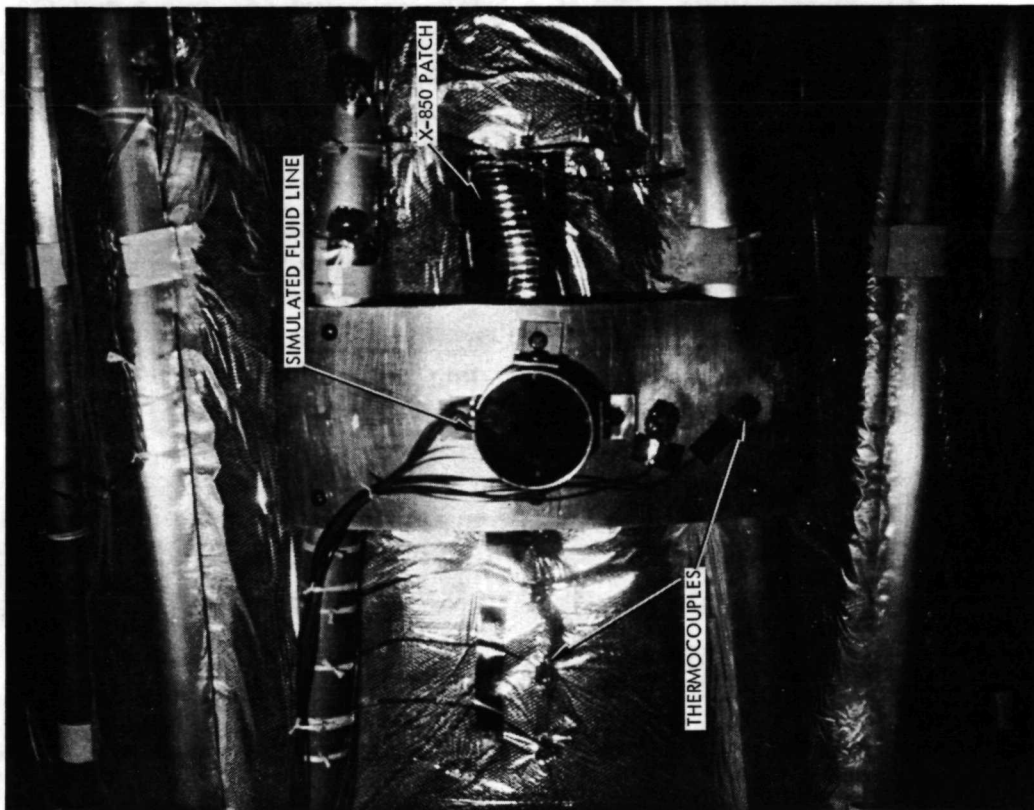


Figure 2.2-11: TEST ARTICLE - FLUID LINE PENETRATION

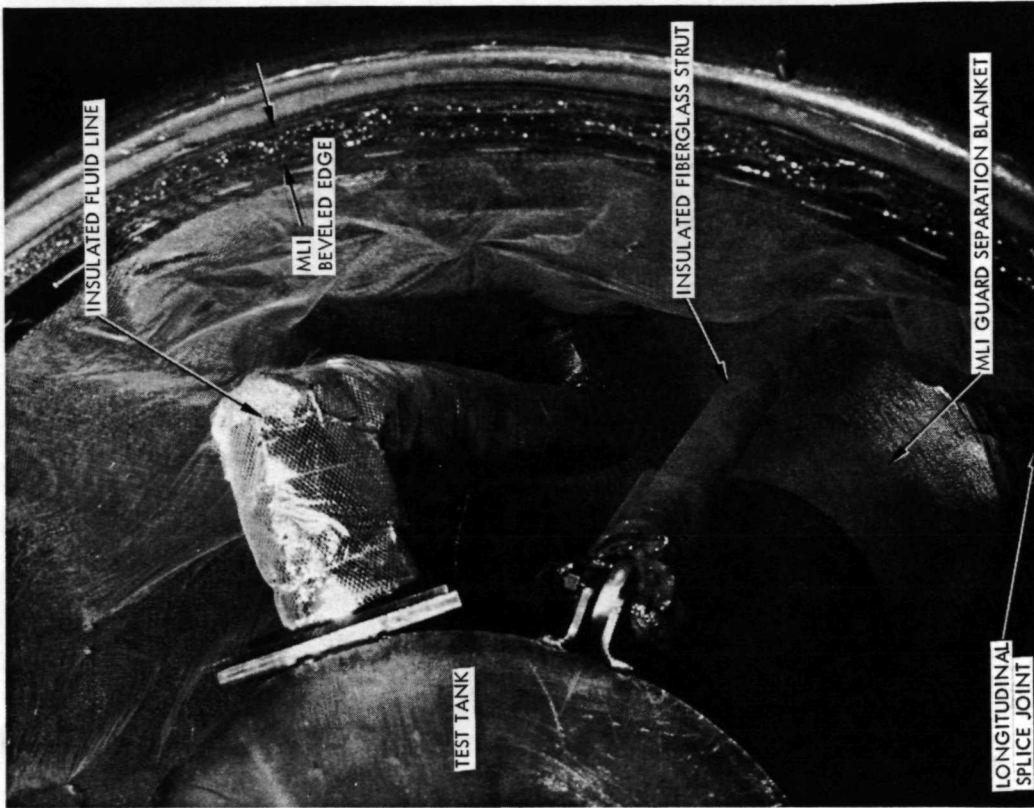


Figure 2.2-12: TEST ARTICLE - FLUID LINE AND SUPPORT STRUT

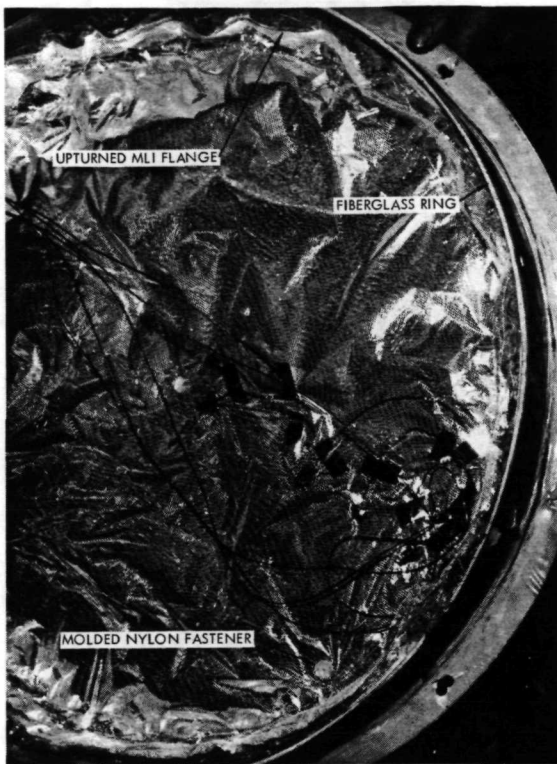


Figure 2.2-13: TEST ARTICLE BASE PLATE

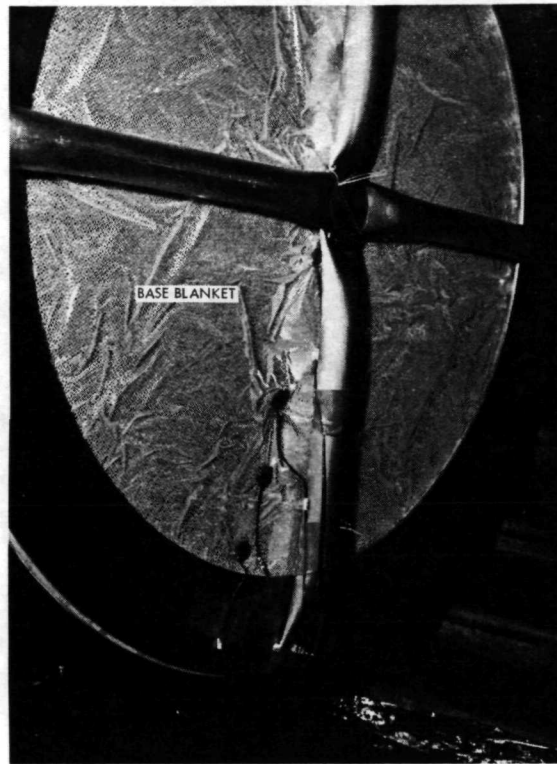


Figure 2.2-14 TEST ARTICLE BASE PLATE

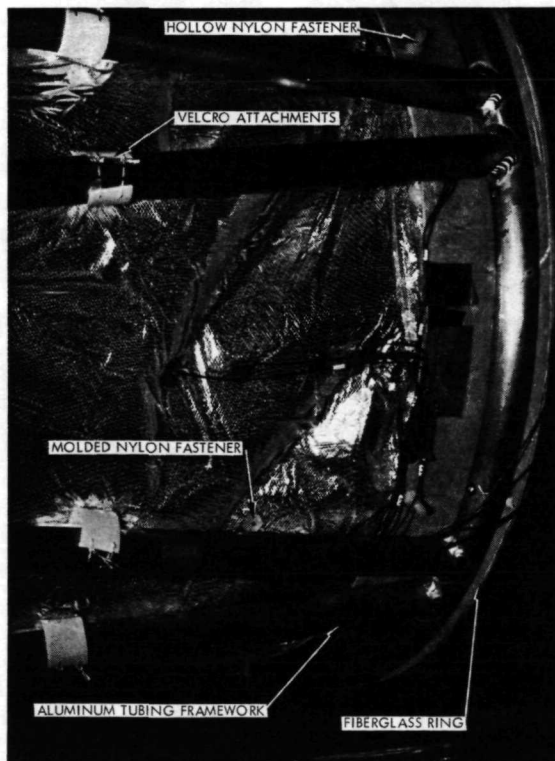


Figure 2.2-15: TEST ARTICLE BASE PLATE INSTALLATION

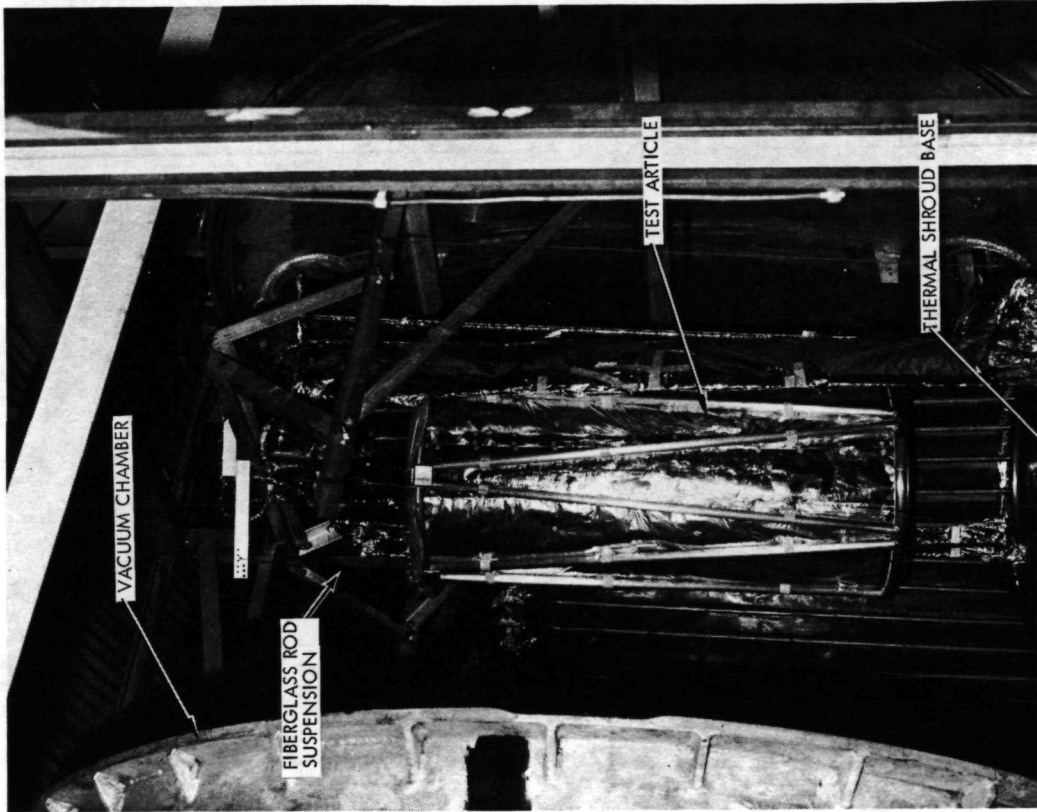


Figure 2.2-17: THERMAL TEST SYSTEM ASSEMBLY



Figure 2.2-16: THERMAL TEST SYSTEM COMPONENTS

The major elements of the test system are shown in Figures 2.2-16 and 2.2-17. Figure 2.2-16 shows the system disassembled. The test article was sitting on the floor. The thermal shroud had been opened and the right half moved away so that the guard and test tanks were visible. The thermal shroud base had been lowered to the floor so that the test article could be installed. Figure 2.2-17 shows the test article in place over the guard tank. Fiberglass suspension rods were used to hang the test article from overhead brackets. The thermal shroud base had been moved into position, prior to closing the shroud halves. The main portion of the vacuum chamber is on the left in the photograph.

### 2.2.3 Test Results and Analysis

The discussion of test results follows the test plan schematic of Figure 2.2-1. Boiloff testing consisted of a succession of test tank fills. Between fills the contents were allowed to boil down to a particular level sensor, usually LL3 or LL4 shown in Figure 2.2-6. The guard and thermal shroud were maintained at their respective temperatures continuously during the entire test. Thermal stabilization was determined by evaluating thermocouple and boiloff data. When the thermocouples on the exterior of the MLI followed the shroud temperature they were considered stabilized. When internal temperatures and boiloff rates were constant for 2 or 3 successive fills stabilization was assumed and one final fill and data run were made.

The objective of correlating the experimental measurements from Task II with corresponding analytical predictions was to provide verification of, or when indicated, empirical corrections to, the final design thermal performance evaluations.

The experimental-analytical correlations were carried out in terms of heat flow through the insulation assembly and in terms of temperatures on the inner and outer surfaces of the insulation blankets. The heat flow correlations in some cases permitted identification of heat flow due to specific test model features such as penetrations, and thus had direct implications to final design thermal performance. Temperature correlations, on the other hand, had no direct implication to vehicle performance but served to indicate the validity of material properties, analytical models, and other assumptions employed in design evaluations.

The analytical predictions of temperatures and heat flow were computed with the aid of a two- or three-dimensional digital program, the Boeing Engineering Thermal Analyzer, BETA program. The program performed a numerical solution of the thermal diffusion equations, accounting for solid conduction, effective conduction through multilayer insulation (combined solid conduction and radiation), and radiation interchanges across spaces. Variation in material thermal properties with temperature were included.

Diagrams of the analytical models, showing temperature nodes and networks of conductances, are included in Appendix E of Volume II, NASA CR-121104,

along with presentation of detailed predicted temperature data for each test. This Appendix also contains the bulk of measured temperature data obtained in the test program. The analytical models included all necessary boundary conditions, i.e., the appropriate temperatures, emittances, and radiation view factors associated with the thermal shroud, test vessel, guard tank, and other details.

The following general assumptions were employed in the analyses of all of the tests:

- (1) Steady state heat flow existed.
- (2) Tank-insulation assembly-shroud geometry adequately represented by a concentric model.
- (3) Heat flow resulting from gas conduction, convection, or diffusion was negligible.
- (4) Thermal shroud was isothermal (Test 8: shroud sides and bottom temperatures uniform at their respective values.)
- (5) Cryogenic (test) tank was isothermal.
- (6) Multilayer insulation thicknesses and layer density were uniform at the design values.
- (7) Localized heat leaks, i.e., those due to strut penetration, plumbing line penetration, fasteners, and the longitudinal joint in the insulation, were mutually independent.

Additional assumptions related to the configuration and conditions of the particular tests were employed and will be described along with the discussions of the correlation results.

Material and configuration properties used in the thermal analyses are given in Table 2.2-1. The expressions for normal and lateral effective conductivity of the multilayer insulation employ the form shown in Table 1.1-9, with coefficients adjusted for best agreement with emittance and cylindrical tank test data derived in this program. The "T" joint conductance expression, employed at the joint between the side wall and the upper cover (top of the guard) and at the joint between the sidewall and the insulation separating the guard and test vessels, was based on the  $K_L$  expression, again employing empirically adjusted coefficients. Other joint conductance or contact resistance values, such as between the main insulation blanket and the plumbing line insulation, were developed for each particular application and are described in the discussions of the individual test correlations. In every case where adjustments were employed in the properties listed in Table 2.2-1 to improve agreement between analytical and experimental

Table 2.2-1:  
PROPERTIES USED IN THERMAL ANALYSES

Multilayer Insulation

(1) Effective Normal Conductivity,  $K_n$ :

$$K_{n,1,2} = \frac{\left[ 4.30 \times 10^{-14} (T_1^2 + T_2^2) + 2.56 \times 10^{-8} \right] [T_1 + T_2]}{\left[ 4.34 \times 10^{-13} (T_1^2 + T_2^2) + 7.97 \times 10^{-8} \right] [T_1 + T_2]} \begin{matrix} \frac{\text{BTU-ft}}{\text{ft}^2\text{-hr-}^\circ\text{R}} \\ \text{W/m-}^\circ\text{K} \end{matrix}$$

(2) Effective Lateral Conductivity,  $K_l$ :

$$K_{l,1,2} = \frac{\left[ 0.750 \times 10^{-10} (T_1^2 + T_2^2) + 16.80 \times 10^{-6} \right] [T_1 + T_2]}{\left[ 7.56 \times 10^{-10} (T_1^2 + T_2^2) + 5.23 \times 10^{-5} \right] [T_1 + T_2]} \begin{matrix} \frac{\text{BTU-ft}}{\text{ft}^2\text{-hr-}^\circ\text{R}} \\ \text{W/m-}^\circ\text{K} \end{matrix}$$

(3) Effective "T" Joint Conductance,  $K_t$ :

$$K_{t,1,2} = \frac{\left[ 1.45 \times 10^{-9} (T_1^2 + T_2^2) + 3.26 \times 10^{-4} \right] [T_1 + T_2]}{\left[ 4.80 \times 10^{-8} (T_1^2 + T_2^2) + 3.33 \times 10^{-3} \right] [T_1 + T_2]} \begin{matrix} \frac{\text{BTU}}{\text{ft}^2\text{-hr-}^\circ\text{R}} \\ \text{W/m-}^\circ\text{K} \end{matrix}$$

(4) Surface Emittance,  $\epsilon$  (Single nylon net outer layer):

$$\epsilon = \begin{matrix} 2.87 \times 10^{-3} T^{0.667} & T \text{ in } ^\circ\text{R} \\ 4.25 \times 10^{-3} T^{0.667} & T \text{ in } ^\circ\text{K} \end{matrix}$$

(5) Longitudinal Joint Butt Interface Clearance,  $B$ :

$$B = 0.050 \text{ in } (.127 \text{ cm})$$

X-850 Film Laminate

(1) Effective Lateral Conductivity,  $K_{X-850}$ :

Table 2.2-1:, (Continued)

PROPERTIES USED IN THERMAL ANALYSES

<u>T</u>	<u>K<sub>X-850</sub></u>
0	0
600°R (333°K)	$6.0 \times 10^{-5} \frac{\text{BTU-ft}}{\text{ft}^2\text{-hr-}^\circ\text{R}} \left( 1.04 \times 10^{-4} \frac{\text{W}}{\text{m-}^\circ\text{K}} \right)$

(2) Outer Surface Emittance:

$$\epsilon_{X-850} = 1.294 \times 10^{-3} T^{0.667} \quad T \text{ in } ^\circ\text{R}$$

$$1.915 \times 10^{-3} T^{0.667} \quad T \text{ in } ^\circ\text{K}$$

Nylon Fastener

(1) Conductivity, K<sub>f</sub> (isotropic):

<u>T</u>		<u>K<sub>f</sub></u>	
40°R (22°K)		.058	$\frac{\text{BTU-ft}}{\text{ft}^2\text{-hr-}^\circ\text{R}} \quad (.100 \text{ W m}^{-1} \text{ }^\circ\text{K}^{-1})$
70°R (39°K)		.092	$(.159 \text{ W m}^{-1} \text{ }^\circ\text{K}^{-1})$
140°R (78°K)		.115	$(.199 \text{ W m}^{-1} \text{ }^\circ\text{K}^{-1})$
270°R (150°K)		.133	$(.230 \text{ W m}^{-1} \text{ }^\circ\text{K}^{-1})$
540°R (300°K)		.142	$(.246 \text{ W m}^{-1} \text{ }^\circ\text{K}^{-1})$

(2) Emittance, ε<sub>f</sub>:

$$\epsilon_f = 0.4$$

(3) Fastener - Multilayer Interface Resistance = 0

Aluminum Components

(1) Conductivity, K<sub>A</sub>:

$$K_A = 41.7 + .1137 T - .48 \times 10^{-4} T^2 \quad \text{BTU-ft/ft}^2\text{-hr-}^\circ\text{R}$$

Table 2.2-1:, (Continued)  
 PROPERTIES USED IN THERMAL ANALYSES

$$72.1 + .354 T - .269 \times 10^{-3} T^2 \quad \text{W/m-}^\circ\text{K}$$

(2) Emittance,  $\epsilon_A$ :

$$\epsilon_A = 0.20$$

(3) Effective Average Radiation Blockage Area of Insulation Support Truss Structure, A:

$$A = 17.5\% \text{ of insulation side wall area}$$

Fiberglass-Epoxy Components:

(1) Emittance,  $\epsilon_{fg}$ :

$$\epsilon_{fg} = 0.80$$

(2) Conductivity of Strut Material,  $K_s$ :

$$K_s = 0.05 + 6.35 \times 10^{-4} T \quad \frac{\text{BTU-ft}}{\text{ft}^2\text{-hr-}^\circ\text{R}}$$

$$0.086 + 1.98 \times 10^{-3} T \quad \text{W/m-}^\circ\text{K}$$

(3) Conductivity of Insulation Support Ring (Test 8)

$$K_{1,2} = \begin{matrix} .501 \times 10^{-1} + .394 \times 10^{-4} (T_1 + T_2) & \text{BTU-ft/ft}^2\text{-hr-}^\circ\text{R} \\ .867 \times 10^{-1} + .123 \times 10^{-3} (T_1 + T_2) & \text{W/m-}^\circ\text{K} \end{matrix}$$

Stainless Steel (347) Components

(1) Conductivity,  $K_{347}$ :

Table 2.2-1; (Continued)  
 PROPERTIES USED IN THERMAL ANALYSES

<u>T</u>	<u>K</u> <u>347</u>		
36°R (20°K)	1.156	$\frac{\text{BTU-ft}}{\text{ft}^2\text{-hr-}^\circ\text{R}}$	(2.00 Wm <sup>-1</sup> °K <sup>-1</sup> )
72°R (40°K)	2.77		(4.79 W m <sup>-1</sup> °K <sup>-1</sup> )
108°R (60°K)	3.82		(6.61 W m <sup>-1</sup> °K <sup>-1</sup> )
144°R (80°K)	4.62		(7.99 W m <sup>-1</sup> °K <sup>-1</sup> )
180°R (100°K)	5.25		(9.08 W m <sup>-1</sup> °K <sup>-1</sup> )
360°R (200°K)	7.51		(12.99 W m <sup>-1</sup> °K <sup>-1</sup> )
540 (300°K)	8.66		(14.98 W m <sup>-1</sup> °K <sup>-1</sup> )

(2) Emittance,  $\epsilon_{347}$ :

$$\epsilon_{347} = 0.40$$

results, such adjustments were applied consistently for all tests. Thus, the empirical property expressions of the table retain justification for use on other similar designs.

Surface emittance for the aluminized mylar/nylon net insulation and for the aluminized X-850 film laminate used the standard T-667 form with coefficients derived from the emittance tests of this program.

The emittance data was obtained on a Hohlraum cavity and was based on a 28 point integration calculation of emittance for a body at 100°F (311°K). The results are tabulated below:

<u>Material</u>	<u>ε</u>
Nylon net over aluminized mylar	0.195
Nylon net over aluminized mylar	0.196
X-850 film laminate (grid side)	0.088
X-850 film laminate (smooth side)	0.063
15 ga. aluminized mylar	0.050

The emittance of the aluminized mylar was higher than the manufacturer's specification. National Metallizing quoted "no single reading above 0.035 as measured by a Lion Emissometer". The surprising results, however, were those obtained with a nylon net layer over the 15 gage aluminized mylar. The test was run twice to verify the data point. The values obtained were significantly higher than with the radiation shield alone.

Conductivity of the fiberglass-epoxy strut material was taken from Reference 2.2-1. The conductivity of other fiberglass-epoxy components and the emissivity of all such material were taken from unpublished Boeing Company data.

Properties for nylon, aluminum, and stainless steel (Type 347) were taken from published data for those materials.

Predictions of heat flow to the test tank were evaluated at a boundary that followed the inner surface of the main MLI blanket. For general areas of the insulation assembly the basic heat flow was computed by integration of the heat flux radiated or conducted to the test tank across the boundary. To this basic heat flow was added, in accordance with assumption (7) above, the incremental heat leaks arising from penetrations or other details. These incremental heat leaks appeared as additional heat radiated by a warmer than normal area of insulation inner surface plus, in the case of strut and plumbing line penetrations, the heat conducted into the strut or pipe itself, that conducted and radiated laterally into the strut or pipe insulation, and that radiated into the strut or pipe interior.

The experimental data for the correlations were selected by examining all data and records from each test and choosing a time at which true steady state conditions were most nearly approached. For each test both the insulation temperature and heat flow data were read at the particular time selected for that test.

The experimental temperature values were taken directly from the test data printouts. No adjustment, modification, or interpretation of the experimental data, other than the selection of the time for reading, was made.

The experimental values of heat flow to the cryogenic test tank were computed by adding the heat flow required to boil the cryogen at the measured rate and the heat flow required to produce the measured temperature rise in the gas outflow. Comparisons between predicted and measured temperatures are shown in Figures 2.2-18 through 2.2-44. Because of changes in instrumentation from test to test and because of the need to illustrate particular problems encountered in certain tests, a consistent format for graphical data presentation was not followed through the test series. A complete tabulation of predicted temperatures is given in Appendix E.

A summary of predicted and measured heat flow values is given in Table 2.2-2. As the test series progressed it became evident in the comparisons between  $Q_{tot, pred}$  and  $Q_{tot, meas}$  that heat leaks not accounted for in the analytical predictions were accumulating. It was for this reason that for some of the later tests the  $Q_{basic}$  values were taken as the  $Q_{tot, meas}$  from appropriate earlier tests. These empirical  $Q_{basic}$  values are so identified in the table. A more detailed breakdown of the heat flow predictions is given in Appendix E of Volume II, NASA CR-121104.

Test T-1: The test was started at approximately 1100 hours on 12-20-71. Data was recorded from that time, however, stabilization did not appear to begin until about 7 hours later. The data plots presented for this test start with "zero" being 1800 hours on 12-20-71.

The boiloff test results are shown in Figure 2.2-45. The interruption of data at 36, 78, and 114 ks was caused by test tank fills. During these fills the wet test meter and back pressure system were valved off allowing tank pressure to return to ambient conditions and upsetting the thermal equilibrium of tank, contents and MLI. Stabilization was obtained about 102 ks into the test and one final fill was made at 114 ks. The gradual decrease in boil-off rate towards the end of the test was attributed to reduced wetted surface area. The heat flow rate as determined by gas flow measurement was 7.6 Btu/hr (2.2 watt). This was the rate when the liquid level was at level sensor 3.

Figure 2.2-46 is an example of the test data printout. Data prints were made each hour. The figure represents a time of 194.4 ks on Figure 2.2-45. The heating rate of one liquid level sensor was subtracted from the measured heat flow rate to obtain the value plotted on the curve of Figure 2.2-45.



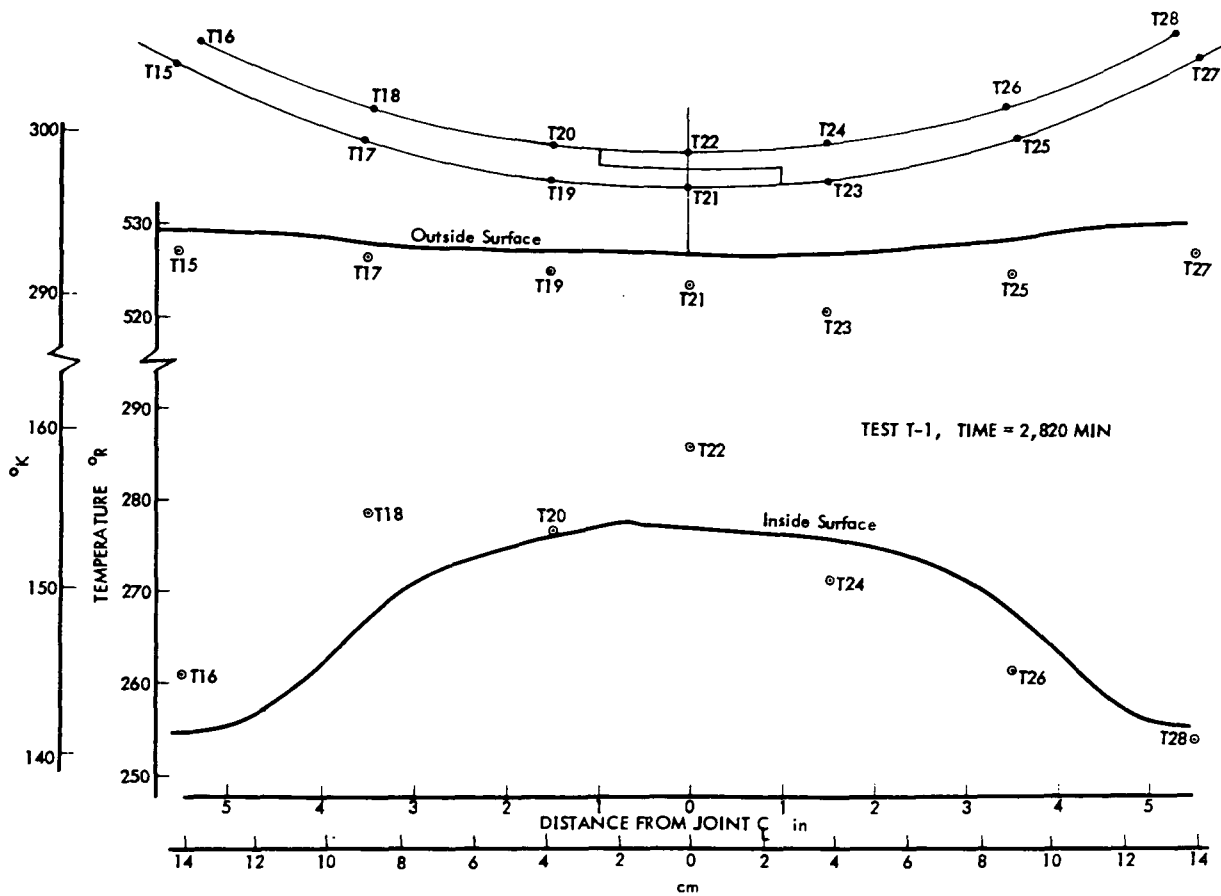


Figure 2.2-20: EXPERIMENTAL AND ANALYTICAL TEMPERATURES LONGITUDINAL JOINT AREA

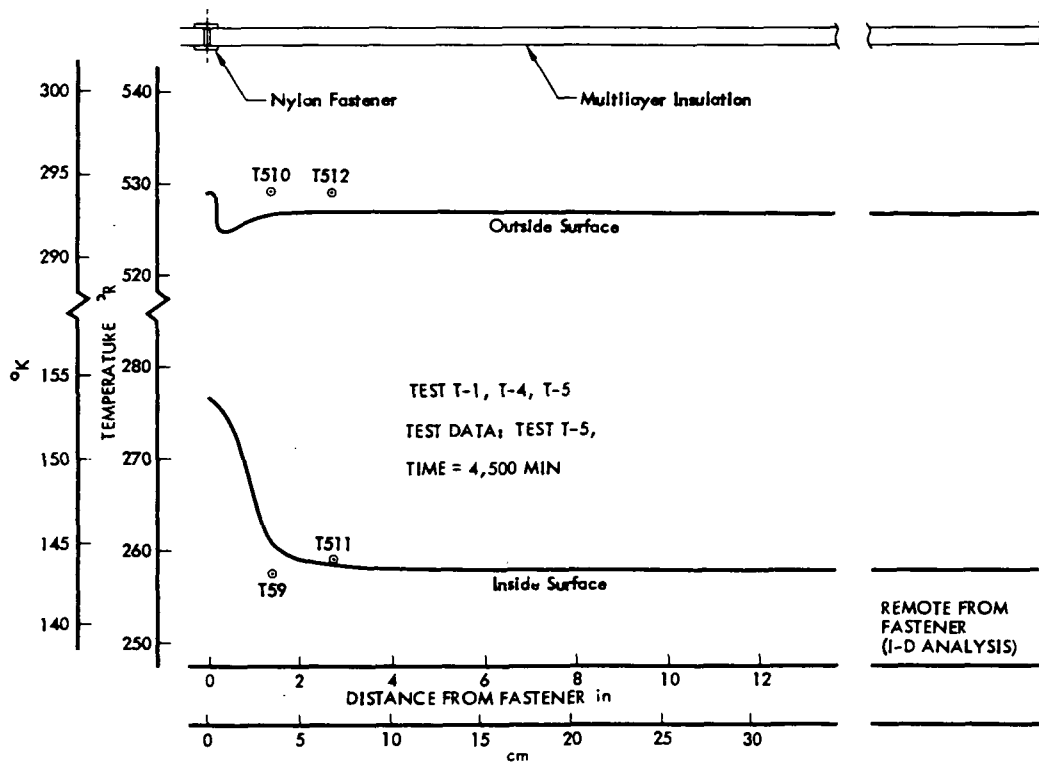


Figure 2.2-21: EXPERIMENTAL AND ANALYTICAL TEMPERATURES TYPICAL FASTENER AREA



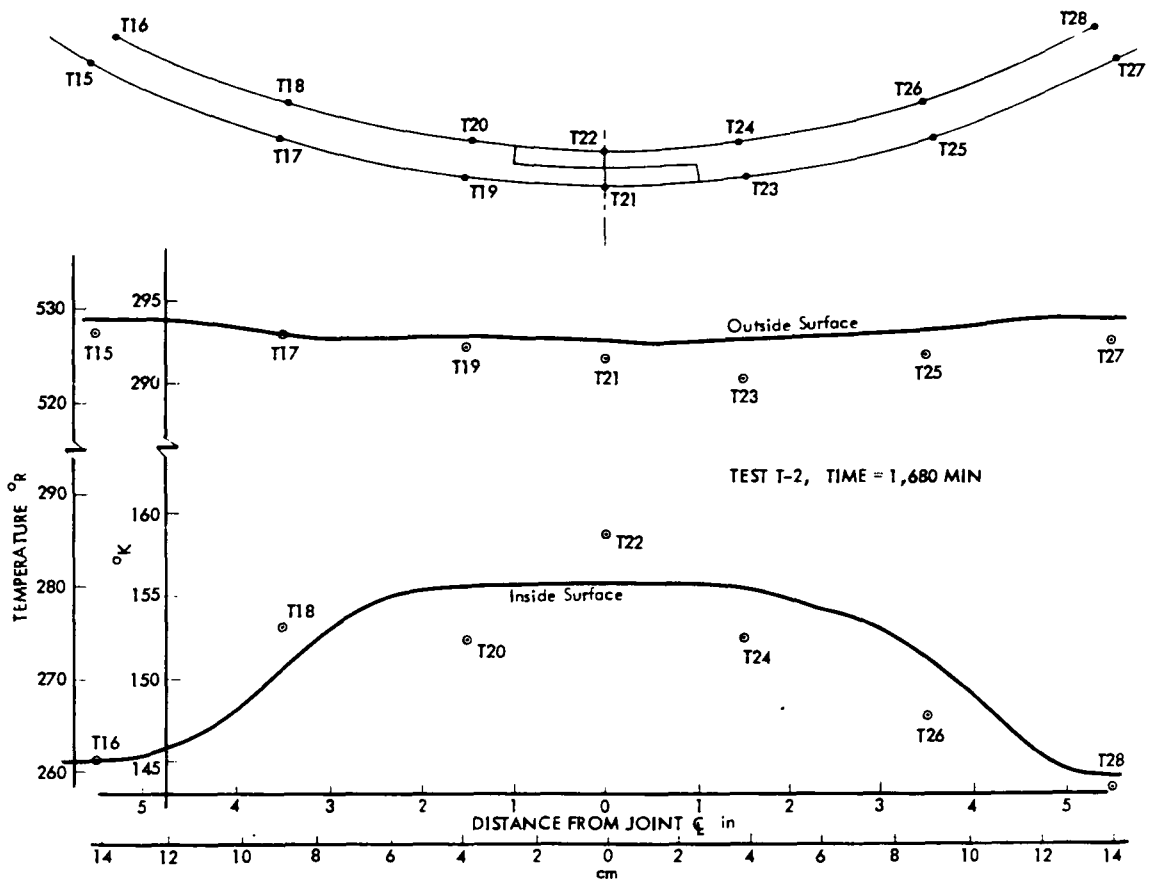


Figure 2.2-24: EXPERIMENTAL AND ANALYTICAL TEMPERATURES LONGITUDINAL JOINT AREA

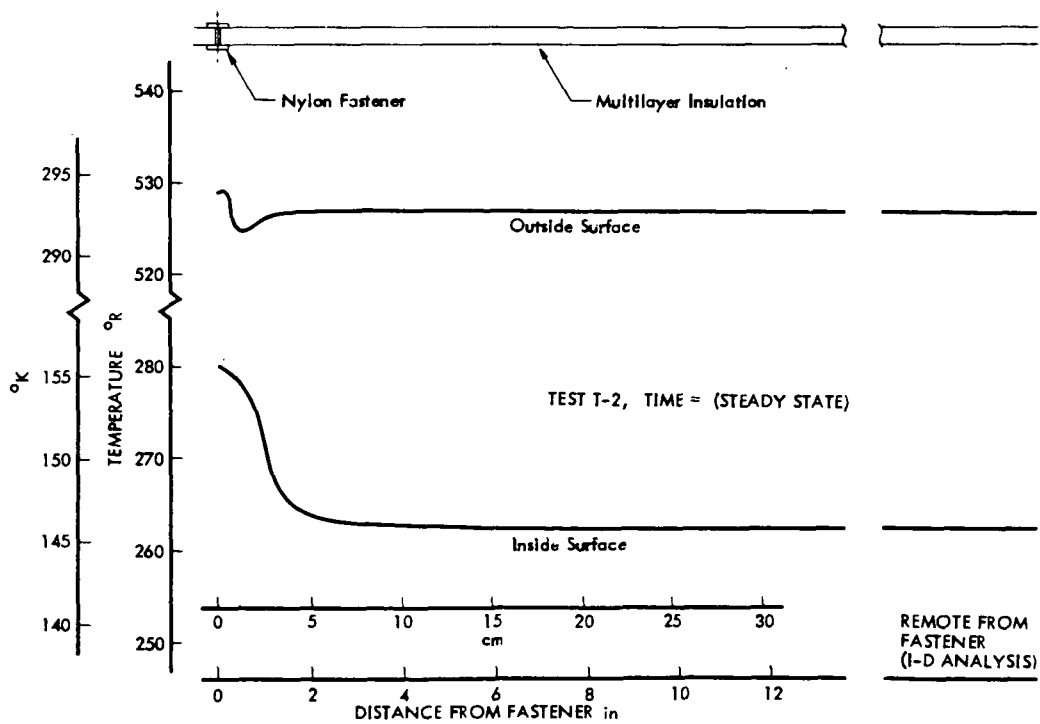


Figure 2.2-25: ANALYTICAL TEMPERATURES TYPICAL FASTENER AREA

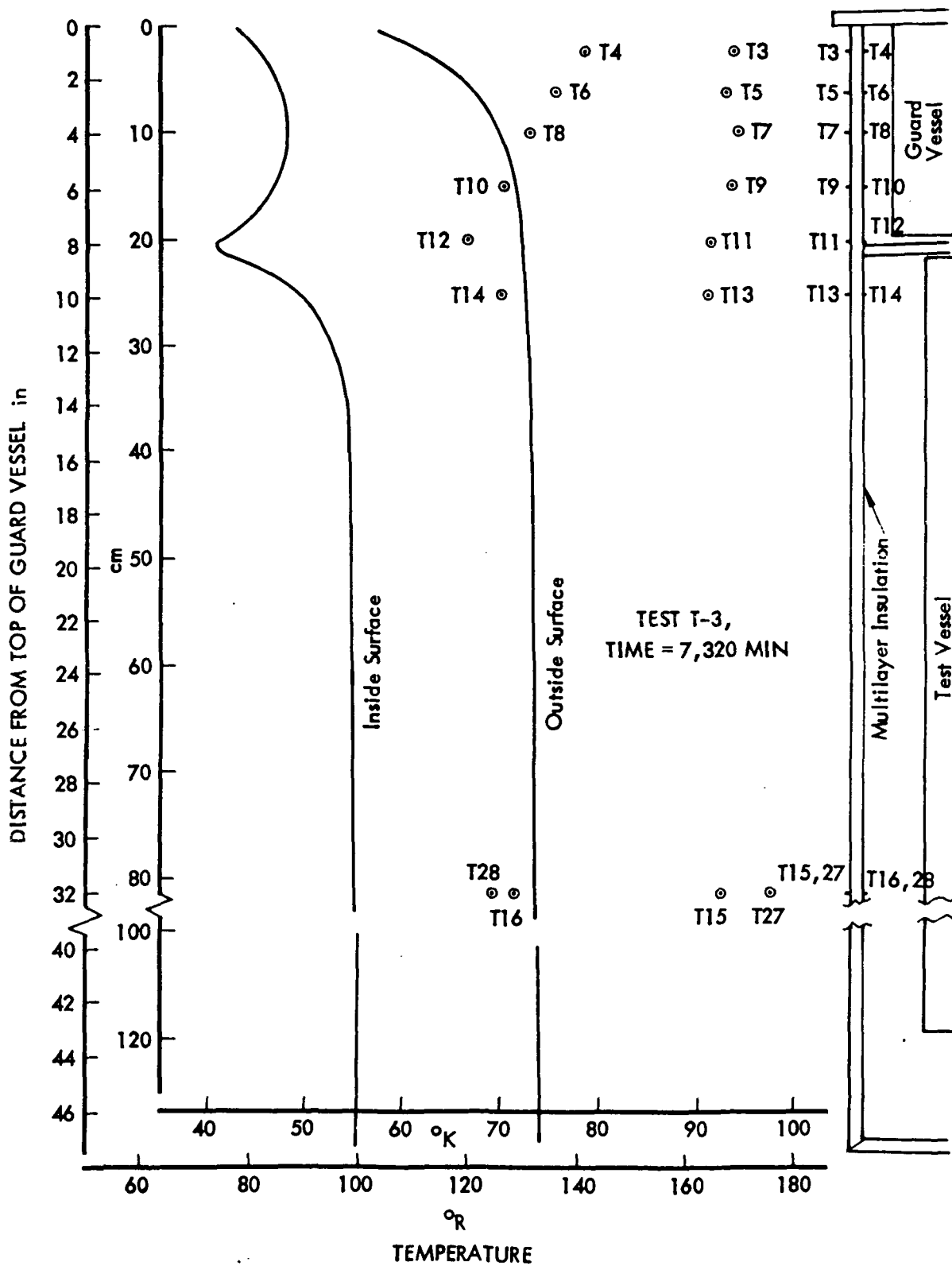


Figure 2.2-26: EXPERIMENTAL AND ANALYTICAL TEMPERATURES  
MAIN INSULATION SIDE WALL AREA

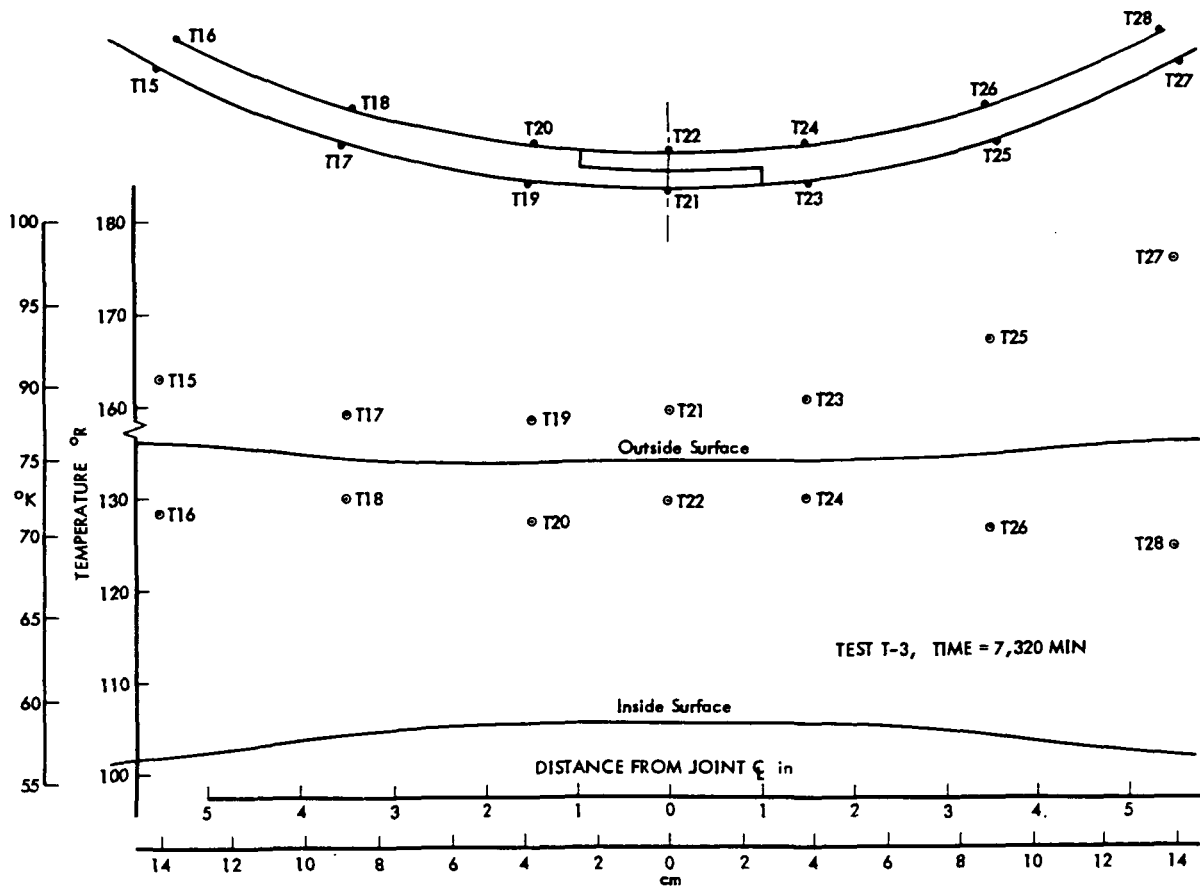


Figure 2.2--27: EXPERIMENTAL AND ANALYTICAL TEMPERATURES LONGITUDINAL JOINT AREA

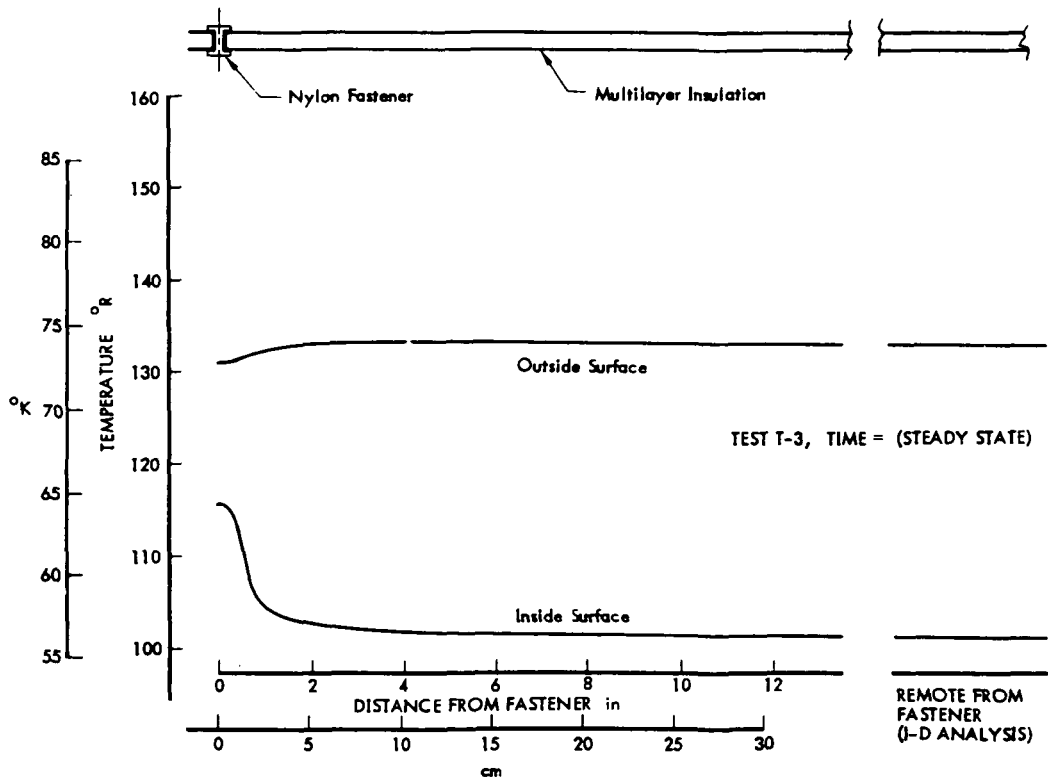


Figure 2.2-28: ANALYTICAL TEMPERATURES TYPICAL FASTENER AREA

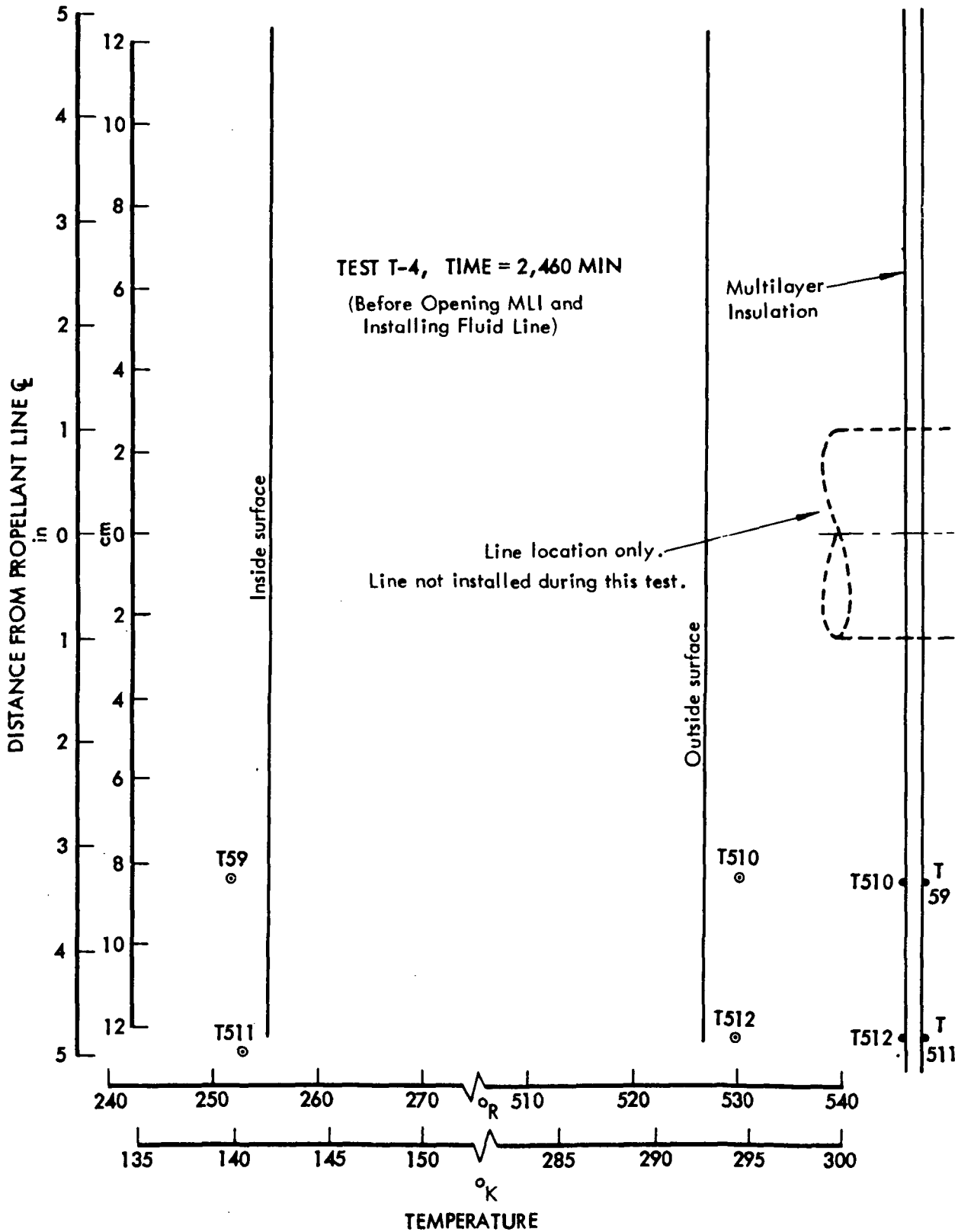


Figure 2.2-29: EXPERIMENTAL AND ANALYTICAL TEMPERATURES  
FLUID LINE PENETRATION AREA

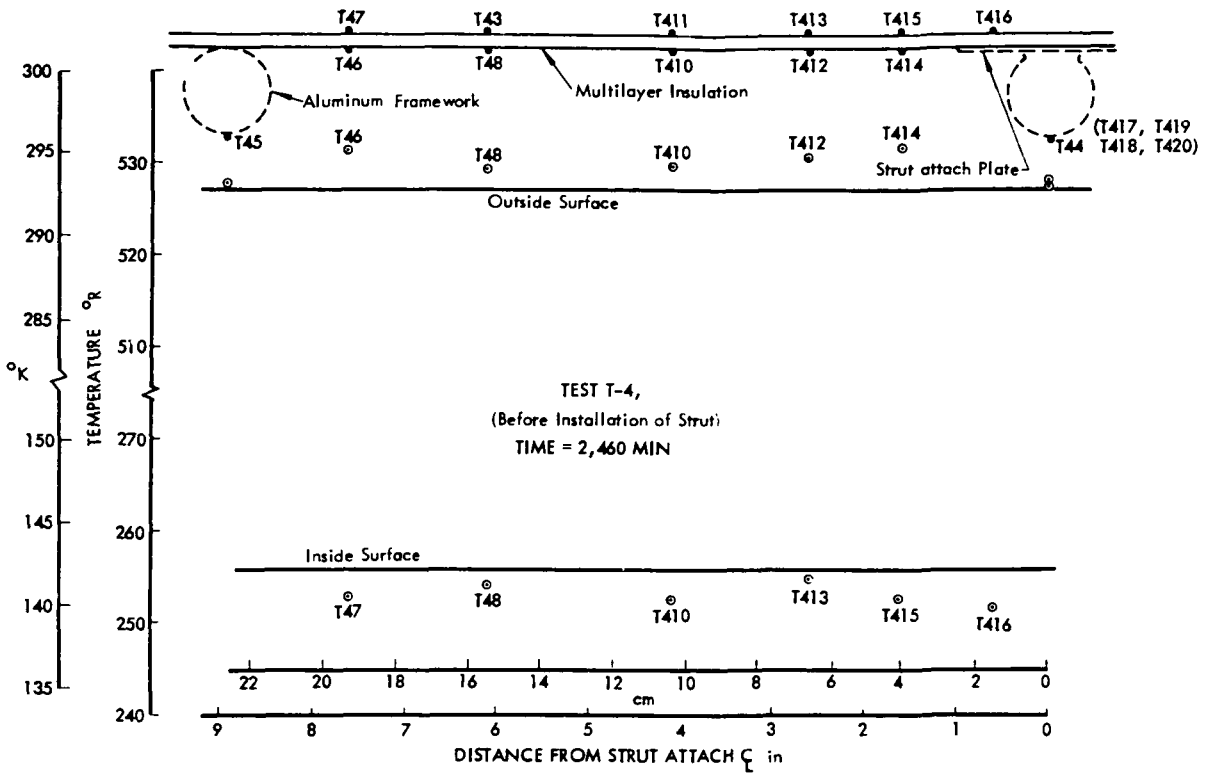


Figure 2.2-30: EXPERIMENTAL AND ANALYTICAL TEMPERATURES STRUT PENETRATION AREA

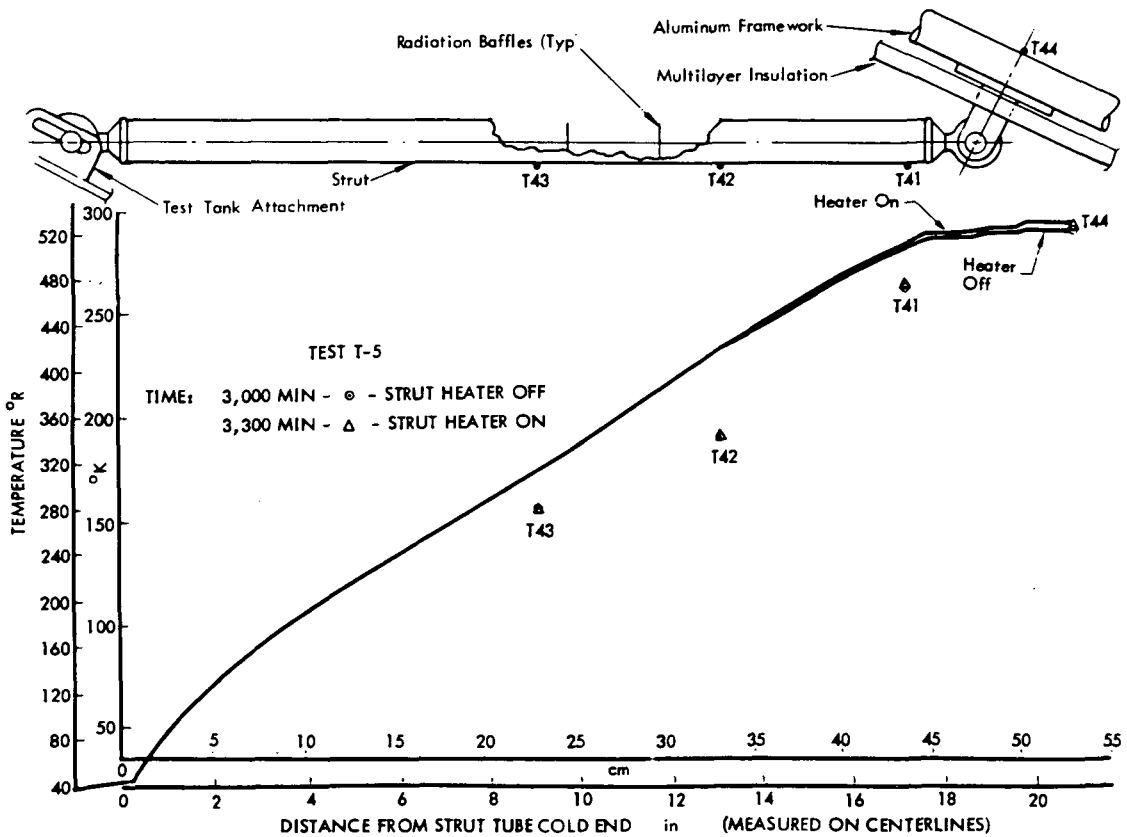


Figure 2.2-31: EXPERIMENTAL AND ANALYTICAL TEMPERATURES TANK SUPPORT STRUT

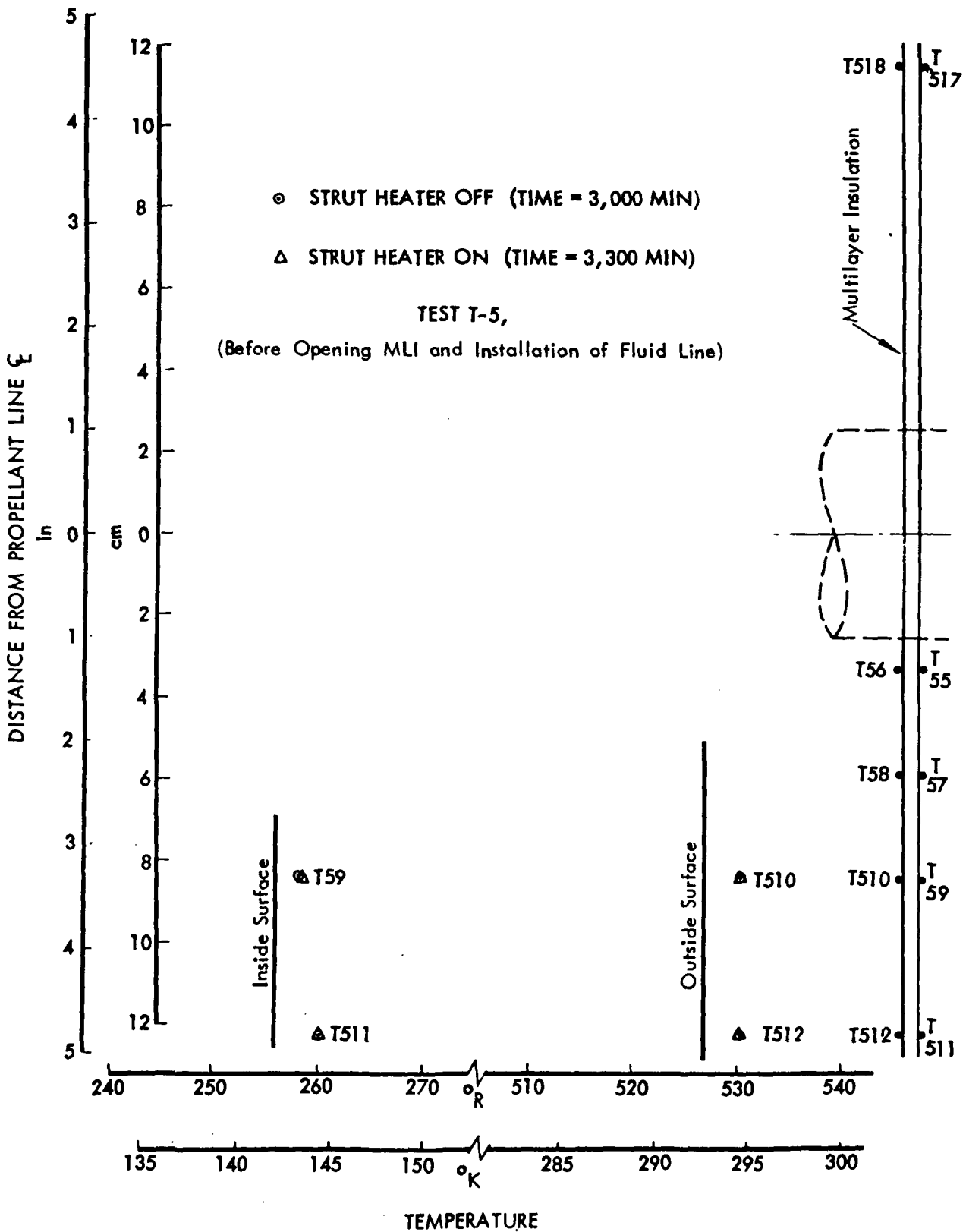


Figure 2.2-32: EXPERIMENTAL AND ANALYTICAL TEMPERATURES  
 FLUID LINE PENETRATION AREA

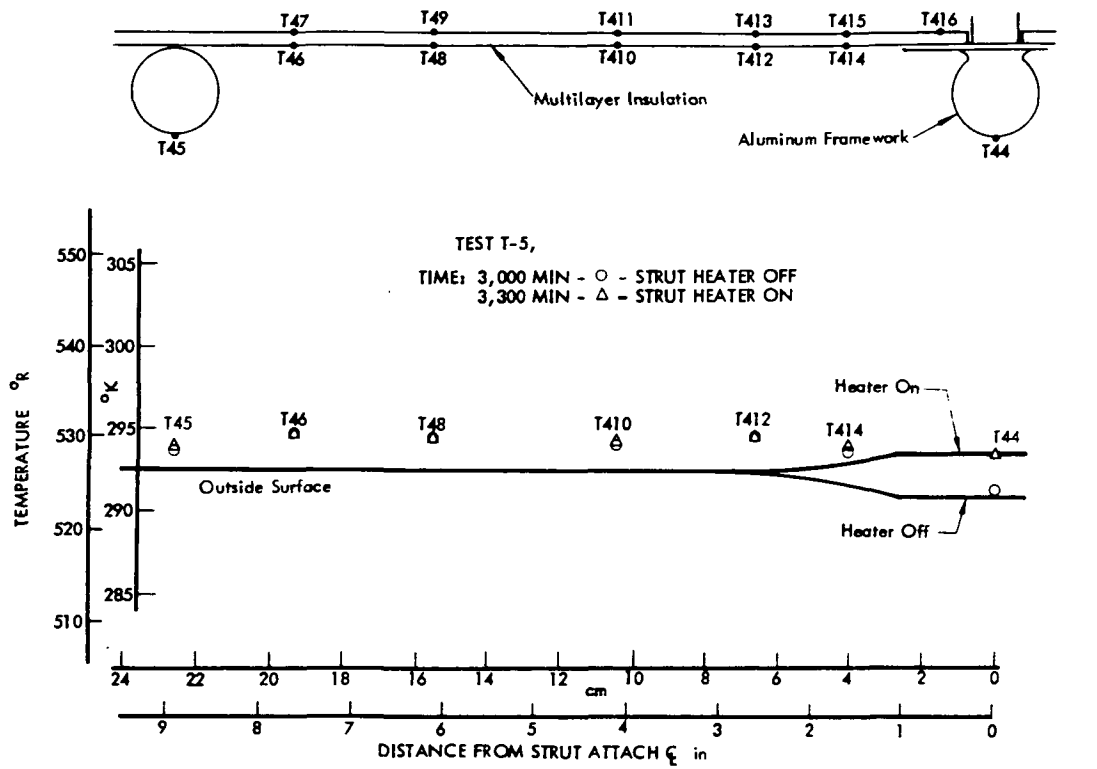


Figure 2.2-33: EXPERIMENTAL AND ANALYTICAL TEMPERATURES STRUT PENETRATION AREA

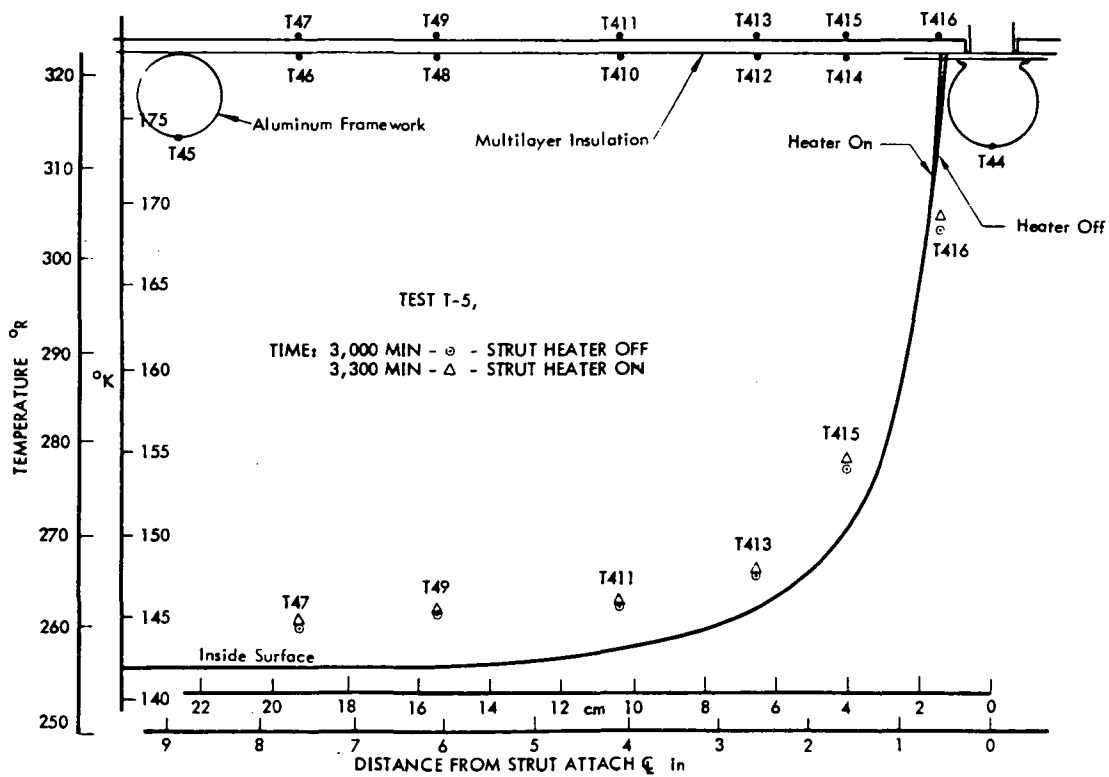


Figure 2.2-34: EXPERIMENTAL AND ANALYTICAL TEMPERATURES STRUT PENETRATION AREA

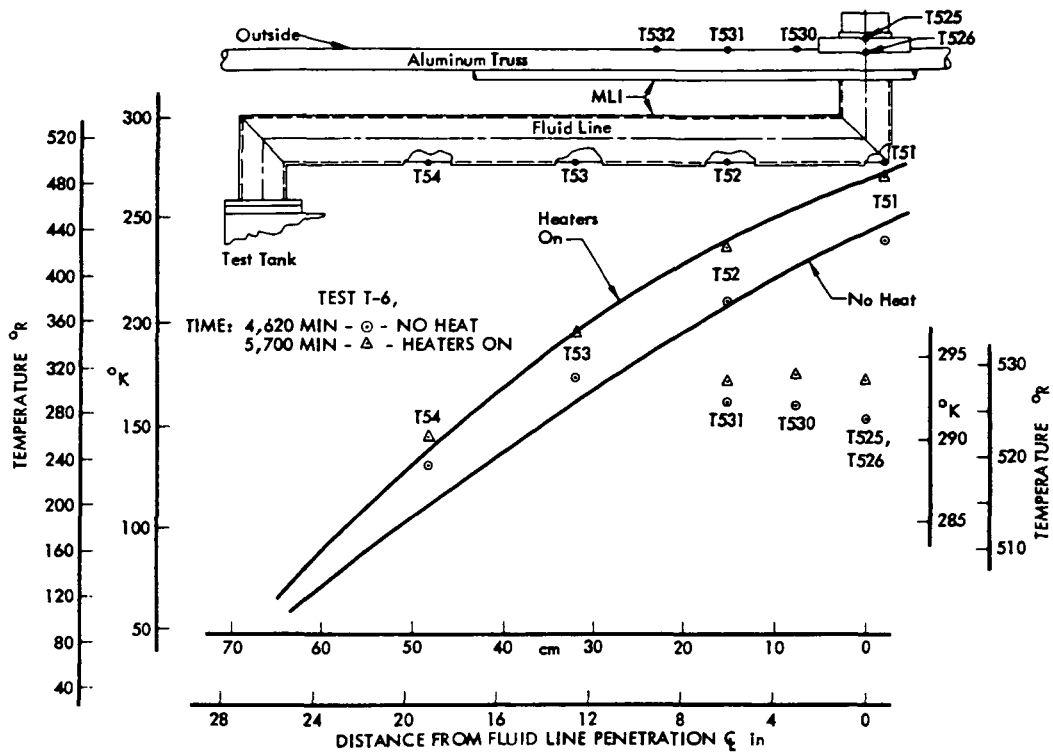


Figure 2.2-35: EXPERIMENTAL AND ANALYTICAL TEMPERATURES FLUID LINE AND TRUSS

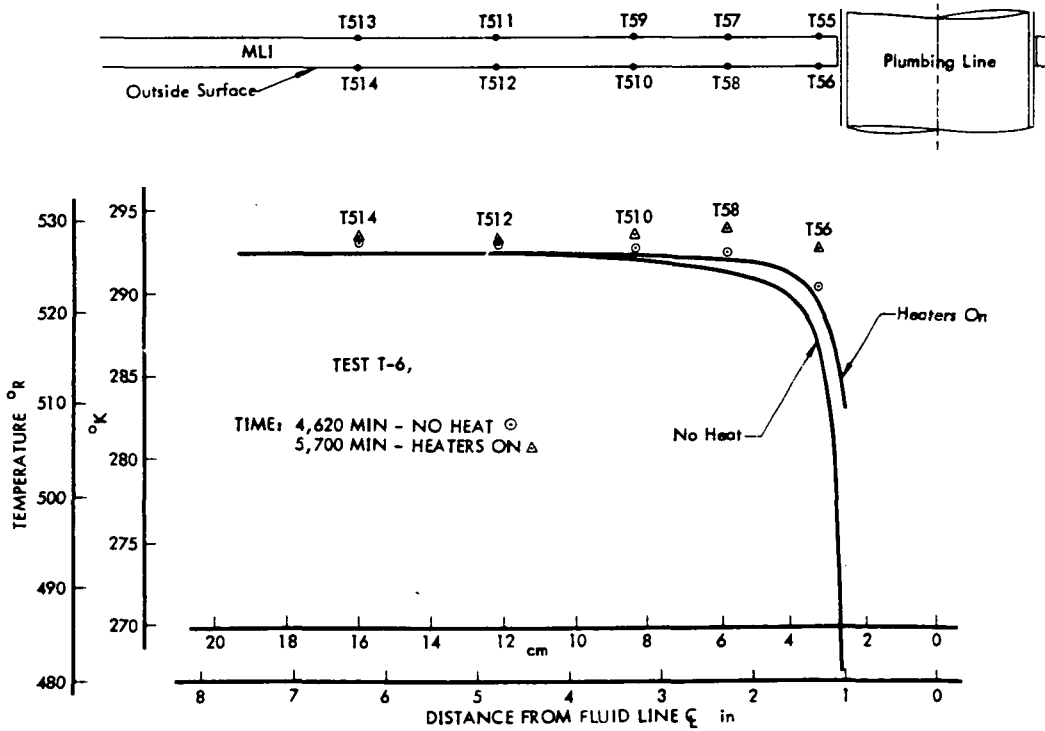


Figure 2.2-36: EXPERIMENTAL AND ANALYTICAL TEMPERATURES FLUID LINE PENETRATION AREA

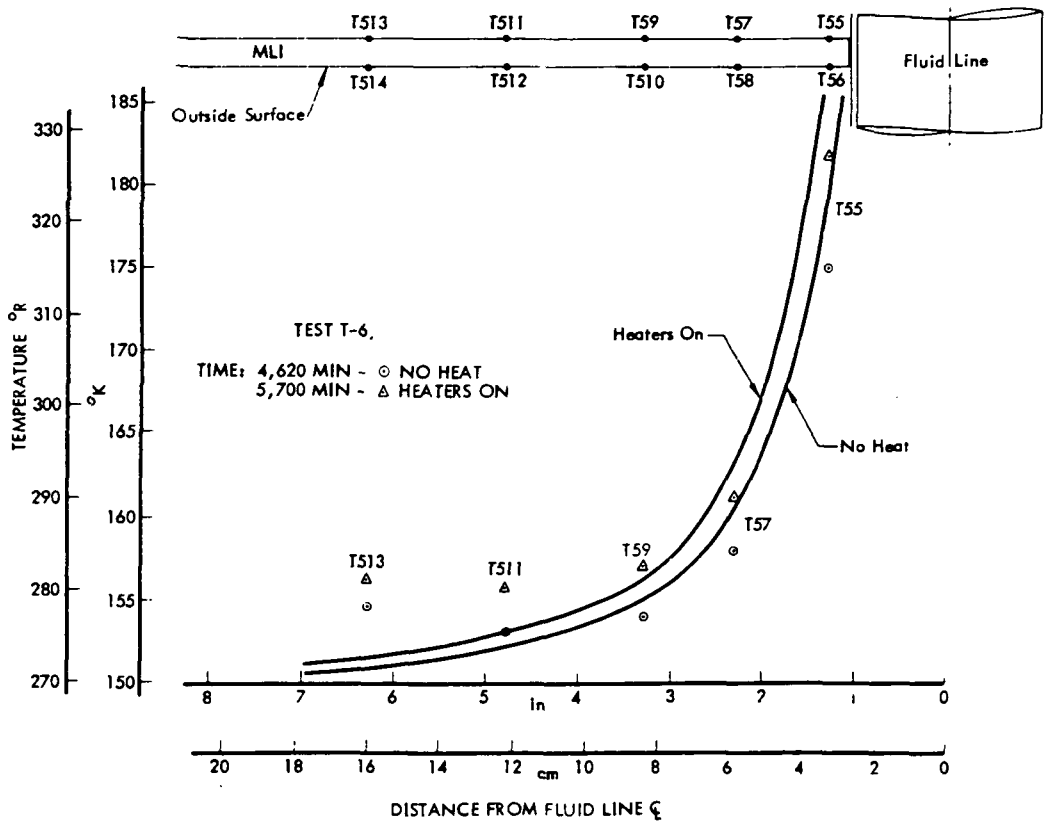


Figure 2.2-37: EXPERIMENTAL AND ANALYTICAL TEMPERATURES  
 FLUID LINE PENETRATION AREA

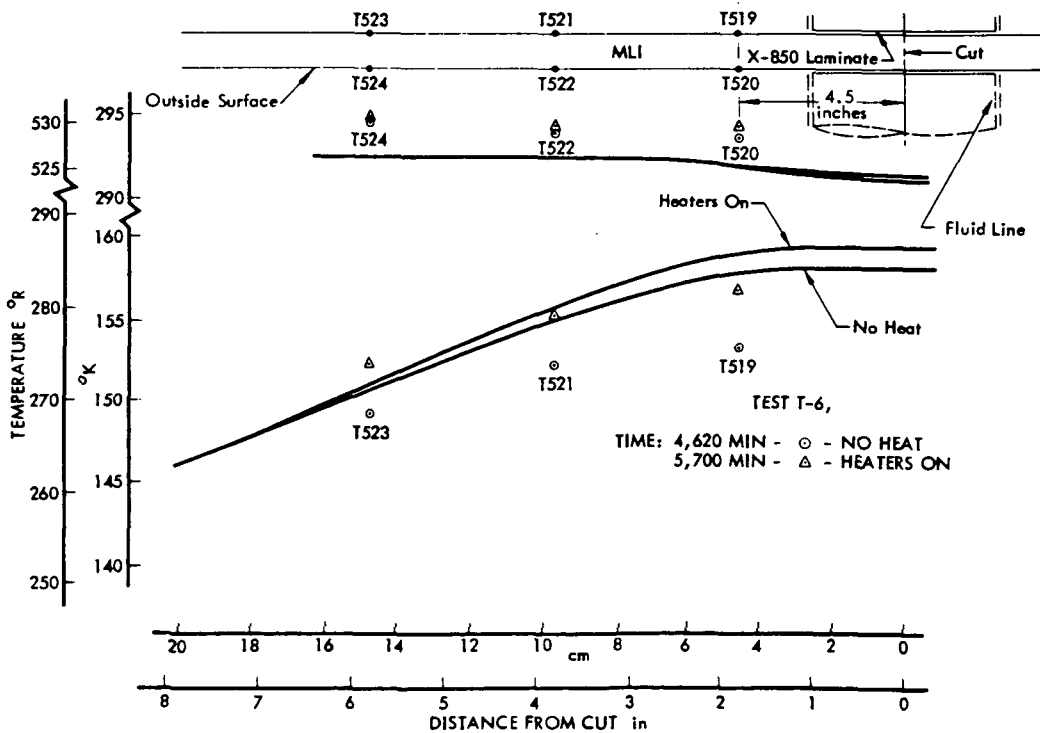


Figure 2.2-38: EXPERIMENTAL AND ANALYTICAL TEMPERATURES  
 FLUID LINE PENETRATION AREA

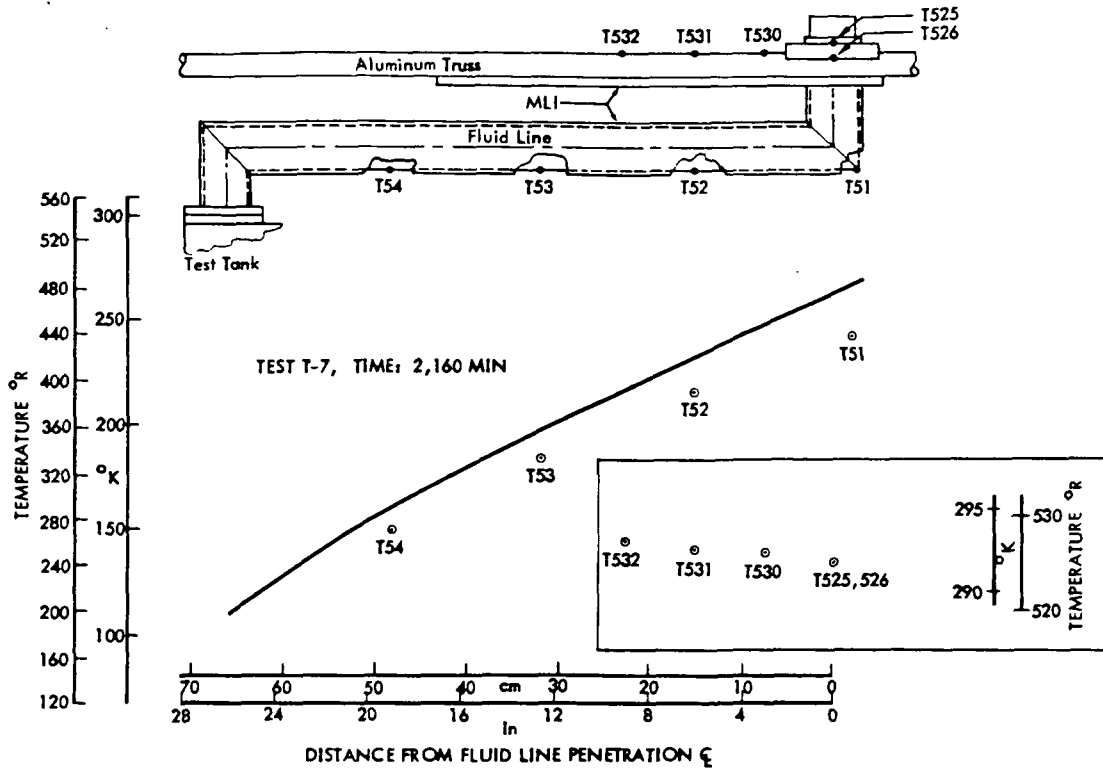


Figure 2.2-39: EXPERIMENTAL AND ANALYTICAL TEMPERATURES FLUID LINE & TRUSS

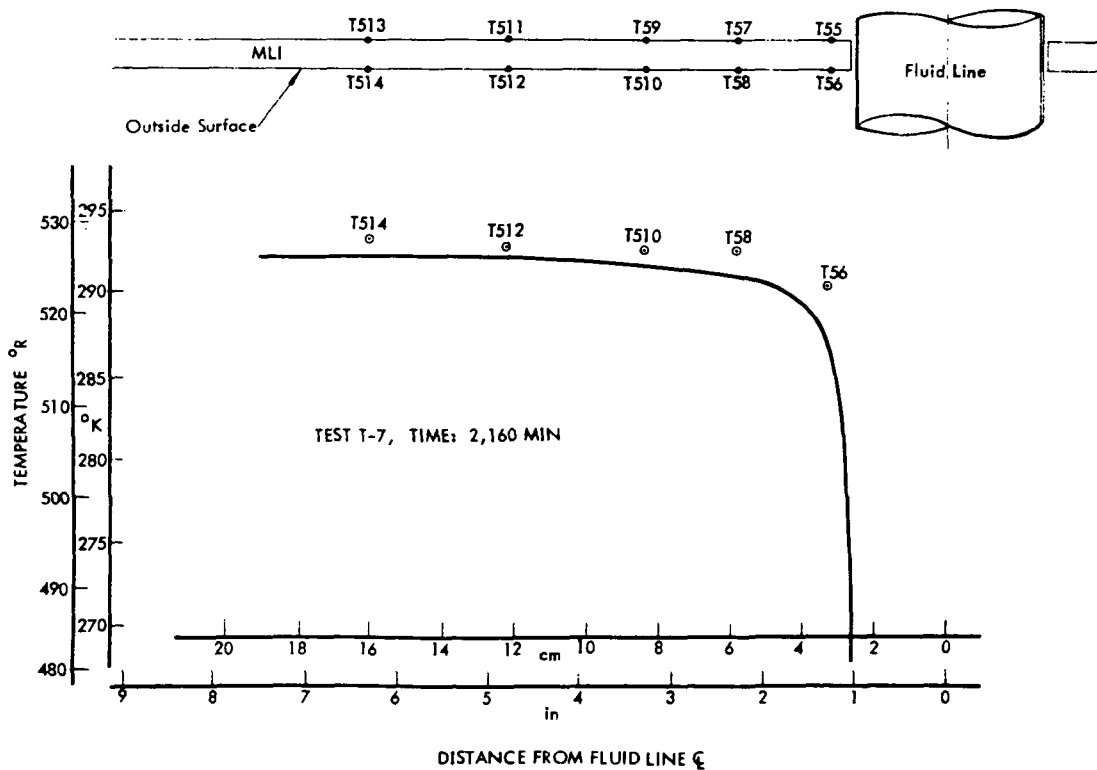


Figure 2.2-40: EXPERIMENTAL AND ANALYTICAL TEMPERATURES FLUID LINE PENETRATION AREA

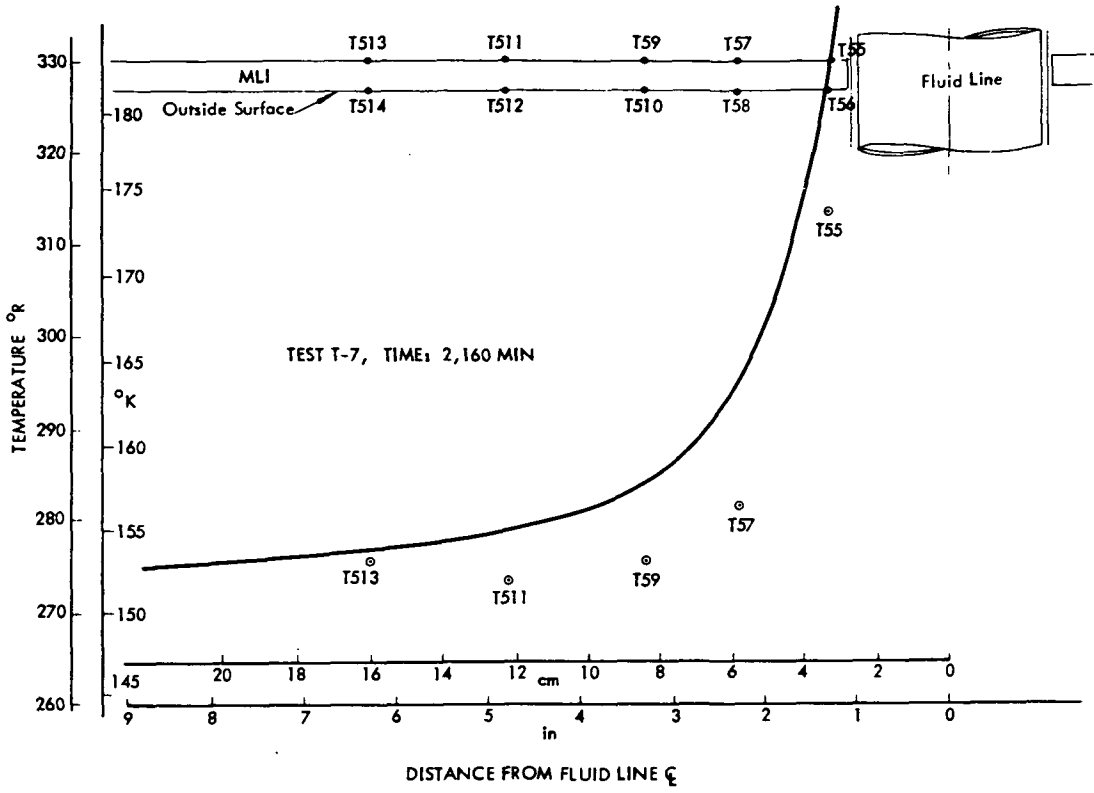


Figure 2.2-41: EXPERIMENTAL AND ANALYTICAL TEMPERATURES FLUID LINE PENETRATION AREA

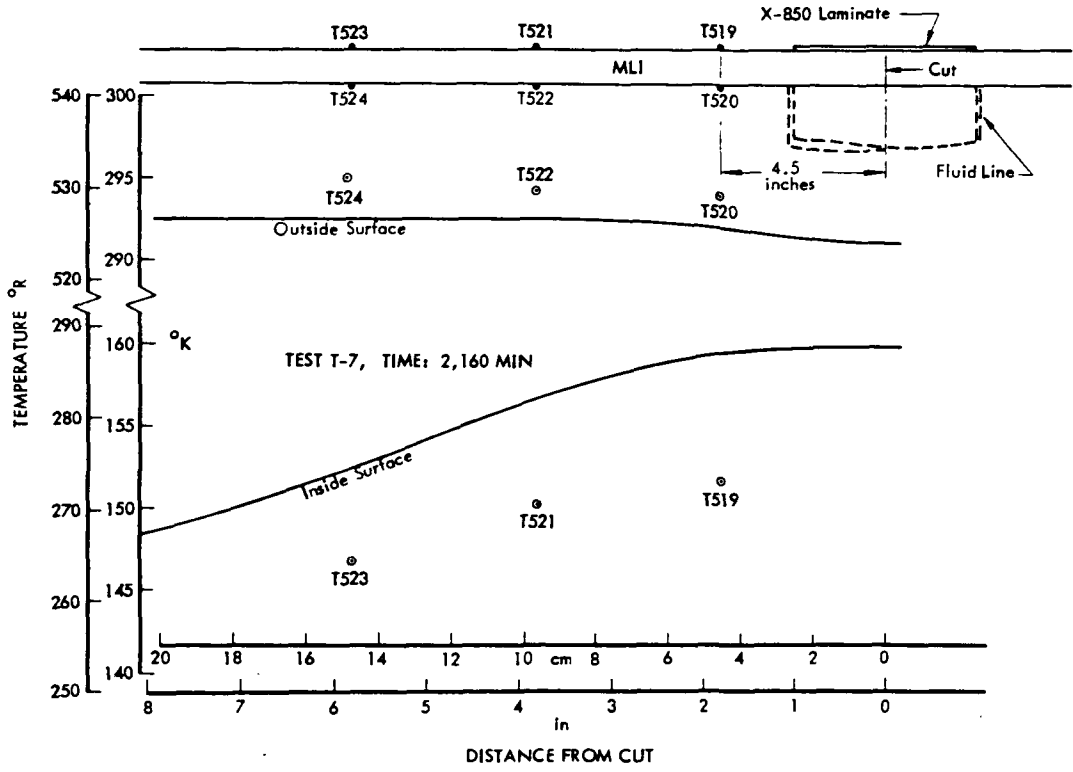


Figure 2.2-42: EXPERIMENTAL AND ANALYTICAL TEMPERATURES FLUID LINE PENETRATION AREA

TEST T-8, TIME = 6,120 MIN

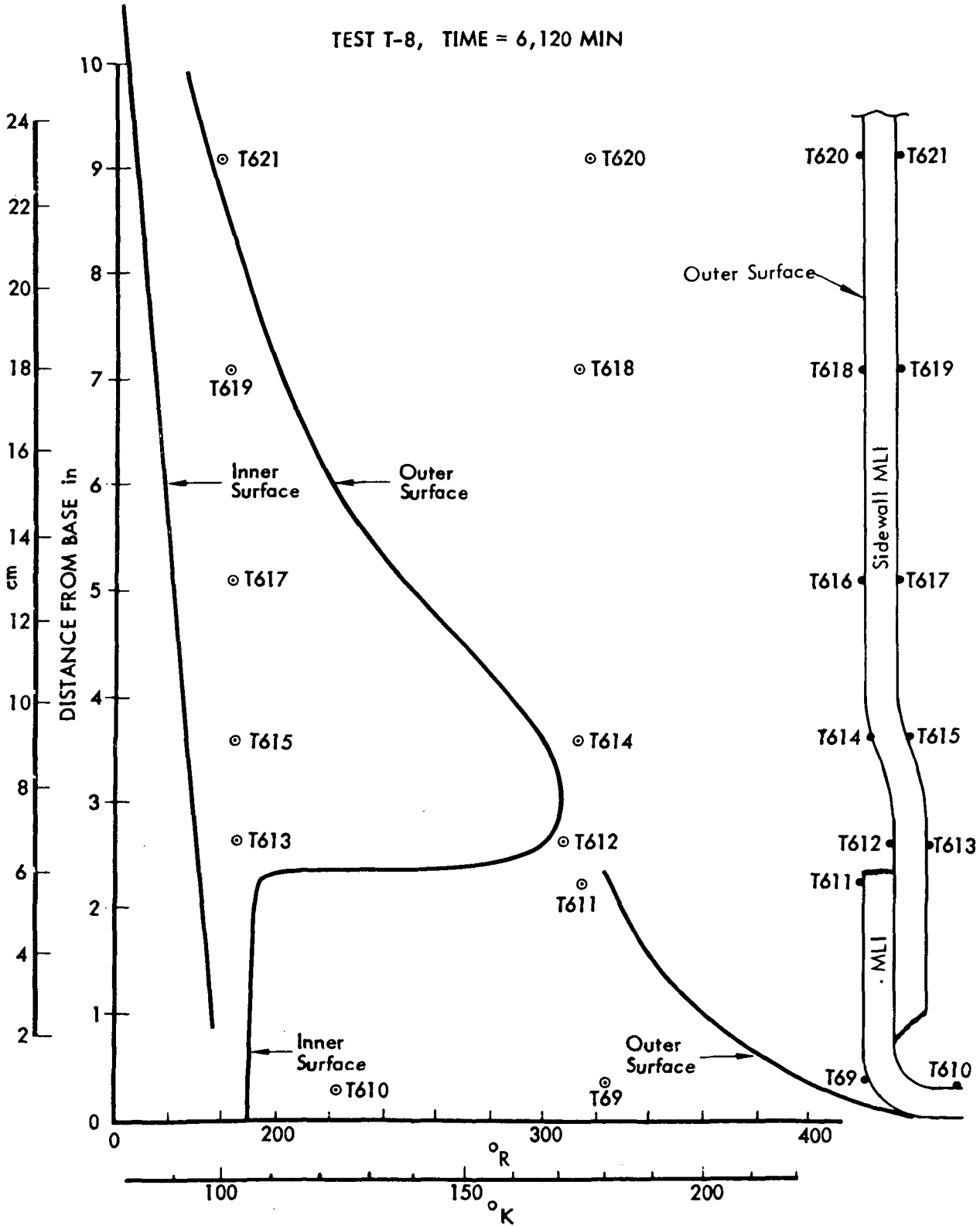


Figure 2.2-43: EXPERIMENTAL AND ANALYTICAL TEMPERATURES  
BASE LAP JOINT AREA

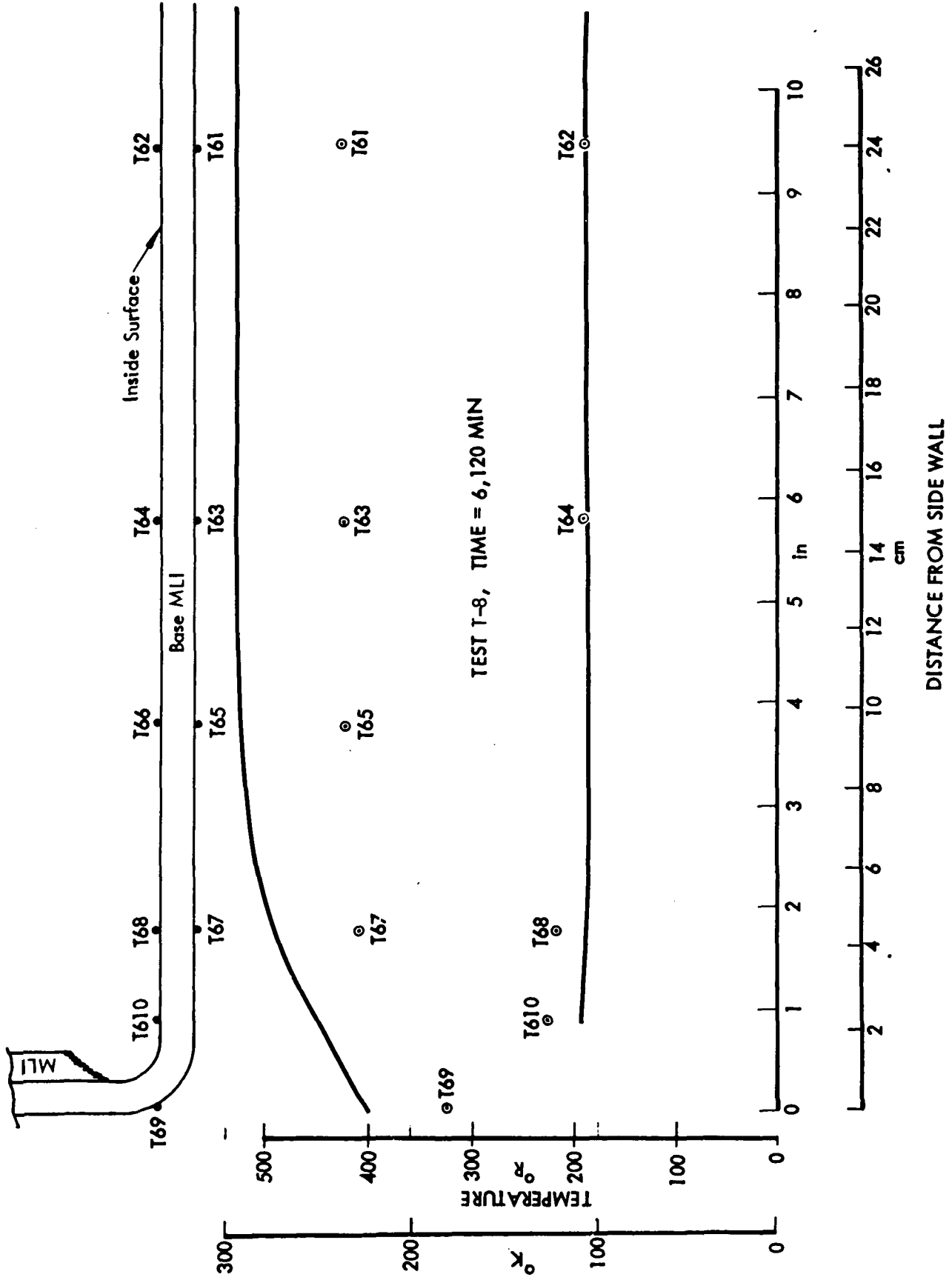


Figure 2.2-44: EXPERIMENTAL AND ANALYTICAL TEMPERATURES BASE AREA

Table 2.2-2: HEAT FLOW SUMMARY

TEST	$\dot{Q}_{\text{Basic}}$		Btu/Hr								Watt		
	$\dot{Q}_{\text{Basic}}$	$\Delta\dot{Q}_{\text{Longitudinal Joint}}$	$\Delta\dot{Q}_{\text{Fasteners}}$	$\Delta\dot{Q}_{\text{Strut}}$	$\Delta\dot{Q}_{\text{Plumbing}}$	$\dot{Q}_{\text{Total Predicted}}$	$\dot{Q}_{\text{Total Measured}}$						
T-1	6.558	1.921	.154	.045	.884	.259	0	0	0	7.596	2.225	8.255	2.418
T-2	6.477	1.897	.132	.039	.963	.282	0	0	0	7.572	2.218	8.833	2.587
T-3	.129	.037	.081	.024	.042	.012	0	0	0	.252	.073	.815	.239
T-4	6.558	1.921	.154	.045	.884	.259	0	0	0	7.596	2.225	8.948	2.621
T-5 $\nabla$	8.948	2.621	$\nabla$	$\nabla$	$\nabla$	$\nabla$	.151	.044	0	9.099	2.665	10.406	3.048
T-5 $\nabla$	8.948	2.621	$\nabla$	$\nabla$	$\nabla$	$\nabla$	.151	.044	0	9.099	2.665	10.500	3.075
T-6 $\nabla$	10.406	3.048	$\nabla$	$\nabla$	$\nabla$	$\nabla$	$\nabla$	$\nabla$	2.155	12.561	3.68	12.805	3.750
T-6 $\nabla$	10.406	3.048	$\nabla$	$\nabla$	$\nabla$	$\nabla$	$\nabla$	$\nabla$	2.699	13.38*	3.92*	13.628	3.991
T-7 $\nabla$	8.833	2.587	$\nabla$	$\nabla$	$\nabla$	$\nabla$	.134	.039	1.911	10.880	3.186	12.550	3.676
T-8	.703	.205	.081	.024	.132	.039	.006	.002	.386	1.307	.383	3.142	.920

$$\dot{Q}_{\text{Total Predicted}} = \dot{Q}_{\text{Basic}} + \Delta\dot{Q}_{\text{Longitudinal Joint}} + \Delta\dot{Q}_{\text{Fasteners}} + \Delta\dot{Q}_{\text{Strut}} + \Delta\dot{Q}_{\text{Plumbing}}$$

$\nabla$   $\dot{Q}_{\text{Basic}}$  is  $\dot{Q}_{\text{Total Measured}}$  from Test T-4

$\nabla$   $\dot{Q}_{\text{Basic}}$  is  $\dot{Q}_{\text{Total Measured}}$  from Test T-5

$\nabla$   $\dot{Q}_{\text{Basic}}$  is  $\dot{Q}_{\text{Total Measured}}$  from Test T-2

$\nabla$  Included in  $\dot{Q}_{\text{Basic}}$

\* Includes assumed 0.279 Btu/hr conducted from heaters into MLI support truss and eventually reaching test tank.

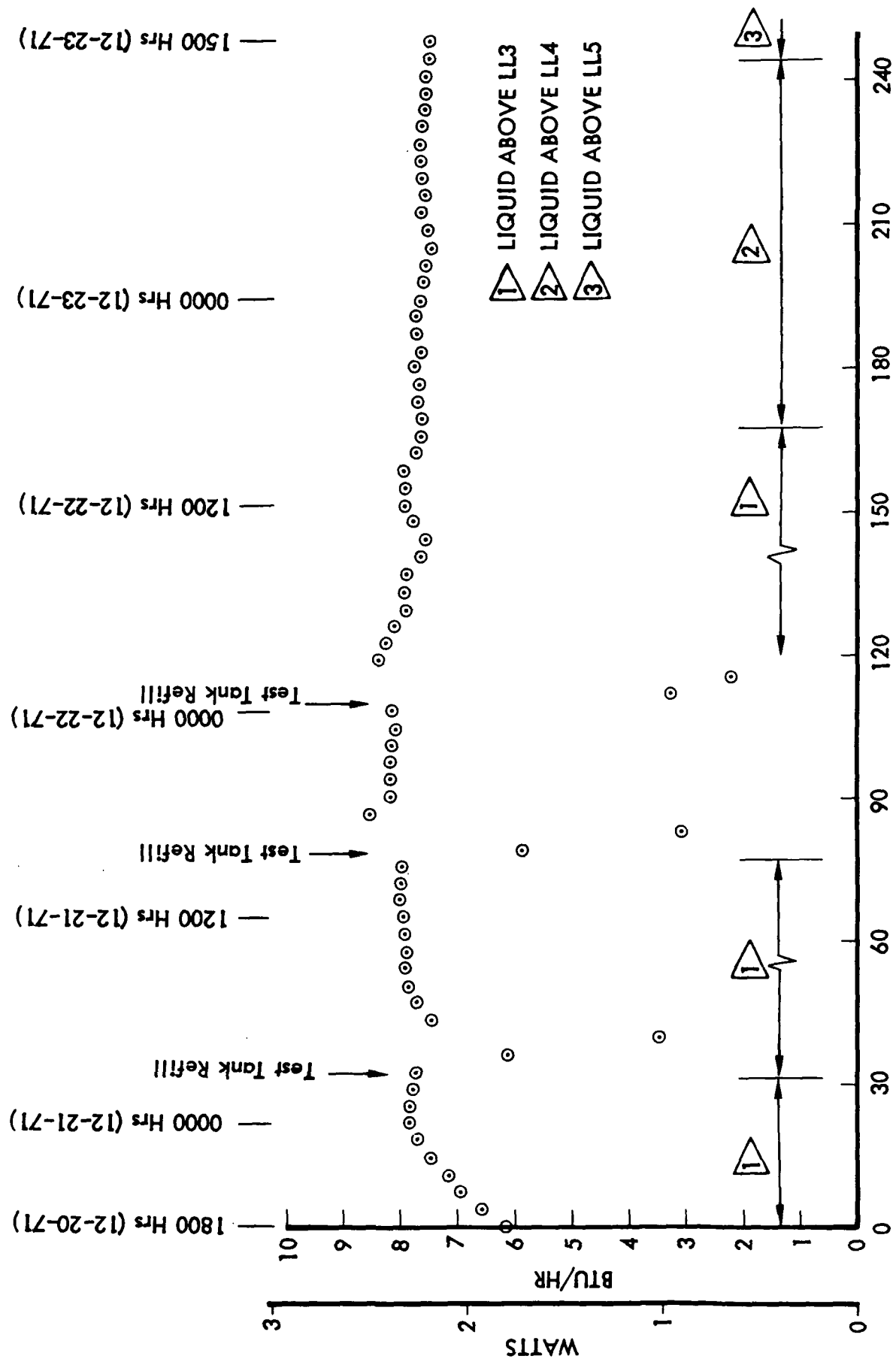


Figure 2.2-45: HEAT FLOW, TEST T-1

THERMAL/INTEGRATED PROTECTION SYSTEM

TEST NO. 7112

RUN NO 1

DATE 1222

HEAT LOSS CALCULATIONS-

PREVIOUS TIME = 23.0093 PRESENT TIME = 24.0088 DELTA TIME = : 0.9995 HRS  
 PREVIOUS VOL = 621.2 PRESENT VOL = 629.5 DELTA VOL = 8.4 CU FT  
 METER TEMP = 69.08 DEG-F TEMP CORR = 1.0018  
 VAPOR PRESS. OVER WATER = 18.20 MM-HG  
 METER PRESS = 749.81 MM-HG PRES CORR = 0.9626  
 CORR. FACTOR (K) = 0.9643  
 METERED VOLUME = 8.1 STD CU FT  
 VOLUMETRIC LOSS RATE = 8.056 STD CU FT/HR  
 WEIGHT LOSS RATE = 0.04196 LBS/HR

HEAT LOSS RATE = 8.044 BTU/HR

8.04  
 - .38  
 -----  
 7.66

ENGINEERING UNIT DATA-

PARAM	DATA	UNITS	PARAM	DATA	UNITS
TIMM	0	HR-MIN	TIMS	3133	SEC-CY
P-1	0.921	PSIG	P-2	1.280	PSIG
P-3	1.419	10-5 T	T-A.MB	12.82	DEG-F
PRAR	749.81	MM-HG	T-7.01	71.26	DEG-F
T-702	71.66	DEG-F	T-7.03	71.79	DEG-F
T-704	71.39	DEG-F	T-7.05	71.17	DEG-F
T-706	74.06	DEG-F	V-H.H	600	FT3
V-LD	29.5	FT3	T-2.9	75.66	DEG-F
T-30	69.08	DEG-F	T-1.	-616.88	DEG-F
T-2	-621.75	DEG-F	T-1.	61.90	DEG-F
T-4	-180.24	DEG-F	T-5.	67.63	DEG-F
T-6	-141.29	DEG-F	T-7	68.93	DEG-F
T-8	-205.52	DEG-F	T-9	69.74	DEG-F
T-10	-216.12	DEG-F	T-11	69.51	DEG-F
T-12	-205.08	DEG-F	T-13	70.00	DEG-F
T-14	-212.52	DEG-F	T-15	70.81	DEG-F
T-16	-199.51	DEG-F	T-17	69.74	DEG-F
T-18	-181.81	DEG-F	T-19	67.63	DEG-F
T-20	-186.35	DEG-F	T-21	66.47	DEG-F
T-22	-174.81	DEG-F	T-23	63.00	DEG-F
T-24	-189.76	DEG-F	T-25	67.36	DEG-F
T-26	-199.51	DEG-F	T-27	69.78	DEG-F
T-28	-208.82	DEG-F	P-1	15.42	PSIA

Figure 2.2-46: TYPICAL DATA PRINTOUT

The temperature at the tank outlet was measured by thermocouple T1. Figure 2.2-47 is a plot of that temperature during the test. The points where tank refills were made can be distinguished by a rise in temperature. The gradual warming trend towards the end of the run occurred as the liquid level dropped.

Barometric and test tank pressure are shown in Figure 2.2-48. It was apparent that the back-pressure system was not functioning correctly during the test. It was later found that a quantity of hydrogen gas had been trapped in a bend of the line connecting the large and small area pots.

Because of the malfunctioning back-pressure system, changes in barometric pressure affected tank internal pressure which, in turn, affected boiloff rate. The changes in boiloff resulting from this effect were not indicative of a change in heat flow to the tank and thus were a source of error in the heat flow to the tank deduced from the measured boiloff.

The time period selected for evaluating Test 1 thermal data was in the neighborhood of 168 ks, a relatively stable period following the last tank refill. As seen in Figure 2.2-48, the barometric and test tank pressure experienced a rise during this period. Increasing pressure decreased the boiling temperature, resulting in some of the incoming heat being stored undetected in both the LH<sub>2</sub> and the tank wall.

The heat stored during the period from 132 ks to 186 ks was calculated as an average of 0.139 Btu/hr (0.04 watt). This value was added to the indicated boiloff heat flow of 7.60 Btu/hr (2.2 watt) (evaluated at 169 ks) to obtain a corrected boiloff heat flow of 7.739 Btu/hr (2.24 watt).

The heat of vaporization of LH<sub>2</sub> is also a function of pressure, but the variation due to the pressure change during the period of interest was not significant to the heat flow calculated from boil-off rates.

The MLI was instrumented in this test to measure gradients along inner and outer surfaces at the longitudinal splice joint and the edge of the test article in the vicinity of the guard. One purpose for this data was to determine the efficiency of the guard's function. Figures 2.2-49 and 2.2-50 are photographs of the internal instrumentation for these two locations.

The heat flow and temperature distributions of Test T-1 were modeled by means of three two-dimensional sections. These were:

- (1) A longitudinal section through the entire insulation assembly, ignoring the longitudinal joint and the nylon pin fasteners. This section is illustrated in part in Figures 2.2-18 and 2.2-19, and the analytical model is shown in detail in Appendix E. Analysis of this section was

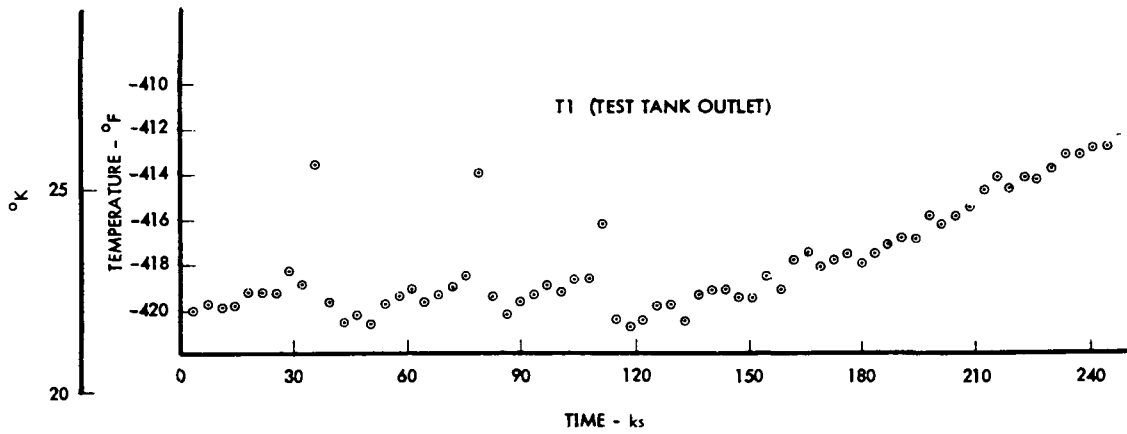


Figure 2.2-47: TEST TANK OUTLET TEMPERATURE, TEST T-1

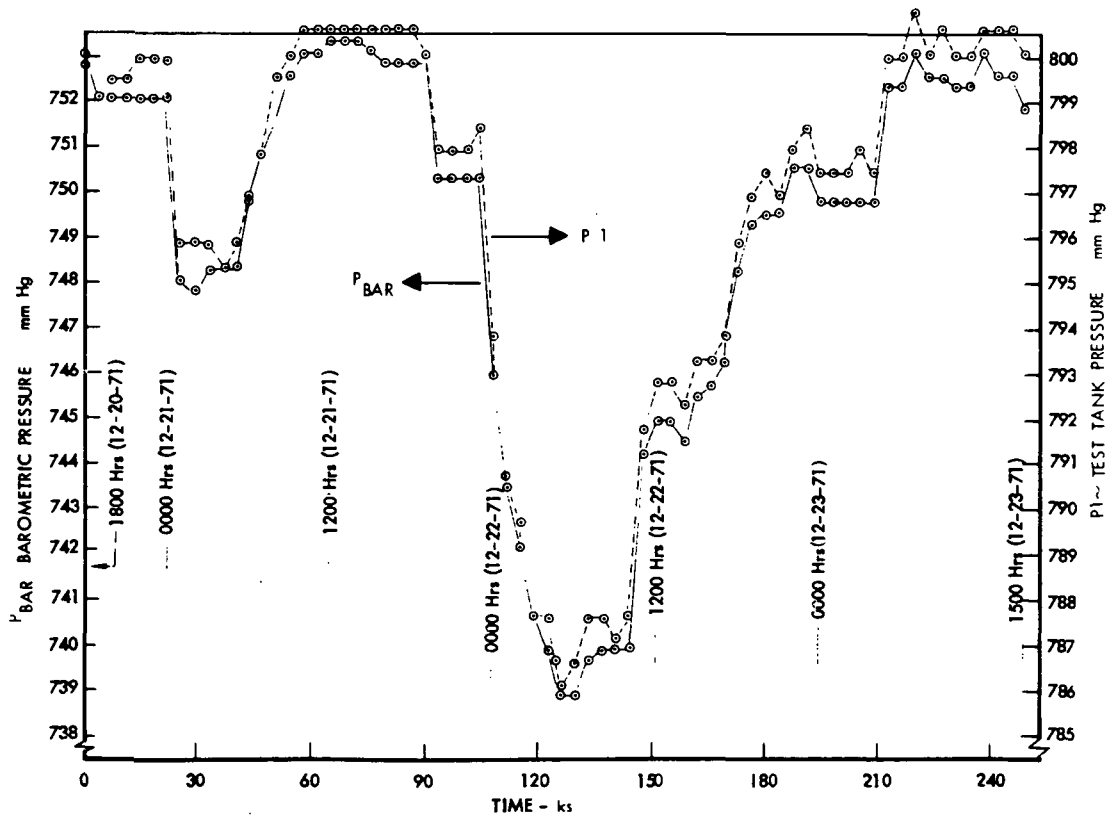


Figure 2.2-48: TEST TANK AND BAROMETRIC PRESSURE, TEST T-1

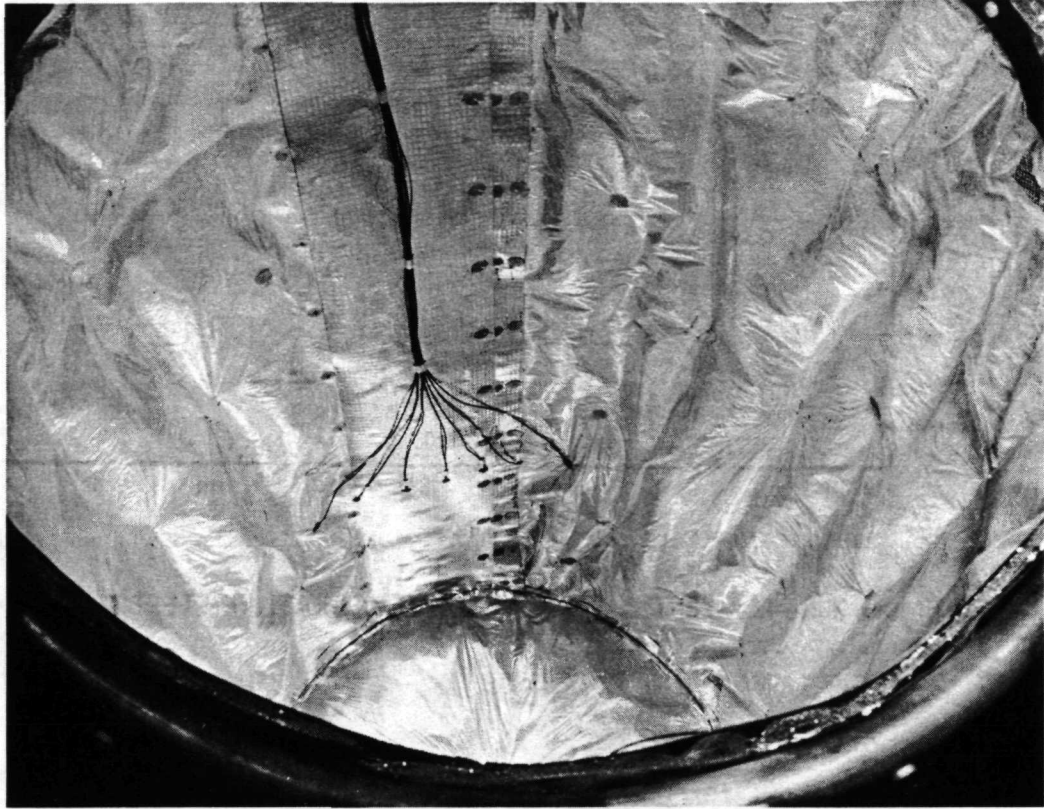


Figure 2.2-49: LONGITUDINAL JOINT INSTRUMENTATION

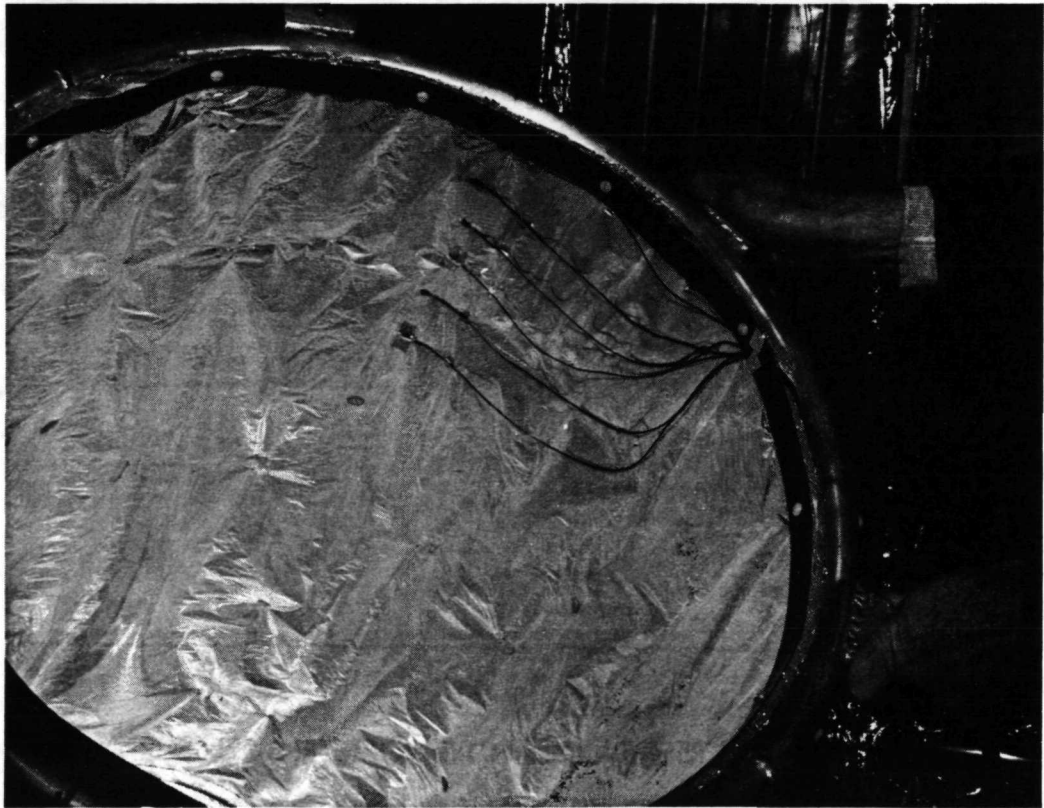


Figure 2.2-50: GUARD AREA INSTRUMENTATION

used to predict temperatures for correlation with the measured values T3 through T14 and to compute the predicted  $Q_{\text{basic}}$  value.

- (2) A partial circumference cross-section through the insulation longitudinal joint. This section is illustrated in Figure 2.2-20 and the conductance network shown in Appendix E. The analysis was used for temperature correlations involving measured T15 through T28 values and to compute the incremental heat leak due to the joint.
- (3) A typical section through a circular area of insulation, approximately 24 in (0.61 m) in diameter, surrounding one of the 47 nylon pin fasteners. This section is illustrated in Figure 2.2-21, with the conductance network shown in Appendix E. The analysis of this section provided the prediction of incremental heat leaks due to fasteners. An attempt was made to verify its accuracy by correlation of temperature predictions with measured T59 and T510 through T512 values from Test T-5.

The analytical models of Items (2) and (3), above, were defined with the intent to include sufficient area of insulation such that the thermal influence of the longitudinal joint and fastener, respectively, were effectively contained within the section analyzed. This isolation of effects was tentatively confirmed by the observation that temperatures predicted for the outlying parts of the joint and fastener section tended to agree with temperatures predicted for the mid-body areas of the main insulation assembly.

In addition to the general assumptions employed throughout the thermal analyses and described in the introductory paragraphs of this section, it was assumed in the analysis of Test T-1 (and of Tests T-2 through T-7, as well) that the multi-layer conductivity through the base miter joint was equivalent to the lateral conductivity of the continuous multilayer.

Figures 2.2-18 and 2.2-19 show temperatures on the surfaces of the side-wall insulation for Test 1. Measured values from T15, T16, T27 and T28 were included in the figure even though they did not lie in the same longitudinal section as T3 through T14. Thermocouples T15, T16, T27 and T28, from the longitudinal joint instrumentation set, were felt to be far enough from the joint to be essentially free from its thermal influence. The analytical results indicate a strong heat flow into the MLI separating the test and the guard tanks, caused primarily by direct contact between the separating insulation and the two tanks and the relatively high lateral conductivity in the insulation.

The apparent anomaly of the T12 measurement has not been explained. Although it is quite possible that this thermocouple was not located exactly where intended, it is difficult to surmise a mislocation that would result in the temperature shown. It is possible that the assumed joint conductance, which contributes to the satisfactory agreement between analytical and experimental temperatures at the other

points, is appropriate only as an average for the whole joint but is not accurate at the particulate locale of T12.

The divergence between analytical and experimental temperatures near the top of the side wall, as seen in Figures 2.2-18 has not been explained but was not felt important because of apparent little influence on test vessel insulation temperatures or heat flow. It is possible that the analytical model does not accurately account for conditions at this location or at the fill and vent lines on top of the assembly.

Figure 2.2-20 presents inside and outside surface temperatures for Test T-1 at the section through the longitudinal joint. Limited attempts were made to analyze a partially separated or misaligned joint in order to improve agreement with the measured inside surface temperatures. These attempts were not successful and the results shown, based on an ideal joint, were accepted. The principal application of the joint thermal analysis was to predict the joint heat leak. The fact that the area (representing total heat flow due to the joint) under a smoothed curve drawn through the test points approximates the area under the analytical curve, lends credence to the analysis for its intended application.

Figure 2.2-21 shows temperatures in the neighborhood of a typical fastener. The analytical predictions, like those for the longitudinal joint, are applicable to Tests T-4, T-5, T-6 and part of Test T-8, as well as to Test T-1. The active thermocouples suitable for providing measured data for temperature correlations were T59 and T510 through T512 from Test T-5. As can be seen from the figure, the thermocouples were insufficient in number and too remote from the fastener to supply useful correlation data. As with the joint thermal analysis, the primary use of the fastener analysis was to predict the fastener heat leak.

The Test T-1 analytical heat flow synthesis and the comparison between predicted and measured total heat flow are shown in Table 2.2-2. The temperature distribution correlations offer no explanation for the difference between the predicted and measured total heat flows. It is pointed out, however, that large areas of the insulation assembly were without experimental verification of predicted temperatures, raising the possibility that the analytical predictions were not entirely representative of the total insulation assembly.

Test T-2: Boil-off data is presented in Figure 2.2-51. The test was started on 12-6-71. The data plots begin at 0500 hours, December 7 (time "zero"), and end at 1200 hours, December 8. At test termination a problem had developed with the mercury back pressure system. Water from the saturator had been forced into the mercury pot because of a change in operating procedure. Mercury was withdrawn to reduce the pressure, and in performing this operation the water migrated to the large diameter mercury equalizing pot and was drawn into the cold trap of the vacuum pumping system. The vacuum system gradually became inoperative and test tank pressure began to rise; therefore, the test was terminated.

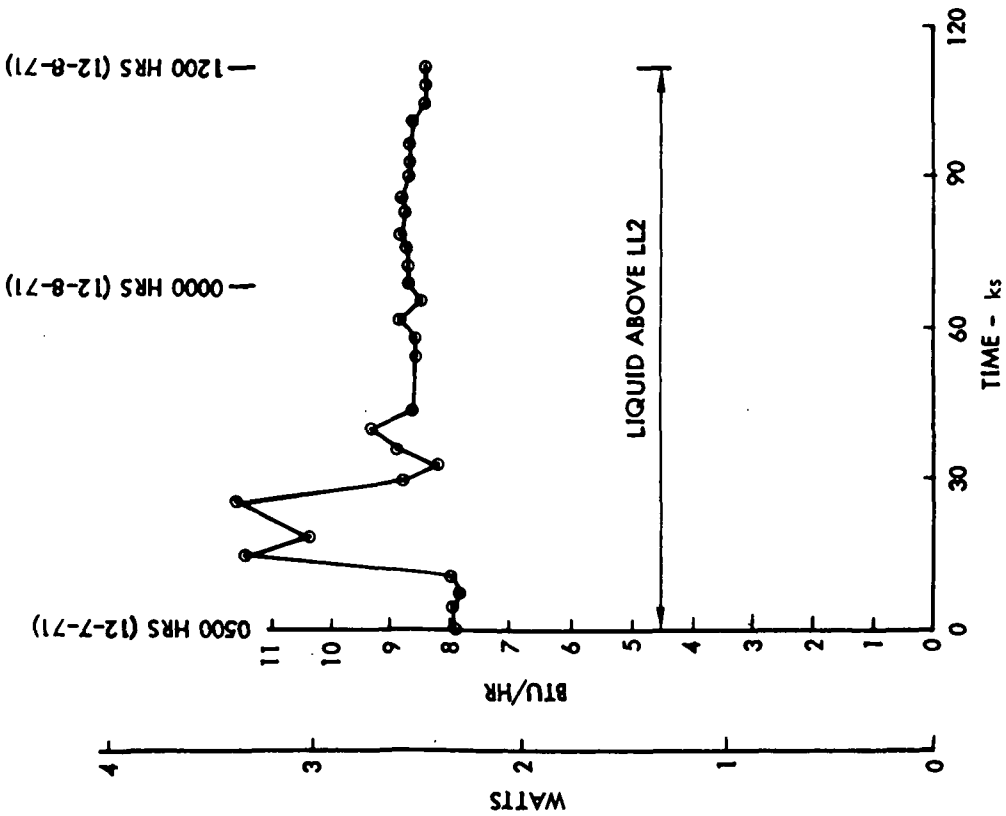


Figure 2.2-51: HEAT FLOW, TEST T-2

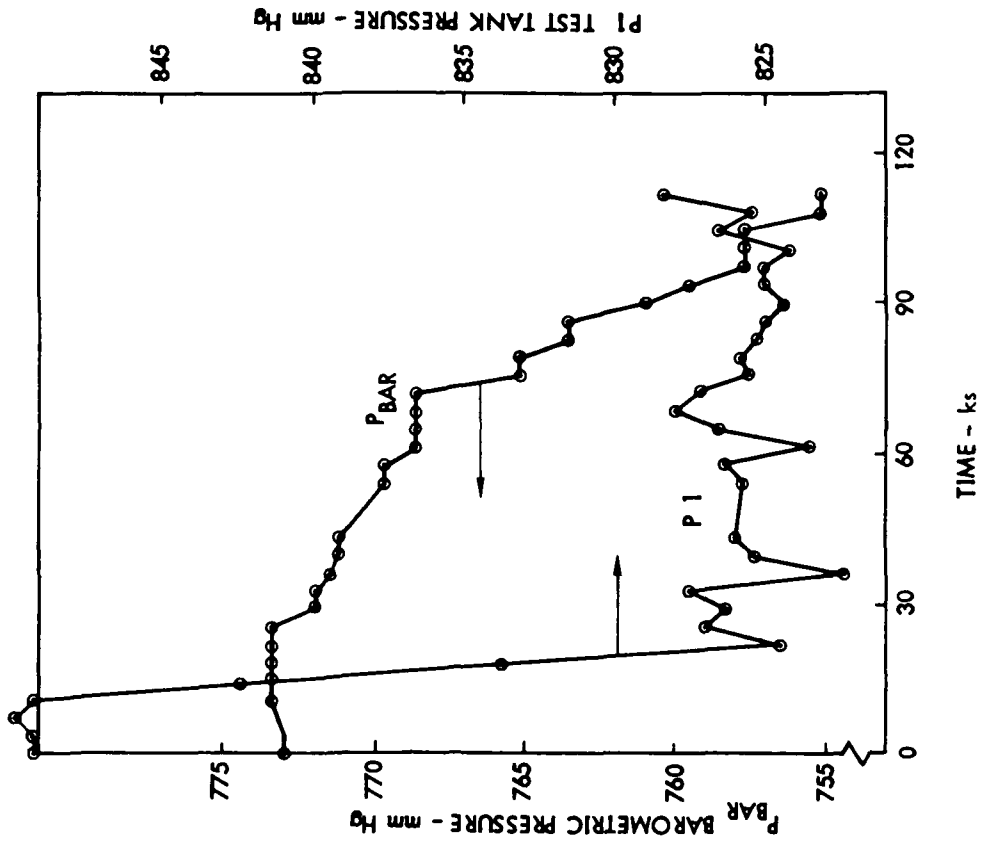


Figure 2.2-52: TEST TANK AND BAROMETRIC PRESSURES, TEST T-2

The system maintained pressure reasonably well during the period of 90 - 102 ks where the boil-off data indicated that stabilization had been attained. The boil-off rate was 8.6 Btu/hr (2.5 watt).

Figure 2.2-52 shows test tank & barometric pressures. The test tank pressure reflects the difficulties encountered with the back pressure system. As the vacuum pumping efficiency was degraded, the mercury level in the large pot dropped, and the level increased in the small pot; thus the height of the hydrogen gas bubble column increased. The abrupt drop in pressure early in the test resulted in a corresponding increase in boil-off rate. This pressure drop was accomplished by withdrawing mercury from the column. Figure 2.2-53 shows the temperature at the tank outlet. The liquid remained above level sensor 2 during the entire test; therefore, a very slight change was noted.

Figures 2.2-22 and 2.2-23 show the insulation side wall temperatures for Test T-2 (LN<sub>2</sub>). The same assumptions and analytical model were employed as for Test 1, and the same characteristics are seen in the correlations. Tests T-1 and T-2 were considered simultaneously in adjusting the MLI properties discussed earlier. Further adjustments that would have improved prediction-measurement agreement for one test at the expense of agreement for the other test were not made. Figure 2.2-24 showing the temperatures at the longitudinal joint section for Test T-2 exhibits characteristics similar to the results for Test T-1. In this case the analytical results more closely approximate experimental values. Again, the area under an experimental temperature distribution approximates that of the analytical distribution, indicating adequacy of the theoretical analysis for heat leak prediction. Examination of the joint revealed the possibility of considerable irregularity in details of the joint configuration along its length. Thus, a representation of the average effect of the joint is all that can be expected without a far more detailed investigation.

Figure 2.2-25 shows the fastener region analysis for Test T-2. No experimental data are shown since there were no suitable active thermocouples near a fastener at the conditions of Test T-2.

The heat flow correlations of Table 2.2-2 show a discrepancy between predicted and measured total heat flow even greater than that of Test T-1. Again, the temperature correlations provide no explanation for the discrepancy.

Test T-3: Referring to the test plan, Figure 2.2-1, Test T-3 utilized the same thermal protection system as Tests T-1 and T-2. However, the external boundary temperature was reduced to -320°F (77.7°K) by means of the thermal shroud. The measurement fluid in the test tank was LH<sub>2</sub>.

This test was started on 12-13-71. Boil-off data, beginning at 0000 hours on 12-15-71, is shown in Figure 2.2-54. The data curve was interrupted by two test tank refills. The boil-off rate appeared to be insensitive to liquid level in

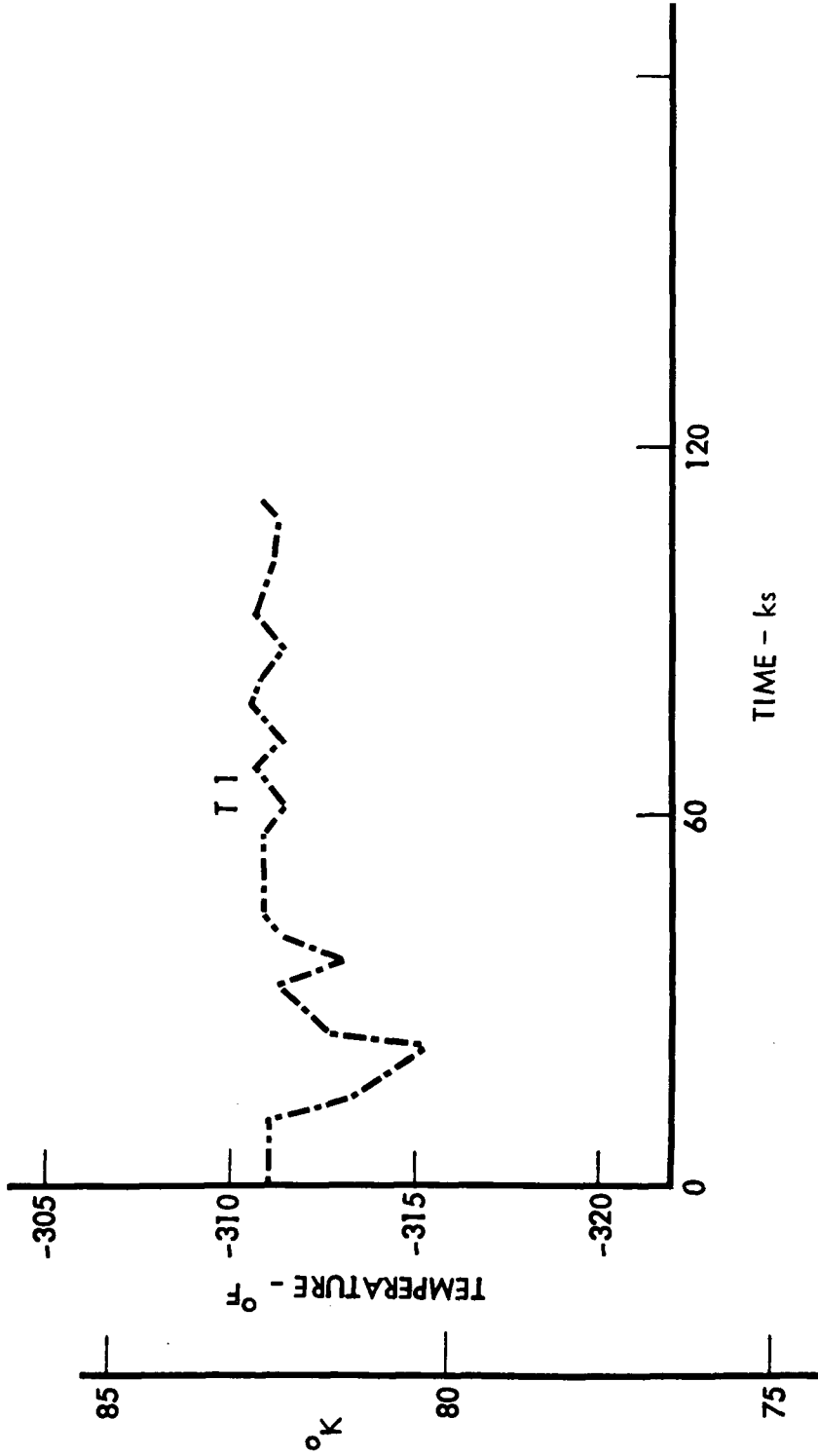


Figure 2.2-53: TEST TANK OUTLET TEMPERATURE, TEST T-2

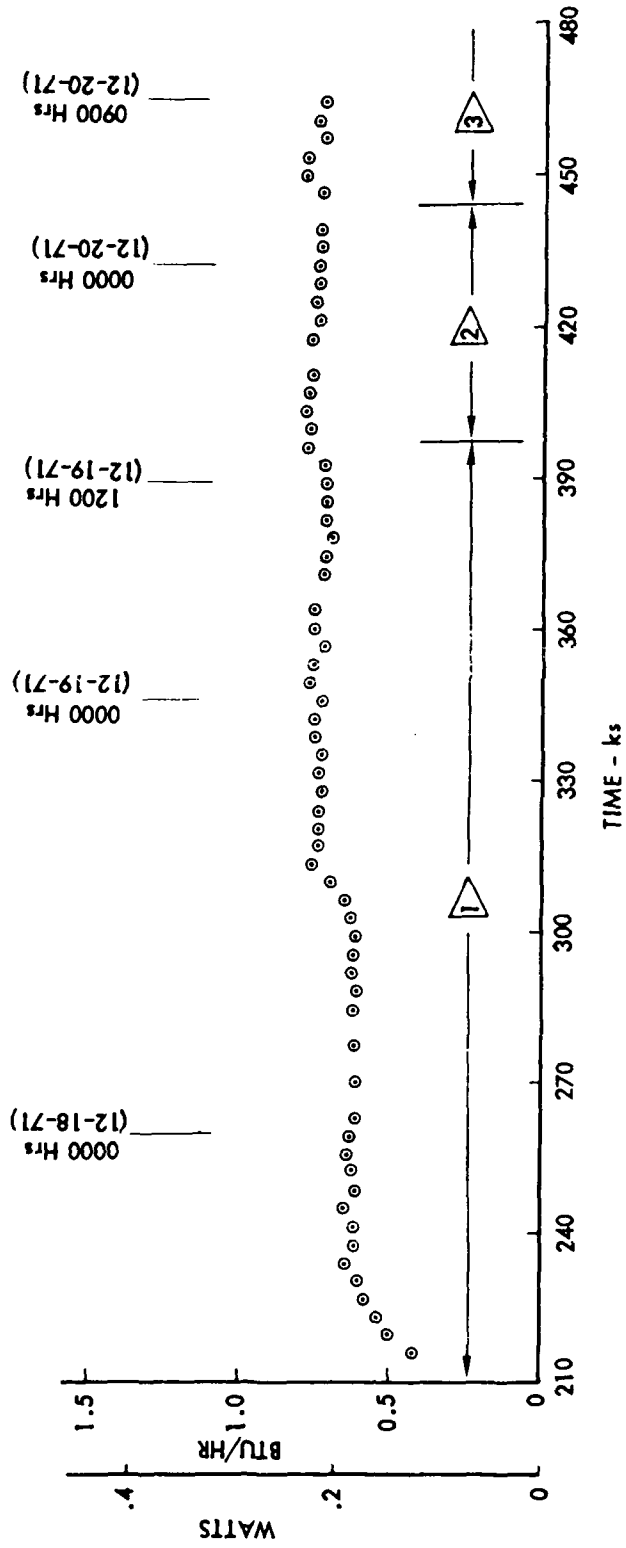
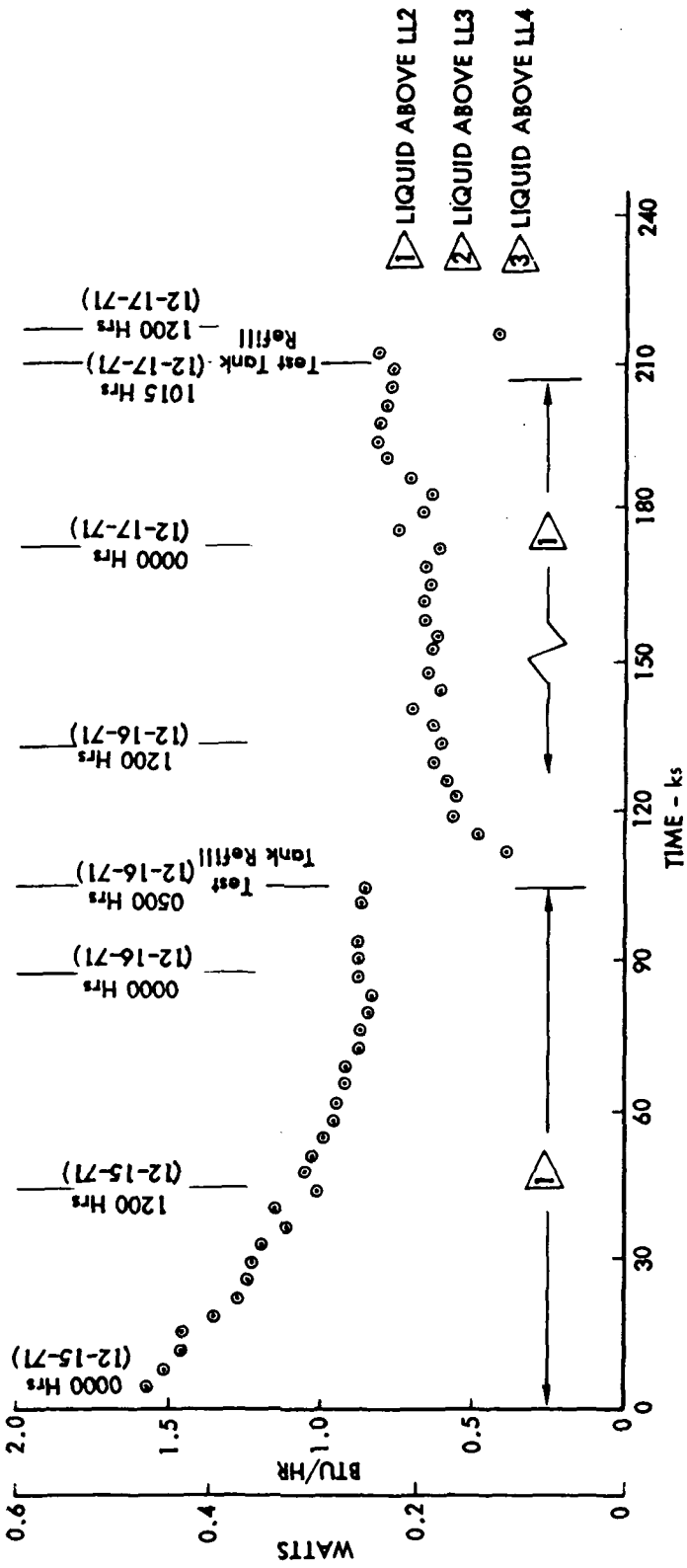


Figure 2.2-54: HEAT FLOW, TEST T-3

the test tank as evidenced from approximately 330 ks to test termination. Figure 2-2-55 presents the test tank outlet temperature. The temperature at the test tank outlet varied less than 3°F (1.7°K) from 240 ksi to test termination.

Barometric and test tank pressures are shown in Figure 2.2-56. The mercury back pressure system functioned properly for the first 36 ks; then test tank pressure followed barometric pressure variations until termination of the run. The trouble was traced to the mercury line connecting the small and large area reservoirs.

The influence of barometric pressure changes on boil-off rate can be seen in Figure 2.2-54. From approximately 240 ks to 312 ks, a heat flow rate of 0.62 Btu/hr (0.18 watt) was obtained. From 312 ks to the end of the test the heat flow was 0.74 Btu/hr (0.22 watt). The test tank pressure of Figure 2.2-56 was seen to increase during the period from 300 ks to 312 ks; then decrease to the end of the test. When the pressure increased, the boiling point was depressed, and thus heat was stored in the LH<sub>2</sub> and tank wall as described in Test T-1. The heat stored during the period from 240 ks to 312 ks was calculated as an average of 0.0367 Btu/hr (0.01 watt). The heat liberated during the period of decreasing pressure was found to be an average of 0.0674 Btu/hr (0.02 watt). The stored heat was then added to the measured boil-off rate during the first period mentioned to derive a value of  $0.62 + 0.04 = 0.66$  Btu/hr (0.19 watt). The heat released during the latter period was subtracted from the measured value to obtain  $0.74 - 0.07 = 0.67$  Btu/hr (0.20 watt). The correlation using this approach was good; thus, a boil-off heat flow value of 0.67 Btu/hr (0.20 watt) was selected for this test series. The heat of vaporization of LH<sub>2</sub> varied only 0.05% through the range of pressure change; thus, the effect in converting mass flow rate to heat flow was negligible.

Figure 2.2-26 shows the inside and outside temperatures on the insulation side wall for Test T-3. Poor correlation is seen throughout. No attempt was made to adjust properties to obtain better agreement for two reasons. First, any significant change in assumed properties would have been detrimental to Tests T-1 and T-2 correlations. Second, little hope was seen in obtaining close correlation, since most of the indicated measured temperatures were higher than boundary temperatures on either side of the insulation.

All data were reviewed carefully and test personnel were consulted in an attempt to correct what appeared to be an error in the measured temperatures. The approximation of true steady-state conditions at the measurement time selected, and the existence of the intended test vessel, guard vessel, and shroud temperatures were verified. No explanation was found for the large difference between expected and measured temperatures. With this large discrepancy in the overall level of temperatures, no attempt was made to examine or explain trend differences between analytical and experimental results.

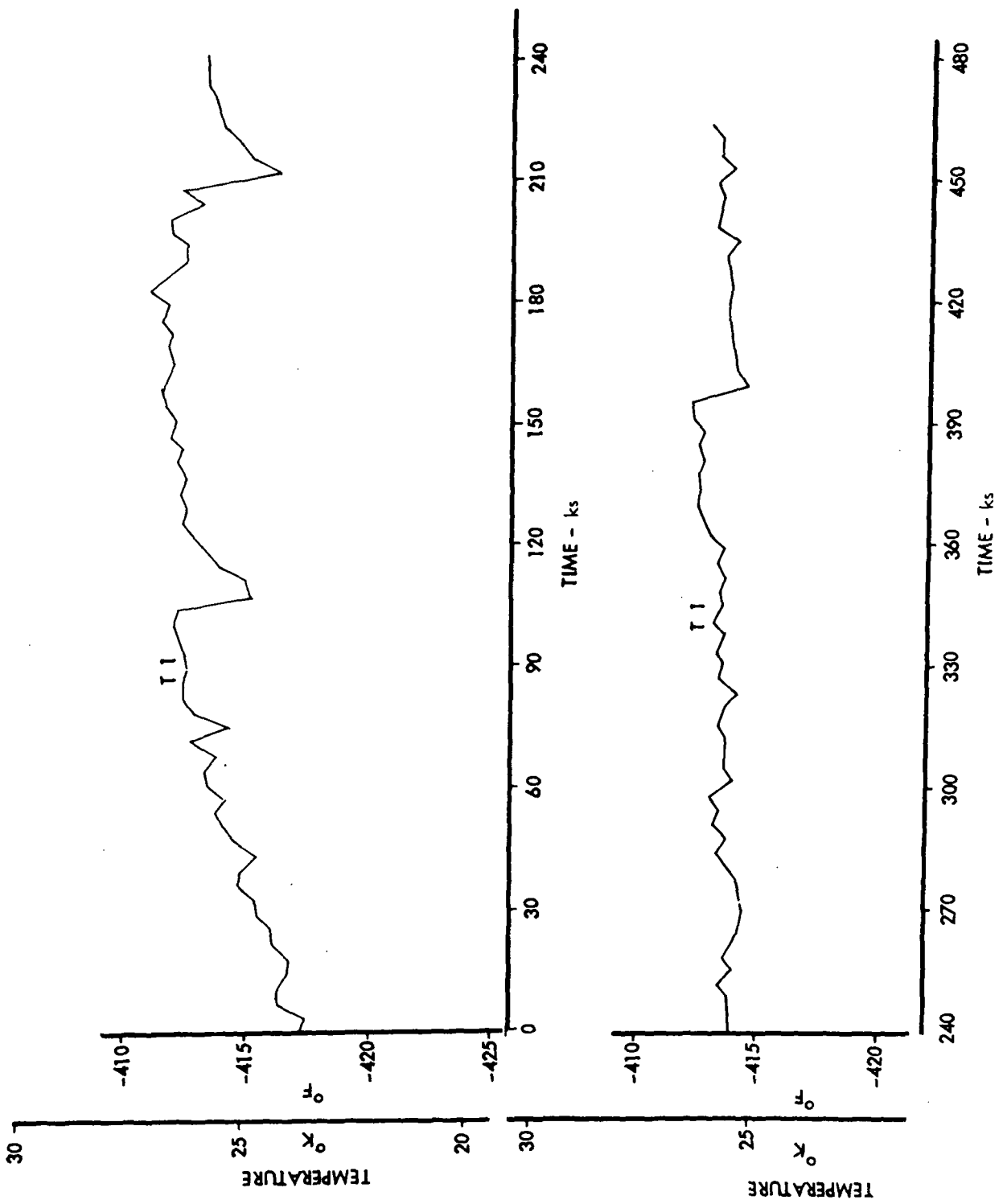


Figure 2.2-55: TEST TANK OUTLET TEMPERATURE, TEST T-3

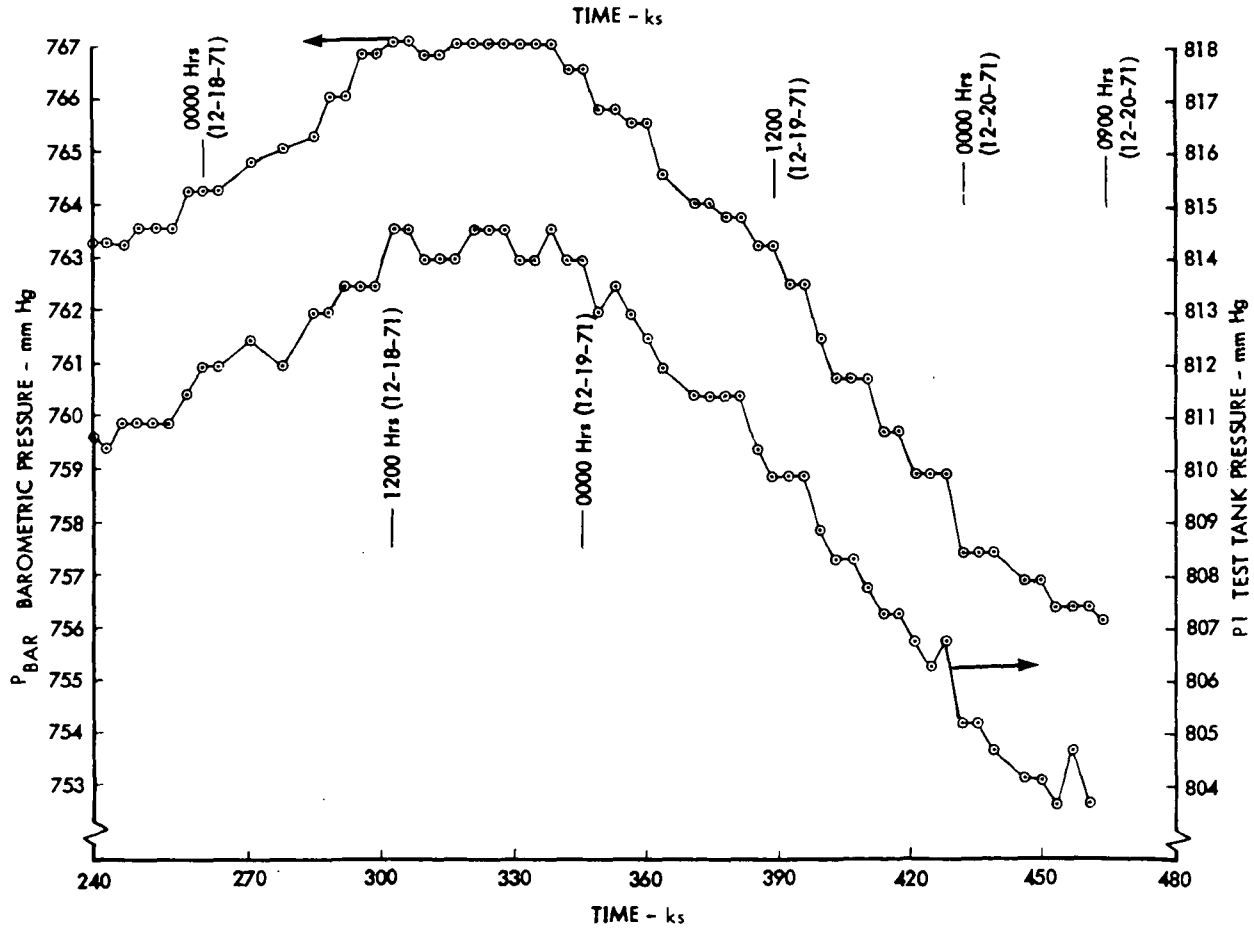
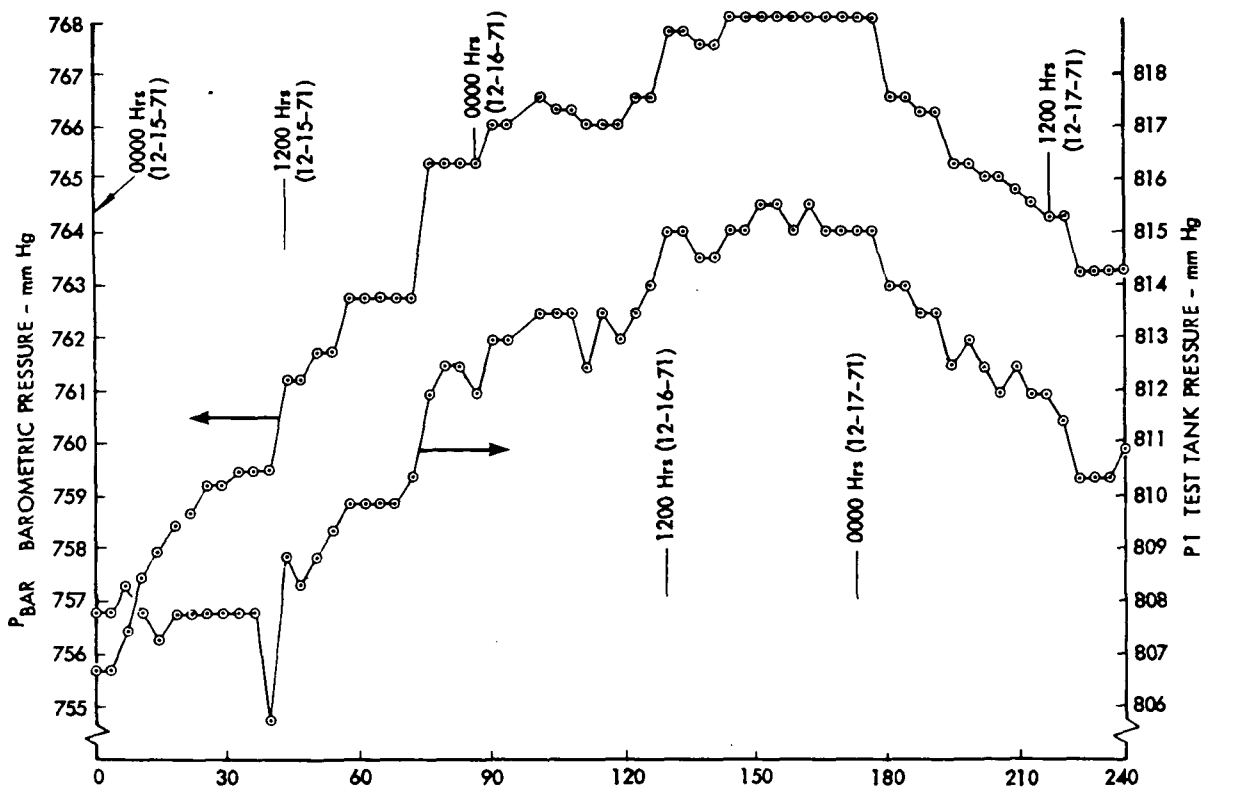


Figure 2.2-56: TEST TANK AND BAROMETRIC PRESSURE, TEST T-3

Figure 2.2-27 which shows longitudinal joint section temperatures for Test T-3 continues the discrepancies seen in Figure 2.2-26, and offers no further clue as to the source of the problem.

Figure 2.2-28 shows analytical predictions of temperatures in the vicinity of a fastener at conditions of Test T-3. Like Test T-2, there are no measured values available for correlation with this distribution.

The heat flow comparison for Test T-3 shown in Table 2.2-2 continues the large, unexplained disparity between predicted and measured thermal results for this test. An additional computation of heat flow for Test T-3 was carried out utilizing measured insulation inner surface temperatures rather than predicted temperatures. Because of the localized instrumentation grouping, considerable extrapolation of measured temperatures was necessary to obtain full area coverage of the insulation surface. The result of this more empirical approach was a slightly improved, but still far from satisfactory predicted heat flow. It is pointed out that regardless of results, this approach could not be regarded without suspicion because a similar computation utilizing insulation outer surface measured temperatures would have yielded a negative basic heat flow ( $Q_{\text{basic}}$ ).

Test S-1: Upon completion of the first three thermal performance tests, the test article was removed from the calorimeter assembly, and all instrumentation on the MLI was removed.

The first structural test involved two axis vibrations. Figure 2.2-57 shows the test article prepared for transverse axis testing. Longitudinal axis testing was performed by rotating the shaker pot  $90^\circ$  to the vertical position and mounting the part on top. Accelerometers were placed at the mid-point and outside end to measure response, and on the shaker table to serve as input control.

The vibration specification for the test is defined in Figure 2.2-58. The curve for the transverse axis test is shown in Figure 2.2-59. This was a full level random vibration test run for five minutes at 3.1 G's RMS. The MLI and frame showed only slight response, so the test was repeated at 6 G's RMS for 3 minutes. This procedure was followed for the longitudinal axis test also. The part was examined for evidence of damage. The only detectable change was two, 1-inch (2.5 cm) long tears in the inner aluminized mylar layer, originating at nylon fasteners. These fasteners can be seen on the interior of the part in Figure 2.2-10. The heads of the fasteners were bonded to the net and adjacent aluminized mylar layer.

Test S-2: The acoustic environment test was conducted by placing the part in a closed cell containing an air horn. In this way the acoustic energy was applied to all surfaces simultaneously. Microphones were located three places,  $120^\circ$  apart to measure input and aid in shaping the test curve. Figure 2.2-60 shows the test setup, and Figure 2.2-61 shows the acoustic environment.

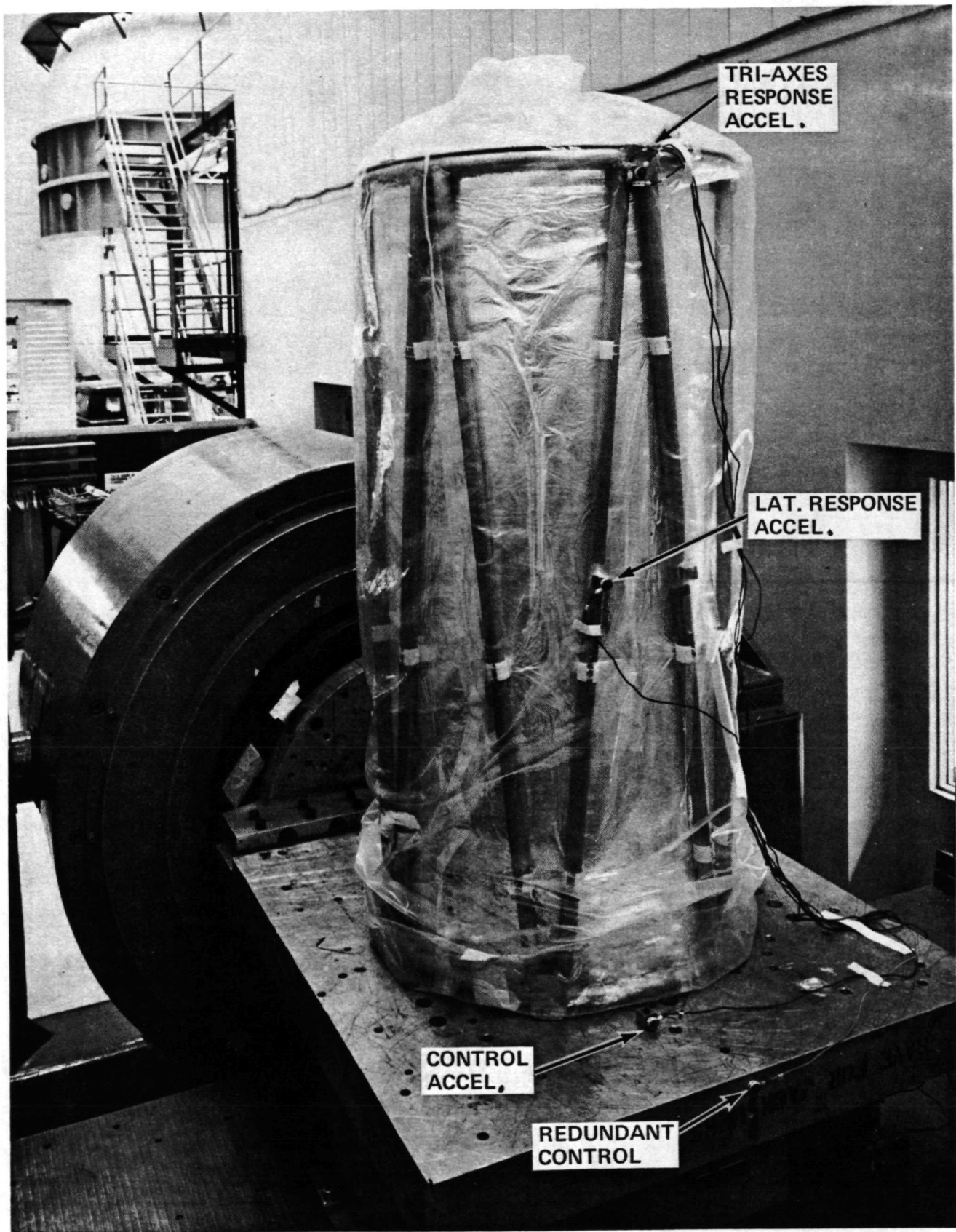


Figure 2.2-57: VIBRATION TEST ASSEMBLY

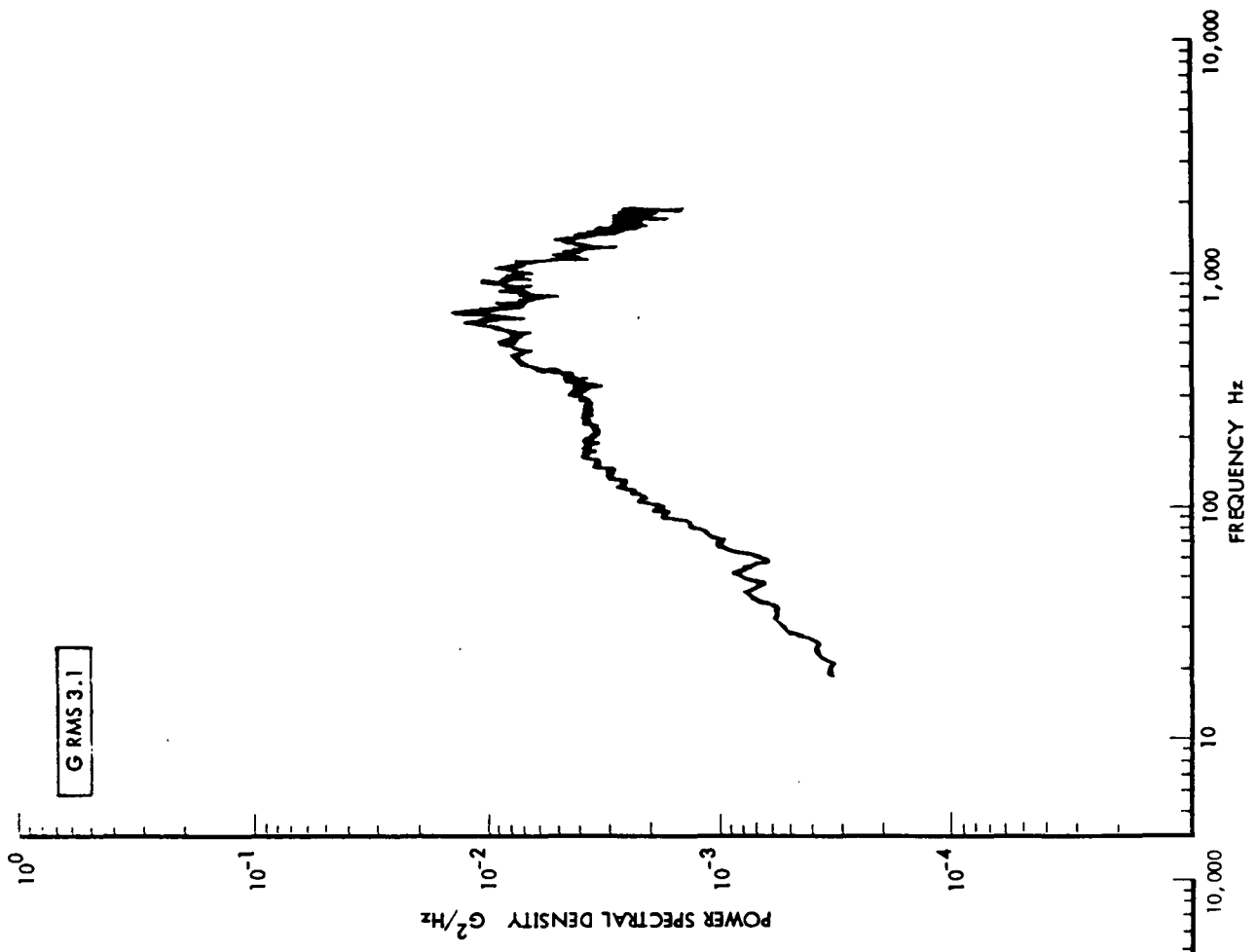


Figure 2.2-58: VIBRATION TEST ENVELOPE

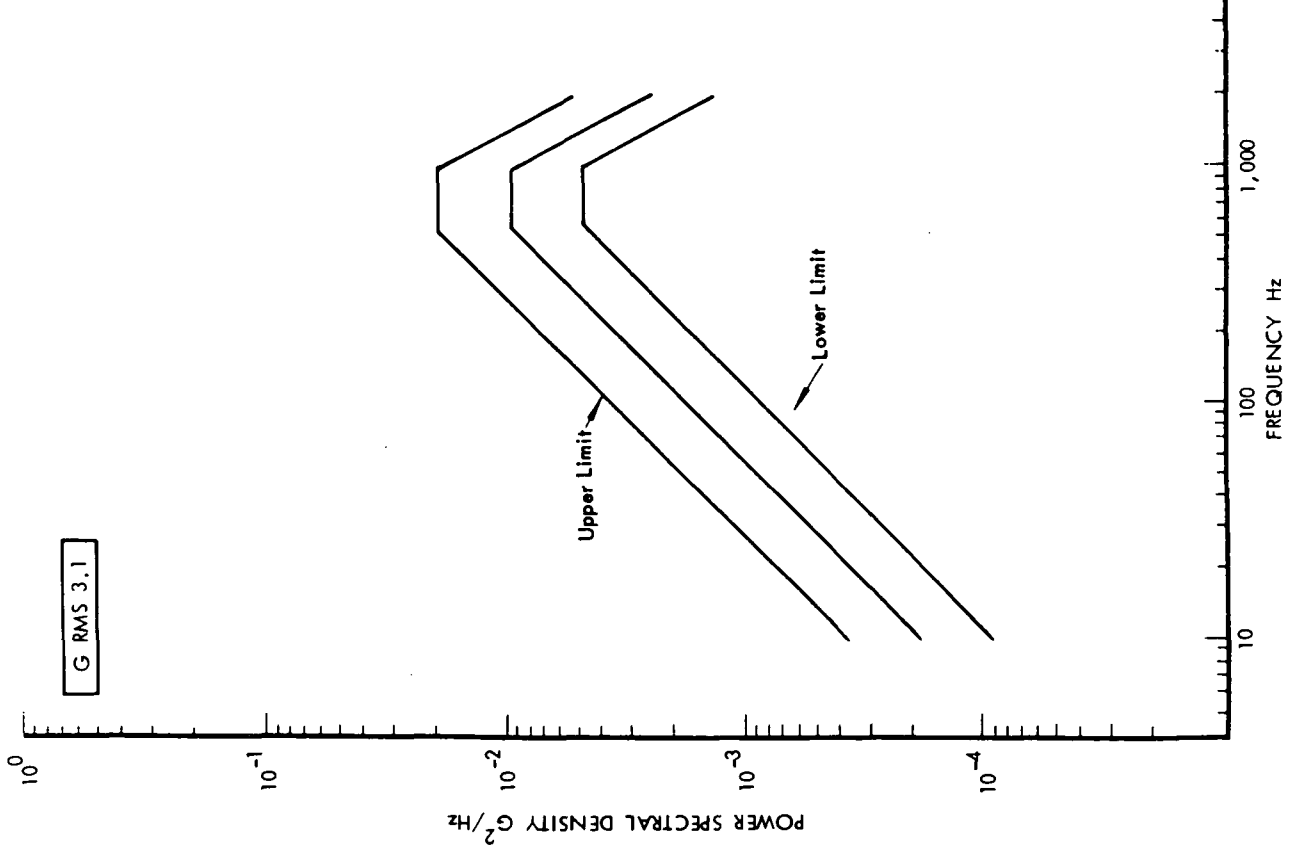


Figure 2.2-59: VIBRATION TEST RESULTS

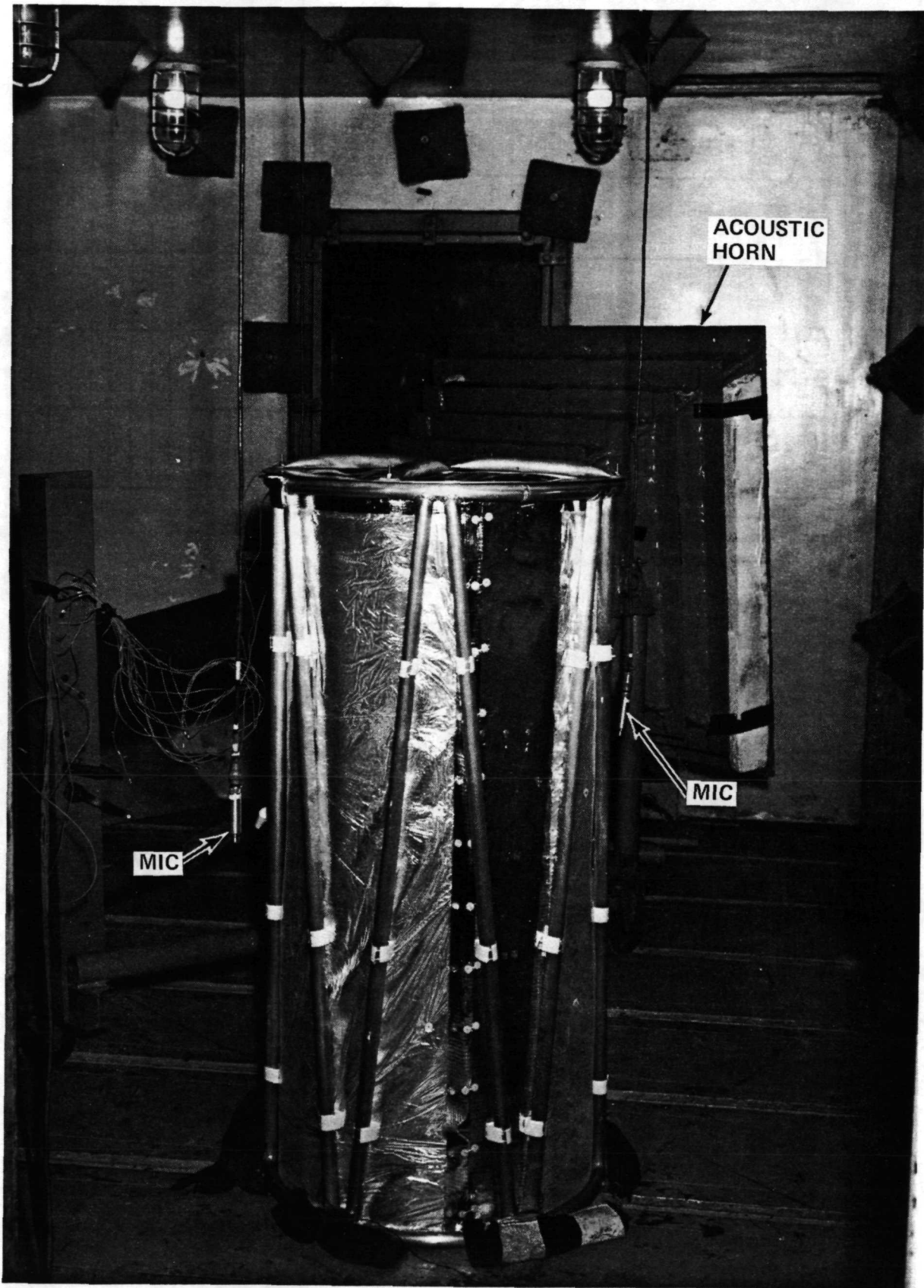


Figure 2.2-60: ACOUSTIC TEST ASSEMBLY

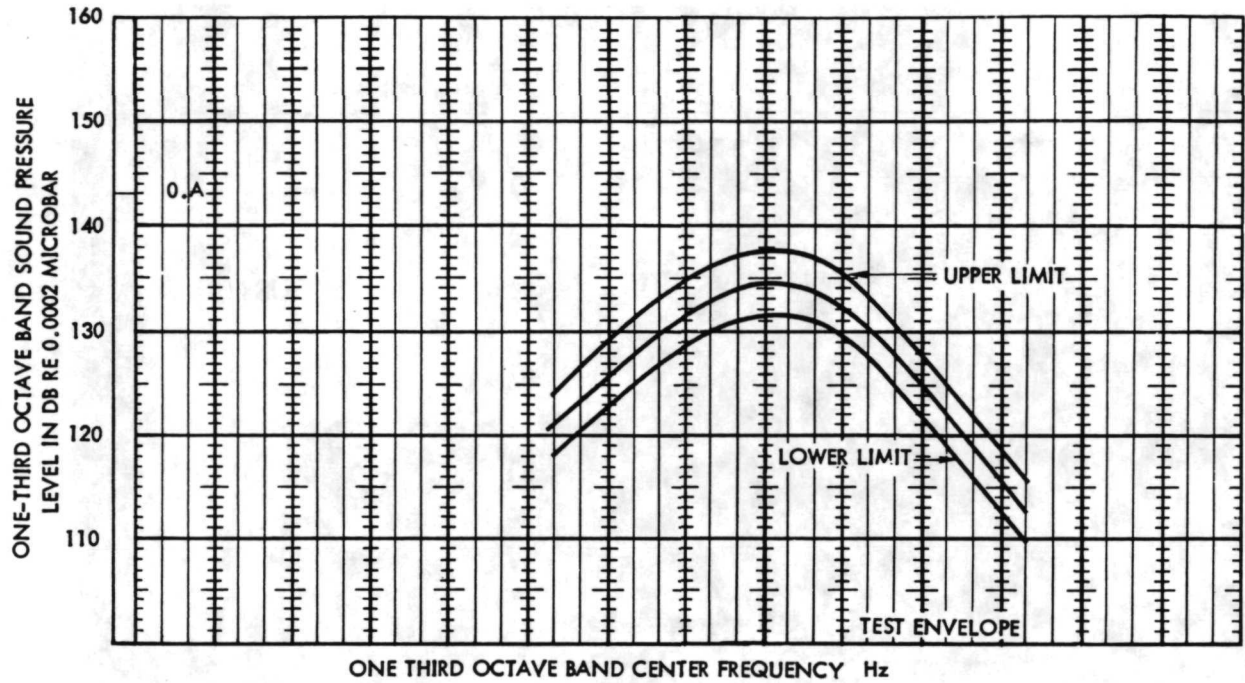


Figure 2.2-61: ACOUSTIC ENVIRONMENT

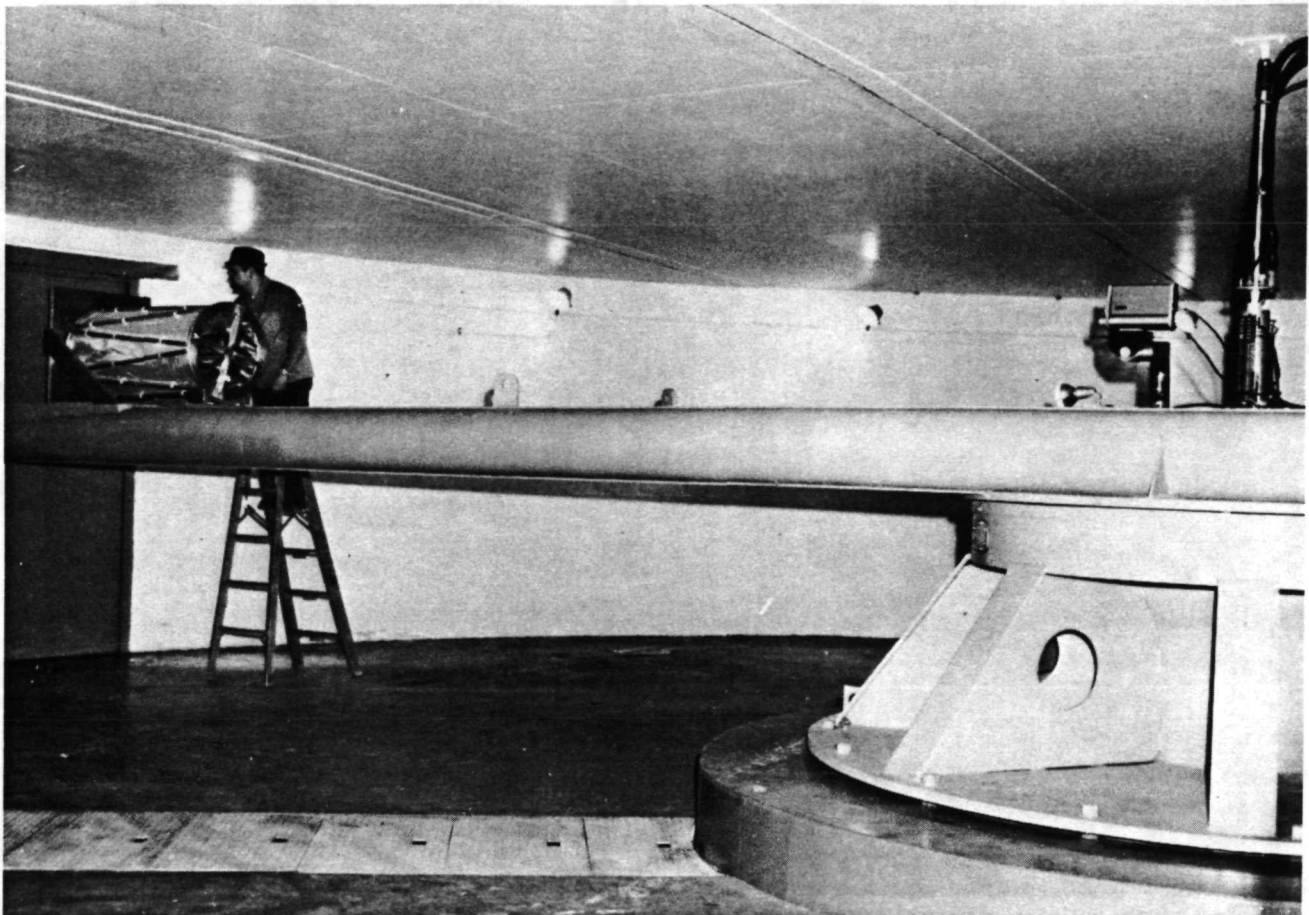


Figure 2.2-62: CENTRIFUGE

An initial run was conducted for 1-1/2 minutes, up to 137 db, to verify the curve. The actual test run took 3 minutes with a peak level of 143 db.

After completion of the test an examination of the part showed that there was no damage. During the test run considerable motion of the outer MLI layer was observed, predominantly in unsupported areas. It appeared that this motion was sufficient to cause tears at the points of attachment; however, none developed.

Test S-3: The acceleration test was conducted on a centrifuge at the Naval Torpedo Station. The test article was mounted with the closed end towards the axis of the centrifuge, 22.7 ft (6.9 m) from the center as shown in the photograph of Figure 2.2-62. The arm was rotated at the rate of 22.75 RPM. There was no visible damage to the part upon examination after test.

Test T-4: The part was returned to the calorimeter test site and instrumented with thermocouples for the next series of tests. Figure 2.2-6 showed the quantity and location of instrumentation. The previous locations were not repeated because similar thermal performance was expected.

The test was a repeat of Test T-1 after application of vibration, acoustic, and acceleration loads. The measured boil-off results are shown in Figure 2.2-63. The value obtained at 227 ks was 8.5 Btu/hr (2.5 watt), 0.9 Btu/hr (0.26 watt) greater than Test T-1.

The mercury backpressure system was functioning correctly for this test as evidenced in Figure 2.2-64.

Figure 2.2-65 shows temperatures at the test tank outlet T1. The spikes in the curves occurred when the test tank was refilled.

Temperature correlations for Test T-4 are shown in Figures 2.2-29 and 2.2-30. Since the conditions and configuration for Test T-4 were the same as for Test T-1, the analysis results for both temperatures and heat flow were taken directly from the analysis of Test T-1. The agreement between the predicted and measured temperatures for Test T-4 was satisfactory, but there was insufficient instrumentation to permit verification of analytical prediction accuracy for large areas of the insulation assembly.

Examination of the heat flow correlations in Table 2.2-2 shows that the disparity between predictions and measurements increased significantly from Test T-1 to Test T-4. Apparently, the structural tests of Test T-4 and possibly thermal and pressure cycling and handling in Tests T-2 and T-3 caused some degradation in MLI performance.

Test T-5: This test incorporated a fiberglass tubular strut connected between the aluminum frame work and the calorimeter tank. The support penetrated the

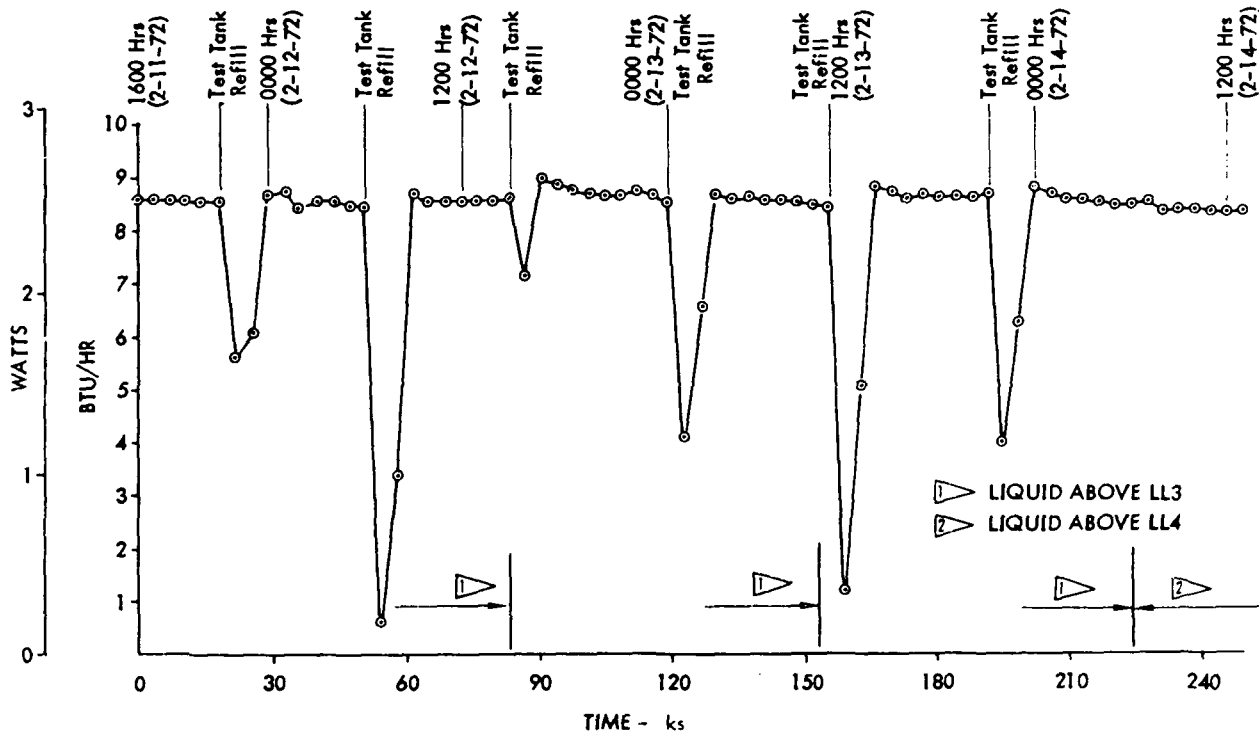


Figure 2.2-63: HEAT FLOW, TEST T-4

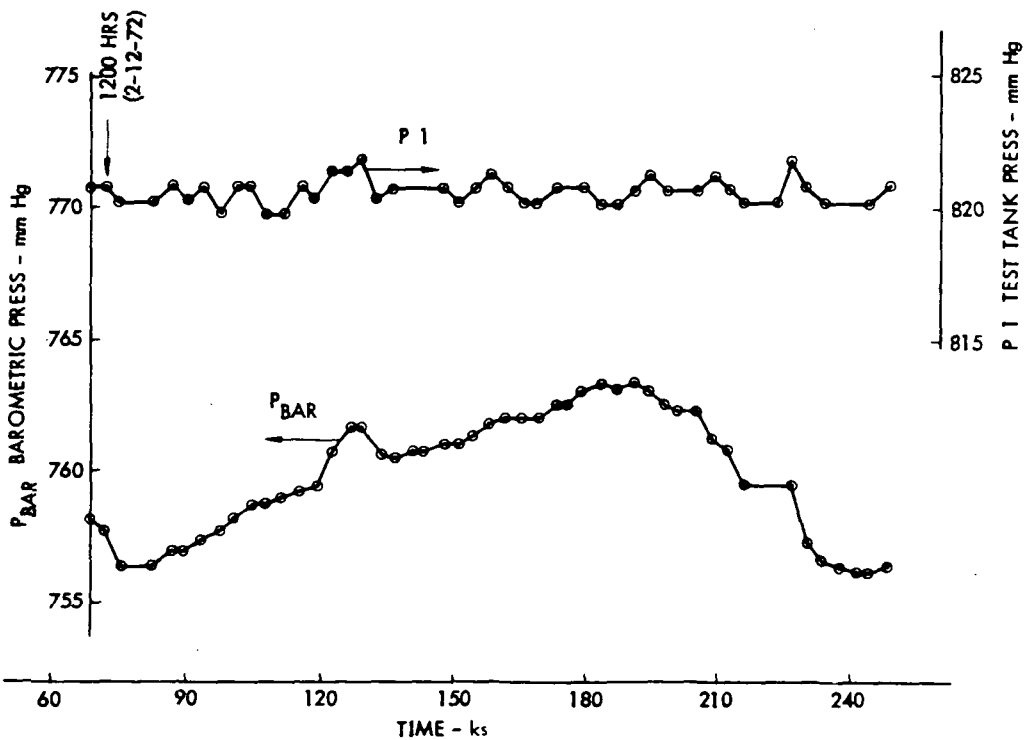


Figure 2.2-64: TEST TANK AND BAROMETRIC PRESSURES, TEST T-4

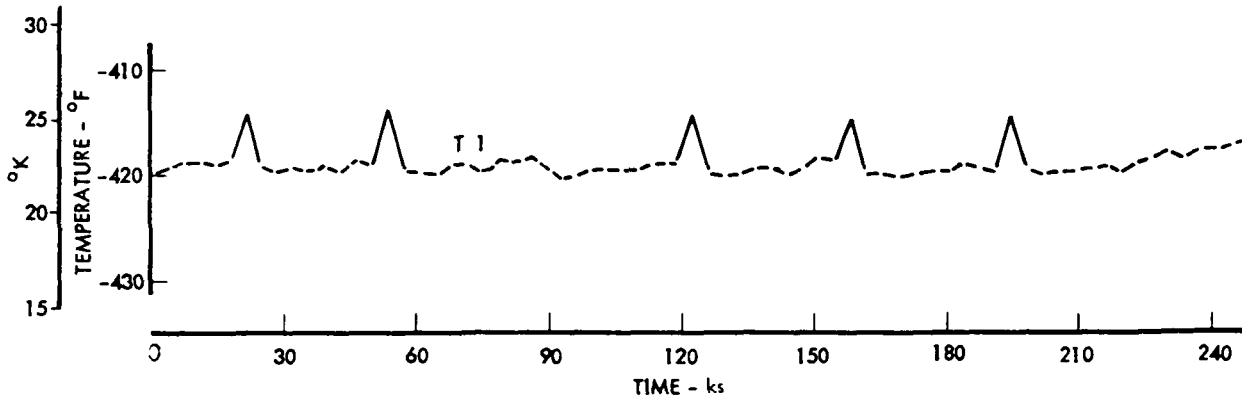


Figure 2.2-65: TEST TANK OUTLET TEMPERATURE, TEST T-4

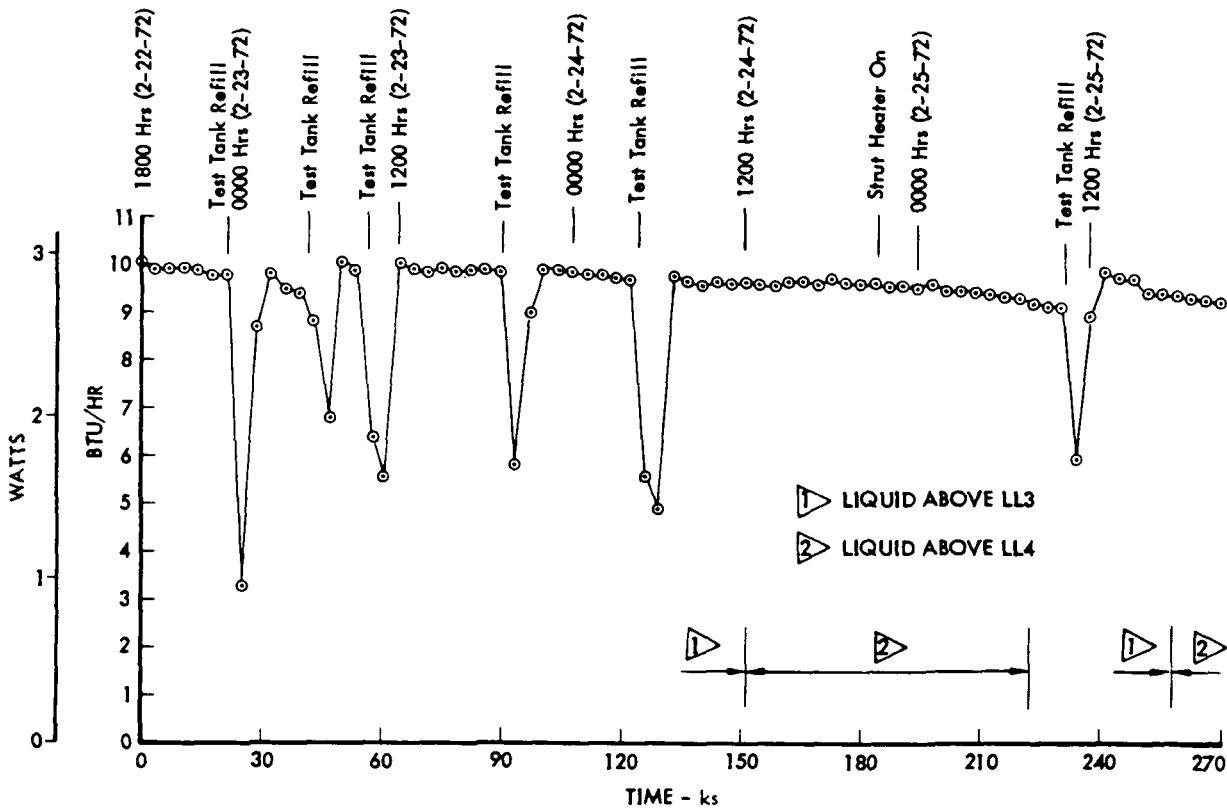


Figure 2.2-66: HEAT FLOW, TEST T-5

MLI through a small rectangle cut from the blanket. The warm end of the strut was equipped with a resistance heater.

Boil-off test results are shown in Figure 2.2-66. A value of 9.6 Btu/hr (2.8 watt) was obtained at approximately 150 ks before the heater was activated. The heater was operated during that same boil-off cycle to balance the warm end temperature with another location on the aluminum frame-work. Prior to heater activation the warm end of the strut had been about 4°F (2.2°K) cooler than the other location. The heater power required to raise the temperature 4°F (2.2°K) ranged from 0.29 to 0.31 watts (1 to 1.1 Btu/hr). The effect of increasing the outboard end temperature disappeared a short distance along the strut towards the calorimeter tank.

The boil-off test was continued with a nearly constant heater power setting. The boil-off curve of Figure 2.2-66 did not reflect the addition of heat at the outboard end of the strut as evidenced at 185 ks. Another test tank fill was made at 232 ks and a heat flow of 9.4 Btu/hr (2.8 watt) was obtained.

Test tank and barometric pressures are shown in Figure 2.2-67, and the temperature at the tank outlet in Figure 2.2-68.

The inclusion of the tank support strut in Test T-5 necessitated the incorporation of an additional analytical model in the thermal analysis of the test. This model is illustrated in Appendix E. It was intended to represent the strut; its insulation, fittings, and interior baffles; and a sufficient area of the main MLI surrounding the penetration to isolate its effects. Analysis of this model provided the predicted temperatures for comparison with the measured values and the incremental heat leak associated with the strut.

A number of additional assumptions were employed along with the strut analytical model in the simulation of Test T-5. These assumptions were:

- (1) Effective normal and lateral conductivities of strut MLI were equal to those of the main MLI.
- (2) Strut MLI was in perfect thermal contact with the strut and strut end fittings.
- (3) There was no radial or circumferential thermal gradient in the strut walls.
- (4) Heat transfer between strut MLI edges and main MLI and between main MLI edges and strut attachment clevis was by radiation only.
- (5) Joint resistance at pinned fittings was equal to twice the resistance of the fitting itself.

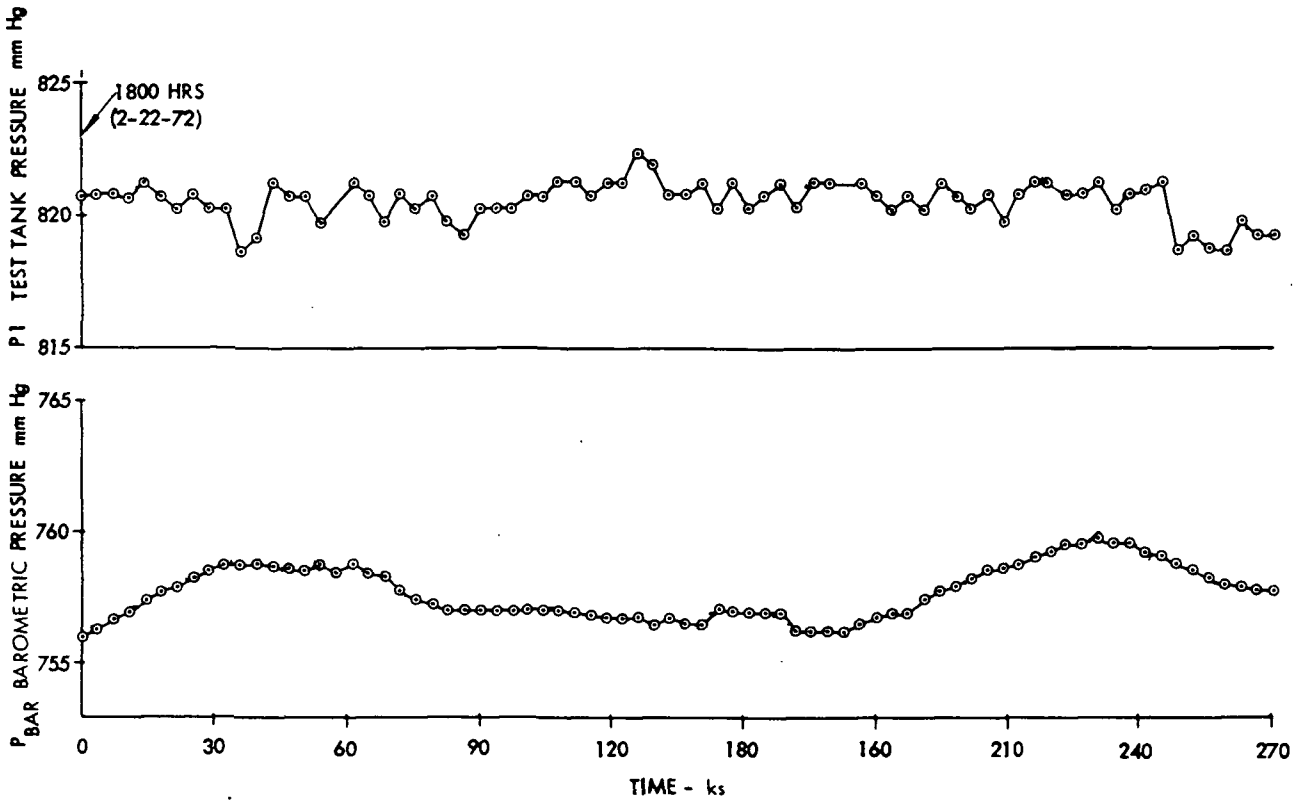


Figure 2.2-67: TEST TANK AND BAROMETRIC PRESSURES, TEST T-5

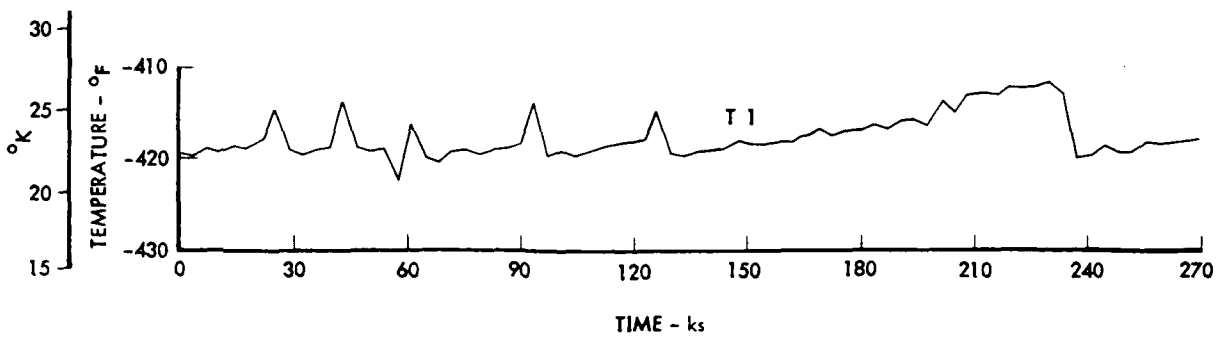


Figure 2.2-68: TEST TANK OUTLET TEMPERATURE, TEST T-5

- (6) Joint conductance of bolted joint (strut fitting to strut attachment pad) was based on conductance through bolt, with perfect thermal contact at bolt head and at threads, no contact elsewhere.
- (7) All bonded interfaces were in perfect thermal contact.
- (8) Aluminized mylar baffles within the tube installed to block internal radiation.

The computation of effective conductivity of the strut, minus its MLI, was accomplished using data interpolated from the tables of Reference 2.2-2 to account for the coupling of conduction and radiation in the presence of the internal baffles.

Although Test T-5 was run with the strut heater both off and operating, the measured total heat flow showed no significant effect of heater activation. It was concluded, therefore, that the heater did not function as a heat source as far as heat flow to the test tank was concerned. It appeared that essentially all heater output found its way to the guard tank, possibly by conduction through the aluminum frame-work.

The possibility of heater power being lost through the frame-work was checked by computing the heat flow indicated by the temperature gradients through T44 and T417 through T420. The result accounted for approximately one-half of the heater power. A re-evaluation, considering thermocouple measurement tolerances, however, indicated that all of the heater power could have been conducted away by the truss.

Influence of the heater was observed at thermocouples T44 and at T41 on the strut (see Figure 2.2-31). These observations formed the basis for the assumed boundary conditions for the analysis of Test T-5. With the heater off, the thermal shroud temperature was taken as the hot boundary temperature, as for previous analyses. With the heater activated, an additional boundary temperature located at the strut attachment (heater) pad, and fixed at the measured value at T44, was established.

Strut temperatures are shown in Figure 2.2-31. The large difference between predicted and measured temperatures near the hot end of the strut, in spite of perfect or near-perfect agreement at T44, strongly indicates a greater than assumed joint resistance at the intervening pin joint. A change in joint resistance to improve temperature correlations, however, would have been detrimental to the heat flow correlation, as will be described later.

Correlations of temperatures on the surfaces of the main MLI in the vicinity of the strut penetrations (Figures 2.2-32, 2.2-33, and 2.2-34) show approximately the same level of agreement as was seen for the same areas in Tests T-1 and T-4.

The fact that the predicted temperature curve of Figure 2.2-34 lies below the measured data at all points except very near the penetration may be an indication that the conductance into the main MLI at the penetration was less than assumed while the lateral conductivity through the MLI at this section was greater than assumed. If this observed difference between predicted and measured temperatures prevailed over the entire MLI area influenced by the strut penetration, a deficiency in the predicted strut penetration heat leak could result.

The details of the temperature predictions (Appendix E) indicate that the area of main MLI surrounding the strut penetration selected for the analytical model was adequate to isolate the penetration effects. This conclusion, however, is not fully confirmed by the experimental temperature distribution (Figure 2.2-34).

The heat flow correlations for Test 5 are shown in Table 2.2-2. The heat leaks unaccounted for at this stage of the test program, as indicated by the difference between predicted and measured values for Test T-4, had become significant. It was decided, therefore, to use the measured total heat flow value from Test T-4 as the basic heat flow value ( $Q_{\text{basic}}$ ) in computing Test T-5 total heat flow predictions. Since this empirical  $Q_{\text{basic}}$  value included the effect of the longitudinal joint and of the fasteners, these incremental contributions were not calculated for Test T-5 and are not shown separately in Table 2.2-2.

With the predicted heat flow for Test T-5 computed as described above, the theoretical value approximates the measured value to an accuracy comparable to that achieved for the other tests (except Test T-3). When the difference in measured heat flow between Tests T-4 and T-5, i.e., the apparent measured strut heat leak, is compared with the predicted strut heat leak ( $Q_{\text{strut}}$ ), however, a large relative difference is seen:

$$Q_{\text{strut, meas}} = Q_{\text{tot, meas}_5} - Q_{\text{tot, meas}_4} = 10.406 - 8.948 = 1.458 \text{ Btu/hr (0.43 watt)}$$

$$Q_{\text{strut, pred}} = Q_{\text{strut}} \text{ (Table 2.2-2)} = 0.1507 \text{ Btu/hr (0.04 watt)}$$

Part of the observed deficiency in predicted strut penetration heat leak was anticipated from the temperature correlations of Figure 2.2-31. The temperature differences are not sufficient to account for the entire difference in heat flow, however, unless the strut penetration thermal influence extended over a much larger area of main MLI than the analysis indicated. Examination of temperature distributions on the strut (Figure 2.2-31) indicated that the effective conductance, and therefore the heat flow contribution of the strut and its fittings were probably less, not greater, than predicted. Thus, no adjustment in analysis properties or assumptions suggested by one set of correlations could be applied without degrading other correlations from this or preceding tests.

Test T-6: A stainless steel fluid line was incorporated in this test configuration. The data from a succession of boil-off test runs is shown in Figure 2.2-69. A stabilized value of 12.1 Btu/hr (3.5 watt) with liquid at level sensor 3 was indicated at 271 ks.

The heaters on the warm ends of the strut and the fluid line were activated at about 300 ks. The boil-off rate increased for a period of time and then stabilized at about 12.5 Btu/hr (3.7 watt) when the liquid level was at sensor 4. Another fill was made and after the fill a value of 13.0 Btu/hr (3.8 watt) was obtained with liquid at level sensor 3. The test was continued until the liquid dropped to LL4. At that point a value of 12.5 Btu/hr (3.7 watt) was obtained, which verified the data point preceding the fill. The test was terminated at that point.

After heater power was applied, the temperatures along the metallic frame members increased as expected. Sufficient power was applied to raise the warm end temperature of each penetration to the same temperature as a remote location on the aluminum framework. The sum of the heater power applied to the strut and fluid line was approximately 5 Btu/hr (1.5 watt). It took less heater power to maintain the required temperature at the warm end of the fiberglass strut in this test than in Test T-5.

Figure 2.2-70 shows barometric and test tank pressures. There was an intentional increase in back-pressure at 192 ks. The mercury back-pressure system was functioning properly during this test.

The temperature at the tank outlet is shown in Figure 2.2-71.

The simulated fluid line installed for Test T-6 necessitated a further addition to the analytical model. This addition was treated in much the same way as the strut addition for the analysis of Test T-5. The analytical model of the fluid line assembly, including an adjacent area of main MLI assumed to contain the penetration influence, is illustrated in Appendix E. As with the strut penetration, certain additional assumptions were made in this penetration analysis. These were:

- (1) Effective normal and lateral conductivities of the line MLI were equal to those of the main MLI.
- (2) Line MLI was in perfect thermal contact with the tube.
- (3) There was no radial or circumferential thermal gradient in the line walls.
- (4) The joint conductance between the main MLI edges and the line was the "T" joint conductance employed for the main MLI (Table 2.2-1).
- (5) There was no thermal resistance at the line-tank joint.

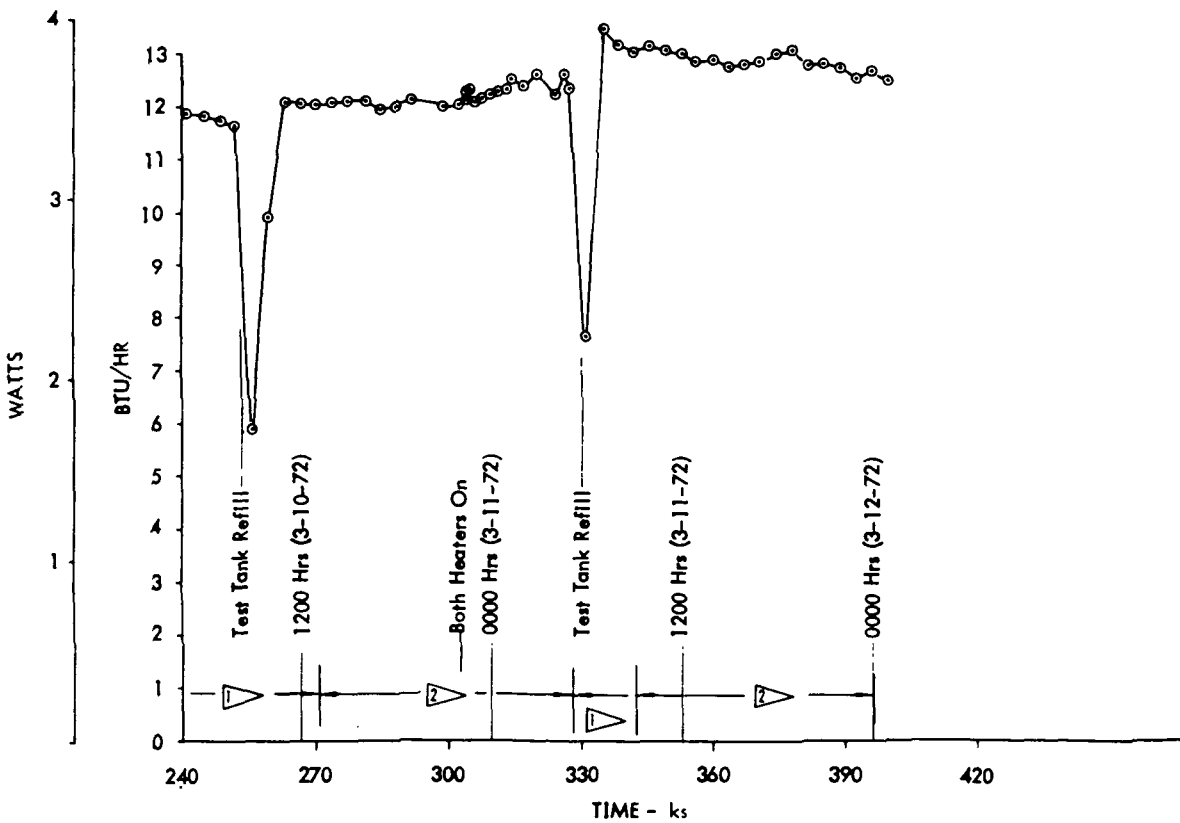
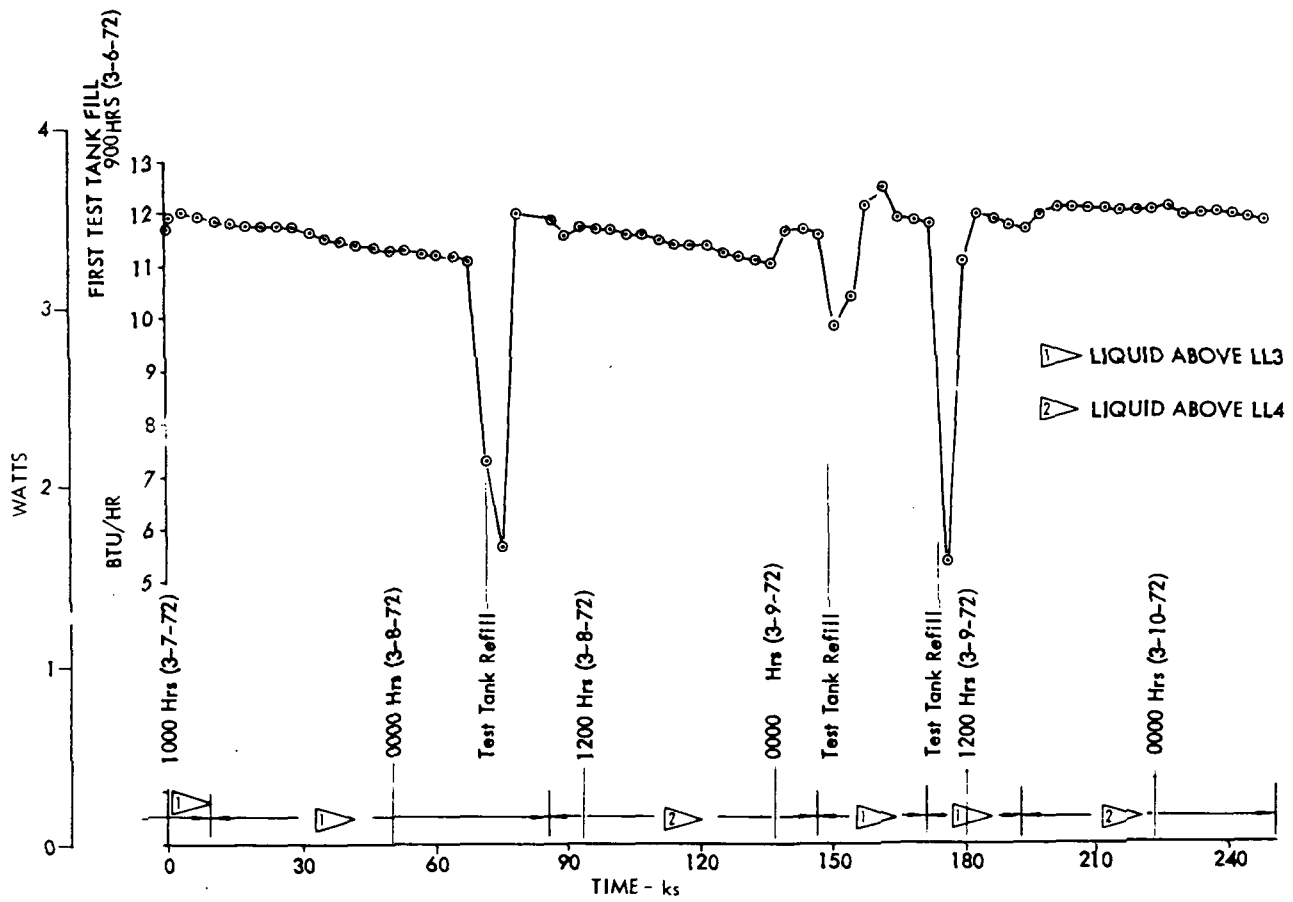


Figure 2.2-69: HEAT FLOW, TEST T-6

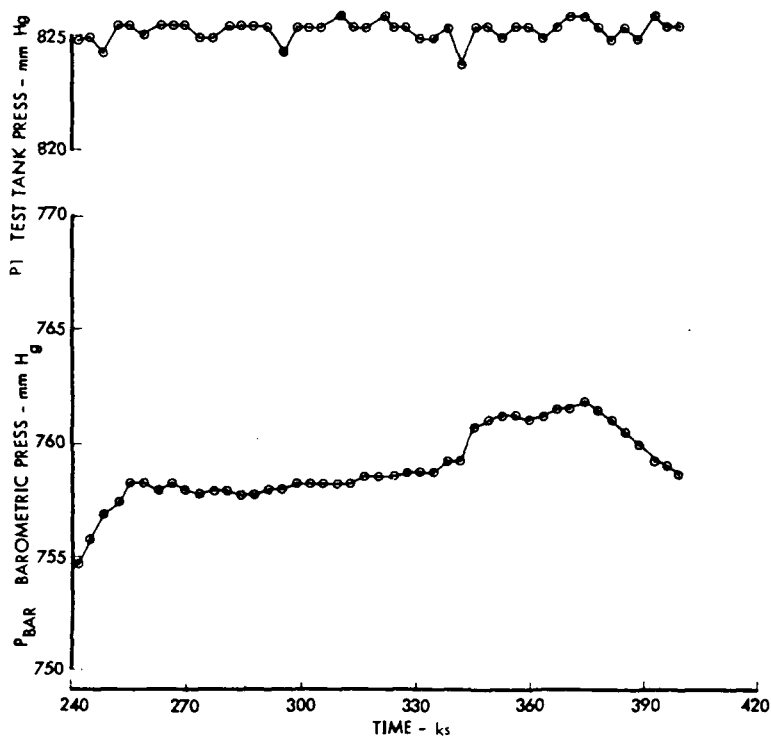
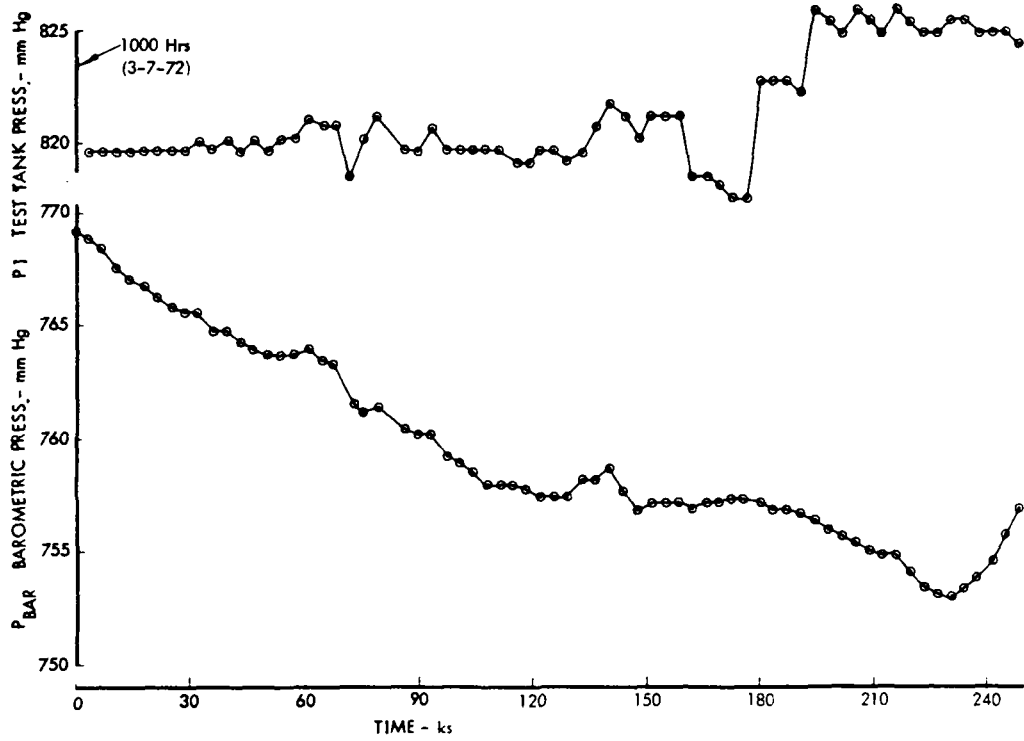


Figure 2.2-70: TEST TANK AND BAROMETRIC PRESSURE, TEST T-6

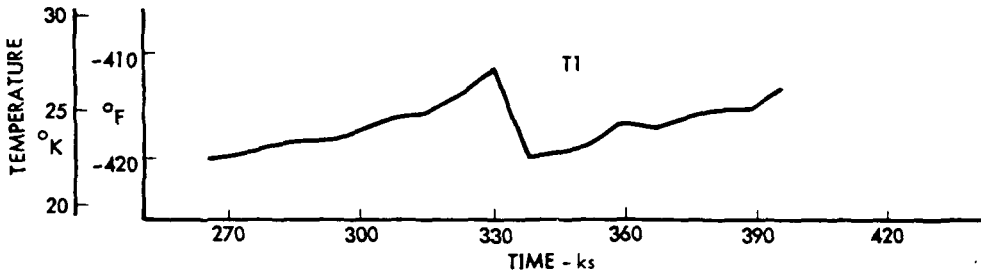
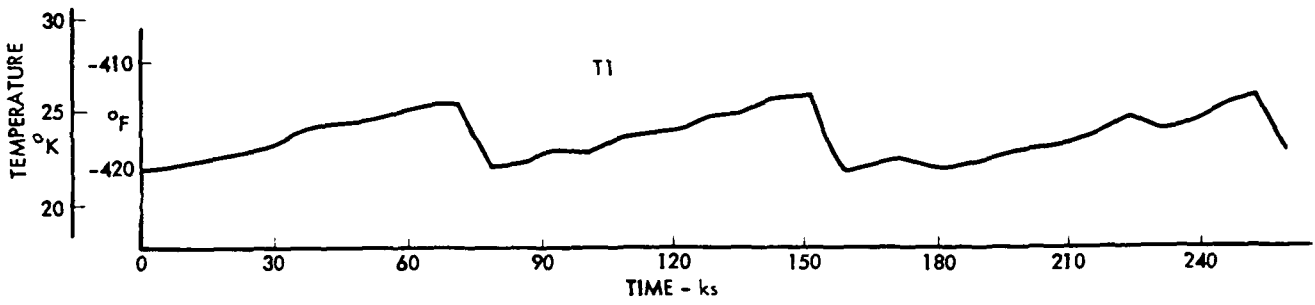


Figure 2.2-71: TEST TANK OUTLET TEMPERATURE, TEST T-6

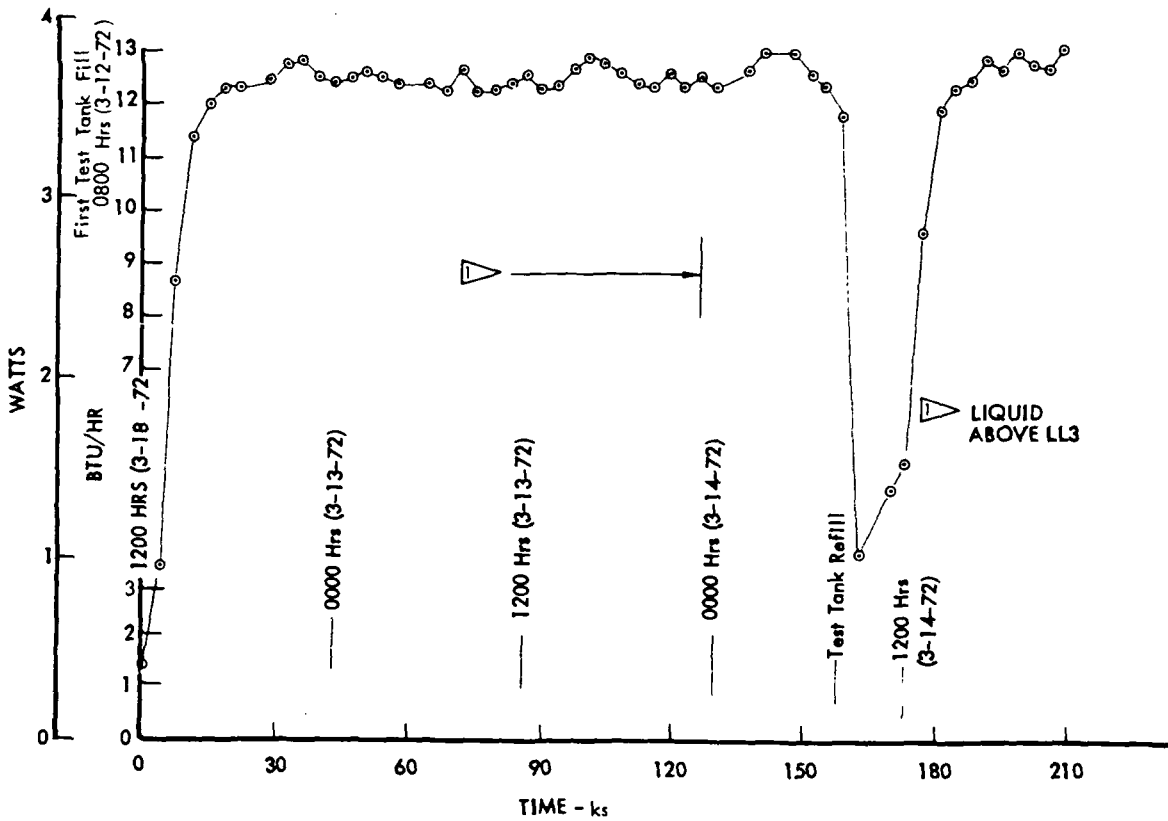


Figure 2.2-72: HEAT FLOW, TEST T-7

- (6) The upper (warm) end of the line was treated as very close but not in thermal contact with the thermal shroud.
- (7) There was no thermal interaction between the fluid line assembly and the strut assembly.
- (8) The cut in the main MLI adjacent to the opening for the line was an ideal cut, i.e., no misalignment of layers occurred and no radiation gap was opened.
- (9) Radiation from warm to cold end within the line was accounted for in the thermal model.

Test T-6, like Test T-5, was conducted with the heaters (line and strut) both off and operating. In contrast with Test T-5, however, the measured heat flow results (Table 2.2-2) from Test T-6 indicate that some, but not all, of the 1.605 watt total heater output reached the test tank. Since there was no way of determining what portion of the fluid line heater output contributed to the line assembly heat leak, the heater was not treated as a heat source in the analysis. Instead, as in the analysis of Test T-5, a temperature boundary condition was established to account for the effect of the heater when operating. The measured temperature employed in this case was that at T525, assumed to exist at the heater location on the line.

Figure 2.2-35 shows measured and predicted temperatures along the fluid line. The temperature distributions indicated the possibility of greater thermal resistance near the lower (cold) end of the line than was assumed. The most probable source of error was the assumption of zero resistance at the line-tank interface. Analytical predictions were not made for the locations of T525, T526, T530, or T531 since the aluminum framework and the line support plate were not included in the analytical model. A large lump of adhesive inside the line near its warm end could have affected heat flow by blocking internal radiation.

Temperatures on the main MLI surfaces at a section through the penetration opening are shown in Figures 2.2-36 and 2.2-37. Correlations for the inner surface show roughly the same trends as for the corresponding section adjacent to the strut penetration in Test T-5. The indicated rise in measured temperature from T511 to T513 has not been explained.

Temperatures predicted for the inner surface of the main MLI around the periphery of the area included in the analytical model (Appendix E) are generally higher than the level predicted for that part of the insulation assembly without penetrations. Thus, it is indicated that the area of main MLI incorporated as a part of the analytical model was not sufficient to entirely isolate the penetration effects. It may be expected, therefore, that some deficiency would exist in the predicted

fluid line penetration incremental heat flow. Experimental temperatures were not measured over a large enough area to confirm or deny this possibility.

Figure 2.2-38 shows temperatures on the MLI surfaces at a section through the cut in the main MLI just below the fluid line penetration. Most of the deviation in temperatures at this section from values at remote locations resulted from lateral conduction from the penetration and from the intervention of the fluid line in the main MLI test tank radiation interchange. Some effect was due to the lower surface emittance of the X-850 laminate as compared to a net covered layer of aluminized mylar covering the cut. No disturbance in predicted temperatures arose from the cut itself, because of the assumptions of no radiation gaps and no layer misalignment and because the cut lay in a plane of thermal symmetry.

The relatively strong influence of the heater on measured temperatures at T519, T521, and T523 has not been explained. A response to radiation from the insulation support truss and the line support plate might have been expected at this section, but the measured outer surface temperatures showed very little such response. Some of the correlation discrepancies near the centerline of the section of Figure 2.2-38 may have resulted from predicted radiation interchange with the rather crude model of the fluid line MLI.

Heat flow correlations for Test T-6 are included in Table 2.2-2. Because of the apparent deficiency in the predicted contribution of the strut penetration for Test T-5, the basic heat flow for Test T-6 ( $Q_{\text{basic}}$ ) was taken as the measured total heat flow ( $Q_{\text{tot, meas}}$ ) from the no-heat part of Test T-5. The  $Q_{\text{basic}}$  for Test T-6 thus includes the strut heat flow, as well as longitudinal joint and fastener heat flow, on an empirical basis.

The comparison of total heater power, 1.605 watt versus total measured heat flow for Test T-6 with heaters on and heaters off indicates that most, but not all, of the heater output escaped through the guard tank. The predicted total heat flow ( $Q_{\text{tot, pred}}$ ) for the heaters-on part of the test also included 0.279 Btu/hr (0.082 watt), which was assumed as that part of the total heater output reaching the test tank by means other than the fluid line as analytically modeled. The figure of 0.279 Btu/hr (0.082 watt) was arrived at by subtracting the difference between the predicted plumbing line heat leak ( $\Delta Q_{\text{line}}$ ) for heaters-on and no-heat conditions from the difference between total measured heat flow for the two conditions. Thus,

$$(13.628 - 12.805) - (2.699 - 2.155) = 0.279 \text{ Btu/hr (0.082 watt)}$$

An assessment of the apparent measured plumbing line heat leak and a comparison with the corresponding predicted value was made in a manner similar to that employed for Test T-5. Thus, for the no-heat condition,

$$\Delta \dot{Q}_{\text{line, meas}} = \dot{Q}_{\text{tot, meas}_6} - \dot{Q}_{\text{tot, meas}_5} = 12.805 - 10.406 = 2.399 \text{ Btu/hr} \\ (0.71 \text{ watt})$$

$$\Delta \dot{Q}_{\text{line, pred}} = \Delta \dot{Q}_{\text{line}} \text{ (Table 2.2-2)} = 2.155 \text{ Btu/hr (0.63 watt)}$$

The comparison between apparent measured and predicted plumbing line heat leak values was qualitatively consistent with some, but not all, of the measured-predicted temperature comparisons. The only suggested change in properties or assumptions that would result in an uncompromised improvement in correlations was the use of a larger area of main MLI in the plumbing line analytical model.

Test T-7: This was a repeat of the preceding test except that LN<sub>2</sub> was used as the fluid instead of LH<sub>2</sub>. The strut and fluid line heaters were inactive during this run.

Figure 2.2-72 shows the boiloff data. The results were more erratic than preceding LN<sub>2</sub> tests and there was no apparent reason for this behavior. An average value of 12.4 Btu/hr (3.6 watt) was selected.

Figure 2.2-73 shows that the back-pressure system was functioning properly. Temperatures at the test tank outlet are presented in Figure 2.2-74.

Test T-7 was conducted on the same configuration as Test T-6. In principle the analysis differed from that of Test T-6 only in the temperature boundary condition of the test tank. The analytical models were the same as employed for analysis of the previous tests and the assumptions were the same as described earlier.

In actual execution the analysis of Test T-7 differed somewhat from that of Test T-6 since it was necessary in the Test T-7 activity to analyze the strut assembly, in addition to the plumbing line assembly, with the liquid nitrogen boundary condition. The model for this component was the same as that used for Test T-5 and illustrated in Appendix E. The Test T-7 analysis differed from the Test T-6 analysis also in the synthesis of the predicted total heat flow, which will be described later.

Temperature distributions for Test T-7 are shown in Figures 2.2-39 through 2.2-42. In general, the trends were similar to those seen in the Test T-6 correlations and the same comments applied. Temperatures related to the strut assembly are not shown in this section since there was no instrumentation in this area for Test T-7. The predicted temperatures for the strut assembly analytical model are given in Appendix E.

Figure 2.2-42 shows an unusually large difference between measured and predicted temperatures on the inner surface of the insulation. It was seen that

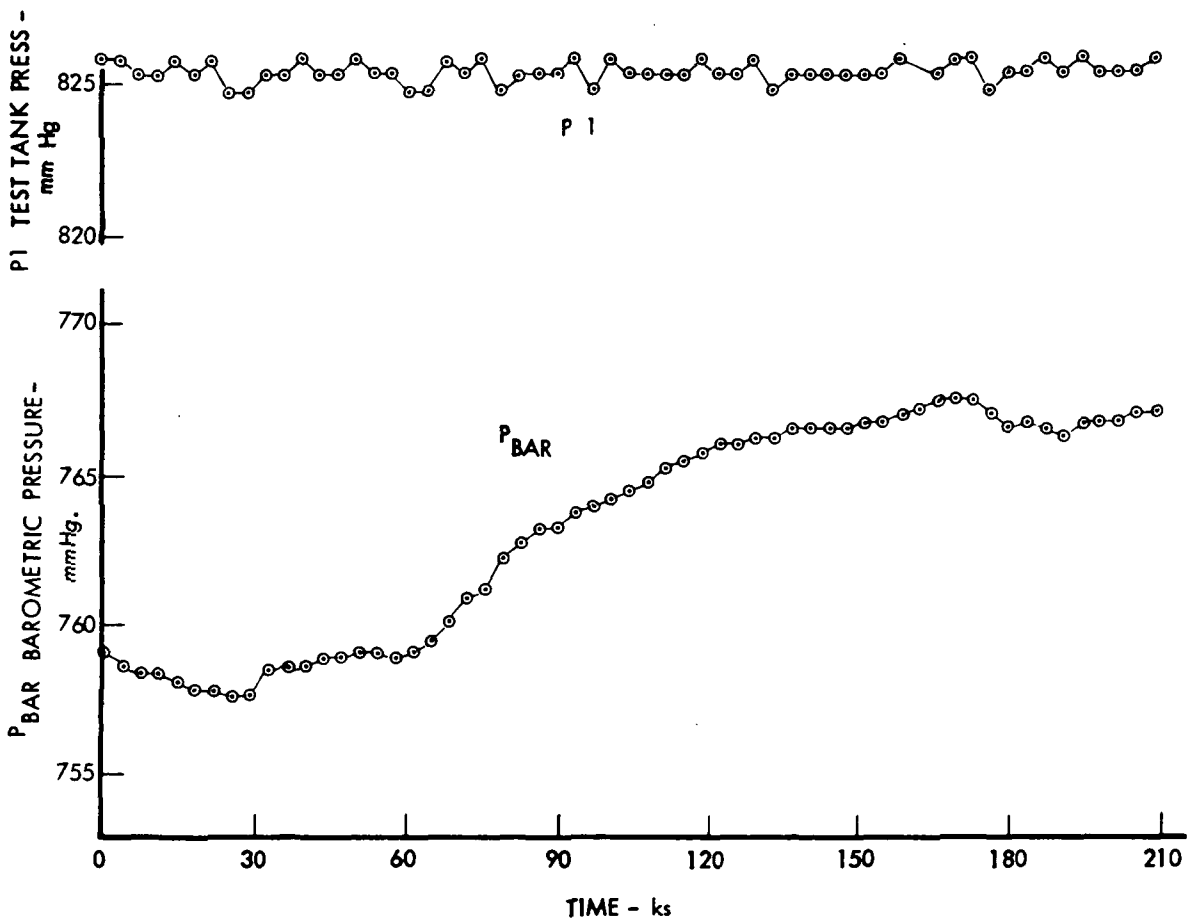


Figure 2.2-73: TEST TANK AND BAROMETRIC PRESSURE, TEST T-7

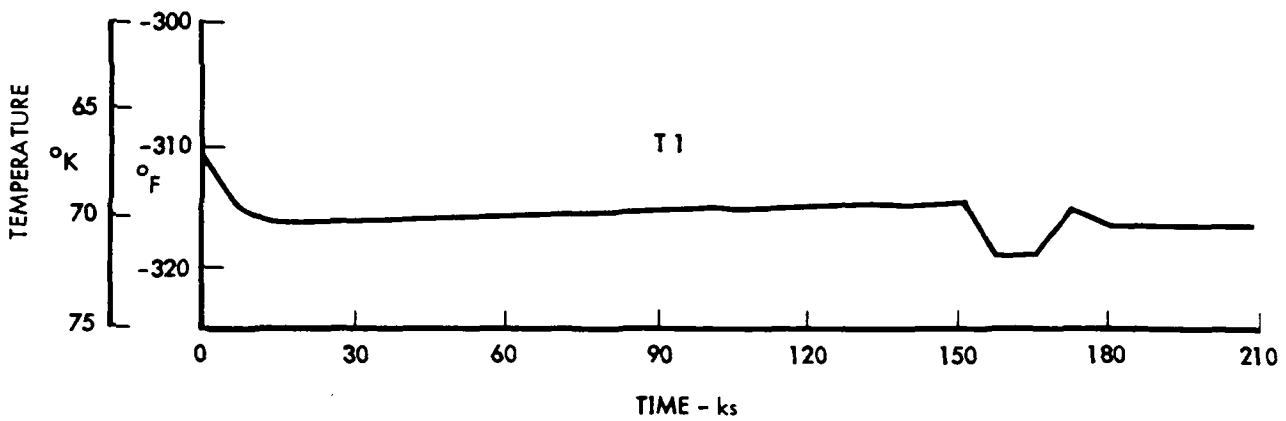


Figure 2.2-74: TEST TANK OUTLET TEMPERATURE, TEST T-7

measured temperatures at T519, T521, and T523, as well as those at T55, T57, T59, T511 and T513 (Figure 2.2-41), were lower than the respective measurements from Test T-6. The predictions, responding as expected to the higher cold boundary temperature, showed higher temperatures for Test T-7. No explanation was found for the behavior of the measured temperatures.

The heat flow correlation for Test T-7 is shown in Table 2.2-2. The basic heat flow ( $Q_{\text{basic}}$ ) for Test T-7 was taken from the measured total heat flow ( $Q_{\text{tot, meas}}$ ) of Test T-2, where the boundary temperatures were the same as for Test T-7. Thus the longitudinal joint and fastener heat leaks were accounted for in  $Q_{\text{basic}}$ . To this value were added the  $Q_{\text{strut}}$  and  $Q_{\text{line}}$  from the Test T-7 thermal analysis, to obtain  $Q_{\text{tot, pred}}$ . The necessity of obtaining  $Q_{\text{basic}}$  from Test T-2 precluded an empirical accounting for the unpredicted increase in heat flow that appeared to result from the structural tests of Test T-4, as was done for Test T-5 and T-6 heat flow correlations.

Test T-8: This test incorporated a lap joint in the MLI and two different warm boundary temperatures. The base of the thermal shroud was controlled to 70°F (294°K) and the sidewall of the shroud was filled with LN<sub>2</sub>. The test fluid was LH<sub>2</sub>. The two shroud components were thermally disengaged by phenolic blocks. The heaters were both inoperative during this run.

The heat flow data is shown in Figure 2.2-75. The initial fill was made at 1500 hours on 3-17-72. The data plots were started approximately a day later. Six boil-off runs are shown in the figure. The boil-off rate was essentially constant throughout these runs. A value of 2.9 Btu/hr (0.9 watt) was selected.

The test system and barometric pressure plots are shown in Figure 2.2-76. Temperature at the tank outlet is shown in Figure 2.2-77.

Simulation of Test T-8 consisted primarily of an analysis of the basic main MLI assembly, accounting for the modified lower (sidewall-base) lap joint and the differing temperatures of the shroud sides and base. The analytical model was very similar to that used for analysis of Tests T-1, T-2 and T-3, and is shown in detail in Appendix E. As for the earlier analyses, the main aluminum framework was not considered part of the analytical model. The lower aluminum and fiberglass support ring was included in the model.

The earlier assumption of mutual thermal independence of the main MLI assembly, the longitudinal joint, the strut assembly, and the fluid line assembly was extended to imply that only the main MLI assembly was affected by the two-level hot boundary temperatures of Test T-8. Thus, the joint, strut, and line analyses at the conditions of Test T-3 were assumed applicable to Test T-8. The total heat leak due to fasteners was the sum of individual fastener leaks with appropriate boundary temperatures. These values were taken from the Test T-1 and T-3 fastener analyses.

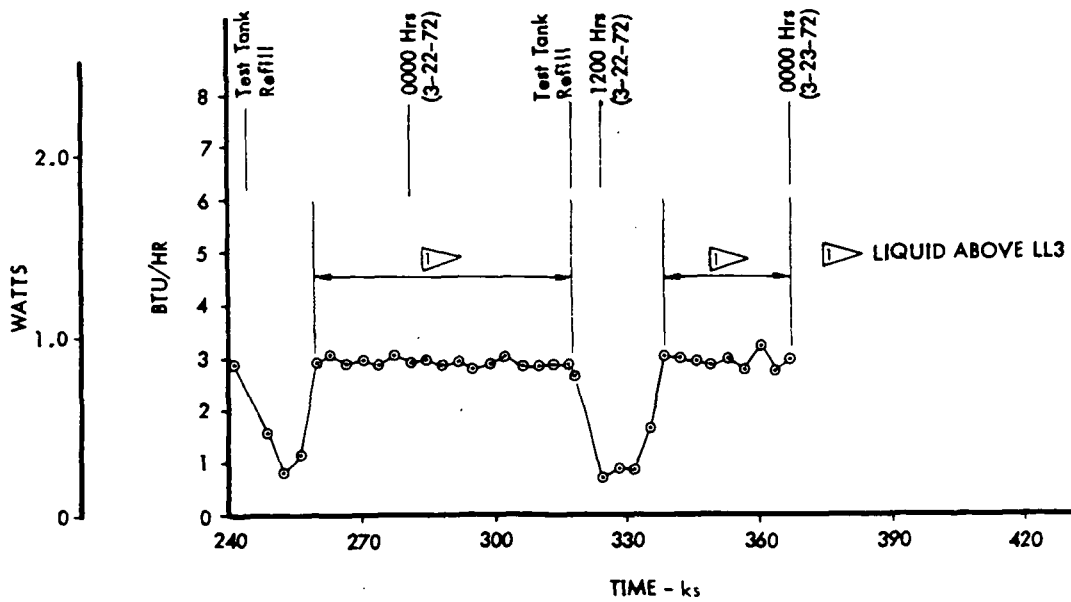
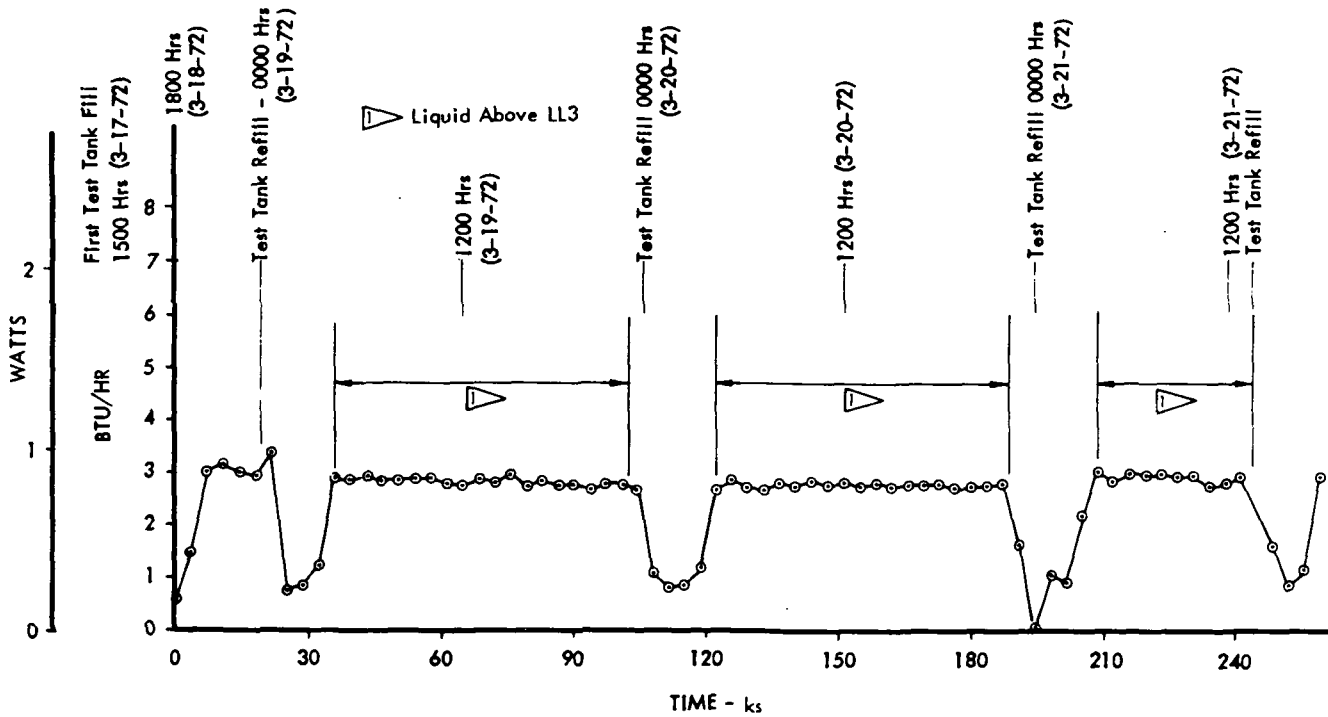


Figure 2.2-75: HEAT FLOW, TEST T-8

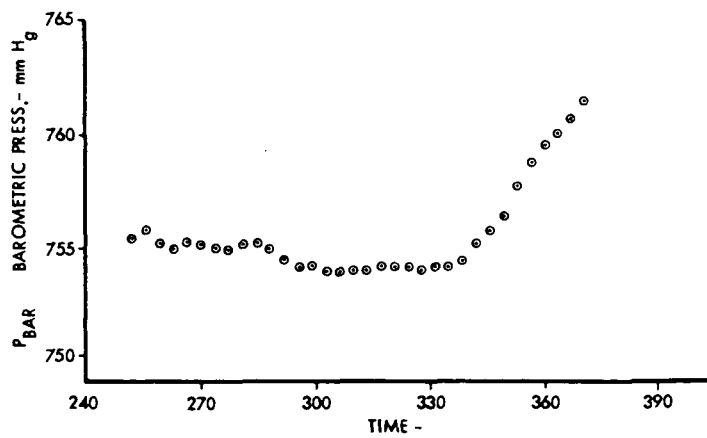
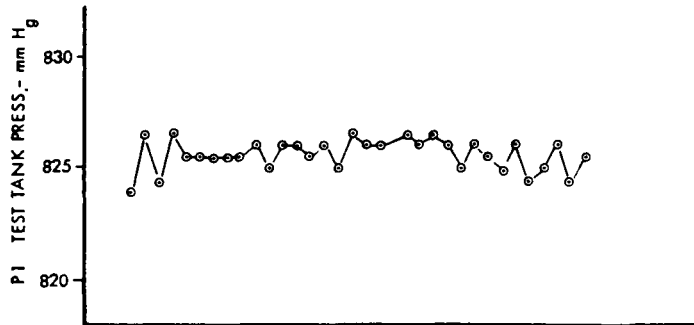
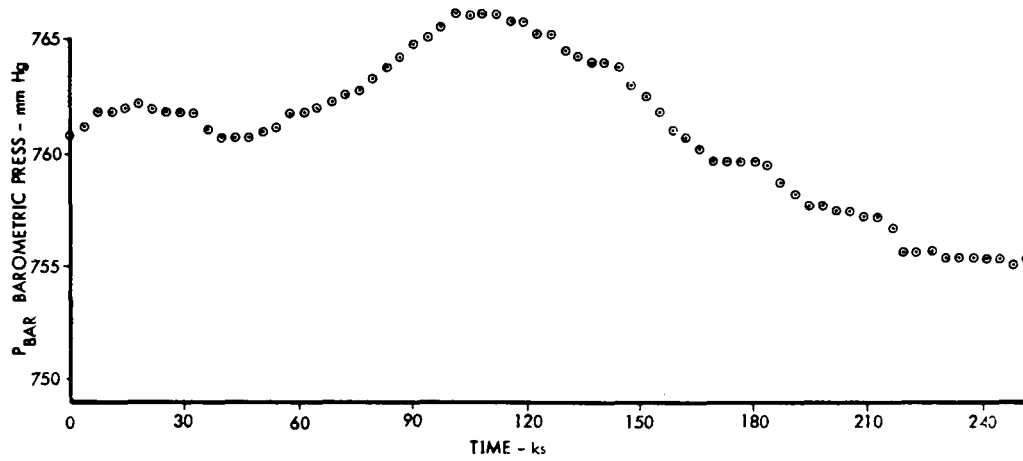
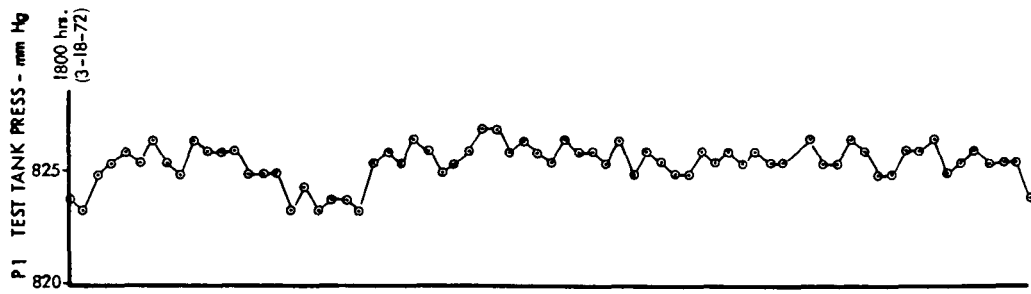


Figure 2.2-76: TEST TANK AND BAROMETRIC PRESSURE, TEST T-8

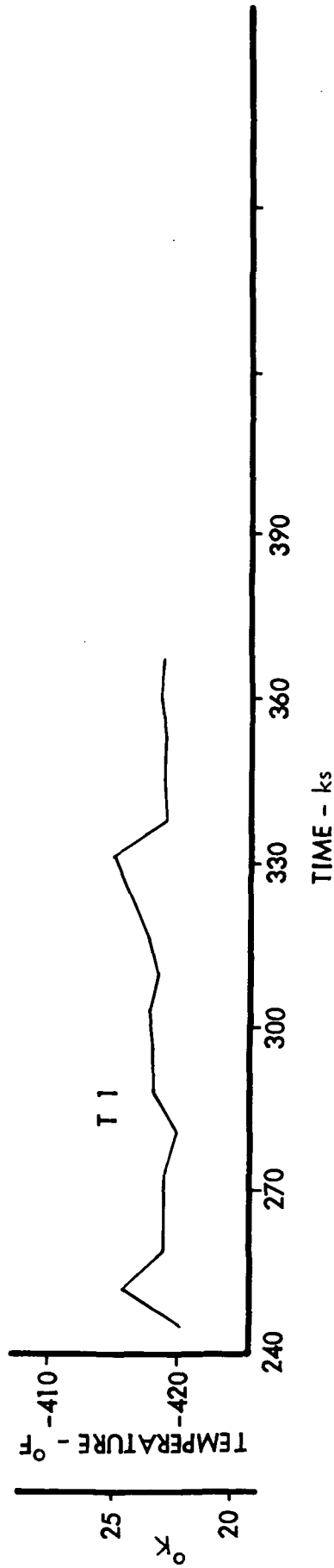
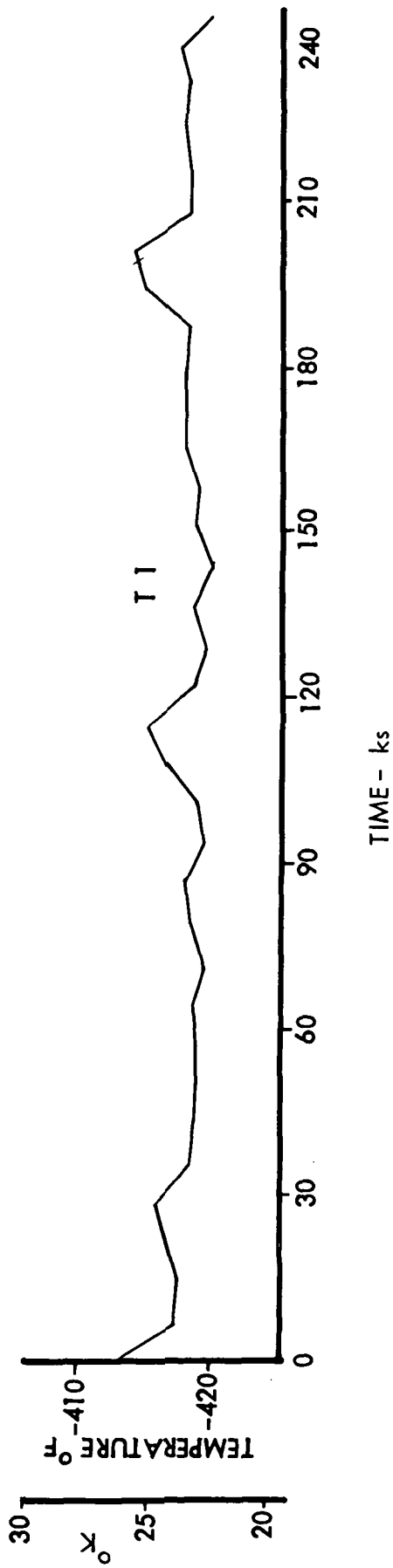


Figure 2.2-77: TEST TANK OUTLET TEMPERATURE, TEST T-8

Additional assumptions employed in the analysis of the lower lap joint are listed below:

- (1) Conductance through the lap interface of the MLI lap joint was equal to the conductance of a continuous thickness of MLI.
- (2) Emittance of MLI exposed edges was 1.0.
- (3) Heat transfer between the support ring assembly and the MLI was by radiation only.
- (4) The aluminum part of the support ring was isothermal and the aluminum and fiberglass parts were in perfect thermal contact.

Temperature correlations for the MLI sidewall in Test T-7 are shown in Figure 2.2-43. Notice that the outer surface of the MLI above the lap joint became the inner surface below the joint. Above the immediate vicinity of the joint the predicted outer surface temperatures, and, to a lesser degree, the inner surface temperatures differed greatly from the measured values. No explanation was found for the discrepancy, but it was observed that the prediction-measurement difference was somewhat similar to that of the Test T-3 correlations.

Temperatures on the MLI base blanket are shown in Figure 2.2-44. The very large difference between predicted and measured values on the outer (hot) surface were not completely explained. Subsequent to the analysis it was discovered that the outer surface of the base blanket was covered with two layers of nylon net rather than the single layer used elsewhere. Thus, the surface emittance used in the analysis (Table 2.2-1) may not have been correct for this surface. No emittance data were available for a double nylon net surface, but, judging from the effect of adding a single layer to a bare aluminized mylar surface, a double net layer was very unlikely to lower the emittance. Therefore, an emittance correction offered little hope for resolving the discrepancy.

Thermocouples T61, T63, T65 and T67 (Figure 2.2-44) were shielded in varying degrees by one of the lower support ring cross members. These cross members were afforded a rather direct thermal conduction connection with the main insulation support truss frame. The main truss frame experienced temperatures lower than the base blanket outer surface, due to the frame's principal exposure to the LN<sub>2</sub>-cooled shroud side wall. Thus, the cross members on the lower support ring could have drawn heat from the base blanket outer surface by radiation, actively cooling the MLI, as well as partially shielding it from the shroud base heat source. This effect which was not accounted for in the analysis was the most plausible explanation for the prediction-measurement discrepancy of Figure 2.2-44. It is not clear why the measured temperatures were nearly constant across the outer surface of the base blanket in view of the thermocouples varying distance from the nearest lower support ring cross member.

Post-test inspection revealed that thermocouple T69 was cemented to both the MLI and the adjacent fiberglass portion of the support ring, contrary to its intended installation. The MLI was badly torn around the thermocouple due to the resulting non-yielding attachment. There was a large tear involving two aluminized mylar layers around thermocouple T62. In addition, there were numerous small tears, mostly at stitching holes, in the MLI lap joint region. The attempt to form a cylindrical surface at the lap joint by folding the edge of the base blanket disc produced considerable puckering and bunching of the MLI, resulting in local variations in thickness and effective layer density. All of these departures from the idealized configuration represented by the analytical model could have contributed to correlation discrepancies.

Heat flow for Test T-8 is summarized in Table 2.2-2. The basic heat flow ( $Q_{\text{basic}}$ ) was computed by integration of heat flux emanating from the inner surface of the main insulation assembly in the same manner as was done for Tests T-1, T-2 and T-3. The incremental heat flow due to the longitudinal joint ( $Q_{\text{long, joint}}$ ) was taken directly from the analysis of Test T-3. The incremental heat flow due to all fasteners ( $Q_{\text{fasteners}}$ ) was computed by adding the appropriate number of individual fastener heat leaks for a  $532^{\circ}\text{R}$  ( $296^{\circ}\text{K}$ ) shroud temperature, taken from Test T-1 analysis, and the appropriate number for a  $140^{\circ}\text{R}$  ( $77.7^{\circ}\text{K}$ ) shroud temperature, taken from Test T-3 analysis. The strut and plumbing line heat leaks were computed using the same analytical models as for preceding test analyses, but with the  $140^{\circ}\text{R}$  ( $77.7^{\circ}\text{K}$ ) shroud temperature boundary condition.

A large relative error is seen in the comparison between predicted and measured heat flow for Test T-8. It is probable that part of the error was due to simplifying assumptions and differences between the analytical model and the test article in the lower joint and base area, as described earlier. Certainly some such error was anticipated in reviewing the temperature correlation results.

The prediction of heat flow for Test T-8 did not have the benefit of a basic heat flow value which included, on an empirical basis, the unpredicted extra heat flow appearing after the structural tests of Test T-4, or the additional heat flow apparently associated with the strut penetration. It is interesting to note that for Test 8 the difference between predicted and measured heat flow, in absolute terms, was approximately the same as for Test T-7, where the predicted heat flow, likewise, did not include the empirical corrections. On the other hand, the difference between predicted and measured heat flow for Test T-6, which did include the empirical corrections, was approximately one-half of the differences for Tests T-7 and T-8. It was concluded that at least a significant portion of the discrepancy between measured and predicted heat flow for Test T-8 was due to those unpredicted increments in heat flow that first appeared in the Test T-4 and T-5 correlations.

Several general conclusions can be drawn from the analysis of test results. These are discussed in the following paragraphs.

Many predicted temperatures agreed with measured values to within approximately  $5^{\circ}\text{R}$  ( $3^{\circ}\text{K}$ ). Most departures from this degree of accuracy occurred in areas where important thermal properties were not accurately known or other analytical modeling deficiencies may have existed. The Test T-3 temperature correlations remained the outstanding case of unexplained disagreement.

Differences between predicted and measured total heat flow rates were less than 2 Btu/hr (0.59 watt) throughout the program. These differences equate to a less than 20% relative error except for Tests T-3 and T-8, where the small absolute values tend to magnify the relative error. Had the predicted heat flow values been computed on a purely theoretical basis, i.e., without the benefit of empirical corrections for unpredicted apparent additional heat leaks, the differences for many of the tests would have been approximately doubled.

Most sources of error thought to be important to the temperature and heat flow correlations were mentioned in discussions of the results for the particular tests. In addition to deviations from the listed assumptions and analytical model deficiencies described, other potential sources of prediction-measurement disagreement existed. The analytical solutions were fundamentally inexact, containing errors from numerical solutions, convergence criteria, and the lumping of physical properties into a finite number of nodes. Perfect steady state conditions probably never existed during the tests and instrumentation tolerances could have accumulated to produce a noticeable error. Numerous small details of the test article were not accounted for in the analytical models. These included heat leaks due to thermocouple leads, and localized areas of double nylon net layers.

### 2.3 Mockup Evaluation

A full scale structural and thermal/meteoroid protection system mockup was made of Vehicle 1-14. A photograph of the structure, fluid lines and electrical systems is shown in Figure 2.3-1.

MLI blankets consisting of aluminized mylar/nylon net layers were assembled in accordance with the vehicle final design drawings and installed on the mockup. The ease of assembly and potential problem areas were noted and where major problems existed an alternate installation was tried. Finally, the mockup and MLI were cut apart so that a photographic log of critical areas could be made.

The design improvements dictated by this phase of the program were incorporated in the final vehicle design drawings Figure 1.3-1 and 1.3-2, and in the assembly of the thermal/structural test article.

## Assembly and Installation

Several thermal/meteoroid protection design deficiencies were found in assembling the panels on the mockup. These deficiencies and the design remedies are discussed in the following paragraphs.

The LH<sub>2</sub> tank fill line penetrated the vehicle sidewall on the conical surface below the lower main-body ring. This necessitated an elongated hole in the MLI blanket which was difficult to fit to the insulated pipe penetration as evidenced in Figure 2.3-2. The design "fix" consisted of moving the line to a point slightly above the lower ring on the cylindrical surface of the vehicle, which permitted the use of a circular hole in the MLI blanket. It was also found that each plumbing penetration should have a flange on the pipe to provide support to the intersecting MLI blanket at the point of penetration. Without this support, motion between the pipe and the blanket would cause MLI damage or gaps, thus degrading the thermal performance. The MLI blanket could be attached to the pipe flanges with Velcro patches.

The fitup of the longitudinal shiplap joints in sidewall and base blankets was good in those areas where the nylon thread ties were tight. If the thread slipped or was tied loosely severe gaps resulted. A spring tensioning device which would clip in place should be designed for this application. A metallic spring could be used since it does not penetrate the blanket. This problem was remedied on the thermal test article by using fiberglass thread and tweezers to make a tight tie. A very good joint was obtained with this approach but considerably more labor was required.

It was found that Velcro patches were necessary on the vehicle sidewall struts to hold the MLI blanket in place and reduce sagging. On the mockup there were strips of hook and pile, bonded to struts and blanket, respectively. Since the blanket was located inside of the structure, the Velcro attachment was made with hand pressure from the inside. When the blanket installation was complete it was impossible to re-engage this attachment from the outside of the vehicle. Detaching and re-engaging the Velcro became necessary to allow positioning of the blanket and to aid in making an efficient longitudinal joint. The problem was solved on the thermal test article by using Velcro strips with "ears" on the MLI blanket. The ears could be grasped and pulled outward to produce a strong attachment. Velcro pile should also be placed on both sides of the strut at the point of attachment to secure the "ears" and provide a shear tie.

Both the compartment separation and top deck MLI blankets were designed with nylon studs and buttons to facilitate handling. Initial problems were experienced with these fasteners when the heat formed heads, which held the washers in place, began to break during installation of the blanket. Examination of the breaks showed that the nylon had become brittle when heat formed. This problem was partly resolved by bonding the washer and the stud together

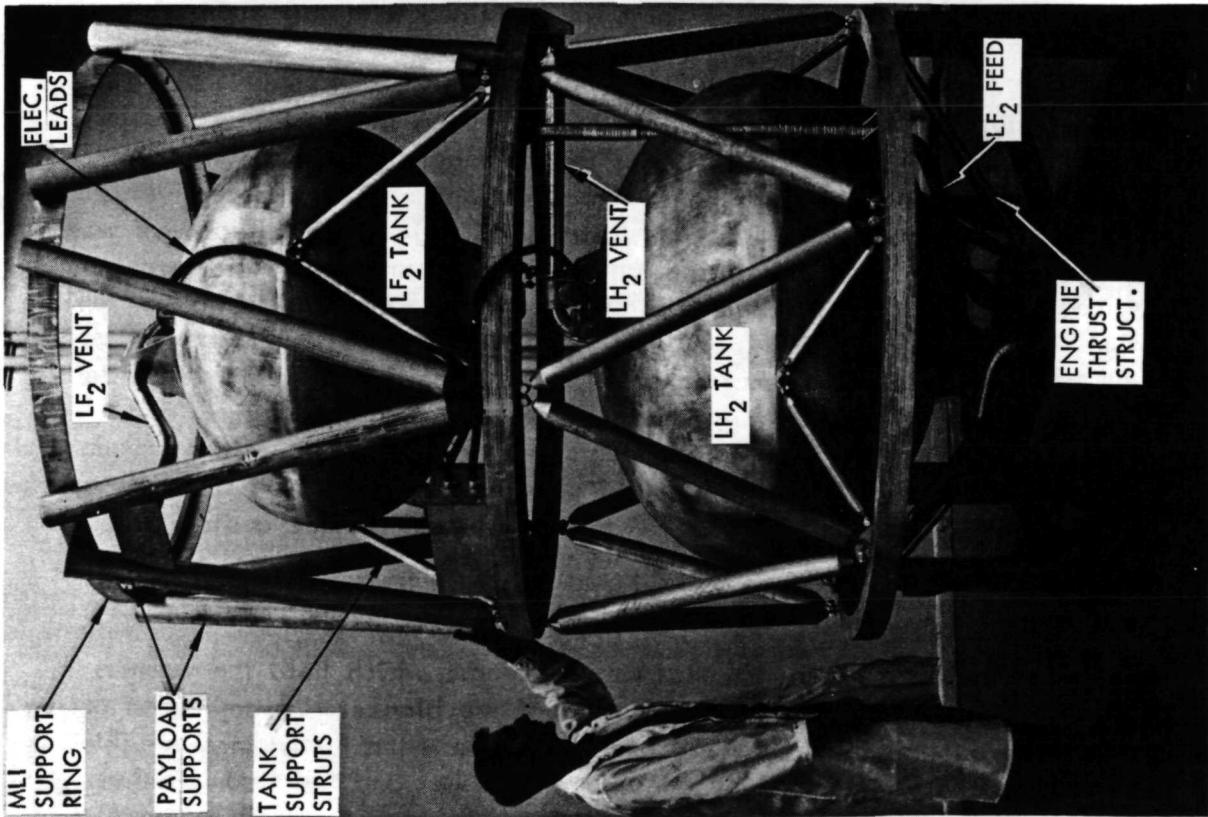


Figure 2.3-1: MOCKUP - VEHICLE I-14 STRUCTURE

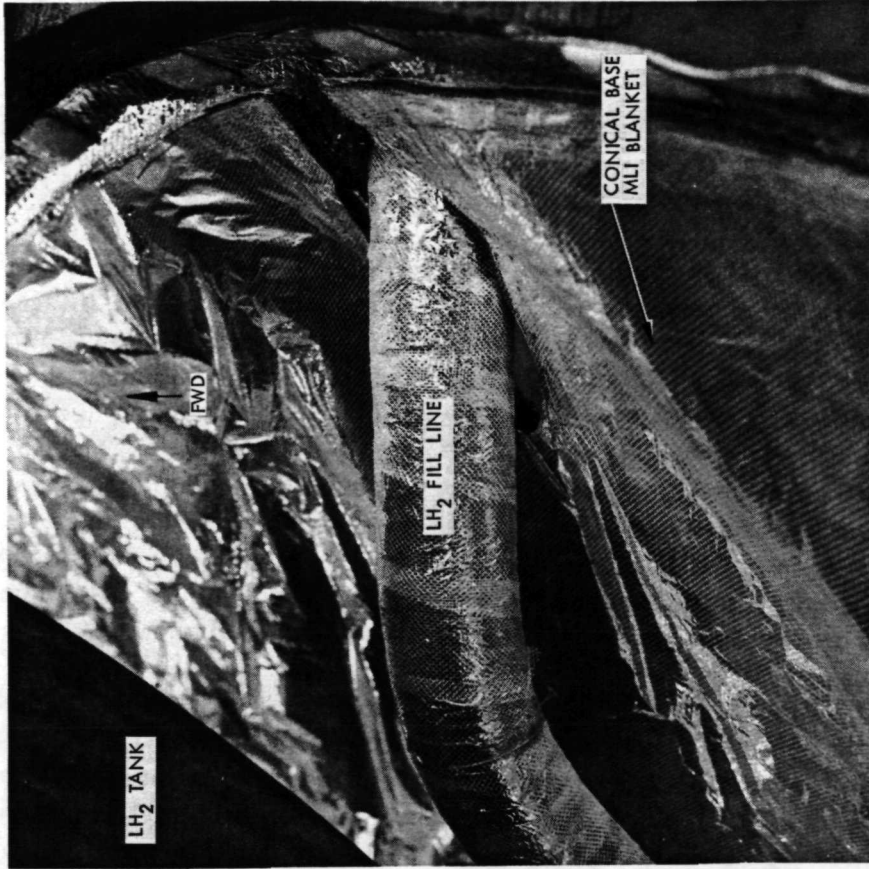


Figure 2.3-2: MOCKUP - LH<sub>2</sub> FILL LINE/MLI PENETRATION

and to the outer MLI layers. After these blankets were installed on the mockup it became apparent that 1/2" (1.27 cm) diameter heads did not support the blanket adequately. This deficiency was remedied by replacing the nylon studs and buttons with a 1 in (2.54 cm) diameter fiberglass washer on the inside of the blanket, tied with thread through the outer X-850 layer. The X-850 material had good tear resistance and strength if the thread tie was looped over several strands of the scrim cloth within the laminate. Care should be exercised to avoid compacting the blanket with the thread tie.

The top deck MLI blanket had a flanged edge which faced aft along the vehicle sidewall. This flange was formed during fabrication of the blanket by cutting radial slits, folding over the edge of the layup tool and taping the cut edge together. It was found that the flange length should be increased to compensate for errors in positioning the blanket within the fiberglass support ring. When the blanket was located off-center the overlap was nearly eliminated from one side.

The compartment separation blanket design utilized X-850 film with Velcro around the perimeter to attach to the lower side of a fiberglass support ring at the mid-body location. This design did not permit tensioning of the X-850 film, and as a consequence the blanket sagged. It was decided to re-locate the X-850 to the top of the support ring where there was access to the entire perimeter. The MLI was separated from the X-850 in this area and placed underneath the ring. Both the top deck and compartment separation blankets contacted the vent line outlets on top of the  $LF_2$  and  $LH_2$  tanks. Since this contact could not be avoided a small platform with Velcro attachment was necessary to support the MLI blanket at this location.

### Disassembly

The mockup was disassembled and photographed. Section cuts were made through structural members and insulation at all the joints to evaluate fitup characteristics. Sidewall blankets were removed so that internal clearances and penetrations could be reviewed.

Figure 2.3-3 is an external view of the insulated mockup. Figure 2.3-4 is a view of the top deck blanket and illustrates the sag problem typical for this and the compartment separation blanket. Figure 2.3-5 is an internal view of the top deck blanket showing contact with the vent plumbing outlet. Figures 2.3-6 and 2.3-7 show the top deck/sidewall blanket joint. Figure 2.3-6 was taken from the inside with a portion of the restraint ring removed for clarity. Figure 2.3-7 is a section cut through the support ring and the insulation showing the lap joint.

The longitudinal ship-lap joint was viewed from the outside at the mid-body ring in Figure 2.3-8. Figure 2.3-9 is a section view of this joint made from

a portion removed from the mockup. The gaps could be avoided by exercising more care in early assembly stages.

A  $LF_2$  tank support penetration is shown in Figure 2.3-10. A portion of the compartment separation blanket is also visible. The compartment separation blanket and  $LF_2$  feedline penetration are shown in Figure 2.3-11. X-850 film laminate was used as a carrier to support this blanket. The junction of compartment separation blanket and mid-body support ring is shown in Figure 2.3-12. This is a view looking down. Figure 2.3-13 is a close-up of the upper and lower sidewall and compartment separation blanket junctions. This joint reflects the design change wherein the X-850 film was relocated to the top of the insulation support ring to facilitate tensioning. Figure 2.3-14 is a view of the lower side of the compartment separation blanket showing the junction with the sidewall.

Figure 2.3-15 is an external view of the vehicle conical base. Figure 2.3-16 shows  $LH_2$  and  $LF_2$  engine feedlines penetrating the base blanket. It was decided that flanges were needed on these and all line penetrations to allow insulation attachment. These attachments would be made with Velcro and would be expected to minimize the gaps evident in the photograph. The blanket was cut from the edge to permit assembly around the lines. A good fit between abutting edges of the conical and base blankets was difficult to obtain because accessibility and clearance were limited. Figure 2.3-17 is a section view of the sidewall/conical blanket junction. This joint tended to peel when tension was placed on either blanket, however, Velcro attachments to the adjacent struts supported the joint.



Figure 2.3-3: MOCKUP - VEHICLE 1-14 MLI ASSEMBLY

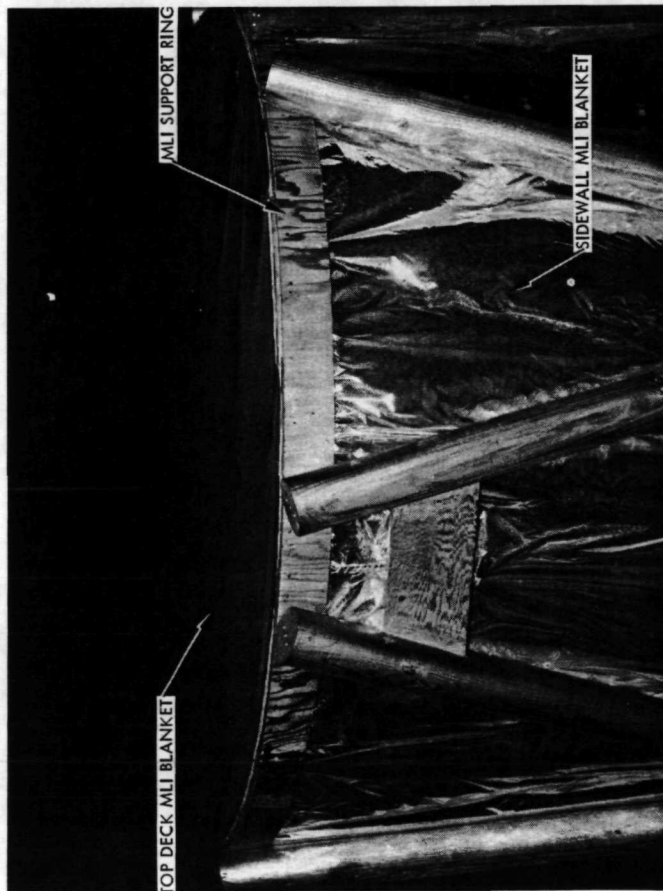


Figure 2.3-4: MOCKUP - TOP DECK MLI BLANKET

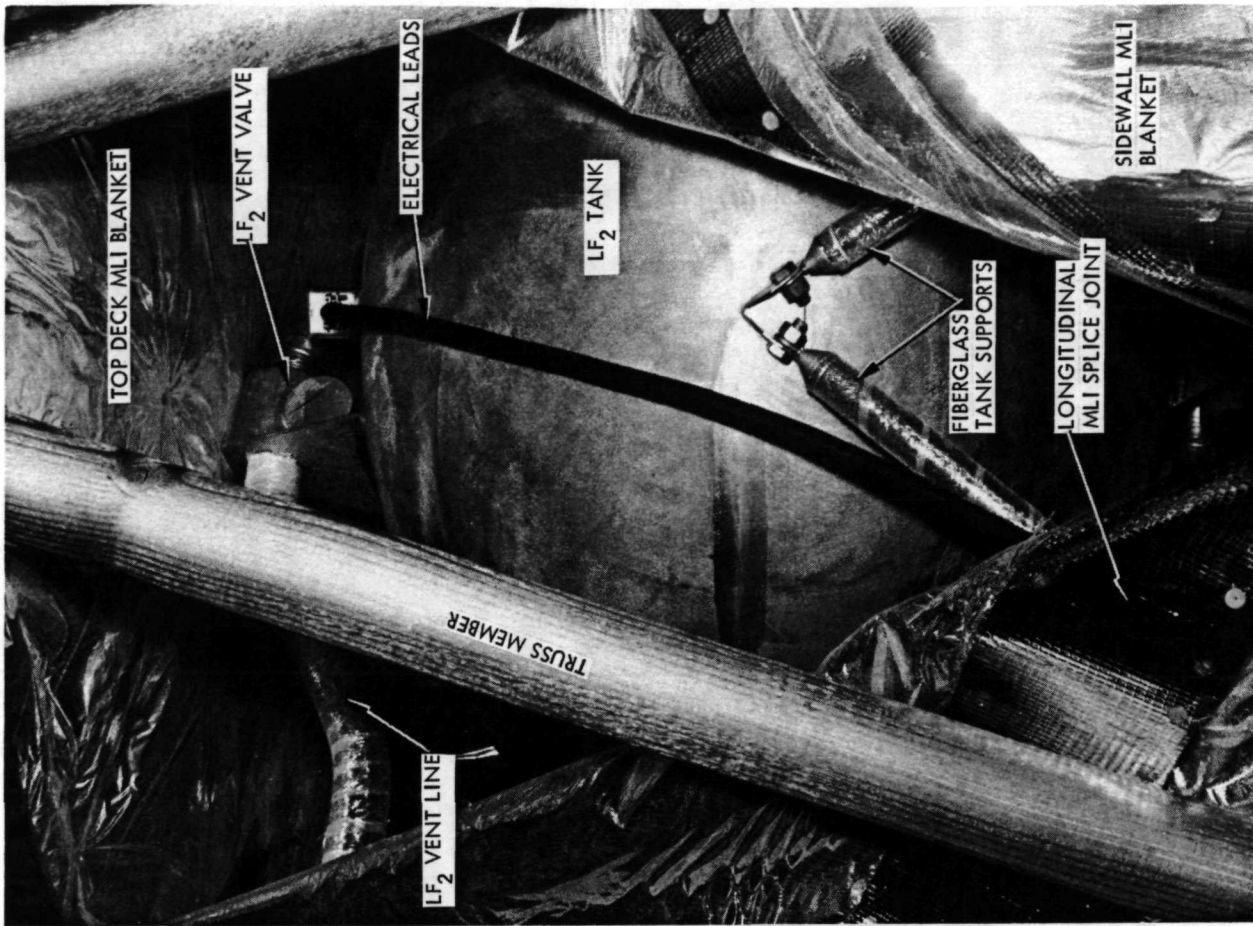


Figure 2.3-5: MOCKUP - INTERNAL VIEW, LF<sub>2</sub> COMPARTMENT: IT

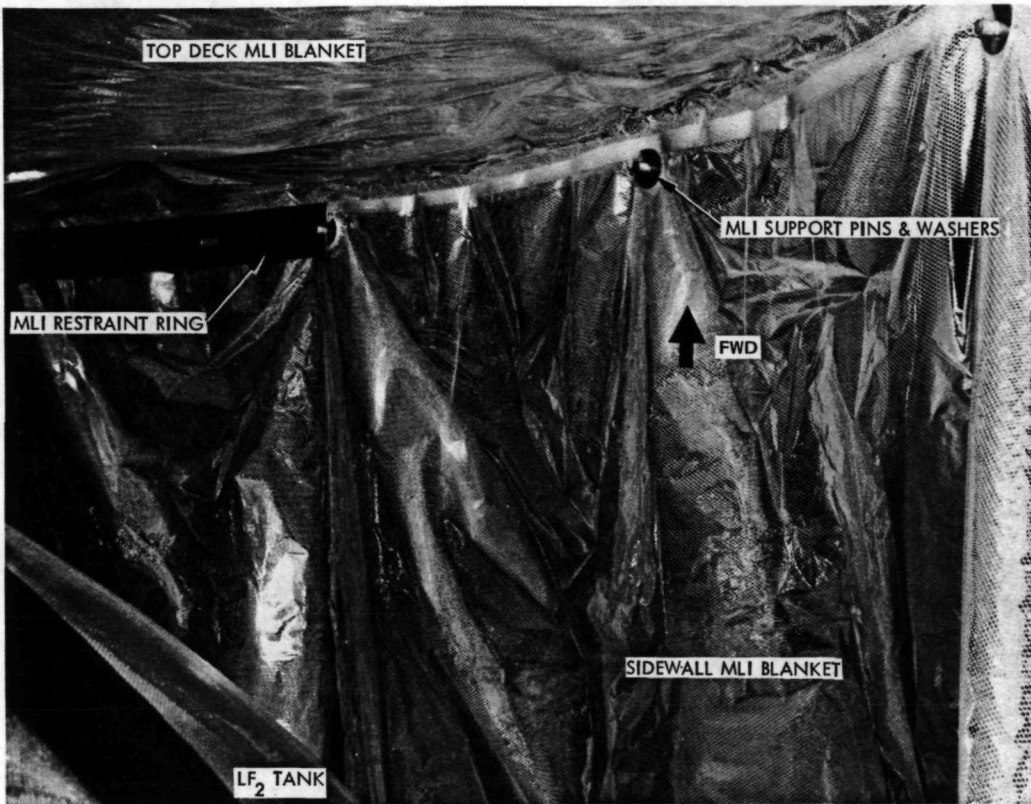


Figure 2.3-6: MOCKUP - INSIDE VIEW, LF<sub>2</sub> COMPARTMENT

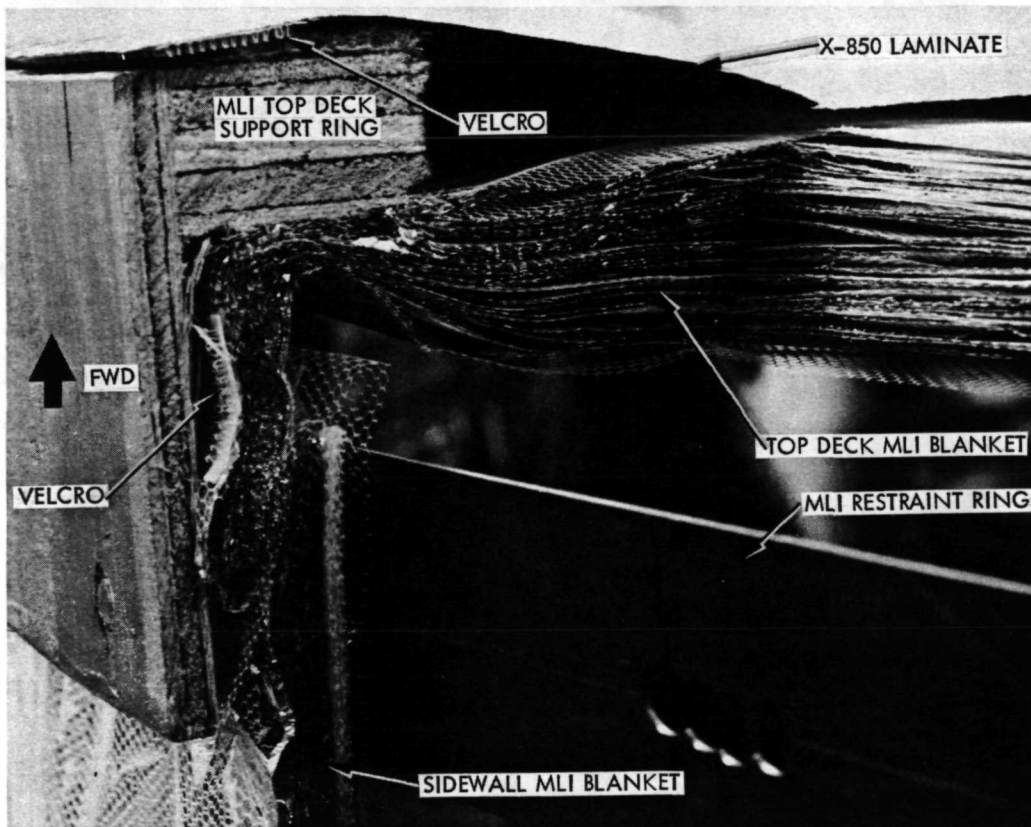


Figure 2.3-7: MOCKUP - TOP DECK/SIDEWALL BLANKET JUNCTION



Figure 2.3-8: MOCKUP - MID BODY RING AND MLI JOINT

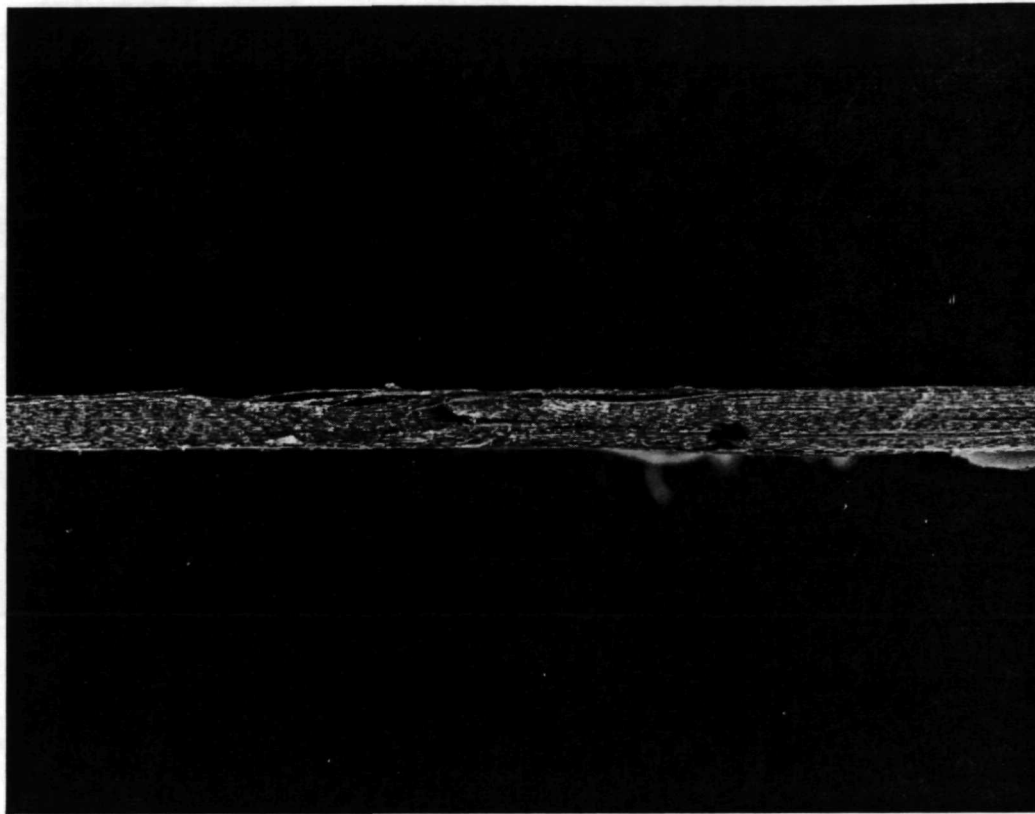


Figure 2.3-9: MOCKUP - SECTION VIEW, LONGITUDINAL JOINT

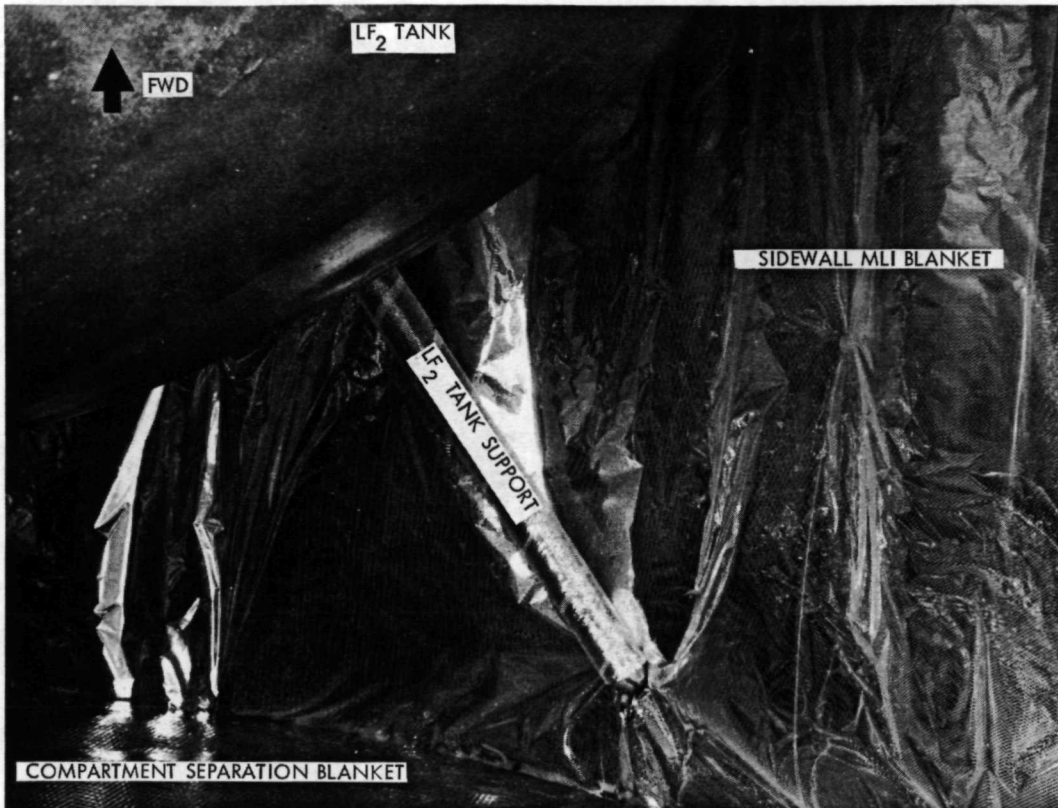


Figure 2.3-10: MOCKUP - TANK SUPPORT/MLI BLANKET PENETRATION

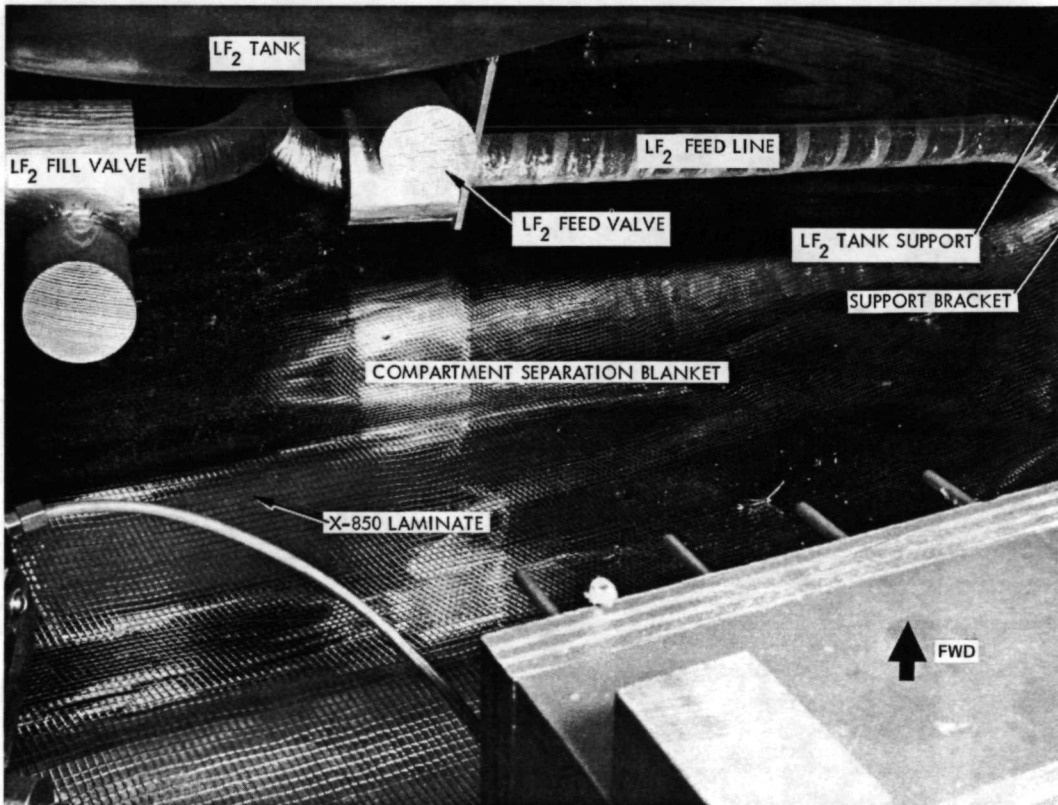


Figure 2.3-11: MOCKUP - COMPARTMENT SEPARATION BLANKET

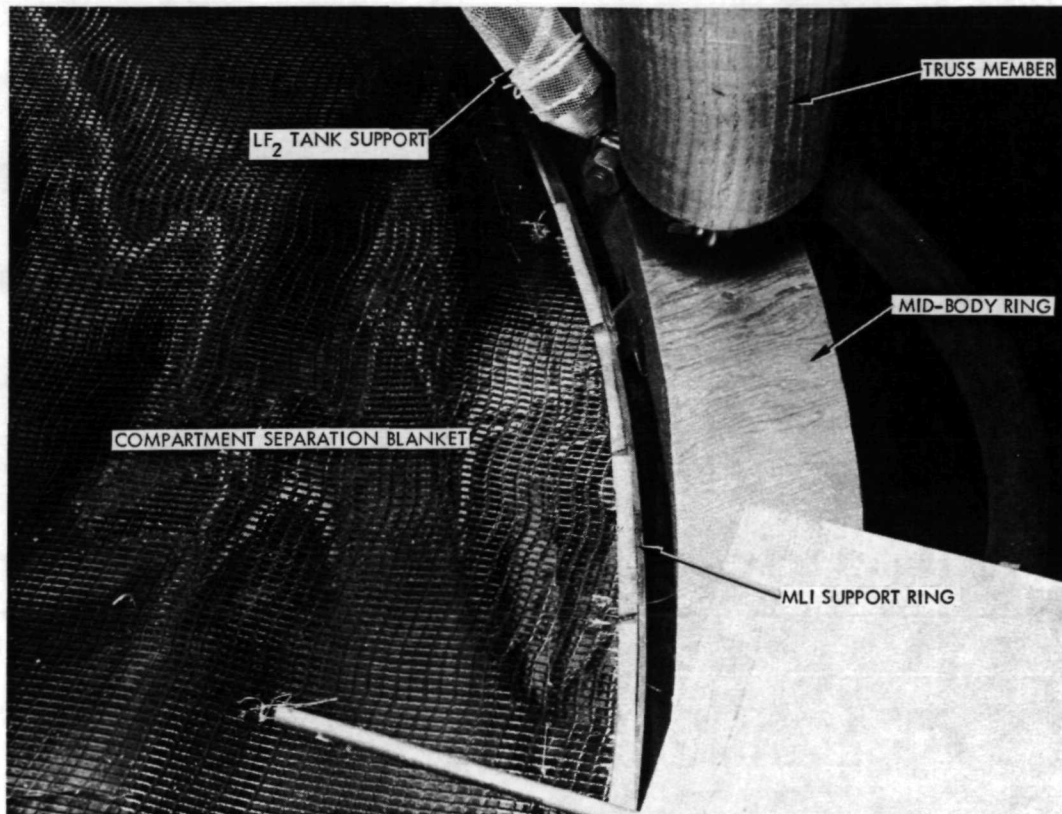


Figure 2.3-12: MOCKUP - COMPARTMENT SEPARATION BLANKET ATTACHMENT

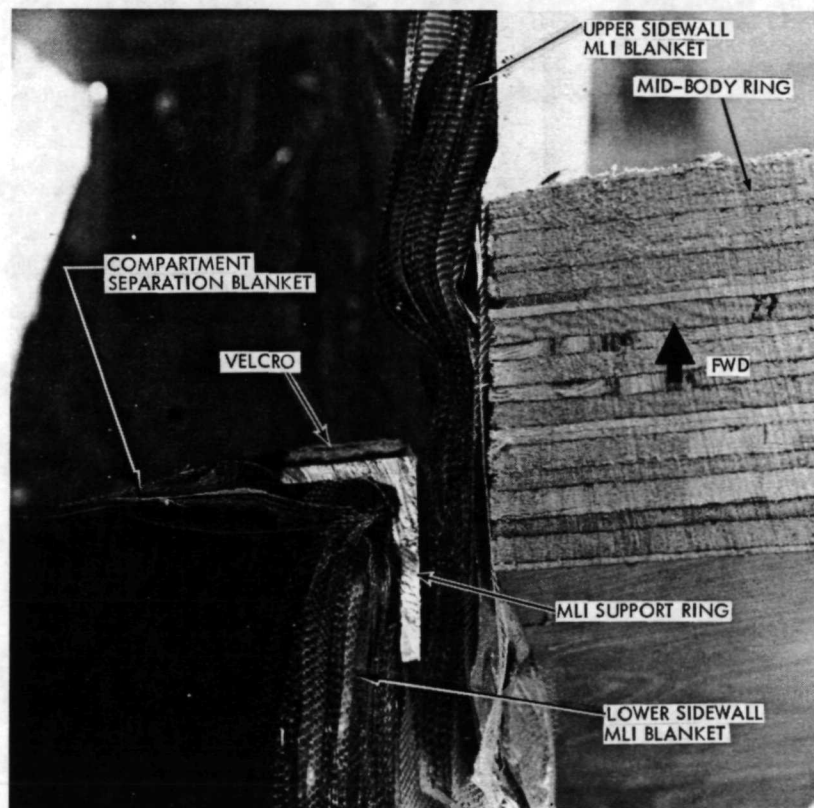


Figure 2.3-13: MOCKUP - COMPARTMENT SEPARATION/SIDEWALL BLANKET JUNCTION

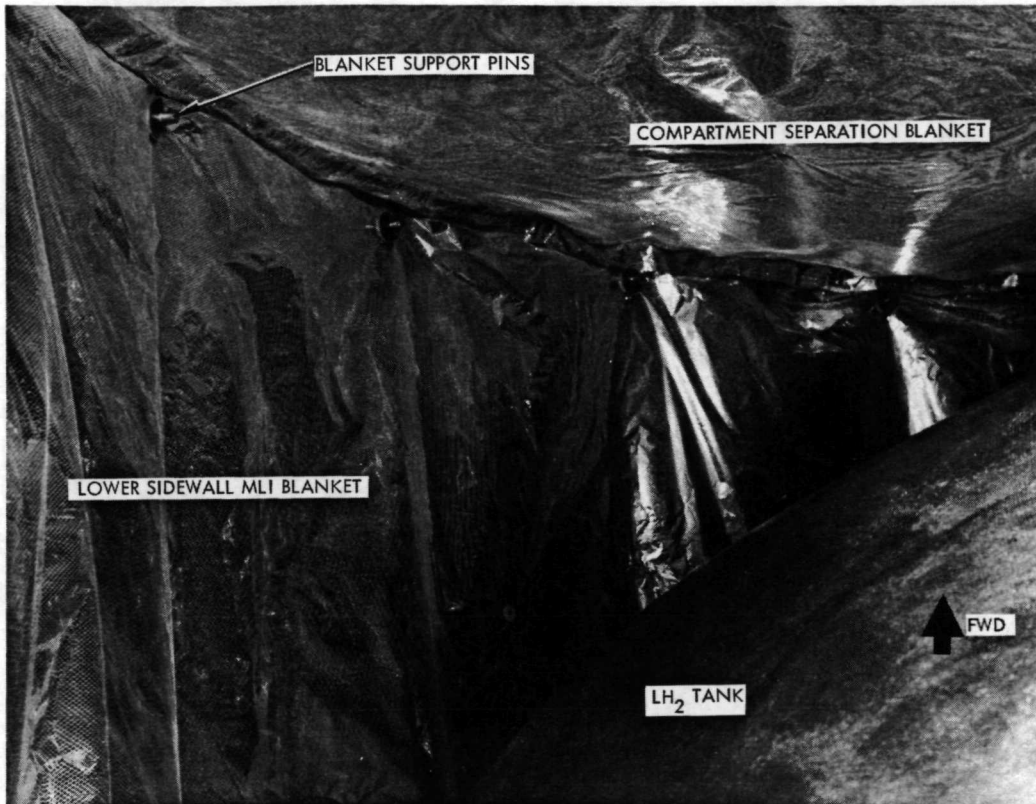


Figure 2.3-14: MOCKUP - COMPARTMENT SEPARATION BLANKET, INSIDE VIEW

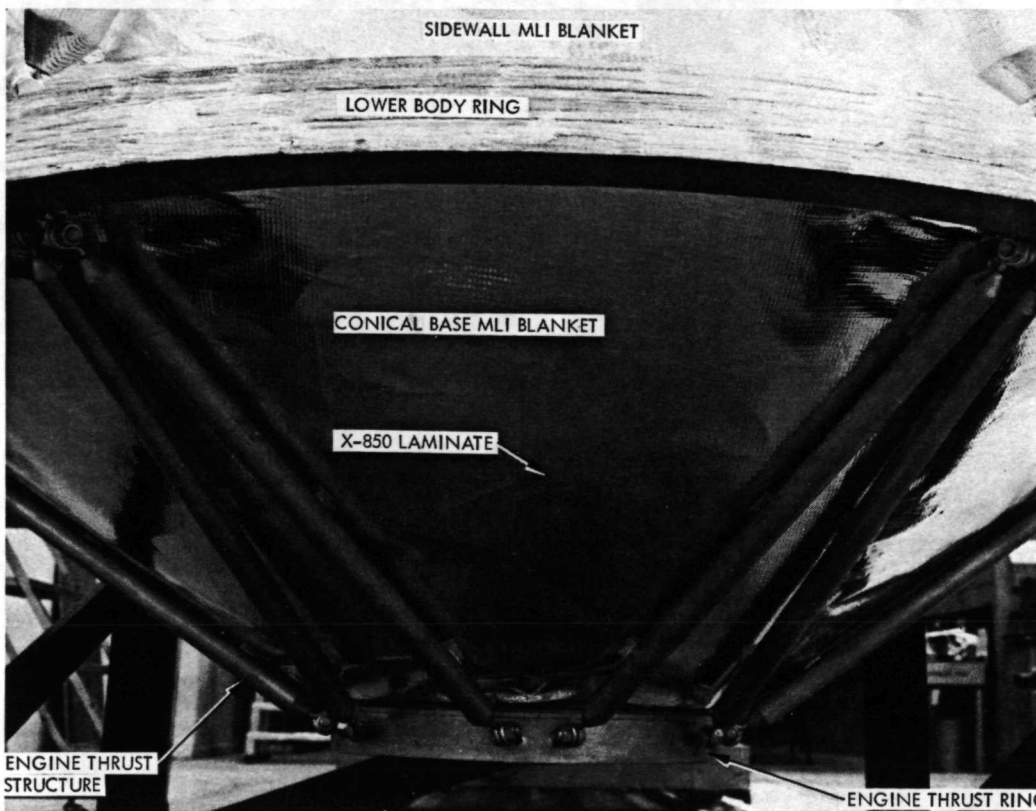


Figure 2.3-15: MOCKUP - CONICAL BASE AREA

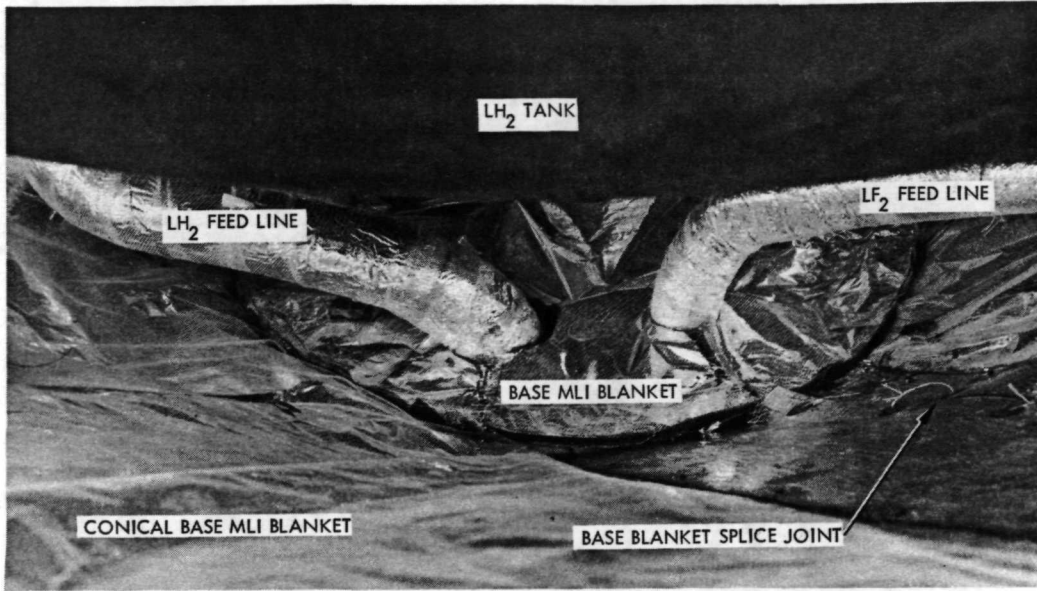


Figure 2.3-16: MOCKUP - BASE BLANKET PENETRATIONS

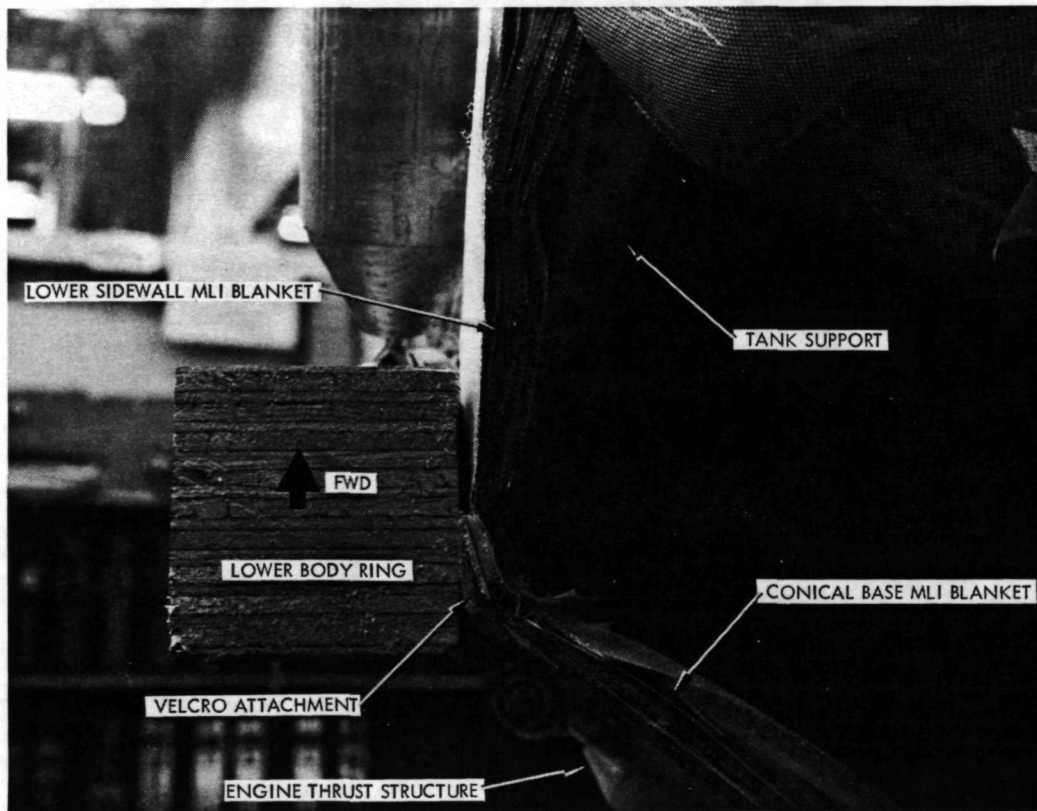


Figure 2.3-17: MOCKUP - SIDEWALL/CONICAL BASE BLANKET JUNCTION

### 3.0 TASK III - DATA EVALUATION AND FINAL DESIGN CORRECTION

#### 3.1 Design Heat Leak Corrections

In order to accomplish the stated objective of the experimental-analytical correlations, to provide verification of, or empirical corrections to, the final designs, the results of the correlation analyses were put into forms suitable for design application. Judgement was necessary to separate the correlation results having valid implications to design from those reflecting conditions or errors related only to the particular test or analysis mode.

The availability of correlations for the same assembly or component with different boundary temperatures made possible the derivation of effective conductivity or conductance expressions involving temperature dependence. Where such expressions dealt with normal conductivity through MLI, or modifications thereof (fastener and longitudinal joint conductivity), the form of the original MLI conductivity expression (Table 2.2-1) was retained. For conductivity of other components (strut and plumbing line assembly) expressions incorporating linear functions of temperature were derived. The correlation expressions were derived specifically from the predicted heat flow results and then modified, as judged appropriate, with factors reflecting the experimental heat flow results.

Table 3.1-1 shows the revised thermal design properties derived from the experimental-analytical correlations. The expression for  $k_n$  includes an empirical factor of 1.2 which was drawn mainly from consideration of the ratio of measured to predicted heat flow for Test T-4. The expressions for incremental conductances of the longitudinal joint and fasteners ( $\Delta K_{lj}$  and  $\Delta K_f$ , respectively), were derived from the analytical predictions with no additional empirical factors. The expressions for strut and plumbing line effective conductivities ( $\Delta k_s$  and  $\Delta k_p$ , respectively) include an empirical factor of 1.1. This factor approximates the ratio of apparent measured heat flow to predicted heat flow for the plumbing line. The much larger ratio that appeared to be associated with the strut was ignored.

Table 3.1-1 includes only those properties that were required for the re-evaluation of the two final designs.

#### 3.2 Thermal Systems Optimization

The re-evaluation of the final designs was accomplished by means of additional TATE (Tank Arrangement Thermal Efficiency) program analyses, as described in Section 1.3.2. These analyses incorporated the revised thermal properties of Table 3.1-1. The BETA (Boeing Engineering Thermal Analyzer) program analyses, which preceded the TATE program analyses in the earlier evaluations of Section 1.3.2, was not repeated. The BETA analyses served only to supply temperatures

Table 3.1-1: REVISED THERMAL PROPERTIES

Multilayer Insulation Effective Normal Conductivity  $K_n$ :

$$K_n = \left[ 5.16 \times 10^{-14} (T_1^2 + T_2^2) + 3.07 \times 10^{-8} \right] (T_1 + T_2), \quad \frac{\text{BTU-ft}}{\text{ft}^2\text{-hr-}^\circ\text{R}}$$

$$\left[ 5.20 \times 10^{-13} (T_1^2 + T_2^2) + 9.56 \times 10^{-8} \right] (T_1 + T_2) \quad \text{W/m-}^\circ\text{K}$$

Longitudinal (Single-Step Lap) Joint Incremental Unit Conductance,  $\Delta K_{lj}$ :

$$\Delta K_{lj} = \left[ -1.2 \times 10^{-14} (T_1^2 + T_2^2) + 9.45 \times 10^{-9} \right] (T_1 + T_2), \quad \frac{\text{BTU}}{\text{hr-}^\circ\text{R}}$$

$$\left[ -1.14 \times 10^{-14} (T_1^2 + T_2^2) + 2.77 \times 10^{-9} \right] (T_1 + T_2) \quad \text{W/}^\circ\text{K}$$

(To obtain true conductance, multiply by total length of joint and divide by thickness of MLI)

Nylon Fastener Incremental Unit Conductance,  $\Delta K_f$ :

$$\Delta K_f = \left[ -.288 \times 10^{-14} (T_1^2 + T_2^2) + 3.42 \times 10^{-9} \right] (T_1 + T_2) \quad \frac{\text{BTU-ft}}{\text{hr-}^\circ\text{R}}$$

$$\left[ -.833 \times 10^{-15} (T_1^2 + T_2^2) + 3.05 \times 10^{-10} \right] (T_1 + T_2), \quad \text{W-m/}^\circ\text{K}$$

(To obtain true conductance, multiply by number of fasteners per unit area, multiply by total area, divide by thickness of MLI)

Fiberglass Strut Effective Conductivity,  $K_s$ :

$$K_s = .0262 + .112 \times 10^{-3} (T_1 + T_2) \quad \text{BTU-ft/ft}^2\text{-hr-}^\circ\text{R}$$

$$.0453 + .349 \times 10^{-3} (T_1 + T_2) \quad \text{W/m-}^\circ\text{K}$$

(Conductivity based on total cross section area of fiberglass tube and length of fiberglass tube)

Fluid Line Effective Conductivity,  $K_p$ :

$$K_p = .185 + .779 \times 10^{-3} (T_1 + T_2) \quad \text{BTU-ft/ft}^2\text{-hr-}^\circ\text{R}$$

$$.320 + 2.43 \times 10^{-3} (T_1 + T_2) \quad \text{W/m-}^\circ\text{K}$$

Conductivity based on total cross section area of line and total length of line

to be used as boundary conditions in the TATE analyses. Experience had shown that changes in thermal conductance properties did not significantly affect boundary temperatures, unless such changes were very large. Therefore, the temperatures from previous BETA analyses were assumed valid and were used in the revised TATE analyses.

The results of the design re-evaluations are shown in Table 3.2-1, which repeats the form of Table 1.3-1 describing the earlier evaluations. The revised thermal design properties employed in the design re-evaluations generally represent increased thermal conduction between tank exteriors and interiors.

In the case of Vehicle 1-14, the low fuel and oxidizer temperatures resulted in a tendency for a net heat flow from outside to inside the tanks throughout the mission. Under these circumstances the increase in conductivity led to design optimization with increased insulation thicknesses, which, as seen in Table 3.2-1, was the primary contributor to the weight increase.

In the case of Vehicle 2-18, the increased effective conductivity, together with higher oxidizer and fuel temperatures, resulted in net heat flow out of the tank during the coast phase of the mission. The critical design condition then became the end-of-ascent condition, for which the optimum design was obtained with decreased insulation thicknesses. The reduced total heat flow into the tank produced lower pressures at the end of the mission, resulting in reduced helium requirements. The re-evaluated Vehicle 2-18 thermal system components (Table 3.2-1) thus weighed less than the original as described in Table 1.3-1.

### 3.3 Recommendations

The experimental-analytical correlations of this program included a number of significant disparities, particularly in the heat flow category. The indications were that the prediction technique employed here would not yield satisfactory accuracy to support detailed design of an actual system. Potential sources of error and potential points of improvement could be identified in the assumptions and approximations used in the analytical predictions.

The determination of which potential design improvements would actually benefit prediction accuracy and which could continue to be ignored would have required more extensive instrumentation of the test article, permitting a greater degree of isolation of the effects under question.

Modular tests, as covered in the literature, appear to adequately verify the fundamentals of thermal performance prediction techniques. In application to complete tank systems, however, where interactions, fabrication and handling effects, design compromises, and other departures from the ideal exist, the prediction accuracy begins to break down. It is therefore recommended that further tests, with the objective of improving thermal performance predictions, be performed with full- or large-scale realistic tank systems, with extensive thermal instrumentation.

Table 3.2-1: FINAL DESIGN SYSTEM WEIGHTS - EXPERIMENTAL THERMAL PROPERTIES

VEHICLE	STRUCTURE	MATERIAL	SEPARATION P/L	INSULATION THICKNESS					TANK GAGE			SYSTEM WEIGHT *	INSULATION LOCATION
				Top in	Side Ox in	Side Fuel in	Bottom in	Inside in	Fuel Head in	Fuel Cylinder in	Oxi- dizer in		
1-14	Truss	Aluminum	14	1.38	.33	.60	.34	.65	.030	.025	.025	90.4	inside
2-18	Truss	Fiberglass	4	.52	.14		.01	-	.025	.025	.025	45.0	inside
				cm	cm	cm	cm	cm	cm	cm	cm	kg	
1-14	Truss	Aluminum	35.6	3.50	.84	1.68	.86	1.7	.076	.076	.064	41.0	inside
2-18	Truss	Fiberglass	10.2	1.32	.36		.025	-	.064	.064	.064	20.40	inside

\* System weight includes tanks, insulation, propellant vapor, helium, helium tank.

## 4.0 CONCLUSIONS

It was concluded that a combined structural/thermal/meteoroid protection system for the size vehicles considered in the study was impractical from a weight standpoint. Significant weight penalties were incurred through the use of continuous shell structures due to the low shell loading.

However, an efficient design was derived by combining the thermal and meteoroid protection system with a vehicle structure consisting of rings and truss framework. The MLI by itself was found to be the most weight-efficient meteoroid protection device evaluated.

When compared to a tank mounted thermal/meteoroid protection system, there was only a slight weight difference. Based on the mockup fabrication results, however, it is believed that the best thermal predictability would be derived from a tank mounted design. MLI blanket penetrations were numerous and difficult to insulate effectively in the shell mounted protection concept.

Various shell mounted protection designs were evaluated, all being about equal in terms of weight penalty. In several cases, concepts were chosen which differed by only 3 or 4 lbs (1.4 or 1.8 kg) from their nearest competitors. It is conceivable that an externally mounted protection system, although slightly heavier, might afford insulation fabrication simplicity at penetrations and thus yield a design with a confidence level comparable to the tank mounted configuration.

The most promising MLI for the intended application was a combination of aluminized mylar radiation shields alternated with net spacers. Edge evacuation rather than broadside pumping through perforated shields was preferred.

Advanced composite materials produced the most weight efficient structural concept for both truss and continuous shell structures.

In order to obtain ground hold capability a refrigeration system or cold gas purge of propellant tank compartments was necessary.

Correlation of thermal test results with predictions was inconclusive, possibly due to cumulative handling and modification effects. A full scale or near-full scale test representing an entire compartment would be required for an accurate appraisal of flight system thermal performance. Extensive instrumentation would also be a necessity.

## 5.0 ACKNOWLEDGEMENTS

The success of this program is in large measure attributable to the guidance afforded by the Project Manager, James R. Barber, and to D. L. Nored.

Appreciation is expressed to the Boeing participants whose efforts and experience contributed to the evaluation.

E. W. Brogren, H. C. Cheng, D. L. French and D. Halstead for thermal analysis and correlation of test results.

D. L. Barclay, D. D. Smith, W. P. Haese and K. W. Osborne for conceptual and detail design development.

J. H. Laakso, L. Rogers, E. Lopez and J. C. McGinnis for structural analysis and optimization studies.

J. E. Erickson, R. Watanabe and G. Miller for definition of the meteoroid environment, meteoroid impact experiments, and analysis of results.

D. E. Giesecking, R. Nelson, P. Smith, E. Nicholson, D. Oliver and F. Kent for mockup and manufacturing evaluations.

A. Kacoroski, B. Pepper and W. Hadley for thermal test operations, calibration and data reduction.

J. Hess for structural tests.

L. Guinn, D. Osmer and G. Woodhead for weights analysis.

K. W. Osborne and D. G. Good for preparation of detail design drawings and graphical illustrations.

## REFERENCES

- 1.1-1 Masters, A. I.; Brooke, A. W.; and Bailey, T. E.: "Space Storable Engine Characterization", Final Report, Contract NAS 3-12010, November 1969.
- 1.1-2 Becker, H. and Gerard, G.: "Elastic Stability of Orthotropic Shells", New York University, Journal of the Aerospace Sciences, Vol. 29, No. 5., May 1962.
- 1.1-3 Block, David L.; Card, Michael F.; and Mikulas, Martin M., Jr.: "Buckling of Eccentrically Stiffened Orthotropic Cylinders", NASA TND-2960, 1965.
- 1.1-4 Sullins, R. T.; Smith, G. W.; and Spier, E. E.: "Manual for Structural Stability Analysis of Sandwich Plates and Shells", General Dynamics Corp., NASA CR-1457, December 1969.
- 1.1-5 Timoshenko and Gere; "Theory of Elastic Stability".
- 1.1-6 McAdams, W. H.: "Heat Transmission", Third Edition, McGraw-Hill Book Company, Inc., New York, 1954.
- 1.1-7 Gueraco, R. A., et al.: "Thermophysical Properties of Selected Gases Below 300°K, Bureau of Mines Information Circular 8317, U.S. Dept. of the Interior, 1967.
- 1.1-8 Coston, R. M.: "Experimental Evaluations of the Equations and Parameters Governing Flow Through Multilayer Insulation During Evacuation", Cryogenic Engineering Conference, 1965.
- 1.1-9 Bruce, G. H.; Peaceman, D. W.; Rachford, H. H. Jr.; and Rice, J. D.: "Calculation of Unsteady-State Gas Flow Through Porous Media", Trans. American Inst. of Mining and Met. Engrs., Vol. 198, p. 79, 1953.
- 1.1-10 Bartlett, D. H.: "Evaluating Depressurization Rates of Gas Filled Multilayer Insulation", Structural Development Research Memo No. 20, The Boeing Company, April 1968.
- 1.1-11 McDonnell-Douglas Astronautics Company, "Ranking and Selection of Insulation Systems for MNV Application", Special Report No. 1, Contract NAS 8-21400.

- 1.1-12 Pogson, J. T. and MacGregor, R. K.: "Effective Conductance Along Parallel Radiation Shields", AIAA 5th Thermophysics Conference, June 1970.
- 1.1-13 Coston, R. M. and Vliet, G. G.: "Thermal Energy Transport Characteristics Along the Laminations of Multilayer Insulation", Thermophysics of Spacecraft and Planetary Bodies, Academic Press, New York, 1968, pp. 909-923.
- 1.1-14 A. D. Little report, "Advanced Studies on Multilayer Insulation Systems", NASA CR-54929, Contract NAS 3-6283, June 1966.
- 1.2-1 Ralph, E. L.: "Performance of Very Thin Silicone Solar Cells", 6th Photo Voltaic Conference, March 1967.
- 1.2-2 Bartlett, D. H. and McGinnis, J. C.: "Design and Development of Techniques for Fabrication of Cryogenic Tank Support Structures for Long Term Storage in Space Flight", Final Report, NASA CR-61309.
- 1.2-3 "The Bidirectional Reflectance of GT1015 Coating as Applied to the Apollo Command Module", GD/C Report GDC-DBE-66-023.
- 1.3-1 Arenz, R. J.: "Influence of Hypervelocity Projectile Size and Density on the Ballistic Limit of Dual-Sheet Structures", 69-376 AIAA Hypervelocity Impact Conference, 1969.
- 1.3-2 Nysmith, C. R.: "An Experimental Investigation of Aluminum Double-Sheet Structures", 69-375 AIAA Hypervelocity Impact Conference, 1969.
- 2.2-1 Bullard, B. R.: "Cryogenic Tank Support Evaluation", Lockheed Missiles and Space Company, Final Report on Contract NAS 3-7979, NASA CR-72546, 1969.
- 2.2-2 Swann, R. T. and Pittman, C. M.: "Analysis of Effective Thermal Conductivities of Honeycomb-Core and Corrugated-Core Sandwich Panels", National Aeronautics and Space Administration, Technical Note D-714, April 1961.

DISTRIBUTION LIST FOR FINAL REPORT

NAS3-13316      Boeing      CR 121103 Vol. I

<u>NO. OF COPIES</u>	<u>RECIPIENT</u>	<u>NO. OF COPIES</u>	<u>RECIPIENT</u>
	National Aeronautics & Space Administration Lewis Research Center 21000 Brookpark Road Cleveland, Ohio 44135	1	National Aeronautics & Space Administration Ames Research Center Moffett Field, California 94035 Attn: Library
1	Attn: Contracting Officer, MS 500-313	1	National Aeronautics & Space Administration Flight Research Center P.O. Box 273 Edwards, California 93523 Attn: Library
5	E. A. Bourke, MS 500-205		
1	Technical Report Control Office, MS 5-5		
1	Technology Utilization Office, MS 3-16		
2	AFSC Liaison Office, 501-3		
2	Library		
1	Office of Reliability & Quality Assurance MS 500-211	1	Director, Technology Utilization Division Office of Technology Utilization NASA Headquarters Washington, D.C. 20546
1	J. W. Gregory, Chief, MS 500-203		
3	J. R. Barber, Project Manager, MS 500-203		
1	D. Petrash, MS 500-204	1	Office of the Director of Defense Research & Engineering Washington, D. C. 20301 Attn: Office of Asst. Dir. (Chem Technology)
1	A. V. Zimmerman, MS 500-318		
1	N. T. Musial, MS 500-113		
1	Director, Physics & Astronomy Programs, SG Office of Space Science NASA, Headquarters Washington, D.C. 20546	1	Office of Aeronautics & Space Technology, R NASA Headquarters Washington, D. C. 20546
1	Director, Planetary Programs, SL Office of Space Science NASA Headquarters Washington, D. C. 20546	10	NASA Scientific and Technical Information Facility P. O. Box 33 College Park, Maryland 20740 Attn: NASA Representative
1	Director, Manned Space Technology Office, RS Office of Aeronautics & Space Technology NASA Headquarters Washington, D. C. 20546	1	National Aeronautics & Space Administration Goddard Space Flight Center Greenbelt, Maryland 20771 Attn: Library
2	Director Space Prop. and Power, RP Office of Aeronautics & Space Technology NASA Headquarters Washington, D. C. 20546	1	National Aeronautics & Space Administration John F. Kennedy Space Center Cocoa Beach, Florida 32931 Attn: Library
1	Director, Launch Vehicles & Propulsion, SV Office of Space Science NASA Headquarters Washington, D. C. 20546	1	National Aeronautics & Space Administration Langley Research Center Langley Station Hampton, Virginia 23365 Attn: Library
1	Director, Materials & Structures Div. RW Office of Aeronautics & Space Technology NASA Headquarters Washington, D.C. 20546		National Aeronautics & Space Administration Lyndon B. Johnson Space Center Houston, Texas 77001 Attn: Library
1	Director, Advanced Programs, MT Office of Manned Space Flight NASA Headquarters Washington, D. C. 20546	1	W. Chandler
		1	W. Dusenberry
		1	C. Yodzis

<u>NO. OF COPIES</u>	<u>RECIPIENT</u>
	National Aeronautics & Space Administration George C. Marshall Space Flight Center Huntsville, Alabama 35912
1	Attn: Library
1	J. M. Stuckey
1	I. G. Yates
1	E. H. Hyde
	Jet Propulsion Laboratory 4800 Oak Grove Drive Pasadena, California 91103
1	Attn: Library
1	L. Stimson
1	J. Kelly
1	R. Breshears
1	Defense Documentation Center Cameron Station Building 5 5010 Duke Street Alexandria, Virginia 22314 Attn: TISIA
1	RTD (RTNP) Bolling Air Force Base Washington, D. C. 20332
1	Arnold Engineering Development Center Air Force Systems Command Tullahoma, Tennessee 37389 Attn: Library
1	Advanced Research Projects Agency Washington, D. C. 20525 Attn: Library
	Aeronautical Systems Division Air Force Systems Command Wright-Patterson Air Force Base Dayton, Ohio 45433
1	Attn: Library
1	AFML (MAAE)
1	AFML (MAAM)
1	Air Force Rocket Propulsion Laboratory (RPM) Edwards, California 93523 Attn: Library
1	Air Force FTC (FTAT-2) Edwards Air Force Base, California 93523 Attn: Library
1	Air Force Office of Scientific Research Washington, D. C. 20333 Attn: Library

<u>NO. OF COPIES</u>	<u>RECIPIENT</u>
1	Space & Missile Systems Organization Air Force Unit Post Office Los Angeles, California 90045 Attn: Technical Data Center
1	Office of Research Analyses (OAR) Holloman Air Force Base, New Mexico 88330 Attn: Library
1	U.S. Air Force Washington, D.C. Attn: Library
1	Commanding Officer U.S. Army Research Office (Durham) Box CM, Duke Station Durham, North Carolina 27706 Attn: Library
1	Bureau of Naval Weapons Department of the Navy Washington, D.C. Attn: Library
1	Director (Code 6180) U.S. Naval Research Laboratory Washington, D.C. 20390 Attn: Library
1	Picatinny Arsenal Dover, New Jersey 07801 Attn: Library
1	Air Force Aero Propulsion Laboratory Research & Technology Division Air Force Systems Command United States Air Force Wright-Patterson AFB, Ohio 45433 Attn: APRP (Library)
1	Electronics Division Aerojet-General Corporation P.O. Box 296 Azusa, California 91703 Attn: Library
1	Space Division Aerojet-General Corporation 9200 East Flair Drive El Monte, California 91734 Attn: Library
1	Aerojet Ordnance and Manufacturing Aerojet-General Corporation 11711 South Woodruff Avenue Fullerton, California 90241 Attn: Library

<u>NO. OF COPIES</u>	<u>RECIPIENT</u>	<u>NO. OF COPIES</u>	<u>RECIPIENT</u>
1	Aerojet Liquid Rocket Company P. O. Box 15847 Sacramento, California 95813 Attn: Technical Library 2484-2015A	1	Chemical Propulsion Information Agency Applied Physics Laboratory 8621 Georgia Avenue Silver Spring, Maryland 20910
1	Aeronutronic Division of Philco Ford Corp. Ford Road Newport Beach, California 92663 Attn: Technical Information Department	1	Chrysler Corporation Missile Division P.O. Box 2628 Detroit, Michigan Attn: Library
1	Aerospace Corporation 2400 E. El Segundo Blvd. Los Angeles, California 90045 Attn: Library-Documents  Arthur D. Little, Inc. 20 Acorn Park Cambridge, Massachusetts 02140	1	Chrysler Corporation Space Division P.O. Box 29200 New Orleans, Louisiana 70129 Attn: Librarian
1	Attn: Library	1	Curtiss-Wright Corporation Wright Aeronautical Division Woodridge, New Jersey Attn: Library
1	R. B. Hinckley	1	University of Denver Denver Research Institute P.O. Box 10127 Denver, Colorado 80210 Attn: Security Office
1	Astropower Laboratory McDonnell-Douglas Aircraft Company 2121 Paularino Newport Beach, California 92163 Attn: Library	1	Fairchild Stratos Corporation Aircraft Missiles Division Hagerstown, Maryland Attn: Library
1	ARO, Incorporated Arnold Engineering Development Center Arnold AF Station, Tennessee 37389 Attn: Library	1	Research Center Fairchild Hiller Corporation Germantown, Maryland Attn: Library
1	Susquehanna Corporation Atlantic Research Division Shirley Highway & Edsall Road Alexandria, Virginia 22314 Attn: Library	1	Republic Aviation Fairchild Hiller Corporation Farmington, Long Island New York  General Dynamics/Convair P.O. Box 1128 San Diego, California 92112
1	Beech Aircraft Corporation Boulder Facility Box 631 Boulder, Colorado Attn: Library	1	Attn: Library
1	Bell Aerosystems, Inc. Box 1 Buffalo, New York 14240 Attn: Library	1	R. Tatro
1	Instruments & Life Support Division Bendix Corporation P.O. Box 4508 Davenport, Iowa 52808 Attn: Library	1	Missiles and Space Systems Center General Electric Company Valley Forge Space Technology Center P. O. Box 8555 Philadelphia, Pa. 19101 Attn: Library
1	Boeing Company 1625 K Street, N.W. Washington, D.C. 20006	1	General Electric Company Flight Propulsion Lab. Department Cincinnati, Ohio Attn: Library

<u>NO. OF COPIES</u>	<u>RECIPIENT</u>
1	Grumman Aircraft Engineering Corporation Bethpage, Long Island, New York 11714 Attn: Library
1	Honeywell Inc. Aerospace Division 2600 Ridgeway Road Minneapolis, Minnesota 55436 Attn: Library
1	IIT Research Institute Technology Center Chicago, Illinois 60616 Attn: Library
1	Ling-Temco-Vought Corporation P. O. Box 5907 Dallas, Texas 75222 Attn: Library
1	Linde-Div. of Union Carbide P. O. Box 44 Tonawanda, N. Y. 11450 Attn: G. Nies
1	Lockheed Missiles and Space Co. P.O. Box 504 Sunnyvale, Calif. 94088 Attn: Library
1	R. T. Parmley
1	Marquardt Corporation 16555 Saticoy Street Box 2013 - South Annex Van Nuys, California 91409  Denver Division Martin-Marietta Corporation P. O. Box 179 Denver, Colorado 80201 Attn: Library
1	G. C. Skartvedt
1	Western Division McDonnell Douglas Astronautics 5301 Bolsa Ave. Huntington Beach, California 92647 Attn: Library
1	P. Klevatt
1	McDonnell Douglas Aircraft Corporation P. O. Box 516 Lambert Field, Missouri 63166 Attn: Library
1	L. F. Kohrs
1	Rocketdyne Division North American Rockwell Inc. 6633 Canoga Avenue Canoga Park, California 91304 Attn: Library, Department 596-306

<u>NO. OF COPIES</u>	<u>RECIPIENT</u>
	Space & Information Systems Division North American Rockwell 12214 Lakewood Blvd. Downey, California
1	Attn: Library
1	E. Hawkinson AC10
1	Northrop Space Laboratories 3401 West Broadway Hawthorne, California 90250 Attn: Library
1	Purdue University Lafayette, Indiana 47907 Attn: Library (Technical)
1	Goodyear Aerospace Corporation 1210 Massillon Road Akron, Ohio 44306 Attn: C. Shriver
1	Hamilton Standard Corporation Windsor Locks, Connecticut 06096 Attn: Library
1	Stanford Research Institute 333 Ravenswood Avenue Menlo Park, California 94025 Attn: Library
1	TRW Systems Inc. 1 Space Park Redondo Beach, California 90278 Attn: Tech. Lib. Doc. Acquisitions
1	United Aircraft Corporation Pratt & Whitney Division Florida Research & Development Center P. O. Box 2691 West Palm Beach, Florida 33402 Attn: Library
1	United Aircraft Corporation United Technology Center P. O. Box 358 Sunnyvale, California 94038 Attn: Library
1	Vickers Incorporated Box 302 Troy, Michigan 48084
1	Airesearch Mfg. Div. Garrett Corp. 9851 Sepulveda Blvd. Los Angeles, California 90009 Attn: Library

<u>NO. OF COPIES</u>	<u>RECIPIENT</u>
1	Airesearch Mfg. Div. Garrett Corp. 402 South 36th Street Phoenix, Arizona 85034 Attn: Library
1	Commanding Officer U.S. Naval Underwater Ordnance Station Newport, Rhode Island 02844 Attn: Library
1	National Science Foundation, Engineering Div. 1800 G. Street NW Washington, D.C. 20540 Attn: Library
1	G. T. Schjeldahl Company Northfield, Minn. 55057 Attn: Library
1	General Dynamics P. O. Box 743 Fort Worth, Texas 76101
1	Cryonetics Corporation Northwest Industrial Park Burlington, Massachusetts 01803
1	Institute of Aerospace Studies University of Toronto Toronto 5, Ontario Attn: Library
1	FMC Corporation Chemical Research & Development Center P. O. Box 8 Princeton, New Jersey 08540
1	Westinghouse Research Laboratories Buelah Road, Churchill Boro Pittsburgh, Pa. 15235
1	Cornell University Department of Material Science & Engr. Ithaca, New York 14850 Attn: Library
1	Marco Research & Development Co. Whittaker Corporation 151 N. Ludlow Street Dayton, Ohio 45402
1	General Electric Company Apollo Support Dept. P.O. Box 2500 Daytona Beach, Florida 32015 Attn: C. Pay

<u>NO. OF COPIES</u>	<u>RECIPIENT</u>
1	E. I. DuPont, DeNemours and Company Eastern Laboratory Gibbstown, New Jersey 08027 Attn: Library
1	Esso Research & Engineering Company Special Projects Unit P.O. Box 8 Linden, New Jersey 07036 Attn: Library
1	Minnesota Mining & Manufacturing Company 900 Bush Avenue St. Paul, Minnesota 55106 Attn: Library